Stability Analysis of a Single Three Dimensional Rock Block:
Effect of Dilatancy and High-velocity Water Jet Impact

Committee:

Fulvio Tonon, Supervisor

Spyridon A Kinnas

Ellen M. Rathje

Anton Schleiss

Kenneth H. Stokoe II

John L. Tassoulas

Stability Analysis of a Single Three Dimensional Rock Block:

Effect of Dilatancy and High-velocity Water Jet Impact

by

Pooyan Asadollahi, B.S.; M.S.

Dissertation

Presented to the Faculty of the Graduate School of

The University of Texas at Austin

in Partial Fulfillment

of the Requirements

for the Degree of

Doctor of Philosophy

The University of Texas at Austin

August 2009

DEDICATION

With all the love in the world,

to my parents, *Maryam* and *Mohammad*,

for their endless love, encouragement, and support

ACKNOLWDGEMENTS

I would like to acknowledge my supervisor, Dr. Fulvio Tonon, for supporting and guiding me throughout my PhD study. He has been a great mentor over the past three years. I really appreciate all he has done for me from the very beginning hours of my landing in Austin. This endeavor would never been succeed without his guidance.

I would also want to express my appreciation to my committee members Dr. Spyridon Kinnas, Dr.Ellen Rathje, Dr.Anton Schleiss,Dr. Kenneth Stokoe, and Dr.John Tassoulas for their time and helpful comments.

I am indebted to Dr. Anton Schleiss and his student, Matteo Federspiel,from Ecole Polytechnique Federale de Laussanne (EPFL). Theygave me the opportunity to use some of their experimental results before being officially published.

I wish to express my gratitude toDr. Alan Cline, Dr. Bob Gilbert, Dr. Thomas Hughes, Dr. Spyridon Kinnas,Dr. Kenneth Stokoe,Dr.John Tassoulas,Dr. Fulvio Tonon, and Dr. Stephen Wright. I learned a lot from their lectures throughout my PhD study at UT-Austin.

Marco Invernizzi and Simone Addotto (former graduate students at Turin Polytechnic and visiting scholars at UT-Austin) contributed a lot to this research. They performed experimental study to validate the modifications proposed to Barton's model. Theyalso helped me in doing a part of analysespresented in Chapter 7 of this manuscript. Moreover, Siamack Khorgami, currently research student at University College London, gave helpful comments on the correlation analyses performed to address some of the weaknesses of Barton's model. In addition, Dr. Ghislaine Kozu, Senior Lecturer at UT-Austin, edited the first draft of Chapter 3 of this dissertation. Their contributions are deeply appreciated.

The last, but the most, my deepest gratitude goes to my father for his endless support. Without doubt, my successes, in all steps of my life, were not achieved without him.

Stability Analysis of a Single Three Dimensional Rock Block: Effect of Dilatancy and High-velocity Water Jet Impact

Pooyan Asadollahi, Ph.D.

The University of Texas at Austin, 2009

Supervisor:Fulvio Tonon

In simulation of closely- or separately-joined rock masses, stability of rock blocks is of primary concern. However, there seems to be no approach that can handle general modes of simultaneous slidingand truly large rotation under general forces, including non-conservative forces such as waterforces. General causes of failure for rock blocks, such as limit points, bifurcation points, anddynamic instability (divergence and flutter), have never been addressed. This research implementsa formulation, called BS3D(an incremental-iterative algorithm introduced by Tonon), for analyzing general failure modesof rock blocks under conservative and non-conservative forces.

Among the constitutive models for rock fractures developed over the years, Barton's empirical model has been widely used because it is easy to apply and includes several important factors associated with fracture characteristics. Although Barton's failure criterion predicts peak shear strength of rock fractures with acceptable precision, it has some weaknesses in estimating the peak shear displacement, post-peak shear strength, dilation, and surface degradation in unloading and reloading. In this dissertation, modifications are made to Barton's original model in order to address these

weaknesses.The modified Barton's model is validated by a series of direct shear tests on rock fractures and implemented in BS3D to consider the dilatant behavior of fractures.

The mechanical behavior of a rock block formed in the roof of a tunnel is governed by its geometry, the mechanical characteristics and the deformability of the fractures forming the block, the deformability of the block and that of the surrounding rock mass, and the stresses within the rock. BS3D, after verification and validation, is used to investigate the effect of dilatancy onstability of rock blocks formed in the roof of a circular tunnel.

High-velocity plunging jets, issuing from hydraulic artificial or natural structures, can result in scouring of the rock riverbed or the dam toe foundation. Assessment of the extent of scour is necessary to ensure the safety of the dam and to guarantee the stability of its abutments. BS3D is used to investigate effect of high-velocity jet impact on stability of rock blocks in plunge pools.

TABLE OF CONTENTS

xiii

LIST OF TABLES

xiv

LIST OF FIGURES

CHAPTER 1:   INTRODUCTION

1.1   PROBLEM STATEMENT AND MOTIVATION

Rock masses are composed of intact rock and fractures (Figure 1.1). This assemblage may fail in several ways [1]:

- The intact rock may yield, either violently or plastically.
- Blocks may move out of their original seat cut out by the fractures (block mould).
- Any combination of the above failure modes may occur.
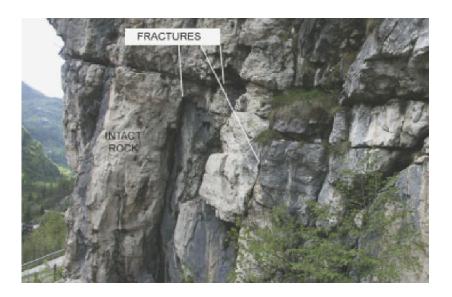
Figure 1.1: Rock fractures forming blocks of intact rock; Mount Pelsa, Triassic dolostone, Dolomites, Italy [1].

This dissertation focuses on the case in which the intact rock is strong enough that failure will only occur because rock blocks move out of their moulds. Single rock block is considered because, if no removable block is unstable, then the entire rock mass is stable [2] (a single block may be formed of several stable blocks [3]). In addition, In simulation of closely- or separately-joined rock masses in rock engineering problem, (for instance, slopes (Figure 1.1), dam foundations (Figure 1.2-a), and underground excavations (Figure 1.2-b)), stability of rock blocks is of primary concern [4, 5].

1

<div align="center">(a)   (b)</div>

Figure 1.2: (a) Karun-3 Dam; (b) Karun-3 Power Tunnel, Khozestan, Iran. Photo courtesy of Iran Water & Power Resource Development Co.

Although several researchers [2, 6-19] proposed different methods to analyze the stability of rock blocks, there seems to be no approach that can handle general modes of simultaneous sliding and truly large rotation under general forces, including non-conservative forces such as water forces. General causes of failure for rock blocks, such as limit points, bifurcation points, and dynamic instability (divergence and flutter), have never been addressed [1].

1.1.2 Stability of rock blocks formed in the roof of a tunnel

The mechanical behavior of a rock block formed in the roof of a tunnel (Figure 1.3) is governed by its geometry, the mechanical characteristics and the deformability of the fractures forming the block, the deformability of the block and that of the surrounding rock mass, and the stresses within the rock [20].

Approaches currently being used to analyze the stability of rock blocks formed in the roof of a tunnel can not handle general modes of simultaneous sliding and truly large rotation.

Among the constitutive models for rock fractures developed over the years, Barton's empirical model [21, 22] has been widely used because it is easy to apply and includes several important factors associated with fracture characteristics. Although

<div align="center">2</div>

Barton's failure criterion predicts peak shear strength of rock fractures with acceptable precision, it has some weaknesses in estimating the peak shear displacement, post-peak shear strength, dilation, and surface degradation upon unloading and reloading. Therefore, approaches used to analyze the stability of tunnel keyblocks suffers from these weaknesses as well.
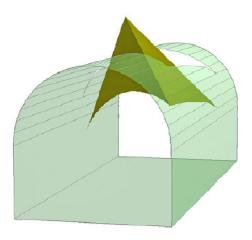
Figure 1.3: A tetrahedral block formed in the roof of a tunnel

1.1.3   Stability of rock blocks in plunge pools

Standard dam risk assessment includes consideration for spillway and spillway energy dissipator scour. For concrete and masonry dams, it also includes consideration for dam overtopping and scour of the foundations. High-velocity plunging jets, issuing from hydraulic artificial or natural structures, can result in scouring of the rock riverbed or the dam toe foundation. Figure 1.4 illustrates the schematic process of rock scour in plunge pools.

Assessment of the extent of scour is necessary to ensure the safety of the dam and to guarantee the stability of its abutments. However, currently, there is no formulation for evaluating scour caused by general failure modes of rock blocks having general shape and subject to general loading (e.g., gravity, reinforcement, dam loads) and to the plunge pool water pressures [23].

1 Jet issuance
2 Jet diffusion in the air (spreading and core contraction)
3 Jet diffusion in the water, macroturbulent pool flows
4 Hydrodynamic pressures at the water-rock interface
5 Pressure propagation inside fissures, crack propagation
6 Rock block ejection, ball-milling
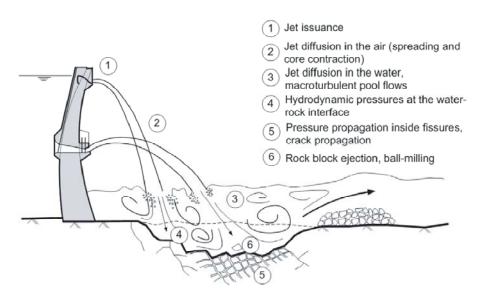
Figure 1.4: Schematic rock scour process in plunge pools [24].

1.2 OBJECTIVES AND SCOPE OF THIS STUDY

Tonon [1] presented an incremental-iterative algorithm for analyzing general failure modes of rock blocks subject to generic forces, including non-conservative forces such as water forces. The block interacts with the surrounding constraint space using a finite number of sensor points. Consistent stiffness matrices were developed that fully exploit the quadratic convergence of the adopted Newton–Raphson iterative scheme. The algorithm takes into account large block displacements and rotations, which together with non-conservative forces make the stiffness matrix non-symmetric.

The objectives of this research is to implement the formulation developed by Tonon [1] for the stability analysis of three dimensional single rock blocks subjected to generic forces including water pressure and high-velocity jet impact. The implemented code (called BS3D) considers the dilatant behavior of fractures using the modified Barton's model developed in this study.

The verified and validated code is used to investigate the following rock engineering problems:

1) Stability of rock blocks formed in the roof of a circular tunnel: effect of dilatancy.
2) Effect of high-velocity jet impact on stability of rock blocks in plunge pools.

4

1.3 ORGANIZATION

Chapter 2 summarizes the method proposed by Tonon [1] to analyze the stability of single rock blocks for general failure modes under conservative and non-conservative forces.

Chapter 3 presents a comprehensive literature review performed to address the limitation of Barton's empirical model for rock fractures [21, 22], known as the most practical model. A database of direct shear tests available in the literature is assembled and analyzed. Modifications are made to Barton's original model in order to address the weaknesses described above.

In Chapter 4, the modified Barton's model introduced in Chapter 3 is validated by a series of direct shear tests on rock fractures.

In Chapter 5, prototype BS3D computer code developed by Tonon [1] in Mathematica is re-written and translated into Fortran 95. Tonon's original code implements the algorithm just for tetrahedrons. However, the generalized version of BS3D developed in this dissertation can analyze general shapes of rock blocks. Furthermore, *in situ* stress and water pressure are implemented from scratch because they were not included in Tonon's code. In Tonon's original code, fracture dilatancy was included in a rudimental fashion by using a simplified version of Barton's model. However, the generalized version of BS3D can deal with both original [21, 22] and modified Barton's model (Chapter 3) as well as Mohr-Coulomb's failure criterion [25].

BS3D is validated in Chapter 6 for analysis of rock wedge stability by comparing the results of BS3D numerical analyses with 64 physical models and 2 case histories available from the literature [18, 26]. This investigation demonstrated the advantages of BS3D in predicting failure modes of a tetrahedron.

In Chapter 7, the effect of dilatancy on the stability of a rock block formed in the roof of a circular tunnel is investigated:

- An analytical approach is presented to analyze stability of a 2D triangular wedge formed in the roof of a circular tunnel. Two different definitions are introduced for the factor of safety of the block. The effects of stiffness and shear strength of

the fractures as well as *in situ* stress conditions on stability of the wedge are investigated.

- A simplified limit equilibrium method is explained to analyze stability of a tetrahedron in the roof of an excavation. The results of the analytical analyses are compared with those obtained from BS3D simulations. Using the analytical limiting equilibrium approach and BS3D, the effects of the normal stiffness of the fractures, dilatancy, the tunnel radius, and the block size on stability of the tetrahedron are investigated.

- A comprehensive sensivity analysis is performed on the effects of the shear strength, the normal stiffness, the *in situ* stress condition, the tunnel radius, and the block size on stability of a prism formed in the roof of a circular tunnel by four fractures that have the same dip angle.

Chapter 8 briefly explains limitations of available approaches to scour evaluation. In this Chapter, water pressures caused by impinging jets have been implemented in BS3D and the stability of single rock blocks in plunge pools is investigated:

- An approach is described to estimate pressure forces generated in plunge pools due to high-velocity jet impacts.

- Failure criterion is introduced for jointed rock masses.

- The scour model implemented in BS3D is calibrated and validated using the results of several experimental studies as well as case histories and prototypes available from the literature [27-31].

- Ability of BS3D in considering *in situ* stress and dilation behavior of rock fractures as well as dealing with dynamic divergence and flutter are demonstrated.

CHAPTER 2:   GENERAL SINGLE ROCK BLOCK STABILITY ANALYSIS METHOD (BS3D)

2.1 INTRODUCTION

Figure 2.1 shows different failure modes for a rock block subject to gravity. Making use of limiting equilibrium methods, John [6], Londe *et al*. [7], Hendron *et al*. [8], Hoek and Bray [9], Warburton [10], Priest [11], and Goodman and Shi [2] considered case (a) (wedge sliding) only. Pioneered by Wittke [12, 13], the study of rotational failure modes (b) and (c) in Figure 2.1 was also pursued using analytical methods by Chan and Einstein [14], Mauldon and Goodman [15] and Tonon [16]. These analytical methods cannot handle general simultaneous sliding and rotation; Yeung and co-workers [17-19] thus used a numerical method, such as the Discontinuous Deformation Analysis (DDA), to overcome the problem.

However, there seems to be no approach that can handle general modes of simultaneous sliding and truly large rotation under general forces, including non conservative forces, such as water forces. General causes of failure for rock blocks have never been addressed: limit points (when the active force cannot be incremented further), static bifurcation points (when more than one static solution exists), and dynamic instability (divergence, when the motion of the block is unbounded in time; and flutter, when the unforced motion of the block is oscillatory and unbounded).

The determination of the factor of safety is a challenge for currently available numerical methods, which typically resort to time-consuming trial and error calculations using the reduction of the strength parameters (e.g., [32]). After each complete analysis, they reduce the strength parameters and repeat the earlier analysis again until failure is reached. Whenever failure is not caused by limited strength (e.g., when the block fails in a pure rotational mode, or in a more complex roto-translational mode), the reduction of the strength parameters cannot yield the factor of safety, but, rather, it yields an incorrect failure mode (e.g., sliding rather than toppling).

| (a) translation | (b) rotation about an edge | (c) rotation about a corner |
| (d) torsional sliding | (e) slumping |
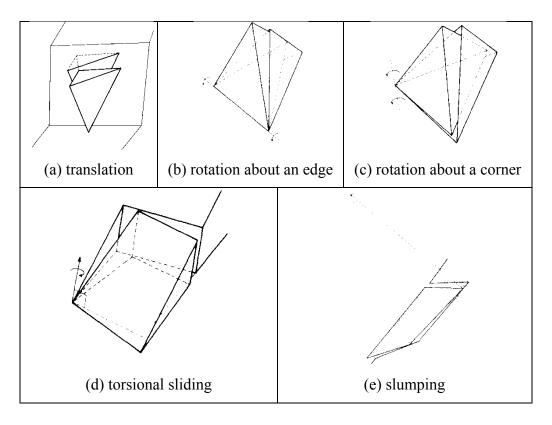
Figure 2.1: Failure modes of a rock block. After Reference [33].

On the other hand, in a typical limiting equilibrium analysis, one would need to know the normal forces exerted by each of the discontinuities, which are indeterminate when contact occurs on more than three non-parallel discontinuities, or on two or more parallel discontinuities. Also, one needs to know the point of application for the frictional forces. In a typical limit equilibrium analysis, this entails knowing the shear stress distribution at limiting equilibrium, which in its turn requires knowledge of the normal stress distribution. The latter is, however, unavailable even if one assumes a linear elastic behavior of the rock mass and discontinuity (to normal stresses) because the application point of the normal force on a contact face is not available unless there is just one contact face. In order to overcome the reaction force indeterminacy, one needs to introduce the deformability of the discontinuities and/or of the bodies (rock block and surrounding rock mass).

BS3D [1] implements an incremental-iterative algorithm for analyzing general failure modes of rock blocks subject to generic forces, including non conservative forces such as water forces. The incremental-iterative nature of the algorithm is only a consequence of the non-linearity of the boundary conditions (contact vs. no contact), and of the constitutive relationships (deformability and yielding); it is not a consequence of the factor of safety determination *per se*. Consistent stiffness matrices have been developed that fully exploit the quadratic convergence of the adopted Newton-Raphson iterative scheme. The algorithm takes into account large block displacements and rotations, which, together with non-conservative forces make the stiffness matrix non symmetric. Also included in the algorithm are *in situ* stress and fracture dilatancy, which introduces non-symmetric rank-one modifications to the stiffness matrix. Progressive failure is captured by the algorithm, which has proven capable of detecting numerically challenging failure modes, such as rotations about only one point.

BS3D determines the stability condition of a rock block by following its equilibrium path: if equilibrium is not possible, the mode of failure is detected. Failure modes may originate from a limit point or from dynamic instability (divergence or flutter); equilibrium paths emanating from bifurcation points are followed by the algorithm. The algorithm identifies both static and dynamic failure modes. The dynamic failure mode, i.e. the possible motion of the body over an infinitesimal interval of time, is calculated based on small rotation theory by imposing no further interpenetration at the constraints during the dynamic failure mode, and by assuming a rigid-perfectly plastic behavior of the discontinuities to shear displacements. The calculation of the factor of safety and associated failure mode(s) is obtained by BS3D with no overhead for any type of failure mode.

Indeed, a typical stability analysis is divided into stages, for example: application of self weight and in situ stresses (Stage 1) followed by excavation (Stage 2), application of water forces (Stage 3), etc.. Within each stage, the active force applied to the block is proportional to a stage control parameter. The factor of safety was shown to be equal to the value of the stage control parameter at failure [1], and only one (non-linear, and thus

incremental-iterative) analysis (with no trial-and-error) is carried out by BS3D to determine the factor of safety.

This chapter describes the basics of general single rock block stability analysis (BS3D). The whole chapter was taken from reference [1].

2.2 KINEMATICS

Let us fix a global Cartesian reference system (O, x, y, z) with unit vectors $\mathbf{e}_x,\ \mathbf{e}_y,\ \mathbf{e}_z$ attached to the rock mass and considered as fixed in time. Let a subscript (0) indicate the base configuration. The rock block is a rigid body that has six degrees of freedom, namely the displacement of the centroid, G, referred to the global reference system, $\mathbf{u}_G \equiv \left(u_{x,G}, u_{y,G}, u_{z,G} \right)^T$, and the pseudo-vector that defines the rotation about the centroid (again referred to the global reference system), $\boldsymbol{\theta} \equiv \left(\theta_x, \theta_y, \theta_z \right)^T = \theta\mathbf{r}$, where $0 \leq \theta < 2\pi$ is the rotation angle and $\mathbf{r}$ is a unit vector about which the rotation occurs [34]. The vector of degrees of freedom is thus $\mathbf{u} := \left(\mathbf{u}_G, \boldsymbol{\theta} \right)^T$. This choice of degrees of freedom allows for a 2π rotation of the rigid body, at difference with Rodrigues parameters [34] or other parameterization that have singularities in the $[0, 2\pi]$ range.

The pseudo-vector $\boldsymbol{\theta}$ allows one to calculate the rotation matrix, $\mathbf{R}_{3\times3}$, which maps a vector $\mathbf{v}$ attached to the rigid body from the base configuration to the current configuration as $\mathbf{v}_{(0)} \mapsto \mathbf{R}\cdot\mathbf{v}$:

$$\mathbf{R} = \mathbf{I} + \frac{\sin\theta}{\theta}\mathbf{S}(\boldsymbol{\theta}) + \frac{2\sin^2(\theta/2)}{\theta^2}\mathbf{S}(\boldsymbol{\theta})\cdot\mathbf{S}(\boldsymbol{\theta}), \tag{2.1}$$

where $\mathbf{S}(.)$ is the spin operator, i.e.:

$$\mathbf{S}(\boldsymbol{\theta}) = \begin{pmatrix} 0 & -\theta_z & \theta_y \\ \theta_z & 0 & -\theta_x \\ -\theta_y & \theta_x & 0 \end{pmatrix} \tag{2.2}$$

Notice that $\lim_{\theta \to 0}\mathbf{R} = \mathbf{I}$, and that, from a numerical standpoint the sine-squared form should be preferred to $1\text{-}\cos\theta$ in order avoid the cancellation in computing $1\text{-}\cos\theta$

for small θ. The spin operator allows one to express the vector product between any two 3-vectors **a** and **b** as:

$$\mathbf{a} \times \mathbf{b} = \mathbf{S}(\mathbf{a}) \cdot \mathbf{b} = -\mathbf{b} \times \mathbf{a} = -\mathbf{S}(\mathbf{b}) \cdot \mathbf{a} \tag{2.3}$$

and, for any 3x3 matrix **c**, has the property

$$\mathbf{S}(\mathbf{a}) \cdot \mathbf{c} = \mathbf{c} \cdot \mathbf{S}(\mathbf{a}) \tag{2.4}$$

The displacement of any point of the block, P, can then be calculated as:

$$\mathbf{u}_P = \mathbf{u}_G + (\mathbf{R} \text{-} \mathbf{I}) \cdot \mathbf{G}_{(0)} \mathbf{P}_{(0)} \tag{2.5}$$

In the following, the derivative of $\mathbf{u}_P$ with respect to the six degrees of freedom will be needed. In order to accomplish this, let us first take the derivative of the rotation matrix with respect to $\boldsymbol{\theta}$. The columns of **R** are an orthonormal base $\mathbf{j}_i$ fixed to the rigid body and initially coincident with the global basis. Therefore, by using Poinsot formulas: $d\mathbf{j}_i / dt = \boldsymbol{\omega} \times \mathbf{j}_i$, one obtains:

$$\dot{\mathbf{R}} = \mathbf{S}(\boldsymbol{\omega}) \mathbf{R} \tag{2.6}$$

The angular velocity, $\boldsymbol{\omega}$, is related to $\dot{\boldsymbol{\theta}}$ as [35]:

$$\boldsymbol{\omega} = \mathbf{J}(\boldsymbol{\theta}) \cdot \dot{\boldsymbol{\theta}}, \tag{2.7}$$

where:

$$\mathbf{J}(\boldsymbol{\theta}) = \frac{1}{\theta^2} \left(\boldsymbol{\theta} \cdot \boldsymbol{\theta}^T + 2\sin^2(\theta/2) \mathbf{S}(\boldsymbol{\theta}) \right) + \frac{\sin\theta}{\theta} \left(\mathbf{I} - \frac{1}{\theta^2} \boldsymbol{\theta} \cdot \boldsymbol{\theta}^T \right) \tag{2.8}$$

After plugging Equation (2.7) into Equation (2.6), and Equation (2.6) into Equation (2.5), one can differentiate the displacement $\mathbf{u}_P$ making use of Equation (2.3) and taking into account that vector $(\mathbf{GP})_{(0)}$ does not change in time because it belongs to the base configuration:

$$\dot{\mathbf{u}}_P = \dot{\mathbf{u}}_G + \dot{\mathbf{R}} \cdot (\mathbf{GP})_{(0)} = \dot{\mathbf{u}}_G + \mathbf{S}(\mathbf{J}(\boldsymbol{\theta}) \cdot \dot{\boldsymbol{\theta}}) \mathbf{R} \cdot (\mathbf{GP})_{(0)} = \dot{\mathbf{u}}_G - \mathbf{S}(\mathbf{R} \cdot (\mathbf{GP})_{(0)}) \mathbf{J}(\boldsymbol{\theta}) \cdot \dot{\boldsymbol{\theta}} = \mathbf{D}_P(\boldsymbol{\theta}) \cdot \dot{\mathbf{u}}$$

$$\tag{2.9}$$

where:

$$\mathbf{D}_P(\boldsymbol{\theta}) := \left(\mathbf{I}_{3 \times 3}, -\mathbf{S}(\mathbf{R} \cdot (\mathbf{GP})_{(0)}) \mathbf{J}(\boldsymbol{\theta}) \right) \tag{2.10}$$

11

$$\dot{\mathbf{u}} := [\dot{\mathbf{u}}_G \quad \dot{\boldsymbol{\theta}}]^T \tag{2.11}$$

Likewise, let $\mathbf{v}$ be any vector attached to the moving frame (e.g., **GP**). Since $\mathbf{v}(\mathbf{u}) = \mathbf{R} \cdot \mathbf{v}_{(0)}$:

$$\dot{\mathbf{v}}(\mathbf{u}) = \dot{\mathbf{R}} \cdot \mathbf{v}_{(0)} = -\mathbf{S}\left(\mathbf{R} \cdot \mathbf{v}_{(0)}\right)\mathbf{J}(\boldsymbol{\theta}) \cdot \dot{\boldsymbol{\theta}} = \mathbf{H}_P\left(\boldsymbol{\theta}, \mathbf{v}_{(0)}\right) \cdot \dot{\mathbf{u}} \tag{2.12}$$

where:

$$\mathbf{H}_P\left(\boldsymbol{\theta}, \mathbf{v}_{(0)}\right) := \left(\mathbf{0}_{3\times 3}, -\mathbf{S}\left(\mathbf{R} \cdot \mathbf{v}_{(0)}\right)\mathbf{J}(\boldsymbol{\theta})\right) \tag{2.13}$$

Notice that: both $\mathbf{D}_P$ and $\mathbf{H}_P$ are skew-symmetric; $\mathbf{J}(\boldsymbol{\theta})$ is neither symmetric nor skew-symmetric; the large rotation contribution is quantified by $\mathbf{J}(\boldsymbol{\theta})$; and that $\lim_{\theta \to 0} \mathbf{J}(\boldsymbol{\theta}) = \mathbf{I}$, for which one retrieves small-rotation formulations.

Now, let $\boldsymbol{\theta}$ be the compound rotation vector corresponding to a first rotation by pseudo-vector $\boldsymbol{\theta}_1$ followed by a second rotation by pseudo-vector $\boldsymbol{\theta}_2$. $\boldsymbol{\theta}$ is calculated making use of quaternion as follows [36, 37]. The quaternion $\mathbf{q}_i$ associated to $\boldsymbol{\theta}_i$ is the paring $(q_{i,0}, \mathbf{q})$, where $q_{i,0}$ is a scalar and $\mathbf{q}$ is a vector defined as, respectively:

$$q_{i,0} = \cos(\theta/2) \quad ; \quad \mathbf{q}_i = \frac{\sin(\theta/2)}{\theta}\boldsymbol{\theta} \tag{2.14}$$

The quaternion, $\mathbf{q}$, associated to $\boldsymbol{\theta}$ is found using the quaternion product of $\mathbf{q}_2$ and $\mathbf{q}_1$:

$$\mathbf{q} := (q_0, \mathbf{q}) = \mathbf{q}_2; \mathbf{q}_1 := \left(q_{i,2} q_{i,1} - \mathbf{q}_2 \cdot \mathbf{q}_1, \, q_{2,0}\mathbf{q}_1 + q_{1,0}\mathbf{q}_2 + \mathbf{q}_2 \times \mathbf{q}_1\right) \tag{2.15}$$

$\boldsymbol{\theta}$ is then calculated by inverting Equation (2.14), and its rotation matrix can be calculated either using Equation (2.1) or (and this reduces numerical inaccuracies) using $\mathbf{q}$ directly:

$$\mathbf{R} = \left(2q_0^2 - 1\right)\mathbf{I} + 2q_0\mathbf{S}(\mathbf{q}) + 2\mathbf{q}\mathbf{q}^T \tag{2.16}$$

The described algorithm is singularity-free and allows one to update a rotation pseudo-vector without multiplying rotation matrices and subsequently extracting the relevant rotation pseudo-vector: this last algorithm is unstable around and singular for $\theta = \pm\pi$. Numerical inaccuracies introduced in matrix multiplication may also lead to non orthonormal matrices after several updates, whereas Equations (2.1) and (2.16) always yield an orthonormal matrix.

2.3　THE REACTION FORCES ARE INDETERMINATE

Let us introduce the following notation: m = mass of the block; $\mathbf{E}_G$ = inertia operator relative to point G [16, 38-41]; $\dot{\boldsymbol{\omega}} = d\boldsymbol{\omega}/dt$ = angular acceleration; $\mathbf{f} = \mathbf{f}_c + \mathbf{f}_a$ = resultant of the external forces (constraint $\mathbf{f}_c$, and active $\mathbf{f}_a$); $\mathbf{m}_G = \mathbf{m}_{G,c} + \mathbf{m}_{G,a}$ = resultant moment of the external forces (constraint $\mathbf{m}_{G,c}$, and active $\mathbf{m}_{G,a}$) with respect to pole G.

The dynamics of the block is controlled by the following system of vector differential equations (e.g., [38, 39]):

$$\begin{cases} m\ddot{\mathbf{u}}_G & = \mathbf{f}_a + \mathbf{f}_c \\ \mathbf{E}_G \cdot \dot{\boldsymbol{\omega}} + \boldsymbol{\omega} \times \mathbf{E}_G \cdot \boldsymbol{\omega} & = \mathbf{m}_a + \mathbf{m}_c \end{cases} = \mathbf{F}_a + \mathbf{F}_c \ , \tag{2.17}$$

where $\mathbf{F}_a = (\mathbf{f}_a, \mathbf{m}_{G,a})^T$ and $\mathbf{F}_c = (\mathbf{f}_c, \mathbf{m}_{G,c})^T$.

The first three scalar equations control the motion of the centroid, while the last three (Euler's) scalar equations control the motion of the body relative to the centroid, considered as a fixed point about which the body rotates. In order to simplify the derivations, in this section small rotations will be used, so that $\mathbf{J}(\boldsymbol{\theta}) \to \mathbf{I}$ in Equation (2.8), $\boldsymbol{\omega} = \dot{\boldsymbol{\theta}}$ in Equation (2.7), and $\dot{\boldsymbol{\omega}} = \ddot{\boldsymbol{\theta}}$. An upper bar will indicate small displacements.

Since only the incipient motion is of interest in this section, let us rewrite Equation (2.17) for t=0, and take into account the initial conditions: $\boldsymbol{\omega}(0) = 0$ (zero initial angular velocity) and $\dot{\mathbf{u}}_G(0) = \mathbf{0}$, so that the displacement of P in the time interval dt is [16]:

$$\bar{\mathbf{u}}_P = \left(\ddot{\mathbf{u}}_G + \dot{\boldsymbol{\omega}} \times \mathbf{GP}\right) dt^2 / 2 \tag{2.18}$$

One obtains the following linear system in the unknown $\ddot{\mathbf{u}} = \left(\ddot{\mathbf{u}}_G, \dot{\boldsymbol{\omega}}\right)^T$ (for simplicity, in the following the index "(0)" will be suppressed):

$$\mathbf{M}\ddot{\mathbf{u}} = \mathbf{F} \ , \tag{2.19}$$

where $\mathbf{M} = \begin{bmatrix} m\mathbf{I}_{3\times3} & \mathbf{0} \\ \mathbf{0} & \mathbf{E}_G \end{bmatrix}$, $\mathbf{F} = \begin{pmatrix} \mathbf{f} \\ \mathbf{m}_G \end{pmatrix}$.

13

Equation (2.19) is supplemented with the constraint equations that prevent the block penetration into the rock mass. Let us assume that we know the contact points, P_i, that remain in contact with a discontinuity. We need to impose that these points move parallel to the discontinuities that bound the block. If P_i remains in contact with the j-th discontinuity, these constraints can be written in the form $\bar{\mathbf{u}}_{P_i} \cdot \mathbf{n}_{c,j} = 0$ or

$$\left(\ddot{\bar{\mathbf{u}}}_G + \dot{\boldsymbol{\omega}} \times \mathbf{GP}_i \right) \cdot \mathbf{n}_{c,j} = 0 , \tag{2.20}$$

where $\mathbf{n}_{c,j}$ is the block side unit normal to the j-th discontinuity. Since these constraints are linear in $\ddot{\bar{\mathbf{u}}}$, they can be written as $\mathbf{A}\ddot{\bar{\mathbf{u}}} = \mathbf{0}$, where matrix $\mathbf{A}$ has as many rows as there are constraints of the type shown in Equation (2.20):

$$\mathbf{A} = \begin{bmatrix} n_{x,c,j} & n_{y,c,j} & n_{z,c,j} & \left(y_{P_i}-y_G\right)n_{z,c,j}-\left(z_{P_i}-z_G\right)n_{y,c,j} & \left(z_{P_i}-z_G\right)n_{x,c,j}-\left(x_{P_i}-x_G\right)n_{z,c,j} & \left(x_{P_i}-x_G\right)n_{y,c,j}-\left(y_{P_i}-y_G\right)n_{x,c,j} \\ . & . & . & . & . & . \end{bmatrix}$$

$$\tag{2.21}$$

A virtual displacement is any non-zero vector, $\boldsymbol{\xi}_{6\times1}$, that lies in the null space of $\mathbf{A}$, i.e. it satisfies $\mathbf{A} \cdot \boldsymbol{\xi} = \mathbf{0}$ [42]. Let the work done under virtual displacements, W^c, by the constraint forces $\mathbf{F}_c$ be formalized through a vector $\mathbf{C}$, so that [41-51]:

$$\boldsymbol{\xi}^T \mathbf{F}_c := W^c = \boldsymbol{\xi}^T \mathbf{C} \tag{2.22}$$

The General Principle of Mechanics [42-51] generalizes Gauss Principle of Least Constraint [42, 52, 53] to mechanical systems with non-ideal constraints. These constraints (such as all frictional constraints) do work for virtual displacements, so that $\mathbf{C} \neq \mathbf{0}$. The General Principle of Mechanics states that: the system evolves in time in such a manner that its acceleration minimizes the quadratic form [50]:

$$\left(\mathbf{M}\ddot{\bar{\mathbf{u}}} - (\mathbf{F}_a + \mathbf{C})\right)^T \mathbf{M}^{-1} \left(\mathbf{M}\ddot{\bar{\mathbf{u}}} - (\mathbf{F}_a + \mathbf{C})\right) \qquad \text{(subject to the constraint } \mathbf{A}\ddot{\bar{\mathbf{u}}} = \mathbf{0}\text{)}$$

Using the General Principle of Mechanics, the acceleration and the resultant forces in the system can be obtained in closed-form [50]:

$$\begin{aligned} \ddot{\bar{\mathbf{u}}} &= \mathbf{a} - \mathbf{M}^{-1/2}\mathbf{B}^+\mathbf{A}\mathbf{a} + \mathbf{M}^{-1/2}(\mathbf{I} - \mathbf{B}^+\mathbf{B})\mathbf{M}^{-1/2}\mathbf{C} \\ \mathbf{M}\ddot{\bar{\mathbf{u}}} &= \mathbf{F}_a - \mathbf{M}^{1/2}\mathbf{B}^+\mathbf{A}\mathbf{a} + \mathbf{M}^{1/2}(\mathbf{I} - \mathbf{B}^+\mathbf{B})\mathbf{M}^{-1/2}\mathbf{C} \end{aligned} , \tag{2.23}$$

14

where a superscript "+" indicates the Moore-Penrose generalized inverse of a matrix [54], $\mathbf{a} = \mathbf{M}^{-1}\mathbf{F}_a$, and $\mathbf{B} = \mathbf{A}\mathbf{M}^{-1/2}$.

In Equation (2.23), the constraint resultant generalized force, $\mathbf{F}_c = \left(\mathbf{f}_c, \mathbf{m}_c \right)^T$ is split into two components: the component caused by the ideal constraints $\mathbf{F}_{c,id} = -\mathbf{M}^{1/2}\mathbf{B}^+\mathbf{A}\mathbf{a}$, and the component caused by the presence of non-ideal constraints $\mathbf{F}_{c,nid} = \mathbf{M}^{1/2}(\mathbf{I} - \mathbf{B}^+\mathbf{B})\mathbf{M}^{-1/2}\mathbf{C}$. Several important consequences can be drawn:

(1) $\mathbf{F}_c$ depends on the mass matrix $\mathbf{M}$ unless $\mathbf{M}$ is of the form $m\mathbf{I}_{6\times 6}$. This is equivalent to requiring that x, y, and z are three principal axes of inertia with moment of inertia equal to m. This is quite a rare event; for example, it may occur if the block is a sphere with radius equal to $\sqrt{5/2}$ or if it is a cube with edge equal to $2\sqrt{3}$.

(2) The work done by a frictional constraint is not zero if there is slippage along that discontinuity. In a typical limit equilibrium analysis, one would need to know the normal force exerted by that discontinuity in order to be able to determine matrix $\mathbf{C}$ in Equation (2.22). Unfortunately, $\mathbf{F}_{c,id}$ is only the resultant (force and moment) of the normal forces exerted by all the discontinuities. Thus, one cannot calculate the normal force on each discontinuity when contact occurs on more than three non parallel discontinuities, or on two or more parallel discontinuities. When three or less non parallel discontinuities are in contact, the normal force on one of those discontinuities is simply found as the projection of the resultant force, $\mathbf{f}_{c,id}$, onto that discontinuity's normal.

(3) Consider the case in which the virtual displacement has non-zero rotational component(s): $\boldsymbol{\xi} = (\boldsymbol{\xi}_G, \boldsymbol{\psi})^T$. The virtual work is equal to $\boldsymbol{\xi}_G \mathbf{f}^T + \boldsymbol{\psi}\mathbf{m}_G^T$. In order to compute the virtual work done by the frictional forces on a given block face, one needs to know $\mathbf{m}_{G,c}$, and thus one needs to know the point of application for the frictional forces. In a typical limit equilibrium analysis, this entails knowing the shear stress distribution at limiting equilibrium, which in its turn requires knowledge of the normal stress distribution. The latter is however unavailable even if one assumes a

15

linear elastic behavior of the rock mass and discontinuity (to normal stresses) because the application point of the normal force on a contact face is not available unless there is just one contact face. Indeed, if there is just one contact face, let P be the application point of the normal force $\mathbf{N}$. The equation $\mathbf{OP} \times \mathbf{N} = \mathbf{m}_{c,id}$ in the three coordinates of P has rank 2, and, together with the plane equation for the contact face, it yields the three coordinates of P.

In order to overcome the reaction force indeterminacy, one needs to introduce the deformability of the discontinuities and/or of the bodies (rock block and surrounding rock mass). For example, 3DEC [55, 56] uses normal and tangential springs at the intersection point between a discontinuity face and a block's vertex. BSM3D [57-59] and 3D-DDA [17, 18, 60-62]   use similar springs located at the vertices of the contact area. In general, these contact points change from one iteration to the next. The thrust of these models is, however, toward analyzing systems composed of many blocks: if only one block is considered, the introduced approximations are too coarse to yield accurate results because:

- If discontinuities display a non-linear behavior, the discontinuity path dependency cannot be modeled when the contact points change at each iteration. To get around this, 3DEC can analyze internally discretized blocks, but this increases considerably the computational effort.

- Only an approximate moment of inertia, α, is calculated in 3DEC based upon the average distance from the centroid to the vertices of the block [56], so that $\mathbf{E}_G = \alpha \mathbf{I}_{3 \times 3}$, and $\mathbf{M}$ becomes close to $m\mathbf{I}_{6 \times 6}$ (see observation 1 above). These approximations may lead to large errors in detecting a block's dynamic failure mode because the angular velocity of the unconstrained motion becomes parallel to the applied resultant moment (Equation (2.19)), and the incipient motion of a block and the resultant constraint force are not accurate (Equation (2.23)).

16

- In 3DEC, the constraint force on a given face (in contact with another face) is placed mid-way between the centroids of the two contacting blocks [56]; if blocks undergo rotation, the position of the centroid is moved based on an empirical factor (for which there is no experimental evidence) [56], and brought back to a point (which has no physical meaning) on the contacting faces if it ends up outside the contacting faces themselves [56]. This whole construction is purely geometrical, and is not based on the actual stress distribution at the contacting faces.

3D-DDA [17, 18, 60, 61] as well as the Manifold Method [63] are based on the assumption that there exists a potential for all forces (active and constraint) acting on the block system. As a consequence, all forces must be conservative and no dissipative forces (e.g., friction) or path-dependent behavior can be modeled. Moreover, since forces are conservative, they must be positional, and therefore non-positional forces (*e.g*., follower loads such as water pressure) cannot be modeled.

2.4 PROPOSED APPROACH

Since the general problem is statically indeterminate, the rock block, B, is thought of as interacting with the rock mass (constraint space) at a finite number of points lying on its boundary, ∂B. These points are termed "sensor points" because they represent the points at which the rock block "feels" the constraint space as in haptic technology (Sections 2.2.5 and 2.2.6). These points can also be seen as a generalization of the "artificial supports" introduced by Chan and Einstein [14], who noticed that the use of artificial supports is appealing because of "its analogy with reality, where surfaces are in contact at a number of points".

Each sensor point is provided with a non-linear normal spring that simulates the deformability of the rock mass, of the discontinuity and of the rock block. At each sensor point, a non-linear tangential spring equipped with a tangential slider simulates the

tangential deformability and the limited shear strength of the discontinuity, respectively. Stiffness and resistance will be dealt with in Section 2.8.

The aim is to determine the stability condition of a rock block: if equilibrium is not possible, the mode of failure will be detected. In static conditions, the left-hand side of Equation (2.17) is equal to zero, and the equilibrium path of the rock block is thus followed using a predictor-corrector (or incremental-iterative) scheme that imposes the vanishing of the residual (right-hand side of Equation (2.17)): $\mathbf{r} := \mathbf{F} = \mathbf{F}_a + \mathbf{F}_c$ (Section 2.5). Large displacements and rotations are accommodated as per Section 2.2.

2.5 THE PREDICTOR-CORRECTOR STRATEGY

The entire calculation is first divided into stages. For example: application of self weight and *in situ* stresses (stage 1) followed by excavation (stage 2), water forces (stage 3), etc. Within each stage, $\mathbf{F}_a$ is assumed to be proportional to one stage control parameter, λ, so that the residual equation that defines the equilibrium path is:

$$\mathbf{r}(\mathbf{u}, \lambda) = \mathbf{F}_c(\mathbf{u}) + \lambda \mathbf{F}_a(\mathbf{u}) = \mathbf{0} \qquad (2.24)$$

Its incremental form is:

$$\frac{\partial \mathbf{r}}{\partial \mathbf{u}} \dot{\mathbf{u}} + \frac{\partial \mathbf{r}}{\partial \lambda} \dot{\lambda} = \mathbf{0} \Rightarrow \mathbf{K}\dot{\mathbf{u}} = \mathbf{F}_a \dot{\lambda} \,, \qquad (2.25)$$

where the stiffness matrix is

$$\mathbf{K} := -\frac{\partial \mathbf{r}}{\partial \mathbf{u}} \qquad (2.26)$$

Equation (2.25) must be solved with the initial conditions: $\mathbf{u}_0 = \mathbf{u}_{\text{previous stage}}$ and $\lambda_0 = 0$. The additional equation that makes it possible to solve Equation (2.25) is the increment control strategy. Let $(\bullet)^{(l)}_{(n)}$ be the value of a variable $(\bullet)$ at the l-th iteration ($l = 0$ refers to the predictor step) during the n-th increment. Let δ indicate iterative change and Δ denote increment change. Let $\mathbf{v}^{(0)}_{(n)} = \mathbf{K}^{(0)-1}_{(n)}\mathbf{F}^{(0)}_{a(n)}$ be the predictor velocity, and define the stiffness ratio, *sr*, as:

18

$$sr_{(n)} = \frac{\Delta\lambda_{(n)}^{(0)}\mathbf{v}_{(n)}^{(0)T}\mathbf{F}_{a(n)}^{(0)}}{\mathbf{v}_{(n)}^{(0)T}\mathbf{v}_{(n)}^{(0)}} \tag{2.27}$$

The stiffness ratio is a measure of the system's stiffness as related to the tangential predictor. If $sr_{(n)}/sr_{(0)} > 0.3$, then the system has lost less than 70% of its stiffness at the first iteration, and load control strategy can be safely applied:

$$c\left(\Delta\mathbf{u}_{(n)}^{(l)}, \Delta\lambda_{(n)}^{(l)}\right) = \Delta\lambda_{(n)}^{(l)} - step_0 = 0 \tag{2.28}$$

A value $step_0 = 0.1$ has been successfully used in the implementation.

Otherwise, the system has lost more than 70% of its stiffness at the first iteration; the adopted control strategy is then the arc-length control [64, 65] because it allows the static solution to safely reach possible critical points. Let $(\mathbf{v}, 1)^{\mathrm{T}}/f$ be the tangent vector to the equilibrium path normalized to unit length. The arc-length control with fixed-step strategy is:

$$c\left(\Delta\mathbf{u}_{(n)}^{(l)}, \Delta\lambda_{(n)}^{(l)}\right) = \frac{1}{f_{(n)}^{(l)}}\left|\mathbf{v}_{(n)}^{(0)T}\Delta\mathbf{u}_{(n)}^{(l)} + \Delta\lambda_{(n)}^{(l)}\right| - step_0 = 0 \tag{2.29}$$

The arc-length controlled forward-Euler predictor is then [66]:

$$\Delta\mathbf{u}_{(n)}^{(0)} = \mathbf{v}_{(n)}^{(0)}\Delta\lambda_{(n)}^{(0)}, \tag{2.30}$$

where: $\mathbf{v}_{(n)}^{(0)} = \mathbf{K}_{(n)}^{(0)-1}\mathbf{F}_{a(n)}^{(0)}$, $\Delta\lambda_{(n)}^{(0)} = step_0 / \sqrt{1 + \mathbf{F}_{a(n)}^{(0)T}\mathbf{v}_{(n)}^{(0)}}$, and $step_0$ is calculated at the first arc-length increment as $step_0 = 1/\left(20\sqrt{1+\mathbf{F}_{a(0)}^{(0)T}\mathbf{v}_{(0)}^{(0)}}\right)$. Since units of displacements and of angles are intermixed in $\mathbf{u}$, stiffness scaling (energy constraint) has been introduced in the increment control via: $\mathbf{F}_{a(n)}^{(0)T}\mathbf{v}_{(n)}^{(0)} = \mathbf{v}_{(n)}^{(0)T}\mathbf{K}_{(n)}^{(0)}\mathbf{v}_{(n)}^{(0)}$.

Since the contact status of a sensor point may change at each iteration, the corrector phase is a full Newton method, which is based on the truncated Taylor expansion of the system of Equations (2.24) and (2.29):

$$\begin{cases} \mathbf{r}_{(n)}^{(l+1)} = \mathbf{r}_{(n)}^{(l)} + \left.\frac{\partial\mathbf{r}}{\partial\mathbf{u}}\right|_{(n)}^{(l)}\delta\mathbf{u}_{(n)}^{(l+1)} + \left.\frac{\partial\mathbf{r}}{\partial\lambda}\right|_{(n)}^{(l)}\delta\lambda_{(n)}^{(l+1)} = \mathbf{0} \\[3mm] c_{(n)}^{(l+1)} = c_{(n)}^{(l)} + \left.\frac{\partial c}{\partial\mathbf{u}}\right|_{(n)}^{(l)}\delta\mathbf{u}_{(n)}^{(l+1)} + \left.\frac{\partial c}{\partial\lambda}\right|_{(n)}^{(l)}\delta\lambda_{(n)}^{(l+1)} = 0 \end{cases}, \tag{2.31}$$

i.e.:
$$\begin{pmatrix} \mathbf{K}_{(n)}^{(l)} & -\mathbf{F}_{a(n)}^{(l)} \\ \mathbf{g}^T & g \end{pmatrix} \begin{pmatrix} \delta\mathbf{u}_{(n)}^{(l+1)} \\ \delta\lambda_{(n)}^{(l+1)} \end{pmatrix} = \begin{pmatrix} \mathbf{r}_{(n)}^{(l)} \\ -c_{(n)}^{(l)} \end{pmatrix} \tag{2.32}$$

where:

$$\mathbf{g} = \frac{\partial c}{\partial \mathbf{u}}\bigg|_{(n)}^{(l)} = \frac{\mathbf{v}_{(n)}^{(0)}}{f_{(n)}^{(l)}} = \frac{\mathbf{v}_{(n)}^{(0)}}{\sqrt{1 + \mathbf{F}_{a(n)}^{(l)\,T} \mathbf{v}_{(n)}^{(0)}}} \; ; \qquad\qquad g = \frac{\partial c}{\partial \lambda}\bigg|_{(n)}^{(l)} = \frac{1}{f_{(n)}^{(l)}} = \frac{1}{\sqrt{1 + \mathbf{F}_{a(n)}^{(l)\,T} \mathbf{v}_{(n)}^{(0)}}}$$

The system of Equations (2.32) is not symmetric but has small order (i.e. 7), and is solved using the LU decomposition (Crout-Banachiewicz) method with partial pivoting [67]. The detection of a critical point in the equilibrium path then comes with no overhead because the minimum diagonal element of matrix $\mathbf{L}$ monitors the smallest eigenvalue of $\mathbf{K}$ [66, 67]. The stopping criterion for the Newton method is:

$$\left\| \mathbf{r}_{(n)}^{(l)} \right\| / \left\| \mathbf{r}_{(n)}^{(0)} \right\| < 10^{-4} \;\; \text{AND} \;\; \left\| \Delta\mathbf{u}_{(n)}^{(l)} \right\| / \left\| \Delta\mathbf{u}_{(n)}^{(0)} \right\| < 10^{-2} \tag{2.33}$$

Divergence is detected using the condition:

$$\left\| \mathbf{r}_{(n)}^{(l)} \right\| / \left\| \mathbf{r}_{(n)}^{(0)} \right\| > 10^{3} \;\; \text{OR} \;\; \left\| \Delta\mathbf{u}_{(n)}^{(l)} \right\| / \left\| \Delta\mathbf{u}_{(n)}^{(0)} \right\| > 10^{3} \tag{2.34}$$

and the maximum number of iterations is 50.

Since the rotation vectors cannot be summed up [53, 68], one cannot accumulate the generalized displacements $\Delta\mathbf{u}_{(n)}^{(l)}$ for a given increment, i.e. one cannot write $\Delta\mathbf{u}_{(n)} = \Delta\mathbf{u}_{(n)}^{(0)} + \sum_l \Delta\mathbf{u}_{(n)}^{(l)}$. Indeed, the updating of the degree-of-freedom vector, $\mathbf{u}$, follows the usual vector laws for its first three components (centroid displacement), and the algorithm in Equation (2.14) and (2.15) for its last three components (rotation about the centroid). The rotation matrix is updated using Equation (2.16).

2.6 THE ROCK BLOCK

Let us first determine the coordinates of the sensor points. Let n_f be the number of faces making up the rock block. Since the rock block, B, is a polyhedron, the i-th face of B, F_i, is a polygon Let S_i be an ordered list of its vertices listed in counterclockwise order along its boundary (hole vertices are listed in clockwise order). Let $n_{v,i}$ be the number of vertices of F_i, i.e. $n_{v,i} = \#S_i$. F_i is first triangulated into a set of $n_{t,i} = n_{v,i} - 2$ triangles using

the efficient procedure of Seidel [69] as implemented by Narkhede and Manocha [70]; it is an incremental randomized algorithm whose expected complexity is $O(n_{v,i} \log n_{v,i})$, but in practice it is almost linear in time for a simple polygon. Subsequently, sensor points are assigned to each triangle as described below.

The j-th triangle in F_i is mapped from a normalized plane using the following (affine) transformation $\mathbf{g}$ shown in Figure 2.2:

$$\begin{cases} x = x_{i,j,1} + \left(x_{i,j,2} - x_{i,j,1}\right) \cdot \xi + \left(x_{i,j,3} - x_{i,j,1}\right) \cdot \eta \\ y = y_{i,j,1} + \left(y_{i,j,2} - y_{i,j,1}\right) \cdot \xi + \left(y_{i,j,3} - y_{i,j,1}\right) \cdot \eta \\ z = z_{i,j,1} + \left(z_{i,j,2} - z_{i,j,1}\right) \cdot \xi + \left(z_{i,j,3} - z_{i,j,1}\right) \cdot \eta \end{cases}, \tag{2.35}$$

where $(x_{i,j,k}, y_{i,j,k}, z_{i,j,k},)$ are the coordinates of the k-th triangle vertex, $A_{i,j,k}$. In the normalized (ξ, η)-plane, each edge is subdivided into the same number of segments, n_{tt}. The same number of segments is used for all triangles in F_i, even though one could use a different n_{tt} for each triangle, if needed. The normalized triangle in the (ξ, η)-plane remains subdivided into n_{tt}^2 subtriangles of equal area, i.e. $1/[2(n_{tt}^2)]$. The subtriangle area in the (x, y, z)-space is thus:

$$a_{i,j} := \frac{\left\| \mathbf{A}_{i,j,1}\mathbf{A}_{i,j,2} \times \mathbf{A}_{i,j,1}\mathbf{A}_{i,j,3} \right\|}{2n_{tt}^2} \tag{2.36}$$
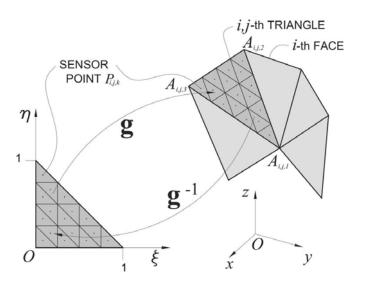
Figure 2.2: Affine transformation g and sensor points for ntt = 4 [1].

21

A sensor point is located at the centroid of each normalized subtriangle in the (ξ, η)-plane. The normalized coordinates of the sensor points in the (ξ, η)-plane may be found using Algorithms 1 and 2 in Figure 2.3.

Algorithm 1:	*Algorithm 2*:

FOR $l=1,\ldots, n_{tt}$
     $(1/3+(l-1), 1/3\ )\ /\ n_{tt}$
	$n_{tt}1 = n_{tt}\text{-}1$
	 FOR $l=1,\ldots, n_{tt}\text{-}1$
	     FOR $m = 1,\ldots, n_{tt}1$
	         $(2/3 + (m-1), 2/3 +(l\text{-}1))\ /$
	 n_{tt}
	         $(1/3 + (m-1), 1/3 + l)\ /\ n_{tt}$
	     $n_{tt}1 = n_{tt}\text{-}1$
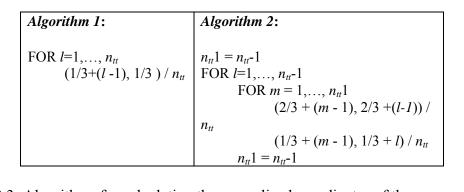
Figure 2.3: Algorithms for calculating the normalized coordinates of the sensor points in the (ξ, η)-plane

For each sensor $P_{i,j,k}$ ($k = 1,\ldots, n_{tt}^2$), the coordinates in the (x, y, z)-space are then found using Equation (2.35). This ensures that $P_{i,j,k}$ in the (x, y, z)-space is the centroid of the i,j,k-th subtriangle. Indeed, consider the subtriangle with normalized centroid coordinates $(1/3, 1/3)/n_{tt}$. Using Equation (2.35), the x-coordinate of the centroid in the (x, y, z)-space is: $(1-2/(3n_{tt}))x_{i,j,1}+(x_{i,j,2}+x_{i,j,3})/(3n_{tt})$. On the other hand, it is known that the coordinates of the centroid of a triangle are the averages of the coordinates of the vertices (e.g., [71]). Since the x-coordinates of the vertices are: $x_{i,j,1}$, $x_{i,j,1}+(x_{i,j,2}-x_{i,j,1})/n_{tt}$, and $x_{i,j,1}+(x_{i,j,3}-x_{i,j,1})/n_{tt}$, respectively, one again obtains $(1-2/(3n_{tt}))x_{i,j,1}+(x_{i,j,2}+x_{i,j,3})/(3n_{tt})$. Likewise for the other subtriangles.

Notice that the normalized coordinates of the sensor points are the same for all triangles in F_i. Additionally, since an incremental scheme is adopted, these initial configuration coordinates will be labeled with a subscript (0). Algorithm 3 in Figure 2.4 sums up the main calculation steps.

The current positions for the sensor points are needed in order to detect contacts (Section 2.7), and, if there is contact, to calculate the correct reaction forces because the

normal and tangential springs are non-linear in the sensor displacement components (Section 2.8). Likewise, the current application points and direction (for follower loads) of the active external forces are needed to calculate the correct resultants. Therefore, at each iteration the coordinates and the stresses at each sensor point are updated using Equation (2.5).

Algorithm 3:

CALCULATE NORMALIZED COORDINATES FOR SENSOR POINTS
FOR $i = 1,\ldots, n_f$
     FOR $j = 1,\ldots, n_{t,i}$
        CALCULATE $a_{i,j}$ (Equation (2.36))
        FOR $k = 1,\ldots, n_{tt}^2 + 1$
           CALCULATE $P_{i,j,k(0)}$ coordinates (Equation (2.35))

Figure 2.4: Algorithm that sums up the main calculation steps

2.7 CONSTRAINT SPACE AND CONTACT DETECTION

The constraint space, C, is the set of points where the sensor points find a reactive force. Oftentimes C is just the rock mass surrounding the block. For example, let D_1 be a block's mould and consider the tunnel example in Figure 2.5(a) and Figure 2.5(b) (in which C has boundary $\partial C = D_1 \cup D_2 \cup D_3$) and the slope example in Figure 2.5(c) (in which C is has boundary $\partial C = D_1 \cup D_3$).

C is assumed to be fixed in the (x, y, z)-space. At each iteration, one needs to know whether a sensor point is in C. In particular, one needs to know whether the iterative displacement $\delta \mathbf{u}_{(n)}^{(l)}$ for B has taken a sensor point into or out of C, or whether it has kept a sensor point inside or outside C. This is accomplished as follows.

The boundary of the constraint space, ∂C, is made up of (or is approximated with) a set of polygons in the (x, y, z)-space: $\{C_i, \ i = 1, \ldots, n_{ci}\}$. Similar to ∂B, each polygon C_i is first triangulated using Seidel's algorithm [69]. Let $\mathbf{n}_{c,i}$ denote the i-th unit normal to C_i, positive into the unconstrained space for B.
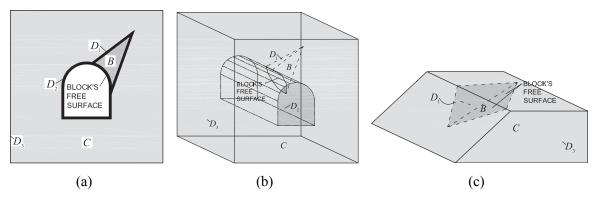
Figure 2.5: (a) and (b) Tunnel example for block B; (c) slope example for block B [1].

Oftentimes the path described by a sensor point until *B* reaches either equilibrium or a critical point is small as compared to the representative dimension of *C*, and sensor points interact with a small subset of ∂C. Thus, triangulation and intersection search can be limited to a small subset of ∂C enclosed in a bounding box around *B*: excellent efficiency has been achieved with a single Axis-Aligned Bounding Box (AABB) [72] inflated 10% on edge. In the common situations exemplified in Figure 2.5, one can even restrict ∂C to D_1, i.e. to the block's mould. In this case, no additional computations are actually necessary because the triangulation and the query structure for internal point location have already been carried out in Section 2.6; consequently, $\forall F_i \in D_1$: $C_i = F_i$ and $\mathbf{n}_{c,i} = \mathbf{n}_i$ (all of *B* quantities referring to the initial configuration).

The logic of the contact algorithm adopted here is based on the three-dimensional extension of the Jordan curve Theorem [71, 73], i.e. a simple closed surface separates the 3D space into two regions of which it is the common boundary. Consider a sensor point $P_{i,j,k}$ that at the (*l*-1)-th iteration during the *n*-th increment is not in *C*. As shown in Figure 2.6(a), at the *l*-th iteration, point $P_{i,j,k}$ is in *C* if $\delta\mathbf{u}_{P_{i,j,k}(n)}^{(l)}$ applied at $P_{i,j,k(n)}^{(l-1)}$ has an odd number of intersections with ∂C; and it remains outside *C* otherwise (Figure 2.6(b)). As shown in Figure 2.6(c) and (d), the other way around is true if $P_{i,j,k}$ is in *C* at the (*l*-1)-th iteration. Notice that if two or more intersections are found, $\delta\mathbf{u}_{P_{i,j,k}(n)}^{(l)}$ is too large, the arclength $step_0$ (Equation (2.29)) must be reduced, and the *n*-th increment must be restarted.

24
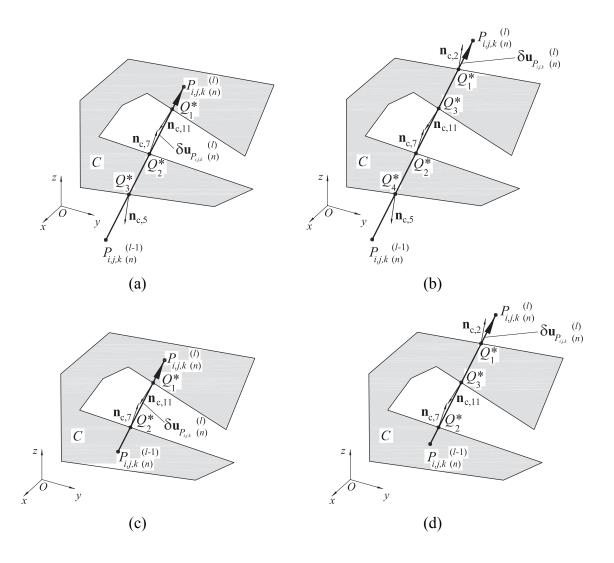
Figure 2.6: (a) and (b) $P_{i,j,k(n)}^{(l-1)}$ is not in C at the (l-1)-th iteration: (a) $\delta\mathbf{u}_{P_{i,j,k}(n)}^{(l)}$ takes the sensor point into C, (b) $\delta\mathbf{u}_{P_{i,j,k}(n)}^{(l)}$ takes the sensor point out of C. (c) and (d) $P_{i,j,k(n)}^{(l-1)}$ is in C at the (l-1)-th iteration: (c) $\delta\mathbf{u}_{P_{i,j,k}(n)}^{(l)}$ keeps the sensor point in C, (d) $\delta\mathbf{u}_{P_{i,j,k}(n)}^{(l)}$ takes the sensor point outside C [1].

In order to check whether $\delta\mathbf{u}_{P_{i,j,k}(n)}^{(l)}$ applied at $P_{i,j,k(n)}^{(l-1)}$ intersects C_h, one first calculates the intersection between a ray from $P_{i,j,k(n)}^{(l-1)}$ in the positive $\delta\mathbf{u}_{P_{i,j,k}(n)}^{(l)}$ direction. This ray has parametric equation $OQ = OP_{i,j,k(n)}^{(l-1)} + d\ \delta\mathbf{u}_{P_{i,j,k}(n)}^{(l)} / \left\| \delta\mathbf{u}_{P_{i,j,k}(n)}^{(l)} \right\|$,

25

with $d > 0$. The idea is to first find the intersection Q^* between this ray and the plane containing C_h, and then check if Q^* lies inside C_h; if it does and $0 \leq d \leq \left\| \delta \mathbf{u}_{P_{i,j,k}(n)}^{(l)} \right\|$, then C_h is counted as an intersection face.

If sensor point $P_{i,j,k}$ crosses into C, in the calculation of the residual one needs to know the distance traveled in C, $\overline{d}_{i,j,k}$. Likewise, if sensor point $P_{i,j,k}$ crosses out of C, one needs to know the distance traveled outside C, $\overline{d}_{i,j,k}$. In the first (second) case, one has $\delta \mathbf{u}_{P_{i,j,k}(n)}^{(l)} \cdot \mathbf{n}_{c,h} < 0$ ($\delta \mathbf{u}_{P_{i,j,k}(n)}^{(l)} \cdot \mathbf{n}_{c,h} > 0$, respectively), and the distance traveled in (outside, respectively) C is $\overline{d}_{i,j,k} = \left\| \delta \mathbf{u}_{P_{i,j,k}(n)}^{(l)} \right\| - d$.

Algorithms for determining whether a point is in a polygon have been reviewed by Haines [74]. Since C_h has already been triangulated, the most efficient algorithm exploits this triangulation by generating a query structure that is then used to determine the location of a point in logarithmic time [70] (the ray tracing algorithm of Franklin [75], for example, works in linear time). Because the algorithm handles polygons embedded in a 2D space, C_h is projected onto a Cartesian plane. To avoid numerical instabilities, the largest component of $\mathbf{n}_{c,h}$ is first identified, say this is the x-component. Then, the projection of vertex $A \in C_h$ is $A \equiv (x, y, z) \mapsto (y, z)$.

Efficient algorithms for contact detection (e.g., RAPID [76] and OPCODE [77]) yield a list of intersecting boundary triangles, but do not provide information on points that are inside two intersecting solids. As a consequence, they cannot be used here.

2.8 SENSOR POINT STIFFNESS, CONSTRAINT FORCES AND THEIR RESIDUAL CONTRIBUTIONS

Let $\mathbf{n}_{c,i,j,k}$ be the normal to ∂C where $P_{i,j,k}$ entered C, and let $\mathbf{I}$ be the identity matrix. In order to simplify the notation, let us suppress the iteration and increment indexes. The normal component of the iterative displacement change and the tangential component of the incremental displacement are, respectively:

$$\delta \mathbf{u}_{n,P_{i,j,k}} = \mathbf{n}_{c,i,j,k} \left(\mathbf{n}_{c,i,j,k} \cdot \delta \mathbf{u}_{P_{i,j,k}} \right) = \mathbf{n}_{c,i,j,k} \mathbf{n}_{c,i,j,k}{}^T \delta \mathbf{u}_{P_{i,j,k}} \qquad (2.37)$$

$$\Delta \mathbf{u}_{t,P_{i,j,k}} = \Delta \mathbf{u}_{P_{i,j,k}} - \Delta \mathbf{u}_{n,P_{i,j,k}} = \Delta \mathbf{u}_{P_{i,j,k}} - \mathbf{n}_{c,i,j,k} \mathbf{n}_{c,i,j,k}{}^T \Delta \mathbf{u}_{P_{i,j,k}} = \left(\mathbf{I} - \mathbf{n}_{c,i,j,k} \mathbf{n}_{c,i,j,k}{}^T \right) \Delta \mathbf{u}_{P_{i,j,k}} \quad (2.38)$$

2.8.1 Normal stiffness

At the l-th iteration of the n-th increment, the normal stiffness at a sensor point, $P_{i,j,k}$, is not zero if and only if $P_{i,j,k(n)}^{(l-1)} \in C$. Let $u_{n,P_{i,j,k}}$ be the accumulated normal displacement into C since $P_{i,j,k}$ entered C: $u_{n,P_{i,j,k}} = -\mathbf{n}_{c,i,j,k}{}^T \mathbf{u}_{P_{i,j,k}}{}^*$, where "*" denotes "since $P_{i,j,k}$ entered C". This normal displacement is the sum of three displacement components caused, respectively, by the deformability of the discontinuity, the rock block, and the constraint space (rock mass):

$$u_{n,P_{i,j,k}} = u1_{n,P_{i,j,k}} + u2_{n,P_{i,j,k}} + u3_{n,P_{i,j,k}} \qquad (2.39)$$

The deformability of the rock block and of the rock mass are taken into account (albeit in a simplified form) in order not to overestimate the forces generated by dilatancy.

Let $kn2_{i,j,k}$ be the normal stiffness of the rock block and let $kn3_{i,j,k}$ be the normal stiffness of the rock mass, which are assumed to be constant, and are calculated as shown below. If $\sigma n_{i,j,k}$ is the current normal stress at $P_{i,j,k}$, then:

$$u2_{n,P_{i,j,k}} = \sigma n_{i,j,k} / kn2_{i,j,k} \; ; \; u3_{n,P_{i,j,k}} = \sigma n_{i,j,k} / kn3_{i,j,k} \qquad (2.40)$$

Goodman's hyperbolic model [78] is adopted for the normal behavior of the discontinuity:

$$\sigma n_{i,j,k} = \frac{s_{i,j,k} \cdot u1_{n,P_{i,j,k}}}{1 - u1_{n,P_{i,j,k}} / v_{i,j,k}} \qquad (2.41)$$

where $s_{i,j,k}$ and $v_{i,j,k}$ are the initial stiffness and the maximum closure, respectively, of the constraint face penetrated by $P_{i,j,k}$.

Substituting Equation (2.40) into Equation (2.39), solving for $u1_{n,P_{i,j,k}}$, and finally substituting into Equation (2.41) yields a quadratic equation in the normal stress. Its positive root is (subscripts have been omitted to reduce clutter):

27

$$\sigma n = \left(\begin{array}{c} kn2 \cdot kn3 \cdot (u_n - v) - (kn2 + kn3) \cdot s \cdot v + \\ \sqrt{4 \cdot (kn2 + kn3) \cdot kn2 \cdot kn3 \cdot s \cdot v \cdot u_n + (kn3 \cdot s \cdot v + kn2(s \cdot v + kn3(v - u_n)))^2} \end{array} \right) / \left[2 \cdot (kn2 + kn3) \right]$$

(2.42)

The normal stiffness of the rock block is assumed to be constant. It is assumed that the normal force at a sensor point causes a settlement equal to that of a circular foundation resting on an isotropic linearly elastic medium whose depth is equal to the distance between the sensor point and the centroid, $h_{i,j,k}$. The equivalent circular foundation is assumed to have the same area as the area of face F_i, a_{F_i}. The equivalent diameter of the foundation is then: $d_i = 2\sqrt{a_{F_i}/\pi}$. Let E_B and v_B be the Young's modulus and the Poisson's ratio of the intact rock. The stiffness is:

$$kn2_{i,j,k} = \frac{E_B}{d_i(1 - v_B^2)} \left[1 + \frac{2h_{i,j,k}}{d_i} - \sqrt{1 + \left(\frac{2h_{i,j,k}}{d_i}\right)^2} - \frac{\frac{2h_{i,j,k}}{d_i}}{2(1 - v_B)} + \frac{\left(\frac{2h_{i,j,k}}{d_i}\right)^2}{2(1 - v_B)\sqrt{1 + \left(\frac{2h_{i,j,k}}{d_i}\right)^2}} \right]^{-1}$$

(2.43)

The boundary element method could be also used to determine this stiffness.

Likewise, the normal stiffness of the rock mass is assumed to be constant. It is assumed that the normal force at a sensor point causes a settlement equal to that of a circular foundation on an isotropic linearly elastic ground of infinite depth. Let E_m and v_m be the Young's modulus and the Poisson's ratio of the rock mass. The stiffness is:

$$kn3_{i,j,k} = \frac{1}{d_i} \frac{E_m}{1 - v_m^2}$$

(2.44)

The contribution of the normal stiffness to the constraint force $\mathbf{F}_c$ in Equation (2.24) is thus:

$$\mathbf{F}_{c,n}(\mathbf{u})_{(n)}^{(l)} = a_{i,j} \cdot \sigma n_{i,j,k(n)}^{(l)} \left(\begin{array}{c} \mathbf{n}_{c,i,j,k} \\ \mathbf{S}\left(\mathbf{G}_{(n)}^{(l)} \mathbf{P}_{i,j,k(n)}^{(l)}\right) \mathbf{n}_{c,i,j,k} \end{array} \right)$$

(2.45)

The derivative $\partial \sigma n_{i,j,k} / \partial \mathbf{u}_P$ will be needed which can be written as:

$$\frac{\partial \sigma n_{i,j,k}}{\partial \mathbf{u}_{P_{i,j,k}}} = \frac{\partial \sigma n_{i,j,k}}{\partial u_{n,P_{i,j,k}}} \frac{\partial u_{n,P_{i,j,k}}}{\partial \mathbf{u}_P} = \frac{\partial \sigma n_{i,j,k}}{\partial u_{n,P_{i,j,k}}} \left(-\mathbf{n}_{c,i,j,k}^{\ T} \right) = -\frac{\partial \sigma n_{i,j,k}}{\partial u_{n,P_{i,j,k}}} \mathbf{n}_{c,i,j,k}^{\ T} , \qquad (2.46)$$

where (subscripts have been again omitted to reduce clutter):

$$\frac{\partial \sigma n_{i,j,k}}{\partial u_{n,P_{i,j,k}}} = kn2 \cdot kn3 \cdot \left[1 + \frac{kn3 \cdot s \cdot v + kn2\left(s \cdot v + kn3\left(u_n - v \right) \right)}{\sqrt{4 \cdot \left(kn2 + kn3 \right) \cdot kn2 \cdot kn3 \cdot s \cdot v \cdot u_n + \left(kn3 \cdot s \cdot v + kn2\left(s \cdot v + kn3\left(v - u_n \right) \right) \right)^2}} \right] / \left[2 \cdot \left(kn2 + kn3 \right) \right]$$

$$(2.47)$$

Likewise, the derivative $\partial \left(\dfrac{\partial \sigma n_{i,j,k}}{\partial u_{n,P_{i,j,k}}} \right) / \partial \mathbf{u}_P$ will be needed. This can be written

as:

$$\partial \left(\frac{\partial \sigma n_{i,j,k}}{\partial u_{n,P_{i,j,k}}} \right) / \partial \mathbf{u}_P = -\frac{\partial^2 \sigma n_{i,j,k}}{\partial u_{n,P_{i,j,k}}^{\ 2}} \mathbf{n}_{c,i,j,k}^{\ T} , \qquad (2.48)$$

where:

$$\frac{\partial^2 \sigma n_{i,j,k}}{\partial u_{n,P_{i,j,k}}^{\ 2}} = \frac{2\left(kn2 \cdot kn3 \right)^3 \cdot s \cdot v^2}{\left[4 \cdot \left(kn2 + kn3 \right) \cdot kn2 \cdot kn3 \cdot s \cdot v \cdot u_n + \left(kn3 \cdot s \cdot v + kn2\left(s \cdot v + kn3\left(v - u_n \right) \right) \right)^2 \right]^{3/2}} \qquad (2.49)$$

Let us now consider possible the special case of sensor points entering C. If $P_{i,j,k(n)}^{(l-1)} \notin C$ and $P_{i,j,k(n)}^{(l)} \in C$, then the normal displacement traveled in C is $\bar{d}_{i,j,k} \delta \mathbf{u}_{n,P_{i,j,k}(n)}^{(l)} / \left\| \delta \mathbf{u}_{n,P_{i,j,k}(n)}^{(l)} \right\|$. The penetration of $P_{i,j,k}$ causes the unbalanced force:

$$\mathbf{no}_{i,j,k(n)}^{(l)} := a_{i,j} \cdot \sigma n_{i,j,k(n)}^{(l)} \bar{d}_{i,j,k} \delta \mathbf{u}_{n,P_{i,j,k}(n)}^{(l)} / \left\| \delta \mathbf{u}_{n,P_{i,j,k}(n)}^{(l)} \right\|^2 , \qquad (2.50)$$

and the unbalanced moment:

$$\mathbf{G}_{(n)}^{(l)} \mathbf{P}_{i,j,k(n)}^{(l)} \times \mathbf{no}_{i,j,k(n)}^{(l)} = \mathbf{S}\left(\mathbf{G}_{(n)}^{(l)} \mathbf{P}_{i,j,k(n)}^{(l)} \right) \mathbf{no}_{i,j,k(n)}^{(l)} \qquad (2.51)$$

Therefore, the following is the $P_{i,j,k}$ contribution to the residual $\mathbf{r}_{(n)}^{(l)}$ in Equation (2.32):

$$-\begin{pmatrix} \mathbf{no}_{i,j,k(n)}^{(l)} \\ \mathbf{S}\left(\mathbf{G}_{(n)}^{(l)} \mathbf{P}_{i,j,k(n)}^{(l)} \right) \mathbf{no}_{i,j,k(n)}^{(l)} \end{pmatrix} \qquad (2.52)$$

2.8.2 Shear stiffness

The Barton-Bandis model for shear strength [79-81] is adopted here because of its wide use and relative ease in parameter estimation. Consider first the case in which $P_{i,j,k(n)}^{(l-1)} \in C$. Let L_i be the characteristic length of face F_i, and let $JRC_{i,j,k}$ and $JCS_{i,j,k}$ be the Joint Roughness Coefficient and the Joint Compressive Strength (respectively) for the discontinuity penetrated by $P_{i,j,k}$, corrected for the length L_i as appropriate [80]. The shear strength is:

$$\tau_{\max,i,j,k(n)}^{(l)} = \sigma n_{i,j,k(n)}^{(l)} \tan\left(JRC_{i,j,k} \log \frac{JCS_{i,j,k}}{\sigma n_{i,j,k(n)}^{(l)}} + \varphi_{b,i,j,k} \right), \tag{2.53}$$

where $\varphi_{b,i,j,k}$ is the base friction angle of the discontinuity penetrated by $P_{i,j,k}$.

Two stiffness models have been considered: in the first model, the shear stiffness is equal to a fraction of the normal stiffness (typically one tenth):

$$ks_{i,j,k(n)}^{(l)} = kn_{i,j,k(n)}^{(l)}/10 = a_{i,j} \cdot \left. \frac{\partial \sigma n_{i,j,k}}{\partial u_{n,P_{i,j,k}}} \right|_{(n)}^{(l-1)} /10 \tag{2.54}$$

In the second model, following Barton and Bandis, it is assumed that the shear stiffness is constant up to the peak shear displacement, $\delta_{peak,i,j,k}$ [81]:

$$ks_{i,j,k(n)}^{(l)} = \sigma n_{i,j,k(n)}^{(l)} \tan\left(JRC \log \frac{JCS}{\sigma n_{i,j,k(n)}^{(l)}} + \varphi_b \right) / \delta_{peak,i,j,k}, \tag{2.55}$$

where the peak shear displacement is (L in m):

$$\delta_{peak,i,j,k} = \frac{L_i}{500} \left(\frac{L_i}{JRC_{i,j,k}} \right)^{-0.33} (m) \tag{2.56}$$

Let $\mathbf{s}_{i,j,k(n-1)}$ be the last converged shear force at $P_{i,j,k}$. In order to avoid spurious unloading, incremental (rather than iterative) updates of the shear force are used (e.g., page 154 in reference [82]). The updated shear force is thus

$$\mathbf{s}_{i,j,k(n)}^{(l)} = \mathbf{s}_{i,j,k(n-1)} + ks_{i,j,k(n)}^{(l)} \Delta \mathbf{u}_{t,P_{i,j,k}(n)}^{(l)} \tag{2.57}$$

The contribution to the constraint force, $\mathbf{F}_c$, in Equation (2.24) is thus:

$$\mathbf{F}_{c,s}\left(\mathbf{u}\right)^{(l)}_{(n)} = -\begin{pmatrix} \mathbf{s}^{(l)}_{i,j,k(n)} \\ \mathbf{S}\left(\mathbf{G}^{(l)}_{(n)}\mathbf{P}^{(l)}_{i,j,k(n)}\right)\mathbf{s}^{(l)}_{i,j,k(n)} \end{pmatrix} \tag{2.58}$$

If, on the other hand, the peak shear strength has been overcome during the previous iteration, then $ks^{(l)}_{i,j,k(n)} = 0$ and the following is the $P_{i,j,k}$ contribution to the residual $\mathbf{r}^{(l)}_{(n)}$ in Equation (2.32):

$$\begin{pmatrix} \mathbf{s}^{(l)}_{i,j,k(n)} := \left[-\sigma n^{(l)}_{i,j,k(n)}\tan\left(JRC_{i,j,k}\log\dfrac{JCS_{i,j,k}}{\sigma n^{(l)}_{i,j,k(n)}}+\varphi_{b,i,j,k}\right)a_{ij}\right]\Delta\mathbf{u}^{(l)}_{t,P_{i,j,k}(n)}/\left\|\Delta\mathbf{u}^{(l)}_{t,P_{i,j,k}(n)}\right\| \\ \mathbf{S}\left(\mathbf{G}^{(l)}_{(n)}\mathbf{P}^{(l)}_{i,j,k(n)}\right)\mathbf{s}^{(l)}_{i,j,k(n)} \end{pmatrix} \tag{2.59}$$

Let us now consider possible special cases of sensor points exiting or entering C. If $P^{(l-1)}_{i,j,k(n)} \in C$ and $P^{(l)}_{i,j,k(n)} \notin C$, then $P_{i,j,k}$ contributes neither to the stiffness nor to the residual. Finally, if $P^{(l-1)}_{i,j,k(n)} \notin C$ and $P^{(l)}_{i,j,k(n)} \in C$, then the shear stiffness becomes active, and the following is the $P_{i,j,k}$ contribution to the residual $\mathbf{r}^{(l)}_{(n)}$ in Equation (2.32):

$$-\begin{pmatrix} \mathbf{s}^{(l)}_{i,j,k(n)} := ks^{(l)}_{i,j,k(n)}\overline{d}_{i,j,k}\delta\mathbf{u}^{(l)}_{t,P_{i,j,k}(n)}/\left\|\delta\mathbf{u}^{(l)}_{t,P_{i,j,k}(n)}\right\| \\ \mathbf{S}\left(\mathbf{G}^{(l)}_{(n)}\mathbf{P}^{(l)}_{i,j,k(n)}\right)\mathbf{s}^{(l)}_{i,j,k(n)} \end{pmatrix} \tag{2.60}$$

2.9 ACTIVE FORCES GENERATED BY HYDROSTATIC WATER PRESSURE

Consider hydrostatic water pressure exerted on the area a_{ij} that surrounds $P_{i,j,k}$. Let $z_{w,i,j,k}$ be the pressure head at $P_{i,j,k}$ in the base configuration; the piezometric surface is assumed to be constant along the equilibrium path. Let $\mathbf{e}_z$ be the unit vector of the z-axis pointing upwards. The contribution to the active force, $\mathbf{F}_a$, in Equation (2.24) is:

$$\mathbf{F}_{a,w}\left(\mathbf{u}\right)^{(l)}_{(n)} = a_{i,j}\begin{pmatrix} \gamma_w\left(z_{w,i,j,k}-\mathbf{e}_z{}^T\mathbf{u}^{(l)}_{P_{i,j,k}(n)}\right)\mathbf{n}^{(l)}_{i(n)} \\ \gamma_w\mathbf{S}\left(\mathbf{G}^{(l)}_{(n)}\mathbf{P}^{(l)}_{i,j,k(n)}\right)\left(z_{w,i,j,k}-\mathbf{e}_z{}^T\mathbf{u}^{(l)}_{P_{i,j,k}(n)}\right)\mathbf{n}^{(l)}_{i(n)} \end{pmatrix} \tag{2.61}$$

2.10 STIFFNESS MATRICES

By compiling the forces derived above, the residual is calculated as:

$$\mathbf{r}(\mathbf{u}, \lambda) = \mathbf{F}_{c,n}(\mathbf{u}) + \mathbf{F}_{c,s}(\mathbf{u}) + \lambda\left(\mathbf{F}_{a,w}(\mathbf{u}) + \mathbf{F}_a{}^*(\mathbf{u}) + \mathbf{F}_a{}^{**}\right), \qquad (2.62)$$

where $\mathbf{F}_a{}^*$ collects all forces (except for hydrostatic water pressure) that depend on $\mathbf{u}$, and $\mathbf{F}_a{}^{**}$ collects all forces that do not depend on $\mathbf{u}$ (e.g., weight).

Per Equation (2.26), each component in Equation (2.62) gives rise to a stiffness matrix component: in the finite element method terminology, the first two components of the residual yield the equivalent to the structural matrix, whereas $\mathbf{F}_{a,w}$ yields a load stiffness matrix.

Except for $\mathbf{F}_a{}^*$, each component is of the form

$$\begin{pmatrix} \mathbf{v}\left(\mathbf{u}_{P_{i,j,k}}\right) \\[2mm] \mathbf{S}\left(\mathbf{GP}_{i,j,k}\right)\mathbf{v}\left(\mathbf{u}_{P_{i,j,k}}\right) \end{pmatrix} \qquad (2.63)$$

By taking the derivative of the first three rows with the aid of Equation (2.9), one obtains:

$$\left.\frac{\partial\mathbf{v}\left(\mathbf{u}_{P_{i,j,k}}\right)}{\partial\mathbf{u}}\right|_{(n)}^{(l)} = \left.\frac{\partial\mathbf{v}\left(\mathbf{u}_{P_{i,j,k}}\right)}{\partial\mathbf{u}_{P_{i,j,k}}}\right|_{(n)}^{(l)} \left.\frac{\partial\mathbf{u}_{P_{i,j,k}}}{\partial\mathbf{u}}\right|_{(n)}^{(l)} = \left.\frac{\partial\mathbf{v}\left(\mathbf{u}_{P_{i,j,k}}\right)}{\partial\mathbf{u}_{P_{i,j,k}}}\right|_{(n)}^{(l)} \mathbf{D}_P\left(\mathbf{\theta}_{(n)}^{(l)}\right) \qquad (2.64)$$

The derivative of the last tree rows may be rewritten as:

$$\frac{\partial\left[\mathbf{S}\left(\mathbf{G}_{(n)}^{(l)}\mathbf{P}_{i,j,k(n)}^{(l)}\right)\mathbf{v}\left(\mathbf{u}_{P_{i,j,k}(n)}^{(l)}\right)\right]}{\partial\mathbf{u}} = -\mathbf{S}(\mathbf{v})\frac{\partial\left[\mathbf{G}_{(n)}^{(l)}\mathbf{P}_{i,j,k(n)}^{(l)}\right]}{\partial\mathbf{u}} + \mathbf{S}\left(\mathbf{G}_{(n)}^{(l)}\mathbf{P}_{i,j,k(n)}^{(l)}\right)\frac{\partial\mathbf{v}\left(\mathbf{u}_{P_{i,j,k}(n)}^{(l)}\right)}{\partial\mathbf{u}}, \quad (2.65)$$

and using Equations (2.9) and (2.12), one obtains:

$$\left.\frac{\partial\left[\mathbf{S}\left(\mathbf{GP}_{i,j,k}\right)\mathbf{v}\left(\mathbf{u}_{P_{i,j,k}}\right)\right]}{\partial\mathbf{u}}\right|_{(n)}^{(l)} = -\mathbf{S}\left[\mathbf{v}\left(\mathbf{u}_{P_{i,j,k}(n)}^{(l)}\right)\right]\mathbf{H}_P\left(\mathbf{\theta}_{(n)}^{(l)},\mathbf{G}_{(0)}\mathbf{P}_{(0)}\right) + \mathbf{S}\left(\mathbf{G}_{(n)}^{(l)}\mathbf{P}_{i,j,k(n)}^{(l)}\right)\frac{\partial\mathbf{v}\left(\mathbf{u}_{P_{i,j,k}(n)}^{(l)}\right)}{\partial\mathbf{u}_{P_{i,j,k}}}\mathbf{D}_P\left(\mathbf{\theta}_{(n)}^{(l)}\right)(2.66)$$

As for hydrostatic water forces, it is easier to take the derivative with respect to $\mathbf{u}$, and therefore one would use:

$$\left.\frac{\partial\left[\mathbf{S}\left(\mathbf{GP}_{i,j,k}\right)\mathbf{v}\left(\mathbf{u}_{P_{i,j,k}}\right)\right]}{\partial\mathbf{u}}\right|_{(n)}^{(l)} = -\mathbf{S}\left[\mathbf{v}\left(\mathbf{u}_{P_{i,j,k}(n)}^{(l)}\right)\right]\mathbf{H}_P\left(\mathbf{\theta}_{(n)}^{(l)},\mathbf{G}_{(0)}\mathbf{P}_{(0)}\right) + \mathbf{S}\left(\mathbf{G}_{(n)}^{(l)}\mathbf{P}_{i,j,k(n)}^{(l)}\right)\left.\frac{\partial\mathbf{v}\left(\mathbf{u}_{P_{i,j,k}}\right)}{\partial\mathbf{u}}\right|_{(n)}^{(l)} \qquad (2.67)$$

For a given sensor point $P_{i,j,k}$, Table 2.1 gives the vectors and matrices needed in Equations (2.64), and (2.66) or (2.67). The complete stiffness matrix is then obtained by summation over the sensor points:

$$\mathbf{K} = \sum_{i,j,k} \left(\mathbf{K}_{n,i,j,k} + \mathbf{K}_{s,i,j,k} + \lambda \cdot \mathbf{K}_{w,i,j,k} + \mathbf{K}_{F_a*} \right) \tag{2.68}$$

Some considerations on the symmetry of $\mathbf{K}$ are in order. $\mathbf{K}$ is always non-symmetric if large rotations occur. In fact, consider the first three rows of $\mathbf{K}$ given in Equation (2.64) and the contribution of the second term in r.h.s. of Equation (2.66) to the last three rows of $\mathbf{K}$. Denote $\mathbf{d} = \partial \mathbf{v}\left(\mathbf{u}_{P_{i,j,k}}\right)/\partial\mathbf{u}$. The definition in Equation (2.10), yields:

$$\begin{pmatrix} \mathbf{dI}_{3\times3} & -\mathbf{d}\cdot\mathbf{S}\left(\mathbf{R}\cdot(\mathbf{GP})_{(0)}\right)\cdot\mathbf{J}(\mathbf{\theta}) \\ \mathbf{S}\left(\mathbf{R}\cdot(\mathbf{GP})_{(0)}\right)\cdot\mathbf{d} & -\mathbf{S}\left(\mathbf{R}\cdot(\mathbf{GP})_{(0)}\right)\cdot\mathbf{d}\cdot\mathbf{S}\left(\mathbf{R}\cdot(\mathbf{GP})_{(0)}\right)\cdot\mathbf{J}(\mathbf{\theta}) \end{pmatrix} \tag{2.69}$$

A necessary and sufficient condition for the upper leading diagonal minor to be symmetric is that $\mathbf{d}$ is symmetric. Under this assumption, the transpose of the upper off-diagonal minor is equal to: $\mathbf{J}(\mathbf{\theta})^T \cdot \mathbf{S}\left(\mathbf{R}\cdot(\mathbf{GP})_{(0)}\right)\cdot\mathbf{d}$. This is equal to the lower off-diagonal minor if and only if one neglects large rotations so that $\mathbf{J}(\mathbf{\theta}) \to \mathbf{I}$. Using Equation (2.4), the lower leading diagonal term can be rewritten as $-\mathbf{d}\cdot\mathbf{S}\left(\mathbf{R}\cdot(\mathbf{GP})_{(0)}\right)\cdot\mathbf{S}\left(\mathbf{R}\cdot(\mathbf{GP})_{(0)}\right)\cdot\mathbf{J}(\mathbf{\theta})$, which is symmetric if and only if $\mathbf{d}$ is symmetric and $\mathbf{J}(\mathbf{\theta}) \to \mathbf{I}$. Thus, $\mathbf{K}$ is symmetric if and only if $\mathbf{d}$ is symmetric and one neglects large rotations. As shown in Table 2.1, $\mathbf{d}$ is symmetric for normal and shear joint stiffness, but it is not symmetric when water forces are applied. In addition, the first term in the r.h.s of Equation (2.66) is always not symmetric under large rotations because it contains $\mathbf{J}(\mathbf{\theta})$. Stiffness matrices in 3D-DDA and BSM3D are symmetric because $\mathbf{d}$ is always assumed to be symmetric and large rotations are neglected.

Table 2.1: Vectors and matrices needed for the calculation of the stiffness matrices [1].

$\mathbf{K}_{i,j,k}$	$\mathbf{v}\left(\mathbf{u}_{P_{i,j,k}(n)}^{(l)}\right)$	$\left.\dfrac{\partial \mathbf{v}\left(\mathbf{u}_{P_{i,j,k}}\right)}{\partial \mathbf{u}_{P_{i,j,k}}}\right\|_{(n)}^{(l)}$ or $\left.\dfrac{\partial \mathbf{v}\left(\mathbf{u}_{P_{i,j,k}}\right)}{\partial \mathbf{u}}\right\|_{(n)}^{(l)}$
$\mathbf{K}_{n,i,j,k} = -\dfrac{\partial \mathbf{F}_{c,n}}{\partial \mathbf{u}}$	$a_{i,j}\cdot \sigma n_{i,j,k(n)}^{(l)}\mathbf{n}_{c,i,j,k}$	$\left.\dfrac{\partial \mathbf{v}\left(\mathbf{u}_{P_{i,j,k}}\right)}{\partial \mathbf{u}_{P_{i,j,k}}}\right\|_{(n)}^{(l)} = -a_{i,j}\cdot \left.\dfrac{\partial \sigma n_{i,j,k}}{\partial u_{n,P_{i,j,k}}}\right\|_{(n)}^{(l)}\mathbf{n}_{c,i,j,k}\mathbf{n}_{c,i,j,k}^{T}$
$\mathbf{K}_{s,i,j,k} = -\dfrac{\partial \mathbf{F}_{c,s}}{\partial \mathbf{u}}$	$ks_{i,j,k(n)}^{(l)}\left(\mathbf{I}-\mathbf{n}_{c,i,j,k}\mathbf{n}_{c,i,j,k}^{T}\right)\mathbf{u}_{P_{i,j,k}(n)}^{(l)}$	$\left.\dfrac{\partial \mathbf{v}\left(\mathbf{u}_{P_{i,j,k}}\right)}{\partial \mathbf{u}_{P_{i,j,k}}}\right\|_{(n)}^{(l)} = -ks_{i,j,k(n)}^{(l)}\left(\mathbf{I}-\mathbf{n}_{c,i,j,k}\mathbf{n}_{c,i,j,k}^{T}\right)$
$\mathbf{K}_{w,i,j,k} = -\dfrac{\partial \mathbf{F}_{a,w}}{\partial \mathbf{u}}$	$a_{i,j}\gamma_w \left(z_{w,i,j,k}-\mathbf{e}_z^{T}\mathbf{u}_{P_{i,j,k}(n)}^{(l)}\right)\mathbf{n}_{i(n)}^{(l)}$	$\left.\dfrac{\partial \mathbf{v}\left(\mathbf{u}_{P_{i,j,k}}\right)}{\partial \mathbf{u}}\right\|_{(n)}^{(l)} =$ $a_{i,j}\gamma_w \begin{bmatrix} -\mathbf{n}_{i(n)}^{(l)}\mathbf{e}_z^{T}\cdot \mathbf{D}_P\left(\boldsymbol{\theta}_{(n)}^{(l)}\right) \\ +\left(z_{w,i,j,k}-\mathbf{e}_z^{T}\mathbf{u}_{P_{i,j,k}(n)}^{(l)}\right)\mathbf{H}_P\left(\boldsymbol{\theta},\mathbf{n}_{i(0)}\right) \end{bmatrix}$

Note: $\dfrac{\partial \sigma n_{i,j,k}}{\partial u_{n,P_{i,j,k}}}$ and $\dfrac{\partial^2 \sigma n_{i,j,k}}{\partial u_{n,P_{i,j,k}}^{2}}$ are given in Equations (2.49) and (2.51), respectively.

2.11 DILATANCY

Discontinuity dilatancy creates a displacement component of a sensor point normal to the discontinuity and directed toward the constrained space. Its magnitude is equal to the shear displacement times the tangent of the dilatancy angle. The dilatancy angle is quantified based on the Barton-Bandis model [79-81] as: $JRC_{i,j,k(n)}^{(l)} \log\left(JCS_{i,j,k}/\sigma n_{i,j,k(n)}^{(l)}\right)$.

In order to account for dilatancy reduction upon shear displacement reversal, a local reference system, $\left(O,\chi,\zeta\right)_{i,j,k}$ with unit vectors $\chi_{i,j,k}$ and $\zeta_{i,j,k}$, is introduced on the constraint plane in contact with $P_{i,j,k}$. $O_{i,j,k}$ is the point at which $P_{i,j,k}$ enters C, and

34

$\chi_{i,j,k}$ and $\zeta_{i,j,k}$ are orthogonal unit vectors along which *JRC* has been measured. The shear displacement is then accumulated along the two local axes, e.g.,:

$$u_{\chi,P_{i,j,k}(n)}^{(l)} = \sum_{ll<l; nn<n} \chi_{i,j,k}{}^{T} \delta \mathbf{u}_{P_{i,j,k}(nn)}^{(ll)} \tag{2.70}$$

Per Barton-Bandis model, the mobilized *JRC* in, say, the $\chi_{i,j,k}$-direction is a function of the ratio $u_{\chi,P_{i,j,k}(n)}^{(l)} / \delta_{peak,i,j,k}$ (e.g., Figure 12 in [81]), where the peak displacement, $\delta_{peak,i,j,k}$, is given in Equation (2.56):

Sign reversal is then detected using flags of the type:

$$flag_{\chi,i,j,k(n)}^{(l)} = \begin{cases} 1 & IF \ \delta_{\chi,i,j,k(n)}^{(l)} \delta \mathbf{u}_{P_{i,j,k}(n)}^{(l)} \cdot \chi_{i,j,k} \geq 0 \\ -1 & IF \ \delta_{\chi,i,j,k(n)}^{(l)} \delta \mathbf{u}_{P_{i,j,k}(n)}^{(l)} \cdot \chi_{i,j,k} < 0 \end{cases} \tag{2.71}$$

and the iterative normal displacement is:

$$\delta \mathbf{u}_{d,P_{i,j,k}(n)}^{(l)} = -\mathbf{n}_{c,i,j,k} \left[\begin{array}{l} \tan\left(JRC_{i,j,k,\chi(n)}^{(l)} \log \dfrac{JCS_{i,j,k}}{\sigma n_{i,j,k(n)}^{(l)}} \right) \left(flag_{\chi,i,j,k(n)}^{(l)} \left| \chi_{i,j,k}{}^{T} \delta \mathbf{u}_{P_{i,j,k}(n)}^{(l)} \right| \right) + \\ \tan\left(JRC_{i,j,k,\zeta(n)}^{(l)} \log \dfrac{JCS_{i,j,k}}{\sigma n_{i,j,k(n)}^{(l)}} \right) \left(flag_{\zeta,i,j,k(n)}^{(l)} \left| \zeta_{i,j,k}{}^{T} \delta \mathbf{u}_{P_{i,j,k}(n)}^{(l)} \right| \right) \end{array} \right] \tag{2.72}$$

If a sensor point enters C, i.e. if $P_{i,j,k(n)}^{(l-1)} \notin$ and $P_{i,j,k(n)}^{(l)} \in C$, then recall that $\bar{d}_{i,j,k}$ is the distance traveled in C. The normal displacement increment is then obtained by multiplying Equation (2.72) by $\bar{d}_{i,j,k} / \left\| \delta \mathbf{u}_{P_{i,j,k}(n)}^{(l)} \right\|$.

Although dilatancy *per se* does not cause any force, and thus any stiffness component, it does add a term to the expression of the displacement, which is now equal to $\mathbf{u}_{P_{i,j,k}}* = \mathbf{u}_{P_{i,j,k}} + \delta \mathbf{u}_{d,P_{i,j,k}}$ where $\mathbf{u}_{P_{i,j,k}}$ is given in Equation (2.5). As a consequence, using Equation (2.9) the derivative $\partial \mathbf{u}_{P_{i,j,k}} / \partial \mathbf{u}$ in Equations (2.64) and (2.66) is replaced by:

$$\frac{\partial \mathbf{u}_{P_{i,j,k}}*}{\partial \mathbf{u}} = \mathbf{D}_P(\theta) + \frac{\partial \delta \mathbf{u}_{d,P_{i,j,k}}}{\partial \mathbf{u}} = \mathbf{D}_P(\theta) + \frac{\partial \delta \mathbf{u}_{d,P_{i,j,k}}}{\partial \mathbf{u}_{P_{i,j,k}}} \frac{\partial \mathbf{u}_{P_{i,j,k}}}{\partial \mathbf{u}} = \left(\mathbf{I} + \frac{\partial \delta \mathbf{u}_{d,P_{i,j,k}}}{\partial \mathbf{u}_{P_{i,j,k}}} \right) \mathbf{D}_P(\theta) \quad (2.73)$$

Let us now consider the derivative in Equation (2.73) for the component in the χ_i-direction:

$$\frac{\partial \delta \mathbf{u}_{d,P_{i,j,k}}}{\partial \mathbf{u}_{P_{i,j,k}}} = -SIGN\left(\boldsymbol{\chi}_i^T \delta \mathbf{u}_{P_{i,j,k}}\right) \tan\left(JRC_{i,j,k,\chi} \log \frac{JCS_{i,j,k}}{\sigma n_{i,j,k}}\right) flag_{\chi,i,j,k} \mathbf{n}_{c,i,j,k} \boldsymbol{\chi}_{i,j,k}^T$$

$$- \mathbf{n}_{c,i,j,k} \frac{\partial}{\partial JRC}\left[\tan\left(JRC_{i,j,k,\chi} \log \frac{JCS_{i,j,k}}{\sigma n_{i,j,k}}\right)\right] \frac{\partial JRC_{i,\chi}}{\partial \mathbf{u}_{P_{i,j,k}}} \left(flag_{\chi,i,j,k} \left|\boldsymbol{\chi}_{i,j,k}^T \delta \mathbf{u}_{P_{i,j,k}}\right|\right)$$

$$- \mathbf{n}_{c,i,j,k} \frac{\partial}{\partial \sigma n_{i,j,k}}\left[\tan\left(JRC_{i,j,k,\chi} \log \frac{JCS_{i,j,k}}{\sigma n_{i,j,k}}\right)\right] \frac{\partial \sigma n_{i,j,k}}{\partial \mathbf{u}_{P_{i,j,k}}} \left(flag_{\chi,i,j,k} \left|\boldsymbol{\chi}_{i,j,k}^T \delta \mathbf{u}_{P_{i,j,k}}\right|\right)$$

(2.74)

Since:

$$\frac{\partial JRC_{i,j,k,\chi}}{\partial \mathbf{u}_{P_{i,j,k}}} = \frac{\partial JRC_{i,j,k,\chi}}{\partial u_{\chi,P_{i,j,k}}} \frac{\partial u_{\chi,P_{i,j,k}}}{\partial \mathbf{u}_{P_{i,j,k}}} = \frac{\partial JRC_{i,j,k,\chi}}{\partial u_{\chi,P_{i,j,k}}} \boldsymbol{\chi}_{i,j,k}^T,$$

(2.75)

the second term is equal to:

$$- flag_{\chi,i,j,k} \cos^{-2}\left(JRC \log \frac{JCS_{i,j,k}}{\sigma n_{i,j,k}}\right) \log \frac{JCS_{i,j,k}}{\sigma n_{i,j,k}} \left|\boldsymbol{\chi}_{i,j,k}^T \delta \mathbf{u}_{P_{i,j,k}(n)}^{(l)}\right| \frac{\partial JRC_{i,j,k,\chi}}{\partial u_{\chi,P_{i,j,k}}} \mathbf{n}_{c,i,j,k} \boldsymbol{\chi}_{i,j,k}^T \quad (2.76)$$

In the third term:

$$\frac{\partial}{\partial \sigma n_{i,j,k}}\left[\tan\left(JRC_{i,j,k,\chi} \log \frac{JCS_{i,j,k}}{\sigma n_{i,j,k}}\right)\right] = \frac{1}{\cos^2\left(JRC_{i,j,k} \log \frac{JCS_{i,j,k}}{\sigma n_{i,j,k}}\right)} JRC_{i,j,k,\chi} \frac{\sigma n_{i,j,k}}{JCS_{i,j,k}} \frac{1}{\ln(10)}\left(-\frac{JCS_{i,j,k}}{\sigma n_{i,j,k}^2}\right)$$

$$= -\frac{JRC_{i,j,k,\chi}}{\sigma n_{i,j,k} \ln(10) \cos^2\left(JRC_{i,j,k,\chi} \log \frac{JCS_{i,j,k}}{\sigma n_{i,j,k}}\right)}$$

(2.77)

and using Equations (2.46) and (2.77) into Equation (2.74), one finally obtains that the third term in Equation (2.74) is equal to:

$$- flag_{\chi,i,j,k} \frac{JRC_{i,j,k,\chi}}{\sigma n_{i,j,k} \ln(10) \cos^2\left(JRC_{i,j,k,\chi} \log \frac{JCS_{i,j,k}}{\sigma n_{i,j,k}}\right)} \frac{\partial \sigma n_{i,j,k}}{\partial u_{n,P_{i,j,k}}} \left|\boldsymbol{\chi}_{i,j,k}^T \delta \mathbf{u}_{P_{i,j,k}}\right| \mathbf{n}_{c,i,j,k} \mathbf{n}_{c,i,j,k}^T \quad (2.78)$$

While the third term contributes a symmetric rank-one modification to the stiffness matrix, the first two terms yield non-symmetric rank-one modifications to the stiffness matrix. To exemplify, consider a parallelepiped (constrained along its vertical faces) that translates downwards, and in which $\mathbf{n}_{c,i,j,k} = \mathbf{e}_x$ (horizontal) and $\boldsymbol{\chi}_i = \mathbf{e}_z$ (vertical up). The net effect of the dilatancy first two terms is to add to the third column of $\partial\mathbf{v}\left(\mathbf{u}_{P_{i,j,k}}\right)/\partial\mathbf{u}_{P_{i,j,k}}$ in Equations (2.64) and (2.66) the first column of $\partial\mathbf{v}\left(\mathbf{u}_{P_{i,j,k}}\right)/\partial\mathbf{u}_{P_{i,j,k}}$ multiplied by an appropriate scalar. Dilatancy couples with normal stiffness because from Table 1, third column and second row, the added term to $\partial\mathbf{v}\left(\mathbf{u}_{P_{i,j,k}}\right)/\partial\mathbf{u}_{P_{i,j,k}}$ is proportional to:

$$\mathbf{e}_x\mathbf{e}_x^{T}\mathbf{e}_x\mathbf{e}_z^{T} = \begin{pmatrix} 0 & 0 & 1 \\ 0 & 0 & 0 \\ 0 & 0 & 0 \end{pmatrix} \tag{2.79}$$

whereas dilatancy does not couple with shear stiffness (Table 2.1, third column and third row) because $\left(\mathbf{I} - \mathbf{e}_x\mathbf{e}_x^{T}\right)\mathbf{e}_x\mathbf{e}_z^{T} = \mathbf{0}$.

Per Equation (2.79), a monotonic downward vertical translation causes the first term in Equation (2.74) to apply a positive force in the positive x-direction, i.e. toward the inside of the block. The second term applies a positive (negative, resp.) force in the positive x-direction if JRC is increasing (decreasing, resp.) with $u_{\chi,P_{i,j,k}}$, i.e. if $u_{\chi,P_{i,j,k}} \leq u_{\chi,peak}$ ($u_{\chi,P_{i,j,k}} > u_{\chi,peak}$, resp.). If the vertical translation is reversed, dilatancy forces change sign: this does not cause the stiffness matrix to become negative definite because the first two terms in Equation (2.74) contribute only off-diagonal terms, and the third term is generally small in comparison with the other terms (except in the vicinity of critical points).

In general, dilatancy introduces a non-symmetric rank-one modification because a displacement in the $\chi_{i,j,k}$-direction creates a displacement (and then a stiffness change) in the $\mathbf{n}_{c,i,j,k}$-direction but the opposite does not necessarily occur. Indeed, there will be

37

symmetry if and only if a constraint face also occurs with normal $\chi_{i,j,k}$, and the point in contact with this face has the same *JRC*, *JCS*, and normal stress as $P_{i,j,k}$.

2.12 INITIAL STRESSES

The initial state of stress acting on the rock mass can be easily included in the calculations of the first stage as follows. Let $\boldsymbol{\sigma}$ be the stress tensor of the initial state of stress, and let $\mathbf{n}_{c,i}$ be the normal to the constraint face C_i that bounds the block. The normal and shear stresses on C_i are, respectively:

$$\sigma n_i = \mathbf{n}_{c,i}^T \cdot \boldsymbol{\sigma} \cdot \mathbf{n}_{c,i} \tag{2.80}$$

$$\tau = \left\| \left(\sigma n_i \cdot \mathbf{I} - \boldsymbol{\sigma} \right) \cdot \mathbf{n}_{c,i} \right\| \tag{2.81}$$

The normal displacement length, $u_{n,i}$, that causes the normal stress σn_i is found by solving the equation:

$$\sigma n \left(u_{n,i} \right) = \sigma n_i, \tag{2.82}$$

where $\sigma n \left(u_{n,i} \right)$ is given in Equation (2.42). The normal displacement vector that creates the initial normal stress is then: $\mathbf{u}_{n,i} = u_{n,i} \mathbf{n}_{c,i}$.

As for the shear displacement, its unit vector is:

$$\mathbf{t} = \left(\sigma n_i \mathbf{I} - \boldsymbol{\sigma} \right) \mathbf{n}_{c,i} / \tau \tag{2.83}$$

If $\tau \leq \tau_{max}$ (Equation (2.53)), the shear displacement associated with the shear stress is equal to:

$$u_{s,i} = \tau / k_{s,i}, \tag{2.84}$$

where $k_{s,i}$ is the shear stiffness calculated with Equations (2.54) or (2.55) for a normal stress equal to σn_i. The shear displacement that creates the initial shear stress is then equal to $\mathbf{u}_{s,i} = -u_{s,i} \mathbf{t}$.

If, on the other hand, $\tau > \tau_{max}$, the *i*-th discontinuity can not take a shear stress equal to τ, and the shear displacement is equal to $\mathbf{u}_{s,i} = -\tau_{max} \mathbf{t}$.

Finally, the initial state of stress is imposed by translating the plane containing C_i by the vector $\mathbf{u}_{n,i} + \mathbf{u}_{s,i}$. Once all constraint planes bounding B have been translated in this way, constraint faces C_i are determined by taking the intersections of the translated planes.

2.13 FAILURE MODES AND FACTOR OF SAFETY

2.13.1 Limit points and static instability

While marching along the equilibrium path, critical points are detected by looking at the eigenvalues of the stiffness matrix. If a diagonal element in the LU decomposition is equal (or close) to zero, eigenvalues and eigenvectors of the stiffness matrix, $\mathbf{z}_i$, are calculated to determine limit points and static instability.

Two cases may occur:

- $\mathbf{z}_i^T \mathbf{F}_{a(n)}^{(l)} \neq \mathbf{0}$: this is a limit point and the active force cannot be incremented further. \hfill (2.85)

- $\mathbf{z}_i^T \mathbf{F}_{a(n)}^{(l)} = \mathbf{0}$: this is a static bifurcation point. \hfill (2.86)

2.13.1.1 Limit point

When the first limit point is reached along the equilibrium path of the block, the active force cannot be incremented further, and the unbalanced resultant force applied to the block is $\left(1 - \lambda_{(n)}\right)\mathbf{F}_a$, where n is the last converged increment, and $\mathbf{F}_a$ is evaluated at the n-th increment. The dynamic failure mode, i.e. the possible motion of the body over an infinitesimal interval of time, is calculated based on small rotation theory by imposing no further interpenetration at the constraints during the dynamic failure mode, and by assuming a rigid-perfectly plastic behavior of the discontinuities to shear displacements. In order to determine the dynamic failure mode, the unconstrained motion of the block is first calculated using Equation (2.19) as (we are not interested in its magnitude)

$$\bar{\mathbf{u}}_u = \left(1 - \lambda_{(n)}\right)\mathbf{M}^{-1}\mathbf{F}_a \hfill (2.87)$$

39

This allows one to detect which of the sensor points are to be constrained. Recall that a unilateral constraint constraints a body's motion only if it is active, i.e. only if there is contact across that constraint. Therefore, the search is limited to the sensor points, $P_{i,j,k}$, that are in C at the n-th increment. For each of these sensor points, the unconstrained displacement is given by Equation (2.18):

$$\overline{\mathbf{u}}_{u,P_{i,j,k}} = \left(\ddot{\overline{\mathbf{u}}}_{u,G} + \dot{\boldsymbol{\omega}}_u \times \mathbf{GP}_{P_{i,j,k}} \right) = \left(\mathbf{I}_{3\times3}, -\mathbf{S}\left(\mathbf{R}_{(n)} \cdot \left(\mathbf{GP}_{P_{i,j,k}} \right)_{(0)} \right) \right) \cdot \overline{\mathbf{u}}_u \qquad (2.88)$$

Let $C_h \in \partial C$ be the active polygon constraint at $P_{i,j,k}$. Then C_h constraints the possible motion of B if and only if $\overline{\mathbf{u}}_{u,P_{i,j,k}}$ is directed into C, i.e.

$$\overline{\mathbf{u}}_{u,P_{i,j,k}} \cdot \mathbf{n}_{c,h} < 0 \ \Rightarrow \mathbf{n}_{c,h}^T \cdot \left(\mathbf{I}_{3\times3}, -\mathbf{S}\left(\mathbf{R}_{(n)} \cdot \left(\mathbf{GP}_{P_{i,j,k}} \right)_{(0)} \right) \right) \cdot \overline{\mathbf{u}} < 0 \qquad (2.89)$$

If C_h constraints the possible motion of B, then an equality constraint must be imposed on the motion of B, $\overline{\mathbf{u}}$, so that $P_{i,j,k}$ can only move parallel to C_h

$$\overline{\mathbf{u}}_{P_{i,j,k}} \cdot \mathbf{n}_{c,h} = 0 \ \Rightarrow \mathbf{n}_{c,h}^T \cdot \left(\mathbf{I}_{3\times3}, -\mathbf{S}\left(\mathbf{R}_{(n)} \cdot \left(\mathbf{GP}_{P_{i,j,k}} \right)_{(0)} \right) \right) \cdot \overline{\mathbf{u}} = 0 \qquad (2.90)$$

If, in addition, $P_{i,j,k}$ has not been sheared off at the n-th increment, then $P_{i,j,k}$ cannot move parallel to C_h either, and thus $P_{i,j,k}$ is fixed in space. Equation (2.90) must be replaced by the three conditions

$$\mathbf{e}_l^T \cdot \left(\mathbf{I}_{3\times3}, -\mathbf{S}\left(\mathbf{R}_{(n)} \cdot \left(\mathbf{GP}_{P_{i,j,k}} \right)_{(0)} \right) \right) \cdot \overline{\mathbf{u}} = 0, \quad l = x, y, z \qquad (2.91)$$

Constraints (2.90) and (2.91) are linear in $\overline{\mathbf{u}}$, and can thus be arranged in matrix form $\mathbf{A} \cdot \overline{\mathbf{u}} = \mathbf{0}$, where the rows of matrix $\mathbf{A}$ are either $\mathbf{n}_{c,h}^T \cdot \left(\mathbf{I}_{3\times3}, -\mathbf{S}\left(\mathbf{R}_{(n)} \cdot \left(\mathbf{GP} \right)_{(0)} \right) \right)$ or $\mathbf{e}_l^T \cdot \left(\mathbf{I}_{3\times3}, -\mathbf{S}\left(\mathbf{R}_{(n)} \cdot \left(\mathbf{GP}_{P_{i,j,k}} \right)_{(0)} \right) \right)$, $l = x, y, z$. Using the General Principle of Mechanics [50], the constrained acceleration (mode of failure) can be obtained in closed-form (Equation (2.23) with $\mathbf{C} = \mathbf{0}$)

$$\ddot{\overline{\mathbf{u}}} = \mathbf{a} - \mathbf{M}^{-1/2} \cdot \mathbf{B}^+ \cdot \mathbf{A} \cdot \mathbf{a}, \qquad (2.92)$$

where a superscript "+" indicates the Moore-Penrose generalized inverse of a matrix [54], $\mathbf{a} = \mathbf{M}^{-1} \cdot \mathbf{F}_a$, and $\mathbf{B} = \mathbf{A} \cdot \mathbf{M}^{-1/2}$. The mode of failure can be visualized by superimposing

the displacement field calculated using Equation (2.18) with $\ddot{\mathbf{u}}$ from Equation (2.92) upon the last converged increment configuration. This procedure can be seen as the generalization of Sagaseta's for two-dimensional blocks [83].

On the other hand, the static mode(s) of failure is (are) associated with the null space of the stiffness matrix at the first limit point along the equilibrium path. More specifically, if $\mathbf{z}$ is in the null space of this stiffness matrix, then its static failure mode is $\mathbf{z}* = \mathbf{z} \cdot Sign\left(\mathbf{z}^T \mathbf{F}\right)$. In general, the static failure modes are different from the dynamic failure modes.

The factor of safety is the ratio between the stabilizing forces and the driving forces at limiting equilibrium. It is thus the maximum ratio between the projection of the constraint forces on $\mathbf{z}*$ and the projection of the active forces on $\mathbf{z}*$ for which there is equilibrium, i.e. $FS = \max\left| \mathbf{z}*^T \mathbf{F}_c / \mathbf{z}*^T \mathbf{F}_a \right|$. Since, during a stage, the active force is proportional to the control parameter, $\left| \mathbf{z}*^T \mathbf{F}_c / \mathbf{z}*^T \mathbf{F}_a \right| = \lambda$, and $\lambda_{(n)}$ at the last converged increment is equal to the factor of safety for the block. As a consequence, the calculation of the safety factor comes with no overhead, whereas other codes such as 3-DEC, BSM3D and 3D-DDA require time-consuming trial and error calculations using the reduction of the strength parameters (e.g., [17]). However, whenever failure is not caused by limited strength (e.g., when the block fails in a pure rotational mode, or in a more complex roto-translational mode), the reduction of the strength parameters cannot yield the factor of safety, but, rather, it yields an incorrect failure mode (e.g., sliding rather than toppling). On the other hand, the presented algorithm always unambiguously yields the correct factor of safety and associated failure mode(s).

If the US Load and Resistance Factor Design (LRFD) or European partial factor design (Eurocodes) are used, then the appropriate factors are applied directly to the input data, and the block is safe if the control parameter is equal to or greater than one.

41

2.13.1.2   *Bifurcation point*

At a bifurcation point, the equilibrium path branches out in as many branches as the dimension of the null space of the stiffness matrix. Collect these normalized eigenvectors in set T. The branch for $\mathbf{z}_i \in T$ is followed by using a predictor equal to $\Delta\mathbf{u}_{(n+1)}^{(0)} = step_0 \cdot \mathbf{z}_i$ and $\Delta\lambda_{(n+1)}^{(0)} = 0$. The solution is then corrected by following the Newton-Raphson algorithm in Section 2.5.

Modes $\mathbf{z}_i \in T$ are associated with rigid-body motions orthogonal to the original path. As illustrated in Example 4 below, the original equilibrium path is also of interest. The original equilibrium path is followed by adding a "spring" aligned with each eigenvector in T. This is effected by adding to the stiffness matrix the rank-one modifications $k_i\mathbf{z}_i\mathbf{z}_i^{\mathrm{T}}$, where k_i is taken as 5% of the largest eigenvalue of $\mathbf{K}$; if this is equal to zero, then the block is unconstrained, and it is considered as failed. Notice that a displacement parallel to the applied force does zero work with these added springs because Equation (2.86) entails that $\mathbf{F}_{a(n)}^{(l)T}\mathbf{z}_i\mathbf{z}_i^{T}\mathbf{F}_{a(n)}^{(l)} = \mathbf{0}$.

If the block has not failed, then the equilibrium paths are followed until a limit point is encountered (Section 2.13.1.1) or an upper limit on the control parameter is reached.

2.13.2 Dynamic instability

Consider the neighborhood of a point in the equilibrium path. In this neighborhood, Equation (2.19) applies with $\mathbf{F} = (\mathbf{f}_c, \mathbf{m}_{G,c})^T = -\mathbf{K}$, and the ODE for the motion of the unforced block is:

$$\mathbf{M}_{(n)}^{(l)}\ddot{\overline{\mathbf{u}}} + \mathbf{K}_{(n)}^{(l)}\overline{\mathbf{u}} = \mathbf{0} \tag{2.93}$$

Using an eigenmodal expansion for the solution, $\overline{\mathbf{u}} = \sum_i \mathbf{z}_i e^{p_i t}$, one recovers the eigenproblem:

$$\left(\mathbf{K}_{(n)}^{(l)} + \mathbf{M}_{(n)}^{(l)}p_i^{\,2}\right)\mathbf{z}_i = \mathbf{0} \tag{2.94}$$

Since **K** is real and is not symmetric (large rotations, applied non-conservative forces such as water pressure), and **M** is real and positive definite, eigenvalues p_i^2 can be either real or complex; if the later, they occur in conjugate pairs. In all cases run by the author, no numerical problem arose in obtaining eigenvalues p_i^2. Three cases are distinguished:

- p_i^2 is real and positive: The motion of the block is unbounded in time, and thus the block is considered as failed (dynamic instability by divergence).

- p_i^2 is real and negative: The unforced motion of the block is harmonic, the block is stable, and the predictor-corrector algorithm continues along the equilibrium path.

- p_i^2 is complex: The unforced motion of the block is oscillatory and unbounded, and thus the block is considered as failed (dynamic instability by flutter). Since these eigenvalues occur in pairs, energy is transferred from one eigenmode to another.

2.14 SUMMARY AND CONCLUSIONS

Tonon's [1] incremental-iterative algorithm described in details. The method is to analyze general failure modes of rock blocks subject to generic forces, including non-conservative forces such as water forces. The block interacts with the surrounding constraint space using a finite number of sensor points. Consistent stiffness matrices were developed that fully exploit the quadratic convergence of the adopted Newton–Raphson iterative scheme. The algorithm takes into account large block displacements and rotations, which together with non-conservative forces make the stiffness matrix non-symmetric.

Also included in the algorithm are fracture dilatancy and *in situ* stress. Dilatancy acts at a kinematic level by adding a normal component to an active sensor point's displacement. As a consequence, dilatancy introduces non-symmetric rank-one modifications to the stiffness matrix.

43

Progressive failure is captured by the algorithm, which has proven capable of detecting numerically challenging failure modes, such as rotations about only one point.

All possible failure modes can be automatically detected along the block's equilibrium path; they may originate from a limit point or from dynamic instability (divergence or flutter); equilibrium paths emanating from bifurcation points are followed by the algorithm.

The algorithm identifies both static and dynamic failure modes. Static analyses (including limiting equilibrium) do not take into account the block's inertia properties, which may lead to detecting an incorrect failure mode. The difference between static and dynamic failure modes is relevant to slow *versus* rapid removal of constraints (e.g. tunnel boring machine *versus* drill- and-blast tunnel excavation), and is the subject of current investigation. Any real block is created by the removal of constraints: the algorithm simulates this natural process, and allows one to investigate the impact of how blocks are constrained on stability and factor of safety.

The calculation of the factor of safety comes with no overhead, and does not require trial and error model runs using the reduction of the strength parameters, which may even lead to erroneous failure modes.

Rock blocks that are typically thought of reaching equilibrium by translation actually rotate about their centroid because the reaction forces create a non-zero moment about the centroid; this is the case of 2-plane wedges subjected to their own weight. The equilibrium path of a rock block that undergoes slumping failure must first pass through a bifurcation point, unless the block is laterally constrained. Rock blocks subjected to water forces (or other non-conservative forces) may undergo flutter failure before reaching a limit point. Thus, existing methods (including limiting equilibrium) may overestimate the safety of a rock block when water forces are important (e.g. dam foundations, rock scour at bridge piers and under dam jets).

CHAPTER 3:   CONSTITUTIVE MODEL FOR ROCK FRACTURES: REVISITING BARTON'S EMPIRICAL MODEL

3.1   INTRODUCTION

In near-surface geotechnical works (for instance, dam foundations, power plants, underground caverns, and slopes), the mechanical behavior of the rock masses is influenced more by the fractures than by the intact rock. Therefore, algebraic calculations and numerical simulations for the mechanical behavior of fractured rock masses require the constitutive law of rock fractures. However, the characteristics of intact rock are better known; for example, the Suggested Methods of the International Society of Rock Mechanics [84] define mathematically the Young's modulus for uniaxial compressive tests but leave out any calculations for the shear and normal stiffnesses of fractures [85].

In the study of the behavior of a single rock fracture under different loading conditions, rock fractures are divided into two main categories: filled and unfilled fractures. The shear behavior of unfilled fractures is a function of the roughness and compressive strength of the fracture [22] walls, while in the case of filled fractures, the physical and mineralogical properties of the material separating the fracture walls are of primary concern [22]. In this chapter, the constitutive models of unfilled rock fractures with dilatancy and surface degradation are investigated.

There are two main approaches to the quantitative description of the mechanical properties of rock fractures: (a) the theoretical approach, which adopts known theories (e.g. plasticity, contact theory, etc.) to simulate the observed behavior (e.g. [86-90]); (b) the empirical approach, in which wide-spanning physical data is analyzed to derive correlations between variables of influence and models are formulated according to observed behavior (e.g. [22, 79, 81, 91-93]). Other efforts combine the above two approaches (e.g. [94]) or treat the problem analytically (e.g. [95]) [96].

Several empirical and theoretical constitutive models were developed by Ladanyi and Archambault [91], Goodman [97], Barton and Choubey [22], Plesha [87], Amadei and Saeb [98], Jing *et al.* [99, 100], Qiu *et al.* [101], etc. Patton [102] proposed bilinear

models of saw-tooth fractures. Plesha [87] idealized Patton's saw-tooth type asperities and developed a constitutive model based on the classical theory of plasticity. Huang *et al.* [103] verified Plesha's exponential degradation law through a series of experiments for fractures having saw-tooth type asperities. Qiu *et al.* [101] revised Plesha's model by idealizing the sinusoidal asperities, but it was less practical due to the complexity of constitutive equation. Saeb [104] modified the failure criterion of Ladanyi and Archmbault [91]. Gens *et al.* [105] proposed an elastoplastic constitutive law for describing the three-dimensional mechanical behavior of rock fractures. Desai and Fishman [106] proposed a constitutive model based on the theory of plasticity for characterizing the mechanical response of simulated fractures under monotonic loading, unloading and reverse loading. Wang *et al.* [107] proposed an elliptic yield function based on associated flow rule to predict the behavior of rock interfaces and fractures. By using the results of a series of experimental work on sandstone, Leichnitz [108] developed a constitutive law for rock fractures that also allows consideration for the non-linearity of the material behavior. Kana *et al.* [109] suggested the interlock-friction model for dynamic shear response; the importance of second order asperities on the dynamic shear behavior was explained by Fox *et al.* [110]. Samadhiya *et al.* [111] introduced a generalized formulation of a three-dimensional joint/interface element to account for dilatancy, roughness, and undulating surface of discontinyities.

The scale effect on fracture shear strength has been studied by many authors, such as Pratt *et al.* [112], Barton and Choubey [22], Bandis [113], Barton and Bandis [114], Barton [115, 116], Hencher *et al.* [117], Hencher and Richard [118, 119], Patton [102], Cording [120, 121], McMahon [122], Lee [123], and OH [124]. In addition, anisotropic shear behavior of rock fractures was considered by some researchers, such as Huang and Doong [125], Jing *et al.* [126] Grasselli *et al.* [127, 128], and Kulatilake *et al.* [129, 130].

Most of the constitutive models were only developed for monotonic shear loading without considering surface roughness degradation. Among these models, Barton's empirical model has widely been used because it is easy to apply and includes several important factors of fracture properties.

In this chapter, Section 3.2 recalls the essential aspects of the most common models for rock fractures including Barton-Bandis and Goodman's empirical models. Section 3.3 addresses some of the inconsistencies of Barton's model in predicting the peak shear displacement, post-peak shear strength, dilation, and surface degradation during unloading and reloading. A database of results from direct shear tests available in the literature was assembled and analyzed. Modifications were made to Barton's original model in order to address some of its weaknesses, and an empirical equation is introduced to predict peak shear displacement of rock fractures. Unlike Barton's model, the proposed peak shear displacement relationship depends on normal stress, and in the revised model, the post-peak mobilized Fracture Roughness Coefficient (*JRC*) is given by a power law, instead of employing Barton's table. This new empirical equation for post-peak mobilized *JRC* works for all ranges of displacements and never gives unusual zero or negative values, even at very large displacements. Moreover, the modified model can predict compression (negative) dilatancy at small shear displacements. Furthermore, the model suggested here for unloading and reloading behaviors takes into account 18 cyclic direct shear tests including the one that Barton used. Section 3.3 shows that the revised model not only addresses some of the weaknesses of Barton's model but also works better in predicting the behavior of rock fractures in the collected data of direct shear tests. Section 3.4 summaries the results of experimental studies on anisotropic dilatant behavior of rock fractures found in the literature. In Section 4, a model is proposed to predict the magnitude of *JRC* in a given direction.

3.2 CONSTITUTIVE MODELS FOR ROCK FRACTURES

3.2.1 The Shear Strength of Rock Fractures

Based on Coulomb's linear relationship [25], the shear strength of rock fractures can be expressed as follows:

$$\tau = c + \sigma_n \cdot \tan(\phi), \tag{3.1}$$

47

in which τ is the peak shear strength under a normal stress of σ_n; c is cohesion and ϕ is the friction angle.

Byerlee [131] suggested that the frictional strength of faults developed through intact rock may be the same for all rocks, independent of lithology. Barton [132] showed that artificial faults and tension fractures in a variety of rocks have the same peak shear strength when the effective normal stress is of the same order or greater than the unconfined compression strength of the rocks. However, under low effective normal stresses, the shear strength of fractures can vary within relatively wide range.

Many researchers have attempted to predict the shear strength of non-planar rock fractures based on their dilatant behavior. Jaeger [133], Krsmanovic and Langof [134], Lane and Heck [135], Patton [136] and Byerlee [131] are among those who first obtained curved relationships between the shear strength of the rock fractures and the normal stress. Patton [102, 136] and Goldstein *et al.* [137] used the following equation, basically developed by Newland and Alley [138] and Rowe *et al.* [139] for granular material, to represent the shear strength of irregular rock surfaces at low normal stresses:

$$\tau = \sigma_n \cdot \tan(\phi_b + i), \tag{3.2}$$

in which i and ϕ_b are the effective roughness and the base friction angle, respectively.

Although Patton [136] initially suggested that only first-order irregularities would contribute to the shear strength of fractures beneath natural slopes, Patton and Deere [140] later emphasized that all scales of roughness are likely to be important. At high normal stresses, when most irregularities would be sheared off, it was assumed that the Coulomb relationship would be valid.

The recognition that the shear strength of an irregular rock surface can be zero at zero normal stress represents a major improvement over the earlier assumption of linear (c and ϕ) properties. Using a cohesion intercept for rock fractures is inherently dangerous, even if the extrapolation is made from the mean effective normal stress level appropriate to the particular engineering problem. The Coulomb concept of cohesion and friction angle is really no more than a simple mathematical convenience since cohesion is not a constant [132].

3.2.1.1 Barton's failure criterion

Barton [21] suggested the following empirical law of friction for the shear strength of rock fractures:

$$\tau = \sigma_n \cdot \tan\left(JRC \cdot \log_{10}\left(\frac{JCS}{\sigma_n}\right) + \phi_r \right)$$

(3.3)

The residual friction angle, ϕ_r, (which is equal to basic friction angle, ϕ_b, for unweathered rock fractures) can be obtained from residual shear tests on flat unweathered rock surfaces. The basic friction angle of the majority of unweathered rock surfaces ranges from 25° to 35°, at least at medium stress levels [92, 136, 141-145]. The residual friction angle of weathered rock fractures can be estimated based on the Schmidt rebound on dry unweathered sawn surfaces and wet fracture surfaces as follows:

$$\phi_r = (\phi_b - 20°) + 20 \times \left(\frac{r}{R}\right),$$

(3.4)

where ϕ_b is basic friction angle of dry unweathered sawn fracture; R is Schmidt rebound on dry unweathered sawn surface; r is Schmidt rebound on wet fracture surface.

The fracture roughness coefficient (JRC) represents a sliding scale of roughness varying from approximately 20 to 0, from the roughest to the smoothest rock surfaces. JRC reduces with the increasing size of the sample [115]:

$$JRC_n = JRC_0 \cdot \left(\frac{L_n}{L_0}\right)^{-0.02 JRC_0},$$

(3.5)

where JRC_n and JRC_0 are fracture roughness coefficients of samples with lengths of L_n and L_0, respectively.

The joint wall compressive strength (JCS) at low stress levels is equal to the unconfined compression strength σ_c of the rock if the fracture is unweathered, but may reduce to approximately $\sigma_c/4$ for weathered fractures [92]. The Schmidt hammer can be employed to measure the JCS values of weathered rock fractures (Miller's method

[146]). However, Barton [132] suggested that in view of the safety requirements of rock engineering structures, the value of $\left(JRC \cdot \log_{10}\left(JCS/\sigma_n\right)+\phi_b\right)$ should be limited to 70°.

Due to the effect of confinement on the compressive strength of rock asperities, the measured shear strength at high normal stress levels is always appreciably higher than the predicted value using Equation (3.3) [132]. At low stress levels, appropriate to most rock engineering problems, the contact area between fracture walls is extremely small [147]; therefore, the strength of asperities can be considered as the unconfined strength. However, as the level of σ_n approaches the value of σ_c, the area of contact across the fracture increases, probably as a result of elastic displacement and possible local failure of any mismatching asperities [132]. The increasing contact area in turn causes the compressive strength of the asperities themselves to increase due to the more effective confinement.

At high stress levels, the JCS value appearing in Equation (3.3) should be considered to be the confined compression strength of the rock, which is equal to the differential stress $(\sigma_1 - \sigma_3)$, where σ_1 is the axial stress at failure and σ_3 is the effective confining pressure [132]. Empirical relationships between the compressive strength of intact rock as a function of confining pressure are proposed by variety of researchers; one of the best one suggested by Bieniawski [148] is as follows:

$$\sigma_1 = k \cdot \sigma_c \cdot \left(\frac{\sigma_3}{\sigma_c}\right)^A + \sigma_c, \tag{3.6}$$

where A and K are constant.

The joint compressive strength reduces with increasing size of the sample [115]:

$$JCS_n = JCS_0 \cdot \left(\frac{L_n}{L_0}\right)^{-0.03 JRC_0}, \tag{3.7}$$

where JCS_n and JCS_0 are joint compressive strengths of samples with lengths of L_n and L_0, respectively.

50

3.2.1.2 Saeb's model

Saeb [104] modified the failure criterion of Ladanyi and Archmbault [91] which is now expressed as follows:

$$\tau_p = \sigma_n \cdot \tan(\phi_u + i) \cdot (1 - a_s) + a_s s_r,$$ (3.8)

where a_s is the proportion of total fracture area sheared through the asperities and can be obtained using the following equation [149]:

$$a_s = 1 - \left(1 - \frac{\sigma_n}{\sigma_c}\right)^{k_1},$$ (3.9)

in which K_1 is an empirical constant; σ_c is the unconfined compressive strength of intact rock. $(1 - a_s)$ is the proportion of total fracture area on which sliding takes place; ϕ_u is the angle of friction for sliding along the asperities; s_r represents the shear strength of the asperity intact rock. Dilation angle, i, can be obtained using the following equation:

$$i = \tan^{-1}\left(\left(1 - \frac{\sigma_n}{\sigma_c}\right)^{k_2} \cdot \tan(i_0)\right),$$ (3.10)

in which K_2 is an empirical constant; $\tan(i_0)$ is the peak rate of dilatancy at zero normal stress.

3.2.1.3 Jing's model

Jing *et al.* [99, 100] proposed the following relationship for the peak friction angle:

$$\phi_p = \phi_r + \alpha_0 \cdot \left(1 - \frac{\sigma_n}{\sigma_c}\right)^b,$$ (3.11)

where α_0 is the initial asperity angle, σ_n is the magnitude of normal stress and σ_c is the magnitude of the uniaxial compressive strength of the material; b is a material constant representing the wearability of the fracture material.

In order to investigate anisotropic behavior of rock fractures Jing *et al.* [126, 150] determined and plotted in polar diagram the mobilized friction angles from shear and tilt tests for 12 shear directions. They found that the distribution of the total friction angles, ϕ_p, on the nominal plane of the fracture surface (lower block), may be generalized as follows: (a) ϕ_p varies with both the shear direction and magnitude of normal stress; (b) the degree of the directional variation of ϕ_p decreases with increasing normal stress; (c) ϕ_p decreases with increasing normal stress; (d) under a certain normal stress, the directional distribution of the friction angle is not completely random, but displays principal directions. These principal directions may or may not be symmetrical, depending very much on the geometrical distribution of the asperities on the fracture surface.

The directional dependency of the shear strength of fractures would then be represented by the directional variation of the asperity angle α_0 in Equation (3.11). To simplify the matter as much as possible, it was assumed that magnitudes of the asperity angle follow an elliptical distribution in the plane of the fracture surface. The magnitude of the asperity angle in a given direction θ can then be written as:

$$\alpha = \sqrt{[C_1 \cdot \cos(\psi) - C_2 \cdot \sin(\psi)]^2 + [C_1 \cdot \sin(\psi) + C_2 \cdot \cos(\psi)]^2}, \qquad (3.12)$$

where $C_1 = \alpha_1 \cdot \cos(\theta - \psi)$ and $C_2 = \alpha_2 \cdot \sin(\theta - \psi)$; α_1 and α_2 are the major and minor semi-axes of the ellipse, and ψ is the angle to the major semi-axis, all of which should be determined experimentally.

3.2.1.4 Grasselli's model

Grasselli *et al.* [128] have digitized and reconstructed a large number of fracture surfaces using a triangulation algorithm. This approach results in a discretisation of the fracture surface into a finite number of triangles, whose geometric orientations were calculated by the authors. Based on their observations and using the triangulated surface data, they described the variation of the potential contact area versus the apparent dip angle of the fracture surface with the expression:

$$A_{\theta^*} = A_0 \cdot \left(\frac{\theta^*_{max} - \theta^*}{\theta^*_{max}} \right)^c, \qquad (3.13)$$

where A_0 is the maximum possible contact area; θ^*_{max} is the maximum apparent dip angle in the shear direction, and c is a ''roughness'' parameter which characterizes the distribution of the apparent dip angles over the surface.

Grasselli and Egger [127] proposed the following empirical relationship for peak shear strength of rock fractures:

$$\tau_p = \sigma_n \cdot \tan \left[\phi_b + \left(\frac{\theta^*_{max}}{C} \right)^{1.18 \cos \alpha} \right] \cdot \left(1 + e^{-(\frac{\theta^*_{max}}{9 A_0 C}) \cdot (\frac{\sigma_n}{\sigma_t})} \right), \qquad (3.14)$$

where σ_t is tensile strength of intact rock and α is the angle between the schistosity plane and the normal to the fracture; if the rock does not exhibit schistosity, α is assumed to be equal to zero.

Using Equation (3.14), Joint Roughness Coefficient (*JRC*) can be determined from the following relationship:

$$JRC = \frac{\arctan \left\{ \tan \left[\phi_b + \left(\frac{\theta^*_{max}}{C} \right)^{1.18 \cos \alpha} \right] \cdot \left(1 + e^{-(\frac{\theta^*_{max}}{9 A_0 C}) \cdot (\frac{\sigma_n}{\sigma_t})} \right) \right\} - \phi_b}{\log_{10} \left(\frac{\sigma_c}{\sigma_n} \right)} \qquad (3.15)$$

3.2.1.5 Kulatilake's model

Kulatilake *et al.* [129, 130] developed a new empirical peak shear strength criterion for anisotropic rock fractures that includes both the effect of dilation and shearing through asperities. They measured roughness profiles at 30° intervals on a model fracture and run direct shear tests of different normal stresses of the replicas. They suggested the following general equation to model the peak shear strength of rock fractures for a specific direction and for $\sigma_n / \sigma_j < 0.1$:

$$\frac{\tau}{\sigma_j} = \frac{\sigma_n}{\sigma_j} \cdot (1 - a_s) \cdot \tan \left[\phi_b + \left(160 D^{5.63} A^{0.88} \pm 1.8 I_{\text{eff}}\right) \cdot \log_{10}\left(\frac{\sigma_j}{10\sigma_n}\right) \right] + a_s \cdot \frac{\tau_r}{\sigma_j}, \qquad (3.16)$$

where σ_j is the joint compressive strength (*JCS*); A is a proportionality constant and D is a fractal dimension in the direction considered; I_{eff} is effective nonstationary trend angle for considered direction, which is conceptually quite different to an inclination angle that exist on a smooth planar joint surface. Because of the irregularities of a rock joint surface, it is difficult to estimate I_{eff}. However, a procedure is given by Kulatilake *et al.* [129] to estimate the effective nonstationary trend angle; a_s is the area proportion where asperities are sheared, which can be estimated for each direction using the following equation:

$$a_s = 10^{-1/4} \cdot D^{1/4} \cdot A^{1/3} \cdot \left(\frac{\sigma_n}{\sigma_j}\right)^{3/4} \pm 10^{-0.85} \cdot I_{\text{eff}} \cdot \left(\frac{\sigma_n}{\sigma_j}\right)^2 \qquad (3.17)$$

The term $a_s \dfrac{\tau_r}{\sigma_j}$ in Equation (3.16) is the contribution to peak shear strength due to shearing through the asperities and τ_r is the shear strength of intact rock.

3.2.1.6 OH's model

OH [124] developed a joint constitutive model by considering both small-scale asperities present in laboratory sample and large-scale waviness observes in the field. He found that the evaluation of strength of rock fractures in the field requires assessment of large-scale irregularities not present in the lab sample. The complete form of OH's joint model for multi-scale asperities is as follows:

$$\tau = \sigma_n \cdot \tan\left(\phi_r + \alpha_n \cdot e^{\left(-c \cdot W_p\right)} + i_0 \cdot f^s\right), \qquad (3.18)$$

where α_n is a shear-through component obtained by laboratory test; i_0 is initial angle of inclination of large scale irregularities; c is a dimensionless asperity degradation constant that can be estimated using the following equation:

$$c = k \cdot \frac{\alpha_0}{\lambda \cdot \sigma_c},$$

(3.19)

in which α_0 is the initial asperity angle; σ_c is the unconfined compressive strength of rock; λ is wavelength of asperity; and k is constant.

f^s in Equation (3.18) is called "sinusoidal function" and mathematically expressed as follows [123]:

$$f^s = \left[\frac{\pi}{4} + \tan^{-1} \left(-\sin \left(\pi \cdot \frac{\delta_s^p}{0.5\lambda_{l \arg e}} \right) - \frac{\pi}{2} \right) \right] / \frac{\pi}{2},$$

(3.20)

where $\lambda_{l \arg e}$ is the wavelength of large-scale irregularity observed in the field.

Plastic work, W_p, is a function of shear strength ($\sigma_t = \sigma_n . \tan\phi$) and plastic shear displacement (δ_s^p):

$$W_p = \sum \Delta\delta_s^p \cdot \sigma_t$$

(3.21)

3.2.2 Rock Fracture Deformation

Goodman *et al.* [151] introduced the terms Normal Stiffness, K_n, and Shear Stiffness, K_s, to describe the rate of change of normal stress, σ_n, with respect to normal displacements, V_j, and of the shear stress, τ, with respect to shear displacements, d_h, respectively.

3.2.2.1 Normal Stiffness

Goodman [93] described the basic mechanics of fracture normal deformation by considering that the maximum closure, V_m, of a fracture should be less than its aperture thickness, a_j, defined as the maximum gap anywhere across the mated walls. Experiments showed that the fracture closure under increasing normal stress varies in a non-linear fashion closely resembling a hyperbola [93, 112, 152, 153]. Bandis *et al.* [80] suggested the following equation for normal stiffness:

$$K_n = K_{ni} \cdot \left(1 - \frac{\sigma_n}{V_m K_{ni} + \sigma_n}\right)^{-2}, \tag{3.22}$$

where the initial normal stiffness, K_{ni}, can be calculated from the following relation [113]:

$$K_{ni} = -7.15 + 1.75 \, JRC + 0.02\left(\frac{JCS}{a_j}\right), \tag{3.23}$$

in which the units of *JCS* and a_j are MPa and mm, respectively. A fair approximation of the initial aperture, a_j, can be obtained from the following empirical relationship [80]:

$$a_j = \frac{JRC}{5} \cdot (0.2\frac{\sigma_c}{JCS} - 0.1) \tag{3.24}$$

The maximum closure, V_m, can be obtained using the following empirical relationship (see Table 3.1 for constants) [80]:

$$V_m = A + B(JRC) + C(\frac{JCS}{a_j})^D \tag{3.25}$$

Table 3.1: Constant values for the maximum closure in Equation (3.25) [80].

Constant	1st Cycle	2nd Cycle	3rd Cycle
A	-0.2960 ± 0.1258	-0.1005 ± 0.0530	-0.1032 ± 0.0680
B	-0.0056 ± 0.0022	-0.0073 ± 0.0031	-0.0074 ± 0.0039
C	2.2410 ± 0.3504	1.0082 ± 0.2351	1.1350 ± 0.3261
D	-0.2450 ± 0.1086	-0.2301 ± 0.1171	-0.2510 ± 0.1029

Goodman [97] suggested that the unloading curves for fractures will follow essentially the same path as that for the intact rock; however, Bandis *et al.* [80] found that the unloading stress-opening curves for fractures are also hyperbolic (essentially similar in shape for the first, second, and third cycles). Equation (3.25) can be used to obtain maximum closure for the second and third cycles where the values of a_j are based on the initial aperture minus the permanent set at the end of first and second cycle. The ratio of irrecoverable closure, V_i, to maximum closure, V_m, can be estimated from Figure 3.1.
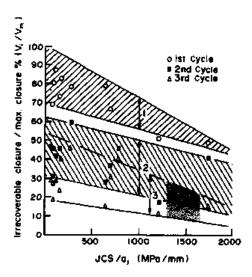
Figure 3.1: Irrecoverable fracture closure reduces with number of load cycle; with JCS_0 value; and with the smallness of the initial fracture aperture, a_j [80].

Comparison between interlocked and dislocated fracture normal stiffness indicated that an assumption of linear decrease in $(K_n)_{mis.}/(K_n)_{int.}$ with shear displacement from zero to δ_{peak} would be sufficiently accurate for numerical simulation purposes. The following empirical relation can be used to obtain the normal stiffness of mismatched rock fracture at peak shear displacement [80]:

$$\frac{(K_n)_{int.}}{(K_n)_{mis.}} \approx 2 + \frac{JRC \cdot JCS.\sigma_n}{2500} \qquad (3.26)$$

Yoshinaka and Yambe [154] used the following equation for normal stiffness proposed by Yoshinaka and Nishimaki [155]:

$$k_n = m \cdot \exp\left(\frac{l \cdot \Delta v}{v_{mc}}\right), \qquad (3.27)$$

where m, l, and $v_{mc} = L/100$ are material constants. The model has no advantageous on Goodman's model.

Alvarez [156] had collected data from hydromechanical experimental studies conducted on both natural and induced rock joints. They re-examined published

57

experiments on the hydromechanical behavior of single joints and found that the initial normal stiffness, K_{ni}, and the maximum closure, V_m, are not independent. These two parameters are related with each other, because both are controlled by the surface topography of the rock joints and the elastic properties of the intact rock. The initial normal stiffness can be estimated as [156]:

$$\frac{5}{V_m^{1.333}} \leq k_{ni} \leq \frac{20}{V_m^{1.333}}, \qquad (3.28)$$

where the units of K_{ni} and V_m are MPa and μm, respectively.

3.2.2.2 Shear Stiffness

The shear displacement, δ_{peak}, required to reach peak shear strength determines the secant stiffness of fractures in shear. This is extremely important input data in the finite element [157] and distinct element [158] analyses. Secant peak shear stiffness, K_s, can be obtained from the following equation:

$$K_s = \frac{\tau_{peak}}{\delta_{peak}} \qquad (3.29)$$

Barton [92] indicated that model tension fractures representing prototype fracture lengths from 225 cm up to 2,925 cm required approximately 1% displacement ($\delta_{peak} = 0.01L$). In addition, Barton and Choubey [22] suggested 1% displacement as a "rule-of-thumb", based on the overall mean obtained for 136 specimen ($\delta_{peak} = 0.0095L$). However, they pointed out that δ_{peak} will eventually reduce to less than $0.01L$ as fracture length increases to several meters. Barton and Bakhtar's [159] survey of almost 300 shear test records revealed that peak shear displacement of lab-size fractures (224 tests) averaged at 1.28% of their corresponding lengths. On the other hand, 71 *in situ* tests gave an average of 0.72% of fracture lengths, thus yielding an overall average of 0.98%. Barton [115], by reviewing of a large number for shear tests reported in literature (650 data points), found that the ratio δ_{peak}/L reduces gradually with increasing block

length. Moreover, he proposed that an approximation to the mean trend of 170 data points (with block lengths from about 50 mm to 1,000 km) is given by the following equation:

$$\delta_{peak} = 0.004 L^{0.6} \tag{3.30}$$

Analysis of data published by Bandis *et al.* [79] indicates that the ratio δ_{peak}/L is related to the JRC of the particular length of fractures tested, and that improved fit to the data is obtained with the following equation [115]:

$$\frac{\delta_{peak}}{L} = \frac{1}{500}\left(\frac{JRC}{L}\right)^{0.33}, \tag{3.31}$$

where L is length of fracture sample (in meters).

Hyperbolic functions are frequently used to express analytically the non-linear behavior of sheared fractures in the pre-peak range. Bandis *et al.* [80] based on Kulhaway's [160] formula suggested the following equation for the tangent shear stiffness of a fracture at any level of shear, τ, and normal, σ_n, stress:

$$K_{st} = K_j (\sigma_n)^{n_j}\left(1 - \frac{\tau \cdot R_f}{\tau_p}\right)^2, \tag{3.32}$$

where τ_p is peak shear strength; n_j is stiffness exponent; R_f is failure ratio (τ/τ_{ult}) ranging from 0.652 to 0.887; and K_j is a "stiffness number" varying from 3.49 to 30.19 MPa/mm. It can be calculated using the following empirical relation:

$$K_j = -17.19 + 3.86 JRC \tag{3.33}$$

Lower R_f values were associated with well-interlocked, unweathered fractures of high *JRC*, while planar, fresh, and especially weathered fractures gave the relatively higher values.

Bandis [96] described the normal and shear stress dependency of the shear stiffness by applying hyperbolic functions to the $\tau - u$ relationship of the type:

$$\tau = \frac{u}{m + n \cdot u}, \tag{3.34}$$

where *m* is the inverse of initial shear stiffness and *n* is the inverse of shear stress asymptote.

Wang *et al*. [107] mentioned that the elastic shear stiffness K_s is a function of normal stress at the interface and can be expressed in terms of:

$$\frac{K_s}{\alpha(\theta)} = K_{s0} + a_1\sigma_n,$$ (3.35)

in which $\alpha(\theta)$ is a shape function that considers the effect of shear anisotropy on elastic deformation. The magnitude of the shape function is unity in isotropic cases. The shear elasticity parameters K_{s0} and a_1 can be directly determined from the shear stiffness-intercept and the gradient of the best straight line, respectively, for the elastic normal stress-shear stiffness response for a particular rock fracture.

Goodman [97] recommended two models to represent the variation of fracture shear stress with shear displacement under constant normal stress; one of which assumes that the fracture shear stiffness is independent of normal stress (constant stiffness model), whereas the other assumes that the peak and residual shear displacements are constant (constant displacement model). Both models show an increase in peak and residual shear strengths with normal stress. Wibowo *et al*. [161], based on the shape of the shear versus shear displacement response curves obtained from their experimental study, proved that neither constant stiffness model nor constant displacement model, by itself, fits the observed behavior [162].

The peak shear displacement measured in the experiments by Wibowo *et al*. [161] was found to increase with the normal load or stress. A linear relation was used to describe the variation of the peak displacement, u_p, with applied normal stress, σ_n, as follows [162]:

$$u_p = a + b \cdot \sigma_n,$$ (3.36)

in which coefficient *a* and *b* are to be determined by linear regression analysis of lab test results.

Jing *et al.* [99, 100] proposed the following empirical relationship for shear stiffness:

$$k_t = \frac{\sigma_n}{\sigma_c} \cdot \left(2 - \frac{\sigma_n}{\sigma_c} \right) \cdot k_t^m,$$ (3.37)

where k_t^m is the maximum shear stiffness and is obtained when the normal stress reaches the magnitude of σ_c, which is a material constant and should be obtained from lab tests.

For shear stiffness Yoshinaka and Yambe [154] used the following equation proposed by Kondner [163] and Duncan and Chang [164]:

$$k_s = k_{si}(1 - R_f \cdot \tau / \tau_f)^2,$$ (3.38)

where k_{si} is the initial shear stiffness. It depends on normal stress and condition of fracture surface; it is defined based on two material constants; τ_f is peak shear strength; and R_f is a material constant.

Plesha's model [87] needs shear and normal stiffness and asperity information as input values, which should be measured from lab tests. Chen [165] used bilinear shear stress-displacement response with shear stiffness which are found from laboratory experiments.

3.2.3   Degradation of fracture asperity

The degradation of fracture asperity can be conceptualized as the variation of asperity angle, which would be evaluated by the secant or tangential slope of dilation curves. Plesha [87] and Zubelewicz *et al.* [166] proposed an exponential model to represent the degradation of asperity angle. Lee at al. [167], based on their experimental results (a series of cyclic shear tests conducted using both the saw-cut and the split tensile fracture specimens) revised Plesha's plastic constitutive model by considering the second order asperities. Homand *et al* [168, 169] proposed a model to predict the evaluation of fracture morphology and the degree of degradation during the course of shearing. Their model is as good as Barton's criteria compared to their experimental results. However, Saeb's model [104] and Ladanyi and Archmabault's model [91] dealing with proportion

of total fracture area sheared through asperities tend to underestimate the observed degradation [169]. Hutson and Dowding [170] and Hutson [171] suggested an exponential wear equation for fracture asperity based on experimental results using artificial fractures in a sinusoidal shapes. Huang *et al*. [103] tested molded fractures in a saw-tooth shape under cyclic shear loading and validated Plesha's theoretical law for fracture asperities degradation [87].

3.2.3.1 Mobilization of Shear Strength

Barton [115] showed that the mobilized (pre- or post-peak) shear strength can be expressed by using the concept of roughness mobilization, $JRC_{mobilized}$, in Equation (3.3). The ratio $JRC_{mobilized} / JRC_{peak}$ can be estimated from the ratio δ / δ_{peak} using the values given in Table 3.2. When $JRC_{mobilized} / JRC_{peak} = 0.5$, the shear strength mobilized is midway between peak and residual values. This point seems to occur at approximately $10\delta_{peak}$ for non-planar fractures and $25\delta_{peak}$ for planar fractures. The slow reduction towards residual strength found in practice suggests that it is more appropriate to use the term "ultimate" strength for the value measured at the end of a shear test [115].

Table 3.2: Recommended model for shear stress-displacement [115].

Non-planar fractures		Planar fractures ($JRC_0 \leq 5$)	
$\dfrac{\delta}{\delta_{peak}}$	$\dfrac{JRC_{mobilized}}{JRC_{peak}}$	$\dfrac{\delta}{\delta_{peak}}$	$\dfrac{JRC_{mobilized}}{JRC_{peak}}$
0	$-\phi_r / i$	0	$-\phi_r / i$
0.3	0	0.3	0
0.6	0.75	0.6	0.75
1.0	1.0	1.0	0.95
2.0	0.85	2.0	1.0
4.0	0.70	4.0	0.9
10.0	0.50	10.0	0.7
25.0	0.40	25.0	0.5
100	0	100	0

3.2.3.2 Unloading and Reversals

Barton [115] found that the shear stiffness measured during the second and subsequent load sequences average approximately 1.5 times the initial shear stiffness. Barton [115] considered three sets of data available in the literature [172-174] that include reversal. Based on the most complete one [174], he explained how the shear stress-displacement performance could be simulated using the $JRC_{mobilized}$ concept (Figure 3.2) as a guideline for unloading, reloading, and reversal. For convenience, the gradient of the various loading, unloading and reversal curves are defined in units of m which is given by the following empirical relation:

$$m = \frac{\phi_r / i}{0.3} \tag{3.39}$$

where i is dilation angle defined as follows:

$$i = JRC \cdot \log_{10}\left(\frac{JCS}{\sigma_n}\right) \tag{3.40}$$
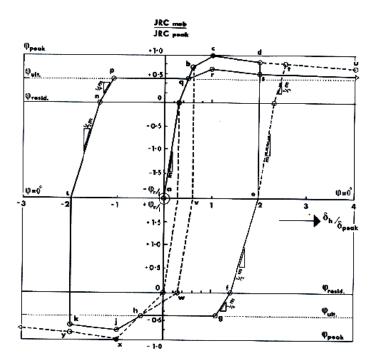
Figure 3.2: A preliminary model for simulating the effects of shear reversal and unloading of rock fractures [115].

Jing *et al*. [99] investigated the cyclic behavior of natural fractures using replicas of natural fracture surfaces. By utilizing these results Jing [100] proposed a conceptual model for the cyclic shear behavior as depicted in Figure 3.3:

-Segment *DE* is called the "unloading stage" because it represents the proportional decrease of shear stress over shear displacement immediately after reversal of shear direction; τ_b is defined as:

$$\tau_b = \sigma_n \cdot \tan(\phi_b),$$
(3.41)

where ϕ_b is called the basic friction angle of the fracture.
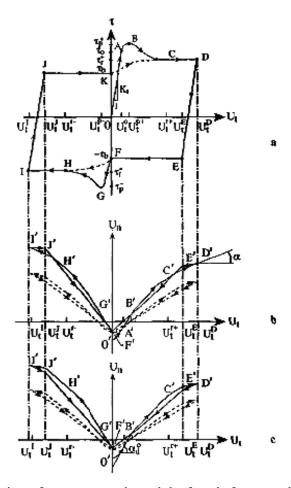
Figure 3.3: Idealized behavior of a conceptual model of rock fracture during shear under constant normal stress, a) Shear stress versus shear displacement; b) normal displacement versus shear displacement for fractures without previous shear; c) shear stress and normal displacement versus shear displacement for fractures with previous shear [99].

64

- The shear stress decreases linearly along the straight segment *DE* which has the same slope k_t as that of segment O-A, until it reaches point E.

- When shear continues in the negative direction past the original point of zero shear displacement, the shear stress and normal deformation displays similar features as in the positive shear direction.

- For fractures with previous shear histories, no peak shear stress occurs even for the first cycle. The dilatancy curves are much less nonlinear.

3.2.4 Dilatancy

The prediction of the dilatancy phenomenon of regular or irregular fractures subjected to direct shear loading has been addressed by numerous researchers such as Patton [102], Ladanyi and Archambault [91], Jaeger [147], Barton [21], Saeb [104], and Homand *et al* [168, 169]. In addition, variations in dilatancy with normal stresses have been modeled by many authors: Ladanyi and Archambault [91], Jaeger [147], Barton [132], Leichnitz [108], etc.

Barton and Choubey [22] used both the peak secant dilation angle also called initial dilation angle, and the peak tangent dilation angle. Their experimental results showed that the peak secant dilation angle is about one-third of the peak tangent dilation angle. Ladanyi and Archmbault [91], Schneider [175], and Jing [100] considered the peak dilation angle only.

The peak secant dilation angle (also called initial dilation angle), $d_{s,peak}$, and the peak tangent dilation angle, $d_{t,peak}$, are defined as follows [22]:

$$d_{s,peak} = \arctan\left(\frac{\tau}{\sigma_n}\right) - \phi_r \tag{3.42}$$

$$d_{t,peak} = \left(\frac{\partial \delta_v}{\partial \delta_h}\right)_{@ \delta_h = \delta_{peak}} \tag{3.43}$$

The experimental evidence indicates that fractures and fractures dilate most strongly when the shear displacement corresponds to the instant of peak shear strength

65

[132]. Both peak tangent and secant dilation angles were occasionally negative or zero [22]. The majority of measured peak tangent dilation angles fell between the following limits:

$$0.5 JRC \cdot \log_{10}(JCS / \sigma_n) < d_{t,peak} < 2 JRC \cdot \log_{10}(JCS / \sigma_n) \qquad (3.44)$$

Barton and Choubey [22] suggested the following relation for the peak tangent and secant dilation angles:

$$d_{t,peak} = (1/M) \cdot JRC \cdot \log_{10}(JCS / \sigma_n) \qquad (3.45)$$

$$d_{s,peak} = (1/3) \cdot JRC \cdot \log_{10}(JCS / \sigma_n), \qquad (3.46)$$

where M is damage coefficient, given values of 1 or 2 for shearing under low or high normal stress respectively [176], or can be obtained from the following relationship [22]:

$$M = \frac{JRC}{12 \log_{10}(JCS / \sigma_n)} + 0.70 \qquad (3.47)$$

Barton [115] indicated that dilation will begin at the instant that $JRC_{mobilized} = 0$ and mobilized dilation angle can be obtained from the following relationship:

$$d_t = (1/M) \cdot JRC_{mobilized} \cdot \log_{10}(JCS / \sigma_n) \qquad (3.48)$$

Ladanyi and Archmbault [91] proposed the following relation between the peak tangent dilatancy rate and the applied normal stress:

$$\tan(i_p) = \left(1 - \frac{\sigma_n}{\sigma_T}\right)^{k_2} \cdot \tan(i_{po}) \qquad (3.49)$$

where k_2 is an empirical coefficient, σ_T is a threshold stress beyond which no further dilatancy takes place and $\tan(i_{po})$ is the peak rate of dilatancy at zero normal stress.

Schneider [175] proposed the following relationship between the peak tangent dilation angle and the normal stress:

$$i_p = i_{po} e^{-k\sigma_n}, \qquad (3.50)$$

where k is an empirical coefficient and i_{po} is the peak tangent dilation angle at zero normal stress.

Jing [100] proposed another relationship between the peak tangent dilation angle and the normal stress as follows:

$$i_p = i_{po} \cdot \left(1 - \frac{\sigma_n}{q_u}\right)^k,$$ (3.51)

where k is another empirical coefficient, i_{po} is the peak tangent dilation angle at zero normal stress, and q_u is the uniaxial compressive strength of the inact material in the fracture wall.

Wibowo [162] modified Ladanyi and Archmbault [91] model, Equation (3.49), as follows:

$$\tan(i_{av}) = \left(1 - \frac{\sigma_n}{\sigma_T}\right)^{k_3} \cdot \tan(i_{avo})$$ (3.52)

where k_3 is an empirical coefficient, σ_T is a threshold stress beyond which no further dilatancy takes place and $\tan(i_{avo})$ is the avarage rate of dilatancy at zero normal stress.

3.2.5 Anisotropic dilatant behavior of fractures

The shearing strength of rock fractures is composed of two components: (1) the base friction angle, ϕ_b, resulting from two sawed surfaces sliding over each other, which is equal for all shearing directions; and (2) the resistance to sliding and/or shearing of the fracture asperities, which is a geometrical parameter. Consequently, the shear strength of rock fractures will be anisotropic as long as the surface is uneven and displays anisotropy in its geometric property [125].

Huang and Doong [125] conducted an experimental study on the anisotropy in shear strength of fractures by shearing silicon rubber replicas of rock fractures in different directions. They found that: (1) the shear strength of the joints with the same surface morphology might be different when sheared in reverse direction; (2) the effect of anisotropy decreases with increasing normal stress. Their results show that the shear direction changes the shear strength of replicas. They adopted Barton's failure criterion [21] together with Tse and Cruden's equation [177] relating the joint roughness

coefficient, *JRC*, with the root mean square, *RMS*, of the asperity angle. However, they had no specific solution for including the shear direction in the shear strength of rock fractures.

Jing *et al.* [126, 150], through their experimental study, found that the distribution of the total friction angles, ϕ_p, on the nominal plane of the fracture surface (lower block), may be generalized as follows: (1) ϕ_p varies with both the shear direction and magnitude of normal stress; (2) the degree of the directional variation of ϕ_p decreases with increasing normal stress; (3) ϕ_p decreases with increasing normal stress; (4) under a certain normal stress, the directional distribution of the friction angle is not completely random, but displays principal directions. These principal directions may or may not be orthogonal, depending very much on the geometrical distribution of the asperities on the fracture surface. They proposed a new model for dilation angle of fractures, in which the magnitudes of the asperity angle follows an elliptical distribution. Wang *et al.* [107] also adopted the elliptical model introduced by Jing *et al.* [126].

Grasselli *et al.* [127, 128] and Kulatilake *et al.* [129, 130] proposed new models for rock fractures. Their respective models do not include shear direction and can not be used to predict shear strength in different directions because the authors measured the geometrical parameters of their models only in the shearing direction.

3.3   MODIFIED BARTON-BANDIS MODEL

Among the constitutive models proposed in the literature to estimate the shear strength of rock fractures, Barton's failure criterion is the one mainly used [127] because it is easy to apply and includes several important aspects off fracture characteristics that can be easily measured or estimated. In addition, Grasselli and Egger [127] stated that researchers studying the contribution of morphology to the shear strength have to deal with the *JRC* criterion proposed by Barton in the 1970s [22], and adopted as a reference by the International Society of Rock Mechanics in 1978 [178].

Although, Barton's failure criterion predicts the peak shear strength of rock fractures with acceptable precision, it shows weaknesses in estimating the peak shear

displacement, post-peak shear strength, dilation, and surface degradation in unloading and reloading. The weaknesses of the model are the following:

- The peak shear displacement is independent of normal stress and is zero for sawed fractures [80]; this is not consistent with experimental observations. For example, peak shear displacements between 0.05 and 2.71 mm were reported in the literature and cited in this chapter.

- Barton suggested zero mobilized *JRC* after 100 times of peak shear displacement. It means that according to Barton's model after this amount of displacement, the behavior of the fracture is the same as a sawed fracture (no dilatancy and $\tau = \sigma_n \tan \phi_r$). This seems to be just an approximation for the end of the curve because there are few experimental results containing post-peak shear strength of rock fractures up to about 100 times of the peak shear displacement. Moreover, even after this amount of displacement, the fracture surface is not the same as a sawed fracture ($JRC_{mobilized} = 0$).

- Barton assumed zero dilation displacement up to one-third of peak shear displacement and eliminated negative dilatancy. However, many experimental studies performed on rock fractures showed that there is a negative dilation at small shear displacements.

- Barton proposed his model for unloading and reloading based on just one cyclic direct shear test.

In this study, the original Barton model is modified to address its weaknesses. As stated in Section 3.1, there are two main approaches to the quantitative description of the mechanical properties of rock fractures: the theoretical approach, and the empirical approach. Moreover, as indicated by Saeb [179] and Saeb and Amadei [180-182], the shear behavior of a rock fracture under any boundary condition can be determined from the response curves of the fracture under constant normal stress. Therefore, in this research, the empirical approach was used, which is consistent with Barton's empirical model and the response curves of the fracture under constant normal stress were

considered. Barton's failure criterion for peak shear strength of rock fracture, Equation (3.3), was adopted. A database of the results of direct shear tests available in the literatures was constructed and analyzed. The ability of Barton's model to predict peak shear displacement, dilation, post peak shear strength, and unloading and shear reversal behavior was investigated and modifications are proposed to improve it in its weakness points.

3.3.1   Database

Two databases were built by collecting the results of direct shear tests available in the literature: Monotonic Direct Shear Tests, called MDST (Appendix A.1), and Cyclic Direct Shear Tests, called CDST (Appendix A.2).

Studies on monotonic shearing [79, 81, 106, 113, 115, 127, 154, 161, 162, 169, 176, 183-210] were investigated to find available monotonic direct shear test results. Peak shear strength, peak shear displacement, peak dilation displacement, maximum negative value of dilation, and shear displacement at which dilation displacement is zero were digitized from the curves. For post peak behavior shear strength, and dilation displacement at 4 different points were digitized.

A large amount of data was collected from a site investigation report series published by Svensk Karnbranslehantering AB (Swedish Nuclear Fuel and Waste Management Co.) and available online (www.skb.com) [188-210]. In these cases, the values of *JCS* was assumed to be equal to the unconfined compressive strength of intact rock, which can be calculated from available results of triaxial tests run on intact rock specimens (using Hoek and Brown failure criterion [211, 212]). In the reports, the magnitudes of peak and residual shear strength were available in tabular format and the corresponding shear displacements were digitized from curves. Base friction angle and *JRC* values were back calculated assuming that: (1) Barton [21] failure criterion can predict the peak and residual shear strength correctly and (2) residual shear strength is reached when $JRC_{mobilized} / JRC_{peak} = 0.5$ [115] and assuming no weathering for fractures ($\phi_r = \phi_b$), base friction angle and *JRC* values were back calculated. *JRC* values may be

different for the same specimens under different normal stresses (due to the damage of asperities in the shear test run under smaller of normal stresses). The value of the peak dilation displacement, the maximum negative value of dilation, and the shear displacement at which dilation displacement is zero were all digitized from the curves.

Results of 18 cyclic direct shear tests were found in the literature [103, 127, 150, 167, 169, 174, 213]. For each available cycle, shear strengths and dilation displacements at different shear displacements were digitized so that shear strength-shear displacement as well as dilation-shear displacement curves could be built with the available information.

In should be mentioned that the correlation analyses, in this Chapter, are performed employing the trial version of SPSS 14.0 available online (www.spss.com) which is a computer program used for data manning and statistical analysis.

3.3.2 Peak shear displacement

Although Bandis *et al*. [80] found that a constant normal peak displacement model [214] is not always realistic, Barton's [115] empirical equation, Equation (3.31), for peak shear displacement was independent of normal stress. The non-linear variation of shear stiffness with normal stress is due to non-linear variation of τ_{peak} with σ_n and small increase in δ_{peak} with σ_n [80]. In addition, Wibowo *et al*. [161, 162] demonstrated that neither the constant stiffness model nor the constant displacement model, by itself, fits the observed shear behavior of rock fractures. The peak shear displacement measured in the experiments by Wibowo *et al*. [161] was found to increase with the normal load or stress. They introduced a linear relation to describe the variation of the peak displacement, δ_{peak}, with applied normal stress, σ_n.

In addition, Barton's empirical model does not have any clear suggestion for peak shear displacement of sawed fractures ($JRC = 0$). The MDST database contained 19 data points with zero *JRC* and peak shear displacement ranging between 0.05 and 2.71mm; in these cases, Equation (3.31) would yield zero peak shear displacement. On the other

hand, Barton had 2 other suggestions for peak shear displacement before proposing Equation (3.31), both of which are independent of *JRC*:

-   $\delta_{peak} = 0.01L$: the result obtained from this equation is the same as the peak shear displacement predicted using Equation (3.31) for a fracture with the same length and $JRC = 12.5$. It is clear that rock fractures with $JRC = 0$ and $JRC = 12.5$ should not have the same peak shear displacements.

-   $\delta_{peak} = 0.004L^{0.6}$: For a lab size specimen with block length of 0.1m, the result obtained from this equation for a fracture with a length of 0.1m is the same as predicted peak shear displacement of a fracture with the same length and $JRC = 13$ using Equation (3.31). Again, it is clear that rock fractures with $JRC = 0$ and $JRC = 13$ should not have the same peak shear displacements.

The purpose of this section is to find an empirical relationship for peak shear displacement considering the effect of normal stress and develop a solution for smooth fractures ($JRC = 0$).

The peak shear displacement, δ_{peak}, of rock fractures may be affected by length of the block (*L*), *JRC*, *JCS*, and normal Stress (σ_n).

The peak shear displacement, δ_{peak}, and the block length, L, have length dimension (L). In addition, JCS and normal stress, σ_n, have stress dimension (FL^{-2}). However, joint roughness coefficient, JRC, is dimensionless. Dimensional analysis [215] was performed. While, there is no idea about the correlation between δ_{peak} and *L*, a dimensionless parameter was defined to be the ratio of the peak shear displacement to the block length and another was introduced as the ratio of the block lengthto the length of the lab specimen, L_0 (0.1 m). Since only normal stress and *JCS* have force in their dimensions, a dimensionless parameter would be their ratio. Therefore, the following dimensionless parameters were found: $\pi_1 = \dfrac{\delta_{peak}}{L}$, $\pi_2 = \dfrac{L}{L_0}$, $\pi_3 = JRC$, and $\pi_4 = \dfrac{\sigma_n}{JCS}$

Correlation analyses were performed to find π_1 as a function of π_2, π_3, π_4:

$$\pi_1 = f(\pi_2, \pi_3, \pi_4) \qquad\qquad (3.53\text{-a})$$

The MDST database contained 362 direct shear test records. Cases that have *JRC* values between 2 and 20 were selected for this part of analyses (317 data points). In order to perform a reliable correlation analyses, all variables should have reasonable distributions. It is shown here that distributions of all variables in the MDST database are acceptable.

The block lengths ($\pi_2 \times L_0$) in the MDST database ranged from 0.049 to 3m with distribution depicted in Figure 3.4. It can be seen in the figure that since the MDST database contained the results of direct shear tests, the size of the blocks are around 0.1m. Therefore, the database may under-represents long fractures. However, the following paragraphs demonstrate that the MDST database is adequate from this point of view.

Distribution of Length of the Block

Legend:
- L < 0.1
- 0.1 < L < 0.2
- 0.2 < L < 0.3
- 0.3 < L < 0.4
- 0.4 < L

Values: 211, 74, 15, 13, 4

Y-axis: Number of Cases
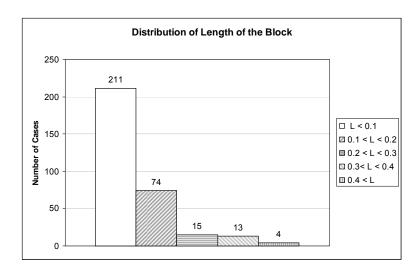
Figure 3.4: Distribution of length of the block in 317 data points of the database used in correlation analysis of peak shear displacement.

Barton [115] found an approximation to the mean trend of 170 data, Equation (3.30), where block length ranged from about 50 mm to 1,000 km (56 samples with

$L \approx L_0$, 94 samples with $L \approx 10 \cdot (L_0)$, 5 samples with $L \approx 80 \cdot (L_0)$, and 15 earthquake fault with block size ranging between 1 and 1000 km).

Non-linear regression analysis performed on the MDST database to correlate peak shear displacement and length of the sample gave the following relationship, which is very close to Barton's Equation (see Figure 3.5 for comparison):

$$\delta_{peak} = 0.0032 \cdot L^{0.61} \tag{3.54}$$

As can be seen in Figure 3.5, the predicted values from these equations are very close; their differences are less than 15% of predicted values from Barton's equation. It is almost impossible to collect all required information, such as *JRC*, *JCS*, normal stress, peak shear stress, and friction angle, from sheared large blocks. Even Barton could only collected the values of peak shear displacement and length of the block. Therefore, the MDST database is adequate from this point of view.
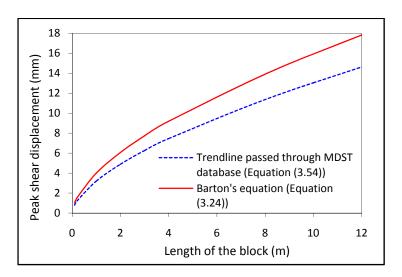
Figure 3.5: Comparison between Barton's equation correlating peak shear displacement and length of the block and trend line passed through our database.

The magnitude of *JRC* (π_3) in MDST ranged from 2 to 20 with a good distribution (close to a normal distribution) depicted in Figure 3.6. In addition, $\dfrac{\sigma_n}{JCS}(\pi_4)$ ranged between 0.001 and 0.6 with distribution illustrated in Figure 3.7.
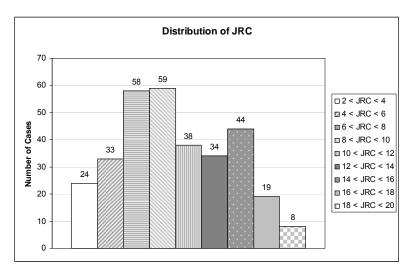
Figure 3.6: Distribution of *JRC* in 317 data points of the database used in correlation analysis of peak shear displacement.
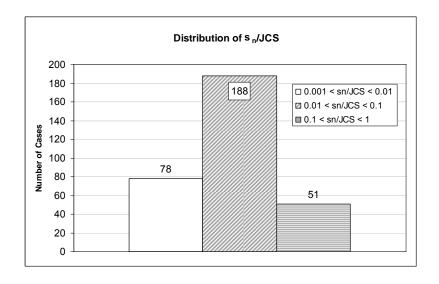
Figure 3.7: Distribution of σ_n/*JRC* in 317 data points of the database used in correlation analysis of peak shear displacement.

A power relationship has been adopted by Barton to relate peak shear displacement with block's length and *JRC*, Equation (3.31). Moreover, the power function is a convenient form to use in calculations. Consequently, in this study, it was first assumed that function *f* in Equation (3.53-ab) is a power function with the following format:

$$\pi_1 = a\pi_2{}^b\pi_3{}^c\pi_4{}^d \tag{3.53-b}$$

Assuming a power function, the problem of non-linear multivariable regression analysis can be simplified to linear multivariable regression analysis, which is much easier to solve and the solution is much more reliable in the case where the type of function is unknown. This can be done by obtaining a natural logarithm of both sides of Equation (3.53-b) as follows:

$$\ln(\pi_1) = \ln(a) + b \cdot \ln(\pi_2) + c \cdot \ln(\pi_3) + d \cdot \ln(\pi_4) \tag{3.53-c}$$

Linear multivariable regression analysis was performed. With coefficient of correlation $R^2 = 0.42$ and standard error of estimate equal to 0.65, the following constants were obtained: $a = 0.0618$; $b = -0.419$; $c = -0.37$; $d = 0.32$.

By substituting the above constants in Equation (3.53-c), the following dimensionless equation for peak shear displacement of the rock fracture was derived:

$$\frac{\delta_{peak}}{L} = 0.0618 \times \left(\frac{L}{L_0}\right)^{-0.49} \times JRC^{-0.37} \times \left(\frac{\sigma_n}{JCS}\right)^{0.32} \tag{3.55}$$

Adopting SI units (meter for length) and choosing the lab specimen size of $L_0 = 0.1m$, Equation (3.56) can be simplified as follows:

$$\delta_{peak} = 0.02 \frac{L^{0.51}}{JRC^{0.37}} \left(\frac{\sigma_n}{JCS}\right)^{0.32} \tag{3.56}$$

There is a major difference between Barton's empirical relationship, Equation (3.31), and what is obtained here by correlation analysis, Equation (3.56): although Barton found that peak shear displacement increases with *JRC*, the opposite is found here. The following analytical calculations show that the peak shear displacement should decrease by increasing *JRC*.

Figure 3.8 depicts a diagram of forces applied in shearing rough fractures. In Figure 3.8, i is the dilation angle or the effective roughness angle, which is the angle between asperities and the horizontal direction and can be defined as follows:

$$i = JRC \cdot \log_{10}\left(\frac{JCS}{\sigma}\right), \tag{3.57}$$

in which σ is normal stress on the horizontal plane.
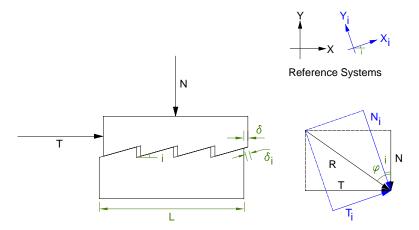
Figure 3.8: Diagram of forces applied at failure in shearing rough fracture.

In addition, R is the forces applied to the uppermost block. T and N are the horizontal and vertical components of R, respectively. These forces can be obtained by projecting R on X and Y axis. At failure, T and N, can be expressed as:

$$T = R \cdot \sin(\varphi + i) \tag{3.58}$$

$$N = R \cdot \cos(\varphi + i) \tag{3.59}$$

A new coordinate system, $X_i - Y_i$, is defined in Figure 3.8. X_i and Y_i are parallel and perpendicular to the inclined plane of the fracture, which makes an angle of i with the horizontal direction, X. T_i and N_i are the components of R in $X_i - Y_i$ coordinate system. Thus, T_i and N_i can be determined as follows:

$$T_i = R \cdot \sin(\varphi) \tag{3.60}$$

$$N_i = R \cdot \cos(\varphi) \tag{3.61}$$

In other words, T_i can be expressed in terms of N_i using the following equation:

$$T_i = N_i \cdot \tan(\varphi) \tag{3.62}$$

By substituting Equation (3.59) into Equation (3.62), N_i can be expressed as:

$$N_i = N \cdot \frac{\cos(\varphi)}{\cos(\varphi + i)} \tag{3.63}$$

77

Normal stress on the horizontal plane can be determined as:

$$\sigma = \frac{N}{L} \qquad (3.64)$$

Normal stress on the inclined plane of fracture is as follows:

$$\sigma_i = \frac{N_i}{L_i}, \qquad (3.65)$$

in which L_i is the length of the fracture along X_i direction and can be obtained from:

$$L_i = L / \cos(i) \qquad (3.66)$$

By substituting, Equations (3.63), (3.64), and (3.66) into Equation (3.65), we have:

$$\sigma_i = \sigma \cdot \frac{\cos(\varphi) \cdot \cos(i)}{\cos(\varphi + i)} \qquad (3.67)$$

It can be seen in Figure 3.8 that the peak shear displacement in X direction, δ, can be expressed in terms of the peak shear displacement in X_i direction, δ_i, as:

$$\delta = \delta_i \cdot \cos(i) \qquad (3.68)$$

In order to find whether the peak shear displacement increases or decreases with *JRC*, two fractures are defined with the following conditions (both have the same shape as what is shown in Figure 3.8):

- Different dilation angle: $0 < i_1 < i_2 < 90$; and based on Equation (3.57), we have:

$$JRC_1 \cdot \log\left(\frac{JCS}{\sigma_1}\right) < JRC_2 \cdot \log\left(\frac{JCS}{\sigma_2}\right) \qquad (3.69)$$

- Equal length along X_i direction: $(L_i)_1 = (L_i)_2$
- Equal normal stress on the inclined plane of fracture: $(\sigma_i)_1 = (\sigma_i)_2$; and using Equation (3.67), we have:

$$\frac{\sigma_1}{\sigma_2} = \frac{\cos(\varphi + i_1)}{\cos(\varphi + i_2)} \cdot \frac{\cos(i_2)}{\cos(i_1)} \qquad (3.70\text{-a})$$

Which can be simplified as:

78

$$\frac{\sigma_1}{\sigma_2} = \frac{1 - \tan(\varphi) \cdot \tan(i_1)}{1 - \tan(\varphi) \cdot \tan(i_2)} \tag{3.70-b}$$

While $0 < i_1 < i_2 < 90$ and since base friction angles, φ, are positive and less than 90 degrees:

$$\frac{\sigma_1}{\sigma_2} = \frac{1 - \tan(\varphi) \cdot \tan(i_1)}{1 - \tan(\varphi) \cdot \tan(i_2)} > 1 \tag{3.70-c}$$

- Both fractures are from the same material and have the same Fracture Compressive Strength (*JCS*) and the same base friction angle (φ_b). While *JCS* is a positive value and $JCS > \sigma2, \sigma3$:

$$\log\left(\frac{JCS}{\sigma_1}\right) < \log_{10}\left(\frac{JCS}{\sigma_2}\right) \tag{3.71}$$

Based on Equation (3.69) and (3.71), it can be concluded:

$$JRC_1 < JRC_2 \tag{3.72}$$

Based on Equation (3.68), peak shear displacements can be expressed as follows:

$$\frac{\delta_1}{\delta_2} = \frac{(\delta_i)_1}{(\delta_i)_2} \cdot \frac{\cos(i_1)}{\cos(i_2)} \tag{3.73}$$

Based on Barton's model, the peak shear displacement is a function of length of the block and *JRC*. This research found that the peak shear displacement is a function of length, *JRC*, and normal stress, Equation (3.56). Let us now apply Equation (3.56) along X_i axis. Since, along the X_i axis, *JRC* is close to zero for all cases and since $(L_i)_1 = (L_i)_2$ and $(\sigma_i)_1 = (\sigma_i)_2$, the peak shear displacements along the X_i direction are equal ($(\delta_i)_1 = (\delta_i)_2$). Thus, Equation (3.73) can be simplified as:

$$\frac{\delta_1}{\delta_2} = \frac{\cos(i_1)}{\cos(i_2)} \tag{3.74}$$

Because dilation angles are different ($0 < i_1 < i_2 < 90$), we have:

$$0 < i_1 < i_2 < 90 \Rightarrow \cos i_1 > \cos i_2 \tag{3.75}$$

79

From Equations (3.73) and (3.75), it can be concluded that the peak shear displacement decreases with the increasing dilation angle (or *JRC*):

$$\delta_1 > \delta_2 \tag{3.76}$$

In order to see whether this conclusion is consistent with Barton's model or not, the peak shear displacements expressed based on Barton's empirical Equation (Equation (3.31)) are as follows:

$$\frac{\delta_1}{\delta_2} = \left(\frac{L_1}{L_2}\right)^{0.67} \cdot \left(\frac{JRC_1}{JRC_2}\right)^{0.33} \tag{3.77}$$

Substituting Equation (3.66) in Equation (3.77) and considering $(L_i)_1 = (L_i)_2$ we have:

$$\frac{\delta_1}{\delta_2} = \left(\frac{\cos(i_1)}{\cos(i_2)}\right)^{0.67} \cdot \left(\frac{JRC_1}{JRC_2}\right)^{0.33} \tag{3.78}$$

It can be shown from Equations (3.72), (3.75), and (3.78) that according to Barton's empirical equation the peak shear displacement increases with increasing *JRC* ($\frac{\delta_1}{\delta_2} < 1$).

On the other hand, using Equation (3.56), the peak shear displacements are expressed as follows:

$$\frac{\delta_1}{\delta_2} = \left(\frac{L_1}{L_2}\right)^{0.51} \cdot \left(\frac{JRC_2}{JRC_1}\right)^{0.37} \cdot \left(\frac{\sigma_1}{\sigma_2}\right)^{0.32} \tag{3.79}$$

Substituting Equation (3.66) in Equation (3.79), and considering $(L_i)_1 = (L_i)_2$ we have:

$$\frac{\delta_1}{\delta_2} = \left(\frac{\cos(i_1)}{\cos(i_2)}\right)^{0.51} \cdot \left(\frac{JRC_2}{JRC_1}\right)^{0.37} \cdot \left(\frac{\sigma_1}{\sigma_2}\right)^{0.32} \tag{3.80}$$

Through Equations (3.70-c), (3.72), and (3.75), it was proved that all terms in the right hand side of Equation (3.80) are bigger than 1. Therefore, their multiplication is higher than 1 and consequently the left hand side is higher than 1 ($\delta_1 > \delta_2$). This is exactly consistent with Equation (3.76) and the fact that the peak shear displacement decreases with the increasing dilation angle (or increasing *JRC*).

The only problem with Equation (3.56) is predicting peak shear displacement of sawed fractures ($JRC = 0$). Based on Equation (3.68), which is consistent with Figure 3.8, the peak shear displacement of sawed fractures has the following relation:

$$\delta_i = \lim_{JRC \to 0} \frac{\delta}{\cos\left(JRC \cdot \log_{10}\left(\frac{JCS}{\sigma}\right)\right)} = \delta \tag{3.81}$$

However, based on Barton's empirical Equation (3.31):

$$\delta_i = \lim_{JRC \to 0} \delta = \lim_{JRC \to 0} \frac{L}{500}\left(\frac{JRC}{L}\right)^{0.33} = 0 \tag{3.82}$$

And based on Equation (3.56):

$$\delta_i = \lim_{JRC \to 0} \delta = \lim_{JRC \to 0} 0.02 \frac{L^{0.51}}{JRC^{0.37}}\left(\frac{\sigma}{JCS}\right)^{0.32} \to \infty \tag{3.83}$$

This shows that although the predicated peak shear displacement using Equation (3.56) changes with normal stress and decreases with increasing JRC, the developed equation still has a weakness in the case of smooth fractures ($JRC \to 0$). Therefore, the power function is a good option, but there may be better choices for relating the peak shear displacement and JRC. Consequently, the regression analysis was revised in accordance with the above mentioned analytical explanation. The goal is to find an empirical equation for the peak shear displacement of sawed fracture, δ_i, and then obtain the peak shear displacement of rough fractures, δ_{peak}, using Equation (3.68).

By performing a dimensional analysis [215], the following dimensionless parameters were found:

- $\pi_1 = \frac{\delta_i}{L_i}$: based on Equations (3.66) and (3.68), it can be simplified as:

$$\pi_1 = \frac{\dfrac{\delta_{peak}}{\cos(i)}}{\dfrac{L}{\cos(i)}} = \frac{\delta_{peak}}{L},$$

where $i = JRC.\log_{10}\left(\frac{JCS}{\sigma_n}\right)$.

81

-    $\pi_2 = \dfrac{L_i}{L_0}$: Based on Equation (3.66), it can be written as:

$$\pi_2 = \frac{L}{L_0 . \cos(i)} .$$

-    $\pi_3 = \dfrac{\sigma_i}{JCS}$: in which σ_i is the normal stress on the inclined plane of fracture and can be expressed in terms of σ_n, the normal stress on the horizontal plane, using Equation (3.67). Therefore, π_3 can be written as

$$\pi_3 = \frac{\sigma_n}{JCS} \cdot \frac{\cos \varphi \cos i}{\cos(\varphi + i)} .$$

All 362 direct shear test records available in the MDST database were used to calculate the three above mentioned dimensionless parameters and perform correlation analyses to find π_1 as a function of π_2, π_3 :

$$\pi_1 = f(\pi_2, \pi_3) \qquad\qquad (3.84\text{-a})$$

Since the power function is a convenient form to be used in calculations, it was assumed that function f in Equation (3.84-a) is a power function as follows:

$$\pi_1 = a\pi_2^{\,b}\pi_3^{\,c} \qquad\qquad (3.84\text{-b})$$

Therefore, the problem of non-linear multivariable regression analysis can be simplified to linear multivariable regression analysis which is much easier to solve and the solution is much more reliable. This can be done by obtaining a natural logarithm of both sides of Equation (3.84-b) as follows:

$$\ln(\pi_1) = \ln(a) + b \cdot \ln(\pi_2) + c \cdot \ln(\pi_3) \qquad\qquad (3.84\text{-c})$$

Linear multivariable regression analysis was performed. With coefficient of correlation $R^2 = 0.38$ and standard error of estimate equal to 0.68, the following constants were derived:

$$a = 0.027 ; \quad b = -0.55 ; \quad c = 0.34$$

By substituting the above constants in Equation (3.84-c), the following dimensionless equation for the peak shear displacement of sawed fractures was obtained:

$$\frac{\delta_i}{L_i} = 0.027\left(\frac{L_i}{L_0}\right)^{-0.55} \cdot \left(\frac{\sigma_i}{JCS}\right)^{0.34} \tag{3.85}$$

Adopting SI units (meter for length) and choosing the lab specimen size of $L_0 = 1$ m, Equation (3.85) can be simplified as follows:

$$\delta_i = 0.0077 L_i^{0.45}\left(\frac{\sigma_i}{JCS}\right)^{0.34} \tag{3.86}$$

Substituting Equations (3.66) to (3.68) into Equation (3.86), the peak shear displacement of the rough fractures can be obtained using the following equation:

$$\delta_{peak} = 0.0077 L^{0.45} \cdot \left(\frac{\sigma_n}{JCS}\right)^{0.34} \cdot \cos(i) \cdot \left[\frac{1}{(\cos i)^{0.45}}\left(\frac{\cos\varphi\cos i}{\cos(\varphi + i)}\right)^{0.34}\right] \tag{3.87}$$

The base friction angle ranges between 25° to 35° for the majority of unweathered rock surfaces [92, 136, 141-145]. Furthermore, in view of the safety requirement of rock engineering structures, the value of $\varphi + i$ is limited to 70°. Therefore, the last part of the right hand side of Equation (3.88), $\left[\frac{1}{(\cos i)^{0.45}}\left(\frac{\cos\varphi\cos i}{\cos(\varphi + i)}\right)^{0.34}\right]$, can range between 1 and 1.45. Thus, for simplicity it can be eliminated from the equation. Consequently, the following empirical relation can be used for the peak shear displacement of fractures:

$$\delta_{peak} = 0.0077 L^{0.45} \cdot \left(\frac{\sigma_n}{JCS}\right)^{0.34} \cdot \cos\left(JRC\log(\frac{JCS}{\sigma_n})\right) \tag{3.88}$$

Table 3.3 compares Equations (3.31), (3.56), and (3.88) with each other, in accordance with their ratio of predicted to the measured peak shear displacement, $\frac{\delta_{predicted}}{\delta_{measured}}$, for the 317 cases of MDST database with JRC between 2 and 20. Correlation analysis Equation (3.88) had a smaller R^2 compared to Equation (3.56) (0.38 compared to 0.42). However, based on the following reasons, it can be concluded from Table 3.3 that Equation (3.88) works the best in predicting peak shear displacement of fractures:

- Although Equation (3.56) has the higher value of $(\dfrac{\delta_{predicted}}{\delta_{measured}})_{Min}$, Equation (3.88) has the minimum value of $(\dfrac{\delta_{predicted}}{\delta_{measured}})_{Average}$, $(\dfrac{\delta_{predicted}}{\delta_{measured}})_{Max}$, and sum of the square of errors, $\sum\left(1-\dfrac{\delta_{predicted}}{\delta_{measured}}\right)^2$, among the other options.

- The correlation factor, which is defined as the ratio of standard deviation to the average, $(\dfrac{\delta_{predicted}}{\delta_{measured}})_{STD} / (\dfrac{\delta_{predicted}}{\delta_{measured}})_{Average}$, is also the minimum in the case of Equation (3.88) (0.68 compared to 0.99 and 0.69 from Barton's equation and Equation (3.56), respectively).

Table 3.3: Comparing Barton's empirical equation with Equations (3.56) and (3.88) in predicating the peak shear displacement of rock fractures.

Parameter	Barton's Equation (3.31)	Equation (3.56)	Equation (3.88)
$(\dfrac{\delta_{predicted}}{\delta_{measured}})_{Average} \pm STD$	1.64+1.63	1.26+0.87	1.11+0.76
$(\dfrac{\delta_{predicted}}{\delta_{measured}})_{Max}$	13.70	6.36	5.59
$(\dfrac{\delta_{predicted}}{\delta_{measured}})_{Min}$	0.12	0.23	0.19
$\sum\left(1-\dfrac{\delta_{predicted}}{\delta_{measured}}\right)^2$	980.22	259.70	188.47

In addition, for the above mentioned 317 data points, Figure 3.9 illustrates predicted peak shear displacement, $\delta_{predicted}$, using Barton's equation and Equation (3.88) versus the measured peak shear displacement, $\delta_{measured}$. It can be seen in the

figure that the distribution of $\delta_{predicted}$ versus $\delta_{measured}$ for the case of Equation (3.88) is closer to the ideal line of $\delta_{predicted} = \delta_{measured}$ compared to those obtained employing Barton's equation.

(a)   (b)
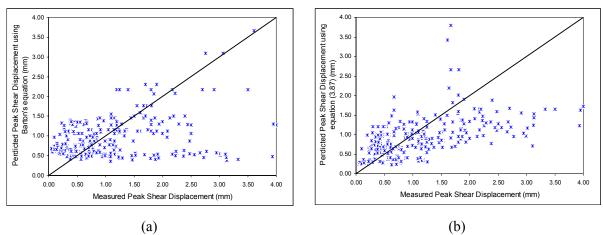
Figure 3.9: Predicted versus the measured peak shear displacement: (a) using Barton's equation; (b) Equation (3.88).

Furthermore, using Equation (3.88) to predict the peak shear displacement of rock fractures has advantages over Equations (3.31) and (3.56), because it is the only one that can be used for all types of rock fractures including sawed, smooth, and rough. Figure 3.10 compares experimental peak shear displacement for sand blasted and sawed fractures ($JRC = 0$) with the values predicted employing Equation (3.88), as the suggested empirical equation of this study. While Equation (3.31) predicts zero peak shear displacement for sawed fractures and Equation (3.56) tends to infinity, Equation (3.88) yields a good estimation, as it can be seen in Figure 3.10.

Figure 3.11 demonstrates the ability of Equation (3.88) to consider the effect of normal stress on the peak shear displacement. Also shown in Figures 3.12 (m) through (p) is Wibowo's linear correlation (Equation (3.36)). Although, Wibowo's approximation performs the best in these Figures, constants a and b in Wibowo's model have to be determined experimentally for each fracture, whereas no additional parameter has to be determined in Equation (3.88).

85

(a) Sand blasted fractures

(b) Diamond sawed fractures

(c) Sawed fractures
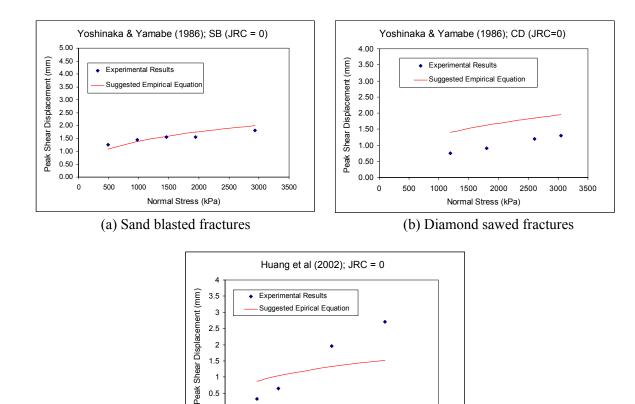
Figure 3.10: Comparing measured peak shear displacement with their predicted values using Equation (3.88) for the case of sawed fractures (*JRC*=0)

3.3.3   Post-peak stress-displacement curve

Barton expressed the post-peak stress-displacement curve by using the concept of roughness   mobilization, $JRC_{mobilized}$,   in   Equation   (3.3)   [115].   The   ratio $JRC_{mobilized} / JRC_{peak}$ can be estimated from the ratio δ / δ_{peak} employing the values given in Table 3.2.

Barton assumed that at a shear displacement of $100\delta_{peak}$, the mobilized *JRC* becomes zero. It seems to be just an approximation for the end of the curve; because obviously there are few experimental results containing post-peak shear strength of rock

fractures up to about $100\delta_{peak}$. Moreover, after even this amount of displacement, the fracture surface is not the same as sawed fracture ($JRC_{mobilized} = 0$).
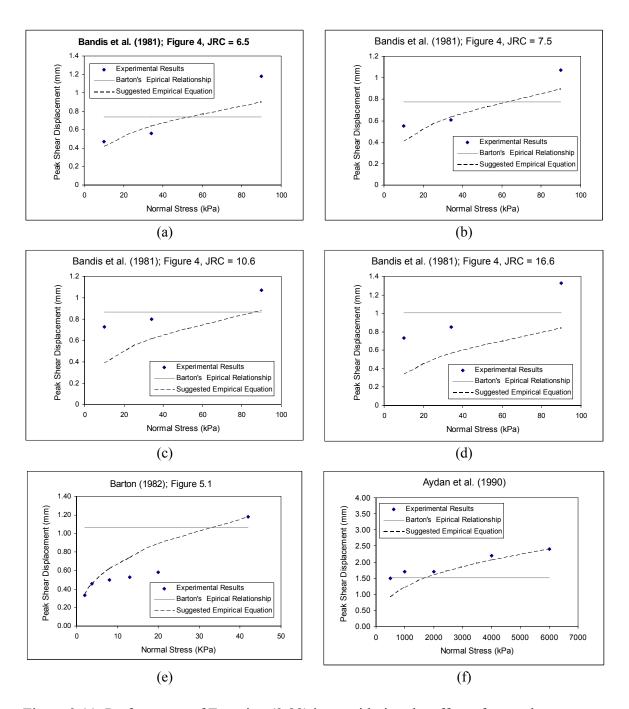
Figure 3.11: Performance of Equation (3.88) in considering the effect of normal stress on the peak shear displacement as compared to Barton's Equation (Equation (3.31))

Figure 3.11-Continued: Performance of Equation (3.88) in considering the effect of normal stress on the peak shear displacement as compared to Barton's Equation (Equation (3.31))
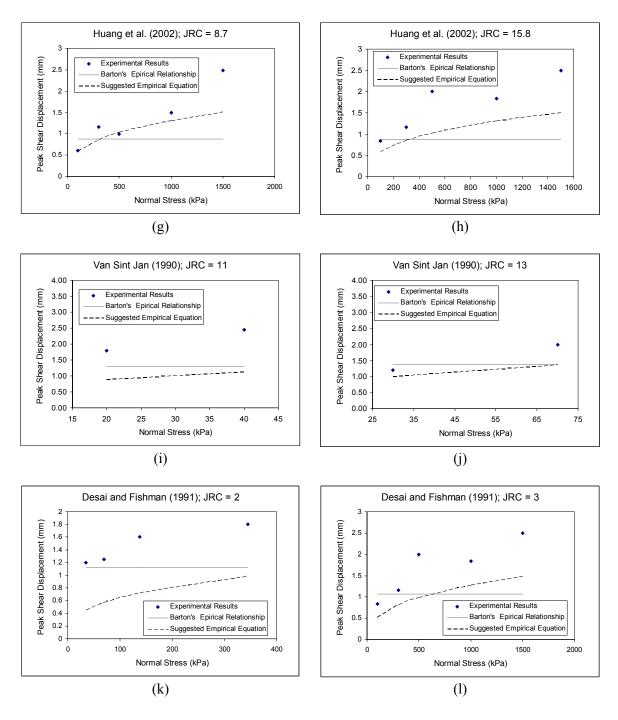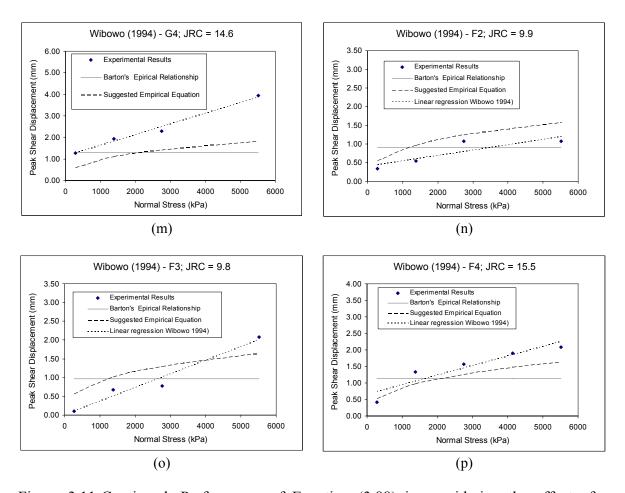
Figure 3.11-Continued: Performance of Equation (3.88) in considering the effect of normal stress on the peak shear displacement as compared to Barton's Equation (Equation (3.31))

In addition, Barton divided the problem of post-peak shear strength into two categories: non-planar ($JRC > 5$) and planar ($JRC \leq 5$) fractures [115]. There is an inconsistency for the case of planar fracture. At peak shear displacement, the mobilized JRC was assumed to be 0.95 times of JRC_{peak}. On the other hand, the mobilized JRC was assigned to be equal to the peak value of JRC, when the shear displacement is twice as much as the peak shear displacement. However, the peak value of JRC, which is coincident with peak shear strength, should be mobilized at the peak shear displacement. Using the values given in Table 3.2 for planar fractures, the post-peak

89

shear strength at a shear displacement of $2\delta_{peak}$ is higher than the shear strength at δ_{peak}. For the case of planar fractures, assume that the actual peak shear displacement is the one related to the mobilized JRC of JRC_{peak} (i.e.: two times as much as it is defined in Table 3.2). As can be seen in Figure 3.12, there is no significant difference between the post-peak values of $JRC_{mobilized} / JRC_{peak}$ given in Table 3.2 for non-planar and planar fractures.

Regarding the above mentioned inconsistencies of Barton's empirical model in predicting the post-peak shear strength of rock fractures, the MDST database was analyzed in order to find an empirical relationship between the mobilized JRC and post-peak shear displacement. Initially, it was assumed that the ratio of $JRC_{mobilized} / JRC_{peak}$ is a function of not only δ / δ_{peak}, but also normal stress, JCS, and JRC_{peak}.
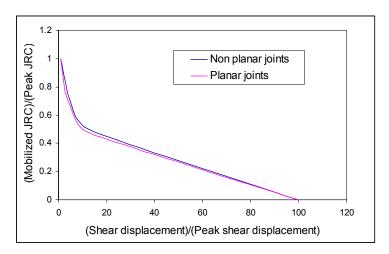
Figure 3.12: Comparing the post-peak values of $JRC_{mobilized} / JRC_{peak}$ given by Barton for planar and non-planar fractures

It should be noted that most of the direct shear tests performed for research or professional purposes are conducted up to a shear displacement of not more than 15 mm. Even according to ASTM D5607-02, the displacement devices used to measure shear displacement in direct shear tests should accommodate a displacement of 13 mm. For a

lab-size specimen of 10 cm, the peak shear displacement is about 1 mm (using the "rule-of-thumb" suggested by Barton [92]) and shear displacement of 15 mm is approximately 15 times the peak shear displacement. Consequently, any database used for correlation analysis suffers from lack of information for post-peak shear strength when shear displacements are greater than $15\delta_{peak}$.

The MDST database contains 255 direct shear test records for which the magnitude of post-peak shear strength are known at 1 to 4 different points; this gives a total number of 762 data points with δ/δ_{peak} ranging between 1 and 40, four of which have δ/δ_{peak} between 25 and 40. Eliminating these four cases, the other 758 data points ($1 < \delta/\delta_{peak} < 25$) have a distribution illustrated in Figure 3.13, which shows that the most of the data points have δ/δ_{peak} between 1 and 15 (730 out of 758).

Therefore, regression analysis performed on the MDST database is reliable up to $\delta/\delta_{peak} = 10$. Clearly, for $\delta/\delta_{peak} > 10$, the obtained relationship from correlation analysis is almost an extrapolation of the approximation through the points with smaller amount of displacements. Thus, for large shear displacements, the correlation analysis of MDST suffers from exactly the same weakness as Barton's model.
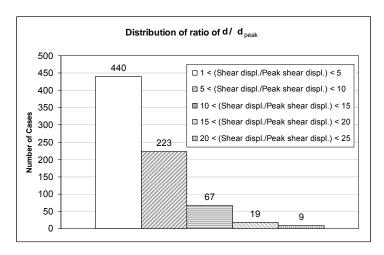
Figure 3.13: Distribution of δ/δ_{peak} for 758 data points of MDST database used in correlation analysis of post-peak shear strength.

By performing a dimensional analysis [215], the following dimensionless parameters were found:

$$\pi_1 = \frac{JRC_{mobilized}}{JRC_{peak}}, \quad \pi_2 = \frac{\delta}{\delta_{peak}}, \quad \pi_3 = JRC_{peak}, \quad \pi_4 = \frac{\sigma_n}{JCS}$$

Correlation analyses were performed to find π_1 as a function of π_2, π_3, π_4:

$$\pi_1 = f(\pi_2, \pi_3, \pi_4) \tag{3.89-a}$$

The magnitude of π_3 (JRC) in 758 data points of the MDST database ranges from 0 to 20 with a normal distribution depicted in Figure 3.14. In addition, Figure 3.7 shows that $\frac{\sigma_n}{JCS}$ ranges between 0.001 and 0.6 with ab acceptable distribution. Initial correlation analysis showed that there is no correlation between π_1 and both π_3 and π_4. Therefore, Equation (3.89-a) can be written as follows:

$$\pi_1 = f(\pi_2) \tag{3.89-b}$$

Since at peak shear displacement ($\delta = \delta_{peak}$), the mobilized JRC should be equal to JRC_{peak}, Equation (3.89-b) should satisfy condition $\pi_1 = f(1) = 1$.

Barton expressed the relationship between π_1 and π_2 in tabular format (Table 3.2). The most common method of using the table is linear interpolation between given values. In order to have an initial idea about the shape of function f, the values presented in Table 3.2 were analyzed. The table can be approximated by the following functions:

- Eliminating the weakest point of the table ($\frac{\delta}{\delta_{peak}} = 100$), the best fit function would be power function ($\pi_1 = \pi_2^a$).

- Eliminating the second weakest point of the table ($\frac{\delta}{\delta_{peak}} = 25$), the best fit function would be logarithmic function ($\pi_1 = 1 - a.\ln(\pi_2)$).

The correlation analysis revealed that the power function fits experimental results the best. Thus, the following empirical equation with R^2 of 0.52 and standard error of estimate of 0.58 is proposed to obtain $JRC_{mobilized}/JRC_{peak}$ from δ/δ_{peak}:

$$\frac{JRC_{mobilized}}{JRC_{peak}} = \left(\frac{\delta}{\delta_{peak}}\right)^{-0.381} \tag{3.90}$$

Table 3.4 compares the predicted versus measured values obtained by using Equation (3.90) against Table 3.2 for 762 data points of the MDST database. In addition, Figure 3.15 illustrates the predicted value of $JRC_{mobilized}/JRC_{peak}$ using Barton's model (Table 3.2) and Equation (3.90) versus the measured value of $JRC_{mobilized}/JRC_{peak}$.
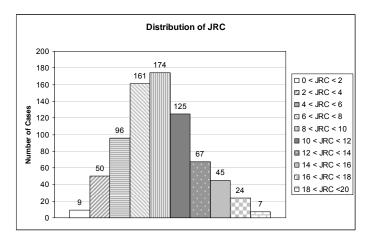
Figure 3.14: Distribution of *JRC* for data points of MDST database used in correlation analysis of post-peak shear strength.

Based on the following reasons, it can be concluded from Table 3.4 and Figure 3.15 that Equation (3.90) works better than Table 3.2 in predicting $JRC_{mobilized}$:

-   Although Equation (3.90) has the smaller value of $\left(\dfrac{(JRC_{mobilized})_{perdicted}}{(JRC_{mobilized})_{measured}}\right)_{Min}$, it

    has the minimum value of $\left(\dfrac{(JRC_{mobilized})_{perdicted}}{(JRC_{mobilized})_{measured}}\right)_{Average}$, $\left(\dfrac{(JRC_{mobilized})_{perdicted}}{(JRC_{mobilized})_{measured}}\right)_{Max}$

, and sum of the square of errors, $\sum\left(1-\dfrac{(JRC_{mobilized})_{perdicted}}{(JRC_{mobilized})_{measured}}\right)^2$, compared to

Table 3.2.

- The correlation factor, which is defined as the ratio of standard deviation to the

average, $\dfrac{\left(\dfrac{(JRC_{mobilized})_{perdicted}}{(JRC_{mobilized})_{measured}}\right)_{STD}}{\left(\dfrac{(JRC_{mobilized})_{perdicted}}{(JRC_{mobilized})_{measured}}\right)_{Average}}$, is also the minimum in the case of

Equation (3.90) (0.77 compared to 0.79).

- It can be seen in Figure 3.15 that the distribution of the predicted value of $JRC_{mobilized} / JRC_{peak}$ versus the measured value of $JRC_{mobilized} / JRC_{peak}$ using

Equation (3.90) is closer to the ideal line of $\dfrac{(JRC_{mobilized})_{perdicted}}{(JRC_{mobilized})_{measured}}=1$ compared

to those obtained employing Barton's equation.

Table 3.4: Comparison between Barton's model proposed in tabular format and Equation (3.90) in predicting the ratio of $JRC_{mobilized}$ from real δ / δ_{peak} .

Parameter	Barton's Model (Table 3.2)	Equation (3.90)
$\left(\dfrac{(JRC_{mobilized})_{perdicted}}{(JRC_{mobilized})_{measured}}\right)_{Average} \pm STD$	1.39+1.10	1.19+0.92
$\left(\dfrac{(JRC_{mobilized})_{perdicted}}{(JRC_{mobilized})_{measured}}\right)_{Max}$	11.97	9.67
$\left(\dfrac{(JRC_{mobilized})_{perdicted}}{(JRC_{mobilized})_{measured}}\right)_{Min}$	0.56	0.43
$\sum\left(1-\dfrac{(JRC_{mobilized})_{perdicted}}{(JRC_{mobilized})_{measured}}\right)^2$	37.83	32.35

| (a) | (b) |
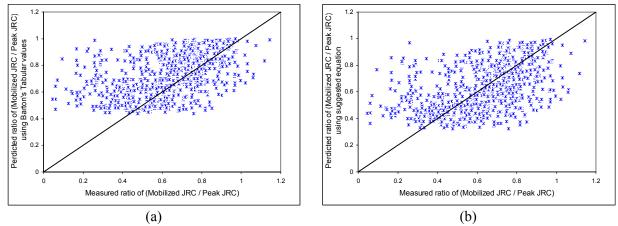
Figure 3.15: Predicted versus the measured $JRC_{mobilized} / JRC_{peak}$: (a) Barton's model (Table 3.2); (b) Equation (3.90)

Barton suggested empirical Equation (3.31) to predict peak shear displacement of rock fractures and Table 3.2 to estimate the mobilized JRC. In this study, Equation (3.88) was proposed to estimate peak shear displacement and Equation (3.90) was introduced to predict the mobilized JRC. In Table 3.5 the ability of Barton's model and the proposed modified equations in predicting $JRC_{mobilized}$ for 762 data points of the MSDT database are compared.

Table 3.5: Comparison between Barton's model (Equation (3.31) and Table 3.2) and proposed model (Equations (3.88) and (3.90)) in predicting $JRC_{mobilized}$

Parameter	Barton's Model	Proposed Model
$\left(\dfrac{(JRC_{mobilized})_{perdicted}}{(JRC_{mobilized})_{measured}} \right)_{Average} \pm STD$	1.44+1.36	1.20+1.12
$\left(\dfrac{(JRC_{mobilized})_{perdicted}}{(JRC_{mobilized})_{measured}} \right)_{Max}$	15.13	12.56
$\left(\dfrac{(JRC_{mobilized})_{perdicted}}{(JRC_{mobilized})_{measured}} \right)_{Min}$	0.47	0.39
$\sum \left(1 - \dfrac{(JRC_{mobilized})_{perdicted}}{(JRC_{mobilized})_{measured}} \right)^2$	45.88	41.74

95

It can be concluded from Table 3.5 that the proposed modified equations work batter than Barton's model in predicting $JRC_{mobilized}$, due to the following reasons:

- Although the proposed modification has the smaller value of $\left(\dfrac{(JRC_{mobilized})_{perdicted}}{(JRC_{mobilized})_{measured}}\right)_{Min}$, it has the minimum value of

$\left(\dfrac{(JRC_{mobilized})_{perdicted}}{(JRC_{mobilized})_{measured}}\right)_{Average}$, $\left(\dfrac{(JRC_{mobilized})_{perdicted}}{(JRC_{mobilized})_{measured}}\right)_{Max}$, and sum of the square of

errors, $\sum\left(1-\dfrac{(JRC_{mobilized})_{perdicted}}{(JRC_{mobilized})_{measured}}\right)^2$, compared to Barton's model.

- The correlation factor, which is defined as the ratio of standard deviation to the

average, $\dfrac{\left(\dfrac{(JRC_{mobilized})_{perdicted}}{(JRC_{mobilized})_{measured}}\right)_{STD}}{\left(\dfrac{(JRC_{mobilized})_{perdicted}}{(JRC_{mobilized})_{measured}}\right)_{Average}}$, is also the minimum in the case of

proposed model (0.93 compared to 0.94).

Just for a comparison, Figure 3.16 depicts the proposed model, Equation (3.90), and Barton's Tabular model (Table 3.2) for δ/δ_{peak} ranging between 1 and 100.

In conclusion, Equation (3.90) is proposed to predict the mobilized JRC after peak shear displacement. In addition to the fact that it works better than Table 3.2 in the MDST database, it has a smoother curve compared to the linear interpolation of the values given in Table 3.2 and is easier to implement numerically. Furthermore, Equation (3.90) is independent of JRC and does not have the same problem as the above mentioned inconsistency of Table 3.2 for the case of planar fractures. Both Table 3.2 and Equation (3.90) suffer from the same problem: lack of information of rock fracture shear strength at shear displacement more than 10 times the peak shear displacement. As a result, the predicted magnitudes of mobilized JRC at high shear displacements (

$\delta / \delta_{peak} > 10$) using either Table 3.2 or Equation (3.90) are just an extrapolation of the relationships obtained by correlation analyses of data points available at smaller displacements. However, in this regard Equation (3.90) has the following advantages over Table 3.2:

- At $\delta / \delta_{peak} = 100$, Table 3.2 suggested $JRC_{mobilized} = 0$, while Equation (3.90) proposed $JRC_{mobilized} = 0.17 JRC_{peak}$, which is more realistic, because, even after this large amount of displacement, one can not expect a rough fracture to behave the same as a sawed fracture.

- After 100 times peak shear displacement, Table 3.2 has no clear suggestion (or maybe proposes a negative value for $JRC_{mobilized}$). However, Equation (3.90) yields positive values for *JRC* regardless of the amount of shear displacement.

- Up to about 50 times the peak shear displacement, the predicted $JRC_{mobilized}$ using Equation (3.90) is smaller than that obtained employing Table 3.2. Before reaching 50 times the peak shear displacement of fractures, using Equation (3.90) instead of Table 3.2 for post-peak shear displacement is conservative.
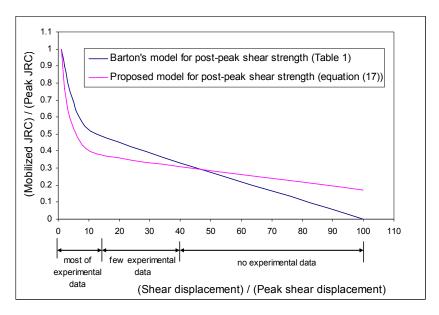
Figure 3.16: Comparison between proposed model for post-peak shear strength (Equation (3.90)) and Barton's model (Table 3.2)

97

3.3.4 Dilatancy

In this section, the dilatancy behavior of rock fractures is investigated. The goal is to find dilation displacement at any shear displacement. The problem is divided into two parts: pre-peak and post-peak dilatancy, which means dilatancy before and after peak shear displacement, respectively.

3.3.4.1 Pre-peak

The MDST database contains the results of 242 direct shear tests for which at least dilation at the peak shear displacement is available. Based on the shape of the vertical displacement versus the shear displacement curve and how much information is available for each test, the results were divided into 4 different categories (Table 3.6).

Table 3.6: Different categories of the MDST database Based on the shape of the vertical displacement versus the shear displacement curve and available information

Categories	Number of tests	Available data	Issues
Category 1	96	- Dilation at peak shear displacement - Shear displacement at which the fracture started to dilate	No negative dilation was depicted. This category contains the results of 96 tests, 34 cases of which come from Barton [115], Barton et al. [81], and Bandis et al. [79]. While they did not consider the negative dilation in their model, there is a possibility that they had eliminated the negative part in presenting their experimental work.
Category 2	91	- Maximum negative dilation - Dilation at peak shear displacement - Shear displacement at which dilation is zero	Fractures initially showed negative dilation followed by positive dilation.
Category 3	38		Dilation was negative at all points. 35 out of 38 cases of this category have experienced shearing under different normal stresses. Thus, there is considerable uncertainty regarding these data including mismatching results. Therefore, this category was not considered in correlation analyses.
Category 4	17	- Dilation at peak shear displacement	This category was used for validation purposes.

Barton [115] indicated that a rock fracture begins to dilate at the instant that $JRC_{mobilized} = 0$. Also, he assumed zero dilation up to $\delta = 0.3\delta_{peak}$. However, in the MDST database, almost in half of the cases, there is a negative dilation which will be eliminated by Barton's model.

On the other hand, Barton [115] proposed Equation (3.48) for the tangent dilation angle at each shear displacement and Table 3.2 for mobilized JRC. Based on Table 3.2, $JRC_{mobilized}$ is negative up to $\delta / \delta_{peak} = 0.3$. Therefore, the tangent dilation angle should be negative up to $\delta / \delta_{peak} = 0.3$. In addition, $JRC_{mobilized}$ is zero at $\delta / \delta_{peak} = 0.3$ and then has a positive value. As a result, dilation displacement should decrease up to $\delta / \delta_{peak} = 0.3$ and then increase. Thus, $\delta / \delta_{peak} = 0.3$ should be the minimum of dilation displacement, not the point at which the fracture starts to dilate. Consequently, Equation (3.48) is inconsistent with Table 3.2.

Barton and Choubey [22] used the peak secant dilation angle, also called initial dilation angle, and the peak tangent dilation angle. Based on their experimental results, they found that the peak secant dilation angle is about one-third of the peak tangent dilation angle. They proposed Equation (3.45) and (3.46) for peak and secant dilation angles, respectively. There are two ways to predict the peak secant dilation angle:

-    Option 1: estimate the peak secant dilation angle using Equation (3.46).

-    Option 2: use Equation (3.45) to estimate the peak tangent dilation angle, employ Equation (3.47) to predict damage coefficient, M, and estimate the peak secant dilation angle to be one-third of the peak tangent dilation angle:

$$d_{s,peak} = (1/3)\cdot\left(\frac{1}{M} JRC.\log_{10}\left(\frac{JCS}{\sigma_n} \right) \right)$$ (3.91)

Regarding the above mentioned inconsistencies and ambiguity, the MDST database was analyzed to find a clear model for dilatancy behavior of rock fractures that can predict dilation at each shear displacement.

In order to find which option works better, all 204 cases (Categories 1, 2, and 4 of the MDST database in Table 3.6) were considered. For each case, the peak secant dilation

angle, $d_{s,peak}$, was estimated using the above mentioned two options. Then, dilation displacement at peak shear displacement, $(\delta_v)_{peak}$, was calculated using the following equation with the measured value of δ_{peak}:

$$(\delta_v)_{peak} = \delta_{peak} \cdot \tan(d_{s,peak}) \tag{3.92}$$

The two options were compared in Table 3.7, in accordance with their ratio of predicted $(\delta_v)_{peak}$ to measured $(\delta_v)_{peak}$. Table 3.7 shows that option 2 is far better than option 1.

Next, the goal was to find at which shear displacement(s), dilation displacement is zero. Barton [115] indicated that dilation will begin at the instant that $JRC_{mobilized} = 0$ (zero dilation up to $\delta / \delta_{peak} = 0.3$). Analysis of the MDST database shows that, on average, zero dilation occurs as follows:

- In category 1 (no negative dilation): up to $\delta / \delta_{peak} = 0.36$.

- In category 2 (with negative dilation): at $\delta / \delta_{peak} = 0.5$.

- In categories 1 and 2 (together): at $\delta / \delta_{peak} = 0.43$.

Table 3.7: Comparison of two available options to predict the peak secant dilation angle at peak shear displacement

Parameter	Option 1	Option 2
$\left(\dfrac{\left((\delta_v)_{peak}\right)_{predicted}}{\left((\delta_v)_{peak}\right)_{measured}} \right)_{Average} \pm STD$	1.52+2.14	1.21+1.41
$\left(\dfrac{\left((\delta_v)_{peak}\right)_{predicted}}{\left((\delta_v)_{peak}\right)_{measured}} \right)_{Max}$	15.57	9.49
$\left(\dfrac{\left((\delta_v)_{peak}\right)_{predicted}}{\left((\delta_v)_{peak}\right)_{measured}} \right)_{Min}$	0.09	0.10
$\sum \left\{ 1 - \left(\dfrac{\left((\delta_v)_{peak}\right)_{predicted}}{\left((\delta_v)_{peak}\right)_{measured}} \right) \right\}^2$	706.18	325.54

As it was mentioned above, from Table 3.2, one can expect that $\delta/\delta_{peak} = 0.3$ is the point with minimum dilation. However, Barton defined it as the point at which the fracture starts to dilate. Here, in order to build a model for dilatancy behavior of rock fractures, the following assumptions were made:

- Dilation displacement is minimum at $\delta/\delta_{peak} = 0.25$

- Dilation displacement is zero at $\delta/\delta_{peak} = 0.50$

Assuming zero dilation at $\delta/\delta_{peak} = 0.50$ is compatible with the average value obtained from Category 2 of the MDST database. In addition, assuming minimum dilation at $\delta/\delta_{peak} = 0.25$ is very close to the average value obtained from Category 1 of the MDST database and what Barton defined in Table 3.2 as far as $JRC_{mobilized}$ or introduced as starting point of dilation.

Finally, the goal was to find an equation with which dilation displacement can be obtained at each shear displacement. The dimensionless forms of displacement are defined as $\dfrac{\delta_h}{\delta_{peak}}$ and $\dfrac{\delta_v}{\delta_{peak}}$ where δ_h is shear displacement, δ_v is normal displacement (dilation displacement), and δ_{peak} is peak shear displacement. The equation should satisfy the following conditions:

1) At $\dfrac{\delta_h}{\delta_{peak}} = 0 : \dfrac{\delta_v}{\delta_{peak}} = 0$

2) At $\dfrac{\delta_h}{\delta_{peak}} = 0.5 : \dfrac{\delta_v}{\delta_{peak}} = 0$

3) At $\dfrac{\delta_h}{\delta_{peak}} = 1 : \dfrac{\delta_v}{\delta_{peak}} = \dfrac{(\delta_v)_{peak}}{\delta_{peak}}$

Thus, a quadratic equation with zero intercept as follows would be a good option:

$$\frac{\delta_v}{\delta_{peak}} = a \cdot \left(\frac{\delta_h}{\delta_{peak}} \right)^2 + b \cdot \left(\frac{\delta_h}{\delta_{peak}} \right) \tag{3.93}$$

101

In order to satisfy the second and third above mentioned conditions, constants in Equation (3.93) should have the following relations:

$$0.5a + b = 0 \tag{3.94}$$

$$a + b = \frac{(\delta_v)_{peak}}{\delta_{peak}} \tag{3.95}$$

Therefore, the constants were obtained as follows:

$$a = 2\frac{(\delta_v)_{peak}}{\delta_{peak}} \tag{3.96}$$

$$b = -\frac{(\delta_v)_{peak}}{\delta_{peak}} \tag{3.97}$$

Substituting Equations (3.96) and (3.97) in Equation (3.93), we have:

$$\frac{\delta_v}{\delta_{peak}} = \frac{(\delta_v)_{peak}}{\delta_{peak}}\left[2\cdot\left(\frac{\delta_h}{\delta_{peak}}\right)^2 - \left(\frac{\delta_h}{\delta_{peak}}\right)\right] \tag{3.98}$$

These constants, Equations (3.96) and (3.97), also satisfy the condition that minimum dilation occurs at $\delta/\delta_{peak} = 0.25$:

$$\left.\begin{array}{l}\dfrac{d(\dfrac{\delta_v}{\delta_{peak}})}{d(\dfrac{\delta_h}{\delta_{peak}})} = 2a\cdot(\dfrac{\delta_h}{\delta_{peak}}) + b = \dfrac{(\delta_v)_{peak}}{\delta_{peak}}\left\{4(\dfrac{\delta_h}{\delta_{peak}}) - 1\right\} \\[4mm] \dfrac{\delta_h}{\delta_{peak}} = 0.25 \end{array}\right\} \Rightarrow \dfrac{d(\dfrac{\delta_v}{\delta_{peak}})}{d(\dfrac{\delta_h}{\delta_{peak}})} = 0$$

Based on the proposed model for pre-peak dilation displacement, the tangent dilation angle of rock fractures at each point can be obtained as follows:

$$d_t = \arctan\left(\frac{d\left(\dfrac{\delta_v}{\delta_{peak}}\right)}{d\left(\dfrac{\delta_h}{\delta_{peak}}\right)}\right) = \arctan\left(\frac{(\delta_v)_{peak}}{\delta_{peak}}\left[4\cdot\left(\frac{\delta_h}{\delta_{peak}}\right) - 1\right]\right) \tag{3.99}$$

Therefore, the peak tangent dilation angle can be obtained as follows:

$$d_p = \arctan\left(3\frac{(\delta_v)_{peak}}{\delta_{peak}}\right) \tag{3.100}$$

Substituting Equation (3.92) in Equation (3.100), we have:

$$d_p = \arctan\left(3\tan(d_{s,peak})\right) \tag{3.101}$$

Recall that the shear strength of a rock fracture at peak shear displacement can be predicted using Equation (3.3). According to Barton's model [21], the tangent dilation angle at peak shear displacement should be as follows:

$$d_p' = JRC \cdot \log_{10}\left(\frac{JCS}{\sigma_n}\right) \tag{3.102}$$

The MDST database contains the results of 341 direct shear tests for which all required information (JRC, JCS, and normal stress) is available in order to calculate d_p'. The analysis proceeded as follows: the peak secant dilation angle was calculated per option 2 by using Equations (3.47) and (3.91), then, the peak tangent dilation angle was obtained employing Equation (3.101). The ratio of d_p / d_p' ranged from 0.2 to 1.31 and had an average of 0.82 with standard deviation of 0.2. While both d_p and d_p' are defined as the tangent dilation angle at peak shear displacement, it is expected that d_p / d_p' to be 1. Therefore, based on Equations (3.101) and (3.102), the secant dilation angle at can be calculated using the following equation:

$$d_{s,peak} = \arctan\left(\frac{1}{3}\cdot\tan\left(JRC\cdot\log_{10}\left(\frac{JCS}{\sigma_n}\right)\right)\right) \tag{3.103}$$

As a result, an empirical model is proposed for pre-peak dilatancy behavior of rock fractures. The model is depicted in Figure 3.17. The dilation displacement can be calculated at each shear displacement using the following equation:

$$\frac{\delta_v}{\delta_{peak}} = \frac{1}{3}\cdot\tan\left(JRC\cdot\log_{10}\left(\frac{JCS}{\sigma_n}\right)\right)\cdot\left(\frac{\delta_h}{\delta_{peak}}\right)\cdot\left\{2\left(\frac{\delta_h}{\delta_{peak}}\right)-1\right\} \tag{3.104}$$
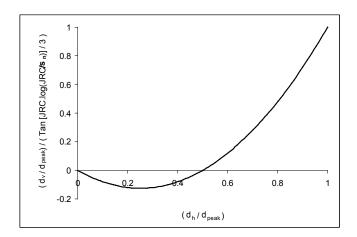
Figure 3.17: Proposed model for pre-peak dilation displacement of rock fractures

The proposed model has none of the inconsistencies and ambiguity of Barton's model described in the initial part of this section. Moreover, it simulates negative dilation, while Barton's model does not. For category 2 of the MDST database using the proposed model, Equation (3.104), it is found that $\left(\dfrac{\left(\delta_{v-\min} \right)_{predicted}}{\left(\delta_{v-\min} \right)_{measured}} \right)_{average} = 0.65$, compared to Barton's model that gave zero. Underestimation of minimum dilation displacement in the suggested model can be justified by considering no negative dilation in category 1. Furthermore, the proposed model predicts zero dilation at $\delta / \delta_{peak} = 0.50$, which is closer to the average measured value, $\delta / \delta_{peak} = 0.43$, compared to what Barton's model suggests, $\delta / \delta_{peak} = 0.33$. In addition, the dilation displacement at each shear displacement can be calculated easily using Equation (3.104); its numerical implementation is also much easier.

3.3.4.2 Post-peak dilatancy

In the previous section, Equation (3.104) was proposed to obtain dilation displacement at each shear displacement before peak shear strength. In this section, the post-peak dilation is considered. The tangent dilation angle defined in Equation (3.99).

104

On the other hand, from an analytical point of view, the tangent dilation angle at each shear displacement should be obtained from $JRC_{mobilized}$ using the following equation:

$$d_t^{'} = JRC_{mobilized} \log_{10}\left(\frac{JCS}{\sigma_n}\right)$$

(3.105)

Substituting Equation (3.105) in Equation (3.99), we have:

$$d(\frac{\delta_v}{\delta_{peak}}) = \tan\left(JRC_{mobilized} \cdot \log_{10}\left(\frac{JCS}{\sigma_n}\right)\right).d(\frac{\delta_h}{\delta_{peak}})$$

(3.106)

Section 3.3.3 proposed Equation (3.90) to predict post-peak mobilized JRC. Substituting, Equation (3.90) in Equation (3.106), we have:

$$d(\frac{\delta_v}{\delta_{peak}}) = \tan\left(JRC_{peak}\left(\frac{\delta_h}{\delta_{peak}}\right)^{-0.381} \cdot \log_{10}\left(\frac{JCS}{\sigma_n}\right)\right).d(\frac{\delta_h}{\delta_{peak}})$$

(3.107-a)

Consequently, dilation displacement between the peak shear displacement and a post-peak point with $\frac{\delta_h}{\delta_{peak}} = l$ can be estimated by obtaining the integral of the right hand side of Equation (3.107-a) between 1 and l, as follows:

$$\frac{\delta_v}{\delta_{peak}} = \int_1^l \tan\left(JRC_{peak}\left(\frac{\delta_h}{\delta_{peak}}\right)^{-0.381} \cdot \log_{10}\left(\frac{JCS}{\sigma_n}\right)\right).d(\frac{\delta_h}{\delta_{peak}})$$

(3.107-b)

Therefore, dilation displacement at a post-peak point with $\frac{\delta_h}{\delta_{peak}} = l$ can be predicted as follows:

$$\delta_v = \delta_{peak}\left\{\int_1^l \tan\left(JRC_{peak}\left(\frac{\delta_h}{\delta_{peak}}\right)^{-0.381} \cdot \log_{10}\left(\frac{JCS}{\sigma_n}\right)\right).d(\frac{\delta_h}{\delta_{peak}})\right\} + \left(\delta_v\right)_{peak}$$

(3.108)

The integral part of Equation (3.108) can be solved by employing numerical methods. For example, using 1/3-Simpson's rule, the integral can be written as follows:

$$\int_{1}^{l} \tan\left(\frac{JRC_{peak}}{\left(\dfrac{\delta_h}{\delta_{peak}} \right)^{-0.381}} \cdot \log_{10}\left(\frac{JCS}{\sigma_n} \right) \right) . d\left(\frac{\delta_h}{\delta_{peak}} \right) =$$

$$= \frac{l-1}{6} \left\{ \begin{array}{l} \tan\left(JRC_{peak} \cdot \log_{10}\left(\dfrac{JCS}{\sigma_n} \right) \right) \\[2mm] + 4\tan\left(\dfrac{JRC_{peak}}{(\dfrac{l+1}{2})^{0.381}} \cdot \log_{10}\left(\dfrac{JCS}{\sigma_n} \right) \right) + \tan\left(\dfrac{JRC_{peak}}{(l)^{0.381}} \cdot \log_{10}\left(\dfrac{JCS}{\sigma_n} \right) \right) \end{array} \right\}$$

The MDST database contains the post-peak dilation displacements of 205 direct shear tests, for which post-peak dilation at 1 to 4 points are available (total number of 700 data points). Table 3.8 summarized the results. It is found that Equation (3.104) works very well in this database.

3.3.5 Pre-peak stress-displacement curve

If one wants to use Equation (3.3) to describe the pre-peak shear stress-displacement curve, then *JRC* and ϕ_b must depend on the displacement δ. This dependency is called "mobilization" of *JRC* and ϕ_b, respectively.

Table 3.8: Performance of proposed model, Equation (3.108), in predicting the post-peak dilation displacements

Parameter	Equation (3.108)
$\left(\dfrac{(\delta_v)_{perdicted}}{(\delta_v)_{measured}} \right)_{Average} \pm STD$	1.44+1.31
$\left(\dfrac{(\delta_v)_{perdicted}}{(\delta_v)_{measured}} \right)_{Max}$	10.49
$\left(\dfrac{(\delta_v)_{perdicted}}{(\delta_v)_{measured}} \right)_{Min}$	0.13

Barton expressed the pre-peak stress-displacement curve by using the concept of roughness mobilization, $JRC_{mobilized}$, in Equation (3.3) [115]. The ratio $\dfrac{JRC_{mobilized}}{JRC_{peak}}$ can be estimated from the ratio $\dfrac{\delta}{\delta_{peak}}$ employing the values given in Table 3.2. In Barton's model, it was assumed, first, that the base friction angle of rock fracture is mobilized and reaches its peak value at shear displacement of $0.3\delta_{peak}$. Then, from $0.3\delta_{peak}$ to the peak shear displacement, JRC is mobilized and reaches its peak value at δ_{peak}. This assumption is consistent with the zero peak shear displacement for a sawed fracture. However, Section 3.3.2 showed that the peak shear displacement of sawed fractures (JRC=0) is significantly different from zero.

The peak shear displacement of lab size rock blocks is very small, about 1mm for a 10 cm block. Therefore, for pre-peak shear strength, collecting data by digitizing shear stress versus shear displacement curves published in the literature is very difficult and may lead to large errors. Therefore, in this section, modification was made to Barton's model for pre-peak shear strength in order to make the modified model consistent. Accordingly, the mobilization of pre-peak shear strength was divided into two parts: mobilization of friction angle and mobilization of JRC.

At zero shear displacement, the shear stress is zero, and thus the mobilized friction angle is zero. At peak shear displacement, the mobilized friction angle is equal to the base friction angle.

For the case of rough fracture ($JRC > 0$), at zero shear displacement, the shear stress is zero. Therefore, the mobilized friction angle and JRC are both zero. At peak shear displacement, the mobilized friction angle is equal to the base friction angle and the mobilized JRC is equal to JRC_{peak}.

Section 3.3.4.1 suggest empirical Equation (3.104) for dilation displacement. Since dilatancy decreases when $0 \leq \delta_h \leq 0.25\delta_{peak}$ and increases when $\delta_h > 0.25\delta_{peak}$, the mobilized JRC is assumed to be zero up to $0.25\delta_{peak}$. The mobilized friction

107

angles at zero and peak shear displacement are known. It was assumed that the shape of shear stress versus shear displacement curve is the same as the linear interpolation used for the results of Barton's model. The MDST database was analyzed in accordance with the above information. Table 3.9 and Table 3.10 summarize the average value of the mobilized friction angle and the mobilized *JRC*, respectively.

Table 3.9: Pre-peak mobilization of the base friction angle

$\dfrac{\delta}{\delta_{peak}}$	$\dfrac{\phi_{mobilized}}{\phi_{base}}$
0	0
0.25	0.75
0.5	0.9
1	1

Table 3.10: Pre-peak mobilization of *JRC*

$\dfrac{\delta}{\delta_{peak}}$	$\dfrac{JRC_{mobilized}}{JRC_{peak}}$
0	0
0.25	0
0.5	0.67
0.6	0.83
1	1

3.3.6 Reversals and unloading

As was mentioned in section 3.2.3.2, Barton [115] explained how the shear stress-displacement could be simulated in unloading, reloading, and reversal (Figure 3.2) based on one direct shear test. The CDST database contains the results of 18 cyclic direct shear tests. These results were investigated to check the accuracy of Barton's model and revise it consistent with the other parts of our modified model.

The revised model for unloading and reversal is illustrated in Figure 3.18 (τ / σ_n versus δ / δ_{peak}) for a rock fracture with the following properties:

$$\phi_b = 30°; JRC = 10; \frac{JCS}{\sigma_n} = 10$$
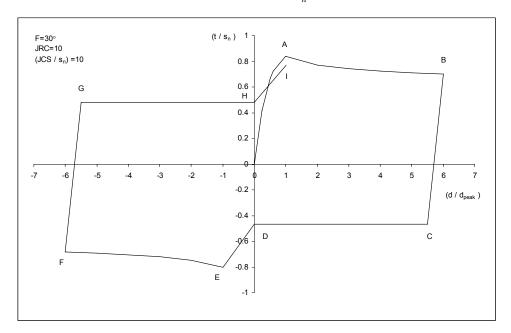
Figure 3.18: Proposed model for shear unloading and reversal of rock fractures

- Point A: the peak shear strength can be calculated using Equation (3.3), as:

$$\frac{\tau}{\sigma_n} = \tan\left(\phi_b + JRC.\log(\frac{JCS}{\sigma_n})\right) = \tan(30 + 10) = 0.84$$

The stress-displacement curve form origin to point A (mobilization of the peak shear strength) can be simulated using Table 3.9 and Table 3.10.

- Point B: the post-peak shear strength at $\delta / \delta_{peak} = 6$ can be estimated using Equation (3.90), as follows:

$$JRC_{mobilized} = JRC_{peak}(\frac{\delta}{\delta_{peak}})^{-0.381} = 10 \times (6)^{-0.381} = 5$$

$$\frac{\tau}{\sigma_n} = \tan\left(\phi_b + JRC_{mobilized}.\log(\frac{JCS}{\sigma_n})\right) = \tan(30 + 5) = 0.7$$

109

- Point C: the CDST database shows that on average the shear strength in unloading is fully mobilized by reversing the shear displacement by an amount equal to the half of peak shear displacement:

$$\delta_c / \delta_{peak} = 6 - 0.5 = 5.5$$

Based on only one cyclic direct shear test, Barton proposed that the mobilized *JRC* in unloading is always equal to $-0.5 JRC_{peak}$. However, our investigation of 18 direct shear tests of the CDST database revealed that the mobilized *JRC* in unloading is the same as the mobilized *JRC* at the end of loading stage (Point B), which can be justified if the problem is approached analytically (see Figure 3.19). During unloading:

$$T' = -N \cdot \tan(\phi - i) = N \cdot \tan(-\phi + i), \qquad (3.109\text{-a})$$

which can be expressed in terms of stress as follows:

$$\tau = \sigma_n \cdot \tan(-\phi + i) \qquad (3.109\text{-b})$$
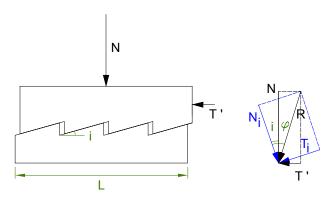
Figure 3.19: Diagram of forces applied to a rough joint at failure during the reversal stage

This means that in this example the mobilized *JRC* is equal to 5. It should be mentioned that both methods consider negative values for base friction angle. Therefore, the shear strength at Point C can be calculated as follows:

$$\frac{\tau}{\sigma_n} = \tan(-30 + 5) = -0.47$$

- Point D: the CDST database shows that the magnitude of shear stress does not change significantly in the unloading stage (from Point C to Point D).

- Point E: based on the result of only one cyclic direct shear test, Barton concluded that the mobilized *JRC* in reversal is equal to $-0.75 JRC_{peak}$. However, our investigation of 18 direct shear tests in the CDST database revealed that the mobilized *JRC* in reversal is equal to $-0.87 JRC_{peak}$. Therefore, the peak value of shear strength in reversal can be calculated as follows:

$$\frac{\tau}{\sigma_n} = \tan\left(-\phi_b - 0.87 JRC_{peak} \cdot \log_{10}\left(\frac{JCS}{\sigma_n}\right)\right) = \tan(-30 - 8.7) = -0.8$$

This peak shear strength will be mobilized at a peak shear displacement related to the new value of *JRC* which can be estimated using Equation (3.88):

$$\delta_E = 0.0077 L^{0.45} \left(\frac{\sigma_n}{JCS}\right)^{0.34} \cos\left(0.87 JRC \cdot \log_{10}\left(\frac{JCS}{\sigma_n}\right)\right)$$

$$\frac{\delta_E}{\delta_{peak}} = -\frac{\cos\left(0.87 JRC \cdot \log_{10}\left(\frac{JCS}{\sigma_n}\right)\right)}{\cos\left(JRC \cdot \log_{10}\left(\frac{JCS}{\sigma_n}\right)\right)} = -\frac{\cos(8.7)}{\cos(10)} = -1.004$$

- Point F: the reversal post-peak shear strength at Point F can be estimated using Equation (3.90), as follows:

$$JRC_{mobilized} = \left(JRC_{peak}\right)_{reversal} \cdot \left(\frac{\delta}{\delta_{peak}}\right)^{-0.381} = -8.7 \times \left(\frac{6}{1.004}\right)^{-0.381} = -4.4$$

$$\frac{\tau}{\sigma_n} = \tan(-30 - 4.4) = \tan(30 + 5) = -0.68$$

- Point G: similar to Point C, in unloading the reversal load, the shear strength is mobilized by a shear displacement increment equal to the half of peak shear displacement:

$$\delta_G / \delta_{peak} = -6 + 0.5 = -5.5$$

In addition, based on only one cyclic direct shear test, Barton proposed that the mobilized *JRC* in unloading is always equal to $0.5 JRC_{peak}$. However, our

investigation of 18 direct shear tests of the CDST database revealed that the mobilized *JRC* in unloading the reversal is the same as the mobilized *JRC* at the end of reversal loading stage (Point F). This means that in this example the mobilized *JRC* is equal to -4.4. It Therefore, the shear strength at Point G can be calculated as follows:

$$\frac{\tau}{\sigma_n} = \tan(30 - 4.4) = 0.48$$

- Point H: the CDST database shows that the shear stress does not change significantly in the unloading stage (from Point G to Point H).
- Point I: based on the result of only one cyclic direct shear test, Barton concluded that the mobilized *JRC* in reloading can be calculated as follows:

$$\left(JRC_{peak}\right)_{relaoding} = -0.75\left(JRC_{peak}\right)_{reversal} = -0.75\left(-0.75JRC_{peak}\right) = 0.56JRC_{peak}$$

However, our investigation of 18 direct shear tests of the CDST database revealed that the mobilized *JRC* in reloading is equal to:

$$\left(JRC_{peak}\right)_{relaoding} = -0.87\left(JRC_{peak}\right)_{reversal} = -0.87\left(-0.87JRC_{peak}\right) = 0.76JRC_{peak}$$

Therefore, the peak value of shear strength in reloading can be calculated as follows:

$$\frac{\tau}{\sigma_n} = \tan\left(\phi_b + 0.76JRC_{peak} \cdot \log_{10}\left(\frac{JCS}{\sigma_n}\right)\right) = \tan(30 + 7.6) = 0.77$$

This peak shear strength will be mobilized at a peak shear displacement related to the new value of *JRC* which can be estimated using Equation (3.88):

$$\delta_I = 0.0077L^{0.45} \cdot \left(\frac{\sigma_n}{JCS}\right)^{0.34} \cos\left(0.76JRC \cdot \log_{10}\left(\frac{JCS}{\sigma_n}\right)\right)$$

$$\frac{\delta_I}{\delta_{peak}} = \frac{\cos\left(0.76JRC \cdot \log_{10}\left(\frac{JCS}{\sigma_n}\right)\right)}{\cos\left(JRC \cdot \log_{10}\left(\frac{JCS}{\sigma_n}\right)\right)} = \frac{\cos(7.6)}{\cos(10)} = 1.007$$

The above mentioned method can be used to simulate shear stress-displacement behavior of rock fractures in the whole process of loading, unloading, reversal, and

reloading. It should be mentioned that the revised method has the following advantages over Barton's model:

- It is based on the results of 18 direct shear tests while Barton's model is based on the results of only one test.
- The 18 direct shear tests considered in this study contain between 1 and 20 cycles, while the only one that Barton considered in his study just had one cycle.
- The predicted mobilized *JRC* value for unloading stages may be justified analytically (Figure 3.19).

Barton's model does not have any specific suggestion for dilation displacement during unloading, reversal, and reloading. However, in employing Barton's model, the dilatancy behavior of rock fractures can be simulated using the mobilized value of *JRC* obtained from Table 3.2. In the revised model, the dilation displacement can also be estimated using the mobilized value of *JRC*. However, our investigation of the CDST database found that at the end of each unloading stage the dilation displacement is almost zero. Figure 3.20 depicts the dilation displacement at each shear displacement (δ_v / δ_{peak} versus δ / δ_{peak}) for the above example:
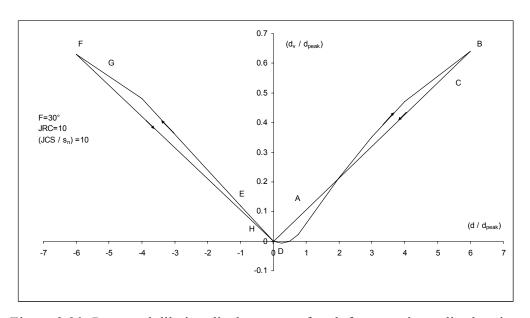
Figure 3.20: Proposed dilation displacement of rock fractures in cyclic shearing

- Dilation displacement of loading stages (from origin to Point B) can be estimated using the model developed in Section 3.3.4.

- As was stated above, the dilation displacement at the end of unloading stage (Point D) is equal to zero. It is assumed here that dilation displacement decreases linearly from Point B to D.

- Dilation displacement at reversal loading (Point E and F) can be calculated using Equation (3.108).

- Again at the end of unloading stage (Point H), the dilation displacement is equal to zero. It is assumed here that dilation displacement decreases linearly from Point F to H.

3.4   A PREDICTIVE MODEL FOR ANISOTROPIC BEHAVIOR OF FRACTURES

In Barton's empirical model, *JRC* and the fracture length are the only geometrical parameters that affect the shear strength, shear deformability, peak shear displacement, and dilatancy of the rock fractures. For a given direction, the fracture length can be easily measured. However, evaluating the magnitude of *JRC* in all directions is not possible and practical. Therefore, in this section, the experimental data available in the literature is used to propose a model to estimate the magnitude of *JRC* in different directions based on given two major and minor values of *JRC* along two orthogonal axes.

Experimental studies performed by Huang and Doong [125] consisted of direct shear tests and roughness measurement on model joints. Silicon rubber replicas of two fracture types were tested under 6 different normal stresses and 12 different directions. Uniaxial compressive strength and base friction angle were equal to 4 MPa and 28°, respectively. In the present study, for each direction, *JRC* was back-calculated for all 6 normal stresses by using Barton's failure criterion. The magnitude of *JRC* in each direction was assumed to be equal to the average of back-calculated *JRC's* at different normal stresses. Figure 3.21 depicts the distribution of the magnitude of *JRC* in different directions for both fracture types.
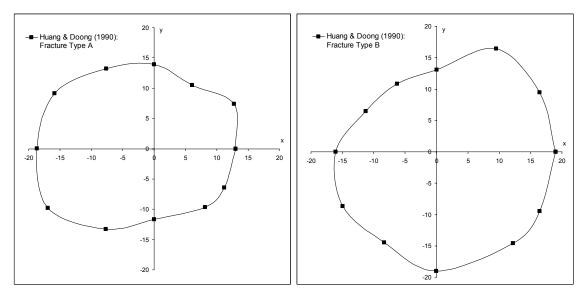
Figure 3.21: Distribution of the magnitude of *JRC* in different directions back calculated by using Huang and Doong's [125] experimental study [216].

In order to investigate anisotropic behavior of rock fractures, Jing *et al.* [126, 150] determined and plotted in polar diagram the mobilized friction angles from shear tests of concrete replicas in 12 shear directions, at 30º intervals, under 4 different normal stresses. Uniaxial compressive strength was equal to 52 MPa. In the present study, the base friction angle was assumed to be equal to 30°. For each direction, *JRC* was back-calculated for all 4 normal stresses using Barton's failure criterion. The magnitude of *JRC* in each direction was assumed to be equal to the average of back-calculated *JRC's* at different normal stresses. Figure 3.22 depicts the distribution of the magnitude of *JRC* in different directions.

A series of direct shear tests performed by Kulatilake *et al.* [129, 130] on replicas in 12 directions and under 5 different normal stresses. Uniaxial compressive strength and base friction angle were equal to 9.70 MPa and 34.5°, respectively. In this research, for each direction, *JRC* was back-calculated for all 5 normal stresses using Barton's failure criterion. The magnitude of *JRC* in each direction was assumed to be equal to the average of back-calculated *JRC's* at different normal stresses. Figure 3.23 depicts the distribution of the magnitude of *JRC* in different directions.

115
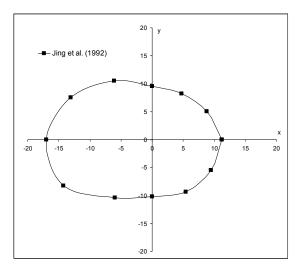
Figure 3.22: Distribution of the magnitude of *JRC* in different directions back calculated by using Jing et al.'s [125] experimental study [216].
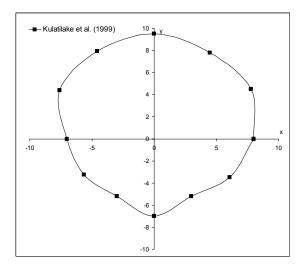
Figure 3.23: Distribution of the magnitude of *JRC* in different directions back calculated by using Kulatilake et al.'s [125] experimental study [216].

Grasselli *et al.* [127, 128] reported anisotropic distribution of peak friction angle for concrete replicas of Valtelina serpentinite. Uniaxial compressive strength and base friction angle were equal to 47 MPa and 13°, respectively. However, a base friction angle of 13° seems to be too low, because the base friction angle of the majority of rock surfaces ranges from 25° to 35°, at least at medium stress levels [92, 136, 141-145].

Using this low value for base friction angle, the back-calculated *JRC* was as large as 31, but, according to Barton [21], the magnitude of *JRC* can range between 0 and 20. Therefore, in this research, the base friction angle was assumed to be equal to 30°. For each direction, *JRC* was back-calculated using Barton's failure criterion. Figure 4 depicts the distribution of the magnitude of *JRC* in different directions, which is comprised between 6 and 19.
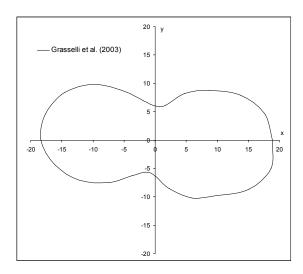
Figure 3.24: Distribution of the magnitude of *JRC* in different directions back calculated by using Grasselli et al.'s [125] experimental study [216].

Jing *et al.* [126, 150] assumed that magnitude of the asperity angle follows an elliptical distribution in the plane of the fracture surface. Since the asperity angle is the only geometrical parameter in Jing *et al.'s* model and *JRC* is the only geometrical parameter in Barton's failure criterion, an option is to adopt an elliptical model for the distribution of the magnitude of *JRC* in different directions. The elliptical model can be described in parametric form as follows:

$$
\begin{aligned}
JRC_x &= JRC_1 \cos(\theta), \\
JRC_y &= JRC_2 \sin(\theta),
\end{aligned}
\tag{3.110}
$$

where JRC_1 and JRC_2 are the magnitude of *JRC* along the major and minor semi-axes of the ellipse, x and y axes (Figure 3.25).
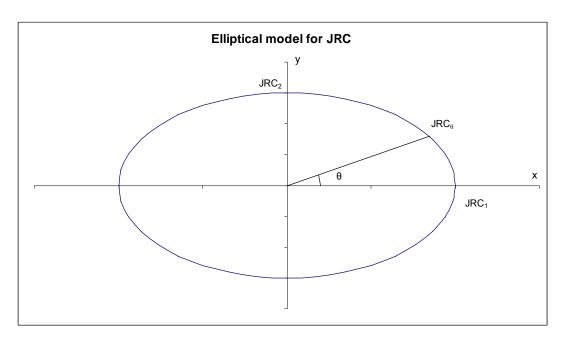
Figure 3.25: Elliptical model for the angular distribution of *JRC* [216].

The magnitude of the *JRC* in a given direction θ can then be written as:

$$JRC_\theta = \sqrt{JRC_x^{\;2} + JRC_y^{\;2}} \qquad (3.111)$$

Correlation analyses conducted in this study show that Equation (3.111) yields a good approximation for all of the 77 available data points collected from the literature. The $JRC_{predicted} / JRC_{measured}$ ratio has an average of 1.19 with maximum, minimum, and standard deviation equal to 2.1, 0.79, and 0.28, respectively. However, Figure 3.21 through Figure 3.24 illustrate that the actual angular distribution of the *JRC* does not have an elliptical shape, but, rather, it has the shape of an "8". The following parametric form better captures the angular distribution of *JRC*:

$$JRC_x = \sqrt{\left[JRC_1 \cos(\theta)\right]^2 + \left[JRC_2 \sin(\theta)\right]^2}\; \cos(\theta)$$
$$JRC_y = \sqrt{\left[JRC_1 \cos(\theta)\right]^2 + \left[JRC_2 \sin(\theta)\right]^2}\; \sin(\theta) \qquad (3.112)$$

Figure 3.26 depicts the suggested model, Equation (3.112). It should be noted that, in the proposed model, the magnitude of *JRC* in a given direction θ can then be estimated using Equation (3.111). Table 3.11 and Figure 3.27 show that the suggested

parametric model, Equation (3.112), works better than the elliptical model in predicting the magnitude of *JRC* in different directions.
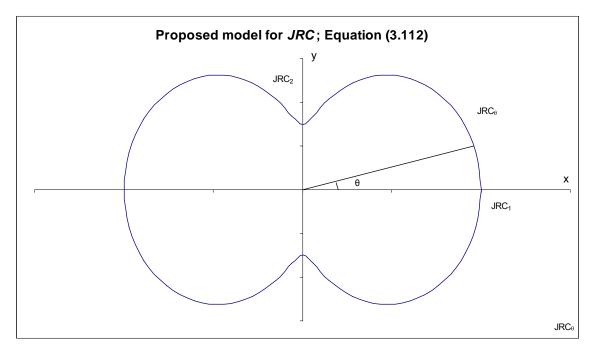
Figure 3.26: Proposed "8" shape model for the angular distribution of *JRC* (Equation (3.112)) [216].

Table 3.11: Comparison of elliptical model and proposed "8" shape model (Equation (3.112)) for the angular distribution of *JRC*

Parameters	$(JRC_x)_{perdicted} / (JRC_x)_{measured}$		$(JRC_y)_{perdicted} / (JRC_y)_{measured}$	
	Elliptical model	Proposed "8" shape model (Equation (3.112))	Elliptical model	Proposed "8" shape model (Equation (3.112))
Average	0.859	0.977	1.388	0.981
Standard deviation	0.234	0.142	0.676	0.136
Maximum	1.267	1.279	3.215	1.279
Minimum	0.311	0.671	0.706	0.671
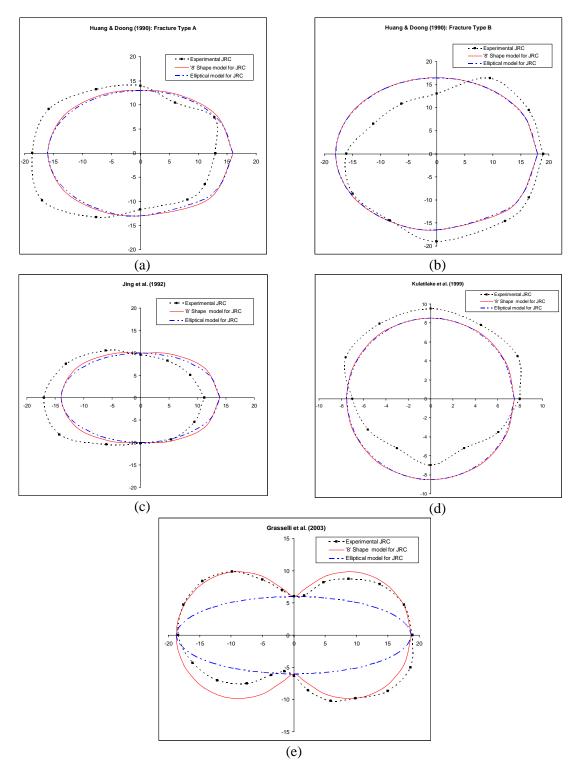
Figure 3.27: Comparison of elliptical model and proposed "8" shape model
(Equation (3.112)) for the angular distribution of *JRC*.

3.5 CONCLUSIONS

Two databases were built by collecting the results of direct shear tests available in the literature: Monotonic Direct Shear Tests (MDST), which contains the results of 362 tests, and Cyclic Direct Shear Tests (CDST), which contains the results of 18 tests.

Analyses of these databases showed that Barton's failure criterion works very well in predicting the shear strength of rock fractures. However, some weaknesses were found in the original Barton model and addressed by correlation analyses performed on collected data. The following modifications to Barton's model are proposed based on the results of correlation analyses:

1) An empirical equation is proposed to predict the peak shear displacement of rock fractures. The equation considers the effect of normal stress on the peak shear displacement, while Barton's equation does not. In addition, this equation can be used for all types of rock fractures, including sawed, smooth, and rough, while Barton's equation predicts an incorrect value of zero for the peak shear displacement of sawed fractures. Finally, the predicted peak shear displacement employing the proposed equation of this study decreases as *JRC* increases. However, the predicted value of peak shear displacement using Barton's equation increases with *JRC*.

2) An empirical equation is proposed to predict the mobilized *JRC*, which is used to calculate the shear stress-displacement curve after peak shear displacement. Besides better matching the MDST database than Barton's Table, the empirical equation gives a smoother curve compared to the linear interpolation of the values given in Barton's Table and is easier to implement numerically.

3) An equation is proposed to obtain pre-peak dilation at any shear displacement. The proposed model has none of the inconsistencies and ambiguity of Barton's model. Moreover, it simulates negative dilation, while Barton's does not. In addition, the dilation displacement at any shear displacement can be calculated easily using this equation; also the numerical implementation is much easier.

4)   An equation is proposed to obtain post-peak dilation at any shear displacement. This equation contains an integral which should be solved using numerical methods.

5)   Two tables are introduced to simulate the pre-peak shear stress-displacement curve (mobilization of pre-peak shear strength): one to estimate the mobilized *JRC* at any shear displacement and another to evaluate the mobilized base friction angle at any shear displacement.

6)   A method is described in detail to simulate shear stress-displacement behavior of rock fractures in the process of loading, unloading, reversal, and reloading.

7)   A method is proposed to simulate the dilatancy behavior of rock fractures in cyclic shearing using the mobilized value of *JRC*. By investigating the CDST database, it was found that at the end of each unloading stage the dilation displacement is almost zero.

8)   The *JRC* angular distribution was found not to have an elliptical shape, but the shape of an "8". Experimental data found in the literature were used to formulate a predictive model for the anisotropic distribution of *JRC* in the plane of a fracture. The input data for the model are the maximum and the minimum *JRC*. The shear strength, shear stiffness, and dilation displacement of rock fractures subjected to shearing in any direction can then be predicted by using either original or modified Barton's model.

CHAPTER 4: VALIDATION OF MODIFIED BARTON'S MODEL

4.1 INTRODUCTION

In order to validate the modified Barton's model developed in Chapter 3, an experimental study was performed in UT Rock Mechanics lab by two MS students, Marco Invernizzi and Simone Addotto, under my supervision. The objective of this study was to validate the proposed empirical equation for the peak shear displacement, the modified shear stress-displacement curve, and the suggested equations for dilation displacement.

This Chapter presents the experimental study conducted on rock fractures. Section 4.2 describes methodology, procedures, and equipment used for testing. Section 4.3 summarized the results of the tests followed by the conclusions in Section 4.4.

4.2 METHODOLOGY AND TESTING EQUIPMENT

The purpose of this experimental study was to validate a newly developed model to predict the shear behavior of rock fractures. In order to validate the model for all rock types and fracture characteristics, a reasonable range of all parameters that may affect the shear behavior of the fractures should be covered in the experimental study. However, covering all ranges of all parameters is not feasible due to the limitations in time, funding, and available equipment.

In order to validate the model independent of rock type and rock hardness, the experimental study was performed on four different rock types:

- Two weak rocks:
    - (1) Weak limestone, called Limestone 1 (Figure 4.1-a)
    - (2) Red sandstone (Figure 4.1-b)
- Two hard rocks:
    - (3) Granite (Figure 4.1-c)
    - (4) Metamorphic limestone, called Limestone 2 (Figure 4.1-d)

(a) Limestone 1 (weak limestone)

(b) Red sandstone

(c) Granite

(d) Metamorphic limestone (Limestone 2)

Figure 4.1: Rock materials used in the experimental study

4.2.2 Uniaxial Compressive Strength

To evaluate the Uniaxial Compressive Strength (*UCS*) of the intact rocks, three different kinds of tests were carried out: the Schmidt Hammer test, the Point Load Test (PLT) and the Uniaxial Compressive Strength (UCS) test with stress-strain curve.

The Schmidt hammer measures the rebound of a spring loaded mass impacting against the surface of the rock (or concrete). Figure 4.2 depicts the L-hammer used in this experimental study (impact energy = 0.075 m.kg) which is suitable for measuring *UCS* values down to about 20 MPa and up to at least 300 MPa. When conducting the test the hammer should be held at right angles to the surface which in turn should be flat and smooth. The rebound reading will be affected by the orientation of the hammer. Thus, the rebound value must be corrected to take into account the effect of orientation of the hammer and the unit weight of the rock. The Schmidt hammer is an arbitrary scale ranging from 10 to 100. The higher rebound gives the higher compressive strength of the rock. Several empirical equations can be found in the literature (e.g. [22, 146, 178, 217-233]) to correlate the rebound value with the uniaxial compressive strength of rock materials. However, most of these relationships have validity ranges in terms of rock type, rebound value, and/or magnitude of *UCS*. In this Chapter, the following empirical equation originally suggested by Miller [146] and adopted later by Barton and Choubey [22] and ISRM [178] is used to correlate *UCS* and rebound number, *R*:

$$\log_{10}(UCS) = 0.0088 \cdot \gamma \cdot R + 1.01, \tag{4.1}$$

where γ is the dry density of rock (kN/m^3) and the unit of *UCS* is MPa.

Figure 4.2: Schmidt hammer

Figure 4.3 illustrates Equation (4.1) relating rock density, compressive strength, and rebound number of Schmidt (L) hammer (hammer held at right angles downwards to the surface). Schmidt hammer tests were performed on each rock type and unconfined compressive strengths were estimated from the rebound values.
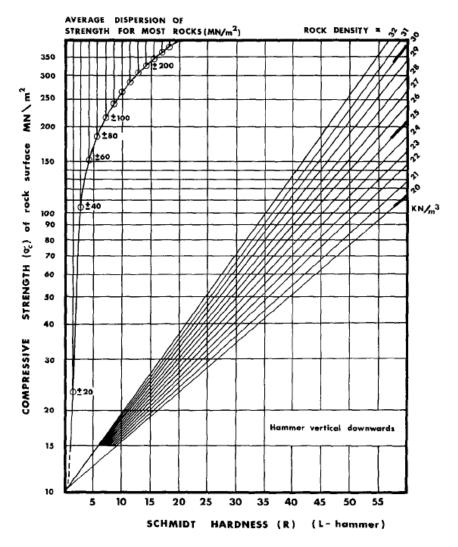
Figure 4.3: Correlation chart for Schmidt (L) hammer, relating rock density, compressive strength, and rebound number [146]

For each rock type, several specimens were prepared by either of the following methods: (1) cutting in pieces of $5 \times 5 \times 2 cm$ using Lapidary Slab Saw (Figure 4.4-a); (2)

coring (with diameter of 5 cm) using core drill press, "Supermax HRD-700H" (Figure 4.4-b). Point Load Test (PLT) was performed on each specimen employing PLT machine, GCTS 8LT100 (Figure 4.5).

<table>
<tr><td>(a)</td><td>(b)</td></tr>
</table>
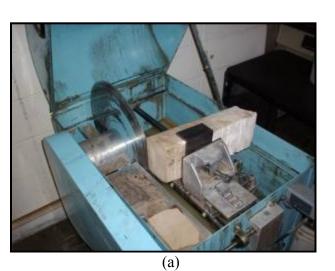
Figure 4.4: (a) Lapidary Slab Saw; (b) Core drill press

Figure 4.5: PLT machine (GCTS 8LT100)

Based on ISRM suggested methods for determining point load strength [234], the Uniaxial Compressive Strength (*UCS*) can be calculated from the point load tests. The point load index is defined as follows:

$$I_{(s)} = \frac{P}{D_e^2},$$ (4.2)

where D_e is the equivalent core diameter. For the case of non-circular cross section it is equal to $\sqrt{\frac{4A}{\pi}}$, in which A is the minimum cross sectional area of a plane trough the specimen and the platen contact points.

The values of the point load index, I_s, should be modified for diameter corrections:

$$I_{(s)50} = F \times I_{(s)},$$ (4.3)

$$F = (D_e / 50)^{0.45},$$ (4.4)

in which D_e has the unit of mm. Two lowest and two highest values of point load indices were removed from the data set and the remaining values were averaged. The ISRM suggested method for determining point load strength proposes that the Uniaxial Compressive Strength is 20-25 times point load index.

The uniaxial compression test with stress-strain curve is to measure the uniaxial or unconfined compressive strength (*UCS*), Young's modulus, and Poisson ratio of the rock material [235]. A cylinder of intact rock with diameter of 5 cm and length of 10 cm (the ratio of length to diameter should be around 2) is loaded axially with no confinement pressure until failure. *UCS* of the intact rock together with stress-strain curve can be obtained from this test. For each rock type (except for Limestone 1), three samples were cored using drill press, "Supermax HRD-700H" (Figure 4.4-b), trimmed, and ground employing specimen grinder (Figure 4.6). A servo hydraulic testing machine (Figure 4.7), designed for uniaxial/triaxial tests, was used for performing uniaxial compression tests. The reason of not performing *UCS* test on Limestone 1 is lack of rock material. Attempts to find exactly the same Limestone were failed, too.

128

Figure 4.6: Grinder

Figure 4.7: Uniaxial/Triaxial testing machine

4.2.3 Joint Compressive Strength

Section 3.2.1.1 explained that the joint compressive strength (JCS) at low stress levels is equal to the unconfined compression strength, σ_c, of the intact rock if the fracture is unweathered, but may reduce to approximately $\sigma_c / 4$ for weathered fractures [92]. The Schmidt hammer can be employed to measure the JCS values of weathered rock fractures (Miller's method [146]).

For the case of artificial sawed fractures, the fracture is unweathered and undamaged and thus *JCS* should be equal to *UCS*. However, the process of making artificial rough joint (shearing the intact rock or breaking by hammer) makes micro-fractures which reduce the joint compressive strength. In order to have an estimation of the ratio of *JCS* to *UCS* for the case of rough joints, 10 Schmidt hammer tests were performed on both sawed and rough fractures of each rock type. The Schmidt hammer tests on rough fractures were done after performing direct shear test and opening the specimen ring. It was found that the uniaxial compressive strengths estimated using the rebound values obtained on (sheared) rough fractures are 0.6 times of those predicted using the rebound values measured on (intact) sawed fractures. While the process of shearing the rough fractures causes some additional damages to the fracture and thus decreases its compressive strength, it is estimated that the ratio of *JCS* to *UCS* should be around 0.8. Therefore, in the rest of the analysis, *JCS* of rough fractures made according to the above mentioned procedure is assumed to be about 0.8 times of *UCS* of the corresponding intact rock.

4.2.4 Direct shear test

Several direct shear tests was performed on artificial sawed and rough fractures of each rock type. The purpose of the direct shear tests performed on sawed fractures was to obtain the base friction angles and to validate the proposed modification in the case of sawed (or planar) fractures. On the other hand, the direct shear tests performed on rough fractures were to validate the modification made on Barton's model regarding the peak shear displacement, stress-displacement curve, and dilation displacement.

130

4.2.4.1 Sample preparation

In the case of limestone 1, Lapidary Slab Saw (Figure 4.4-a) was used to cut samples of 8 x 8 x 8 cm. However, the drill press (Figure 4.4-b) was employed to core samples with 5 cm diameter from the sandstone, the granite, and limestone 2. The samples were cut in half by the slab saw whenever a sawed fracture was required.

In the case of weak rocks (limestone 1 and the sandstone), artificial rough fractures were made by shearing the sample under 1 MPa normal stress up to failure of intact rock and returning shear actuator to the original position. However, in the case of hard rocks (the granite and limestone 2), artificial rough fractures were made by breaking the samples in half by hammer.

For each direct shear test, the sample was prepared in the following procedure (Figure 4.8):

1- Four marks were placed on the outside of the both halves of the specimen to remind us of the specimen orientation. These marks would help us to adjust the position of the upper half of the specimen on its lower half after taking them apart during the later steps of sample preparation.

2- A thick plastic or aluminum sheet was placed on a suitable level surface and the lower half of the specimen holding ring was placed on the sheet.

3- The inner surface of the bottom specimen ring was greased with white petroleum USP jelly produced by Vaseline (Figure 4.8-a).

4- *Anchoring and Patching Cement* manufactured by *Rockite* was used to encapsulate the specimen in the specimen ring. This expanding, fast-setting, pourable, hydraulic type cement has more than twice the strength of fully cured, conventional concrete[1]. The encapsulating compound was prepared according to manufacturer instruction.

5- The lower half of the specimen was positioned centrally in the lower half of the specimen holder.

---

[1] Compressive (28-day) strength of conventional concrete is about 30 MPa

(a) Placing the lower half of the specimen ring on a sheet of aluminum and greasing the inner surface of the ring

(b) Positioning the lower half of the specimen in the lower half of the ring

(c) Pouring the encapsulating material

(d) Placing guide rods and modeling clay on the lower ring

(e) Placing the lower half of the specimen and ring

(f) pouring encapsulating compound in upper ring

Figure 4.8: Procedure of sample preparation for direct shear test
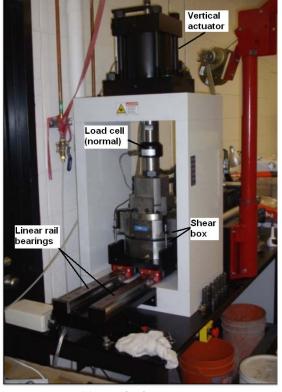
6- The orientation of the specimen was noted relative to the specimen ring.

7- A mark was placed on the outside of the specimen ring to remind the specimen orientation after the cement has covered the specimen completely.

8- Adequate support was provided to the specimen using modeling clay to maintain it in its position while the encapsulating material cures (Figure 4.8-b).

9- The encapsulating material was poured carefully into the annular space between the lower half of the specimen and the lower half of the specimen holding ring. The mix was cured for 10 to 20 minutes (Figure 4.8-c).
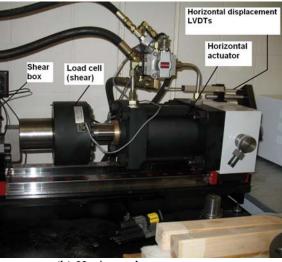
10- After the bottom encapsulated has sufficiently cured, two guide rods were place together with modeling clay on the lower ring such that its cutout edge encircles the encapsulated lower half of the specimen and encompasses the test zone thickness (Figure 4.8-d).

11- The upper half of the specimen was placed onto the encapsulated lower half.

12- The position of the upper half of the specimen was adjusted until the surfaces of the test horizon correctly matched by using the four marks on the specimen.

13- The upper half of the specimen ring was lowered onto the guide rods and modeling clay layer without disturbing the position of the top half of the specimen (Figure 4.8-e).

14- The two halves of the specimen holding ring were connected with bolts.

15- Encapsulating compound was poured into the annular space between the top half of the specimen holder and the top of the specimen (Figure 4.8-f).

16- A layer of fine sand was placed on top of the cement and leveled with the rim of the upper specimen ring using a straight edge.

4.2.4.2 Mechanical testing

A servo hydraulic testing machine, designed for direct shear tests, has been employed for the direct shears tests. The direct shear system (RDS-300) manufactured by Geotechnical Consulting and Testing Systems (GCTS) is depicted in Figure 4.9. The machine is supplied with one shear boxed made up of an upper and a lower part. The upper part can be moved vertically and the lower part can be moved horizontally. Two actuators, one acting vertically and one acting horizontally, are used to apply the forces in the two directions (degrees of freedoms). Two linear rail bearings are used for guidance of the lower box in order to have a controlled linear movement.

The servo hydraulic testing machine is composed of a compression frame of 500 KN, a direct shear apparatus, and electro-hydraulic shear and normal load actuators with 300 kN and 500 kN load capacity, respectively. The maximum stroke is 100 mm in the vertical direction and $\pm$ 50 mm in the shear direction.

(a) Vertical actuator   (b) Horizontal actuator

Figure 4.9: Servo hydraulic testing machine (*GCTS* direct shear test system, RDS-300)

In the shear test, the normal and shear displacements are measured by means of Linear Variable Differential Transducers (LVDTs). The vertical displacement between the shear box is measured by four LVDTs, positioned in a square pattern around the specimen, one in each corner (Figure 4.10). Each of the LVDTs has a measurement range of 12 mm. The average value of these four LVDTs is used to represent the vertical (normal) displacement presented in the results section. The relative displacement between the shear box in the horizontal (shear) direction is measured by one LVDT (Figure 4.9), which has a 100 mm range. The sensitivities of the LVDTs are 0.025 mm for shear displacement and 0.0025 mm for normal displacement.

The procedure of assembling the ring in the shear box and performing the test is as follows:

| (a) Front view | (b) Top view |
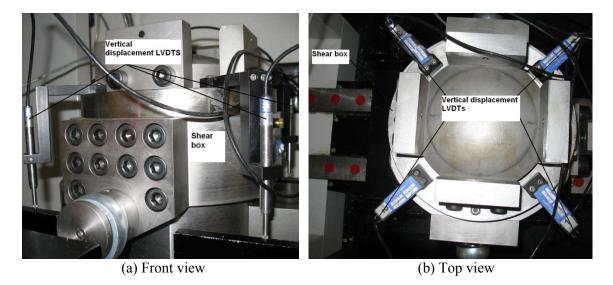
Figure 4.10: Vertical displacement LVDTs

1- Encapsulated specimen was mounted and oriented in the bottom shear box of the testing machine.

2- The top half of the shear box was lowered onto the upper half of the specimen.

3- The bolts connecting the upper and lower halves of the ring were removed.

4- Four vertical displacement LVDTs were places on the lower surface of the testing machine, at the four corners of the lower half of the shear box.

5- The horizontal/shear displacement LVDTs was mounted on the machine in such a manner that measures the shear displacement of the specimen during the test.

6- The lower part of the shear box with the specimen rings was moved under the top part of the shear box.

7- The top specimen ring was aligned with the upper part of the shear box and the normal actuator was commanded to move down with displacement control.

8- A small seating normal load was applied (on the order of 450 to 900 N).

9- The swivel lock plates were removed for any desired direction to allow rotation on any direction as required.

10- The shear actuator was moved under computer control to the "home" or "zero" position.

11- The load normal to the shear zone was increased continuously at a constant rate until the lowest selected load was attained, and consequent normal displacements were recorded.

12- The shear load was not applied until normal displacement has stabilized.

13- Stabilization was considered to be complete when normal displacement reading oscillated less than 0.05 mm in 10 min.

14- After the selected normal load had been stabilized, the shear load was applied continuously at the selected rate of 1 mm shear displacement per minute.

15- After reaching the peak shear strength, loading was continued and readings were taken until residual shear strength was achieved.

4.3 RESULTS

4.3.1 UCS and JCS

In order to obtain the uniaxial compressive strength of intact rocks, three different kinds of tests were performed:

1) Schmidt hammer tests (the results are summarized in Table 4.1 which also includes the measured unit weights of rock materials required for estimating *UCS* from rebound value using Equation (4.1))

2) Point Load Tests (the results are summarized in Table 4.2)

3) Uniaxial Compressive Strength tests with stress-strain curve (the results are summarized in Table 4.3)

Table 4.1: Results of Schmidt hammer tests

Rock type	Number of tests	Average rebound value	Unit weight, γ (kN/m^3)	*UCS* (MPa)
Limestone 1	15	18.6	25.0	26
Sandstone	10	27.0	25.5	41
Granite	20	48.4	26.5	138
Limestone 2	10	49.6	27.0	155

Table 4.2: Results of Point Load Tests (PLT)

Rock Type	Test No.	Height (mm)	P (N)	D_e (mm)	I_S (MPa)	F	$I_{S(50)}$ (MPa)	$I_{S(50), Average}$ (MPa)	UCS (MPa)
Limestone 1	1	18.14	1570	30.42	1.70	0.80	1.36	1.34	30
	2	18.44	2410	33.15	2.19	0.83	1.82		
	3	18.11	1920	33.46	1.72	0.83	1.43		
	4	20.43	1310	35.52	1.04	0.86	0.89		
	5	18.64	1760	30.76	1.86	0.80	1.49		
	6	20.79	2140	34.81	1.77	0.85	1.50		
	7	20.72	1910	34.94	1.56	0.85	1.33		
	8	20.17	1300	35.07	1.06	0.85	0.90		
Sandstone	1	18.70	3890	34.88	3.20	0.850	2.72	2.42	53
	2	19.73	4020	35.76	3.14	0.860	2.70		
	3	23.55	4390	39.03	2.88	0.895	2.58		
	4	20.07	4150	35.99	3.20	0.863	2.76		
	5	16.14	3150	32.35	3.01	0.822	2.47		
	6	21.45	2930	37.27	2.11	0.876	1.85		
	7	18.47	3410	34.60	2.85	0.847	2.41		
	8	22.11	3780	37.89	2.63	0.883	2.32		
	9	17.95	2750	34.07	2.37	0.841	1.99		
Granite	1	27.62	7170	42.40	3.99	0.928	3.70	4.00	88
	2	17.27	6290	33.50	5.60	0.835	4.68		
	3	19.08	7890	35.19	6.37	0.854	5.44		
	4	20.17	4100	36.18	3.13	0.865	2.71		
	5	18.41	5880	34.58	4.92	0.847	4.17		
	6	19.49	7030	35.56	5.56	0.858	4.77		
	7	17.73	5890	33.97	5.10	0.840	4.29		
	8	20.5	4420	36.49	3.32	0.868	2.88		
	9	17.78	4620	33.96	4.01	0.840	3.37		
	10	25.99	7370	40.98	4.39	0.914	4.01		
Limestone 2	1	23.69	3840	39.02	2.52	0.894	2.26	2.86	63
	2	28.81	4660	43.08	2.51	0.935	2.35		
	3	13.53	3770	29.69	4.28	0.791	3.38		
	4	19.31	2920	35.43	2.33	0.856	1.99		
	5	21.86	5800	37.31	4.17	0.877	3.65		
	6	31.65	6930	45.44	3.36	0.958	3.22		
	7	22.41	3560	38.07	2.46	0.885	2.17		
	8	17.44	5240	33.71	4.61	0.837	3.86		
	9	19.42	5840	35.54	4.62	0.858	3.96		

It can be seen that the magnitudes of *UCS* evaluated using Schmidt hammer tests, PLT tests, and UCS test with stress-strain curve are consistent with each other.

Table 4.4 summarizes the measured (or evaluated) magnitudes of *UCS* and *JCS* for different rock types. These values are adopted based on the results of Schmidt hammer, PLT, and UCS tests.

Table 4.3: Results of Uniaxial Compressive Strength tests

Rock Type	Test No.	Height (mm)	Diameter (mm)	*UCS* (MPa)
Sandstone	1	110.06	51.02	43.9
	2	105.01	51.00	44.2
	3	111.53	51.91	34.8
	Average *UCS*			41
Granite	1	105.52	51.23	108.1
	2	94.49	51.19	130.2
	3	96.26	51.34	141.5
	Average *UCS*			127
Limestone 2	1	104.75	50.06	173.0
	2	95.16	50.58	188.5
	3	102.20	50.53	157.8
	Average *UCS*			173

Table 4.4: The measured/evaluated magnitudes of *UCS* and *JCS* for different rock types

Rock type	*UCS* (MPa)	$JCS_{sawed\ fractures}$ (MPa)	$JCS_{rough\ fractures}$ (MPa)
Limestone 1	28	28	22.5
Sandstone	41	41	33
Granite	127	127	101
Limestone 2	155	155	124

4.3.2 Direct shear tests on sawed fractures

Direct shear tests were performed on two to four samples of each rock type under different normal stresses ranging between 0.2 and 6 MPa. Table 4.5 presents the peak shear strength and peak shear displacement of these tests together with the applied normal stresses and length of the samples.

Figure 4.11 depicts shear strength versus normal stress for all direct shear tests performed on sawed fractures. While *JRC* is equal to zero, the inclination of the trendline passed through the origin would be equal to $\tan(\phi_b)$. The base friction angle of each rock type is given in Figure 4.11, too.

Table 4.5: Results of direct shear tests performed on sawed joints

Rock Type	Specimen Number	L (mm)	σ_n (MPa)	τ (MPa)	δ_P (mm)
Limestone 1	1	95.03	1.0	0.749	0.96
			5.0	3.518	J 20
	2	80.96	0.5	0.326	0.42
			1.0	0.726	1.10
			2.0	1.540	1.70
			4.0	3.100	1.25
	3	100.00	5.0	3.500	1.80
			3.0	2.100	1.20
			3.0	2.120	1.10
			3.0	2.098	1.35
	4	86.70	0.4	0.360	0.55
			0.6	0.480	0.40
			0.8	0.650	0.55
Sandstone	1	50.90	0.3	0.358	0.42
			0.5	0.392	0.50
			0.8	0.656	0.58
			1.0	0.726	0.63
			1.5	0.884	0.72
	2	51.10	0.2	0.224	0.36
			0.4	0.367	0.46
			0.6	0.420	0.53
			1.2	0.785	0.67
			2.0	1.400	0.79
			4.0	2.503	1.01
			6.0	3.481	1.15
Granite	1	51.15	0.5	0.152	0.30
			1.0	0.299	0.60
			1.5	0.479	0.90
			2.0	0.793	0.52
			4.0	1.792	0.80
	2	51.15	0.8	0.246	0.65
			1.8	0.635	0.55
			2.5	1.350	0.77
			3.5	1.575	0.56
			4.5	2.360	0.90
Limestone 2	1	51.03	0.2	0.380	0.57
			0.4	0.445	0.60
			0.6	0.582	0.95
			0.8	0.712	0.65
			1.2	0.891	0.69
	2	50.90	0.5	0.568	0.92
			0.7	0.592	0.78
			0.9	0.722	0.95
			1.1	0.832	0.85
			1.3	0.985	1.06

(a) Limestone 1 ($\phi_b = 35.7°$) (b) Sandstone ($\phi_b = 31.4°$)

(c) Granite ($\phi_b = 24.9°$) (d) Limestone 2 ($\phi_b = 39.2°$)
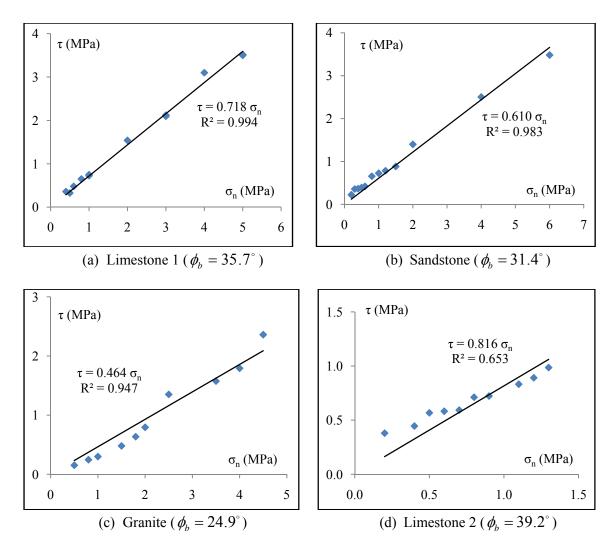
Figure 4.11: Calculation of base friction angle

Barton's empirical equation (Equation (3.31)) suggests zero for peak shear displacement of the sawed fractures. However, Chapter 3 introduced Equation (3.88) for peak shear displacement which works for all ranges of *JRC*, even sawed joints. Table 4.6 and Figure 4.12 show the ability of Equation (3.88) in predicting the peak shear displacement of sawed fractures. It can be seen, except for Limestone 2 (very hard rock), Equation (3.88) works very well. However, predictions of Equation (3.88) are much better than zero given by Barton's equation (Equation (3.31)).

Table 4.6: Ability of Equation (3.88) in predicating the peak shear displacement of sawed fractures

Rock Type and adopted magnitude of JCS	$(\dfrac{\delta_{predicted}}{\delta_{measured}})_{Average} \pm STD$	$(\dfrac{\delta_{predicted}}{\delta_{measured}})_{Max}$	$(\dfrac{\delta_{predicted}}{\delta_{measured}})_{Min}$
Limestone 1 ($JCS = 28$ MPa)	1.05+0.33	1.73	0. 60
Sandstone ($JCS = 41$ MPa)	0.79+0.25	1.46	0.56
Granite ($JCS = 127$ MPa)	0.78+0.19	1.06	0.50
Limestone 2 ($JCS = 155$ MPa)	0.41+0.08	0.56	0.31

(a) Limestone 1

(b) Sandstone

(c) Granite

(d) Limestone 2
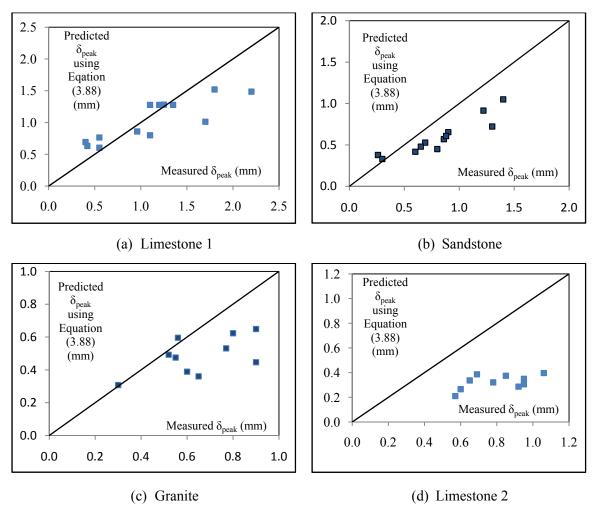
Figure 4.12: Predicted versus measured peak shear displacement using Equation (3.88) for sawed fractures

Figure 4.13 demonstrates the ability of Equation (3.88) to consider the effect of normal stress on the peak shear displacement.

(a) Limestone 1; Specimen 1

(b) Limestone 1; Specimen 2

(c) Limestone 1; Specimen 3

(d) Limestone 1; Specimen 4

(e) Sandstone; Specimen 1

(f) Sandstone; Specimen 2

Figure 4.13: Comparison between measured peak shear displacement and their predicted values using Equation (3.88) for the case of sawed fractures (*JRC=0*)

(g)　Granite; Specimen 1　　　　　　　　(h)　Granite; Specimen 2

(i)　Limestone 2; Specimen 1　　　　　　(j)　Limestone 2; Specimen 2
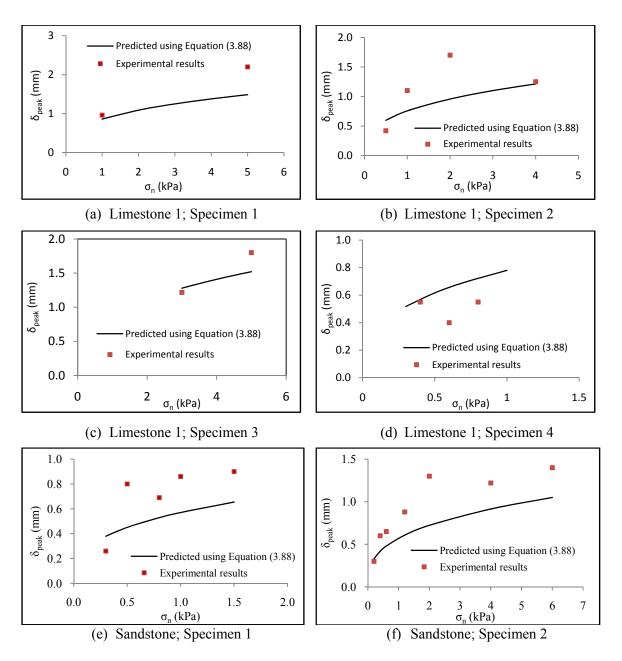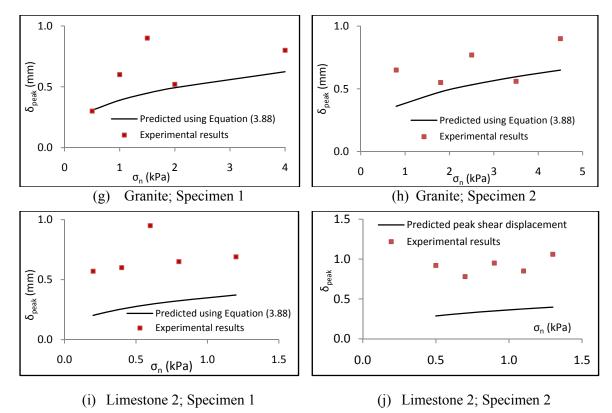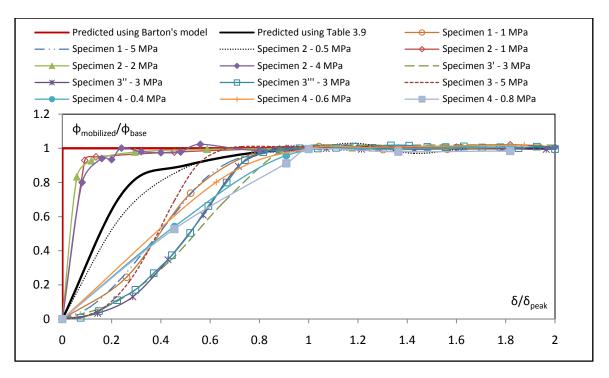
Figure 4.13-Continued: Comparison between measured peak shear displacement and their predicted values using Equation (3.88) for the case of sawed fractures (*JRC*=0)

Although Barton's original model has no suggestion for stress-displacement curve for the case of sawed joints, the modified model proposed in this dissertation suggested Table 3.9 to quantify the mobilization of base friction angle. Figure 4.14 compares the measured $\varphi_{mobilized}/\varphi_{base}$ at each shear displacement with the predicted values using Table 3.9. The measured values of ϕ_{base} and $\phi_{mobilized}$ are obtained using the follow equations:

$$\phi_{base} = \arctan\left(\frac{\tau_{peak}}{\sigma_n}\right), \tag{4.5}$$

$$\phi_{mobilized} = \arctan\left(\frac{\tau}{\sigma_n}\right), \tag{4.6}$$

where σ_n is the normal stress; τ_{peak} is the peak shear strength; and τ is the shear stress at a given shear displacement. It can be seen that Table 3.9 works better than Barton's original model.

(a) Limestone1

(b) Sandstone
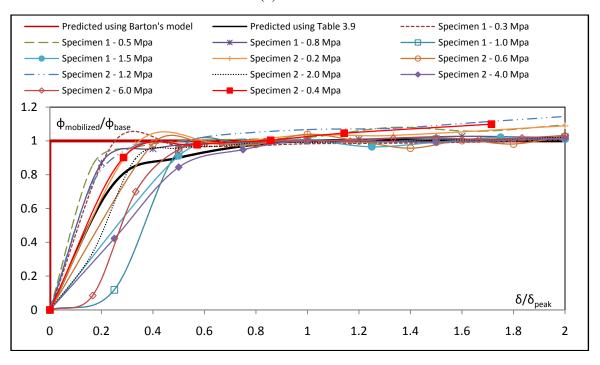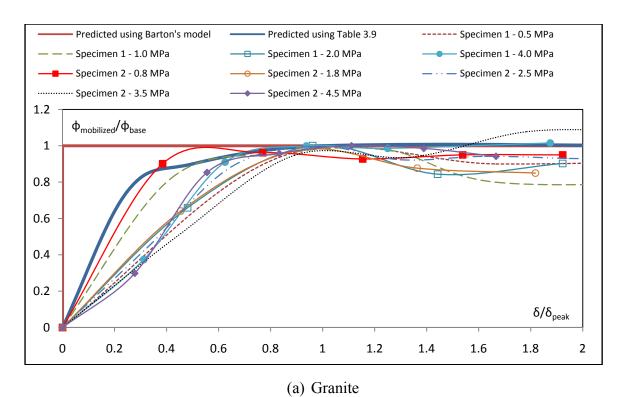
Figure 4.14: Comparison between measured ratio of $\varphi_{mobilized}/\varphi_{base}$ at each shear displacement and predicted one using Table 3.9 (sawed fractures)

144

(a) Granite

(b) Limestone 2
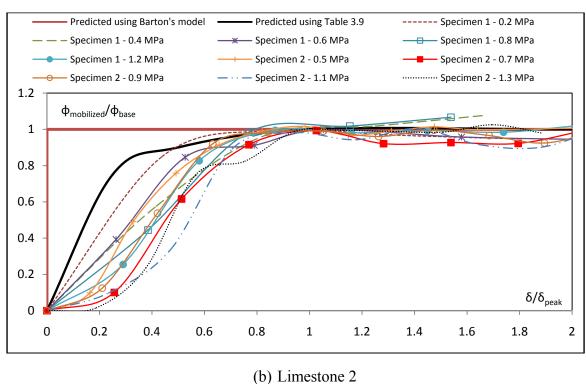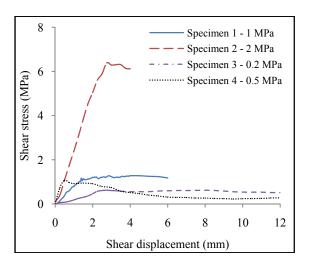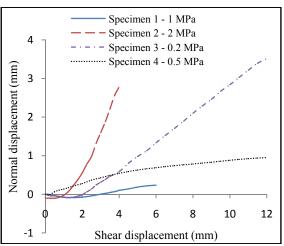
Figure 4.14-Continued: Comparison between measured ratio of $\varphi_{mobilized}/\varphi_{base}$ at each shear displacement and predicted one using Table 3.9 (sawed fractures)

4.3.3 Direct shear tests on rough fractures
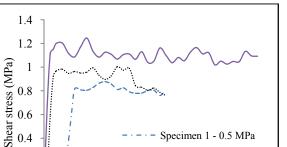
Direct shear tests were performed on three to four samples of each rock type under different normal stresses ranging between 0.2 and 2 MPa. Figure 4.15 and Table 4.7 summarize the results of direct shear tests conducted on the rough fractures of different rock types.

(a-1) Shear stress vs. shear displacement curve   (a-2) Normal vs. shear displacement curve

(a) Limestone
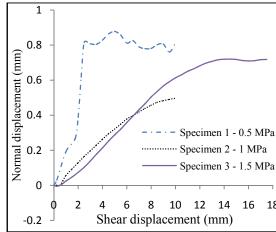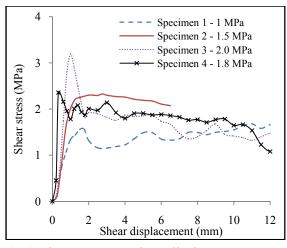
(b-1) Shear stress vs. shear displacement curve   (b-2) Normal vs. shear displacement curve
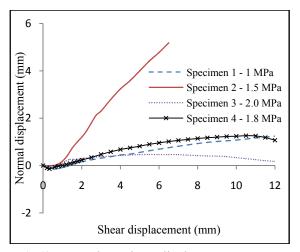
(b) Sandstone

Figure 4.15: Shear stress-shear displacement curves and normal displacement-shear displacement curves obtained from direct shear tests performed on rough fractures
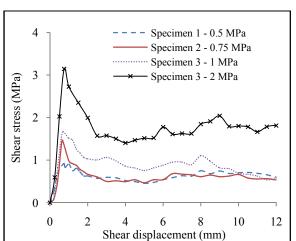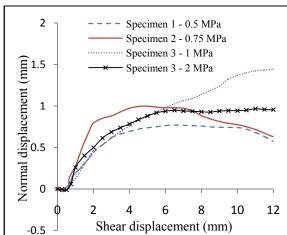
(c-1) Shear stress vs. shear displacement curve   (c-2) Normal vs. shear displacement curve

(c) Granite

(d-1) Shear stress vs. shear displacement curve   (d-2) Normal vs. shear displacement curve

(d) Limestone 2

Figure 4.15-Continued: Shear stress-displacement curves and normal displacement-shear displacement curves obtained from direct shear tests performed on rough fractures

4.3.3.1 Prediction of shear displacement at failure

For each sample, *JRC* was back-calculated based on the measured values of other parameters (*JCS*, base friction angle, normal stress, and shear strength). Table 4.8

summarizes the calculations of *JRC* and peak shear displacements both using Barton's equation (Equation (3.31)) and modified empirical equation (Equation (3.88)).

Table 4.7: Results of direct shear tests on rough fractures

Rock type	Specimen number	L (mm)	σ_n (MPa)	τ_P (MPa)	δ_p (mm)
Limestone 1	1	76.6	1.0	1.22	2.26
	2	66.2	2.0	2.53	2.78
	3	79.9	0.2	0.63	2.72
	4	76.9	0.5	1.08	0.44
Sandstone	1	51.01	0.5	0.82	2.42
	2	51.03	1.0	1.00	1.4
	3	50.40	1.5	1.23	1.36
Granite	1	51.1	1.0	1.56	1.46
	2	51.2	1.5	2.33	1.8
	3	51.2	2.0	3.19	0.92
	4	51.4	1.8	2.36	0.33
Limestone 2	1	51.1	0.5	0.92	0.72
	2	50.7	0.8	1.47	0.66
	3	50.7	1.0	1.67	0.7
	4	51.1	2.0	3.17	0.73

Table 4.8: Calculations of *JRC* and peak shear displacement of rough fractures

Rock Type and adopted magnitude of *JRC*	Sample No.	*JRC*	$\delta_{predicted}$ (mm)	$\dfrac{\delta_{predicted}}{\delta_{measured}}$	$\delta_{predicted}$ (mm)	$\dfrac{\delta_{predicted}}{\delta_{measured}}$
			Equation (3.88)		Barton's equation	
Limestone 1 (*JCS* = 22.5 MPa)	1	10.6	0.81	0.36	0.79	0.35
	2	14.3	0.96	0.34	0.80	0.29
	3	17.3	0.40	0.15	0.95	0.35
	4	17.1	0.58	1.32	0.93	2.11
Sandstone (*JCS* = 33 MPa)	1	15.0	0.43	0.18	0.67	0.27
	2	8.9	0.60	0.43	0.56	0.40
	3	5.9	0.86	0.63	0.66	0.49
Granite (*JCS* = 101MPa)	1	6.2	0.35	0.24	0.68	0.47
	2	17.7	0.41	0.23	0.70	0.39
	3	19.4	0.45	0.48	0.73	0.79
	4	15.8	0.46	1.38	0.68	2.06
Limestone 2 (*JCS* = 124 MPa)	1	9.1	0.29	0.40	0.57	0.79
	2	10.5	0.32	0.49	0.59	0.90
	3	9.3	0.37	0.52	0.57	0.81
	4	10.1	0.47	0.64	0.59	0.81

Figure 4.16 and Table 4.9 compare Equations (3.31) and (3.88) with each other, in accordance with their ratio of predicted to the measured peak shear displacement, $\dfrac{\delta_{predicted}}{\delta_{measured}}$, for rough fractures of different rock types.

(a) Limestone 1 (b) Sandstone

(c) Granite (d) Limestone 2
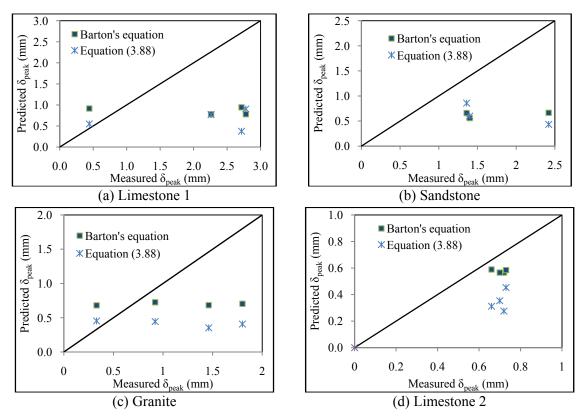
Figure 4.16: Predicted versus the measured peak shear displacement using equation (3.88) and Barton's equation for rough fractures

Table 4.9: Comparison between Barton's equation (Equation (3.31)) and Equation (3.88) in predicting peak shear displacement of rough fractures

Rock Type and adopted magnitude of *JRC*	Sample No.	$(\dfrac{\delta_{predicted}}{\delta_{measured}})_{Average} \pm STD$	$(\dfrac{\delta_{predicted}}{\delta_{measured}})_{Max}$	$(\dfrac{\delta_{predicted}}{\delta_{measured}})_{Min}$
Limestone 1 (*JCS*= 26.4 MPa)	Equation (3.88)	0.54±0.53	1.32	0.15
	Barton's equation	0.77±0.89	2.11	0.29
Sandstone (*JCS* = 32.8 MPa)	Equation (3.88)	0.41±0.23	0.63	0.18
	Barton's equation	0.39±0.11	0.49	0.27
Granite (*JCS* = 101.3 MPa)	Equation (3.88)	0.56±0.54	1.38	0.23
	Barton's equation	0.93±0.78	2.06	0.39
Limestone 2 (*JCS* = 138.5 MPa)	Equation (3.88)	0.51±0.10	0.64	0.40
	Barton's equation	0.83±0.05	0.90	0.79

The following conclusions can be driven from Table 4.8, Table 4.9, and Figure 4.16:

- Equation (3.88) works better than Equation (3.31) in predicting peak shear displacement of rock fractures of Limestone 1, because:

  - Although the value of $(\frac{\delta_{predicted}}{\delta_{measured}})_{Average}$ calculated using Equation (3.31) is closer to one, the correlation factor, $(\frac{\delta_{predicted}}{\delta_{measured}})_{STD} / (\frac{\delta_{predicted}}{\delta_{measured}})_{Average}$, is smaller in the case of Equation (3.88) (0.98 from Equation (3.88) compared to 1.16 from Barton's equation).

  - For specimens 1 and 2, the ability of Equations (3.31) and (3.88) in predicting the peak shear displacement are the same.

  - For specimen 3, Barton's equation works a little bit better than Equation (3.88).

- The abilities of Equations (3.31) and (3.88) in predicting peak shear displacements of rough fractures of the sandstone are almost the same, because:

  - Although the value of $(\frac{\delta_{predicted}}{\delta_{measured}})_{Average}$ calculated using Equation (3.88) is closer to one, the correlation factor, $(\frac{\delta_{predicted}}{\delta_{measured}})_{STD} / (\frac{\delta_{predicted}}{\delta_{measured}})_{Average}$, is smaller in the case of Equation (3.31) (0.28 from Equation (3.31) compared to 0.56 from Equation (3.88)).

  - For specimen 1, Barton's equation works a little bit better than Equation (3.88).

  - For specimens 2 and 3, Equation (3.88) has better predictions for the peak shear displacement comparing to those of Barton's equation.

- Barton's equation (Equation (3.31)) works better than Equation (3.88) in predicting the peak shear displacements of rough fractures of the granite, because:

- The value of $(\frac{\delta_{predicted}}{\delta_{measured}})_{Average}$ calculated using Equation (3.88) is closer to one.

- The correlation factor, $(\frac{\delta_{predicted}}{\delta_{measured}})_{STD} / (\frac{\delta_{predicted}}{\delta_{measured}})_{Average}$, is smaller in the case of Equation (3.88).

- For specimens 1 to 3, Barton's equation works better than Equation (3.88).

- For specimens 4, Equation (3.88) has better predictions for the peak shear displacement comparing to those of Barton's equation.

- Barton's equation (Equation (3.31)) works better than Equation (3.88) in predicting peak shear displacement of rock fractures of limestone 2.

4.3.3.2 Prediction of shear stress-displacement curve

Figure 4.17 compares the stress-displacement curve predicted using Barton's original model and the modified model with the stress-displacement curves obtained from direct shear tests on rough fractures of Limestone 1. In addition, Table 4.10 compares Barton's model and the modified model in accordance with their ratio of predicted to the measured ratio of $\frac{\tau}{\sigma}$ for rough fractures.

It can be seen in Figure 4.17 and Table 4.10 that both models work very well in predicting the stress-displacement curve. For shear displacements smaller than about 8 times of the peak shear displacement, both models underestimate the stresses and, after that, both overestimate the stresses. It can be concluded that the modified model is a little bit better than the original model due to the following reasons:

- The value of $\left(\frac{\left(\frac{\tau}{\sigma}\right)_{predicted}}{\left(\frac{\tau}{\sigma}\right)_{measured}} \right)_{Average}$ obtained using the modified model is closer to one comparing to those calculated using Barton's model.

151

(a) Limestone 1; Specimen 1

(b) Limestone 1; Specimen 2

(c) Limestone 1; Specimen 3

(d) Limestone 1; Specimen 4

(e) Sandstone; Specimen 1

(f) Sandstone; Specimen 2
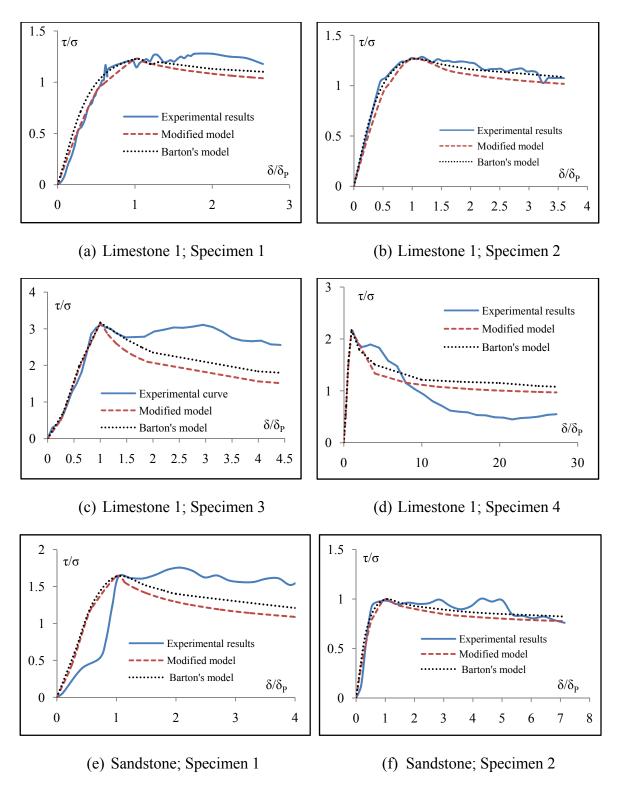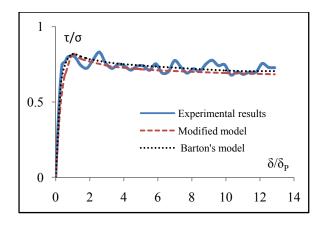
Figure 4.17: Comparison between Barton's original model and the modified model in predicting stress-displacement curve for rough fractures

(g) Sandstone; Specimen 3

(h) Granite; Specimen 1

(i) Granite; Specimen 2

(j) Granite; Specimen 3

(k) Granite; Specimen 4

Figure 4.17-Continued: Comparison between Barton's original model and the modified model in predicting stress-displacement curve for rough fractures

153

(l) Limestone 2; Specimen 1
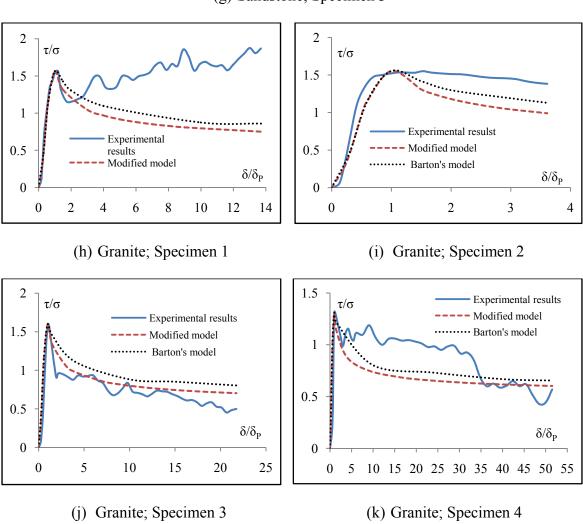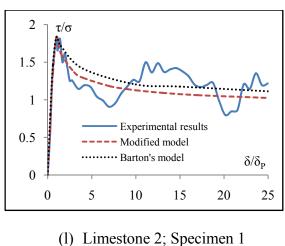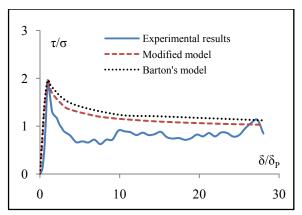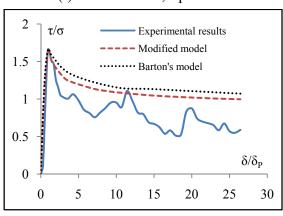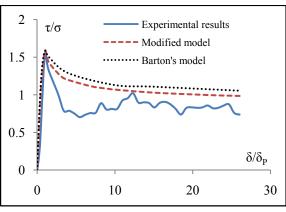
(m) Limestone 2; Specimen 2

(n) Limestone 2; Specimen 3

(o) Limestone 2; Specimen 4

Figure 4.17-Continued: Comparison between Barton's original model and the modified model in predicting stress-displacement curve for rough fractures

Table 4.10: Comparison between Barton's original model and the modified model in predicting tress-displacement curve for rough fractures

Rock Type	Constitutive model	$\left(\dfrac{\left(\frac{\tau}{\sigma}\right)_{predicted}}{\left(\frac{\tau}{\sigma}\right)_{measured}}\right)_{Average} \pm STD$	$\left(\dfrac{\left(\frac{\tau}{\sigma}\right)_{predicted}}{\left(\frac{\tau}{\sigma}\right)_{measured}}\right)_{Max}$	$\left(\dfrac{\left(\frac{\tau}{\sigma}\right)_{predicted}}{\left(\frac{\tau}{\sigma}\right)_{measured}}\right)_{Min}$
Limestone 1	Barton's model	1.09+0.38	2.36	0.69
	Modified model	1.02+0.32	2.07	0.59
Sandstone	Barton's model	1.09+0.42	2.68	0.74
	Modified model	1.02+0.41	2.58	0.67
Granite	Barton's model	1.11+0.82	4.19	0.4
	Modified model	1.23+0.87	4.11	0.46
Limestone 2	Barton's model	1.52+1.01	6.45	0.78
	Modified model	1.70+1.35	7.04	0.84

154

- The correlation factor, the ratio of $\left(\dfrac{\left(\dfrac{\tau}{\sigma}\right)_{predicted}}{\left(\dfrac{\tau}{\sigma}\right)_{measured}}\right)_{STD}$ to $\left(\dfrac{\left(\dfrac{\tau}{\sigma}\right)_{predicted}}{\left(\dfrac{\tau}{\sigma}\right)_{measured}}\right)_{Average}$, is smaller in

the case of the modified model.

- The value of $\left(\dfrac{\left(\dfrac{\tau}{\sigma}\right)_{predicted}}{\left(\dfrac{\tau}{\sigma}\right)_{measured}}\right)_{Max}$ obtained using the modified model is smaller than

those calculated using Barton's model.

4.3.3.3 Prediction of normal displacement-shear displacement curve (dilatancy)

Figure 4.18 compares the normal displacement-shear displacement curves predicted using Barton's original model and the modified model with the normal displacement-shear displacement curves obtained from direct shear tests on rough fractures. In addition, Table 4.11 compares Barton's model and the modified model in accordance with their ratio of $r = \left|\dfrac{\left(\delta_v\right)_{predicted} - \left(\delta_v\right)_{measured}}{\left(\delta_v\right)_{measured}}\right|$ at the same shear displacements for rough fractures.

Figure 4.18 and Table 4.11 show that both Barton's model and the modified model have lots of errors in predicting the dilation displacement. An ideal model has the ratio of r equal to zero. However, both models give this ratio between 1 and 2.5. Both models have lots of approximations and from statistical point of view Barton's model works a little bit better than the modified model. However, due to the following reasons, it can be concluded that the modified model should be used for predicting the dilation behavior of rock fractures:

- Barton's model can predict dilation displacement only at the peak shear displacement. The dilation displacements predicted using Barton's model in this Chapter is not calculated exactly from the model proposed by Barton. However, they were estimated based on our interpretation, in the lack of direct suggestion, which was explained in Section 3.3.4.

155

(a) Limestone 1; Specimen 1 (*JCS* = 22.5 MPa) (b) Limestone 1; Specimen 1 (*JCS* = 22.5 MPa)

(c) Limestone 1; Specimen 3 (*JCS* = 22.5 MPa) (d) Limestone 1; Specimen 4 (*JCS* = 22.5 MPa)

(e) Sandstone; Specimen 1 (*JCS* = 33 MPa) (f) Sandstone; Specimen 2 (*JCS* = 33 MPa)
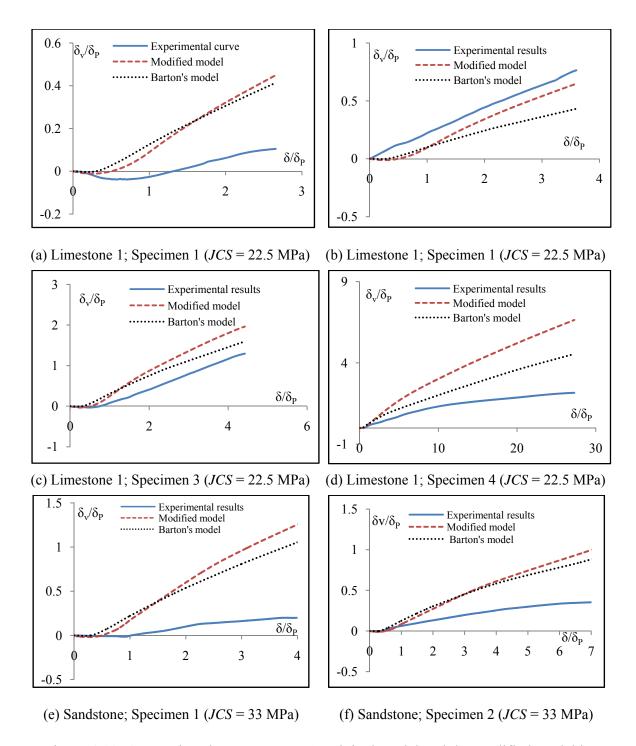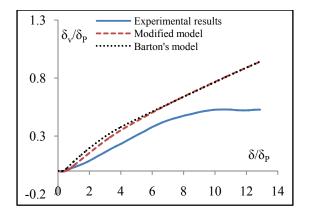
Figure 4.18: Comparison between Barton's original model and the modified model in predicting dilation displacement for rough fractures

(g) Sandstone; Specimen 3 (*JCS* = 33 MPa)
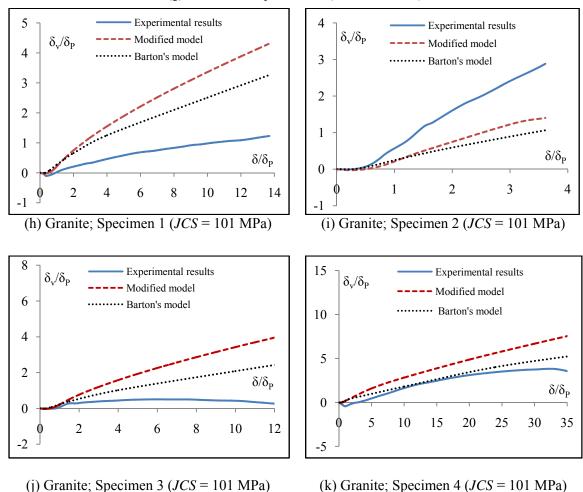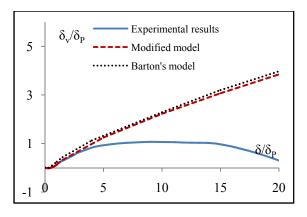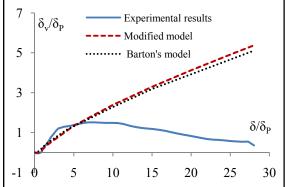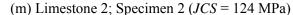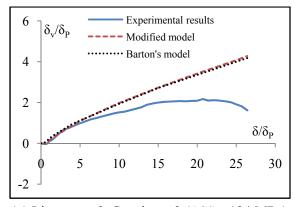
(h) Granite; Specimen 1 (*JCS* = 101 MPa)

(i) Granite; Specimen 2 (*JCS* = 101 MPa)

(j) Granite; Specimen 3 (*JCS* = 101 MPa)

(k) Granite; Specimen 4 (*JCS* = 101 MPa)

Figure 4.18-Continued: Comparison between Barton's original model and the modified model in predicting dilation displacement for rough fractures
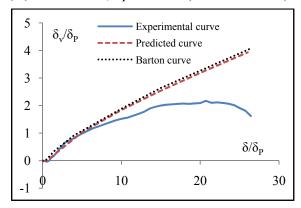
(l) Limestone 2; Specimen 1 (*JCS* = 124 MPa)   (m) Limestone 2; Specimen 2 (*JCS* = 124 MPa)

(n) Limestone 2; Specimen 3 (*JCS* = 124 MPa)   (o) Limestone 2; Specimen 4 (*JCS* = 124 MPa)

Figure 4.18-Continued: Comparison between Barton's original model and the modified model in predicting dilation displacement for rough fractures

Table 4.11: Comparison between Barton's original model and the modified model in predicting dilation displacement for rough fractures

Rock Type	Constitutive model	*JRC*	$r_{Average} \pm STD$	r_{max}	r_{Min}
Limestone 1	Barton's model	22.5	1.96±1.68	5.94	0.23
	Modified model		2.12±1.81	7.46	0.15
Sandstone	Barton's model	33	2.50±2.56	11.03	0.45
	Modified model		2.39±2.26	8.47	0.30
Granite	Barton's model	101	2.25±2.32	10.50	0.51
	Modified model		1.85±1.79	6.90	0.11
Limestone 2	Barton's model	124	1.52±1.79	7.11	0.06
	Modified model		1.10±1.73	7.79	0.01

$$r = \left| \frac{(\delta_v)_{predicted} - (\delta_v)_{measured}}{(\delta_v)_{measured}} \right|$$

- In 13 cases out of 15 cases of rough fractures, it can be seen can see negative dilation (compression) at small shear displacements. These negative dilations are not considered in Barton's model, which can cause overestimation of factor of safety in some analysis such as stability of rock blocks in tunnels. These negative dilations are included in the modified model.

4.4 CONCLUSIONS

The experimental study presented in Section 4.3 validated the modifications proposed in Chapter 3 to Barton's original model. The following conclusions can be driven based on the results of our testing:

1) The modified empirical equation proposed for peak shear displacement of rock fractures (Equation (3.88)) can predict the peak shear displacement of sawed (and planar) fractures with acceptable precision. However, Barton's original equation gives zero peak shear displacement for sawed fractures.

2) The modified empirical equation proposed for peak shear displacement of rock fractures (Equation (3.88)) can consider the effect of normal displacement on increasing the peak shear displacement, while Barton's original equation cannot.

3) Chapter 3 proposed Table 3.9 for shear stress-displacement of sawed fractures (mobilization of the base friction angle). Using Table 3.9, the shear stress-displacement curve of sawed fractures can be predicted with great precision. Barton's original model has no suggestion in this regard.

4) As far as sawed (or planar) fractures, the modified model works much better than the original Barton's model.

5) The modified equation proposed for peak shear displacement of rock fractures (Equation (3.88)) works better than Barton's equation (Equation (3.31)) in the case of rough fractures of Limestone 1. However, in the case of rough fractures of granite and Limestone 2, Barton's equation works better. In addition, the abilities of both equations in the case of sandstone were almost the same.

6) Since the granite and Limestone 2 are hard rocks and while Limestone 1 and sandstone are weak rocks, one may conclude that Barton's model works better for

hard rocks. However, MDST database [188-210] contains many cases of hard rock fractures in which modified model works better.

7) Figure 3.7 shows that, in MDST database, most of the tests have a ratio of σ / JCS between 0.01 and 0.1. It can be seen that, in our experimental study, for the cases located within the above domain, the modified model works better than Barton's model.

8) In the cases of the Granite and Limestone 2, *JRC's* are between 10 and 20. However, in the cases of Limestone 1 and the Sandstone, *JRC's* are between 6 and 17. Furthermore, for the sawed joints, it can be seen that modified model works much better than Barton's model. It can be concluded that modified model works better in the case of planar fractures and Barton's model works better in the case of rough fractures.

9) Table 4.12 shows that, for rough fractures, Barton's equation (Equation (3.31)) works a little bit better than the modified equation (Equation (3.88)). Although the value of $(\dfrac{\delta_{perdicted}}{\delta_{measured}})_{Average}$ calculated using Equation (3.31) is closer to one, the correlation factor, $(\dfrac{\delta_{perdicted}}{\delta_{measured}})_{STD} /(\dfrac{\delta_{perdicted}}{\delta_{measured}})_{Average}$, is smaller in the case of Equation (3.88) (0.57 from Equation (3.88) compared to 0.74 from Barton's equation).

10) Modified model works better than Barton's original model in predicting shear stress-shear displacement curve (for all types of rocks and for both planar and rough fractures).

11) Table 4.13 compares Barton's model and the modified model in accordance with the ratio of $\dfrac{\left(\dfrac{\tau}{\sigma}\right)_{predicted}}{\left(\dfrac{\tau}{\sigma}\right)_{measured}}$.

Table 4.12: Comparison between Barton's equation and Equation (3.88) in predicting the peak shear displacement of rough fractures

Parameter	Equation (3.88)	Barton's equation (Equation (3.31))
$(\dfrac{\delta_{perdicted}}{\delta_{measured}})_{Average} \pm STD$	0.61±0.35	0.72±0.53
$(\dfrac{\delta_{perdicted}}{\delta_{measured}})_{Max}$	1.28	2.07
$(\dfrac{\delta_{perdicted}}{\delta_{measured}})_{Min}$	0.13	0.27

Table 4.13: Comparison between Barton's model and the modified model in predicting stress-displacement curve

Constitutive model	$\left(\dfrac{\left(\frac{\tau}{\sigma}\right)_{predicted}}{\left(\frac{\tau}{\sigma}\right)_{measured}}\right)_{Average} \pm STD$	$\left(\dfrac{\left(\frac{\tau}{\sigma}\right)_{predicted}}{\left(\frac{\tau}{\sigma}\right)_{measured}}\right)_{Max}$	$\left(\dfrac{\left(\frac{\tau}{\sigma}\right)_{predicted}}{\left(\frac{\tau}{\sigma}\right)_{measured}}\right)_{Min}$
Barton's model	1.20±0.71	6.45	0.59
Modified model	1.29±0.88	7.04	0.69

12) One of the advantages of modified model in predicting stress-displacement curve lies in its ability to predict the curve for high values of the δ_h/δ_P ratio which is very difficult to achieve in lab tests. Just in one case (rough fracture of the granite; specimen 4), the ratio of δ_h/δ_P is high and it can be seen that the modified model works better than Barton's model (Figure 4.17-k).

13) It is almost impossible to make a fracture with *JRC* smaller than 5 in laboratory scales (specimen of about 10 cm). However, direct shear tests performed on planar fractures not only can reveal the advantage of the modified model in predicting stress-displacement curve, but also can show the advantage of Equation

(3.88) on Equation (3.31). It should be noted that, considering the scale effect, a fracture with $JRC > 5$ may have a lab size specimen with $JRC < 5$.

14) Our experimental study shows that both the modified model and Barton's model display substantial approximation in predicting dilation displacement of rough fractures. However, due to the following reasons, it is believed that the modified model should be used for predicting the dilation behavior of rock fractures:

- Barton's model can predict dilation displacement only at the peak shear displacement. The dilation displacements predicted using Barton's model in this Chapter is not calculated exactly from the model proposed by Barton. However, they were estimated based on our interpretation, in the lack of direct suggestion, which was explained in Chapter 3.

- In 13 out of 15 cases of rough fractures tested in our study, it can be seen negative dilation (compression) at small shear displacements. These negative dilations are not considered in Barton's model, which can cause overestimation of factor of safety in some analysis such as stability of rock blocks in tunnels. The negative dilation is included in the modified model.

CHAPTER 5:   IMPLEMENTATION AND VERIFICATION OF BS3D

5.1   INTRODUCTION

In this dissertation, prototype BS3D computer code developed by Tonon [1] in Mathematica has been re-written and translated into Fortran 95. The implementation has been done in the platform of *Microsoft Visual Stodio.Net*. *Intel Visual Fortran* has been used as Fortran compiler. The code implements Tonon's [1] incremental-iterative algorithm for analyzing general failure modes of rock blocks subject to generic forces. Consistent stiffness matrices fully exploit the quadratic convergence of the adopted Newton-Raphson iterative scheme. The algorithm takes into account large block displacements and rotations, which, together with non-conservative forces make the stiffness matrix non symmetric. Tonon's original code implements the algorithm just for tetrahedrons. However, the generalized version of BS3D developed in this dissertation can analyze general shapes of rock blocks. Furthermore, *in situ* stress and water pressure have been implemented from scratch because they were not included in Tonon's code. In Tonon's original code, fracture dilatancy was included in a rudimental fashion by using a simplified version of Barton's model. However, the generalized version of BS3D can deal with both original [21] and modified Barton's model (Chapter 3) as well as Mohr-Coulomb's failure criterion [25].

Section 5.2 describes the implementation of BS3D with a brief explanation of strategies, algorithms, and formulations implemented in the code but not explained in the other chapters of this dissertation. In Section 5.3, the implementation is verified using direct shear test examples. In Section 5.4, the *in situ* stress implementation is verified using the example of a Cauchy tetrahedron. The section also deals with the effect of a circular tunnel on the stresses acting on a block's faces. Section 5.5 introduces an example to verify the implementation of *in situ* stress and the Boundary Element Method (for normal stiffness of the rock block) in BS3D. Section 5.6 briefly deals with hydrostatic water pressure followed by the summary of the Chapter in Section 5.7.

163

5.2 IMPLEMENTATION OF BS3D

5.2.1 Reading input variables

BS3D reads physical and mechanical properties of the block and its mould together with information regarding applied forces and intended analyses from an input file, *"input.dat"*. Table 5.1 summarizes the list of input variables read by BS3D from the main input file. A sample input file is given in Appendix B.

Table 5.1: List of input variables of BS3D (*input.dat*)

Category	Description	Symbols
General	Number of vertices (required for defining the block and its mould)	$n_{vertices}$
Block geometry	Coordinate of i-th vertex (i changes between 1 and $n_{vertices}$)	$V_{i,x...z}$
	Number of faces of the block	n_f
	Number of faces of the block with more than one boundary	n_{fwmo}
	Number of boundaries in i-th face that has more than one boundary (i changes between 1 and n_{fwmo}); nb_i = 1+number of holes in the face. If there is no hole in the face, nb_i = 1 and there is no need to allocate it here.	nb_i
	Number of vertices in j-th boundary of i-th face	$nv_{i,j}$
	List of vertices of j-th boundary of i-th face (for outermost boundary, vertex indices should be given here in counterclockwise order along its boundary and, for hole, vertices should be listed in clockwise order)	$lv_{i,j}$
General	Number of segments (sensor points) per edge	n_{tt}
Mould geometry	Number of faces of the mould	$n_{f,mould}$
	Number of faces that are in common between the block and its mould	$n_{f,shared}$
	Index of a face of the block that is in common with i-face of the mould (i changes between 1 and $n_{f,shared}$)	sf_i
	Number of faces of the mould (not shared with a face of the block) with more than one boundary	$n_{fwmo,mould}$
	Number of boundaries in i-th face of the mould (not shared with a face of the block) that has more than one boundary (j changes between 1 and $n_{fwmo,mould}$)	nbm_i
	Number of vertices in j-th boundary of i-th face of the mould (not shared with a face of the block)	$nvm_{i,j}$
	List of vertices of j-th boundary of i-th face of the mould (not shared with a face of the block)	$lvm_{i,j}$
Mechanical properties	Unit weight of the block (MN/m^3)	γ
	Gravity acceleration (m/s)	g
	Young's modulus of the block	E_b
	Poisson's ratio of the block	v_b
	Young's modulus of rock mass	E_{mass}
	Poisson's ratio of rock mass	v_{mass}

164

Table 5.1-Continued: List of input variables of BS3D (*input.dat*)

Category	Description		Symbols
Mechanical properties	Dilatancy characteristics of *i*-th face of the mould (*i* changes between 1 and $n_{f,mould}$)	Initial normal stiffness	s_i
		Maximum closure	v_i
		Length of lab size specimen for which fracture properties are given	$L_{0,i}$
		Base friction angle	$\Phi_{b,i}$
		JCS	$JCS_{0,i}$
	Isotropic *JRC* of *i*-th face of the mould (*i* changes between 1 and $n_{f,mould}$)		$JRC_{0,i}$
	Anisotropic dilatancy characteristics of *i*-th face of the mould (*i* between 1 and $n_{f,mould}$)	Length of block along *j*-th shearing direction (*j*=1,2)	$L_{n,i,j}$
		JRC of block along *j*-th shearing direction (*j*=1,2)	$JRC_{0,i,j}$
		Direction of *j*-th shearing direction (*j*=1,2)	ShD_j
Analyses characteristics	Number of permanent faces of the mould (number of faces which are not removed in the excavation stage)		$n_{perFace}$
	Number of stages		N_{stage}
	Additional forces and moments applied to the block at *i*-th stage		$F_{add,i}$
	Step stage for *i*-th stage		$Step_{0,i}$
	Maximum increment number		*MaxInc*
	Maximum iteration number		*MaxIter*
	Maximum λ at *i*-th stage		λ_i
	Fractures Constitutive model (Mohr-Coloumb, Bartons's, or Modified Barton's model)		
	Normal stiffness of the block should be calculated using approximation or BEM (see Section 5.2.5 for details)		
	Considering *in situ* stress around circular tunnel (Yes or No; see Section 5.4.2 for details)		
	Considering water pressure due to high-velocity jet impact (Yes or No; see Section 5.6 and Chapter 8 for details)		

5.2.2 Dilatant behavior of rock fractures

Section 3.4 introduced a predictive model for anisotropic dilatant behavior of rock fractures for which dilatancy characteristics of fractures should be given in two perpendicular directions. There are two options in BS3D for entering fracture dilatancy properties: isotropic and anisotropic. For anisotropic dilatancy, all information should be given in the input file. However, for the case of isotropic dilatancy, the maximum length of the block along each face of the mould can be calculated by BS3D automatically. The direction is called the 1ˢᵗ shearing direction of the discontinuity. In addition, the length of the block along direction perpendicular to the 1ˢᵗ shearing direction is determined and the direction is called the 2ⁿᵈ shearing direction of the fracture.

The size effect is applied to the given lab size magnitudes of *JRC* and *JCS* using Equations (3.5) and (3.7), respectively. The peak shear displacements of all faces of the mould along both shearing directions are determined using Equations (3.31) or (3.88) according to Barton's model or Modified Barton's model, respectively.

5.2.3 Triangulation

All faces of the block and its mould are triangulated using the efficient procedure of Seidel [69] as implemented by Narkhede and Manocha [70] in C++. The triangulation subroutine is called by the main Fortran routine of BS3D using capabilities of *Microsoft Visual Stodio.Net* in multilanguage programming.

The triangulation subroutine can divide a 2D polygon into triangles. Thus, all faces of the block and the mould should be projected into a 2D plane. However, the 2D plane on which each face is to be projected can not be chosen randomly. Numerical inaccuracy of floating point errors can occur when the face normal has little or no component in the projection direction; in the extreme situation (no component), the face projects to a line segment [236]. To reduce such errors for a given face the α-β-γ coordinates are always chosen as a right-handed ($\hat{\alpha} \times \hat{\beta} = \hat{\gamma}$) permutation of the *x-y-z* coordinates such that $\left|\hat{N}_\gamma\right|$ is maximized. This choice maximizes the area of the projected shadow in α-β plane (see Figure 5.1). Note that a choice can always be found such that $\left|\hat{N}_\gamma\right| > \sqrt{3}^{-1}$ [236].
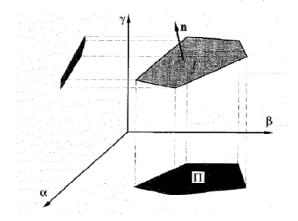
Figure 5.1: The α-β-γ axes are a right-handed permutation of the *x-y-z* axes chosen to maximize the size of the face's projected in the α-β plane [236].
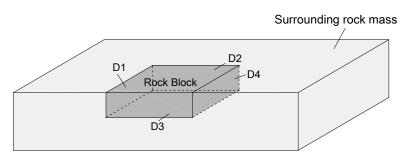
Therefore, before calling triangulation subroutine all faces of the block and the mould are projected on the best 2D plane (found by the method proposed by Mirtich [236]).

5.2.4 Mass properties

Mass properties of the block including centroid, volume, weight, and inertia tensor are determined using a subroutine developed in this research based on the method proposed by Mirtich [236] to compute polyhedral mass properties (see Appendix C for the pseudo code of the algorithm).

5.2.5 Normal stiffness of rock mass and rock block

Figure 5.2 depicts a rock block constrained in its mould by surrounding rock mass. In rock block stability analyses, in addition to the deformability of the rock fractures, the deformability of the rock block and of the rock mass must be taken into account in order not to overestimate the forces generated by dilatancy along the fractures that bound the block. In order to analyze the stability of a single rock block, Tonon [1] adopted Goodman's hyperbolic model [78] for the normal stiffness of the fractures that bound the block. Although the simplified analytical equation (Equation (2.44)) proposed by Tonon [1] works very well for the normal stiffness of the surrounding rock mass, the suggested approximation for the normal stiffness of the rock block (Equation (2.43)) depends on the loading conditions and results may be affected by large errors.

D1... D4: Block faces   (rock fractures that bound the block)

Figure 5.2: Block surrounded by rock mass in its mould.

The deformability of the blocks can conveniently be simulated using the Boundary Element Method (BEM). However, all boundary conditions are given as stresses, and the direct BEM [237-240] is applied to the solution of the traction boundary value problem (TBVP) on the boundary of a domain. The displacement solution of a TBVP is not unique because it is defined up to a rigid body motion (RBM), which has zero strain energy and thus also zero stresses [241] .

Taking into account that the symmetric Galerkin Boundary Element Method (SGBEM) [242] has some strong similarity with the FEM, Vodicka *et al.* [241] applied the method successfully used in the FEM, e.g. [243, 244], in the SGBEM. The method, referred to as Method S by Blazquez *et al.* [245], enforces additional point supports in the displacement field which can be carried out by zeroing the appropriate rows and columns in the linear system of equations and defining the corresponding diagonal elements equal to a non-zero number [241].

Starting from the Fredholm theory of linear operators with zero index [246, 247], different mathematical approaches, referred to as Methods F by Blazquez *et al.* [241], have been proposed by various authors [245, 246, 248-257] with the aim of removing rigid body motions in elastostatic BEM problems. Methods F can be subdivided into two categories: (a) Method F1, also called the *augmenting method* or *bordering method*, has been considered by various researchers [245, 246, 248-250]; (b) Method F2, sometimes called the *completion method*, has been considered by various authors [245, 252-257].

In removing RBMs from the TBVP solution, it should be considered that although the load prescribed is always equilibrated on the continuum level, after discretization its global equilibrium can be slightly perturbed [241]. Nevertheless, it is convenient to search for a reasonable approximation of the TBVP solution on the continuum level. These difficulties were studied theoretically [246, 258] and numerically [245, 259] for the classical BEM. However, it seems that these methods may lack a simple interpretation from an engineering point of view as well as a relation between the rigid-body motion and global equilibrium conditions.

In this Section, an algorithm is proposed to remove rigid body motions in the solution of the boundary form of Somigliana identity discretized by the direct BEM formulation. The algorithm is validated using an example of calculating of the normal stiffness of a rock block. The results of BEM analyses are compared with those obtained by means of the approximation given by Equation (2.43).

Given the stresses on the block's boundary, the problem is to obtain the displacements at each point of the block's boundary due to the deformability of the rock block. However, if a finite elastic body is completely free (i.e. all prescribed boundary conditions are given as stresses), the displacement solution is not unique because the body can freely translate and/or rotate in some directions. There are infinite solutions generating the same state of stresses; the only difference between two such solutions being rigid body motions.

5.2.5.2 Proposed Method

Application of BEM to elstostatic problems consists of the numerical solution of a Boundary Integral Equation, Somigliana identity [239]. Let consider a polyhedral rock block made of a number of faces (polygons). BS3D triangulates each face of the block into a set of triangles and subdivides each triangle into a set of subtriangles. Subsequently, a point (node) is assigned to the centroid of each subtriangle. Figure 5.3 schematically depicts the discretization process.
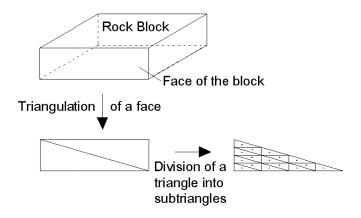
Figure 5.3: Discretization of the boundary of the block

169

Discretization of the boundary by boundary elements (triangles in BS3D) leads to a system of linear equations that can be represented as [239]:

$$HU = GP + B, \qquad\qquad (5.1)$$

where H and G are $3N \times 3N$ coefficient matrices, with N equal to the number of nodes used in the discretization. U, P, and B are displacement, traction, and body force vectors, respectively, of dimension $3N$. In BS3D, all elements of H and G matrices are calculated by using Gaussian integration over triangles [260-263]. G_{ii} components are calculated by following Li's and Han's method [264] for evaluating singular integrals in stress analysis of solids by the direct BEM. Body force vector, B, is obtained using Galerkin Vector approach, which transforms the domain integrals into boundary integrals [237] (see Appendix D for pseudo code of implemented subroutines that calculate BEM matrices together with verification examples).

In BS3D, at the end of each increment, all tractions, P, are known. Displacements at all boundary nodes are unknown, and can formally be calculated by solving Equation (5.1) for U:

$$U = H^{-1}(GP + B) \qquad\qquad (5.2)$$

However, H is singular and there are infinite solutions for U because the block is in equilibrium and free to translate and/or rotate.

In order to remove the rigid-body motions from the solution, the following approach is adopted:

- The displacements of one arbitrarily chosen boundary node, say Q, are assumed to be zero. It should be noted that any boundary node can be selected.
- 3 equations and 3 unknowns corresponding to the fixed node, Q, can be eliminated from the system of Equations (5.1).
- Although the rigid-body translations have been removed from the displacement solution, H should still be singular due to the rigid-body rotation degrees of freedom. However, round-off errors turn H^{-1} from singular to ill-conditioned. Therefore H^{-1} can be calculated by the algorithm proposed by Rump [265] to

inverse extremely ill-conditioned matrices. As a consequence, displacements at all boundary nodes can be calculated with respect to the fixed node, *Q*.

- The displacement of the block's centroid is calculated as the average displacement of all nodes, including the fixed one, *Q*.
- Relative displacements of all nodes to the centroid are calculated.
- The new normal unit vector to each boundary face can be obtained because the new position of all nodes is known.
- The normal displacement component of each node (due to the deformability of rock block) can be determined given the node's displacement vector (relative to the centroid) and the new normal unit vector to the node's triangle.

The normal stiffness due to the deformability of the rock block at each node will be equal to the ratio of the normal stress to the normal displacement at that node. The magnitude of this stiffness depends on the boundary conditions and should be updated at the end of each increment.

5.2.5.3 Results and Discussion

In order to verify the above mentioned boundary element formulation, consider a $0.1 \times 0.1 \times 0.1 m$ cubic block shown in Figure 5.4. The block has Young's modulus of 1,000 MPa and Poisson's ratio of 0.25; and it is subjected to compression load of 0.5 MPa in 1, 2, and 3 directions perpendicular to faces.
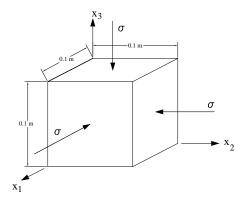
Figure 5.4: Dimension of the cubic block considered in verification and the stress components on the cub

171

The normal stiffness of the block can be calculated based on the theory of elasticity. Figure 5.4 depicts stress components around the cube subjected to compression stress, σ, in 3 directions. For linear elastic materials, the strain along the x_i axis can be calculated as follows [266]:

$$\varepsilon_i = \frac{\Delta l_i}{l_i} = \frac{\sigma}{E}(1 - 2v),$$

(5.3)

where E and v are Young's modulus and Poisson's ratio of the block, respectively; l_i and Δl_i are length of the block and the total displacement along the x_i axis, respectively. The relative displacement of each face to the centroid is equal to half of the total displacement of the block along the normal vector of that face. Thus, the normal stiffness of each face can be calculated analytically as follows:

$$K_{n_i} = \frac{\sigma}{\Delta l_i / 2} = \frac{2E}{l_i(1 - 2v)}$$

(5.4)

For the cases of loading in 1 and 2 directions, the normal stiffness of the loaded faces can be calculated using the following equations, respectively:

$$K_{n_i} = \frac{2E}{l_i}$$

(5.5)

$$K_{n_i} = \frac{2E}{l_i(1 - v)}$$

(5.6)

In addition, the block normal stiffness at the nodes located on the top and the bottom faces was determined by using both approximation (Equation (2.43)) and the proposed algorithm based on Boundary Element Method described in this Section. Knowing the solution (5.4), (5.5), or (5.6) as the correct one, Figure 5.5 depicts the maximum percent error in estimating the block normal stiffness (at the nodes located on the top and the bottom faces) calculated using Tonon's approximation and the proposed BEM-based algorithm for 8 to 72 elements per face.

(a) Compression in 1 direction (along x_3 axis)

(b) Compression in 2 directions (along x_3 and x_1 axes)

(c) Compression in 3 directions (along x_1, x_2, and x_3 axes)
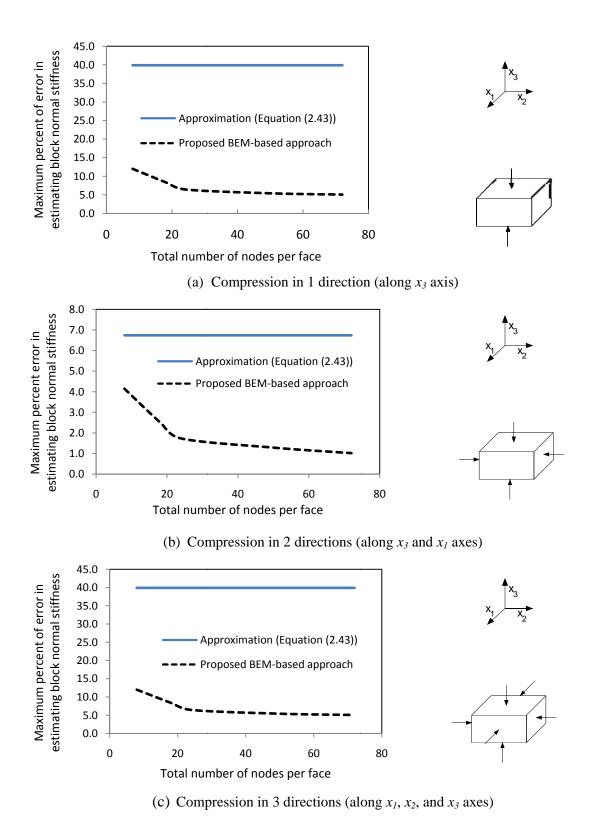
Figure 5.5: Maximum percent error in estimating the block normal stiffness

Figure 5.5 shows that the BEM-based algorithm of this Section works very well in estimating the normal stiffness. Although increasing the number of nodes increases the accuracy of BEM formulation, it has no effect on the accuracy of the approximation. In addition, the accuracy of the approximation depends on the loading condition. The maximum error in estimating the normal stiffness calculated using Tonon's approximation is 30, 6.7, and 40 percent in the cases of loading in 1, 2, and 3 directions, respectively. In the case of loading in 2 directions, the approximation works very well. However, the proposed BEM-based algorithm works with acceptable accuracy for all boundary conditions. There are still small errors in the BEM calculation, which come from different sources, such as:

- Gaussian integration over triangles: components of *H* and *G* matrices are calculated using Gaussian integration over triangles with 16 Gauss points. This approximation causes some errors. Increasing the number of Gauss points increases the accuracy of the calculations. However, even with 48 Gauss points, there are still some very small errors.

- Calculation of new normal vectors: new normal vectors of each face are calculated obtaining the average of new normal vectors of all triangles of that face. The new normal vectors of each triangle, in turn, are calculated based on the new position of three points closest to the vertices of the triangle, assuming the triangle remains planar after deformation. Definitely, this assumption causes some errors due to deformability of the block.

- Round-off errors in calculating coefficient matrices (*H* and *G* matrices)

- Ill-conditioning matrices: matrix *H* is ill-conditioned due to round-off errors (with condition number in order of $10^3 - 10^4$, for the above explained example with 8 to 72 elements per face). The condition number associated with the linear equation gives a bound on how inaccurate the solution will be after approximate solution. Note that this is before the effects of round-off error (in solving the system of equations) are taken into account; conditioning is a property of the matrix, not the

174

algorithm or floating point accuracy of the computer used to solve the corresponding system.

5.2.5.4 Summary and conclusion

An algorithm was proposed to remove the rigid-body motions in the solution of an elastostatic problem discretized by the direct BEM approach. The algorithm fixes one boundary point to prevent rigid-body translations. Finally, the rigid-body rotations are eliminated from the displacement solution. The method was applied to the calculation of the normal stiffness of rock blocks. The algorithm was verified with a simple example for which analytical solution is available based on the theory of elasticity. This example shows the increased accuracy of the proposed algorithm with respect to the approximation proposed by Tonon [1].

5.2.6   Matrix operation

As it was mentioned in Section 2.5, the system of Equations (2.32) is non-symmetric but has small order (i.e. 7), and is solved using LU decomposition (Crout-Banachiewicz) method with partial pivoting [67]. The detection of a critical point in the equilibrium path then comes with no overhead because the minimum diagonal element of matrix $\mathbf{L}$ monitors the smallest eigenvalues of $\mathbf{K}$ [66, 67]. If a diagonal element is equal (or close) to zero, eigenvalues and eigenvectors of the stiffness matrix are calculated to determine limit points and static instability.

As it was mentioned in Section 2.13.2, since $\mathbf{K}$ is a real and non-symmetric (large rotations, applied non-conservative forces such as water pressure) matrix, and $\mathbf{M}$ is real, symmetric, and positive definite, eigenvalues can be either real or complex (Appendix E proves that $\mathbf{M}$ is a real, symmetric, and positive definite matrix). Thus, BS3D should be able to solve generalized eigenvalue problems in which eigenvalues may be real or complex. A subroutine has been developed in this research to solve generalized eigenvalue problems based on the approach proposed by Vandebril *et al* [267]. The problem is to find eigensystem of matrix $\mathbf{K}$ with respect to matrix $\mathbf{M}$ as follows:

$$\mathbf{K} \cdot x = \lambda \cdot \mathbf{M} \cdot x, \qquad\qquad (5.7)$$

where λ is the eigenvalue and x is the eigenvector. The positive definite real matrix $\mathbf{M}$ can be expressed as follows by applying Cholesky factorization [268]:

$$\mathbf{M} = L \cdot L^T \tag{5.8}$$

Thus, the generalized eigenvalue problem in Equation (5.7):

$$L^{-1} \cdot \mathbf{K} \cdot L^{-T} \left(L^T \cdot x \right) = \lambda \cdot \left(L^T \cdot x \right), \tag{5.9}$$

which is the same as determining the eigensystem of matrix $\bar{\mathbf{K}} = L^{-1} \cdot T \cdot L^{-T}$.

In order to calculate the eigenvalues and eigenvectors of matrix $\bar{\mathbf{K}}$ (or any other matrices), BS3D uses a Fortran subroutine developed by Moreau [269] based on algorithm given by Engeln-Mueller and Uhlig [270]. The subroutine can determine both real and complex eigenvalues and corresponding eigenvectors of a square matrix via the QR method [271-273].

In order to calculate $\bar{\mathbf{K}}$, the inverse of matrix L is needed. To determine the inverse of a matrix, BS3D calls a Fortran subroutine developed by Rego [274] based on an algorithm explained by McFarlat [275] and Sniedovich [276].

5.3 VERIFICATION OF BS3D USING DIRECT SHEAR TEST EXAMPLES

5.3.1 Direct shear test up to peak shear strength

An example of monotonic direct shear test up to peak shear strength (with normal stress in the range of 0.625 and 10 MPa) was simulated using BS3D. The problem statement is summarized in Table 5.2 and the block geometry is depicted in Figure 5.6.

In BS3D simulations, after applying the normal stress as an external force in the first stage, the shear stress was applied by adding a longitudinal force in the second stage. However, in BS3D the additional forces are applied to the centroid of the block and, thus, a shear force may cause a moment which does not occur in a well-conducted direct shear test. In order to avoid this kind of unreal moment, in this example, the centroid of the block was artificially moved to the lowermost face of the block.

Since the block has a high Young's modulus (73.64 GPa) in this example, the normal stiffness of the rock block was estimated using Equation (2.43) rather than BEM.

Table 5.2: Statement of the direct shear test problem used to verify BS3D implementation

Parameter	Value
Length of the block (m)	0.2
Width of the block (m)	0.2
Height of the block (m)	0.1
Unit weight of the block (kN/m^2)	25.5
Young's modulus (GPa)	73.64
Poisson ratio	0.23
Initial normal stiffness of fractures (MPa/mm)	8.3
Maximum closure of fractures (mm)	0.4
Lab size joint length (m)	0.1
JRC_0	8
JCS_0 (MPa)	30
Base friction angle, φ_b (º)	20
Number of sensor points per edge, n_{tt}	6

Number of stages:
   • Stage 1: Applying the normal force (step stage = 0.5; λ_{max}=1)
   • Stage 2: Applying the shear force (step stage = 0.01; λ_{max}=2)
	2

Max increment number	500
Max iteration number	50
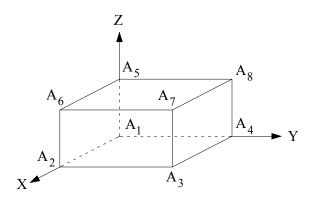
Figure 5.6: Geometry of the cubic block considered in verification example

Figure 5.7 summarizes the results of BS3D simulations for normal stress between 0.625 MPa and 10 MPa. UDEC User manual [277] introduced a table (Table 5.3) for *JRC$_{mobilized}$* which is a little bit different from Barton's table (Table 3.2). In this Section, the direct shear test example was also simulated using the UDEC suggested *JRC$_{mobilized}$* (Table 5.3 has been implemented in BS3D).

(a-1) Stress-displacement curve   (a-2) Normal displacement-shear displacement curve

(a) Normal stress = 0.625 MPa; BS3D analyses

(b-1) Stress-displacement curve   (b-2) Normal displacement-shear displacement curve

(b) Normal stress = 1.25 MPa; BS3D analyses

(c-1) Stress-displacement curve   (c-2) Normal displacement-shear displacement curve

(c) Normal stress = 2.5 MPa; BS3D analyses
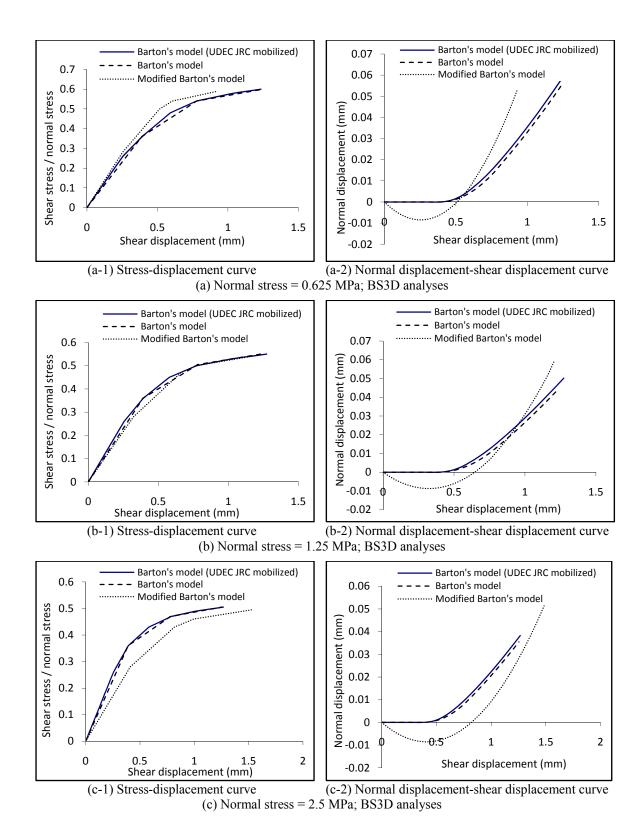
Figure 5.7: Results of BS3D analyses (direct shear test verification example)

(d-1) Stress-displacement curve (d-2) Normal displacement-shear displacement curve
(d) Normal stress = 5 MPa; BS3D analyses

(e-1) Stress-displacement curve (e-2) Normal displacement-shear displacement curve
(e) Normal stress = 10 MPa; BS3D and UDEC analyses
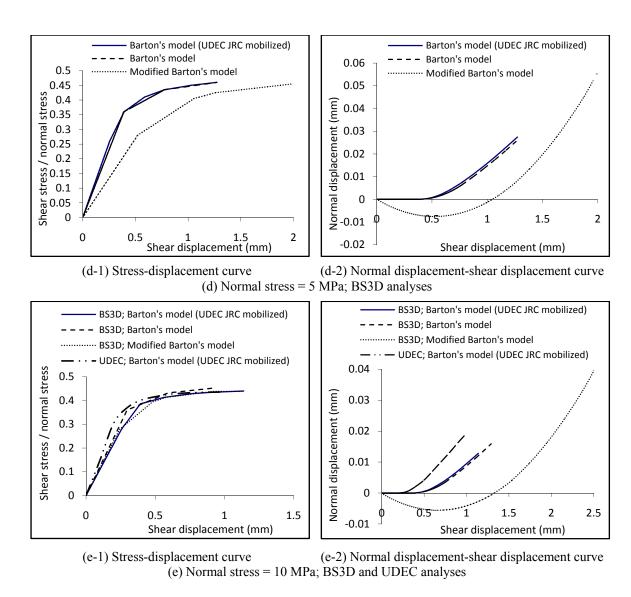
Figure 5.6-Continued: Results of BS3D analyses (direct shear test verification example)

Table 5.3: UDEC Mobilized *JRC* at each shear displacement [277]

$\dfrac{\delta}{\delta_{peak}}$	0	0.2	0.3	0.45	0.6	0.8	1	1.5	2	3	4	6	8	20	40	60	80	100
$\dfrac{JRC_{mobilized}}{JRC_{peak}}$	$-\dfrac{\phi_r}{i}$	$-\dfrac{\phi_r}{4i}$	0	0.5	0.75	0.9	1	0.85	0.75	0.7	0.6	0.55	0.5	0.4	0.3	0.2	0.1	0

In addition, Figure 5.7-(e) shows the results of UDEC analyses (given in UDEC User manual [277] and rerun in this study) for the case of normal stress equal to 10 MPa. In UDEC simulation, after applying the normal stress on the lowermost face ($A_1A_2A_3A_4$), the block was moved with constant horizontal velocity [277] which causes no unreal moment.

The example introduced in this Section is a very simple direct shear test. Thus, the stress-displacement curves and the normal displacement versus shear displacement curves (for all constitutive models) were easily drawn by developing a spreadsheet in Excel. Comparing the curves obtained employing Excel spreadsheet and the results of BS3D simulations, it is found that in all cases the results of BS3D are exactly the same as what models predict. In addition, it can be seen in Figure 5.7 that there are differences between BS3D results obtained using UDEC $JRC_{mobilized}$ model in Table 5.3 and the results of UDEC simulations. However, comparing these results with the curves given by Excel spreadsheet, it is found that BS3D results are exactly the same as what the model in Table 5.3 predicts.
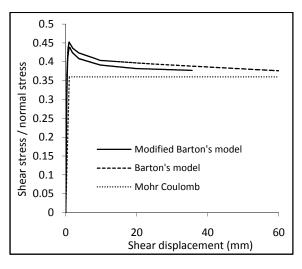
In order to verify the implementation of anisotropic dilatancy, the same model was sheared in eight different shearing directions (every 45˚). Since JRC is the same in all directions, the results should not depend on the direction considered. For all cases, the results were indeed exactly the same as depicted in Figure 5.7.
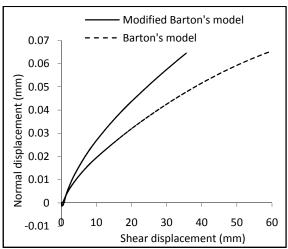
Moreover, in order to verify the implementation of the predictive model introduced in Section 3.4 for anisotropic dilatant behavior of fractures, the same model was sheared in a direction with an angle of θ (the angle between x-axis and the shearing direction depicted in Figure 3.26) equal to 43.85º. JRC_1 and JRC_2 are assumed to be 10 and 5, respectively. Therefore, JRC_θ (JRC along the shearing direction) is estimated using Equations (3.111) and (3.112) to be 10 which is the same as the magnitude of JRC in the above introduced isotropic example. Consequently, the results for anisotropic dilatancy should be the same as those depicted in Figure 5.7 (for isotropic dilatancy), which indeed is the case.

180

5.3.2 Progressive failure

In order to verify BS3D implementation for post-peak behavior of rock fractures, the above example (normal stress equal to 10 MPa) were simulated. At peak shear strength, all sensor points (located at the lowermost face of the block; $A_1A_2A_3A_4$ in Figure 5.7) which were in contact with the block support are sheared off and, thus, the code reports failure. Since the lowermost face of the block ($A_1A_2A_3A_4$) is parallel to x-y plane (see Figure 5.7), after all sensor points are sheared off, the block has no resistance against translation along x- and y-axes and rotation about the z-axis. However, the code reports failure along the given direction of shear force. In order to prevent from failure detection and being able to check the post-peak behavior, three springs were artificially added to the model: two longitudinal springs along x- and y-axes with spring constants of 4000 MN/m and one rotational spring (to prevent rotational failure about the z-axis) with a spring constant of 4000 MN.m/rad.

The results of BS3D simulations in Figure 5.8 were compared with the stress-displacement curves and the normal displacement versus shear displacement curves drawn using Excel spreadsheet. It is found that in all cases the results of BS3D are exactly the same as what models predict.

| (a) Stress-displacement curve | (b) Normal displacement-shear displacement curve |

Figure 5.8: Results of BS3D analyses (direct shear test; progressive failure)

181

This example was simulated by two approaches:

- Applying shear load in one stage
- Applying shear load in two different stages: (1) Stage 1: shear stress of 1 MPa; (2) Stage 2: shear stress of 5 MPa

The results are exactly the same, which verifies that the code works well for multistage analyses.

5.3.3 Rotation about vertical axis

To verify the ability of BS3D in analyzing large rotations, the block in Section 5.3.1 was subjected to a normal stress of 10 MPa and then was applied a torsion of 0.4 MN.m about vertical axis as the shear load. It should be mentioned that, in this case, at peak (rotational) shear strength, all sensor points located at the lowermost face of the block ($A_1A_2A_3A_4$ in Figure 5.7 which were in contact) are sheared off. In order to prevent from failure detection, three springs has been artificially added to the model: two longitudinal springs along x- and y-axes with spring constants of 4000 MN/m and one rotational spring (to prevent rotational failure about the z-axis) with a spring constant of 4000 MN.m/rad. Since the block has a high Young's modulus (73.64 GPa) in this example, the normal stiffness of the rock block was estimated using Equation (2.43) rather than BEM. The result is depicted in Figure 5.9.
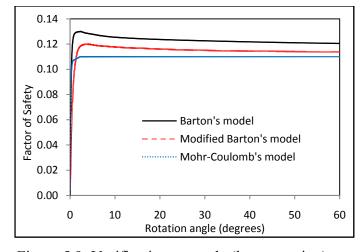
Figure 5.9: Verification example (large rotation)

Considering dilatant behavior of the fracture and different moment arms for fracture shear resistant, there is no simple method to check the results predicted using BS3D. However, the following points are notable:

- The block shape after a large rotation of 60˚ does not change (see Table 5.4 for the coordinates of block vertices before and after 60˚ rotation). However, using DDA, the block expands when simulating problems involving large rotations [278-285].

Table 5.4: Coordinates or the block edge before and after 60º rotation (BS3D analysis of rotation about vertical axis)

	Before rotation	After 60º rotation
Coordinates of the block vertices	$A_1 = [0 \quad 0 \quad 0]^T$ $A_2 = [0.2 \quad 0 \quad 0]^T$ $A_3 = [0.2 \quad 0.2 \quad 0]^T$ $A_4 = [0 \quad 0.2 \quad 0]^T$ $A_5 = [0 \quad 0 \quad 0.1]^T$ $A_6 = [0.2 \quad 0 \quad 0.1]^T$ $A_7 = [0.2 \quad 0.2 \quad 0.1]^T$ $A_8 = [0 \quad 0.2 \quad 0.1]^T$	$A_1 = [0.14 \quad -0.04 \quad 0]^T$ $A_2 = [0.24 \quad 0.14 \quad 0]^T$ $A_3 = [0.06 \quad 0.24 \quad 0]^T$ $A_4 = [-0.04 \quad 0.06 \quad 0]^T$ $A_5 = [0.14 \quad -0.04 \quad 0.1]^T$ $A_6 = [0.24 \quad 0.14 \quad 1]^T$ $A_7 = [0.06 \quad 0.24 \quad 0.1]^T$ $A_8 = [-0.04 \quad 0.06 \quad 0.1]^T$

- The rotation matrices (Equation (2.1)), which map a vector attached to the rigid body from the base configuration to current configuration are orthogonal throughout the simulation as shown in Table 5.5 at different angles.

Table 5.5: Examples of rotation matrix (BS3D analysis of rotation about vertical axis)

Rotation angle	30º	45º	60º
Rotation matrix	$\begin{bmatrix} \frac{\sqrt{3}}{2} & -\frac{1}{2} & 0 \\ \frac{1}{2} & \frac{\sqrt{3}}{2} & 0 \\ 0 & 0 & 1 \end{bmatrix}$	$\begin{bmatrix} \frac{\sqrt{2}}{2} & -\frac{\sqrt{2}}{2} & 0 \\ \frac{\sqrt{2}}{2} & \frac{\sqrt{2}}{2} & 0 \\ 0 & 0 & 1 \end{bmatrix}$	$\begin{bmatrix} \frac{1}{2} & -\frac{\sqrt{3}}{2} & 0 \\ \frac{\sqrt{3}}{2} & \frac{1}{2} & 0 \\ 0 & 0 & 1 \end{bmatrix}$

5.4 IN SITU STRESSES

5.4.1 Implementation and verification

In this dissertation, *in situ* stress has been implemented from scratch (in the same approach that was explained in Section 2.12) because it was not included in Tonon's Mathematica code. In order to verify implementation of *in situ* stresses, an example of Cauchy tetrahedron (Figure 5.10; $\hat{n} = \dfrac{\sqrt{3}}{3} \cdot \begin{bmatrix} 1 & 1 & 1 \end{bmatrix}^T$) with the following *in situ* stresses is simulated using BS3D:

1) *In situ* principal stresses are assumed to act vertically and horizontally with lateral pressure coefficient equal to one (hydrostatic state of stress). The vertical (horizontal) stress is equal to 1.5 MPa.

2) *In situ* principal stresses are assumed to act vertically and horizontally with lateral pressure coefficient equal to two. The vertical and horizontal stresses are equal to 1.5 MPa and 3 MPa, respectively.

3) *In situ* stresses are given by the following tensor: $\sigma = \begin{bmatrix} 0.5 & 0.1 & 0.4 \\ 0.1 & 1 & -0.3 \\ 0.4 & -0.3 & 3 \end{bmatrix}$
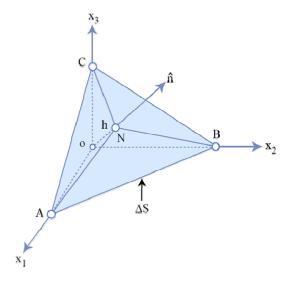
Figure 5.10: Cauchy tetrahedron

184

Normal and shear stresses on all four faces are calculated using BS3D and the results are checked against the analytical solution. The maximum error is about 0.1% which comes from round-off error in floating point arithmetic.

5.4.2 *In situ* stresses around a circular tunnel

In order to implement the effect of a circular tunnel on the state of stresses in the surrounding rock mass, formulation of stress distribution around a circular hole of radius *a* in a 3D stress field (consider a Continuum Homogenous Isotropic Linearly Elastic, CHILE, medium) is used (Figure 5.11). This formulation is based on generalized (or complete) plain strain condition, in which all components of stress, strain, displacement, body and surface forces are to be identical in all planes perpendicular to the hole axis [286-290]:

$$\frac{\partial U}{\partial Z} = \frac{\partial V}{\partial Z} = \frac{\partial W}{\partial Z} = 0, \tag{5.10}$$

where *U*, *V*, and *W* are displacements (of any point of the medium) along the *x*, *y*, and *z* axes.
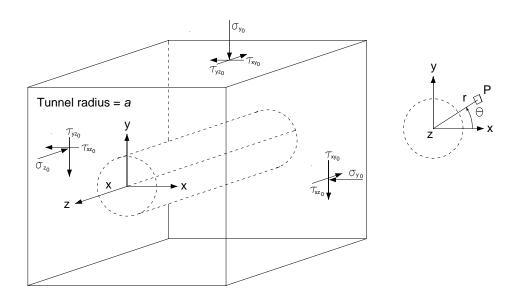
Figure 5.11: Stress distribution around circular tunnel (state of stresses)

Effect of distance from excavation face, d, can be simulated using the following ratio [291]:

$$\lambda = \frac{U}{U_\infty} = 0.27 + 0.71\left(1 - \exp\left(-1.5\left(\frac{d}{a}\right)\right)\right) \tag{5.11}$$

Different components of stresses (in the polar reference system of $r\theta z$) at point P (depicted in Figure 5.11) can be calculated using the following equations [287]:

$$\sigma_r = \left(1 - \lambda\frac{a^2}{r^2}\right)\left(\frac{\sigma_{x_0} + \sigma_{y_0}}{2}\right) + \left(1 + \lambda\frac{3a^4}{r^4} - \lambda\frac{4a^2}{r^2}\right)\left(\frac{\sigma_{x_0} - \sigma_{y_0}}{2}\right)\left(\cos 2\theta + \tau_{xy_0}\sin 2\theta\right) \tag{5.12}$$

$$\sigma_\theta = \left(1 + \lambda\frac{a^2}{r^2}\right)\left(\frac{\sigma_{x_0} + \sigma_{y_0}}{2}\right) - \left(1 + \lambda\frac{3a^4}{r^4}\right)\left(\frac{\sigma_{x_0} - \sigma_{y_0}}{2}\right)\left(\cos 2\theta + \tau_{xy_0}\sin 2\theta\right) \tag{5.13}$$

$$\sigma_z = \sigma_{z_0} - 4\upsilon\lambda\frac{a^2}{r^2}\left(\frac{\sigma_{x_0} - \sigma_{y_0}}{2}\right)\left(\cos 2\theta + \tau_{xy_0}\sin 2\theta\right) \tag{5.14}$$

$$\tau_{r\theta} = -\left(1 - \lambda\frac{3a^4}{r^4} + \lambda\frac{2a^2}{r^2}\right)\left(\frac{\sigma_{x_0} - \sigma_{y_0}}{2}\right)\left(\sin 2\theta + \tau_{xy_0}\cos 2\theta\right) \tag{5.15}$$

$$\tau_{rz} = -\left(1 - \lambda\frac{a^2}{r^2}\right)\left(\tau_{yz_0}\sin\theta + \tau_{xy_0}\cos\theta\right) \tag{5.16}$$

$$\tau_{\theta z} = \left(1 + \lambda\frac{a^2}{r^2}\right)\left(\tau_{yz_0}\cos\theta - \tau_{xy_0}\sin\theta\right) \tag{5.17}$$

BS3D converts the state of stresses from the polar reference system (calculated using Equations (5.12) through (5.17)) to the global reference system (see Figure 5.11 for definition of reference systems). Once the stress tensor in the global reference system, σ, is known, the normal and shear stresses applied to each face of the block are determined using the approach described in detail in Section 2.12

The above mentioned analytical method has been implemented in BS3D. If user wishes to consider the effect of excavation (a circular tunnel) on *in situ* stresses, the choice should be indicated in the main input file, "*input.dat*". In this case, BS3D looks for another input file, "*tunnel_stress.dat*", which includes values for the parameters summarized in Table 5.6 (see Appendix B for an example of the input files).

186

Table 5.6: Parameters required to consider the effect of circular tunnel on *in situ* stresses

Description		Symbols
The origin of the global reference system should be on the tunnel axis		
Tunnel diameter		*2a*
Unit vector along tunnel axis in global reference system		*Tunnel$_{axis}$*
Distance of excavation face from the origin		*d*
Tunnel reference system is the same as principal stress directions:	Depth of the tunnel axis	*Depth*
	Unit weight of the rock mass	*γ*
	Lateral pressure coefficient	K_0
Tunnel reference system is not the same as principal stress direction:	Stress tensor: $(\sigma_{xx}, \sigma_{yy}, \sigma_{zz}, \tau_{xy}, \tau_{xz}, \tau_{yz})$	

It should be noted that verification of commercial software (e.g.: UDEC) is conducted by comparing numerical results with those obtained using the above mentioned analytical method. In this research, the implementation has been checked by comparing the results of BS3D analyses with hand calculations.

5.5   VERIFICATION OF BEM AND *IN SITU* STRESS IMPLEMENTATIONS

In order to verify the implementation of BEM and in situ stresses, an example is introduced here. A cubic block with edge length of 1 m is shown in Figure 5.12-(a). The mechanical properties of intact rock, rock mass, and fractures are summarized in Table 5.7. The block is first constrained along all its six faces while it is subjected to gravity and hydrostatic in situ stress of 0.2 MPa. BS3D analyses have been performed using three constitutive models for fractures (Mohr-Coulomb's model, Barton's Model, and Modified Barton's model) and employing both Equation 2.43 and BEM (Section 5.2.5) to determine the normal stiffness of rock fractures. The calculated safety factors versus the absolute vertical displacement of the block are depicted in Figure 5.12-(b) through (d).

The safety factors and the vertical displacements of the block at failure are exactly the same as what models predict (calculated using Excel spreadsheet), which verify the implementation of *in situ* stresses (and constitutive models). In addition, it can be seen in Figure 5.12 that the results obtained from Equation (2.43) and BEM approach are the same, which is to be expected because:

1- The block is not as deformable as fractures and rock mass. Thus, the deformability of the block should not be too effective and the method of predicting the normal stiffness of the block should not affect the results.

2- It was shown in Section 5.2.5.3 that although Equation (2.43) may lead to large errors in general, it works very well for the case of a block loaded in two directions. The block is exactly loaded in two directions here. Thus, the approximation has negligible errors in this case.

(a) Geometry of the cubic rock block considered in verification example

(b) Results of BS3D analyses using Mohr-Coulomb's model

(c) Results of BS3D analyses using Barton's model

(d) Results of BS3D analyses using Modified Barton's model
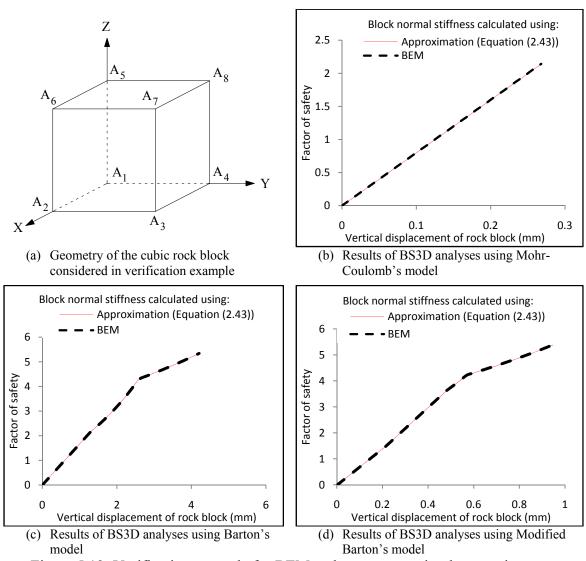
Figure 5.12: Verification example for BEM and *in situ* stress implementations

Table 5.7: Mechanical properties of intact rock, rock mass, and fractures (verification example; *in situ* stresses and BEM implementations)

Parameter	Value
Unit weight of the block (kN/m^2)	30
Young's modulus (GPa) of rock block	30
Poisson ratio of rock block	0.3
Young's modulus (GPa) of rock mass	7
Poisson ratio of rock mass	0.2
Initial normal stiffness of fractures (GPa)	10
Maximum closure of fractures (mm)	0.1
Lab size joint length (m)	1
JRC_0	10
JCS_0 (MPa)	70
Base friction angle, φ_b (°)	30

5.6 WATER PRESSURE

Hydrostatic water pressure is implemented in BS3D in the same approach that was explained in Section 2.9. The implementation has been verified using the example of the direct shear test introduced in Section 5.3 (Figure 5.6); the normal and shear forces are now applied by using hydrostatic water pressure instead of additional forces:

- Applying normal and shear forces as additional forces:
  - Stage 1: a normal stress of 1 MPa was applied by considering a 0.04 MN additional force in the negative vertical direction.
  - Stage 2: a shear stress of 1 MPa was applied by considering a 0.04 MN additional foce in horizontal direction.
- Applying normal and shear forces using hydrostatic water pressure:
  - Stage 1: a normal stress of 1 MPa was applied by considering the hydrostatic water pressure caused by a column of water with a height of 101.94 m on the uppermost face of the block.
  - Stage 2: a shear stress of 1 MPa was applied by considering the hydrostatic water pressure caused by a column of water with a constant height of 101.94 m on one of the vertical faces of the block.

It is expected that the results obtained using both methods of applying normal and shear stresses be exactly the same (which was indeed found in BS3D results). It should be mentioned that these results are different from the results obtained in Section 5.3 for the case of normal stress of 1 MPa because, in Section 5.3, the centroid of the block was artificially moved to the lowermost face of the block ($A_1A_2A_3A_4$ in Figure 5.7) to prevent any moment, which was not done in this Section. Since the purpose of this Section is to verify the hydrostatic water pressure implementation, this moment was counterbalanced by applying additional forces. Although the simulated example is not the same as a real direct shear test, it works for verifying the implementation of the hydrostatic water pressure implementation.

Hydrodynamic water pressures caused by high-velocity jet impacts are also incorporated in BS3D using the method described in detail in Chapter 8. In the cases that user wants to consider the hydrodynamic pressure caused by high-velocity jet impact at the bottom of plunge pools, another input file, "*water_pressure.dat*", is read by BS3D. The input variables of "*water_pressure.dat*" are given in Table 5.8 (see Appendix B for an example of the input files).

Table 5.8: Input variables required for considering hydrodynamic water pressure caused by high-velocity jet impact (*water_pressure.dat*)

Description	Symbols
Depth of water in the pool (m)	*depth*
Distance to the jet center line (m)	*r*
Jet diameter at pool surface (m)	D_j
Jet is circular or rectangular	
Type of turbulence: rough, moderate, or smooth	
Jet length (m)	*L*
Jet velocity (m/s)	V_j

5.7 SUMMARY

In this Chapter, algorithms and formulations implemented in BS3D but not explained in other parts of this dissertation were briefly described. List of variables read by BS3D to define the stability problem of a single rock block were introduced (see

Appendix B for examples of input files). An algorithm was proposed to remove the rigid-body motions in the solution of an elastostatic problem discretized by the direct BEM approach. The method was applied to the calculation of the normal stiffness of rock blocks and verified with a simple example.

BS3D implementations (including fracture constitutive models, *in situ* stresses, BEM, etc.) were verified using examples of direct shear test and Cauchy tetrahedron.

CHAPTER 6: VALIDATION OF GENERAL SINGLE ROCK BLOCK STABILITY ANALYSIS (BS3D)

6.1 INTRODUCTION

In computational mechanics, verification and validation have received increasing attention because critical decisions are made based on the results of computational means [292-297]. If verification is the process of determining that a model implementation accurately represents the developer's conceptual description of the model and the solution to the model, validation is the process of determining the degree to which a model is an accurate representation of the real world from the perspective of the intended uses of the model. The problems entailed in a validation process are exacerbated in rock engineering, where it is very difficult, or even impossible to test a rock mass at a convenient and representative scale.

Rock engineers have attacked this issue by resorting to two validation methods, namely case histories, and model tests. In order to validate BS3D with regard to one of the most common failure modes, i.e. wedge failures, Section 6.2 uses the results from physical model tests reported by Yeung *et al.* [18] as well as two case histories of slope failures occurred in Turkey and reported by Kumsar *et al.* [26].

6.2 WEDGE FAILURE

6.2.1 Physical models used for validation

Physical models were constructed and tested by Yeung *et al.* [18] in order to validate Block Theory and 3D-DDA as wedge stability analysis methods. In this Section, the results of their study on tetrahedral rock blocks are used to validate BS3D [1] for wedge failure.

As shown in Figure 6.1, a typical model considered by Yeung *et al.* [18] consisted of a plaster wedge block placed on a supporting block, which contained the ''mould'' of the wedge block. The plaster supporting block was attached to a wood base block, which in its turn was attached to a tilt table inclined at an angle α with the horizontal direction.

The wedge block could move freely without being obstructed by the tilt table. The orientation of the model with respect to the dip direction of the tilt table was quantified by angle β between the table dip direction and the orthogonal to the wedge intersection vector. In each test, a model was fixed in the desired position corresponding to the chosen α and β values; the wedge block was held in place and then released.

Yeung *et al.* [18] considered two different models. The dimensions of the two wedge blocks, named Block 1 and block 2, are shown in Figure 6.2. The angle α varied from 0° to 90° in 10° increments while the angle β was equal to 60°, 80°, and 240° for Block 1 and equal to 60°, 80°, and 320° for Block 2.
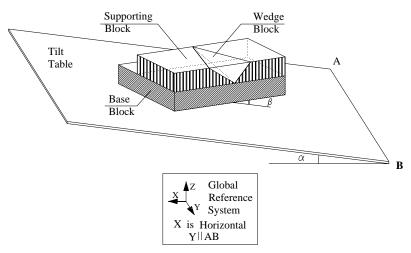
Figure 6.1: Physical model [298].

Block-1　　　　　　　Block-2
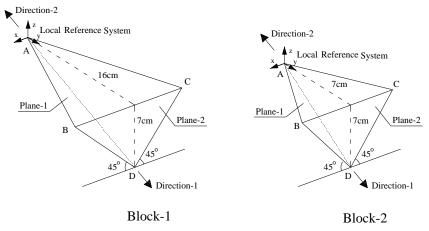
Figure 6.2: Wedge Blocks [298].

193

The coordinates of the block vertices in each of these cases are summarized in Tables 6.1 and 6.2 (in the global reference system, which is illustrated in Figure 6.1).

Table 6.1: Coordinates of the block vertices in the global reference system - Block 1 (see Figures 6.1 and 6.2)

β	α	Block's vertices			
		A	B	C	D
60	0	(13.9, 8.0, 0.0)	(3.5, 22.1, 0.0)	(-3.5, 9.9, 0.0)	(0.0, 16.0, -7.0)
60	10	(13.6, 8.0, 2.4)	(3.4, 22.1, 0.6)	(-3.4, 9.9, -0.6)	(1.2, 16.0, -6.9)
60	18.25	(13.2, 8.0, 4.3)	(3.3, 22.1, 1.1)	(-3.3, 9.9, -1.1)	(2.2, 16.0, -6.6)
60	20	(13.0, 8.0, 4.7)	(3.3, 22.1, 1.2)	(-3.3, 9.9, -1.2)	(2.4, 16.0, -6.6)
60	30	(12.0, 8.0, 6.9)	(3.0, 22.1, 1.8)	(-3.0, 9.9, -1.8)	(3.5, 16.0, -6.1)
60	40	(10.6, 8.0, 8.9)	(2.7, 22.1, 2.2)	(-2.7, 9.9, -2.2)	(4.5, 16.0, -5.4)
60	50	(8.9, 8.0, 10.6)	(2.2, 22.1, 2.7)	(-2.2, 9.9, -2.7)	(5.4, 16.0, -4.5)
60	60	(6.9, 8.0, 12.0)	(1.8, 22.1, 3.0)	(-1.8, 9.9, -3.0)	(6.1, 16.0, -3.5)
60	70	(4.7, 8.0, 13.0)	(1.2, 22.1, 3.3)	(-1.2, 9.9, -3.3)	(6.6, 16.0, -2.4)
60	80	(2.4, 8.0, 13.6)	(0.6, 22.1, 3.4)	(-0.6, 9.9, -3.4)	(6.9, 16.0, -1.2)
60	90	(0.0, 8.0, 13.9)	(0.0, 22.1, 3.5)	(0.0, 9.9, -3.5)	(7.0, 16.0, 0.0)
80	0	(15.8, 13.2, 0.0)	(1.2, 22.9, 0.0)	(-1.2, 9.1, 0.0)	(0.0, 16.0, -7.0)
80	10	(15.5, 13.2, 2.7)	(1.2, 22.9, 0.2)	(-1.2, 9.1, -0.2)	(1.2, 16.0, -6.9)
80	17.17	(15.1, 13.2, 4.7)	(1.2, 22.9, 0.4)	(-1.2, 9.1, -0.4)	(2.1, 16.0, -6.7)
80	20	(14.8, 13.2, 5.4)	(1.1, 22.9, 0.4)	(-1.1, 9.1, -0.4)	(2.4, 16.0, -6.6)
80	30	(13.6, 13.2, 7.9)	(1.1, 22.9, 0.6)	(-1.1, 9.1, -0.6)	(3.5, 16.0, -6.1)
80	40	(12.1, 13.2, 10.1)	(0.9, 22.9, 0.8)	(-0.9, 9.1, -0.7)	(4.5, 16.0, -5.4)
80	50	(10.1, 13.2,12.1)	(0.8, 22.9, 0.9)	(-0.8, 9.1, -0.9)	(5.4, 16.0, -4.5)
80	60	(7.9, 13.2, 13.6)	(0.6, 22.9, 1.1)	(-0.6, 9.1, -1.1)	(6.1, 16.0, -3.5)
80	70	(5.4, 13.2, 14.8)	(0.4, 22.9, 1.1)	(-0.4, 9.1, -1.1)	(6.6, 16.0, -2.4)
80	80	(2.7, 13.2, 15.5)	(0.2, 22.9, 1.2)	(-0.2, 9.1, -1.2)	(6.9, 16.0, -1.2)
80	90	(0.0, 13.2, 15.8)	(0.0, 22.9, 1.2)	(0.0, 9.1, -1.2)	(7.0, 16.0, 0.0)
240	0	(-13.7, 24.0, 0.0)	(-3.5, 9.9, 0.0)	(3.5, 22.1, 0.0)	(0.0, 16.0, -7.0)
240	10	(-13.6, 24.0, -2.4)	(-3.4, 9.9, -0.6)	(3.4, 22.1, 0.6)	(1.2, 16.0, -6.9)
240	20	(-13.0, 24.0, -4.7)	(-3.3, 9.9, -1.2)	(3.3, 22.1, 1.2)	(2.4, 16.0, -6.6)
240	30	(-12.0, 24.0, -6.9)	(-3.0, 9.9, -1.8)	(3.0, 22.1, 1.8)	(3.5, 16.0, -6.1)
240	40	(-10.6, 24.0, -8.9)	(-2.7, 9.9, -2.2)	(2.7, 22.1, 2.2)	(4.5, 16.0, -5.4)
240	50	(-8.9, 24.0, -10.6)	(-2.2, 9.9, -2.7)	(2.2, 22.1, 2.7)	(5.4, 16.0, -4.5)
240	60	(-6.9, 24.0, -12.0)	(-1.8, 9.9, -3.0)	(1.8, 22.1, 3.0)	(6.1, 16.0, -3.5)
240	68.1	(-5.2, 24.0, -12.9)	(-1.3, 9.9, -3.2)	(1.3, 22.1, 3.2)	(6.5, 16.0, -2.6)
240	70	(-4.7, 24.0, -13.0)	(-1.2, 9.9, -3.3)	(1.2, 22.1, 3.3)	(6.6, 16.0, -2.4)
240	80	(-2.4, 24.0, -13.6)	(-0.6, 9.9, -3.4)	(0.6, 22.1, 3.4)	(6.9, 16.0, -1.2)
240	90	(0.0, 24.0, -13.9)	(0.0, 9.9, -3.5)	(0.0, 22.1, 3.5)	(7.0, 16.0, 0.0)

Table 6.2: Coordinates of the block vertices in the global reference system - Block 2 (see Figures 6.1 and 6.2)

β	α	Block's vertices			
		A	B	C	D
60	0	(6.1, 3.5, 0.0)	(3.5, 13.1, 0.0)	(-3.5, 0.9, 0.0)	(0.0, 7.0, -7.0)
60	10	(6.0, 3.5, 1.1)	(3.4, 13.1, 0.6)	(-3.4, 0.9, -0.6)	(1.2, 7.0, -6.9)
60	20	(5.7, 3.5, 2.1)	(3.3, 13.1, 1.2)	(-3.3, 0.9, -1.2)	(2.4, 7.0, -6.6)
60	30	(5.3, 3.5, 3.0)	(3.0, 13.1, 1.8)	(-3.0, 0.9, -1.8)	(3.5, 7.0, -6.1)
60	40	(4.6, 3.5, 3.9)	(2.7, 13.1, 2.2)	(-2.7, 0.9, -2.2)	(4.5, 7.0, -5.4)
60	50	(3.9, 3.5, 4.6)	(2.2, 13.1, 2.7)	(-2.2, 0.9, -2.7)	(5.4, 7.0, -4.5)
60	60	(3.0, 3.5, 5.3)	(1.8, 13.1, 3.0)	(-1.8, 0.9, -3.0)	(6.1, 7.0, -3.5)
60	70	(2.1, 3.5, 5.7)	(1.2, 13.1, 3.3)	(-1.2, 0.9, -3.3)	(6.6, 7.0, -2.4)
60	80	(1.1, 3.5, 6.0)	(0.6, 13.1, 3.4)	(-0.6, 0.9, -3.4)	(6.9, 7.0, -1.2)
60	90	(0.0, 3.5, 6.1)	(0.0, 13.1, 3.5)	(0.0, 0.9, -3.5)	(7.0, 7.0, 0.0)
80	0	(6.9, 5.8, 0.0)	(1.2, 13.9, 0.0)	(-1.2, 0.1, 0.0)	(0.0, 7.0, -7.0)
80	10	(6.8, 5.8, 1.2)	(1.2, 13.9, 0.2)	(-1.2, 0.1, -0.2)	(1.2, 7.0, -6.9)
80	20	(6.5, 5.8, 2.4)	(1.1, 13.9, 0.4)	(-1.1, 0.1, -0.4)	(2.4, 7.0, -6.6)
80	30	(6.0, 5.8, 3.4)	(1.1, 13.9, 0.6)	(-1.1, 0.1, -0.6)	(3.5, 7.0, -6.1)
80	40	(5.3, 5.8, 4.4)	(0.9, 13.9, 0.8)	(-0.9, 0.1, -0.8)	(4.5, 7.0, -5.4)
80	50	(4.4, 5.8, 5.3)	(0.8, 13.9, 0.9)	(-0.8, 0.1, -0.9)	(5.4, 7.0, -4.5)
80	60	(3.4, 5.8, 6.0)	(0.6, 13.9, 1.1)	(-0.6, 0.1, -1.1)	(6.1, 7.0, -3.5)
80	70	(2.4, 5.8, 6.5)	(0.4, 13.9, 1.1)	(-0.4, 0.1, -1.1)	(6.6, 7.0, -2.4)
80	80	(1.2, 5.8, 6.8)	(0.2, 13.9, 1.2)	(-0.2, 0.1, -1.2)	(6.9, 7.0, -1.2)
80	90	(0.0, 5.8, 6.9)	(0.0, 13.9, 1.2)	(0.0, 0.1, -1.2)	(7.0, 7.0, 0.0)
320	0	(-4.5, 1.6, 0.0)	(5.4, 2.5, 0.0)	(-5.4, 11.5, 0.0)	(0.0, 7.0, -7.0)
320	10	(-4.4, 1.6, -0.8)	(5.3, 2.5, 0.9)	(-5.3, 11.5, -0.9)	(1.2, 7.0, -6.9)
320	10.25	(-4.4, 1.6, -0.8)	(5.3, 2.5, 1.0)	(-5.3, 11.5, -1.0)	(1.2, 7.0, -6.9)
320	20	(-4.2, 1.6, -1.5)	(5.0, 2.5, 1.8)	(-5.0, 11.5, -1.8)	(2.4, 7.0, -6.6)
320	30	(-3.9, 1.6, -2.2)	(4.6, 2.5, 2.7)	(-4.6, 11.5, -2.7)	(3.5, 7.0, -6.1)
320	40	(-3.4, 1.6, -2.9)	(4.1, 2.5, 3.4)	(-4.1, 11.5, -3.4)	(4.5, 7.0, -5.4)
320	50	(-2.9, 1.6, -3.4)	(3.4, 2.5, 4.1)	(-3.4, 11.5, -4.1)	(5.4, 7.0, -4.5)
320	60	(-2.4, 1.6, -3.9)	(2.7, 2.5, 4.6)	(-2.7, 11.5, -4.6)	(6.1, 7.0, -3.5)
320	70	(-1.5, 1.6, -4.2)	(1.8, 2.5, 5.0)	(-1.8, 11.5, -5.0)	(6.6, 7.0, -2.4)
320	80	(-0.8, 1.6, -4.4)	(0.9, 2.5, 5.3)	(-0.9, 11.5, -5.3)	(6.9, 7.0, -1.2)
320	85	(-0.4, 1.6, -4.5)	(0.5, 2.5, 5.3)	(-0.5, 11.5, -5.3)	(7.0, 7.0, -0.6)
320	90	(0.0, 1.6, -4.5)	(0.0, 2.5, 5.4)	(0.0, 11.5, -5.4)	(7.0, 7.0, 0.0)

Figure 6.2 shows the possible wedge sliding directions (Direction 1 or Direction 2) and describes the local reference system. Each wedge block was bounded by two joint planes (Plane 1 and Plane 2) and two free surfaces, one horizontal and one vertical for α=0). The average friction angle determined by Yeung *et al.* [18] out of 10 direct shear

test measurements was equal to 32.5°; the density of the blocks was equal to 1400 kg/m³; the Young's modulus was equal to 1×10^7 N/m²; and the Poisson's ratio was equal to 0.49 [18]. BS3D implements both Mohr-Coulomb and Barton [21, 22, 92, 132] failure criteria. Since BS3D takes joint deformability into account using Goodman [78] and Barton-Bandis models [79, 80, 299] (or Modified Barton's model, developed in Chapter 3), it also requires additional input data, such as initial stiffness and maximum closure of the discontinuities. The appropriate magnitude of these two parameters were assumed in this study as described below because they were not available in Ref. [18].

The constitutive model for the rock joints used in the BS3D analysis was Mohr-Coulomb failure criterion with no dilatancy, because this is what is assumed in Block Theory and 3D DDA and because only the friction angle was reported by Yeung *et al.* [18]. In addition, the shear stiffness was assumed to be proportional to (one tenth of) the normal stiffness. Thus, the allocated values of *JCS* and *JRC* have no effect on the results; they are effective only when Barton-Bandis model is used for discontinuities.

Appropriate ranges for the initial stiffness and the maximum closure of joints were determined based on a literature review and a parametric study carried out to find the effect of these parameters on the stability of a wedge. A stable case, Block 1 with β=60° and α=10°, and an unstable case, Block 1 with β=60° and α=30°, were considered. The initial stiffness was changed from 100 to 10,000 MPa/m and the maximum closure was changed from 0.01 to 0.5 mm, considering their possible ranges for different types of rocks as reported by Bandis *et al.* [80]. It was found that in these ranges the failure modes are the same as in the physical model and the safety factors are the same as calculated using limiting equilibrium analysis in Block Theory. Thus, changing the initial stiffness and the maximum closure has no effect on the results; because the stress level is low as compared to the initial stiffness range, the normal stiffness is very close to the initial normal stiffness. The investigation was continued to find when these parameters have an effect on the results. It was found that for a very low value of initial stiffness (40 MPa/m) and the maximum closure of 0.1 mm, the results changed (The safety factor of Block 1 with β=60° and α=10° decreased from 1.4 to 0.9 by decreasing the initial stiffness from

100 MPa/m to 40 MPa/m and the safety factor of Block 1 with β=60° and α=30° decreased from 0.7 to 0.4 by decreasing the initial stiffness from 100 MPa/m to 40 MPa/m). Based on the normal stiffness values reported by Bandis *et al.* [80], Kulhawy and Fred [160], Panet and Guenot [291], and Rosso [300], the initial stiffness of the discontinuities was assumed to be equal to 300 MPa/m with a maximum closure of 0.1mm, which are reasonable values for the plaster used to make the physical models.

6.2.2 VALIDATION USING PHYSICAL MODELS

Tables 6.3 and 6.4 give the results obtained from the physical model tests (failure modes) [18], Block Theory analyses based on limiting equilibrium (factors of safety and modes of failure), and BS3D (safety factors, static and dynamic failure modes). Block Theory analyses were independently carried out by the author and the results were found to be in agreement with those reported in Yeung *et al.* [18]. In Tables 6.3 and 6.4, wedge failures are indicated as "Wedge-i" and plane failures are indicated as "Plane-i" ", where "i" indicates the plane number (either 1 or 2 as indicated in Figures 6.2). Dynamic failure modes are given using the block centroid's displacements and the rotation vectors about the centroid.

It should be considered that static and dynamic failure modes can be different from each other. In order to illustrate the static and dynamic failure modes, the base configuration versus static and dynamic failure modes of Block 1 when β=60° and α=30° are depicted in Figure 6.3. It is shown that the static failure mode is wedge sliding in Direction 1, for which the displacement vector in the global reference system is (-0.49, 0.46, -0.74, 0, 0, 0)^T, while the dynamic failure mode is roto-translational sliding with displacement vector equal to (-0.75, 0.5, -0.43, 0.5, 0.87, 0.04)^T in the global reference system. In the physical model tests, four different types of failure modes were observed by Yeung *et al.* [18]: sliding on a single plane (plane 1 or 2), sliding on two planes simultaneously (wedge sliding in direction 1 or 2), free falling, and torsional sliding.

Table 6.3: Results from physical models [18], Block Theory, and BS3D analyses for Block 1

β	α	Physical Model Failure Mode	Block Theory F.S.	Block Theory Failure Mode	BS3D F.S.	BS3D Static Failure Mode	Dynamic Failure Mode Centroid dir. of Displacement Global	Local	Vector about which rotation occur Global	Local
60	0	Stable	1.98	Stable	2.0	Stable	-	-	-	-
60	10	Stable	1.37	Stable	1.4	Stable	-	-	-	-
60	18.3	Wedge-1	1.04	Wedge-1	1.0	Wedge-1	(-0.82, 0.5, -0.27)	(0, 1, 0)	(0.46, 0.85, 0.24)	(1, 0, 0)
60	20	Wedge-1	0.99	Wedge-1	1.0	Wedge-1	(-0.81, 0.5, -0.3)	(0, 1, 0)	(0.45, 0.85, 0.26)	(1, 0, 0)
60	30	Wedge-1	0.72	Wedge-1	0.7	Wedge-1	(-0.75, 0.5, -0.43)	(0, 1, 0)	(0.5, 0.87, 0.04)	(0.98, 0.04, -0.21)
60	40	Wedge-1	0.51	Wedge-1	0.5	Wedge-1	(-0.75, 0.5, -0.43)	(0, 1, 0)	(0.37, 0.86, 0.35)	(1, 0 , 0)
60	50	Plane-2	0.36	Plane-2	0.4	Wedge-1	(-0.75, 0.5, -0.43)	(0, 1, 0)	(0.22, 0.84, 0.5)	(0.99, -0.03, 0.15)
60	60	Plane-2	0.28	Plane-2	0.3	Plane-2	(-0.75, 0.5, -0.43)	(0, 1, 0)	(0.21, 0.86, 0.47)	(1, 0 , 0)
60	70	Plane-2	0.21	Plane-2	0.2	Plane-2	(-0.75, 0.5, -0.43)	(0, 1, 0)	(0.02, 0.94, 0.33)	(0.98, 0.2, 0.09)
60	80	Plane-2	0.13	Plane-2	0.1	Plane-2	(-0.75, 0.5, -0.43)	(0, 0.99, 0.11)	(-0.63, 0.57, -0.54)	(0.17, 0.83, 0.52)
60	90	Plane-2	0.05	Plane-2	0.1	Plane-2	(-0.75, 0.5, -0.43)	(0, 0.96, 0.28)	(-0.57, 0.26, -0.78)	(-0.16, 0.81, 0.57)
-	0	Stable	1.97	Stable	2.0	Stable		-	-	-
-	10	Stable	1.31	Stable	1.3	Stable		-	-	-
80	17.17	Wedge-1	1.00	Wedge-1	1.0	Wedge-1	(-0.94, 0.17, -0.29)	(0, 1, 0)	(0.16, 0.98, 0.08)	(1, 0, 0)
80	20	Wedge-1	0.92	Wedge-1	0.9	Wedge-1	(-0.93, 0.17, -0.34)	(0, 1, 0)	(0.16, 0.98, 0.09)	(1, 0, 0)
80	30	Wedge-1	0.64	Wedge-1	0.6	Wedge-1	(-0.85, 0.17, -0.49)	(0, 1, 0)	(0.17, 0.99, 0.04)	(1, 0, 0)
80	40	Wedge-1	0.44	Wedge-1	0.4	Wedge-1	(-0.75, 0.17, -0.63)	(0, 1, 0)	(0.22, 0.98, -0.05)	(0.98, 0.04, -0.18)
80	50	Wedge-1	0.26	Wedge-1	0.2	Wedge-1	(-0.63, 0.17, -0.75)	(0, 1, 0)	(0.08, 0.98, 0.17)	(1, 0, 0)
80	60	Plane-2	0.12	Plane-2	0.1	Wedge-1	(-0.49, 0.17, -0.85)	(0, 1, 0)	(0.01, 0.98, 0.22)	(0.99, -0.02, 0.1)
80	70	Plane-2	0.04	Plane-2	0.0	Plane-2	(-0.34, 0.17, -0.93)	(0, 1, 0)	(-0.04, 0.98, 0.18)	(1, 0, 0)
80	80	Free fall.	0.00	Free fall.	0.0	Free fall.	(-0.17, 0.17, -0.97)	(0, 1, 0)	(0.01, 0.98, 0.18)	(1, 0, 0)
80	90	Free fall.	0.00	Free fall.	0.0	Free fall.	(-0.16, 0.14, -0.98)	(-0.03, 0.99, 0.16)	(-0.02, 0.61, -0.79)	(0.46, 0.89, 0.02)
240	0	Stable	1.97	Stable	2.0	Stable	-	-	-	-
240	10	Stable	3.24	Stable	3.2	Stable	-	-	-	-
240	20	Stable	8.04	Stable	8.0	Stable	-	-	-	-
240	30	Stable	16.85	Stable	17.0	Stable	-	-	-	-
240	40	Stable	3.94	Stable	4.0	Stable	-	-	-	-
240	50	Stable	2.11	Stable	2.2	Stable	-	-	-	-
240	60	Stable	1.35	Stable	1.4	Stable	-	-	-	-
240	68.1	Wedge-2	0.98	Wedge-2	1.0	Wedge-2	(-0.03, 0.26, 0.97)	(-0.67, 0.64, 0.39)	(0.66, 0.73, -0.18)	(-0.68, -0.3, -0.68)
240	70	Wedge-2	0.91	Wedge-2	0.9	Wedge-2	(-0.69, 0.68, 0.24)	(-0.58, -0.33, 0.73)	(0.66, 0.73, -0.15)	(-0.68, -0.3, -0.68)
240	80	Plane-1	0.63	Plane-1	0.6	Wedge-2	(-0.98, 0, 0.17)	(0, 0, 1)	(-0.13, 0.93, -0.33)	(-0.63, -0.77, 0.07)
240	90	Plane-1	0.47	Plane-1	0.5	Wedge-2	(-1, 0, 0)	(0, 0, 1)	(0, 1, 0)	(-0.82, -0.57, 0.05)

Table 6.4: Results from physical models [18], Block Theory, and BS3D analyses for Block 2

β	α	Physical Model	Block Theory			BS3D				
							Dynamic Failure Mode			
							Centroid dir. of Displacement		Vector about which rotation occur	
		Failure Mode	F.S.	Failure Mode	F.S.	Static Failure Mode	Global	Local	Global	Local
60	0	Wedge-1	0.78	Wedge-1	0.8	Wedge-1	(-0.87, 0.5, 0)	(0, 1, 0)	(0.5, 0.87, 0)	(1, 0, 0)
60	10	Wedge-1	0.57	Wedge-1	0.6	Wedge-1	(-0.85, 0.5, -0.15)	(0, 1, 0)	(0.5, 0.86, -0.05)	(0.99, 0.01, -0.14)
60	20	Wedge-1	0.41	Wedge-1	0.4	Wedge-1	(-0.81, 0.5, -0.3)	(0, 1, 0)	(0.53, 0.81, -0.23)	(0.92, 0.04, -0.4)
60	30	Plane-2	0.27	Plane-2	0.3	Wedge-1	(-0.75, 0.5, -0.43)	(0, 1, 0)	(0.56, 0.82, -0.11)	(0.93, 0.03, -0.4)
60	40	Plane-2	0.21	Plane-2	0.2	Plane-2	(-0.66, 0.5, -0.56)	(0, 1, 0)	(0.43, 0.87, 0.25)	(1, 0, 0)
60	50	Plane-2	0.14	Plane-2	0.1	Plane-2	(-0.56, 0.5, -0.66)	(0, 1, 0)	(0.43, 0.86, 0.26)	(0.99, 0.01, -0.16)
60	60	Plane-2	0.07	Plane-2	0.1	Plane-2	(-0.43, 0.5, -0.75)	(0, 1, 0)	(0.38, 0.86, 0.34)	(0.99, 0.01, -0.16)
60	70	Plane-2	0.00	Plane-2	0.0	Plane-2	(-0.3, 0.5, -0.81)	(0, 1, 0)	(0.34, 0.86, 0.39)	(0.98, 0.10, -0.18)
60	80	Plane-2	0.07	Plane-2	0.1	Plane-2	(-0.2, 0.5, -0.84)	(0, 1, 0)	(-0.23, 0.35, 0.91)	(0.73, -0.56, 0.39)
60	90	Plane-2	0.14	Plane-2	0.1	Plane-2	(-0.22, 0.49, -0.85)	(0, 0.98, 0.22)	(0.3, 0.95, 0.08)	(0.86, 0.41, -0.3)
80	0	Wedge-1	0.78	Wedge-1	0.8	Wedge-1	(-0.98, 0.17, 0)	(0, 1, 0)	(0.17, 0.98, 0)	(1, 0, 0)
80	10	Wedge-1	0.55	Wedge-1	0.6	Wedge-1	(-0.97, 0.17, -0.17)	(0, 1, 0)	(0.18, 0.98, -0.03)	(1, 0, 0)
80	20	Wedge-1	0.37	Wedge-1	0.4	Wedge-1	(-0.93, 0.17, -0.34)	(0, 1, 0)	(0.19, 0.98, -0.06)	(0.99, 0.01, -0.12)
80	30	Wedge-1	0.21	Wedge-1	0.2	Wedge-1	(-0.85, 0.17, -0.49)	(0, 1, 0)	(0.21, 0.97, -0.07)	(0.99, 0.01, -0.17)
80	40	Plane-2	0.09	Plane-2	0.1	Wedge-1	(-0.75, 0.17, -0.63)	(0, 1, 0)	(0.17, -0.98, -0.05)	(1, 0, 0)
80	50	Plane-2	0.01	Plane-2	0.0	Plane-2	(-0.63, 0.17, -0.75)	(0, 1, 0)	(0.71, 0.21, -0.67)	(0.2, 0.09, -0.98)
80	60	Free fall.	0.00	Free fall.	0.0	Free fall.	(-0.5, 0.17, -0.85)	(0, 1, 0)	(0.09, 0.98, 0.14)	(1, 0, 0)
80	70	Free fall.	0.00	Free fall.	0.0	Free fall.	(-0.34, 0.17, -0.92)	(0, 1, 0)	(0.57, 0.81, -0.11)	(0.82, 0.05, -0.57)
80	80	Free fall.	0.00	Free fall.	0.0	Free fall.	(-0.17, 0.17, -0.97)	(0, 1, 0)	(0.18, 0.97, 0.13)	(0.99, 0.01, -0.16)
80	90	Free fall.	0.00	Free fall.	0.0	Free fall.	(0, 0.17, -0.98)	(0, 1, 0)	(0.16, 0.97, 0.16)	(0.99, 0.01, -0.16)
320	0	Wedge-1	0.78	Wedge-1	0.8	Wedge-1	(0.64, 0.77, 0)	(0, 1, 0)	(0.77, -0.64, 0)	(1, 0, 0)
320	10	Wedge-1	0.98	Wedge-1	1.0	Wedge-1	(0.63, 0.77, 0.11)	(0, 1, 0)	(0.79, -0.6, -0.13)	(0.96, 0.02, -0.27)
320	10.3	Wedge-1	0.99	Wedge-1	1.0	Wedge-1	(0.63, 0.77, 0.11)	(0, 1, 0)	(0.79, -0.6, -0.13)	(0.96, 0.02, -0.27)
320	20	Stable	1.26	Stable	1.3	Stable	-	-	-	-
320	30	Stable	1.70	Stable	1.7	Stable	-	-	-	-
320	40	Stable	2.61	Stable	2.6	Stable	-	-	-	-
320	50	Stable	5.89	Stable	5.9	Stable	-	-	-	-
320	60	Stable	5.39	Stable	5.4	Stable	-	-	-	-
320	70	Stable	2.24	Stable	2.2	Stable	-	-	-	-
320	80	Stable	1.33	Stable	1.3	Stable	-	-	-	-
320	85	TTS[1]	1.07	Plane-2	1.1	TTS[2]	(-0.99, 0.02, 0.1)	(0, 0, 1)	(0.15, 0.98, -0.15)	(-0.73, 0.66, -0.16)
320	90	Plane-2	0.89	Plane-2	0.9	Plane-2	(-1, 0, 0)	(0, 0, 1)	(0.15, 0.96, -0.23)	(-0.79, 0.6, -0.15)
320	0	Wedge-1	0.78	Wedge-1	0.8	Wedge-1	(0.64, 0.77, 0)	(0, 1, 0)	(0.77, -0.64, 0)	(1, 0, 0)

1 Two possible failure modes: (1) Translational sliding on plane 2, and (2) torsional sliding on Plane 2.

2 Two possible failure modes: (1) Translational sliding on plane 2, and (2) torsional sliding on Plane 2:

    Direction of centroid displacement in the global reference system is (-0.67,0.60,-0.44) and in the local one is (-0.76,0.14,0.63).

    Vector about which rotation occur in the global reference system is (-0.5,0.07,0.86) and in the local one is (0.58,0.58,0.58).

(a)

(b)
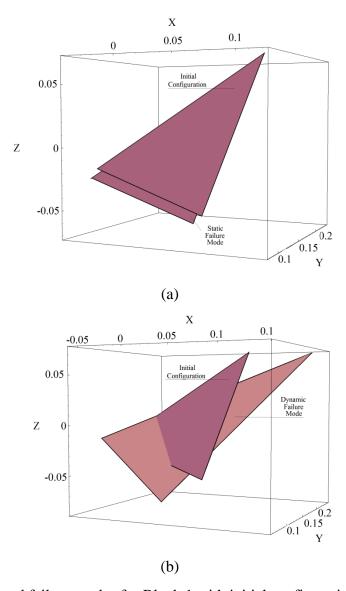
Figure 6.3: Calculated failure modes for Block 1 with initial configuration of β=60° and α=30°: (a) Static failure mode versus initial configuration (b) Dynamic failure mode versus initial configuration [301].

BS3D analyses were performed for all combinations of β and α for which the results of physical models were available. Each analysis consisted of two stages: in the first stage, the block is unilaterally constrained on all its faces, and the rock block "consolidates" under its own weight. In the second stage, the constraints are removed except along the two faces of the supporting block shown in Figure 6.1; this simulates the

block's release occurred in the physical model. In each stage, loads were increased by using increments of the control parameter equal to 0.1. Therefore, the precision of the safety factors is equal to 0.1. When comparing the results obtained using BS3D with Block Theory analyses, it can be seen that the safety factors calculated using BS3D are the same as the rounded safety factors obtained using Block Theory.

The static failure modes predicted by BS3D agree well with those observed in the physical model tests of Yeung *et al.* [18]. Disagreement occurs only for six cases (out of 64 total cases considered in this study), in which sliding on one plane was observed in the physical models, whereas BS3D predicts sliding on two planes, although the safety factors obtained from both methods are the same. To illustrate the reason for such differences, the safety factors and directions of sliding on one or two planes for these six cases are determined using Block Theory and associated limiting equilibrium analysis; the results are summarized in Table 6.5.

Table 6.5: Safety factor and sliding direction for sliding on 1 or 2 planes

Block number	β	α	Sliding on one plane[1]		Sliding on two planes[1]	
			F.S.	displacement direction	F.S.	displacement direction
Block 1	60	50	0.36	(-0.27, 0.42, -0.87)	0.41	(-0.2, 0.46, -0.87)
Block 1	80	60	0.12	(-0.13, 0.14, -0.98)	0.14	(-0.1, 0.16, -0.98)
Block 1	240	80	0.63	(-0.55, 0.43, -0.71)	0.65	(-0.53, 0.46, -0.71)
Block 1	240	90	0.47	(-0.5, 0.32, -0.8)	0.59	(-0.4, 0.46, -0.79)
Block 2	60	30	0.27	(-0.2, 0.34, -0.92)	0.30	(-0.18, 0.35, -0.92)
Block 2	80	40	0.09	(-0.1, 0.1, -0.99)	0.12	(-0.08, 0.12, -0.99)

[1] The Block theory analysis using limiting eqilibrium method

In these six cases, the safety factors and displacement directions for sliding on one or two planes are very close to each other, which can hardly be distinguished in physical models. The differences between the results of BS3D analysis and those obtained from either physical models or Block Theory analyses originate from the following reasons:

1)   Since the directions of sliding are so close one to the other, it could have been difficult to distinguish between one-plane and two-plane sliding

modes occurred in the physical models. Probably sliding on two planes in the physical models could have been easily mistaken for sliding on one plane.

2)   BS3D considers the deformability of the discontinuities, whereas Block Theory does not.

In addition, it can be seen in Table 6.4 that BS3D correctly predicts the failure mode of Block 2 when $\beta=320°$ and $\alpha=85°$, while Block Theory does not. In some repeated tests, the observed failure modes were either translation or torsional sliding on Plane 2; a vertex of the tetrahedral wedge appeared to be stuck to the supporting plane, thus causing rotation about the vertex [18]. The failure mode predicted by Block Theory is only (translational) sliding on Plane 2 because Block Theory does not consider torsional sliding as a failure mode. However, BS3D can deal with rotational as well as translational failure modes, and thus it very well captures these failure modes. In this case, BS3D correctly predicted two possible static failure modes: (1) translational sliding on Plane 2, and (2) torsional sliding on Plane 2; they correspond exactly to the observed failure modes. Figure 6.4 shows the initial configuration together with the static and dynamic failure modes predicted by BS3D, which are both torsional sliding on Plane 2.

Moreover, 3D DDA analysis was carried out for Block 2 when $\beta=320°$ and $\alpha=85°$ by Yeung *et al.* [18] and Figure 6.5 shows the failure mode predicted using 3D DDA. For this case, to simulate the torsional sliding mode observed in the physical model, Yeung *et al.* fixed the vertex of the wedge that appeared to be stuck during the test in the analysis, thus using 3D DDA artificially by forcibly inducing the rotation about this vertex [18]. If the vertex were not fixed, 3D DDA would give a mode of "translational sliding on Plane 2", as observed sometimes in the tests for this case [18]. It should be considered that 3D DDA can only find one of the failure modes at a time, and some previous information on failure mode may be necessary to correctly obtain torsional sliding from 3D DDA. However, BS3D could correctly find both possible failure modes (torsional sliding and translational sliding), without resorting to any prior information or numerical artifacts.
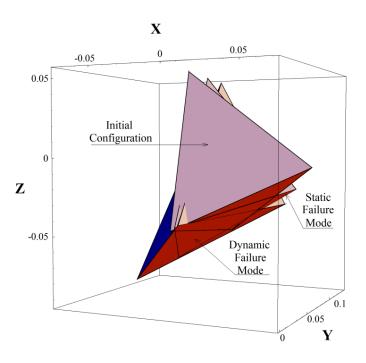
Figure 6.4: Calculated failure modes for Block 2 with initial configuration of α = 85° and β = 320° [301].
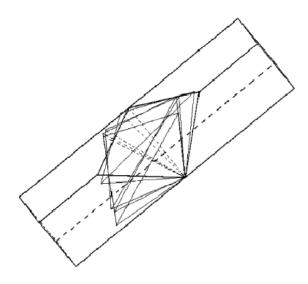
Figure 6.5: 3D DDA result for torsional sliding case; Block 2 with initial configuration of β=320° and α=85° [18].

For each of the other three observed different failure modes, one case was chosen and 3D DDA analysis was conducted by Yeung *et al.* [18]. The results of these three cases agree very well with those observed in the physical model tests as well as the results obtained by Block Theory and BS3D analysis. According to the 3D DDA analysis, the failure mode of Block 1 was predicted to be "free falling" when β=80° and α=80°. Figure 6.6 shows failure modes predicted using 3D DDA and BS3D.

(a)   (b)
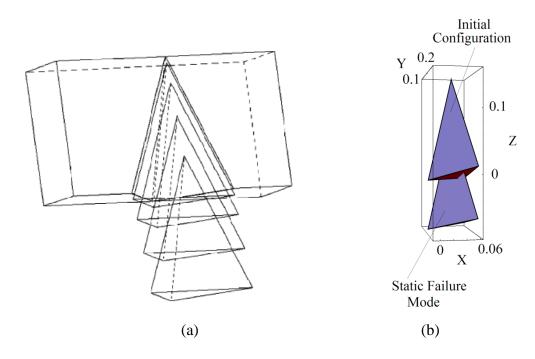
Figure 6.6: Results of analyses for free falling case; Block 1 with initial configuration of β=80° and α=80°: (a) 3D DDA [18] (b) BS3D [301].

Furthermore, the failure mode of Block 1 when β=60° and α=60° should be "sliding on Plane 2", based on 3D DDA analysis. Figure 6.7 shows failure modes predicted using 3D DDA and BS3D. In addition, 3D DDA predicted that Block 1 would fail by wedge sliding in Direction 1, when β=60° and α=30°. Figure 6.8 shows failure modes predicted using 3D DDA and BS3D.

(a)   (b)
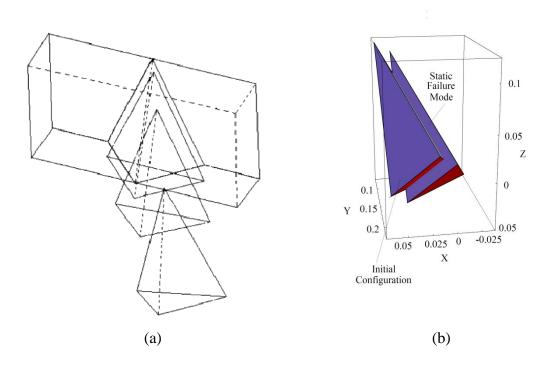
Figure 6.7: Results of analyses for plane 2 sliding case; Block 1 with initial configuration of β=60° and α=60°: (a) 3D DDA [18] (b) BS3D [301].

(a)   (b)
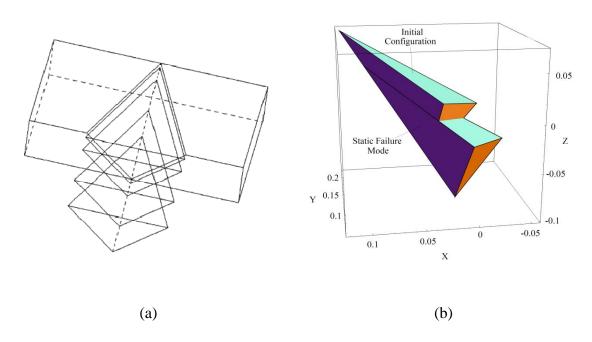
Figure 6.8: Result of analyses for wedge sliding case; Block 1 with initial configuration of β=60° and α=30°: (a) 3D DDA [18] (b) BS3D [301].

In addition, Tonon [1] demonstrated the ability of BS3D to deal with simultaneous translational and rotational failure modes in two examples; examples 2 and 3 in ref. [1]. In order to compare the ability of 3D DDA and BS3D in stability analysis of blocks with rotational failure modes, the literature was reviewed to find suitable examples. Shi [61] explained 3D DDA using three examples, none of which contains a rotational failure mode. Four examples were solved using 3D DDA by Liu *et al.* [302]: block sliding along an incline under the action of gravity; a rigid block excited by the movement of the foundation; lift-off motion of a rigid block resting on a rigid foundation; and scattering of a system of packed cubes. Wang *et al.* [303] solved three examples using 3D DDA: wedge failure analysis; stability analysis of a gravity dam; and dynamic stability analysis of the upper part of Konya dam. Hatzor and Feintuch [304] demonstrated the validity of dynamic block displacement using DDA by a 2D example of block sliding. Moreover, Hatzor *et al.* [305] reported a case history of dynamic stability of jointed rock slope which was simulated by DDA. None of the above examples can be used to compare the capabilities of 3D DDA and BS3D in analyzing the stability of single blocks that may have rotation in their failure modes.

6.2.3 Validation using case histories

Besides physical models, two case histories of slope wedge failure are used to validate BS3D. The case histories used in this study were reported by Kumsar et al [26] and were also used by Yeung *et al.* [18].

6.2.3.1 Case 1: Wedge failure in an Open Museum

A wedge failure occurred in a thick and soft tuff layer of Zelve Open Museum in the Cappadocia Region of Central Anatolia, Turkey [26]. Two joints with dip/dip direction equal to 85°/318° and 82°/208°, respectively, bound a tetrahedral wedge. These discontinuities had slightly rough surfaces with a friction angle of 30°. The slope surface had dip/dip direction equal to 81°/255°.

Considering the fact that gravity is the only active load, BS3D analysis calculated a safety factor of 0.2, with static failure mode consisting of sliding on two planes, and

dynamic failure mode being roto-translational sliding. This agrees not only with the observation that the wedge has already failed, but also with the safety factor obtained from Block Theory analysis.

6.2.3.2 *Case 2: Wedge failure near Ankara Castle*

A wedge failure occurred in a jointed andesite rock mass near Ankara Castle in Bent Deresi region of Ankara City, Turkey [26]. Two joints with dip/dip direction equal to 44°/194° and 71°/103°, respectively, formed a tetrahedral wedge. These discontinuities had a friction angle of 30°. A house sat on top of the wedge failure. The slope surface had a dip/dip direction equal to 69°/162°.

Considering gravity as the only active load, BS3D analysis calculated a safety factor of 0.7, with static failure mode consisting of sliding on two planes, and dynamic failure mode being roto-translational sliding. These results agree with both the actual observation and the safety factor calculated using Block Theory analysis.

6.3   CONCLUSIONS

Wedge failure validation under gravity loading has been carried out for BS3D [1], an algorithm for analysis of single rock blocks that can handle general failure modes under conservative and non-conservative forces.

Sixty four physical models and two case histories were analyzed using this method. For the wedge stability problem, physical modeling and BS3D give the same failure modes except for six cases in which sliding on one plane were observed in physical models while BS3D predicted sliding on two planes. This is due to the fact that the two failure modes have very similar factors of safety and sliding directions, and BS3D considers the deformability of the sliding planes.

In all cases, safety factors obtained using BS3D analyses were the same as obtained using Block Theory limiting equilibrium analysis. The results of BS3D analyses for two case histories agree well with the observations that the wedges have already failed.

CHAPTER 7: STABILITY OF ROCK BLOCKS FORMED IN THE ROOF OF A CIRCULAR TUNNEL: EFFECT OF DILATANCY

7.1 INTRODUCTION

The mechanical behavior of a rock block formed in the roof of a tunnel is governed by its geometry, the mechanical characteristics of the joints forming the block, the deformability of the fractures forming the block, the deformability of the block and that of the surrounding rock mass, and the stresses within the rock [20].

In this Chapter, the effect of dilatancy on the stability of a rock block formed in the roof of a circular tunnel is investigated. Section 7.2 presents an analytical approach to analyze stability of a 2D triangular wedge formed in the roof of a circular tunnel. Two different definitions are introduced for the factor of safety of the block. The effects of stiffness and shear strength of the fractures as well as *in situ* stress conditions on stability of the wedge are investigated. Section 7.3 explains a simplified limit equilibrium method to analyze stability of a tetrahedron in the roof of an excavation. The results of the analytical analyses are compared with those obtained from BS3D simulations. Using the analytical approach and BS3D, the effects of the normal stiffness of the fractures, dilatancy, the tunnel radius, and the block size on stability of the tetrahedron are investigated. Section 7.4 presents a comprehensive sensivity analyses on the effects of the shear strength, the normal stiffness, the *in situ* stress condition, the tunnel radius, and the block size on stability of a prism formed in the roof of a circular tunnel by four fractures with the same dip angles. All of these sensivity analyses are performed using BS3D. Finally, the summary and conclusions made based on the sensivity analyses are presented in Section 7.5.

7.2 SYMMETRIC 2D WEDGE IN THE ROOF OF A CIRCULAR TUNNEL

This Section investigates the stability of a symmetric 2D wedge in the roof of a circular tunnel. The effects of stiffness and shear strength of the fractures as well as *in situ* stress conditions on stability of the wedge are studied.

7.2.1 Stability analysis (analytical solution)

An analytical solution has been proposed by Bray [306] to analyze the stability of a block confined by rock mass. The solution contains a two-stage relaxation procedure (Figure 7.1):

1- The fractures are assumed to be infinitely stiff. The excavation is performed in a homogeneous, isotropic, linearly elastic, weightless medium. The confining lateral force, H_o, acting horizontally on the wedge is evaluated at this stage.

2- Assuming flexible fractures and rigid rock mass, loads due to the block weight, W, as well as the resultant of the supporting forces, S, are applied during this stage.
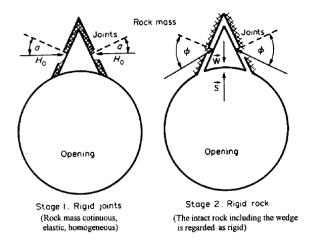
Figure 7.1: Loading stages in the analytical solution proposed by Bray [20].

For the symmetric 2D wedge of Figure 7.1, the factor of safety is defined as:

$$FS = \frac{S + P_0}{W},$$ (7.1)

where P_0 is the pullout resistance of the wedge, which is the resultant of all forces applied to the wedge except for its weight and the supporting forces. It can be evaluated as follows [306, 307]:

$$P_0 = 2MH_0,$$ (7.2)

209

in which M is a function of the mechanical properties of the fractures and the apical angle of the wedge; and H_0 is the horizontal force applied to the wedge by the surrounding rock mass at the end of the first stage. The values of M and D are, respectively [20, 306]:

$$M = \frac{\left(\cos^2\alpha \times \cos i \times \frac{k_s}{k_n} + \sin(\alpha - i) \times \sin\alpha\right) \times \sin(\phi - \alpha)}{D \times \cos i}, \qquad (7.3)$$

$$D = \cos\alpha \times \cos\phi \times \frac{k_s}{k_n} + \sin\phi \times \frac{\sin(\alpha - i)}{\cos i}, \qquad (7.4)$$

where α is the semi-apical angle of the wedge; ϕ and i are the effective friction (the sum of the basic friction angle and the dilation angle) and dilation angles of the fractures; and k_s and k_n are the fractures shear and normal stiffness.

At the end of the relaxation stage, the horizontal force, H_0, applied to a wedge formed in the roof of a circular tunnel can be evaluated by modifying Elsworth's [308] analytical expression, in a hydrostatic stress field, as follows [20]:

$$\frac{H_0}{p \times R} = \frac{\cos\theta \times \cos(\theta - 2\alpha)}{\sin\alpha \times \cos(\theta - \alpha)}, \qquad (7.5)$$

where θ is the angle denoted in Figure 7.2.

Sofianos *et al.* suggested the following equation to evaluate the horizontal force, H_0, confining a wedge in the roof of a circular tunnel in non-hydrostatic stress field [20]:
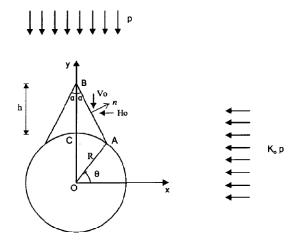
Figure 7.2: Symmetric wedge in the roof of a circular tunnel (biaxial stress field) [20].

Sofianos *et al.* suggested the following equation to evaluate the horizontal force, H_0, confining a wedge in the roof of a circular tunnel in non-hydrostatic stress field [20]:

$$H_0 = \frac{p \times R}{2} \times C_H,$$ (7.6)

where:

$$C_H = (1 + K_0) \cdot C_{H1} - (1 - K_0) \cdot C_{H2}$$ (7.7)

$$C_{H1} = \left(\frac{h}{R} + 1\right) - \frac{1}{(h/R + 1)}$$ (7.8)

$$C_{H2} = \left(\frac{h}{R} + 1\right) - \frac{1}{(h/R + 1)^3}$$ (7.9)

In hydrostatic stress field Equation (7.6) is reduced to:

$$\frac{H_0}{p \times R} = \left(\frac{h}{R} + 1\right) - \frac{1}{(h/R + 1)}$$ (7.10)

Moreover, Nomikos *et al.* [309] introduced the following analytical solution to evaluate the horizontal force applied to a symmetric wedge in the roof of a circular tunnel excavated in an inclined stress field (Figure 7.3):

$$H_0 = \frac{p \times R}{2}\left[(1 + K_0) \cdot C_{H1} - (1 - K_0) \cdot C_{H2} \cdot \cos 2\beta\right]$$ (7.11)
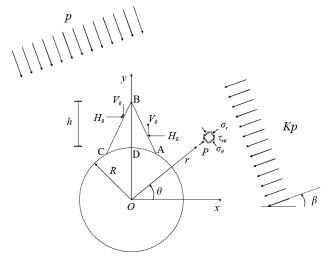
Figure 7.3 Circular opening in an inclined biaxial stress field [309].

211

7.2.2 Effect of fracture stiffness on 2D wedge stability

Hudson and Harrison [310] performed a sensivity analysis to show the variation in M (defined in Equation (7.3)) as a function of the semi-apical angle, α in Figure 7.2, for different ratios of normal to shear stiffness of discontinuities. The effective friction angle was assumed to be 30˚ with zero dilation angle. Figure 7.4 presents the results of Hudson's and Harrison's sensivity analyses (recalculated in this dissertation). They concluded that there is a tendency for the prism to be expelled from the surface when the semi-apical angle exceeds the effective friction angle, which is exacerbated for high values of k_s/k_n.
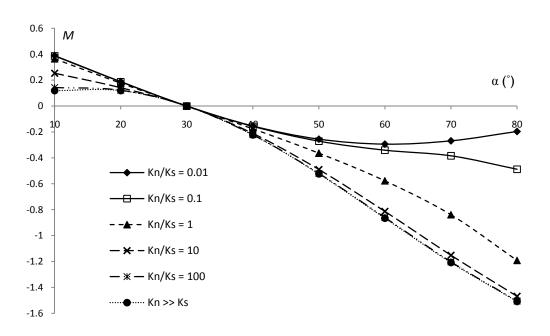
Figure 7.4: Effect of semi-apical angle and discontinuity stiffness on the constraining force applied on symmetric triangular roof wedge

Stability of a block is usually expressed by a safety factor rather than the value of M. Therefore, in this study, the factor of safety of the unsupported block is calculated using Equation (7.1). However, in order to obtain the factor of safety, one should estimate

the block weight and the horizontal force, H_0, confining the wedge, which in turn requires the unit weight of the rock, the tunnel radius, the block height, and the *in situ* stress condition. The unit weight of the rock is assumed to be 27 kN/m^3. The factor of safety is calculated for the maximum triangular block formed in the roof of a tunnel with diameter of 4 m. The semi-apical angle of the wedge is changed between 10 and 80˚, which means that the fractures forming the block dip between 80 and 10˚ below horizontal, respectively. In order to calculate the weight of the block and the normal and shear forces applied to each face, it is assumed that the length of the block along the tunnel axis is 1 m. Hydrostatic *in situ* stress of 0.5 MPa is assumed to act prior to excavation of the tunnel. Figure 7.5 depicts the factors of safety calculated using Equation (7.1) for different semi-apical angles (α) and ratios of normal to shear stiffness (k_s/k_n). In order to present changes in FS with α and k_s/k_n for the case of stable blocks ($10˚ \le α \le 30˚$) more clearly, the results are shown in two different scales of FS.
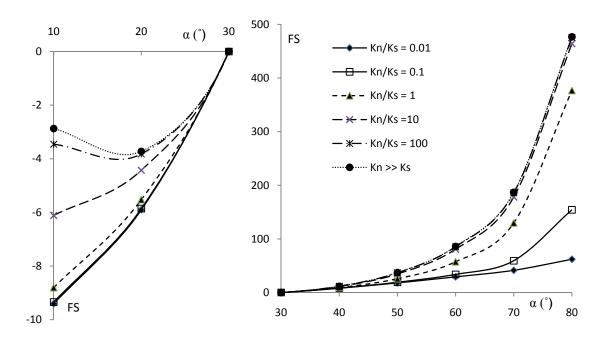
Figure 7.5: Variation of FS (Bray's definition) of maximum 2D wedge formed in the roof of a circular tunnel with semi-apical angle and fractures stiffness (hydrostatic stress field of 0.5 MPa)

It can be seen in Figure 7.5 the tendency of the wedge to be expelled from its mould is exacerbated for high values of k_s/k_n. The factor of safety defined in Equation (7.1), for stable blocks, gives FS $\leq$ -1 and, for unstable blocks, gives FS > -1. However, in most geotechnical engineering (or civil engineering) problems, the FS is always positive: at equilibrium, FS is equal to one; for stable cases, FS is higher than one; and, for unstable cases, FS is between 0 and 1.

In order to limit the factor of safety in the conventional range, the factor of safety is now defined as the ratio of passive to active forces (or the ratio of available shear strength to the required shear stress at equilibrium). The same definition is adopted by Rocscience in their commercial block theory software, Unwedge [311]. Figure 7.6 depicts diagram of forces applied on a symmetric triangular roof prism. The factor of safety of unsupported 2D wedge is defined as the ratio of passive to active forces as follows:

$$FS = \left| \frac{2S \cdot \cos \alpha}{2N \cdot \sin \alpha + W} \right|, \tag{7.12}$$

where N and S are normal and shear forces and can be calculated as follows [235, 306]:

$$N = \frac{H_0 \left(K_s \cos^2 \alpha + K_n \sin^2 \alpha \right) \cdot \cos \phi}{K_s \cos \alpha \cdot \cos \phi + K_n \sin \alpha \cdot \sin \phi} \tag{7.13}$$

$$S = \frac{H_0 \left(K_s \cos^2 \alpha + K_n \sin^2 \alpha \right) \cdot \sin \phi}{K_s \cos \alpha \cdot \cos \phi + K_n \sin \alpha \cdot \sin \phi} \tag{7.14}$$
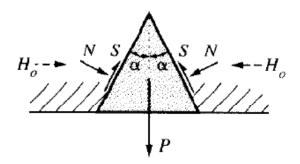
Figure 7.6: Diagram of forces applied on a symmetric triangular roof prism [310]

Figure 7.7 depicts the factors of safety calculated using Equation (7.12) for different semi-apical angles (α) and ratios of normal to shear stiffness (k_s/k_n) of discontinuities. It can be seen that, except for the case of α=10˚, the factor of safety is almost independent of the ratio of k_s/k_n. In the case of α=10˚, the maximum block has much larger size compared to the other values of semi-apical angles, and therefore, the weight of the block is not negligible compared to the values of normal and shear forces applied to the faces. For the case of weightless block (or the case that the weight is negligible compared to the *in situ* stresses), the factor of safety defined in Equation (7.12) can be simplified as follows:

$$FS = \frac{\tan \phi}{\tan \alpha},$$

(7.15)

which is independent of the ratio of k_s/k_n. At a depth of about 20 m, one may expect to have a hydrostatic *in situ* stress of 0.5 MPa. For a 4-meter-diameter tunnel, this depth is almost considered as a limit between shallow and deep tunnels. However, considering the fact that, for a wedge with semi-apical angle of 10˚, the height of the maximum block is 9.52 m, a depth of 20 m for the tunnel axis is shallow.
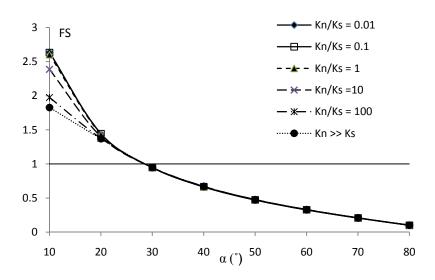
Figure 7.7: Variation of FS (our definition) of maximum 2D wedge formed in the roof of a circular tunnel with semi-apical angle and fractures stiffness (hydrostatic stress field of 0.5 MPa)

Figure 7.8 depicts the factor of safety of a wedge subjected to hydrostatic stress field of 5 MPa calculated using Equation (7.12) for different semi-apical angles (α) and ratio of normal to shear stiffness (k_s/k_n). It can be seen that, when the weight of the block is negligible compared to the *in situ* stress (which is the case almost in all tunneling applications), the factor of safety is independent of the ratio of normal to shear stiffness.
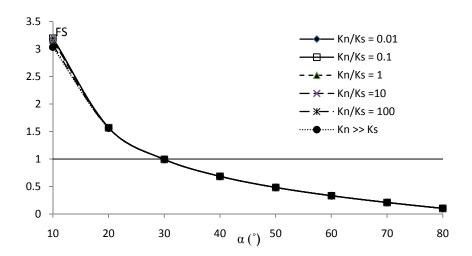
Figure 7.8: Variation of FS (our definition) of maximum 2D wedge formed in the roof of a circular tunnel with semi-apical angle and fractures stiffness (hydrostatic stress field of 5 MPa)

7.2.3 Effect of shear strength of fractures on stability of 2D wedges

Let us consider a 4-meter-diameter tunnel and the maximum triangular prism formed in the roof of the tunnel by two fractures dipping 60˚ below horizontal plane. The rock mass is assumed to be subjected to a hydrostatic stress field of 0.5 MPa. The ratio k_s/k_n is assumed to be equal to 0.1. In order to investigate the effect of shear strength of rock fractures on stability of the wedge, the effective friction angle, ϕ, is varied between 20˚ and 70˚ and the factors of safety are calculated using both Equation (7.1) and Equation (7.12). Figure 7.9 summarizes the results of the analyses.

Figure 7.9 shows that the FS of the wedge increases with increasing the effective friction angle of the fractures. Changing the friction angle from 20 to 70˚ changes the FS

216

calculated using Equation (7.1) from -6.6 to 58.9 and increases the FS determined employing Equation (7.12) from 0.6 to 4.47. It can be seen that the order of magnitudes of the factors of safety calculated using Equations (7.1) and (7.12) are different from each other. However, adopting either definition for the factor of safety, the effective friction angle strongly affects stability of the wedge.
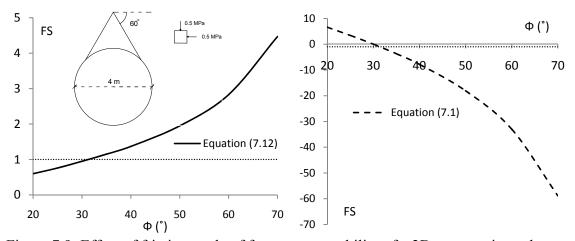
Figure 7.9: Effect of friction angle of fractures on stability of a 2D symmetric wedge

7.2.4 Effect of *in situ* stress condition on stability of 2D wedges

7.2.4.1 Depth of the tunnel (hydrostatic state of stress)

Let us consider a 4-meter-diameter tunnel and the maximum symmetric wedge formed in the roof of the tunnel by two fractures dipping 60° below horizontal plane. The ratio of k_s/k_n is equal to 0.1; the effective friction angle is assumed to be 30°; the rock mass is subjected to hydrostatic state of stress before the excavation. The magnitude of the stress is changed from 0.3 to 10 MPa and the factors of safety are calculated using both Equations (7.1) and (7.12). Figure 7.10 presents the results of the analyses. It can be seen that the FS calculated using Equation (7.1) is zero and does not change with the vertical stress (depth of the tunnel). However, the FS determined employing Equation

(7.12) increases slightly with vertical stress (especially in the low values of *in situ* stresses).
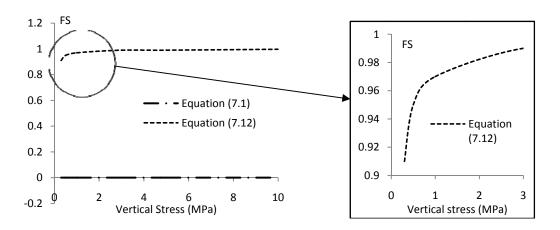
Figure 7.10: Effect of *in situ* stress on stability of 2D wedge ($\phi = 30°$)

The conclusion made based on the definition of FS given by Equation (7.1) seems to be counterintuitive. Thus, the same sensivity analysis is performed choosing an effective friction angle of 25°. Figure 7.11 depicts the results of the analyses. It can be seen that the trend in the FS calculated using Equation (7.12) remains the same as in Figure 7.10. However, the FS determined using Equation (7.1) increases (the stability decreases) with increasing tunnel depth.
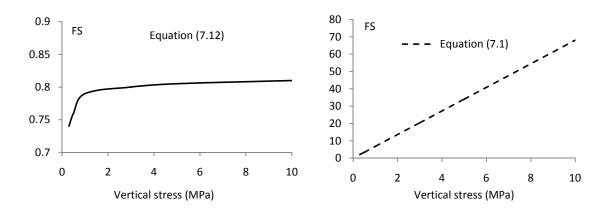
Figure 7.11: Effect of *in situ* stress on stability of 2D wedge ($\phi = 25°$)

The same senivity analysis is performed choosing an effective friction angle of 35°. Figure 7.12 depicts the results of the analysis. Again, it can be seen that the trend in the FS calculated using Equation (7.12) remains the same as in Figure 7.10. However, the FS determined using Equation (7.1) decreases (the stability increases) with increasing the tunnel depth.
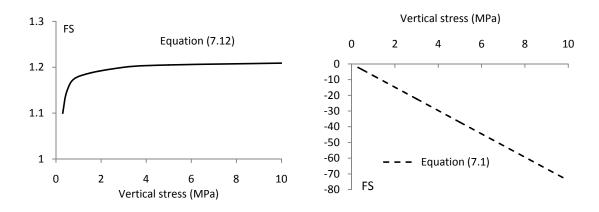
Figure 7.12: Effect of *in situ* stress on stability of 2D wedge ($\phi = 25°$)

It can be seen that, adopting Equation (7.12) as the definition of the FS, the conclusion is consistent: increasing the tunnel depth slightly increases the stability of the block in low stress regimes and has no effect on the factor of safety in high stress regimes. However, the sensivity analyses performed based on the definition of FS given by Equation (7.1) leads to the following conclusions:

- For a friction angle equal to the semi-apical angle, the vertical stress has no effect on the stability of the block.
- For a friction angle smaller than the semi-apical angle, the FS of the block increases (the stability decreases) with increasing *in situ* stress.
- For a friction angle larger than the semi-apical angle, the FS of the block decreases (the stability increases) with increasing *in situ* stress.

219

7.2.4.2 Lateral pressure coefficient

Let us consider a 4-meter-diameter tunnel and the maximum symmetric prism formed in the roof of the tunnel by two fractures dipping 60 below horizontal plane. The ratio of k_s/k_n is equal to 0.1 and the effective friction angle is assumed to be equal to 30˚, 25˚, or 35˚. The rock mass is subjected to a vertical stress of 1 MPa. Figure 7.13, Figure 7.14, Figure 7.15 present the FS calculated using both Equations (7.1) and (7.12) when the lateral pressure coefficient is changed from 0.5 to 4 .
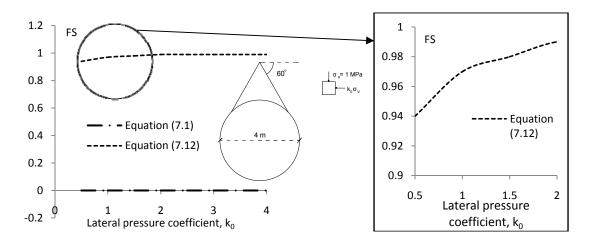
Figure 7.13: Effect of lateral pressure coefficient on stability of 2D wedge ($\phi = 30°$)
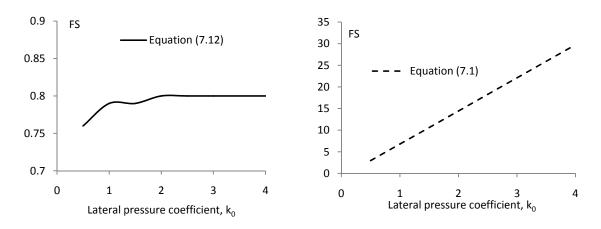
Figure 7.14: Effect of lateral pressure coefficient on stability of 2D wedge ($\phi = 25°$)
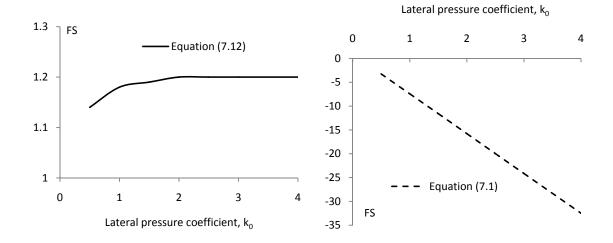
Figure 7.15: Effect of lateral pressure coefficient on stability of 2D wedge ($\phi = 35°$)

The same as what found in Section 7.2.4.1 for the effect of the vertical stress, it can be seen that, defining the FS as Equation (7.12), the conclusion is consistent: increasing the lateral pressure coefficient slightly increases the stability of the block in low k_0 regimes and has no effect on the factors of safety in high k_0 regimes. However, the sensivity analysis performed based on the definition of FS given by Equation (7.1) leads to the following conclusions:

- For a friction angle equal to the semi-apical angle, the lateral pressure coefficient has no effect on the stability of the block.
- For a friction angle smaller than the semi-apical angle, the FS increases (the stability decreases) with increasing the lateral pressure coefficient.
- For a friction angle larger than the semi-apical angle, the FS decreases (the stability increases) with increasing the lateral pressure coefficient.

7.2.5 Summary

An analytical method has been presented for stability analysis of 2D triangular prism formed in the roof of a circular tunnel from References [20, 235, 306-310]. In addition, a new definition for the factor of safety of the block is presented in this Chapter. Based on sensivity analyses, the following conclusions were made:

221

1- Different definitions of the FS may lead to different conclusions in sensivity analyses.

2- Adopting Equation (7.1) as FS definition, it is found that the tendency for the prism to be expelled from the surface is exacerbated for high values of k_s / k_n. However, defining the FS as given in Equation (7.12), it is found that the stability of a 2D triangular wedge is independent of the ratio of k_s / k_n.

3- Stability of 2D wedge is strongly affected by the friction angle of the fractures.

4- Adopting Equation (7.12) as the definition of the FS, it is found that increasing the *in situ* stress slightly increases the stability of the block in low stress regimes and has no effect on the factor of safety in high stress regimes. However, the sensivity analyses performed based on the definition of FS given by Equation (7.1) leads to the following conclusions: for a friction angle equal to the semi-apical angle, the vertical stress has no effect on the stability of the block; for a friction angle smaller than the semi-apical angle, the FS of the block increases (the stability decreases) with increasing the vertical stress; and for a friction angle more than the semi-apical angle, the FS of the block decreases (the stability increases) with increasing the vertical stress.

5- Defining the FS as Equation (7.12), it is found that increasing the lateral pressure coefficient slightly increases the stability of the block in low k_0 regimes and has no effect on the factors of safety in high k_0 regimes. However, the sensivity analysis performed based on the definition of FS given by Equation (7.1) leads to the following conclusions: for a friction angle equal to the semi-apical angle, the lateral pressure coefficient has no effect on the stability of the block; for a friction angle less than the semi-apical angle, the FS of the block increases (the stability decreases) with increasing the lateral pressure coefficient; and for a friction angle more than the semi-apical angle, the FS of the block decreases (the stability increases) with increasing the lateral pressure coefficient.

Based on the above mentioned conclusions obtained from senivity analyses, one may say that although the definition of the factor of safety given in Equation (7.1) is not wrong, it may lead to incorrect conclusions in sensivity analyses. In addition, FS introduced in Equation (7.12) is limited to positive values, the same as most geotechnical engineering (and civil engineering) applications: at equilibrium, FS=1, for stable blocks, FS > 1, and for unstable blocks, 0<FS< 1. Consequently, it is believed that Equation (7.12) can define the factor of safety of a 2D symmetric prism better than Equation (7.1).

7.3 ROOF STABILITY ANALYSIS FOR A TETRAHEDRON

A relaxation analysis for a non-regular 3D tetrahedral block in the roof of an excavation presents some conceptual difficulties, which arise from extra number of degrees of freedom. For instance, on any face of the block it is necessary to consider two components of orthogonal shear displacement as well as a normal displacement component. Maintaining the statical determinacy during the relaxation process would require that the block be almost isotropically deformable. Thus, a complete analysis of the stability of a tetrahedron is not handled conveniently by relaxation method presented earlier for 2D problem [235].

7.3.1 Limit equilibrium approach

Using limit equilibrium methods, it is possible to estimate the wedge (Figure 7.16) stability considering the frictional properties of the fractures.
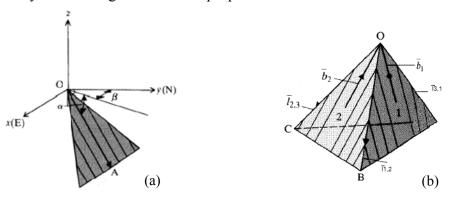
Figure 7.16: (a) Geometry for determination of the unit normal vector to a plane; (b) lines of action of mobilized shear forces on the face of a tetrahedral wedge [235].

223

Suppose the orientation of the dip vector *OA* of a fracture surface is defined by the dip angle α and dip direction β, illustrated in Figure 7.16-(a).

The direction cosines of the outward normal to the plane are given by [235]:

$$\mathbf{n} = (n_x, n_y, n_z) = (\sin\alpha \cdot \cos\beta, \sin\alpha \cdot \sin\beta, \cos\alpha) \qquad (7.16)$$

The normal component of traction at any point on the fracture surface can be estimated from the stress components and the direction cosines by substitution in the equation [235]:

$$t_n = n_x^2 \sigma_{xx} + n_y^2 \sigma_{yy} + n_z^2 \sigma_{zz} + 2(n_x n_y \sigma_{xy} + n_y n_z \sigma_{yz} + n_z n_x \sigma_{zx}) \qquad (7.17)$$

If the normal traction, t_n, is determined at a sufficient number of points on the fracture surface, its average value and the area of the surface can be used to estimate the total normal force *N*. Thus, for each of the three confined faces of the tetrahedron, the respective normal forces N_1, N_2, and N_3, can be calculated directly from the surface geometry and the elastic stress distribution [235].

In determining the stability of a wedge under surface and gravitational forces, it is necessary to take account of the directions of the shear resistances mobilized by the joint normal forces. Suppose the outward normals to the *i*-th face of the tetrahedron OABC shown in Figure 7.16-(b) are given as follows [235]:

$$\mathbf{n}_i = (n_{xi}, n_{yi}, n_{zi}), \qquad \text{etc.} \qquad (7.18)$$

and that the faces are numbered in a sense compatible with the right-handed system of reference axes. The lines of intersection of the faces are then given by cross products of the normals to faces, i.e.:

$$\mathbf{l}_{1,2} = \mathbf{n}_1 \times \mathbf{n}_2 \qquad \text{etc.} \qquad (7.19)$$

The bisector of an apical angle of a face of the tetrahedron, and directed towards the apex, as shown in Figure 7.16-(b), is obtained from the orientations of the adjacent lines of intersection which define the face, i.e.:

$$\mathbf{B}_1 = -\frac{1}{2}(\mathbf{I}_{1,2} + \mathbf{I}_{3,1}) \qquad (7.20)$$

One can establish the unit vector parallel to the *i*-th bisector [235]:

$$\mathbf{b}_i = \left(b_{xi}, b_{yi}, b_{zi}\right) \qquad \text{etc.} \qquad (7.21)$$

It can be reasonably assumed that, in the case where the crown trihedral angle of the tetrahedron includes the z axis, the mobilized shear resistance on any face is directed parallel to the bisector of the face apical angle. Also, the inward unit normal to any face, the line of action of the normal component of the surface force, is given by [235]:

$$\mathbf{a} = (a_x, a_y, a_z) = -(\sin \alpha \cdot \cos \beta, \sin \alpha \cdot \sin \beta, \cos \alpha) \qquad (7.22)$$

The magnitude of the maximum shear forces that can be mobilized on the various faces are given as follows:

$$S_1 = N_1 \tan \phi_1 \qquad (7.23)$$

and the x, y, and z components of the shear resistance on any face can be determined directly from its magnitude and the components of the appropriate unit vector for the face, defined by Equation (7.21). Taking account of all applied normal forces and mobilized shear resistances, the net vertical force associated with surface forces is [235]:

$$F_z = \sum_{i=1}^{3} N_i \left(b_{zi} \tan \phi_i + a_{zi}\right) \qquad (7.24)$$

Introducing the wedge weight, if the resultant vertical force satisfies the condition

$$F_z + W \leq 0, \qquad (7.25)$$

the wedge is potentially stable under the set of surface and body forces [235]. Therefore, based on Bray's [306] and Sofianos's [307] definition for the safety factor of 2D wedges (Equation (7.1)), the factor of safety of 3D tetrahedrons can be defined as follows:

$$FS = \frac{F_z}{W}, \qquad (7.26)$$

For stable blocks, FS $\leq$ -1 and, for unstable blocks, FS > -1.

In order to show the order of magnitude of the factor of safety calculated using Equation (7.26), a tetrahedral rock block is analyzed. The height of the block is assumed to be 1 m. The block is formed by 3 fractures with dip directions of 0, 120, and 240˚. The dip angle is changed from 10˚ to 80˚ and the factor of safety is calculated using Equation (7.26). The effective friction angle of the fracture is equal to 25˚. In addition, it is assumed that a hydrostatic *in situ* stress of 0.5 MPa is applied and the effects of

excavation on *in situ* stresses are eliminated. Figure 7.17-(a) depicts the factor of safety of the block versus dip angle of its fractures.

It can be seen in Figure 7.17-(a) that the FS calculated using Equation (7.26) changes from -50 to 90. The factor of safety defined in Equation (7.26), gives positive value for stable blocks and negative value for unstable blocks. However, in most geotechnical engineering (or civil engineering) problems, the FS is always positive. In order to limit the factor of safety in the conventional range, the factor of safety is defined as the ratio of passive to active forces (or the ratio of available shear strength to the required shear stress at equilibrium). Thus, the factor of safety of unsupported wedges is defined as follows:

$$FS = \left| \frac{\sum\limits_{i=1}^{3} N_i b_{zi} \tan \phi_i}{W + \sum\limits_{i=1}^{3} N_i a_{zi}} \right| \tag{7.27}$$

Figure 7.12-(b) depicts the FS of the tetrahedron calculated using Equation (7.27) versus the dip angle of the fractures, for the same example described earlier in this Section. It can be seen that the FS is equal to one when the block is at equilibrium, is higher than one for stable blocks, and is smaller than one for unstable block.

(a) Equation (7.26)   (b) Equation (7.27)
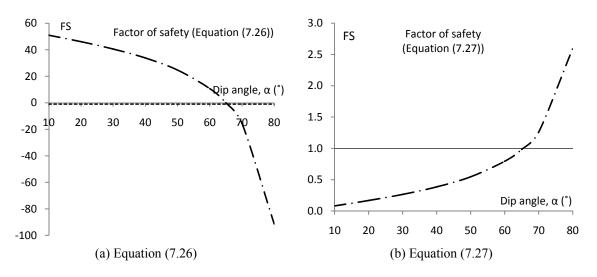
Figure 7.17: Variation of FS of 1-meter-heigth tetrahedron with dip angle of its fracture

7.3.2 Numerical simulation using BS3D

The stability of a single rock block with general shapes can be analyzed using BS3D, in which the factor of safety is defined as the ratio between the stabilizing forces and the driving forces at limiting equilibrium. This definition is the same as in Equation (7.27) for 3D tetrahedrons and Equation (7.12) for 2D wedges. In addition, this definition is consistent with the definitions used in the most civil engineering/geotechnical engineering applications (ex.: Rocscience commercial software: Unwedge). Moreover, our definition (Equation (7.12) and (7.27), for 2D and 3D wedges, respectively) has some advantages over Bray's [306] and Sofianos's [307] definition (Equation (7.1)), as demonstrated in Section 7.2. Thus, in the rest of this Chapter, Equation (7.27) is used to obtain the analytical factor of safety.

Although the definition of the factor of safety (Equation (7.27)) in the analytical method is the same as the definition of the factor of safety in BS3D, if a block is analyzed using both approaches, the factors of safety will be different because:

- BS3D takes into account the deformability of the rock block, fractures, and the rock mass surrounding the block, while the analytical approach (Equation (7.27)) does not.
- BS3D considers the progressive failure and the mobilization of shear strength, while the analytical limit equilibrium method does not.
- In analytical limit equilibrium solution, the *in situ* stresses are assumed to be independent of the block displacement. However, in BS3D analysis, the part of the *in situ* stresses applied to the block changes with block movement.

The tetrahedron that was introduced in Section 7.3.1 is simulated using BS3D. The factors of safety obtained from BS3D analyses together with the safety factors calculated using the analytical method are depicted in Figure 7.18 where the effective friction angle is assumed to be equal to 41˚. The ratio of the shear to normal stiffness of the fractures, k_s/k_n, is assumed to be constant (1/10) with an initial normal stiffness of 2000 MPa/m. In addition, a hydrostatic *in situ* stress of 0.5 MPa is applied without considering the effect of excavation on *in situ* stresses around the excavation.
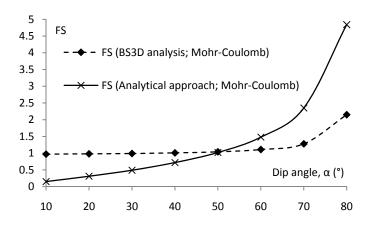
Figure 7.18: Comparing the factors of safety calculated using BS3D and the analytical approach for a tetrahedral rock block

It can be seen in Figure 7.18 that two curves intersect each other at α equal to 49˚ when FS = 1. It means that both found that the block is at limiting equilibrium when semi-apical angle (90˚ - α) is equal to the effective friction angle (41˚). It is found from both BS3D analyses and the analytical calculations that the tetrahedron is stable if the semi-apical angle is larger than the effective friction angle, (90˚- α) > 41˚ or α < 49˚ because in these cases the normal stresses applied to the fractures due to *in situ* stresses push the block into its mould and increase the stability of the block. In addition, both methods report instability if the semi-apical angle is smaller than the effective friction angle, α > 49˚; because in these cases the normal stresses applied to the fractures due to *in situ* stresses push the block outside of its mould and decrease the stability of the block.

Moreover, it can be seen in Figure 7.18 that, for the case of stable blocks, the factors of safety calculated using the analytical approach are higher than those determined from BS3D analysis, while for the case of unstable blocks, BS3D gives higher factors of safety comparing to those calculated using the analytical approach. These differences in factors of safety can be explained based on the fact that the analytical approach does not consider the deformability of the fractures, the rock block, and the rock mass, while BS3D does. Eliminating the effect of deformability is the same as assuming rigid fractures, rock block, and rock mass (or very high stifnesses). Thus, the

228

analytical approach overestimates the normal stresses applied to the fractures due to *in situ* stresses:

- For the case of stable blocks (FS > 1), the normal forces applied to the fractures push the block into its mould and increase the stability of the block. Consequently, overestimating the normal stresses applied to the fractures due to *in situ* stresses overestimates the factor of safety. Therefore, for the case of stable blocks, the factors of safety calculated using the analytical approach is higher than those determined from BS3D analysis.

- For the case of stable blocks (FS < 1), the normal forces applied to the fractures push the block out of its mould and decrease the stability of the block. Consequently, overestimating the normal stresses applied to the fractures due to *in situ* stresses underestimates the factor of safety. Therefore, for the case of unstable blocks, BS3D gives higher factors of safety compared to those calculated using the analytical approach.

7.3.3 Effect of the fractures' normal stiffness on stability of tetrahedron

Unlike the analytical approach, BS3D takes into account the deformability of rock fractures in calculating the factor of safety. In order to check the effect of the normal stiffness of the fracture on stability of tetrahedron, a sensivity analysis is performed considering the same wedge introduced in Section 7.3.2. The effective friction angle is assumed to be equal to 41˚. In addition, a hydrostatic *in situ* stress of 0.5 MPa is applied. As it was mentioned in Chapter 5, excavations change the *in situ* stresses in the surrounding rock mass near the excavation perimeter. In this part of analyses, the effects of excavation on *in situ* stresses are not considered and it is assumed that the *in situ* stresses around the underground opening are the same before and after excavation. The initial normal stiffness of the fractures, k_{ni}, is ranged between 200 and 5000 MPa/m. Figure 7.19 depicts the changes in the FS of the block with the initial normal stiffness and the dip angle of the block, considering Mohr-Coulomb as constitutive model of rock fractures. It should be noted that the ratio of the shear to normal stiffness of the fractures,

k_s/k_n, is assumed to be constant (1/10). It can be seen that the initial normal stiffness of the fractures has no effect on stability of 3D wedges.
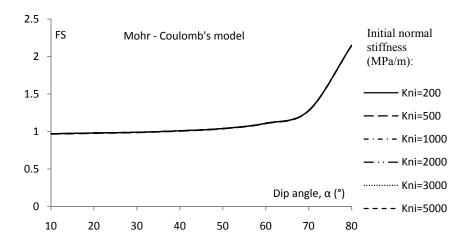
Figure 7.19: The effect of the initial normal stiffness of fractures on stability of tetrahedral rock blocks (Mohr-Coulomb's failure criterion)

The same sensivity analyses are performed adopting the original and the modified Barton's model as the constitutive model of the fractures. In these cases, the mechanical properties of the rock fractures are assumed to be $\phi_b = 25°$, $JRC = 10$, and $JCS = 20$ MPa. Therefore, the effective friction angle of the fractures is 41°:

$$\phi = JRC \cdot \tan\left(\frac{JCS}{\sigma_n}\right) + \phi_b = 10 \cdot \tan\left(\frac{20}{0.5}\right) + 25 \approx 41°$$

Figure 7.20 depicts the changes in FS of the block with the initial normal stiffness and the dip angle of the block, considering Baron's original and modified models as constitutive model of rock fractures. It can be seen that adopting Barton's original or modified model, the factor of safety of tetrahedral rock block decreases with increasing initial normal stiffness of fractures. This effect is more obvious in the case of stable blocks with dip angles greater than 50°. The reason is that, for a given displacement increment, the normal stresses decrease more quickly on stiffer fractures. The drop in

normal stress lowers the available shear strength before shear stresses become large enough to support the block [312].
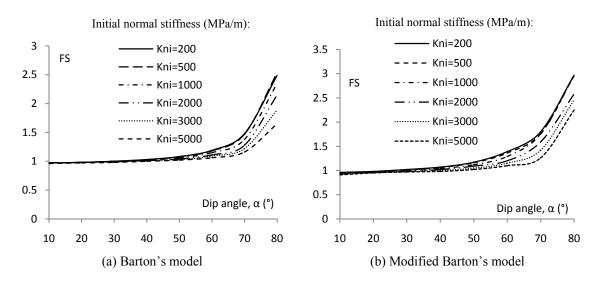
Figure 7.20: The effect of the initial normal stiffness of fractures on stability of tetrahedral rock blocks

7.3.4 Effect of fracture dilatancy on stability of tetrahedron

In order to investigate the effect of dilatancy on stability of tetrahedral rock blocks, a sensivity analysis is performed on the wedge introduced in Section 7.3.2. The mechanical properties of the rock fractures are assumed to be $\phi_b = 25°$, $JRC = 10$, and $JCS = 20$ MPa. In addition, a hydrostatic in $situ$ stress of 0.5 MPa is applied. The effects of excavation on in $situ$ stresses are not considered and it is assumed that the in $situ$ stresses around the underground opening are the same before and after excavation. The initial normal stiffness of rock block is 2000 MPa/m. The factors of safety of the wedges are calculated using BS3D adopting the following constitutive models:

- Mohr-Coulomb: Mohr-Coulomb failure criterion with effective friction angle of 41˚ and Barton's empirical equation for the peak shear displacement and

the shear stiffness (everything is the same as Barton's model except for dilation displacement which is considered to be zero).

- Barton's original model
- Modified Barton's model
- Simplified Barton's model: everything is the same as Barton's model expect for dilation displacement. It is assumed that dilation displacement at a shear displacement of δ_p is equal to $\delta_p \cdot \tan(JRC \cdot \log(JCS / \sigma_n))$. It means that dilatancy starts at zero shear displacement (origin of the shear stress-displacement curve).

Figure 7.21 depicts the factors of safety versus the dip direction of the fractures forming the tetrahedron.
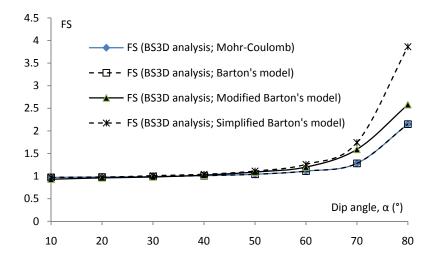
Figure 7.21: The effect of fractures dilatancy on stability of tetrahedral rock blocks

It can be seen in Figure 7.21 that the safety factors calculated using Barton's and Mohr-Coulomb models are exactly the same. The only difference between these two models is the dilation displacement. In the case of Mohr-Coulomb's model, it is assumed that dilation is zero, while in the case of Barton's model, dilation displacement is calculated as explained in Section 3.2.4. Let us explain the reason of having the same

factors of safety in the case of the wedge formed by fractures dipping 70° below horizontal. In Barton's model, it is assumed that dilation starts at 30% of the peak shear displacement. BS3D analyses (adopting Baron's model as the constitutive model of rock fractures) show that the wedge fails by loosing contact (free falling) before any face reaches 30% of its peak shear displacement; the ratio of the shear displacement at block's failure to the peak shear displacement of the fractures is 0.14. Therefore, no dilation displacement develops when adopting Baron's model. Consequently, there is no difference between the factors of safety calculated using Barton's model and Mohr-Coulomb model.

On the other hand, assuming that dilation starts from zero shear displacement (origin of the shear stress-displacement curve), the factors of safety increase comparing to those of Barton's model (or Mohr-Coulomb's model). One of the reasons is dilation displacement increases the normal forces on the face of the block and thus increases the shear strength of the fractures. Consequently, the factors of safety increase. It is found that the ratio of the shear displacement to the peak shear displacement of the fractures of the wedge is 0.21 in this case (adopting the simplified Barton's model). It means that another reason for having higher factors of safety is that more shear strength is mobilized for each fracture using the simplified Barton's model. In other words, not only the peak shear strength is higher in simplified Barton's model, but also the ratio of mobilized to peak shear strengths is larger.

Modified Barton's model uses a different equation for the peak shear displacement (Equation (3.88) instead of Equation (3.31)). In all these examples, the peak shear displacements predicted using Equation (3.88) is smaller than those estimated using Barton's empirical equation (Equation (3.31)). In addition, in the modified model, the positive dilation starts from 0.5 times the peak shear displacement. BS3D analyses show that, at block's failure, all fractures of the wedge (formed by fractures dipping 70° below horizontal) experienced a displacement equal to 30% of peak shear displacement, which caused negative dilation and decreased the normal stresses across fractures. However, the factors of safety calculated using the modified model are higher than those of the original

Barton's model because the fracture mobilized shear strength is higher in the case of the modified model. Very small negative dilation (in the order of 10^{-2} mm) causes a very small decrease in the normal stresses applied to each face (in the order of 0.05 MPa compared to 0.5 MPa due to the *in situ* stresses). Assuming 0.45 MPa as normal stress applied to each face, the mobilized shear strength of each fracture at failure can be predicted using the modified model as follows:

$$\frac{\delta_h}{\delta_{peak}} = 0.3 \rightarrow \frac{\phi_{mobilized}}{\phi_{base}} = 0.78 \quad \text{(Using Table 3.9)} \rightarrow \phi_{mobilized} = 0.78 \times 25 = 19.5°$$

$$\frac{\delta_h}{\delta_{peak}} = 0.3 \rightarrow \frac{JRC_{mobilized}}{JRC_{peak}} = 0.134 \text{(Using Table 3.10)} \rightarrow JRC_{mobilized} = 0.134 \times 10 = 13.4$$

$$\tau_{mobilized} = \sigma_n \cdot \tan\left(\phi_{mobilized} + JRC_{mobilized} \cdot \log\left(\frac{JCS}{\sigma_n}\right)\right) =$$

$$= 0.45 \times \tan\left(19.5 + 1.34 \cdot \log\left(\frac{20}{0.45}\right)\right) \approx 0.18 \quad MPa$$

However, for the case of Barton's model, the mobilized shear strength of each face can be predicated as follows:

$$\frac{\delta_h}{\delta_{peak}} = 0.14 \rightarrow \frac{JRC_{mobilized}}{JRC_{peak}} = -0.83 \text{ (Using Table 3.2)} \rightarrow JRC_{mobilized} = -0.83 \times 10 = -8.3$$

$$\tau_{mobilized} = \sigma_n \cdot \tan\left(\phi_{base} + JRC_{mobilized} \cdot \log\left(\frac{JCS}{\sigma_n}\right)\right) = 0.5 \times \tan\left(25 - 8.3 \cdot \log\left(\frac{20}{0.5}\right)\right) \approx 0.1 \quad MPa$$

This simplified calculation shows that the mobilized shear strength on each face is higher for the case of modified Barton's model. It is clear that BS3D analysis is not as simple as above and it is a complicated incremental-iterative algorithm that takes into account the interaction between the rock block and rock mass as well as the deformability of the fractures.

The same simplified calculation can show why the factor of safety of the simplified Barton's model is higher than those of Barton's model, Modified Barton's model, and Mohr-Coulomb's model. It is found that the ratio of shear displacement to the peak shear displacement of the fractures of the wedge (formed by fractures dipping 70°

234

below horizontal) is 0.21 in the case of simplified model. Assuming dilation starts from zero shear displacement and dilation displacement is $\tan\left(JRC \cdot \log\left(\dfrac{JCS}{\sigma_n}\right)\right)$ times the shear displacement; the normal displacement at failure is calculated to be in the order of 10^{-4} m. This normal displacement causes an increase in normal stress of the fracture in the order of 0.2 MPa. The mobilized shear strength of each face can be obtained as follows:

$$\frac{\delta_h}{\delta_{peak}} = 0.21 \ \rightarrow \frac{JRC_{mobilized}}{JRC_{peak}} = -0.47 \text{ (Using Table 3.2)} \rightarrow JRC_{mobilized} = -0.47 \times 10 = -4.7$$

$$\tau_{mobilized} = \sigma_n \cdot \tan\left(\phi_{base} + JRC_{mobilized} \cdot \log\left(\frac{JCS}{\sigma_n}\right)\right) = 0.7 \times \tan\left(25 - 4.7 \cdot \log\left(\frac{20}{0.7}\right)\right) \approx 0.23 \quad MPa$$

Therefore, the mobilized shear strength predicted using the simplified Barton's model is higher than those predicted employing Barton's model and the modified model. Thus, the factor of safety is higher.

7.3.5 Effect of size of the tetrahedron on its stability

In order to investigate the effect of size of the tetrahedron on its stability, a sensivity analysis is performed. The above introduced tetrahedron formed by fractures dipping 60° below horizontal is considered. The height of the block is changed from 1 to 10 m and the factors of safety are calculated. The mechanical properties of the rock fractures are assumed to be $\phi_b = 25°$, JRC = 10, and JCS = 20 MPa. In addition, a hydrostatic *in situ* stress of 0.5 MPa is applied. The effects of excavation on *in situ* stresses are not considered and it is assumed that the *in situ* stresses around the underground opening are the same before and after excavation. The initial normal stiffness of rock block is 2000 MPa/m. The factors of safety of the wedges are calculated using the analytical approach (with Mohr-Coulomb's model) as well as employing BS3D adopting the following constitutive models: (1) Mohr-Coulomb with effective friction angle of $\phi_b + JRC \cdot \log(JCS / \sigma_n)$; (2) Barton's original model; (3) Modified Barton's model; and (4) Simplified Barton's model (dilatancy starts at zero shear displacement)

Figure 7.22 depicts variation of the factor of safety with height of tetrahedron formed by fractures dipping 60˚ below horizontal. It can be seen that the factor of safety decreases with increasing size of the wedge. The reasons are as follows:

- The weight of the block increases with increasing height of the block and therefore active forces increase.

- The length of the block in shearing direction increases with size of the wedge. Therefore, the scaled *JRC* obtained from Equation (3.5) decreases with the size of the block which in turn causes a decrease in the shear strength of the fractures. Consequently, the factor of safety decreases with the size of the block.
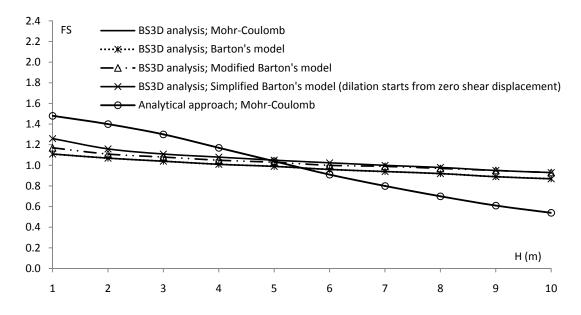
Figure 7.22: FS versus height of tetrahedron formed by 3 fractures dipping 60˚ below horizontal

7.3.6   Effect of changes in *in situ* stress due to excavation on stability of tetrahedron

In the all above analysis, the effects of excavation on *in situ* stresses were not considered and it was assumed that the *in situ* stresses around the underground opening

236

are the same before and after excavation. This assumption was made to be able to simplify the analytical limit equilibrium analysis and to be able to compare its results with those of BS3D analyses. In this Section, the effect of excavation on *in situ* stresses around a circular tunnel is investigated to find how it affects the stability of a wedge formed in the roof of the tunnel.

The above introduced tetrahedron formed from fractures dipping 60° below horizontal is considered. The height of the block is 1 m. The mechanical properties of the rock fractures are assumed to be $\phi_b = 25°$, *JRC* = 10, and *JCS* = 20 MPa. In addition, a hydrostatic *in situ* stress of 0.5 MPa is assumed to be applied prior to excavation. It is assumed that a circular tunnel with a radius changing from 1 to 10 m is excavated and the *in situ* stress condition is modified accordingly. The initial normal stiffness of rock block is 2000 MPa/m. The factors of safety of the wedges are calculated using BS3D adopting different constitutive models. Figure 7.23 depicts variation of the factor of safety with the radius of the circular tunnel.
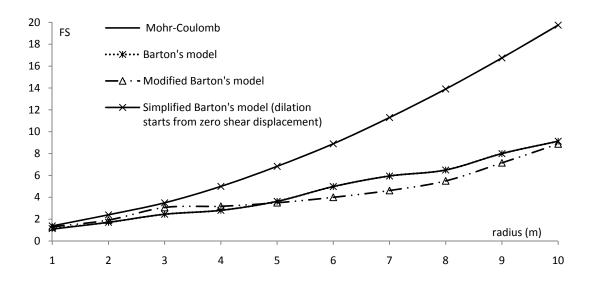
Figure 7.23: FS versus the radius of the circular tunnel (tetrahedron formed by 3 fractures dipping 60° below horizontal with height of 1 m)

It can be seen that the factor of safety of the wedge increases with increasing the radius of the circular tunnel because the normal forces applied to each face of the wedge increases with increasing radius of the tunnel. Assume that the rock mass is subjected to hydrostatic state of stress with magnitude of P. The stress tensor after excavating a circular tunnel with radius of r at distance a from the center of the tunnel can be determined as follows (plane strain conditions) [313-315]:

$$\frac{\sigma_r}{P} = \left(1 - \frac{a^2}{r^2}\right) \; ; \; \frac{\sigma_\theta}{P} = \left(1 + \frac{a^2}{r^2}\right); \sigma_z = \sigma_{z_0}; \tau_{r\theta} = \tau_{rz} = \tau_{\theta z} = 0, \tag{7.28}$$

where σ_r and σ_θ are radial and tangential component of stress. These components are the only ones that are affected by excavation. The *in situ* stresses around circular tunnel of radius 1 to 10 m are calculated using Equation (7.28). Then, the normal stresses applied to each face of the wedge are calculated. Figure 7.24 depicts variation of the ratio of the average normal stress applied to each fracture to the magnitude of the *in situ* hydrostatic pressure with radius of the circular tunnel.

It can be seen in Figure 7.24 that the normal stress applied to each face increases with increasing radius of the tunnel, which in turn causes an increase in the normal forces applied to each face.
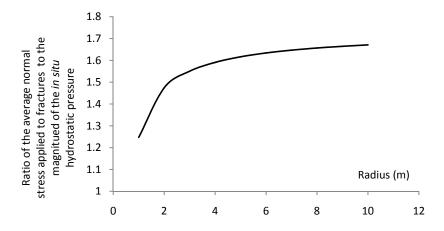
Figure 7.24: Variation of the ratio of the average normal stress applied to each fracture to *in situ* hydrostatic pressure with radius of the circular tunnel

7.4   Sᴛᴀʙɪʟɪᴛʏ ᴏғ ᴀ ᴘʀɪsᴍ ɪɴ ᴛʜᴇ ʀᴏᴏғ ᴏғ ᴀ ᴄɪʀᴄᴜʟᴀʀ ᴛᴜɴɴᴇʟ

Yow and Goodman [312] presented a numerical model for keyblock stability. Using the field observations of keyblocks reported by Yow [316], they performed sensivity analyses on effects of different parameters such as block geometry, *in situ* stresses, and discontinuity properties on stability of keyblocks. In their study, they defined the factor of safety as follows:

$$FS = 1 - F/W, \qquad\qquad (7.29)$$

in which F is the resultant of all forces (including the block weight) with positive upward direction; and W is the keyblock weight (a negative force). The factor of safety is equal to one when the block is at limiting equilibrium. For stable blocks, the factor of safety is higher than one; for unstable blocks, the factor of safety is smaller than one and can be negative. It can be seen that this definition is deferent from what Bray [306] and Sofianos [307] introduced as a safety factor. It is also different from the definition of the factor of safety in BS3D and the proposed factors of safety in this Section 7.3 (Equations (7.12) and (7.27)).

As far as constitutive model for rock fractures, Yow and Goodman [312] used Barton's model assuming that the peak shear displacement is equal to one percent of the length of the block. They investigated the effect of the fracture base friction angle, the magnitudes of *JRC* and *JCS*, the initial normal stiffness, the magnitude of vertical stress, and the lateral pressure coefficient on stability of keyblocks in the roof of a circular tunnel.

In this Section, the same sensivity analyses are performed using BS3D. The differences of the analyses done here with respect to those of Yow and Goodman [312] are as follows:

- The definition of the factor of safety is different.
- The progressive failure along rock fracture is considered.
- Wider ranges of parameters are checked.
- Different constitutive models for rock fractures are adopted.
- The effect of dilation displacement on the stability of the block is investigated.

239

- The effect of principal stress direction on the stability of the block is investigated.

- The effects of distance from the excavation face, the size of the block, and the diameter of the tunnel on the stability of the keyblock are investigated.

7.4.1 Problem statement

The parametric study simulates a symmetrical three-dimensional keyblock in a horizontal tunnel with a radius of 1.8 m. The radius from the tunnel centerline to the block apex is equal to 2.4 m. Figure 7.25 depicts the typical geometry of pyramidal keyblock in the roof of a circular tunnel. Each discontinuity forming a block face dips at 60˚ below horizontal, and fracture apertures for negligible normal stress are equal to 1 mm. *In situ* principal stresses prior to excavation of the tunnel are assumed to act vertically and horizontally with lateral pressure coefficient equal to one (hydrostatic state of stress). The vertical (horizontal) stress is equal to 3.45 MPa. The unit weight of the rock block is assumed to be equal to 27 kN/m^3. The mechanical properties held fixed in the parametric analyses are summarized in Table 7.1.
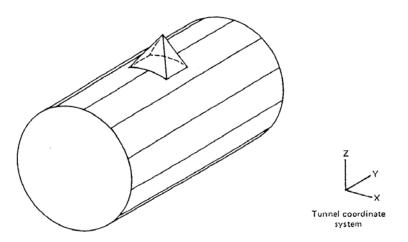
Figure 7.25: Typical geometry of pyramidal keyblock [312].

240

Table 7.1: Mechanical properties held fixed in the parametric analyses

Parameter	Value
Young's modulus of the rock block	30,000 MPa
Poisson's ratio of the rock block	0.26
Young's modulus of the rock mass	12,000 MPa
Maximum closure of the fractures	0.75 mm

Based on Yow 's and Goodman's [312] analysis, the factor of safety of this prism is 5.1. As the constitutive model of rock fractures, they adopted the old version of Barton's model in which the peak shear displacements of fractures are predicted to be one hundredth of the length of the block in the shearing direction. BS3D analyses are performed to obtain the factor of safety of the prism with choosing different constitutive models for the fractures. The results are as follows:

- Mohr-Coulomb's model (Barton's model excluding dilation): FS = 3.92

- Barton's model: FS = 4.04

- Modified Barton's model: FS = 3.35

- Simplified Barton's model (dilation starts from the origin of shear stress-displacement curve): FS = 4.3

- Old Barton's model (peak shear displacement = block length / 100): FS = 3.59

It can be seen even using the old Barton's model the factor of safety calculated using BS3D is different from the result of Yow 's and Goodman's [312] analysis. The reason is that the definition of the factor of safety is different and BS3D considers the progressive failure of the fractures, while Yow 's and Goodman's [312] analyses do not.

In addition, in BS3D analyses, the factor of safety calculated using simplified Barton's model (dilation starts from zero shear displacement) is the highest, followed by those determined using Barton's model, Mohr-Coulomb's model, and the modified Barton's model. As it was explained before, the Mohr-Coulomb's model, the Barton's model, and the simplified Barton's model used in our sensivity analyses are exactly the same except for the dilation displacement. The simplified Barton's model has the highest

dilation displacement and, thus, the highest normal forces applied to the fractures, the highest shear strength of discontinuities, and the highest factor of safety. The modified Barton's model differs from Barton's model in terms of the peak shear displacement, the mobilized shear strength, and the dilatancy behavior. Therefore, the factor of safety calculated using the modified Barton's model is different (smaller for this prism) from those obtained employing the Barton's model.

7.4.2 Parametric study (sensivity analyses)

Yow and Goodman [312] performed sensivity analyses on the effect of the following parameters on stability of a keyblock (the above defined prism):

- The shear strength of discontinuities:
  - o dilatancy components:
    - *JRC*
    - *JCS*
  - o Base friction angle
- The discontinuity initial normal stiffness
- *In situ* stress condition: vertical stress and lateral pressure coefficient

In this Section, parametric studies are performed employing BS3D and adopting five different fracture constitutive models, defined as follows: (1) Mohr-Coulomb's model (Barton's model excluding dilation); (2) Barton's model; (3) Modified Barton's model; (4) Simplified Barton's model (dilation starts from zero shear displacement); (5) Old Barton's model (peak shear displacement = length of the block / 100)

In addition to the effect of parameters investigated by Yow and Goodman [312], the following senivity analyses are performed in this Section:

- Effect of principal stress directions
- Effect of distance from excavation face
- Effect of the tunnel radius

Yow's and Goodman's [312] sensivity analysis on the effect of stresses and loads on stability of keyblocks was limited to investigating the effect of vertical stress and lateral pressure coefficient. In all cases, they assumed that the principal stress directions are vertical and horizontal. However, the principal stress directions may not be vertical and horizontal. In engineering applications, an easy method to estimate the *in situ* stress condition is to evaluate the vertical stress by multiplying the depth to the unit weight of the rock mass and estimate the lateral pressure coefficient from values available in the literature. More expensive and time-consuming methods can be employed to measure the values of *in situ* stresses and obtain the stress tensor (i.e. the principal stresses and their directions) [310]. Therefore, in order to see whether these expensive time-consuming methods are necessary or not, the effect of principal stress directions on keyblock stability is also investigated in this Section.

Figure 7.26 depicts the global reference system (*x*-axis is parallel to the tunnel axis and *z*-axis is vertical and directed unpward). Table 7.2 summarizes the sensivity analyses performed in this Section.
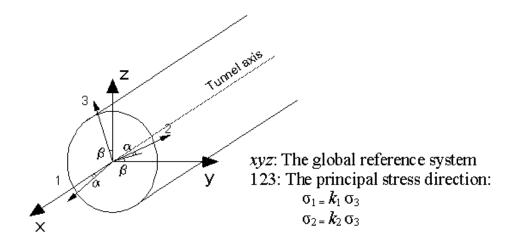
Figure 7.26: Principal stress directions and the global reference system

243

Table 7.2: Summary of parametric studies (effect of different parameters on stability of the prism)

Investigating Effect of …	Type of analyses	JRC	JCS (MPa)	ϕ_b (°)	k_{ni} (MPa)	Stress condition prior to excavation					r^{**} (m)	D^{***} (m)	Figures	Relative influence on stability / Decreasing the parameter from The given max to min changes FS by…. ****
						k_1	k_2	σ_3	α					
JRC	YG*	0 – 5	20.69	25	0.1	3.45	3.45	3.45	0	0	1.8	Far	Figure 7.27	Very strong / decreases 100%
	BS3D	0 – 20			2									Weak / decreases 30%
JCS	YG*	4	4 – 20	25	0.1	3.45	3.45	3.45	0	0	1.8	Far	Figure 7.28	Strong / decreases 75%
	BS3D		5 – 100		2									Weak / decreases 5%
ϕ_b	YG*	4	20.69	21 – 25	0.1	3.45	3.45	3.45	0	0	1.8	Far	Figure 7.29	Strong / decreases 88%
	BS3D			20 – 40	2									Strong / decreases 42%
k_{ni}	YG*	4	20.69	25	0.1 – 2.5	3.45	3.45	3.45	0	0	1.8	Far	Figure 7.30	Weak / increases 48%
	BS3D				0.15 - 5									Weak / increases 16%
Vertical stress (tunnel depth)	YG*	4	20.69	25	0.1	0.5	0.5	0 – 6	0	0	1.8	Far	Figure 7.31	$\sigma_3<$1.5MPa: Strong/decreases 86% / $\sigma_3>$1.5MPa: weak/decreases 13%
	BS3D				2			0 - 27						$\sigma_3<$1.5MPa: Strong/decreases 90% / $\sigma_3>$1.5MPa: weak/decreases 27%
Lateral pressure Coefficient (K_0)	YG*	4	20.69	25	0.1	0.3 - 2		3.45	0	0	1.8	Far	Figure 7.32	$K_0<$0.5: Strong / decreases 76% / $K_0>$0.5: Weak / decreases 20%
	BS3D				2	0.15 - 4								$K_0<$0.5: Strong / decreases 90% / $K_0>$0.5: Weak / decreases 6%
Principal stress direction	BS3D	4	20.69	25	2	1.5	0.5	3.45	0 - 90	0 - 90	1.8	Far	Figure 7.33	Very strong
Distance from excavation face	BS3D	4	20.69	25	2	3.45	3.45	3.45	0	0	1.8	0.5 - 20	Figure 7.34	D < 5r: Strong / decreases 35% / D > 5r: Not effective
Tunnel radius	BS3D	4	20.69	25	2	3.45	3.45	3.45	0	0	1 – 10	Far	Figure 7.35	Strong / decreases 76%

* Yow's and Goodman's analyses

** The tunnel radius

*** Distance from the excavation face

**** In the cases of BS3D analyses, percentages of changes in FS are reported from analyses performed using Modified Barton's model.
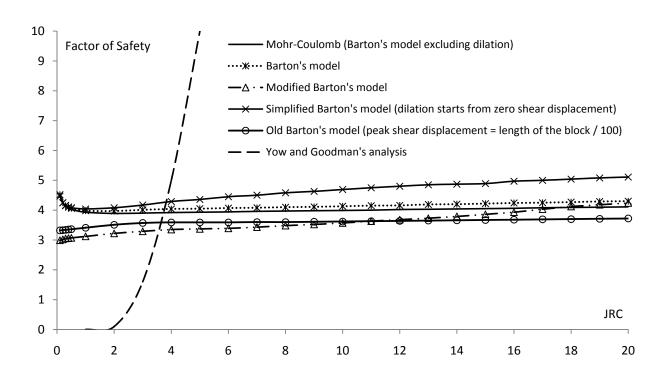
Figure 7.27: Variation of FS of the prism with Joint Roughness Coefficient (*JRC)*
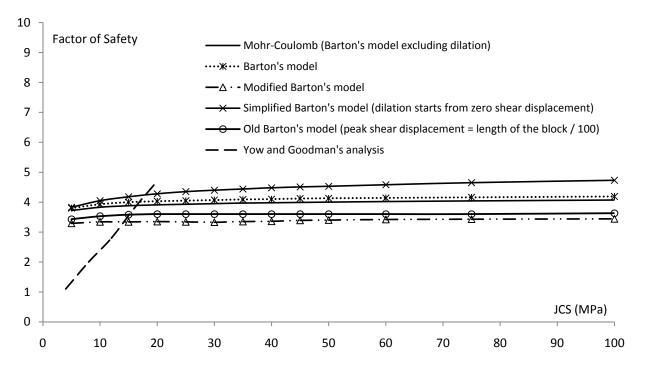
Figure 7.28: Variation of FS of the prism with Joint Compressive Strength (*JCS)*
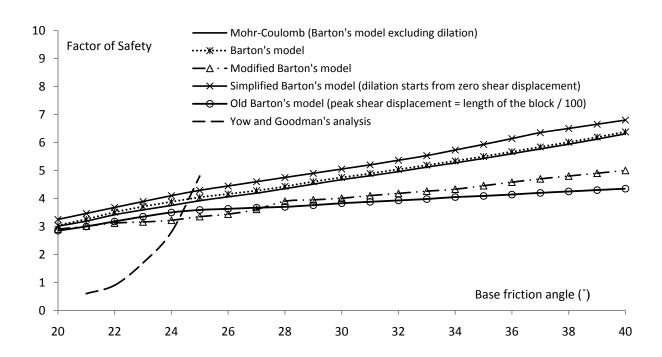
Figure 7.29: Variation of FS of the prism with the base friction angle
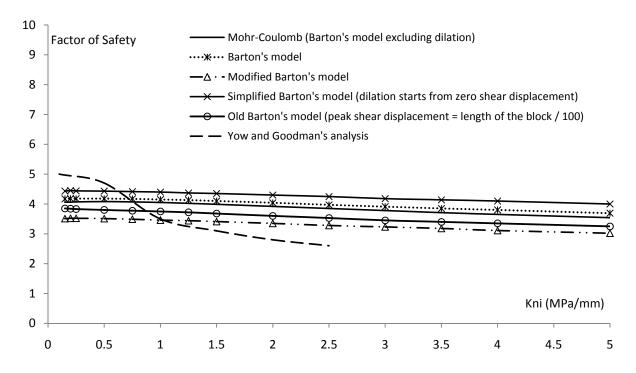
Figure 7.30: Variation of FS of the prism with fracture initial normal stiffness

246
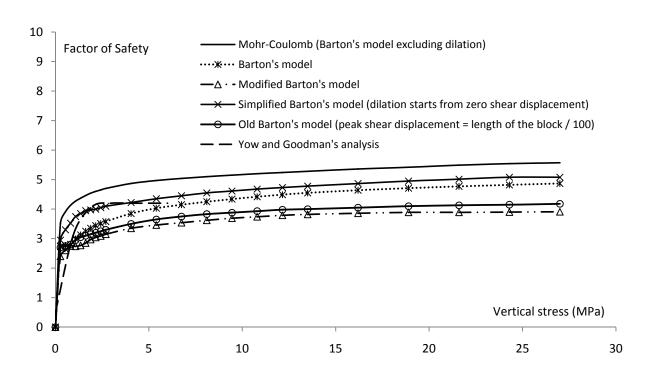
Figure 7.31: FS of the prism versus vertical stress with 0.5 lateral stress ratio
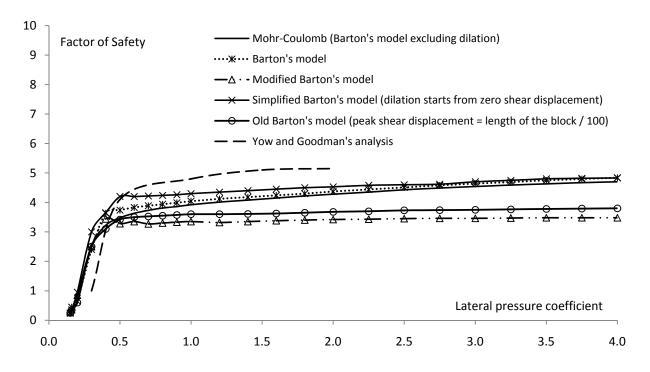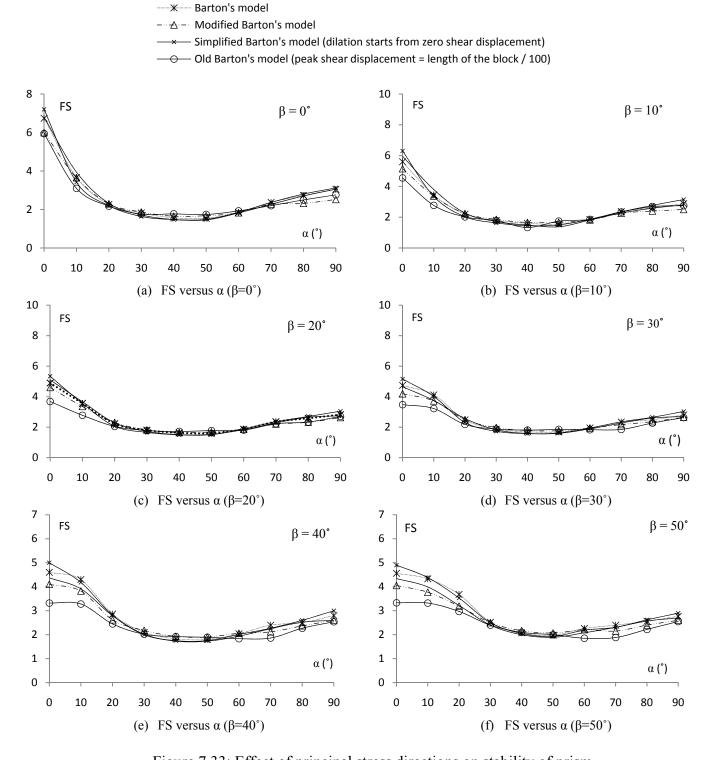
Figure 7.32: FS of the prism versus lateral pressure coefficient at a constant *in situ* vertical stress of 3.45 MPa

Mohr-Coulomb (Barton's model excluding dilation)
Barton's model
Modified Barton's model
Simplified Barton's model (dilation starts from zero shear displacement)
Old Barton's model (peak shear displacement = length of the block / 100)

(a) FS versus α (β=0°)

(b) FS versus α (β=10°)

(c) FS versus α (β=20°)

(d) FS versus α (β=30°)

(e) FS versus α (β=40°)

(f) FS versus α (β=50°)

Figure 7.33: Effect of principal stress directions on stability of prism

Mohr-Coulomb (Barton's model excluding dilation)
Barton's model
Modified Barton's model
Simplified Barton's model (dilation starts from zero shear displacement)
Old Barton's model (peak shear displacement = length of the block / 100)

(g) FS versus α (β=60˚)

(h) FS versus α (β=10˚)

(i) FS versus α (β=20˚)

(j) FS versus α (β=30˚)

(k) FS versus angles α and β (Mohr-Coulomb's model)

Figure 7.33-Continued: Effect of principal stress directions on stability of prism

249
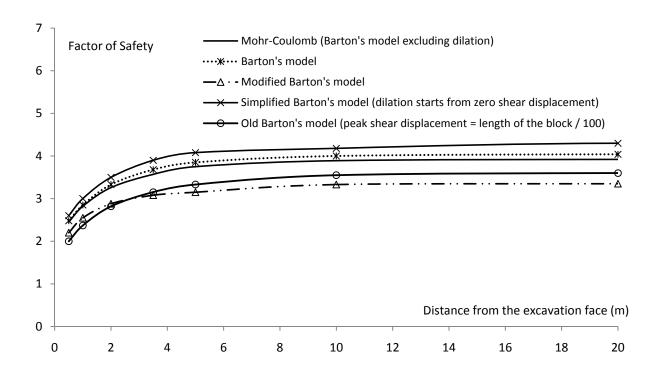
Figure 7.34: FS versus distance from the excavation face
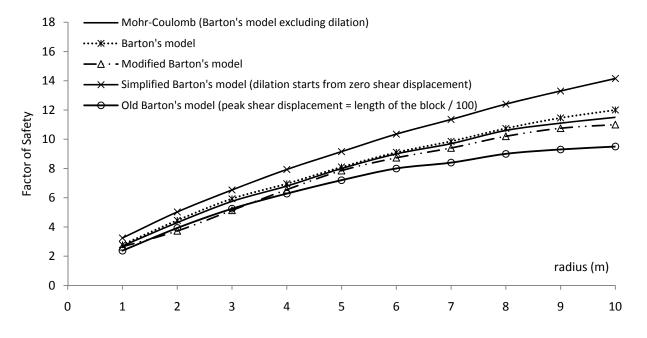
Figure 7.35: FS versus radius of the tunnel for a prism

250

The following conclusions can be made based on comparison between the sensivity analyses performed in this Section using BS3D and Yow's and Goodman's [312] analyses (all depicted in Figure 7.27 through Figure 7.33):

1) Effect of *JRC* on stability of the prism (Figure 7.27):

   a. The stability of the prism weakly depends on *JRC* (decreasing *JRC* from 5 to 0 decreases FS by 100%). However, Yow and Goodman [312] found that the block stability strongly (decreasing *JRC* from 20 to 0 decreases FS by 30%) depends on *JRC*.

      The Barton's model, the simplified Barton's model, and the Mohr-Coulomb's model have counterintuitive behavior for very small *JRC*'s. Increasing *JRC* from 0 to 1, the factors of safety decrease instead of increasing. The peak shear displacements are predicted using Barton's empirical equation (Equation (3.31)), which predicts zero shear displacement for sawed fractures (*JRC* = 0). If *JRC* goes to zero, the predicted shear displacement goes to zero. Thus, the shear stiffness (the ratio of shear strength to the peak shear displacement) goes to infinity. It is not possible to perform a BS3D analysis with *JRC* = 0, using Barton's model, old Barton's model, or Mohr-Coulomb's model because these constitutive relationships would return a "division by zero" runtime error. For *JRCs* close to zero, the very high values of the shear stiffness of the fractures cause some numerical issues in the calculations. In Barton's empirical equation for the peak shear displacement (Equation (3.31)), $JRC^{0.33}$ is in numerator. Consequently, the shear stiffness of the fractures changes with $1/JRC^{0.33}$. Figure 7.36 depicts changes in $1/JRC^{0.33}$ with *JRC*, which can represent changes in the shear stiffness with *JRC*. For *JRC* smaller than one, $1/JRC^{0.33}$ decreases rapidly with *JRC* and does not change dramatically for higher values of *JRC*. In analyses, BS3D assumes that the fractures are very stiff and with small shear displacements, it predicts high shear strength.
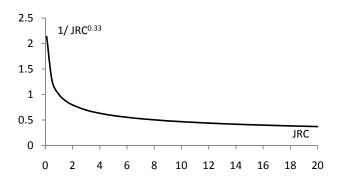
Figure 7.36: Variation of $1/JRC^{0.33}$ with JRC

Figure 7.36 shows that the rate of the changes in the fracture shear stiffness for very small $JRCs$ ($JRC<1$) is different from the rest of the domain. This problem was one of the reasons that modifications were proposed in Chapter 3 to Barton's empirical model.

2) Effect of JCS on stability of the prism (Figure 7.28):

   a. Yow and Goodman [312] found that the effect of JCS on the stability of the prism is not as strong as that of JRC, but it is quite effective. JCS reflects the strength of the discontinuity asperities; a higher JCS value implies that fewer asperities fail during shearing and that more asperities must be overridden.

   b. BS3D analyses found that the stability of the prism weakly depends on JCS.

   c. The FS flattens out after a specific value of JCS, which depends on other aspects of the problem because the asperities does not fail and increasing JCS almost has no effect on the stability of the block.

3) Effect of base friction angle on stability of the prism (Figure 7.29):

   a. Yow and Goodman [312] found that the base friction angle is quite effective on the stability of keyblocks. However, its effect is not as strong as that of JRC because the base friction angle affects only the available shear strength

while dilatancy (expressed in terms of *JRC*) affects both shear strength and the normal stress brought about by fracture closure.

b. BS3D analyses show that the factor of safety of the prism increases with the base friction angle.

4) Effect of fracture normal stiffness on stability of the prism (Figure 7.30):

a. Yow and Goodman [312] found that stability decreases as normal stiffness increases because, for a given displacement increment the normal stresses change more quickly on stiffer discontinuities. The drop in normal stress lowers the available shear strength before the shear stresses become large enough to support the block.

b. BS3D analyses show that the factor of safety of the prism decreases with the initial stiffness of the fractures. Figure 7.37 depicts the trade-off between smaller normal displacements and normal stresses (initial normal stiffness ranges between 200 and 5000 MPa/m). It depicts normal stresses and normal displacements of a face of the prism versus λ (incremental step) for BS3D analyses performed using Barton's model.
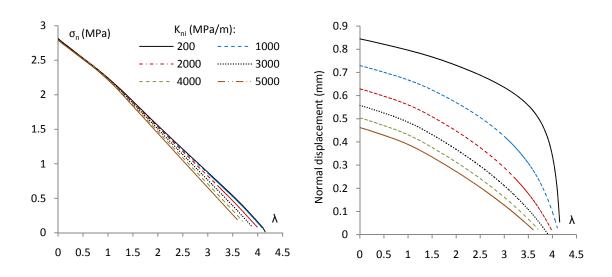
Figure 7.37: Trade-off between smaller normal displacements and normal stresses (Barton's model)

253

Figure 7.37 shows that the normal stresses change more quickly on stiffer discontinuities (the same as Yow and Goodman's [312] statement). Thus, the quicker drop in normal stress decreases more rapidly the fracture shear strength. Consequently, the stiffer the fractures is, the lower is the safety factor of the block.

Moreover, Figure 7.38 illustrates the magnitude of centroid displacement at failure versus the initial normal stiffness obtained using BS3D. It shows that for all models failure occurs at a smaller vertical displacement when the initial stiffness increases.
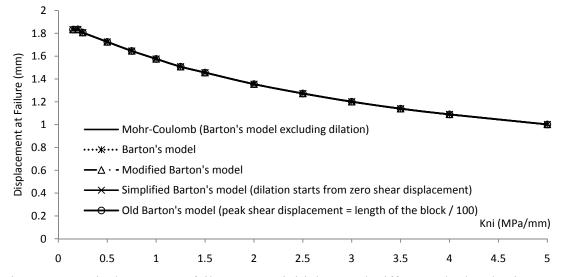
Figure 7.38: Displacement at failure versus initial normal stiffness calculated using BS3D

5) Effect of *in situ* stress condition of the prism (Figure 7.31 through Figure 7.33):

a. Yow and Goodman [312] found that aside from the shear strength, the most critical condition affecting keyblock stability is the stress environment. The block becomes less stable as the initial confining stresses decrease; the trend accelerates as stress magnitudes become very small (smaller than about 1.5 MPa). The same conclusion has been made based on BS3D analyses.

b. Yow and Goodman [312] found that the block becomes less stable as the lateral stress ratio decreases; the trend accelerates as the ratio goes below

about one-half. The same conclusion has been made based on BS3D analyses.

c. In this Section, another sensivity analysis was performed to investigate the effect of principal stress directions on stability of the prism (the stress tensors in the global reference system of

Figure 7.26 are given in Appendix F). It is found that the principal stress directions strongly affect the stability of keyblocks.

d. It can be concluded that the *in situ* stresses strongly affect the stability of the block, even more than the shear strength of fractures (Figure 7.33 versus Figure 7.27 through Figure 7.29). However, the actual stress field in the rock mass surrounding the excavation is not taken into account in the default Unwedge [317] analysis which is based upon the assumption that the wedges are subjected to gravitational loading only.

6) Effect of distance from excavation face of the prism (Figure 7.34): the factor of safety increases with distance from excavation face up to approximately five times the tunnel radius.

7) Effect of the tunnel radius on stability of the prism (Figure 7.35): the factor of safety of the prism increases with increasing tunnel radius. The same observation was found in Section 7.3.6 (Figure 7.23 shows that the safety factor of the tetrahedron increases with increasing the tunnel radius). The reason is that the normal forces applied to fractures increase with increasing diameter (the reason is explained in details in Section 7.3.6).

8) General comments (Figure 7.27 through Figure 7.35):

a. Because of different dilation displacements, the factors of safety obtained using the simplified Barton's model are higher than those calculated using the Barton's model, which is higher than those determined employing the Mohr-Coulomb model. The higher the dilation displacements are, the

higher are the normal forces applied to the fractures, the shear strength of the fractures, and, finally, the factor of safety of the block.

b. The modified Barton's model and the old Barton's model may yield smaller or higher factors of safety compared the other models.

7.4.3 Effect of size of the block on stability of a prism

In order to investigate the effect of keyblock size on its stability, three sensivity analyses are performed. The analyses consider prisms that may be formed by four fractures dipping 60° below horizontal with $JRC = 4$, $JCS = 20.69$ MPa, and $\phi_b = 25°$. A hydrostatic stress field prior to excavation is assumed with a stress magnitude of 3.45 MPa. BS3D analyses were performed adopting five different fracture constitutive models and the factors of safety were calculated. The sensivity analyses are as follows:

1) Assuming constant tunnel radius (10 m), the height of the prism was changed between 0.5 and 10 m (Figure 7.39). The factor of safety of the block decreases with increasing size of the prism. The reasons are: (a) the weight of the block increases with its height and (b) the scaled JRC and therefore the shear strength of the block fractures decreases with increasing size of the block.
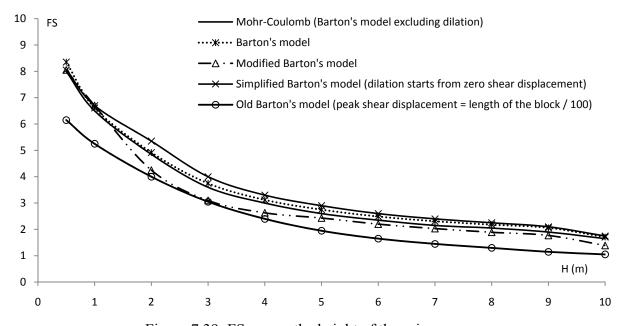
Figure 7.39: FS versus the height of the prism

256

It should be noted that the area of the faces increases with increasing height of the prism. However, this increase in the area increases the area on which both normal stresses and shear stresses are applied and, thus, increases both the normal forces and shear forces applied to the faces. Therefore, increases in the area of the faces may have negligible effect on stability of the prism.

In addition, increasing height of the prism increases its volume (and in turn its weight) more than the area of the faces. Figure 7.40 depicts the prism considered in this parametric study ($\alpha = 60°$ in this Section). The area of each triangular face can be determined as follows:

$$Area = \frac{a \cdot b}{2} = \frac{\left(\frac{2b}{\tan(\beta)}\right) \cdot b}{2} = \frac{b^2}{\tan(\beta)} = \frac{(H \cdot \sin(\alpha))^2}{\tan(\beta)} = \frac{\sin^2(\alpha)}{\tan(\beta)} \cdot H^2$$

Therefore, the area of each triangular face is proportional to square of prism height. However, the volume of the prism can be calculated as follows:

$$Volume = \frac{a^2 \cdot H}{3} = \frac{\left(\frac{2b}{\tan(\beta)}\right)^2 \cdot H}{3} = \frac{4(H \cdot \sin(\alpha))^2 \cdot H}{3\tan^2(\beta)} == \frac{4\sin^2(\alpha)}{3\tan^2(\beta)} \cdot H^3$$

Thus, the volume (and in turn the weight) of the prism is proportional to cube of prism height. Consequently, increasing the prism's height increases the weight more than the area of the faces, which means that the active forces increase more than passive forces. As a consequence, the factor of safety decreases.
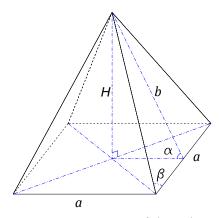
Figure 7.40: Geometry of the prism

2) The tunnel radius and the block height were changed with a same scale. The analysis considers prisms with a height equal to 1/3 of radius of the tunnel. The results shown in Figure 7.41 indicate that the factor of safety of the block decreases (by 20%) with increasing radius of the tunnel (from 1 to 10 m) and size of the prism accordingly. The change is very small. This is the combination effect of the tunnel radius (which increases the FS) and the size of the block (which decrease the FS).
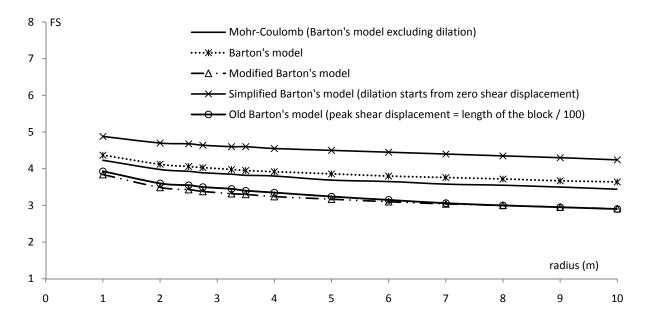
Figure 7.41: FS versus the tunnel radius for the prism with height equal to 1/3 of the tunnel radius

3) The tunnel radius was changed (from 1 to 10 m) and the stability of the maximum block formed from four fractures dipping 60° below horizontal was investigated. As illustrated in Figure 7.42, the factor of safety of the maximum block remains almost constant with increasing tunnel radius. This is the combination effect of the tunnel radius (which increases the FS) and the size of the block (which decreases the FS).

258
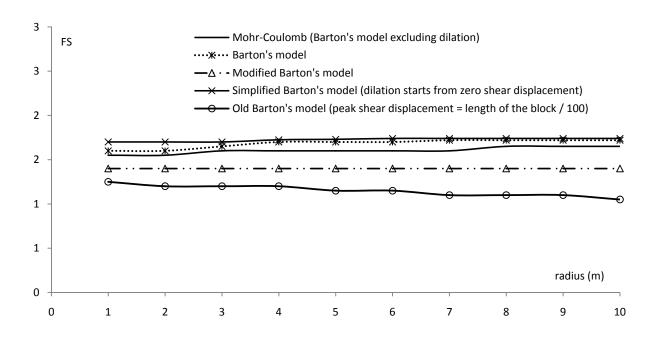
Figure 7.42: FS versus the tunnel radius for the maximum prism

7.5   SUMMARY AND CONCLUSIONS

An analytical method has been presented for stability analysis of 2D triangular prism formed in the roof of a circular tunnel from References [20, 235, 306-310]. In addition, a new definition for the factor of safety of the block is presented in this Chapter. Based on sensivity analyses, the following conclusions were made:

1) Different FS definitions may lead to different conclusions in sensivity analyses.

2) Adopting Equation (7.1) as the definition of the FS, it is found that the tendency for the prism to be expelled from the surface is exacerbated for high values of k_s / k_n. However, defining the FS as given in Equation (7.12), it is found that the stability of 2D triangular wedge is independent of the ratio of k_s / k_n.

3) Stability of 2D wedge is strongly affected by the friction angle of the fractures.

4) Adopting Equation (7.12) as the definition of the FS, it is found that increasing the *in situ* stress (or lateral pressure coefficient) slightly increases the stability of the block in low stress (or k_0) regimes and has no effect on the factor of safety in

259

high stress (or k_0) regimes. However, the sensivity analyses performed based on the definition of FS given by Equation (7.1) leads to the following conclusions: for a friction angle equal to the semi-apical angle, the vertical stress (or lateral pressure coefficient) has no effect on the stability of the block; for a friction angle smaller than the semi-apical angle, the FS of the block increases (the stability decreases) with increasing the vertical stress (or lateral pressure coefficient); and for a friction angle more than the semi-apical angle, the FS of the block decreases (the stability increases) with increasing the vertical stress.

Based on the above mentioned conclusions obtained from senivity analyses, one may say that although the definition of the factor of safety given in Equation (7.1) is not wrong, it may lead to incorrect conclusions in sensivity analyses. In addition, FS introduced in Equation (7.12) is limited to positive values, the same as most geotechnical engineering (and civil engineering) applications: at equilibrium, FS=1 for stable blocks, FS > 1, and for unstable blocks, $0 <$ FS < 1. Consequently, it is believed that Equation (7.12) can define the factor of safety of a 2D symmetric prism better than Equation (7.1).

An analytical approach was presented using limit equilibrium methods to analyze the stability of a tetrahedron formed in the roof of a tunnel. Two different definitions were introduced to calculate the factor of safety of the wedge. The following definition is adopted in the analytical analyses performed in this Chapter: the factor of safety is defined as the ratio of passive to active forces (or the ratio of available shear strength to the required shear stress at equilibrium).

The sensivity analyses performed using the analytical approach and BS3D have the following conclusions:

1) Although the definition of the factor of safety (Equation (7.27)) in the analytical method is the same as the definition of the factor of safety in BS3D, if a block is analyzed using both approaches, the factors of safety will be different because:

260

- BS3D takes into account the deformability of the rock block, fractures, and the rock mass surrounding the block, while the analytical approach (Equation (7.27)) does not.
- BS3D considers the progressive failure and the mobilization of shear strength, while the analytical limit equilibrium method does not.
- In analytical limit equilibrium solution, the *in situ* stresses are assumed to be independent of the block displacement. However, in BS3D analysis, the part of the *in situ* stresses applied to the block change with block movement.

2) Adopting Mohr-Coulomb as constitutive model of fractures, the initial normal stiffness of the fractures (and in turn the normal stiffness of the fractures) has no effect on stability of 3D wedges.

3) Adopting Barton's original or modified model, the factor of safety of tetrahedral rock block decreases with increasing initial normal stiffness of fractures. This effect is more obvious in the case of stable blocks with dip angles greater than 50˚.

4) The safety factors calculated using the Barton's model and the Mohr-Coulomb model are exactly the same, if the shear displacements of fractures are smaller than 30% of the peak shear displacement.

5) Assuming that dilation starts from zero shear displacement (origin of the shear stress-displacement curve), the factors of safety increase compared to those of Barton's model (or Mohr-Coulomb's model).

6) Modified Barton's model uses a different equation for the peak shear displacement (Equation (3.88)) and has a different FS (higher in the case of the tetrahedron analyzed in this Chapter) compared to those of other models.

7) The factor of safety decreases with increasing size of the wedge.

Yow and Goodman [312] presented a numerical model for keyblock stability. Using the field observations of keyblocks reported by Yow [316], they performed sensivity analyses on effects of different parameters such as block geometry, *in situ* stresses, and discontinuity properties on stability of keyblocks. As far as constitutive

261

model for rock fractures, Yow and Goodman [312] used Barton's model assuming the peak shear displacement is equal to one percent of the length of the block. They investigated the effect of the fracture base friction angle, the magnitudes of *JRC* and *JCS*, the initial normal stiffness, the magnitude of vertical stress, and the lateral pressure coefficient on stability of keyblocks in the roof of a circular tunnel. In this Chapter, the same sensivity analyses are performed using BS3D. The differences of the analyses done here with respect to those of Yow and Goodman [312] is as follows:

- The definition of the factor of safety is different.
- The progressive failure of rock fracture is considered.
- Wider ranges along parameters are checked.
- The analyses are performed adopting different constitutive models for rock fractures.
- The effect of dilation displacement on the stability of the keyblock is investigated.
- The effect of principal stress direction on the stability of the keyblock is investigated.
- The effects of distance from the excavation face, the size of the block, and the diameter of the tunnel on the stability of the keyblock are investigated.

The sensivity analyses performed in this Chapter have the following conclusions:

1) Even using the old Barton's model the factor of safety calculated using BS3D is different from the result of Yow 's and Goodman's [312] analysis. The reason is that the definition of the factor of safety is different and BS3D considers the progressive failure of the fractures, while Yow 's and Goodman's [312] analysis does not.

2) In BS3D analyses, the factor of safety calculated using simplified Barton's model (dilation starts from zero shear displacement) is the highest, followed by those determined using Barton's model, Mohr-Coulomb's model, and the modified Barton's model. As it was explained before, the Mohr-Coulomb's

262

model, the Barton's model, and the simplified Barton's model used in our sensivity analyses are exactly the same except for the dilation displacement. The simplified Barton's model has the highest dilation displacement and, thus, the highest normal forces applied to the fractures, the highest shear strength of discontinuities, and the highest factor of safety.

3) The modified Barton's model differs from Barton's model in terms of the peak shear displacement, the mobilized shear strength, and the dilatancy behavior. Therefore, the factor of safety calculated using the modified Barton's model is different (smaller for this prism) from those obtained employing the Barton's model.

4) The stability of the prism weakly depends on *JRC* (decreasing *JRC* from 20 to 0 decreases FS by 30%). However, Yow and Goodman [312] found that the block stability strongly (decreasing *JRC* from 5 to 0 decreases FS by 100%) depends on *JRC*.

5) The Barton's model, the simplified Barton's model, and the Mohr-Coulomb's model have counterintuitive behavior for very small *JRC*'s. Increasing *JRC* from 0 to 1, the factors of safety decrease instead of increases.

6) Yow and Goodman [312] found that the effect of *JCS* on the stability of the prism is not as strong as that of *JRC*, but it is quite effective. BS3D analyses found that the stability of the prism is weakly dependent on *JCS*.

7) The FS flattens out after a specific value of *JCS*, which depends on other aspects of the problem because the asperities does not fail and increasing *JCS* almost has no effect on the stability of the block.

8) Yow and Goodman [312] found that the base friction angle is quite effective on the stability of keyblocks. In addition, BS3D analyses show that the factor of safety of the prism increases with the base friction angle.

9) Stability decreases as normal stiffness increases (the same as Yow's and Goodman's [312] conclusion).

10) Effect of in situ stress condition of the prism: Yow and Goodman [312] found that aside from the shear strength, the most critical condition affecting keyblock stability is the stress environment. The block becomes less stable as the initial confining stresses decrease; the trend accelerates as stress magnitudes become very small (smaller than about 1.5 MPa). The same conclusion has been made based on BS3D analyses.

11) Yow and Goodman [312] found that the block becomes less stable as the lateral stress ratio decreases; the trend accelerates as the ratio goes below about one-half. The same conclusion has been made based on BS3D analyses.

12) The principal stress directions strongly affect the stability of keyblocks.

13) The *in situ* stresses strongly affect the stability of the block, even more than the shear strength of fractures (Figure 7.33 versus Figure 7.27 through Figure 7.29).

14) The factor of safety increases with distance from excavation face up to approximately five times of the tunnel radius.

15) The factor of safety of the prism increases with increasing radius of the tunnel.

16) Because of different dilation displacements, the factors of safety obtained using the simplified Barton's model are higher than those calculated using the Barton's model which itself is higher than those determined employing the Mohr-Coulomb model. The higher the dilation displacements are, the higher are the normal forces applied to the fractures, the shear strength of the fractures, and, finally, the factor of safety of the block.

17) The modified Barton's model and the old Barton's model may have smaller or higher factors of safety compared the other models, while they have colloquial differences with them.

18) The factor of safety of the block decreases with increasing size of the prism.

19) The factor of safety of the block decreases (by 20%) with increasing radius of the tunnel (from 1 to 10 m) and size of the prism accordingly. The change is

very small. This is the combination effect of the tunnel radius (which increases the FS) and the size of the block (which decrease the FS).

20) The factor of safety of the maximum block remains almost constant with increasing tunnel radius. This is the combination effect of the tunnel radius (which increases the FS) and the size of the block (which decrease the FS).

Finally, it can be concluded from the sensivity analyses performed in this Chapter that, in stability of keyblocks, *in situ* stresses have the highest effect. In addition, the type of constitutive model has strong effect, even higher than those of the shear strength of the fractures. The shear strength and stiffness of the fractures have weak effect on stability of keyblocks.

CHAPTER 8: EFFECT OF HIGH-VELOCITY JET IMPACT ON STABILITY OF SINGLE ROCK BLOCKS IN PLUNGE POOLS

8.1 INTRODUCTION

Standard dam risk assessment includes consideration for spillway and spillway energy dissipator scour. For concrete and masonry dams, it also includes consideration for dam overtopping and scour of the foundations. High-velocity plunging jets, issuing from hydraulic artificial or natural structures, can result in scouring of the rock riverbed or the dam toe foundation. Assessment of the extent of scour is necessary to ensure the safety of the dam and to guarantee the stability of its abutments.

Currently, there is no formulation for evaluating scour caused by general failure modes of rock blocks having general shape and subject to general loading (e.g., gravity, reinforcement, dam loads) and to the plunge pool water pressures [23]. Limitations of available approaches to scour evaluation are briefly explained in Section 8.2.

Water pressure has been implemented in BS3D. Water forces cause the stiffness matrix for the block to be non-symmetric, which opens the doors to additional failure modes, such as [318-321]:

1) Divergence, i.e. the motion is aperiodic and exponentially growing in time.
2) Flutter, i.e. the motion is periodic and exponentially growing in time. This is a self-starting vibration of the block that may occur when a block face rotates under hydrodynamic load.

In this Chapter, the stability of single rock blocks in plunge pools is investigated. Section 8.3 describes an approach to estimate pressure forces generated in plunge pools due to high-velocity jet impacts. Section 8.4 introduces failure criteria for jointed rock mass. The scour model implemented in BS3D is calibrated and validated using the results of several experimental studies as well as case histories and prototypes in Section 8.5. Ability of BS3D in considering *in situ* stress and dilation behavior of rock fractures as

266

well as dealing with dynamic divergence and flutter are also demonstrated by an example in Section 8.5 followed by summary and conclusion in Section 8.6.

It should be acknowledged that Sections 8.2 through 8.4.1 are taken from reference [23] with some integrations and modifications.

8.2 LIMITATIONS OF AVAILABLE APPROACHES TO SCOUR EVALUATION

8.2.1 Bollaert's approaches

Bollaert's Dynamic Impulsion (DI) method [30, 31] is limited to vertical translational failure (static failure mode) of parallelepiped rock blocks with one face at the plunge pool bottom. Indeed, roto-translational failures are common even for parallelepiped blocks subjected to pressure fluctuations [322].

Bollaert's Comprehensive Fracture Mechanics (CFM) method has only been applied to scour extent for the Cabora-Bass dam [30, 31], built in Mozambique on "excellent quality granitic gneiss with slight schistosity" [323]. Typical values for the unconfined compressive strength, *UCS*, of gneiss are in the order of 100-200 MPa. However, in order to match the prototype scour extent, the author had to use a *UCS* of only 13 MPa. This raises some concerns on the use of this method for predicting scour extent based on actual rock properties [23].

8.2.2 Annandale's Erodibility Index

Annandale's erodibility index (EI) method [324, 325] is a classification method (as opposed to an analytical or numerical method based on mechanical principles) applicable to rock masses as a whole, and is not applicable to single rock blocks, which typically are critical in dam stability as recognized by Goodman and Powell by working on USBR dams [326]. In addition, the EI only approximately accounts for the distinctive property of rock masses, i.e. their directionality [33]. Indeed, the EI is obtained by multiplication of the following terms:

$$EI = M_s \cdot K_b \cdot K_d \cdot J_s,$$ (8.1)

where:

267

- $M_s = \gamma_r/27\ UCS$, in which γ_r is the unit weight of the rock in kN/m^3 (typically 25-33 kN/m^3), and can have values in the range of 0 to 300.
- $K_b = RQD/J_n$: block size, and can have values in the range of 1 to 100.
- $K_d = J_r/J_a$: shear strength, and can have values in the range of 0.2 to 4.
- J_s = fracture orientation, and can have values in the range of 0.4 to 1.2.

It is evident that shear strength and relative orientation have little weight on the overall EI as compared to unconfined compressive strength and block size [23]. An indication that the unconfined compressive strength of the intact rock plays a disproportionate role in the EI comes from Bollaert's application of EI to the Coborra-Bassa dam [30, 31]. In order to match the prototype scour depths, the unconfined compressive strength of the intact rock had to be lowered to 13 MPa, i.e by an order of magnitude. This unbalance has been noticed by USBR personnel as well while applying the EI on some USBR dams [23].

Annandale's table for determining the unconfined compressive strength of the intact rock disagrees with the table proposed by the Geological Society of America (GSA), and adopted by the International Society of Rock Mechanics [178], the USBR Engineering Geology Field Manual [327], and the British Standards [328]. In particular, Annadale's estimates for soft to very hard rocks rock are much lower than what is generally accepted by the rock mechanics community. One would obtain much higher EI values by using actual testing than by using Annandale's table. This may dangerously mislead the user, and, since *UCS* has a major role in determining EI, it may lead to quite different estimates of EI, and thus quite different estimates of scour potential [23].

8.2.3 Discrete Element Method

As for numerical methods for discontinuous rock masses, 3DEC by Itasca [56] has serious limitations in the dynamics of rigid bodies because it assumes that the inertia tensor is always diagonal [55, 56], i.e. rotations are assumed to be parallel to the applied resultant moment. Both 3DEC and 3D-DDA [17, 18, 60, 61] use contact points at the vertices of the contact areas to calculate constraint forces: this does not allow for path-

dependent behavior of discontinuities. 3D-DDA assumes that all forces must be conservative, and thus cannot handle follower forces, such as water pressure forces, and cannot detect divergence or flutter failure modes [23].

Finally, all numerical methods for discontinuous rock masses need to resort to time consuming sensitivity studies in order to calculate the factor of safety of a block. These sensitivity studies entail changing the strength parameters, e.g., multiplying the cohesion and tangent of the friction angle of fractures by a same amount. If failure is not caused by overcoming of the shear strength (e.g., block rotation), then these sensitivity studies will not yield the correct safety factor. BS3D formulation overcomes the abovementioned limitations and has been validated experimentally on prototypes in Chapter 6.

8.3   PRESSURE FORCES GENERATED IN PLUNGE POOLS

Plunging jets occur in various engineering applications, including overtopping dams, at the ends of spillway chutes, emanating from gates and valves, and the like [325]. Figure 8.1 shows a jet discharging over a dam.
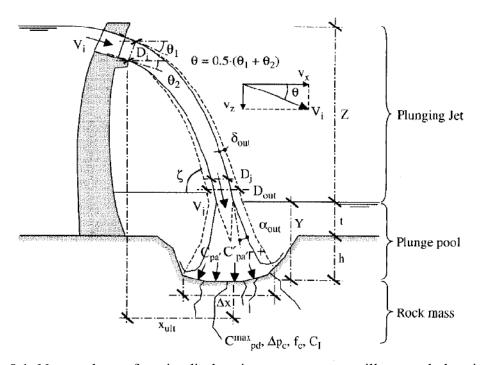
Figure 8.1: Nomenclature for a jet discharging over an ogee spillway and plunging into a pool [30]

The issuance turbulence intensity, defined as [325]:

$$T_u = \frac{V'}{V},$$
(8.2)

is an important parameter, at jet issuance, determining overall jet characteristics. The variable V' is the root mean square value of the fluctuating velocity, and V is the mean axial flow velocity of the jet. Table 8.1 contains estimates of issuance turbulence intensity for use in practice.

Table 8.1: Typical values of issuance turbulence intensity at various outlet structure [30]

Type of outlet structure	Turbulence intensity T_u (%)
Free fall	0 – 3
Ski jump outlet	3 – 5
Valve, intermediate outlet, or bottom outlet	3 – 8

When a jet is completely developed (Figure 8.2), it no longer contains a core but essentially consists of blobs of water that disintegrate into finer and finer drops. Individual blobs and drops of water slow down due to air drag and eventually reach terminal velocity [325]. Equations that can be used to estimate jet breakup length, L_b, and issuance turbulence intensity, T_u, are summarized in Table 8.2. In these equations, Q is the total flow rate, q is the flow rate per unit length of the rectangular jet, and D_j is the jet diameter at the pool surface.

8.3.1 Plunge pool floor

Studies on pressure fluctuation in plunge pools have been conducted by Ervine *et al.* [329], Franzetti and Tanda [330, 331], Xu-Duo-Ming [332], Tao *et al.* [333], Lopardo [334], Armengou [335], May and Willoughby [336], Puertas and Dolz [337], Hartung and Hausler [338], Beltaos and Rajartnam [339], Cola [340], Bollaert [30], Bollaert and Schleiss [341, 342], etc.
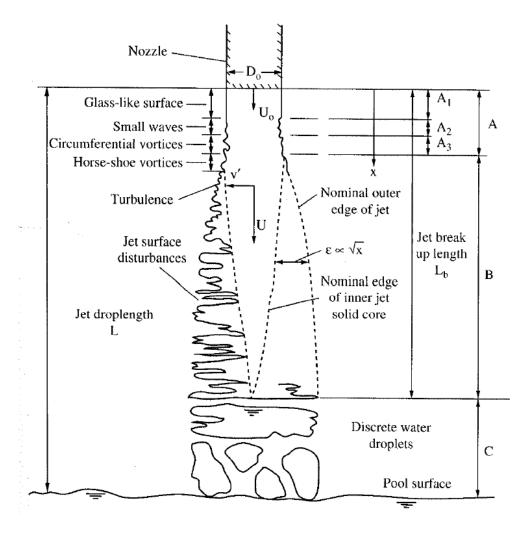
Figure 8.2: Jet characteristics [329]

Table 8.2: Equations for estimating jet breakup length
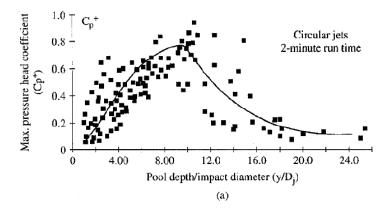
Jet type	L_b	Turbulence intensity T_u (%)	Reference
Rectangular jets	$6q^{0.32}$		Horeni [343]
Circular jets	$60Q^{0.39}$	0.3	Ervine *et al.* [329]
	$17.4Q^{0.31}$	3	
	$4.1Q^{0.20}$	8	
	$50D_j$ to $100D_j$	3 to 8	Ervine and Falvey [344]

271

On the floor of a plunge pool, the maximum and minimum dynamic pressures, respectively, can be calculated as follows [329]:

$$P_{max} = \left(C_{pa} + C_p^{+}\right)\cdot \gamma_w \cdot \frac{V_j^{2}}{2g},$$ (8.3)

$$P_{min} = \left(C_{pa} - C_p^{-}\right)\cdot \gamma_w \cdot \frac{V_j^{2}}{2g},$$ (8.4)

where C_{pa} is the mean dynamic pressure coefficient; C_p^{+} (C_p^{-}, respectively) is the positive (negative, respectively) extreme fluctuation dynamic pressure coefficient (Figure 8.3), V_j is the jet velocity at the pool surface ($V_j = \sqrt{V_i^{2} + 2gZ}$, in which V_i is the jet velocity at issuance and Z is the plunging jet length depicted in Figure 8.1), and γ_w is the unit weight of water.

(a)

(b)
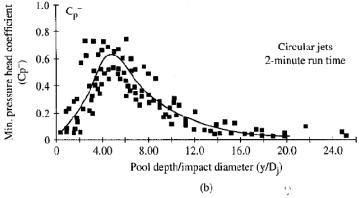
Figure 8.3: (a) Maximum and (b) minimum fluctuation dynamic pressure coefficient at pool floor [329]

If the ratio of the jet length to the jet breakup length (L/L_b) is equal to 0.5, C_{pa} can be calculated with the following expression [329]:

$$C_{pa} = \begin{cases} \dfrac{38.4}{(1+\beta)}(D_j/Y)^2 & if \quad Y/D_j > 4 \\ 0.875 & otherwise \end{cases}, \tag{8.5}$$

where D_j is the jet diameter at the pool surface ($D_j = D_i\sqrt{\dfrac{V_i}{V_j}}$, in which D_i is the jet diameter at issuance depicted in Figure 8.1) and Y is the pool depth. β is the free air content and, for circular plunging jets, can be estimated using the following equation [329, 345-348]:

$$\beta = K'\sqrt{\dfrac{L}{D_j}} \cdot \left(1 - \dfrac{V_0}{V_j}\right), \tag{8.6}$$

in which K' is empirically obtained parameter (Table 8.3) and ranges between 0.2 and 0.4; V_0 (=1 m/s) is the minimum plunging velocity leading to commencement of aeration. In addition, for rectangular plunging jets, β can be estimated as follows [346]:

$$\beta \approx 0.13\sqrt{\dfrac{L}{D_j}} \tag{8.7}$$

The maximum air content that could reasonably be expected to occur in water is on the order of about 65 to 70% [349].

Corrections can be made to take into account different breakup length [30, 325] and turbulence intensity [30]. The following equation can be used to calculate the values of the average dynamic pressure coefficient for rectangular jets as a function of jet breakup length ratio and dimensionless plunge pool depth [325, 350]:

Table 8.3: Constant K' values [344]

Turbulence	Circular jets	Rectangular jets	Application limit
Rough turbulent	0.40	0.20	$L/D_j \leq 50$
Moderate turbulent	0.30	0.15	$L/D_j \leq 100$
Smooth turbulent	0.20	0.10	$L/D_j \leq 100$

$$C_{pa} = a \cdot \exp\left(-b\frac{Y}{B}\right),$$ (8.8)

where B is the width (i.e. thickness) of a rectangular jet. The values of the parameters a and b as a function of jet breakup length ratio are presented in Table 8.4.

8.3.2 Fractures

As shown in Figure 8.4, Bollaert [30] determined experimentally the pressures in a closed-ended fracture (U-joint) and in an open-ended fracture (D-joint), respectively, under an impinging jet. The maximum dynamic pressure can be calculated as [30]:

$$P_{\max,d} = \left(C_{pd} + C_{pd}^+\right) \cdot \gamma_w \cdot \frac{V_j^2}{2g},$$ (8.9)

where coefficients C_{pd} and C_{pd}^+ are given in Figure 8.5. Bollaert noticed that the coefficients for the U-joint and for the D-joint are very similar. As a consequence, in this research, it is assumed that the actual hydraulic connectivity (of a fracture around a rock block with the pool bottom) does not change significantly the pressure field on the block's faces. This entails that predictions based on the D-joint pressure field should be robust.

Table 8.4: Parameters for estimating dynamic pressure coefficient as a function of jet breakup length ratio [325, 350]

L/L_b	a	b	$C_{pa}(Y/B < 4)$
0.4-0.5	0.98	0.070	0.78
0.5-0.6	0.92	0.079	0.69
0.6-0.8	0.65	0.067	0.50
1-1.10	0.65	0.163	0.33
1.1-1.3	0.65	0.185	0.31
1.5-1.6	0.55	0.200	0.24
1.8-1.9	0.55	0.250	0.20
2.2-2.3	0.50	0.250	0.18
2.3-3.0	0.50	0.400	0.10
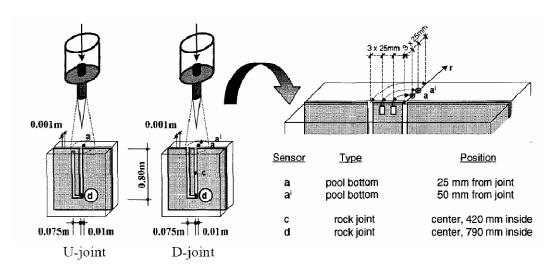
Figure 8.4: Dimensions of joints tested by Ballaert [30]
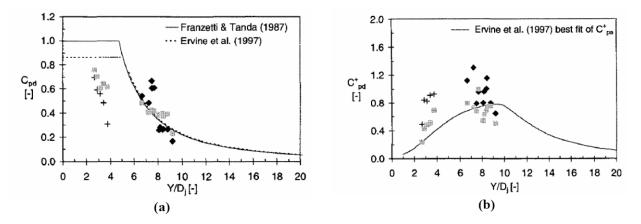
Figure 8.5: a) Mean and b) positive extreme fluctuation dynamic pressure coefficients at sensor "d" in the D-joint of Figure 8.4 (cross and diamond symbols). Gray symbols indicate coefficients at sensor "d" in the U-joint of Figure 8.4 [30]. Lines indicate experimental results for pool bottom.

8.3.3   Proposed approach for pressures at jet centerline

Based on the literature review, at the jet centerline, it is proposed to calculate pressures in the fractures using the experimental results for the D-joint. The pressures on the rock block faces at the pool bottom can be calculated using Equations (8.3) and (8.4).

It is assumed that the maximum (minimum, respectively) pressure in a fracture occurs at the same time as the minimum (maximum, respectively) pressure on the pool floor.

In order to validate this assumption, consider the maximum difference between the pressure at point "d" (Figure 8.4) and the pressure at the pool bottom (points "a" and "a^i" in Figure 8.4). First, consider the ratio Y/D_j in the 3 to 4 range. Equations (8.4) and (8.5) and Figure 8.3-(b) yield a minimum pressure at the pool bottom equal to

$P_{min} = 0.5 \cdot \gamma_w \cdot \dfrac{V_j^2}{2g}$, whereas Equation (8.9) and Figure 8.5 yield a maximum pressure at

the bottom of the block equal to $P_{max,d} = 1.6 \cdot \gamma_w \cdot \dfrac{V_j^2}{2g}$. The net uplift pressure coefficient

is thus about 1.1: this value corresponds well with the difference (experimentally measured by Bollaert) between the pressure at point "d" and the average of pressures at points "a" and "a^i" shown in Figure 8.4. This difference is expressed by Bollaert as [30]:

$$P_{up} = C^{up}_p \cdot \gamma_w \cdot \frac{V_j^2}{2g},$$
(8.10)

where C^{up}_p is given in Figure 8.6.
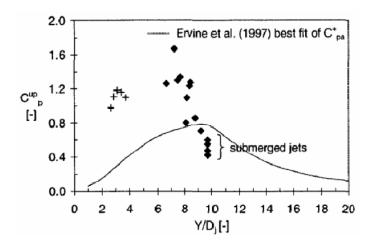
Figure 8.6: Net upward pressure coefficient for D-joints [30]. Lines indicate experimental results for pool bottom.

Likewise, for $Y/D_j = 8$, one obtains a net uplift pressure coefficient of about $1.7 - 0.2 = 1.5$, which compares well with the data in Figure 8.6. These values are in line with the values obtained by Liu et al. [351] by measuring net uplift forces on scaled versions of rock blocks in plunge pools. Finally, maximum pressure fluctuations (as opposed to root-mean-square values) are also typically used in the stability analysis of stilling basin slabs [322, 352, 353].

Since the maximum and minimum dynamic pressure coefficients were obtained from 2-min records, their values must be doubled for a 24 hour run time, which is typically understood to be representative of continuous operation of a plunge pool or stilling basin [329, 352].

The literature review has revealed that the integral scale of the correlation function for pressure fluctuations is very small as compared to the typical dimension of a rock block [354]. If the horizontal characteristic dimension of the block is at least twice the integral scale, then the pressure fluctuations at two fractures are independent [322]. Recall that the net uplift pressure for the D-joint is obtained using the maximum and the minimum pressure coefficients for the fracture and the floor, respectively. Since the distance between the two vertical fractures in the D-joint is only 7.5 cm, Bollaert's result would confirm this assumption. This assumption is a worst-case scenario because it entails that the minimum pressure at one fracture can occur simultaneously with the maximum pressure at another fracture, and vice versa. As a consequence, if a block has n faces, the stability analysis will be run 2^n times to cover all possible combinations of pressure distributions on the block's faces.

8.3.4 Proposed approach for pressures not at jet centerline

Since the 1960's [355], it has been observed experimentally that the pressure on the pool floor decreases radially from the jet centerline. The literature research has revealed that:

1- The mean and extreme pressures decrease more rapidly for developed jets, and less rapidly for core jets.

277

2- The extreme pressure fluctuations decrease less rapidly than the mean pressures.

3- The minimum extreme pressure fluctuation coefficients are very small (about 0.1) and are independent of the radial distance and nature of the jets [23].

4- The extreme pressure fluctuations are proportional to the root mean square pressure fluctuations.

It is thus proposed to apply radially decreasing pressures to the block faces lying on the pool floor. The mean and maximum extreme pressure coefficients are taken as follows [30, 331, 336]:

$$C_{pr} = \exp\left(-3(r/r_{max})^2\right) \cdot C_{pa}, \qquad \text{for core jets} \qquad (8.11)$$

$$C_{pr} = \exp\left(-6(r/r_{max})^2\right) \cdot C_{pa}, \qquad \text{for developed jets} \qquad (8.12)$$

$$C_{pr}^{+} = C_{p}^{+}, \qquad \text{for core jets and } r < 0.5r_{max} \qquad (8.13)$$

$$C_{pr}^{+} = \exp\left(-3(r/r_{max} - 0.5)^2\right) \cdot C_{p}^{+}, \quad \text{for core jets and } r > 0.5r_{max} \qquad (8.14)$$

$$C_{pr}^{+} = \exp\left(-3(r/r_{max})^2\right) \cdot C_{p}^{+}, \qquad \text{for developed jets} \qquad (8.15)$$

where $C_{pr}\left(C_{pr}^{+}\right)$ is the mean (maximum extreme, respectively) pressure coefficient at distance r to the jet centerline, and $r_{max} = 0.5D_j + 0.25Y$. Core jets and developed jets can be distinguished from each other using the following criteria [30]:

$$\begin{cases} 0 < \dfrac{Y}{D_j} < 4-6 & \Rightarrow \quad core \quad jet \\ 4-6 < \dfrac{Y}{D_j} < 20-40 & \Rightarrow \quad developed \quad jet \end{cases} \qquad (8.16)$$

In this research, the minimum extreme pressure fluctuation coefficient on the pool floor is estimated using the following two steps:

1- The minimum extreme pressure fluctuation coefficient, C_{pr}^{-}, is estimated as follows:

278

$$C_{pr}^{-} = C_{p}^{-} \qquad\qquad \text{for core jets and } r < 0.5r_{max} \quad (8.17)$$

$$C_{pr}^{-} = \exp\left(-3(r/r_{max} - 0.5)^2\right) \cdot C_{p}^{-} \qquad \text{for core jets and } r > 0.5r_{max} \quad (8.18)$$

$$C_{pr}^{-} = \exp\left(-3(r/r_{max})^2\right) \cdot C_{p}^{-} \qquad\qquad \text{for developed jets} \qquad\qquad (8.19)$$

2- If $0.1 > C_{pr}^{-}$ or $C_{pr}^{-} < C_{pr}$, then it will be assumed that $C_{pr}^{-} = 0.1$. The reason is the higher value for the minimum extreme pressure fluctuation coefficient gives the lower pressure on the pool floor which should be a positive value. Thus, C_{pr}^{-} can not be higher than C_{pr}. In addition, the literature review shows that the minimum extreme pressure fluctuation coefficients may be very small (about 0.1). Therefore, $C_{pr}^{-} = 0.1$ will be considered whenever it gives the lowest minimum pressure on the pool floor.

8.3.5 Summary of pressure distributions on a block

To account for long duration events, all of the pressure values will be doubled.

8.3.5.1 Faces lying on the pool floor

The average pressure distribution on floor is obtained using Equations (8.11) or (8.12), where C_{pa} is given by Equations (8.5). The maximum pressure distribution is obtained by adding the maximum pressure coefficient given by Equations (8.13) through (8.15) with C_{p}^{+} as in Figure 8.3. The minimum pressure distribution is obtained by subtracting the minimum pressure coefficient to the average pressure distribution. The minimum pressure coefficient is estimated using Equations (8.17) through (8.19) with C_{p}^{-} as in Figure 8.3 or is assumed to be constant and equal to 0.1. The maximum value for the minimum pressure coefficient should be adopted.

8.3.5.2 All other faces

The pressure is assumed to be uniformly distributed. Its maximum value is

$$P_{\max,fracture,r} = \left(C_{p,fracture,r} + C_{p,fracture,r}{}^{+}\right) \cdot \gamma_w \cdot \frac{V_j^2}{2g}, \tag{8.20}$$

where:

$$C_{p,fracture,r} = \exp\left(-3(r/r_{\max})^2\right) \cdot C_{pd}, \qquad \text{for core jets} \tag{8.21}$$

$$C_{p,fracture,r} = \exp\left(-6(r/r_{\max})^2\right) \cdot C_{pd}, \qquad \text{for developed jets} \tag{8.22}$$

$$C_{p,fracture,r}{}^{+} = C_{pd}{}^{+}, \qquad \text{for core jets and } r < 0.5r_{\max} \tag{8.23}$$

$$C_{p,fracture,r}{}^{+} = \exp\left(-3(r/r_{\max}-0.5)^2\right) \cdot C_{pd}{}^{+}, \quad \text{for core jets and } r > 0.5r_{\max} \tag{8.24}$$

$$C_{p,fracture,r}{}^{+} = \exp\left(-3(r/r_{\max})^2\right) \cdot C_{pd}{}^{+}, \qquad \text{for developed jets} \tag{8.25}$$

where C_{pd} and $C_{pd}{}^{+}$ are given in Figure 8.5, and r is the minimum distance of the block's face to the jet centerline.

The minimum pressure is taken as:

$$P_{\min,fracture,r} = \left(C_{p,fracture,r} - 0.1\right) \cdot \gamma_w \cdot \frac{V_j^2}{2g}, \tag{8.26}$$

where $C_{p,fracture,r}$ is calculated using Equations (8.21) and (8.22) with r equal to the maximum distance of the block's face to the jet centerline.

Let n be the number of faces making up the block. The stability analysis is run for all 2^n face pressure combinations, and the factor of safety is the minimum control parameter at failure calculated in the 2^n runs.

As scour deepens, the configuration and geometry of the plunge pool may affect the above pressures. This effect may be introduced through the expressions derived by Manso [24] in his experimental work. However, the objective of this dissertation is to develop a method to analyze the stability of a single rock block (considering the effect of dilatancy and high-velocity jet impact). Therefore, the simulation of the progressive failure of blocks at the bottom of the plunge pool (which causes changes in the configuration and geometry of the pool) is out of the scope of this research. Since the plunge pool geometry is not further defined, in this Chapter, all analyses are performed assuming that the plunge pool has a flat bottom during the whole scour process.

8.4 FAILURE CRITERIA FOR JOINTED ROCK

8.4.1 Impulsive nature of the applied forces

The typical duration of maximum pressure fluctuations is in the order of 5 ms [24, 30]. Manso [24] found that pressure fluctuation with probability higher than 75% persist less than 6 ms at the pool bottom. For core jet conditions, this value drops to 4 ms. For developed jet impact conditions, the persistence for equivalent probability is higher than for core impact conditions.

In this dissertation, it is assumed to subject the block to its constant unbalanced force at failure for the maximum duration of an extreme pressure fluctuation, i.e. 5 ms. This assumption has been successfully used in stilling basins [352].

As mentioned in Chapter 2, the proposed stability analysis follows the block in its static condition until equilibrium is possible between active and reaction forces. When the block fails, the active force that cannot be equilibrated by the constraints (nearby blocks) imparts an acceleration to the block. The formulation then computes the initial acceleration of the block and its subsequent displacement by taking into account the inertia of the rock block. This is accomplished by applying rigorous rigid body dynamics. This displacement under maximum pressure fluctuations has been observed experimentally by Yuditskii [356, 357] to be the beginning of and always conduct to block's ejection.

Indeed, Yuditskii [356, 357] presented what is probably the first conceptual model of the rock scouring process based on pressure fluctuations on rock blocks. His procedure is similar to the one proposed here, in that it is based on an evaluation of the maximum instantaneous pressure that can separate a rock block from the matrix. For increasing pool depths, he compared the maximum pressure gradient amplitude originated by jet impact with a limit pressure value corresponding to the equilibrium situation. He also conducted experimental work (more than 2,000 tests) focusing on the mechanisms of block ejection for varying scour depths, relative size of blocks, block density, and joint thickness. One interesting observation is as follows: "the block is ejected, neither by one pressure fluctuation of high amplitude nor by a succession of

pressure fluctuations of high amplitude, but by one large average pressure that is established in the joint underneath the block following a small vertical displacement. The opening of the joint that allows this small vertical displacement is done by one pressure fluctuation of high amplitude."

BS3D formulation can calculate the small displacement observed experimentally by Yuditskii under maximum pressure fluctuation. What is interesting is that the flow and rock mass conditions that led to a small displacement of the blocks then led to the blocks' ejection from the rock mass. In other words, there is experimental evidence that a block is ejected if and only if it first fails according to one of the failure modes captured by the proposed stability analysis.

8.4.2 Scour threshold (translational failure mode)

In this Section, a scour threshold is introduced for the cases in which analysis predicts that the block fails in a translational mode, i.e. the dynamic failure mode obtained using BS3D is an acceleration in one direction with no rotation.

It is assumed that the block is subjected to a constant unbalanced force at failure for the maximum duration of an extreme pressure fluctuation, i.e. 5 ms. This unbalance force causes an initial velocity as follows:

$$F_{\Delta t} = F \cdot \Delta t = m \cdot v_{\Delta t} = m \cdot a \cdot \Delta t, \tag{8.27}$$

in which F is unbalance force due to the maximum dynamic pressure fluctuation; Δt is the maximum duration (i.e. 5 ms); $F_{\Delta t}$ is the net impulse on the block; m is the block mass; $v_{\Delta t}$ is the initial velocity; and a is the acceleration of the block caused by the unbalance force.

It is assumed that the block moves with the initial velocity, $v_{\Delta t}$, for a time duration equal to the half of the natural period of the fissure. The natural period of an open-ended joint can be obtained as follows [325]:

$$T_c = \frac{2L}{c}, \tag{8.28}$$

where c is the pressure wave celerity and for a mixed fluid, like a mixture of water containing air, can be estimated using the following equation (valid for $\beta \leq 50\%$) [325]:

$$c_{mix} = \sqrt{\frac{1}{\rho_{mix}} \cdot \frac{1}{\dfrac{(1-\beta)}{\rho_{liq} \cdot c_{liq}^2} + \dfrac{\beta}{\rho_{air} \cdot c_{air}^2}}}, \qquad (8.29)$$

in which c_{liq} is the pressure wave celerity in the liquid (assume 1000 m/s for water); c_{air} is the pressure wave celerity in air (assume 340 m/s); ρ_{liq} is the density of the liquid (assume 1000 kg/m^3); ρ_{air} is the density of the air (assume 1.29 kg/m^3); and ρ_{mix} can be estimated as follows [30]:

$$\rho_{mix} = \rho_{air} \cdot \beta + \rho_{liq} \cdot (1 - \beta) \qquad (8.30)$$

L is the fissure length and can be evaluated as follows [30, 325]:

$$L = x_b + 2z_b \qquad (8.31)$$

where x_b and z_b are length and height of the block, respectively.

The block is assumed to be subjected to all forces except for the fluctuation dynamic pressure for a duration equal to half of the natural period of the fissure followed by an unbalance force in opposite direction which changes the direction of the block motion (stops the upward displacement of the block). Thus, the maximum upward displacement of the block, h_{up}, can be estimated based on the above given assumptions.

Criteria for determining if rock blocks from a jointed rock mass will experience incipient motion, have been proposed by Bollaert [30] (Table 8.5). Bollaert and Schleiss [31] found that ultimate scour depth of Cabora-Bassa Dam corresponds to a $\dfrac{h_{up}}{z_b}$ ratio of 0.20, which is not consistent with values given in Table 8.5.

In this dissertation, BS3D was used to simulate Martins' [29] scour experimental study. Based on these simulations, it is suggested to consider that the block is most likely to be removed when $\dfrac{h_{up}}{z_b} > 0.25$ (see Section 8.4.2 for detailed analyses). This assumption together with the above described method is validated in the next Section using previously solved examples, experimental studies, and case histories.

283

Table 8.5: Criteria to assess rock scour potential by dynamic impulsion [30]

$\dfrac{h_{up}}{z_b} \leq 0.1$	Rock block remains in place.
$0.1 < \dfrac{h_{up}}{z_b} < 0.5$	Rock block vibrates and most likely remains in place.
$0.5 \leq \dfrac{h_{up}}{z_b} < 1$	Rock block vibrates and is likely to be removed depending of ambient flow conditions.
$\dfrac{h_{up}}{z_b} > 1$	Rock block is definitely removed from its matrix.

8.5 APPLICATION, CALIBRATION, AND VALIDATION OF THE SCOUR MODEL

By using Federspiel's experimental study [27, 28], this Section validates the above explained method to estimate the dynamic water pressure and BS3D to determine the stability of the rock block together with its displacements. Secondly, employing Martins' experimental study [29], the failure criterion of the rock block is calibrated. Section 8.4.3. shows the application of the scour model in a fictious rock mass (good quality granite) introduced initially by Bollaert [30]. The whole scour model and BS3D algorithm are then validated using three case histories and prototypes [29-31]. Finally, Section 8.4.6 demonstrates the ability of BS3D in predicting more complicated failure modes (divergence and flutter) together with dealing with *in situ* stress and dilation behavior of rock fractures with a fictious example.
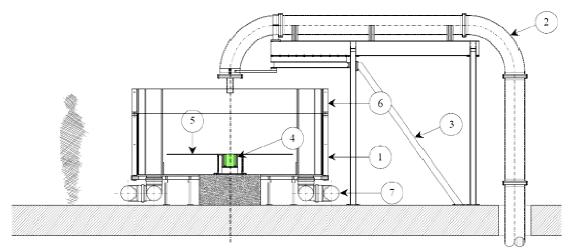
8.5.1 Federspiel's experimental study (response of an intelligent block to core jet impact)

A large-scale experimental facility has been developed in Laboratory of Hydraulic Constructions (LHC), Ecole Polytechnique Federale de Laussanne (EPFL) which reproduces high velocity plunging jet [27, 30]. After employing the installation to study the behavior of a plunge pool with a flat bottom and one- or two-dimensional joints by

Bollaert [30], different plunge pool geometries have been studied for a simple one-dimensional joint by Manso [24].

Federspiel *et al.* [27, 28] have been doing an experimental study using the above mentioned facility to investigate the behavior of a single rock block generated by a 3-dimensional joint network and impinged by a high-velocity water jet. The block is modeled by a hollow steel cube instrumented with a large series of pressure transducers, accelerometers, and displacement transducers.

The experimental facility is depicted in Figure 8.7. The plunge pool is a 3-meter-diameter cylindrical basin in steel reinforced Lucite. The bottom of the basin is made of a rigid steel frame and the height of the basin is 1.4 m. The water supply is a conduit with a 72-mm-diameter cylindrical jet outlet. The water restitution consists of four conduits simulating the downstream conditions. The maximum discharge is 250 l/s, which corresponds to jet outlet velocities of max 30 m/s [27].

(1) The plunge pool, (2) the water supply, (3) his structure, (4) the plunge pool bottom, (5) the level of the plunge pool bottom, (6) the plunge pool max. water level, and (7) the water restitution

Figure 8.7: General view of the experimental facility (transversal section) [27].

The measurement box (length = width = 402 mm and height = 340 mm) is a structure composed of steel plates (Figure 8.8-a). The thickness of the steel plates is 20 mm. Inside this box, a large series of cavities allow inserting pressure and displacement

285

transducers. In the center of the measurement box, a large cavity (length = width = 202 mm and height = 201 mm) allows inserting the intelligent block (a cube with a side length of 200 mm). The width of the steel plates has been optimized to have a density similar to real rock (2,400 – 2,500 kg/m^3). On the top of the "intelligent block", some holes have been pre-perforated to fix the pressure transducers. Between the measurement box, and the intelligent block, a 3-dimensional fissure of 1 mm width is created. Inside the intelligent block, pressure and vibration transducers have been inserted to measure the pressure at the pool bottom under high-velocity jet impact and to measure the vibration of the block. Finally, both the measurement box and the intelligent block have been placed inside the basin simulating the plunge pool (Figure 8.8-b) [27].

(a)   (b)
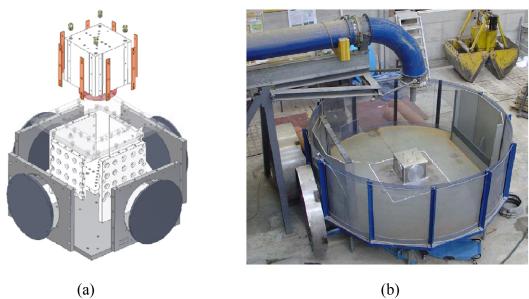
Figure 8.8: (a) axonometric view of the experimental facility; (b) picture of the facility with the measurement box and the intelligent block [27].

Electronic data acquisition equipment consists of a data acquisition system, 12 pressure transducers, two displacement transducers (with an absolute measurement range between 0 and 8 mm and a precision of less than 0.005 mm (static) or less than 0.01 mm (dynamic)), and an accelerometer transducer (which has a sensitivity of 5 mV/g and a frequency range between 1 and 10 kHz) [27].

286

The pressure transducers were fixed within the same vertical plane to reconstruct the pressure field around the block (Figure 8.9). Four transducers are installed inside the block and measure the pressure at the plunge pool bottom (309-312): the first on the jet axis, the second at 25 mm, the third at 50 mm and the fourth at 75 mm from the jet axis Four transducers are installed on one of the vertical walls of the measurement box (313-317): the first at 50 mm from the plunge pool bottom and the following at a 50 mm interval. Four transducers are situated underneath the block (318-321): they have the same relative position as the four transducers that are installed inside the block. The displacement transducer (D1D and D2D not on the Figure 8.9) and the accelerometer (ACC) have a fixed position: displacement transducers under the block in "measurement box" and the accelerometer in the block [27].
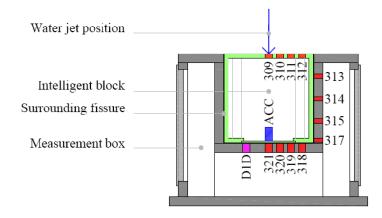
Figure 8.9: Transducers position [27].

Preliminary tests have been performed with a flat bottom and a water jet centered on the middle of the intelligent block. Two plunge pool water levels (Y = 0.1 m and 0.6 m) and four jet outlet velocities (19.6, 22.1, 24.6 and 27.0 m/s) have been tested. The 0.1 m water level in the plunge (Y) generates a core jet (Y/D ratio of only 1.39), while the 0.6 m water level generates a developed jet (Y/D ratio of 8.33). For each water level and jet velocity, three runs have been performed. The data acquisition frequency was 1 kHz and the recording time was 60 seconds (60'000 samples for each transducer) [27].

Based on the results of the preliminary tests, Federspiel *et al.* [27] made comment on the mean and fluctuating coefficients (Figure 8.10). The mean pressure coefficients recorded directly under the jet axis for core jet impact are in good agreement with the theoretical curves developed by Ervine *et al.* [329] and with previous pressure records made by Bollaert [30] and Manso [24]. The mean pressure coefficients recorded away from the jet axis and inside the joints around the block are generally less than the mean pressures under the jet axis, which could reasonably be expected. For developed jet impact, however, the recorded values are higher than the theoretical curves and rather correspond to values for core jet impact. This is most probably due to the jet deflecting the plunge pool water level and locally lowering somewhat this water level [27]. In the same way, the pressure fluctuation coefficients are in good agreement with theory for core jets but differ somewhat from theory for developed jets. As such, the fluctuating part is lower than the theoretical curves, which again would correspond to a core jet rather than a developed jet [27].
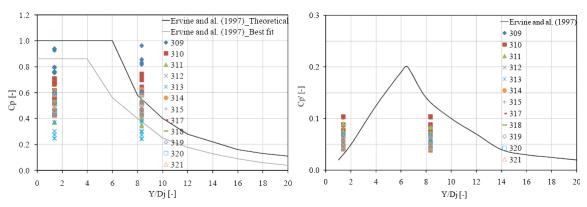
Figure 8.10: C_p mean pressure coefficient and C_p' pressure fluctuations coefficient (the root-mean-square value (*RMS*) of the fluctuating part of the dynamic pressures) [27].

In this dissertation, analyses have been performed on the results of Federspiel's experimental study [28]. For each water level and jet velocity, by investigating the results of all three experimental runs, the following parameters are obtained and presented in Table 8.6:

1) The maximum vertical displacement of the block

2) The maximum net uplift hydrodynamic pressure: difference between the maximum dynamic water pressure on the lowermost fracture (measured using pressure transducer 309 to 312) and the minimum dynamic water pressure on the floor of the plunge pool (measured using pressure transducer 318 to 321)

3) The duration of maximum pressure fluctuation: 1 ms for all cases

Table 8.6: Summary of Federspiel's experimental study and BS3D analyses

Y (m)	V_j (m/s)	Max experimental vertical displacement (mm)	Max experimental net uplift hydrodynamic pressure (m H_2O)	Vertical displacement predicted using BS3D analysis (mm)	
				Using the max experimental net uplift hydrodynamic pressure	Dynamic water pressure estimated using the approach explained in Section 8.2
0.1	19.6	0.995	5.77	0.894	0.38
	22.1	0.996	7.26	1.186	0.56
	24.6	1.004	8.23	1.376	0.75
	27.0	1.025	8.7	1.468	0.95
0.6	19.6	1.052	10.28	1.778	4.50
	22.1	1.060	5.25	0.791	5.79
	24.6	1.069	5.24	0.789	7.23
	27.0	1.055	6.74	1.084	8.76

For each water level and jet velocity, BS3D analyses are performed to predict the maximum vertical displacement of the block using either the following assumption for dynamic water pressure:

1) Measured maximum net uplift hydrodynamic pressure

2) Estimated hydrodynamic pressure applied on fractures and the bottom of the plunge pool using the approach explained in Section 8.3

Since the experimental studies were performed in a short period of time, in the numerical simulations, the dynamic pressure magnitudes are estimated without considering the coefficient two introduced in Section 8.3.5 to account for long duration events.
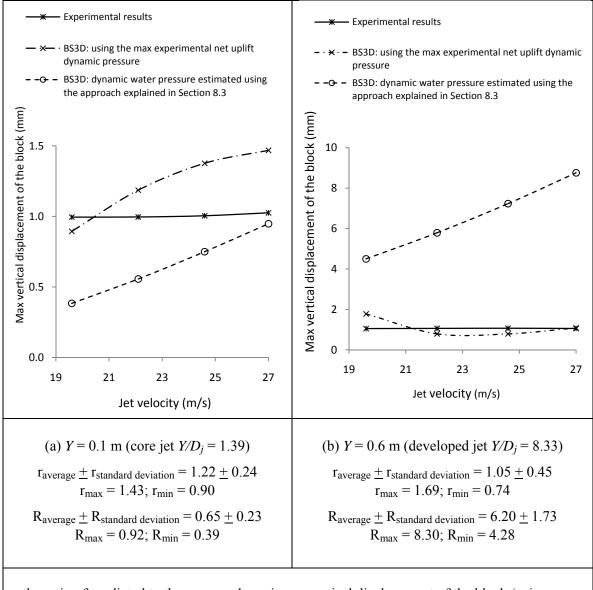
In the lack of any information regarding the air content, β, the pressure wave celerity is assumed to be 100 m/s (which correspond to β of about 15%). Thus, the natural frequency of open-ended fracture is estimated using Equation (8.28) to be 0.012 second, knowing the fact that $L = 0.6$ m (determined using Equation (8.31)).

In BS3D simulation, the Young's modulus and Poisson's ratio of the block and the mould is adopted to be 200 GPa and 0.3, respectively. Table 8.6 summarizes the results of BS3D analyses. In addition, Figure 8.11 compares the measured and predicted (using BS3D) maximum vertical displacement of the block.

It can be seen in Figure 8.11 that, for both core and developed jet, BS3D works well in predicting the maximum displacement of the block when the hydrodynamic pressure is adopted to be equal to the experimental net uplift dynamic water pressure. These results validate BS3D algorithm excluding the part that deals with estimating hydrodynamic pressure. In addition, the results of BS3D analyses with dynamic water pressure estimated using the approach explained in Section 8.3 show that:

- Core jet: the maximum vertical displacement of the block is underestimated.
- Developed jet: the maximum vertical displacement of the block is overestimated.

It seems that the errors in predicting the maximum vertical displacement of the block came from the errors in estimating the dynamic water pressure using the approach explained in Section 8.3. This approach seems to be the best method which can be found in the literature. However, Federspiel *et al.* are trying to find the weakness of current approaches in estimating hydrodynamic pressure caused by high-velocity jet impact, experimentally. In the next step of their experimental study, they will employ the above introduced facility (intelligent block) to do series of test with jet velocities between 5 and 30 m/s, for plunge pool water levels between 0.1 m and 1.0 m (with steps of 0.1 m). In addition, similar tests but with different jet impact position on the intelligent block will be performed (aside from the jet axis: from the middle of the intelligent block to the axis of the vertical fissure).

Figure 8.11: Comparison between measured and predicted maximum vertical
displacement of the block (Federspiel's experimental study)

(a) $Y = 0.1$ m (core jet $Y/D_j = 1.39$)

$r_{average} \pm r_{standard\ deviation} = 1.22 \pm 0.24$
$r_{max} = 1.43$; $r_{min} = 0.90$

$R_{average} \pm R_{standard\ deviation} = 0.65 \pm 0.23$
$R_{max} = 0.92$; $R_{min} = 0.39$

(b) $Y = 0.6$ m (developed jet $Y/D_j = 8.33$)

$r_{average} \pm r_{standard\ deviation} = 1.05 \pm 0.45$
$r_{max} = 1.69$; $r_{min} = 0.74$

$R_{average} \pm R_{standard\ deviation} = 6.20 \pm 1.73$
$R_{max} = 8.30$; $R_{min} = 4.28$

r: the ratio of predicted to the measured maximum vertical displacement of the block (using
   BS3D with maximum experimental net uplift dynamic pressure)
R: the ratio of predicted to the measured maximum vertical displacement of the block (BS3D
   with dynamic water pressure estimated using the approach explained in Section 8.3)

8.5.2 Martins' experimental study (action of free jets on rocky river-beds)

The river-bed test facility was made up of equal, cubic, comparatively large blocks, systematically arranged, without cohesion. The number of tests carried out was 90, which is resulted from the combination of three angles of impact, α, with three openings of the gate closing the orifice discharging the jet, with two values of the sides of the blocks, *a*, with five depth of the water cushion, *e*. The opening of the gates was chosen so as to ensure an approximately square form in the initial cross section of the jet. The blocks were made of cement/sand mortar with a unit weight of about 2.2 g/cm^3 [29].

Table 8.7 summarizes the results of Martins' [29] experimental study for the cases with the sides of blocks equal to 4.7 cm. In the numerical simulation performed in this Chapter using BS3D, the air content, β, is assumed to be 30%. Thus, the pressure wave celerity is estimated (using Equation (8.29)) to be 25 m/s and the natural frequency of open-ended fracture is estimated (using Equation (8.28)) to be 0.014 second, knowing the fact that L = 14.1 cm (determined using Equation (8.31)). The maximum duration of extreme pressure fluctuation is assumed to be 5 ms.

In addition, Table 8.8 summarizes the results of Martins' [29] experimental study for the cases with the sides of blocks equal to 3 cm. The natural frequency of open-ended fracture is estimated using Equation (8.28) to be 8 ms, knowing the fact that L = 9 cm and c = 25 m/s (β = 30%). Since the maximum duration of extreme pressure fluctuation can not be higher than half the natural period, it is assumed to be 4 ms.

BS3D analyses are also summarized in Table 8.7 and Table 8.8. Since the experimental studies were performed in a short period of time, in the numerical simulations, the dynamic pressure magnitudes are estimated without considering the coefficient two introduced in Section 8.3.5 to account for long duration events. For each case, the acceleration, the initial velocity, and the maximum upward displacement of the block are calculated together with the ratio of h_{up}/z_b.

Table 8.7: Summary of Martins' experimental study ($a = 4.7$ cm) and BS3D analyses

α	e (m)	Q (l/s)	H, Fall, (m)	V_j m/s	D_j (m)	Scour Depth (m)	Y (m)	Acceleration (m/s^2)	$V_{\Delta T}$ (m/s)	h_{up} (m)	$\dfrac{h_{up}}{z_b}$
	0.30	150	1.10	7.23		0.097	0.397	752	3.76	0.026	0.55
	0.24	150	1.34	7.99		0.148	0.388	586	2.93	0.020	0.43
	0.18	160	1.49	8.40	0.05	0.197	0.377	472	2.36	0.016	0.35
	0.12	170	1.63	8.80		0.149	0.269	495	2.48	0.017	0.36
	0.06	180	1.79	9.22		0.148	0.208	427	2.14	0.015	0.31
	0.30	221	1.23	7.64		0.196	0.496	399	2.00	0.014	0.29
	0.24	235	1.37	8.07		0.246	0.486	367	1.84	0.013	0.27
40	0.18	253	1.56	8.60	0.06	0.189	0.369	423	2.12	0.015	0.31
	0.12	259	1.68	8.92		0.194	0.314	378	1.89	0.013	0.28
	0.06	270	1.82	9.29		0.15	0.210	363	1.82	0.012	0.27
	0.30	301	1.27	7.75		0.246	0.546	329	1.65	0.011	0.24
	0.24	324	1.41	8.19		0.246	0.486	329	1.65	0.011	0.24
	0.18	343	1.57	8.69	0.07	0.196	0.376	359	1.80	0.012	0.26
	0.12	353	1.71	9.01		0.198	0.318	329	1.65	0.011	0.24
	0.06	371	1.85	9.37		0.196	0.256	292	1.46	0.010	0.21
	0.30	134	1.50	6.63		0.152	0.452	323	1.62	0.011	0.24
	0.24	136	1.59	6.82		0.198	0.438	280	1.40	0.010	0.20
	0.18	144	1.70	7.04	0.05	0.197	0.377	326	1.63	0.011	0.24
	0.12	146	1.79	7.24		0.148	0.268	333	1.67	0.011	0.24
	0.06	153	1.89	7.43		0.105	0.165	312	1.56	0.011	0.23
	0.30	201	1.53	6.68		0.192	0.492	314	1.57	0.011	0.23
	0.24	208	1.62	6.88		0.245	0.485	265	1.33	0.009	0.19
55	0.18	215	1.71	7.08	0.06	0.194	0.374	279	1.40	0.010	0.20
	0.12	220	1.81	7.28		0.143	0.263	286	1.43	0.010	0.21
	0.06	226	1.91	7.48		0.148	0.208	232	1.16	0.008	0.17
	0.30	269	1.54	6.72		0.243	0.543	246	1.23	0.008	0.18
	0.24	278	1.64	6.93		0.198	0.438	262	1.31	0.009	0.19
	0.18	289	1.74	7.13	0.07	0.199	0.379	241	1.21	0.008	0.17
	0.12	293	1.81	7.28		0.146	0.266	244	1.22	0.008	0.18
	0.06	301	1.93	7.51		0.193	0.253	185	0.93	0.006	0.13
	0.30	110	1.77	6.27		0.099	0.399	553	2.77	0.019	0.41
	0.24	112	1.85	6.41		0.155	0.395	362	1.81	0.012	0.26
	0.18	115	1.92	6.54	0.05	0.149	0.329	328	1.64	0.011	0.24
	0.12	116	2.00	6.67		0.129	0.249	301	1.51	0.010	0.22
	0.06	119	2.08	6.79		0.097	0.157	269	1.35	0.009	0.20
	0.30	165	1.78	6.29		0.099	0.399	466	2.33	0.016	0.34
	0.24	166	1.86	6.43		0.148	0.388	313	1.57	0.011	0.23
70	0.18	171	1.94	6.56	0.06	0.149	0.329	278	1.39	0.009	0.20
	0.12	178	2.15	6.91		0.099	0.219	315	1.58	0.011	0.23
	0.06	179	2.09	6.82		0.106	0.166	218	1.09	0.007	0.16
	0.30	221	1.79	6.31		0.104	0.404	388	1.94	0.013	0.28
	0.24	227	1.87	6.45		0.151	0.391	267	1.34	0.009	0.19
	0.18	232	1.95	6.58	0.07	0.101	0.281	306	1.53	0.010	0.22
	0.12	229	2.03	6.71		0.15	0.270	203	1.02	0.007	0.15
	0.06	238	2.1	6.84		0.102	0.162	193	0.97	0.007	0.14

Table 8.8: Summary of Martins' experimental study ($a = 3$ cm) and BS3D analyses

α	e (m)	Q (l/s)	H, Fall, (m)	V_j m/s	D_j (m)	Scour Depth (m)	Y (m)	Acceleration (m/s²)	$V_{\Delta T}$ (m/s)	h_{up} (m)	$\dfrac{h_{up}}{z_b}$
	0.40	13.2	0.91	6.58		0.06	0.46	503	2.01	0.008	0.27
	0.32	14.3	1.11	7.25		0.16	0.48	550	2.20	0.009	0.29
	0.24	15.5	1.30	7.85	0.05	0.25	0.49	611	2.44	0.010	0.32
	0.16	16.8	1.50	8.43		0.22	0.38	1028	4.11	0.016	0.55
	0.08	17.6	1.68	8.94		0.15	0.23	825	3.30	0.013	0.44
	0.40	19.2	0.95	6.73		0.13	0.53	575	2.30	0.009	0.30
	0.32	21.2	1.12	7.29		0.22	0.54	651	2.60	0.010	0.34
40	0.24	23.4	1.32	7.93	0.06	0.28	0.52	833	3.33	0.013	0.44
	0.16	25.8	1.54	8.55		0.25	0.41	988	3.95	0.016	0.52
	0.08	27.1	1.72	9.04		0.19	0.27	828	3.31	0.013	0.44
	0.40	27.2	0.98	6.82		0.28	0.68	470	1.88	0.007	0.25
	0.32	30.0	1.17	7.46		0.31	0.63	682	2.73	0.011	0.36
	0.24	32.2	1.35	8.01	0.07	0.28	0.52	914	3.66	0.015	0.48
	0.16	34.6	1.56	8.60		0.19	0.35	821	3.28	0.013	0.44
	0.08	36.8	1.74	9.10		0.19	0.27	729	2.92	0.012	0.39
	0.40	12.4	1.31	6.20		0.13	0.53	274	1.10	0.004	0.14
	0.32	12.9	1.44	6.49		0.19	0.51	353	1.41	0.006	0.19
	0.24	13.8	1.57	6.78	0.05	0.22	0.46	534	2.14	0.008	0.28
	0.16	14.3	1.70	7.06		0.16	0.32	643	2.57	0.010	0.34
	0.08	14.6	1.83	7.31		0.13	0.21	506	2.02	0.008	0.27
	0.40	19.0	1.34	6.25		0.16	0.56	437	1.75	0.007	0.23
	0.32	20.1	1.47	6.55		0.28	0.60	397	1.59	0.006	0.21
55	0.24	20.8	1.59	6.82	0.06	0.28	0.52	614	2.46	0.010	0.32
	0.16	21.8	1.73	7.11		0.15	0.31	569	2.28	0.009	0.30
	0.08	22.2	1.85	7.35		0.10	0.18	360	1.44	0.006	0.19
	0.40	26.1	1.36	6.30		0.22	0.62	500	2.00	0.008	0.26
	0.32	26.8	1.49	6.59		0.31	0.63	530	2.12	0.008	0.28
	0.24	28.8	1.62	6.87	0.07	0.19	0.43	593	2.37	0.009	0.31
	0.16	28.9	1.75	7.14		0.16	0.32	520	2.08	0.008	0.27
	0.08	30.3	1.88	7.41		0.13	0.21	366	1.46	0.006	0.19
	0.40	10.5	1.63	6.01		0.06	0.46	418	1.67	0.007	0.22
	0.32	10.9	1.73	6.20		0.13	0.45	468	1.87	0.007	0.25
	0.24	11.2	1.83	6.38	0.05	0.16	0.40	616	2.46	0.010	0.33
	0.16	11.7	1.94	6.56		0.09	0.25	473	1.89	0.007	0.25
	0.08	11.7	2.03	6.71		0.07	0.15	299	1.20	0.005	0.16
	0.40	15.8	1.64	6.04		0.06	0.46	526	2.10	0.008	0.28
	0.32	16.8	1.75	6.23		0.13	0.45	552	2.21	0.009	0.29
70	0.24	16.6	1.84	6.39	0.06	0.12	0.36	504	2.02	0.008	0.27
	0.16	17.3	1.95	6.58		0.13	0.29	462	1.85	0.007	0.24
	0.08	18.4	2.08	6.79		0.10	0.18	306	1.22	0.005	0.16
	0.40	21.4	1.66	6.06		0.03	0.43	460	1.84	0.007	0.24
	0.32	22.1	1.76	6.25		0.16	0.48	524	2.10	0.008	0.28
	0.24	22.8	1.86	6.43	0.07	0.19	0.43	518	2.07	0.008	0.27
	0.16	23.4	1.96	6.60		0.13	0.29	406	1.62	0.006	0.21
	0.08	23.7	2.09	6.81		0.10	0.18	260	1.04	0.004	0.14

It can be seen in Table 8.7 that the ratio of h_{up}/z_b ranges between 0.13 and 0.55 with an average of 0.25 and a standard deviation of 0.08. In addition, the ratio of h_{up}/z_b, in Table 8.8, ranges between 0.14 and 0.55 with an average of 0.29 and a standard deviation of 0.10.

Section 8.5.1 showed that the method described in Section 8.3 may underestimate or overestimate the hydrodynamic pressure caused by jet impact. Although all overestimations occurred for developed jets and all underestimations occurred for core jets, since the number of tests are limited to four tests per jet type, it is assumed here that the hydrodynamic pressure caused by jet impact may be underestimated or overestimated regardless of jet type. Therefore, it is reasonable to choose the average ratio of h_{up}/z_b as a scour threshold. Consequently, it can be concluded that the block is most likely to be removed from its mould when $h_{up}/z_b > 0.25$.

Using BS3D together with the method described in Section 8.3 to estimate hydrodynamic pressure caused by jet impact and calibrated scour threshold ($h_{up}/z_b > 0.25$), scour depths are predicted for all 90 cases reported by Martins [29]. The results are summarized in Table 8.9. The ratio of predicted to measured scour depth, $\frac{d_{predicted}}{d_{measured}}$, ranges beween 0.39 and 1.52 (0.44 and 1.70) with an average of 0.88 (1.07) and a standard deviation of 0.30 (0.31) for the cases with the sides of blocks equal to 4.7 (3.0) cm. These results validate the ability of the suggested approach in predicting scour depth.

8.5.3 Example of a good quality granite

Bollaert [30] introduced a fictious rock mass to points out his methodology and the major parameters of interest. After dealing with the break-up phase of the closed-end joints of the rock using the Comprehensive Fracture Mechanics (CFM) model, he described the possibility of the ejection of rock blocks from their mass using Dynamic Impulsion (DI) model and compared the results with Annandale's Erodibility Index (EI) Method.

Table 8.9: Predicted scour depth (Martins' experimental study) using BS3D

α	D_j (m)	e (m)	$d_{measured}$	$d_{predicted}$ (BS3D)	$\dfrac{d_{predicted}}{d_{measured}}$	e (m)	$d_{measured}$	$d_{predicted}$ (BS3D)	$\dfrac{d_{predicted}}{d_{measured}}$
				a = 4.7 cm				a = 3.0 cm	
			Scour Depth, d (m)				Scour Depth, d (m)		
40	0.05	0.30	0.097	0.147	1.52	0.40	0.06	0.06	1.00
		0.24	0.148	0.198	1.34	0.32	0.16	0.16	1.00
		0.18	0.197	0.247	1.25	0.24	0.25	0.28	1.13
		0.12	0.149	0.199	1.34	0.16	0.22	0.37	1.70
		0.06	0.148	0.198	1.34	0.08	0.15	0.21	1.37
	0.06	0.30	0.196	0.196	1.00	0.40	0.13	0.16	1.26
		0.24	0.246	0.246	1.00	0.32	0.22	0.28	1.28
		0.18	0.189	0.189	1.00	0.24	0.28	0.37	1.31
		0.12	0.194	0.194	1.00	0.16	0.25	0.37	1.46
		0.06	0.15	0.15	1.00	0.08	0.19	0.27	1.43
	0.07	0.30	0.246	0.196	0.80	0.40	0.28	0.28	1.00
		0.24	0.246	0.196	0.80	0.32	0.31	0.37	1.19
		0.18	0.196	0.196	1.00	0.24	0.28	0.34	1.20
		0.12	0.198	0.148	0.75	0.16	0.19	0.31	1.66
		0.06	0.196	0.096	0.49	0.08	0.19	0.28	1.44
55	0.05	0.30	0.152	0.152	1.00	0.40	0.13	0.06	0.47
		0.24	0.198	0.148	0.75	0.32	0.19	0.13	0.69
		0.18	0.197	0.197	1.00	0.24	0.22	0.22	1.00
		0.12	0.148	0.148	1.00	0.16	0.16	0.25	1.56
		0.06	0.105	0.055	0.52	0.08	0.13	0.13	1.00
	0.06	0.30	0.192	0.142	0.74	0.40	0.16	0.13	0.83
		0.24	0.245	0.145	0.59	0.32	0.28	0.25	0.90
		0.18	0.194	0.144	0.74	0.24	0.28	0.34	1.21
		0.12	0.143	0.143	1.00	0.16	0.15	0.21	1.38
		0.06	0.148	0.058	0.39	0.08	0.10	0.06	0.63
	0.07	0.30	0.243	0.143	0.59	0.40	0.22	0.22	1.00
		0.24	0.198	0.148	0.75	0.32	0.31	0.31	1.00
		0.18	0.199	0.099	0.50	0.24	0.19	0.22	1.16
		0.12	0.146	0.096	0.66	0.16	0.16	0.16	1.00
		0.06	0.193	0.093	0.48	0.08	0.13	0.06	0.45
70	0.05	0.30	0.099	0.149	1.51	0.40	0.06	0.03	0.47
		0.24	0.155	0.155	1.00	0.32	0.13	0.13	1.00
		0.18	0.149	0.149	1.00	0.24	0.16	0.19	1.21
		0.12	0.129	0.097	0.75	0.16	0.09	0.09	1.00
		0.06	0.097	0.047	0.48	0.08	0.07	0.03	0.44
	0.06	0.30	0.099	0.149	1.51	0.40	0.06	0.06	1.00
		0.24	0.148	0.148	1.00	0.32	0.13	0.13	1.00
		0.18	0.149	0.099	0.66	0.24	0.12	0.12	1.00
		0.12	0.099	0.099	1.00	0.16	0.13	0.13	1.00
		0.06	0.106	0.056	0.53	0.08	0.10	0.06	0.61
	0.07	0.30	0.104	0.104	1.00	0.40	0.03	0.03	1.00
		0.24	0.151	0.101	0.67	0.32	0.16	0.16	1.00
		0.18	0.101	0.101	1.00	0.24	0.19	0.19	1.00
		0.12	0.15	0.1	0.67	0.16	0.13	0.10	0.79
		0.06	0.102	0.05	0.49	0.08	0.10	0.06	0.63

The rock is assumed to be a very good quality granite with a tensile strength, T, of 19 MPa and an unconfined compressive strength, UCS, of 296 MPa. The unit weight of the rock block is 2,650 kg/m^3. It exhibits moderately semi-elliptical jointing in the x-direction (Figure 8.12) and moderately to highly single-edge jointing in the y-direction. The rock is considered to consist of horizontal layer of 1 m of height (z_b = 1m). The length of each side of the block, x_b, is assumed to be 2 m.
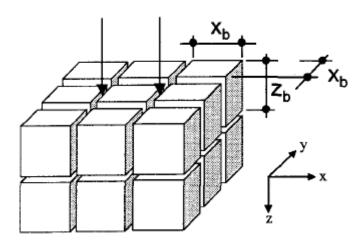
Figure 8.12: Cubic blocks in the rock mass [30].

The jet is issuing from an intermediate outlet structure and its initial turbulence intensity, T_u, is estimated at 5%. The jet is vertically impinging with an impact velocity of V_j = 40 m/s and an estimated diameter at its point of impact of D_j = 4 m. The distance from this point of impact down to the water-rock interface is estimated to be Y = 36 m. As such, the ratio of pool depth to jet diameter Y/D_j = 9 and developed jet impact conditions govern. The air content is assumed to be negligible and the natural period of the fracture is given to be 0.12 seconds [30].

Bollaert [30] estimated the ultimate scour depth from the bottom of the plunge pool to be 11, 9, and 1 m using CFM, DI, and Annandale's EI method, respectively. In this Section, the scour depth is estimated using BS3D (together with the above explained approach for estimating the dynamic water pressure and the given failure criteria). Comprehensive Fracture Mechanics (CFM) and Annandale's EI methods consider

developing new fractures in the rock mass due to jet impact. However, Dynamic Impulsion (DI) method and BS3D analysis just focus on possibility of the ejection of the rock block from its mould. Thus, in this Section, the comparison is made between the results of DI method and BS3D analysis.

Bollaert [30] (in his DI method) assumed that the average net impulsion which can be estimated using Equation (8.10) and Figure 8.6 is applied to the block during the fissure natural period. This net impulsion was then set equal to the product of the mass of the block times the velocity. This results in the maximum velocity that could be given to the block. This velocity or kinetic energy is transformed into potential energy by ejection of the block. The maximum displacement of the block can be evaluated as follows [30]:

$$h_{up} = \frac{V_{\Delta t-pulse}^2}{2 \cdot g} \tag{8.32}$$

Table 8.10 summarizes the determination of the ultimate scour depth using both Bollaert's DI Method and BS3D.

Table 8.10: Determination of the scour depth using Bollaert DI Method and BS3D

Depth of scour (m)	Y (m)	Y/D_j	Bollaert (DI Method)			BS3D; dynamic water pressure estimated using the approach explained in Section 8.3			
			V_{up} (m/s)	h_{up} (m)	$\dfrac{h_{up}}{z_b}$	Acceleration (m/s^2)	$V_{up}(V_{\Delta T})$ (m/s)	h_{up} (m)	$\dfrac{h_{up}}{z_b}$
1	37	9.3	12.4	7.84	7.84	2647	13.24	0.78	0.78
2	38	9.5	10.46	5.58	5.58	2480	12.40	0.73	0.73
4	40	10.0	8.52	3.70	3.70	2144	10.72	0.63	0.63
5	41	10.3	6.58	2.21	2.21	1910	9.55	0.56	0.56
7	43	10.8	5.61	1.60	1.60	1561	7.81	0.45	0.45
8	44	11.0	4.64	1.10	**1.10**	1387	6.94	0.39	0.39
9	45	11.3	3.67	0.69	0.69	1212	6.06	0.35	0.35
10	46	11.5	2.7	0.37	0.37	1038	5.19	0.29	**0.29**
11	47	11.8	1.73	0.15	0.15	863	4.32	0.24	0.24
12	48	12.0	0.76	0.03	0.03	737	3.69	0.20	0.20

Assuming that the ultimate scour depth is reached when the rock block displacement becomes less than the height of the block ($h_{up}/z_b < 1$), Bollaert [30] found that the ultimate scour depth is about 9 m (see Table 8.10). In addition, assuming that the

ultimate scour depth is reached when the rock block displacement becomes less than a quarter of the height of the block ($h_{up}/z_b < 0.25$), BS3D analyses (adopting the maximum fluctuation duration of 5 ms) estimated that the ultimate scour depth from the plunge pool bottom is about 11 m.

In Section 8.5.1, it was found that the method described in Section 8.3 may overestimate dynamic water pressure caused by developed jets. Therefore, the calculated vertical displacement of the block and, in turn, the scour depth may be overestimated. The jet in Table 8.10 that the jet is a developed one and, thus, the scour depth may be overestimated in this case. However, the ultimate scour depths estimated using BS3D and DI method agree well with each other (11 and 9 m from the plunge pool bottom, respectively).

8.5.4   Case study of Cabora-Bassa dam

The Cabora-Bassa Dam, a double curvature arch dam, is located on the Zambezi River in Mozambique and has a total spillway discharge capacity of 13,100 m^3/s at a maximum reservoir level of 326 m a.s.l.. The corresponding tailwater level is at 225 m a.s.l. with a depth of nearly 50 m above the natural riverbed. The spillway consists of eight identical sluice gates with a height of 6 m and a width of 7.8 m. The exit lip of the gates is at elevation 244.30 m a.s.l. and makes an angle of 32.3° with the horizontal. The riverbed is very irregular and has its elevations varying from 170 to 180 a.s.l.. The rock is mainly granitoide gneiss with little cracking, but with a few gabbro and lamprophyre dykes [30, 31].

Hydraulic model tests at a 1/75 scale have been conducted at LNEC, Lisbon, Portugal [358]. A moveable bed model was used, made with gravel weakly aggregated with aluminous cement. The test results predicted the maximum scour depth at an elevation of 150 m a.s.l. and a downstream distance from the jet outlet of 250 m [30, 31].

The prototype behavior of the dam is characterized by two important operating periods. The first one happened in 1975 during 42 days, for a discharge of 6,000 m^3/s (=4 gates). The scour depth after this operation was measured at about 170 m a.s.l.. The

tailwater level was at 215 m a.s.l.. The second period occurred in 1978. The spillway was being operated for four and a half consecutive months. The maximum reservoir level was at 327.74 m a.s.l.. An extensive survey of the scour pit in 1980 showed that the deepest point of the scour pit was situated at 158 m a.s.l., i.e., 22 m deeper than the original riverbed. This occurred at a downstream distance from the jet outlet ranging from 240 to 260 m [30, 31].

Bollaert [30] assumed that the rock mass is soft rock with a *UCS* = 13 MPa and very little cracking, thus a *RQD* = 90%, which seems to be unreal assumption for gneiss. Annandale's [324] Erodibility Index Method has been calibrated based on the equilibrium scour depth of 160 m a.s.l. attained on the prototype after 1978 [324].

The diameter of the jet at issuance from the dam has been estimated as the equivalent hydraulic diameter of the $6m \times 7.8m$ rectangular outlet. This results in an initial jet diameter D_i = 7.7 m. The jet trajectory has been calculated based on ballistic equations and air drag [30, 31]. Bollaert [30] and Bollaert and Schleiss [31] estimated the initial turbulence intensity of the jet, T_u, to be 4% and 5%, respectively. Table 8.11 summarizes jet characteristics of the dam estimated by Bollaert [30] and Bollaert and Schleiss [31] based on different assumptions for the initial turbulence intensity. The air concentration at jet impact is considered very high (β = 60%) [31].

Bollaert [30] and Bollaert and Schleiss [31] performed different analyses using CFM and DI method to estimate the ultimate scour depth based on different assumptions, some of which are described above. In this Section, two series of analyses have been performed to estimate scour depth using BS3D and either Bollaert's [30] or Bollaert's and Schleiss's [31] assumptions.

Table 8.11: Jet characteristics of Cabora-Bassa dam

Parameter	Bollaert [30]	Bollaert and Schleiss [31]
Initial turbulence intensity of the jet, T_u	4%	5%
Jet impact velocity, V_j, (m/s)	35	42
Impact diameter, D_j, (m)	8	7.2
Outer jet diameter, D_{out}, (m)	20	17
Jet break-up length, L_b, (m)	167	152
Downstream distance from the jet outlet, X_{ult}, (m)	150	145

8.5.4.2 Ultimate scour depth of Cabora-Bassa dam (Bollaert's assumptions)

Bollaert [30] based on his Comprehensive Fracture Mechanics (CFM) model found that instantaneous crack grows until an elevation of 170 m a.s.l.. Further scouring to 160 m a.s.l. needed 137 days of discharge, whether this elevation was obtained *in situ* after 139 days. Further scouring down to 150 m a.s.l. will need another 140 days of similar discharge conditions. Then, the phenomenon slows down due to jet diffusion effects. The elevation of 140 m a.s.l. is considered as a practical limit of the ultimate scour depth [30].

The characteristic block dimensions are based on model tests performed at LNEC, Lisbon. These tests represented *in situ* blocks with a weight between 50 and 290 kN [358]. Assuming a cubic shape, this corresponds to side lengths ranging from 1.2 to 2.2 m. A side length of 2 m has been used. Due to the high aeration rate small wave celerity of 100 m/s is taken. The natural period of the open-ended fracture is estimated to be 0.18 s, knowing the fact that $L = 6$ m. The unit weight of the rock block is assumed to be equal to 2,000 kg/m^3 [30]. The results of Bollaert's DI analyses are summarized in Table 8.12.

Table 8.12: Determination of the ultimate scour depth of Cabora-Bassa dam based on the DI model [30]

Y (m)	D_j (m)	V_j (m/s)	Y/D_j	V_{up} (m/s)	h_{up} (m)	h_{up}/z	EI m a.s.l.
166			0.53	10.23	5.33	2.67	160.2
168			0.52	10.11	5.21	**2.60**	**159.5**
170			0.52	9.98	5.08	2.54	158.7
180			0.49	9.37	4.48	2.24	154.8
190			0.46	8.79	3.93	1.97	150.9
200	20	35	0.43	8.22	3.44	1.72	147.0
210			0.41	7.67	3.00	1.50	143.1
220			0.38	7.14	2.60	1.30	139.2
230			0.36	6.63	2.24	1.12	135.3
234			0.35	6.43	2.11	1.05	133.7
236			0.35	6.33	2.04	**1.02**	**132.9**
238			0.34	6.23	1.98	0.99	132.1

It can be seen in Table 8.12 that, using DI method, the scour depth of 160 m a.s.l. that was attained after 1978 corresponds to a critical displacement of 2.6 times the height of the characteristic rock block. In the other words, the ultimate scour depth based on the dynamic uplift criterion is much deeper. The theoretical critical displacement of one times the height of the block is attained at an elevation of 133 m a.s.l. [30].

BS3D analyses is performed in this Section to estimate the ultimate scour depth using the jet characteristics given in the second column of Table 8.11. The maximum duration of extreme pressure fluctuation is adopted to be 5 ms. Assuming that the block is most likely to be removed when $h_{up}/z_b < 0.25$, the ultimate scour depth is estimated to be 161 m a.s.l. ($Y = 164$ m; $a = 1239$ m/s^2; $V_{up} = 6.2$ m/s; $h_{up} = 0.52$; and $h_{up}/z = 0.26$).

It should be mentioned that, in predicting the ultimate scour depth, the effect of pool geometry introduced by Manso [24] was not considered (it is assumed that the pool bottom is flat during the whole scour process). In addition, the maximum value that BS3D gives for the ratio of h_{up}/z, in this problem, is 0.3. It can be seen that the ultimate scour depth predicted using BS3D (and the method explained in Section 8.3 to estimate hydrodynamic pressure and failure criterion) agrees very well with what was attained after 1978.

8.5.4.3 Ultimate scour depth of Cabora-Bassa dam (Bollaert's and Schleiss's assumptions)

Bollaert and Schleiss [31] indicated that the CFM method results that are in good agreement with the prototype observations: a depth of 170 m a.s.l. is attained after 43 days of discharge (42 days on prototype), and the depth of 158 m a.s.l., observed on the site after the 1978 spillage of 139 days is obtained by the CFM method after 114 days of additional spillage. Further scouring down to 154 m a.s.l. would need another 380 days of discharge. After, the phenomenon slows down, due to jet diffusion effects, and an additional scouring down to 150 m a.s.l. would need about 2,500 days of discharge. Stating that the 1978 discharges were exceptional, and accounting for a reasonable

302

lifetime of the dam, it can be argued that the elevation of 150 m a.s.l. constitutes a practical limit of ultimate scour depth, in accordance with the model tests [31].

Bollaert and Schleiss [31] estimated the scour depth using DI method (Table 8.13). In their simulation, they assumed cubic shape blocks with a side length of 2 m. Due to the high aeration rate, the wave celerity is defined at 100 m/ s. They found that [31]:

- The theoretically necessary displacement of one times the height of the block is already attained at an elevation of 176 m a.s.l.

- The scour depth of 158 m a.s.l., observed on the prototype after the 1978 discharge period, corresponds to a h_{up}/z ratio of 0.30.

- The ultimate scour depth based on the dynamic uplift criterion, however, should be somewhat deeper, and has been chosen at 152 m a.s.l., corresponding to a h_{up}/z ratio of 0.20.

Bollaert and Schleiss [31] stated that this calibration reasonably agrees with the ultimate depths found by the CFM method and observed during the model tests [31].

Table 8.13 summarizes the results of BS3D analyses performed in this Section using the jet characteristics given in the third column of Table 8.11. In these simulations, it is assumed that the maximum duration of extreme pressure fluctuation is 5 ms. Assuming that the block is most likely removed when $h_{up}/z_b > 0.25$, the ultimate scour depth is estimated to be at 155 m a.s.l. which agrees with the ultimate depths found by the CFM and DI method by Bollaert and Schleiss [31] and observed during the model tests by Ramos [358]. It should be mentioned that, in predicting the ultimate scour depth, the effect of pool geometry introduced by Manso [24] was not considered (it is assumed that the pool bottom is flat during the whole scour process).

Table 8.13: Determination of ultimate scour depth of Cobara-Bassa dam using DI method [31] and BS3D

Y (m)	D_j (m)	V_j (m/s)	z (m)	Y/D_j	Bollaert's and Schleiss's [31] DI analyses			BS3D (using jet characteristics given in the 3rd column of Table 8.11); dynamic water pressure estimated using the approach explained in Section 8.3			Elevation m a.s.l.
					V_{up} (m/s)	$\dfrac{h_{up}}{z}$	Uplift	Acceleration (m/s^2)	V_{up} (m/s)	$\dfrac{h_{up}}{z}$	
62.3				8.6	3.46	0.61	Uplift	1626	8.13	0.69	168.9
63.4				8.8	3.37	0.58	Uplift	1459	7.295	0.62	168.1
65.3				9.0	3.22	0.53	Uplift	1367	6.835	0.57	166.7
66.4				9.2	3.14	0.5	Uplift	1315	6.575	0.55	165.9
69				9.5	2.95	0.44	Vibrations	1191	5.955	0.49	164.0
71.6				9.9	2.74	0.38	Vibrations	1068	5.34	0.44	162.1
74.2	7.2	42	1	10.3	2.57	0.34	Vibrations	997	4.985	0.41	160.1
77.2				10.7	2.38	0.29	Vibrations	841	4.205	0.34	158.0
79.8				11.0	2.23	0.25	Vibrations	706	3.53	0.28	156.0
82.4				11.4	2.08	0.22	Vibrations	572	2.86	0.22	154.1
84.6				11.7	1.96	0.2	Stability	457	2.285	0.17	152.5
87.9				12.2	1.78	0.16	Stability	397	1.985	0.14	150.0
90.5				12.5	1.66	0.14	Stability	375	1.875	0.13	148.1

8.5.5 Two cases of scour in prototypes (Picote and Kondopoga)

Two cases of scour in prototypes found in the literature [29, 359, 360] are analyzed using BS3D (and the method explained in Section 8.3 to estimate hydrodynamic pressure). The results of analyses are summarized in Table 8.14.

For each case, the maximum vertical displacement of the block at the given scour depth are calculated. It can be seen that, at the reported ultimate scour depth, the ratios of h_{up}/z determined using BS3D are 0.30 and 0.28 for Picote and Kondopoga prototypes, respectively. This agrees with the failure criterion introduced in Section 8.4.2 (the block is most likely to be removed when $h_{up}/z_b > 0.25$).

Table 8.14: BS3D analyses of two cases of scour in prototypes (Picote and Kondopoga)

Parameter / Scheme	Picote (Portugal) [359]	Kondopoga (USSR) [360]
Side length of cubic shape block, a, (m)	1.05	0.14
Cushion of water, e, (m)	36	1.45
Discharge, Q, (m³/s)	7000	70
Fall height, H, (m)	45	11.4
Jet velocity, V_j, (m/s)	29.71	14.95
Jet diameter, D_j, (m)	17.32	2.44
Estimated air entrainment (air content, β)	Intermediate (10%)	Negligible (2.5%)
Wave celerity, c, (m/s)	40	70
Fissure length, L, (m)	3.15	0.42
Fissure natural period, T, (s)	0.16	0.012
Actual scour depth (m)	19	4.8
Y (m)	55	6.25
Y/D_j	3.18	2.65
Acceleration (m/s²)	858.70	1304
Max duration of extreme pressure (ms)	5	5
Initial velocity of the block, V_{up}, (m/s)	4.29	6.52
Maximum vertical displacement of the block, h_{up}, (m)	0.311	0.039
h_{up}/z_b	0.30	0.28

8.5.6 Example of flutter and divergence

In order to demonstrate the ability of BS3D in predicting more complicated failure modes (divergence and flutter) together with dealing with *in situ* stress and dilation behavior of rock fractures, a fictious example is introduced in this Section.

A cubic rock block with edge length of 1 m is assumed to be in its mould at the bottom of a plunge pool. The block is subjected to gravity (unit weight of 2,550 kg/m³) and hydrostatic *in situ* stress of 50 kPa (which applies a normal stress of 50 kPa on fractures). The plunge pool has a depth, Y, of 15 m. The jet is assumed to be a moderately turbulent circular jet with diameter, D_j, and velocity, V_j, at plunge pool surface of 10 m and 45 m/s (at the end of a fall height of about 100 m), respectively. The air content, β, is 35% and the distance of the block centroid to the jet centerline is 7 m.

As illustrated in Figure 8.13, water flows in the negative y-direction along face $A_3A_4A_8A_7$ and applies a hydrodynamic water pressure equal to $p_{hyd} = 1$ MPa (which can

be generated by water flow with a velocity of about 45 m/s) to the portion of the block boundary that moves out of its mould. In order to simplify this example, hydrodynamic shear stress is not considered.

The following constitutive models are considered for the rock fractures:

- Mohr-Coulomb model (with an effective friction angle of 50°)
- Original and modified Barton-Bandis model ($JRC = 10$, $JCS = 70$ MPa, and $\varphi_b = 25$ °)

It should be mentioned that, considering the normal stress applied to the fractures (50 kPa), the effective friction angle of 50° in Mohr-Coulomb model simulates the same fracture shear strength as original or modified Barton-Bandis model does with $JRC = 10$, $JCS = 70$ MPa, and $\varphi_b = 25$ °.

(a)   (b)
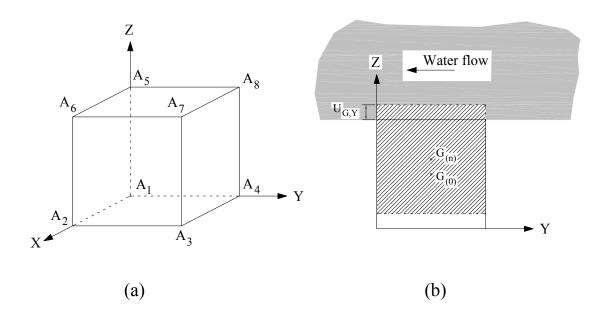
Figure 8.13: (a) Geometry of the cubic rock block considered in the example of flutter and divergence; (b) view of the block in YZ-plane and applied pressure due to water flow

Eliminating the dilation behavior of the fractures and more complicated failure modes (dynamic flutter and divergence), the block is expected to have a factor of safety

of 0.25 with static failure mode along z-axis. However, BS3D analyses give the following factors of safety and failure modes (see Figure 8.14 for displaced configurations):

- Mohr-Coulomb model: the failure mode of the block is dynamic divergence along z-axis with a factor of safety of 0.18.
- Original and modified Barton-Bandis model: the failure modes and the factors of safety obtained using these models are almost the same. The failure mode of the block is dynamic flutter with a factor of safety of 0.2 and directions $(u_x, u_y, u_z, \theta_x, \theta_y, \theta_z)^T$ equal to:

    1- Direction 1: $(0.196, -0.98, 0, 0, 0, 1)^T$

    2- Direction 2: $(0.99, -0.01, 0, 0, 0, 1)^T$

The natural period of the open-ended fracture is estimated to be 0.23 s, because L = 3 m (determined using Equation (8.31)) and c = 25 m/s (estimated employing Equation (8.29)). The scour depths predicted using different approaches are given in

Table 8.15. Notice that the DI approach (Section 8.2.1) predicts that the block will be stable.

This example shows that a block may be fail by dynamic divergence or flutter before its static failure mode can be reached. These failure modes can be detected by BS3D which can also deal with *in situ* stress and dilation behavior of the fractures.
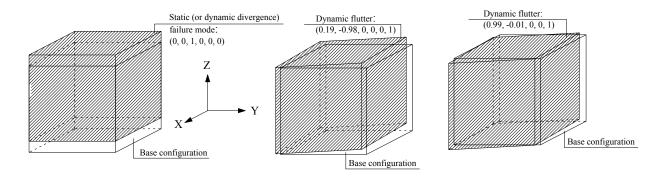
Figure 8.14: Displaced configuration of the block (predicted using different approaches)

Table 8.15: Predicted scour depth (using different approaches) for the fictious example
introduced to demonstrate the ability of BS3D in dealing with flutter and divergence

Analysis description	Fracture constitutive model	FS	$\dfrac{h_{up}}{z_b}$	Scour depth (m)	Observations (prediction)
BS3D[*]; Eliminating fractures' dilation behavior and more complicated failure modes (dynamic flutter and divergence)	Mohr-Coulomb model, Barton's model, and modified Barton's model	0.25	0.230	0	The block remains in place.
BS3D[*]	Mohr-Coulomb model	0.18	0.252	1	The block will be removed.
BS3D[*]	Barton's model and modified Barton's model	0.20	0.245	1	The block most likely will be removed.
DI (Net uplift dynamic water pressure is predicted using Figure 8.6 considering the effect of distance from jet centerline. The maximum vertical displacement of the block is evaluated using Equation (8.32))	Mohr-Coulomb model	N/A	0	0	The net uplift force is smaller than the shear strength of the fractures.

[*] In BS3D analyses, hydrodynamic pressure caused by jet impact is estimated using the approach given in Section 8.3. In addition, the maximum vertical displacement of the block, h_{up}, is evaluated using the method described in Section 8.4.1.

8.6 SUMMARY AND CONCLUSIONS

In this Chapter, the stability of single rock blocks in plunge pools was investigated. An approach was introduced to estimate pressure forces generated in plunge pools due to high-velocity jet impacts. This method together with the ability of BS3D in determining the stability of the rock block and its displacement were validated using Federspiel's experimental study.

Based on the simulation of Martins' [29] experimental study using BS3D, it was proposed to consider that the block is most likely to be removed when $h_{up}/z_b > 0.25$.

The application of the scour model was explained by a fictious rock mass (good quality granite) initially introduced by Bollaert. The whole scour model and BS3D algorithm are then validated using three case histories and prototypes.

Finally, the ability of BS3D in predicting more complicated failure modes (divergence and flutter) together with dealing with *in situ* stress and dilation behavior of rock fractures was demonstrated using a fictious example. It was shown that scour threshold and depth may be underestimated if divergence and flutter are not taken into account.

CHAPTER 9:   CONCLUSIONS AND RECOMMENDATIONS

9.1   SUMMARY AND CONCLUSIONS

9.1.1   Single rock block stability analysis approach

BS3D, a single rock block stability analysis approach, which is an incremental-iterative algorithm introduced by Tonon's [1], was described in detail. The method is to analyze general failure modes of rock blocks subject to generic forces, including non-conservative forces such as water forces. The block interacts with the surrounding constraint space using a finite number of sensor points. Consistent stiffness matrices were developed that fully exploit the quadratic convergence of the adopted Newton–Raphson iterative scheme. The algorithm takes into account large block displacements and rotations, which together with non-conservative forces make the stiffness matrix non-symmetric.

Also included in the algorithm are fracture dilatancy and *in situ* stress. Moreover, progressive failure is captured by the algorithm, which has proven capable of detecting numerically challenging failure modes, such as rotations about only one point.

All possible failure modes can be automatically detected along the block's equilibrium path; they may originate from a limit point or from dynamic instability (divergence or flutter); equilibrium paths emanating from bifurcation points are followed by the algorithm.

The algorithm identifies both static and dynamic failure modes. Static analyses (including limiting equilibrium) do not take into account the block's inertia properties, which may lead to detecting an incorrect failure mode. The calculation of the factor of safety comes with no overhead, and does not require trial and error model runs using the reduction of the strength parameters, which may even lead to erroneous failure modes.

Rock blocks that are typically thought of reaching equilibrium by translation actually rotate about their centroid because the reaction forces create a non-zero moment about the centroid; this is the case of 2-plane wedges subjected to their own weight. The

equilibrium path of a rock block that undergoes slumping failure must first pass through a bifurcation point, unless the block is laterally constrained.

9.1.2 Modified Barton's model (a constitutive model for rock fractures)

Two databases were built by collecting the results of direct shear tests available in the literature: Monotonic Direct Shear Tests (MDST), which contains the results of 362 tests, and Cyclic Direct Shear Tests (CDST), which contains the results of 18 tests.

Analyses of these databases showed that Barton's failure criterion works very well in predicting the shear strength of rock fractures. However, some weaknesses were found in the original Barton model and addressed by correlation analyses performed on collected data. The following modifications to Barton's model are proposed based on the results of correlation analyses:

1) An empirical equation is proposed to predict the peak shear displacement of rock fractures. The equation considers the effect of normal stress on the peak shear displacement, while Barton's equation does not. In addition, this equation can be used for all types of rock fractures, including sawed, smooth, and rough, while Barton's equation predicts an incorrect value of zero for the peak shear displacement of sawed fractures. Finally, the predicted peak shear displacement employing the proposed equation of this study decreases as *JRC* increases. However, the predicted value of peak shear displacement using Barton's equation increases with *JRC*.

2) An empirical equation is proposed to predict the mobilized *JRC*, which is used to calculate the shear stress-displacement curve after peak shear displacement. Besides better matching the MDST database than Barton's Table, the empirical equation gives a smoother curve compared to the linear interpolation of the values given in Barton's Table and is easier to implement numerically.

3) An equation is proposed to obtain pre-peak dilation at each shear displacement. The proposed model has none of the inconsistencies and ambiguity of Barton's model. Moreover, it simulates negative dilation, while Barton's does not. In

311

addition, the dilation displacement at any shear displacement can be calculated easily using this equation; also the numerical implementation is much easier.

4) An equation is proposed to obtain post-peak dilation at each shear displacement. This equation contains an integral which should be solved using numerical methods.

5) Two tables are introduced to simulate the pre-peak shear stress-displacement curve (mobilization of pre-peak shear strength): one to estimate the mobilized *JRC* at any shear displacement and another to evaluate the mobilized base friction angle at any shear displacement.

6) A method is described in detail to simulate shear stress-displacement behavior of rock fractures in the process of loading, unloading, reversal, and reloading.

7) A method is proposed to simulate the dilatancy behavior of rock fractures in cyclic shearing using the mobilized value of *JRC*. By investigating the CDST database, it was found that at the end of each unloading stage the dilation displacement is almost zero.

8) The *JRC* angular distribution was found not to have an elliptical shape, but the shape of an "8". Experimental data found in the literature were used to formulate a predictive model for the anisotropic distribution of *JRC* in the plane of a fracture. The input data for the model are the maximum and the minimum *JRC*. The shear strength, shear stiffness, and dilation displacement of rock fractures subjected to shearing in any direction can then be predicted by using either original or modified Barton's model.

The proposed modifications to Barton's original model were validated by performing an experimental study from which the following conclusions can be drawn:

- For sawed (or planar) fractures, the modified model works much better than the original Barton's model.

- Both the modified model and Barton's original model display substantial approximation in predicting the dilatant behavior of rough fractures. However,

due to the following reasons, it is believed that the modified model should be used for predicting the dilation behavior of rock fractures:

1- Barton's empirical equation for peak shear displacement of rock fractures can not consider the effect of normal stress on the increase of the peak shear displacement.

2- Barton's model can predict dilation displacement only at the peak shear displacement.

3- The modified model works better than Barton's model in predicting stress-displacement curve for high values of the δ_h/δ_{peak} ratio.

4- The negative dilation (found also in the experimental study) is not considered in Barton's model, which can cause overestimation of factor of safety analysis such as stability of rock blocks in tunnels.

9.1.3 Estimating normal stiffness of rock blocks using direct BEM

An algorithm was proposed to remove the rigid-body motions in the solution of an elastostatic problem discretized by the direct BEM approach. The algorithm fixes one boundary point to prevent rigid-body translations. Finally, the rigid-body rotations are eliminated from the displacement solution. The method was applied to the calculation of the normal stiffness of rock blocks. The algorithm was verified with a simple example for which analytical solution is available based on the theory of elasticity. This example shows the increased accuracy of the proposed algorithm with respect to the approximation proposed by Tonon [1].

9.1.4 Validation of BS3D for wedge failure

Wedge failure validation under gravity loading has been carried out for BS3D [1]. Sixty four physical models and two case histories were analyzed using this method. For the wedge stability problem, physical modeling and BS3D give the same failure modes except for six cases in which sliding on one plane were observed in physical models while BS3D predicted sliding on two planes. This is due to the fact that the two failure

modes have very similar factors of safety and sliding directions, and BS3D considers the deformability of the sliding planes.

In all cases, safety factors obtained using BS3D analyses were the same as obtained using Block Theory limiting equilibrium analysis. The results of BS3D analyses for two case histories agree well with the observations of failed wedges.

9.1.5 Stability of rock blocks formed in the roof of a circular tunnel

9.1.5.1 2D triangular prism formed in the roof of a circular tunnel

An analytical method has been presented for stability analysis of 2D triangular prism formed in the roof of a circular tunnel. In addition, a new definition for the factor of safety of the block was presented. Based on sensivity analyses, the following conclusions were made:

1) Different safety factor's definitions may lead to different conclusions in sensivity analyses.

2) The factor of safety defined in this study is limited to positive values, the same as most geotechnical engineering (and civil engineering) applications: at equilibrium, FS=1 for stable blocks, FS > 1, and for unstable blocks, 0 < FS < 1.

3) Contrary to what established in the literature (by Hudson and Harrison [310]), the stability of 2D triangular wedge is independent of the ratio of k_s / k_n.

4) 2D wedge stability of is strongly affected by the friction angle of the fractures.

5) Increasing the *in situ* stress (or lateral pressure coefficient) slightly increases the stability of the block in low stress (or k_0) regimes and has no effect on the factor of safety in high stress (or k_0) regimes.

9.1.5.2 3D tetrahedron formed in the roof of a tunnel

An analytical approach was presented using limit equilibrium methods to analyze the stability of a tetrahedron formed in the roof of a tunnel. The factor of safety of the

314

wedge was defined as the ratio of passive to active forces (or the ratio of available shear strength to the required shear stress at equilibrium).

The sensivity analyses performed using the analytical approach and BS3D lead to the following conclusions:

1) Although the definition of the factor of safety in the analytical method is the same as the definition of the factor of safety in BS3D, if a block is analyzed using both approaches, the factors of safety will be different because:

    - BS3D takes into account the deformability of the rock block, fractures, and the rock mass surrounding the block, while the analytical approach does not.

    - BS3D considers the progressive failure and the mobilization of shear strength, while the analytical limit equilibrium method does not.

    - In analytical limit equilibrium solution, the *in situ* stresses are assumed to be independent of the block displacement. However, in BS3D analysis, the part of the *in situ* stresses applied to the block changes with block movement.

2) Adopting Mohr-Coulomb as constitutive model of fractures, the initial normal stiffness of the fractures (and in turn the normal stiffness of the fractures) has no effect on stability of 3D wedges.

3) Adopting Barton's original or modified model, the factor of safety of tetrahedral rock block decreases with increasing initial normal stiffness of fractures.

4) The safety factors calculated using the Barton's model and the Mohr-Coulomb model are exactly the same, if the shear displacements of fractures are smaller than 30% of the peak shear displacement.

5) Modified Barton's model uses a different equation for the peak shear displacement and has a different FS compared to those of other models.

6) The factor of safety decreases with increasing size of the wedge.

9.1.5.3 3D prism in the roof of a circular tunnel

Yow and Goodman [312] presented a numerical model for keyblock stability. Using the field observations of keyblocks reported by Yow [316], they performed sensivity analyses on effects of different parameters such as block geometry, *in situ*

stresses, and discontinuity properties on stability of keyblocks. As far as constitutive model for rock fractures, Yow and Goodman [312] used Barton's model assuming the peak shear displacement is equal to one percent of the length of the block. They investigated the effect of the fracture base friction angle, the magnitudes of *JRC* and *JCS*, the initial normal stiffness, the magnitude of vertical stress, and the lateral pressure coefficient on stability of keyblocks in the roof of a circular tunnel. The same sensivity analyses were performed using BS3D. The differences of the analyses done here with respect to those of Yow and Goodman [312] are as follows:

- The definition of the factor of safety was different.
- The progressive failure of rock fracture with different constitutive models was considered.
- Wider parameter ranges were checked.
- The effects of dilation displacement, principal stress directions, distance from the excavation face, the block size, and the tunnel diameter on the stability of the keyblock were investigated.

The following conclusions may be drawn from the sensivity analyses:

1) Even using the old Barton's model (peak shear displacement is equal to one percent of the length of the block) the factor of safety calculated using BS3D is different from the result of Yow 's and Goodman's [312] analysis. The reason is that the definition of the factor of safety is different and BS3D considers the progressive failure of the fractures, while Yow 's and Goodman's [312] analysis does not.

2) In BS3D analyses, the factor of safety calculated using simplified Barton's model (dilation starts from zero shear displacement) was the highest, followed by those determined using Barton's model, Mohr-Coulomb's model, and the modified Barton's model. The Mohr-Coulomb's model, the Barton's model, and the simplified Barton's model used in this study are exactly the same except for the dilation displacement. The simplified Barton's model has the highest dilation

316

displacement and, thus, the highest normal forces applied to the fractures, the highest shear strength of discontinuities, and the highest factor of safety.

3) The modified Barton's model differs from Barton's model in terms of the peak shear displacement, the mobilized shear strength, and the dilatancy behavior. Therefore, the factor of safety calculated using the modified Barton's model is different (smaller for this prism) from those obtained employing the Barton's model.

4) The stability of the prism weakly depends on *JRC* (decreasing *JRC* from 20 to 0 decreases FS by 30%). However, Yow and Goodman [312] found that the block stability strongly (decreasing *JRC* from 5 to 0 decreases FS by 100%) depends on *JRC*.

5) The Barton's model, the simplified Barton's model, and the Mohr-Coulomb's model have counterintuitive behavior for very small *JRC*'s. When *JRC* increases from 0 to 1, the factors of safety decrease instead of increasing.

6) Yow and Goodman [312] found that the effect of *JCS* on the stability of the prism is not as strong as that of *JRC*, but it is quite effective. BS3D analyses found that the stability of the prism is weakly dependent on *JCS*.

7) The FS flattens out after a specific value of *JCS*, which depends on other aspects of the problem because the asperities do not fail and increasing *JCS* almost has no effect on the stability of the block.

8) Yow and Goodman [312] found that the base friction angle is quite effective on the stability of keyblocks. In addition, BS3D analyses show that the factor of safety of the prism increases with the base friction angle.

9) Stability decreases as normal stiffness increases (the same as Yow's and Goodman's [312] conclusion).

10) Effect of in situ stress condition of the prism: Yow and Goodman [312] found that aside from the shear strength, the most critical condition affecting keyblock stability is the stress environment. The block becomes less stable as the initial confining stresses decrease; the trend accelerates as stress magnitudes become

317

very small (smaller than about 1.5 MPa). The same conclusion has been made based on BS3D analyses.

11) Yow and Goodman [312] found that the block becomes less stable as the lateral stress ratio decreases; the trend accelerates as the ratio goes below about one-half. The same conclusion has been made based on BS3D analyses.

12) The principal stress directions strongly affect the stability of keyblocks.

13) The *in situ* stresses strongly affect the stability of the block, even more than the shear strength of fractures.

14) The factor of safety increases with distance from excavation face up to approximately five times of the tunnel radius.

15) The factor of safety of the prism increases with increasing radius of the tunnel.

16) Because of different dilation displacements, the factors of safety obtained using the simplified Barton's model are higher than those calculated using the Barton's model which itself is higher than those determined employing the Mohr-Coulomb model. The higher the dilation displacements are, the higher are the normal forces applied to the fractures, the shear strength of the fractures, and, finally, the factor of safety of the block.

17) The modified Barton's model and the old Barton's model may have smaller or higher factors of safety compared the other models, while there are minimal differences between them.

18) The factor of safety of the block decreases with increasing size of the prism.

19) The factor of safety of the block decreases (by 20%) with increasing radius of the tunnel (from 1 to 10 m) and size of the prism accordingly. The change is very small. This is the combination effect of the tunnel radius (which increases the FS) and the size of the block (which decrease the FS).

20) The factor of safety of the maximum block remains almost constant with increasing tunnel radius. This is the combination effect of the tunnel radius (which increases the FS) and the size of the block (which decrease the FS).

Finally, it can be concluded from the sensivity analyses performed that, in stability of keyblocks, *in situ* stresses have the highest effect. In addition, the type of constitutive model has strong effect, even higher than those of the shear strength of the fractures. The shear strength and stiffness of the fractures have weak effect on stability of keyblocks.

9.1.6 Effect of high-velocity jet impact on stability of rock blocks in plunge pools

The stability of single rock blocks in plunge pools has been investigated. An approach is introduced to estimate pressure forces generated in plunge pools due to high-velocity jet impacts. This method together with the ability of BS3D to determine the stability of a rock block and its displacements are validated using Federspiel's experimental study [27, 28].

Based on the simulation of Martins' [29] experimental study using BS3D, it is proposed to consider that the block is most likely to be removed when $h_{up}/z_b > 0.25$.

The application of the scour model is explained by a fictious rock mass (good quality granite) initially introduced by Bollaert [30]. The whole scour model and BS3D algorithm are then validated using three case histories and prototypes [29-31].

Finally, the ability of BS3D in predicting more complicated failure modes (divergence and flutter) together with dealing with *in situ* stress and dilation behavior of rock fractures is demonstrated using a fictious example. It was shown that rock blocks subjected to water forces (or other non-conservative forces) may undergo flutter failure before reaching a limit point. Thus, existing methods (including limiting equilibrium) may overestimate the safety of a rock block and, thus, underestimate scour depth when water forces are important (e.g. dam foundations and rock scour at bridge piers).

9.2 RECOMMENDATIONS FOR FUTURE STUDIES

9.2.1 Constitutive model for rock fractures

In this dissertation, modifications have been proposed to Barton's model for rock fractures based on correlation analyses of the results of direct shear tests found in the

literature. The database is given in Appendix A. Although this database presents a great source of information, it does not include all direct shear tests done in the past. Adding significant number of data to the given database and reanalyzing them may lead to some improvements in the modified model.

In addition, the modified model still suffers from weaknesses mostly in cyclic shearing. Performing a series of cyclic direct shear tests on wide ranges of rock fractures may lead to a better understanding of behavior of rock joints subjected to load reversal and reloading.

9.2.2   Scour of plunge pools

An experimental study should be performed to validate predictions of BS3D in terms of flutter/divergence versus static failure modes.

The implemented formulation for the stability analysis of single rock blocks in a plunge pool can be folded into a probabilistic approach to evaluate probability of scour threshold and extent. This study will deliver a formulation and a computer program for the evaluation of:

- The probability of scour as a function of plunge pool elevation.
- The probability of scour retrogression in the walls of the plunge pool toward the dam, its foundation, or the appurtenances.

The approach should be validated at a couple of dam sites where rock scour is a possible failure mechanism as highlighted by available risk analyses. The results of this study will allow one to carry out a quantitative risk assessment for scour.

9.2.3   Scour of bridge foundations

Scour is one of the first causes of bridge collapse in the USA. BS3D can be used to investigate the problem of scour at bridge foundation on rock. BS3D simulation will enhance the understanding of rock block removal under fluctuating turbulence. The scour zone is to be estimated and recommendations are to be proposed based on this study.

9.2.4 Coupling Digital Terrain Method and BS3D

Laser and photogrammetric methods for rock face characterization produce Digital Terrain Method (DTM) that can be used to locate removable blocks. The stability of these removable blocks may be studied using BS3D. The developed version of the code can be used to remotely analyze stability of rock slopes and/or tunnels to propose a guideline for design.

9.2.5 Stability of rock slopes during earthquake and heavy rains

Stable natural or artificial rock slopes may become unstable during an earthquake or heavy rains (ex: earthquake in Chalous road, Iran, 2005). The effect of earthquakes and heavy rains on stability of rock slopes can be investigated using BS3D. Reduction in shear strength of rock fracture due to cyclic shearing and/or water flow should be considered using an appropriate approach.

APPENDIX A: DIRECT SHEAR TEST DATABASE

A.1. MONOTONIC DIRECT SHEAR TESTS (MDST) DATABASE

Studies on monotonic shearing [79, 81, 106, 113, 115, 127, 154, 161, 162, 169, 176, 183-210] were investigated to find available monotonic direct shear test results. Peak shear strength, peak shear displacement, peak dilation displacement, maximum negative value of dilation, and shear displacement at which dilation displacement is zero were digitized from the curves (see Table A.1)   For post peak behavior shear strength, and dilation displacement at 4 different points were digitized (see Table A.2).

A large amount of data was collected from a site investigation report series published by Svensk Karnbranslehantering AB [188-210]. In these cases, the values of *JCS* was assumed to be equal to the *UCS* of intact rock, which can be calculated from available results of triaxial tests run on intact rock specimens.   Base friction angle and *JRC* values were back calculated assuming that: (1) Barton [21] failure criterion can predict the peak and residual shear strength correctly and (2) residual shear strength is reached when $JRC_{mobilized} / JRC_{peak} = 0.5$ [115] and assuming no weathering for fractures ($\phi_r = \phi_b$). *JRC* values may be different for the same specimens under different normal stresses (due to the damage of asperities in the shear test previously run under smaller normal stresses).

A.2. CYCLIC DIRECT SHEAR TESTS (CDST) DATABASE

Results of 18 cyclic direct shear tests were found in the literature [103, 127, 150, 167, 169, 174, 213]. For each available cycle, shear strengths and dilation displacements at different shear displacements were digitized so that shear strength-shear displacement as well as dilation-shear displacement curves could be built with the available information (see Table A.3).

Table A.1: Monotonic Direct Shear Test (MDST) database: pre-peak behavior

Case No.	Source and Description	L (m)	ϕ_b (°)	JRC	JCS (kPa)	δ_p (mm)	σ_n (kPa)	τ_p (kPa)	$(\delta_h)_p$ (mm)	$(\delta_v)_{@(\delta_h)=0}$	$\min(\delta_h)$
1	Barton [115]; Figure 5.1; Tension Fracture	0.1	30	16	450	0.33	2	-	0.083	0.083	0
2		0.1	30	16	450	0.46	3.8	-	0.058	0.300	0
3		0.1	30	16	450	0.50	8	-	0.067	0.300	0
4		0.1	30	16	450	0.53	13	-	0.062	0.300	0
5		0.1	30	16	450	0.58	20	-	0.026	0.300	0
6		0.1	30	16	450	1.18	42	-	0.088	0.710	0
7	Bandis [113]	0.06	32	15.0	2000	0.72	24.5	44.22	-	-	-
8		0.12	32	12.2	1464.1	0.92	24.5	34.65	-	-	-
9		0.18	32	10.8	1219.9	0.97	24.5	29.42	-	-	-
10		0.36	32	8.8	893.02	1.85	24.5	23.18	-	-	-
11	Barton [115]; Figure 6.2	0.06	32	12.5	9554.4	0.78	24.5	50.52	0.22	0.09	0
12		0.12	32	11.5	4026.1	1.25	24.5	39.78	0.17	0.36	0
13		0.18	32	11.0	2304.7	1.80	24.5	34.61	0.18	0.73	0
14		0.36	32	9.0	1679.6	2.22	24.5	32.02	0.11	0.93	0
15	Barton et al. [81]; Figure 20	0.25	30	8.3	57000	1.64	6000	4170	0.07	0.74	0
16		0.25	30	8.3	57000	1.61	24000	13410	0.03	0.8	0
17		0.75	30	6.7	41000	2.76	6000	3720	0.08	1.01	0
18		0.75	30	6.7	41000	3.07	24000	12570	0.03	1.08	0
19	Barton et al. [81]; Figure 22	0.30	30	8.0	72000	1.55	1000	1020	0.076	0.83	0
20		0.30	30	8.0	72000	1.71	3000	2570	0.061	0.83	0
21		0.30	30	8.0	72000	1.67	10000	7530	0.039	0.83	0
22		0.30	30	8.0	72000	1.67	30000	19670	0.012	0.83	0
23	Barton et al. [81]; Figure 23	0.10	30	10.0	100000	0.84	10000	8440	0.04	0.42	0
24		0.30	30	8.0	72000	1.81	10000	7620	0.06	0.77	0
25		1.00	30	6.3	50000	3.61	10000	7050	0.08	1.35	0
26		3.00	30	5.1	36000	7.34	10000	6640	0.02	2.55	0
27	Olson and Barton [176]; Figure 16	0.20	31	9.7	169000	0.87	2000	2350	-0.02	0.93	-0.03
28	Jacobsson & Flansbjer [192, 202]; KLX06A; Avro Granite	0.06	33	12.0	184000	0.13	500	1020	0.04	0.04	0.00
29		0.06	33	7.4	184000	0.6	5000	4930	0.065	0.031	-0.02
30		0.06	33	6.5	184000	2.17	20000	16370	0.06	1.18	-0.05
31		0.06	33	7.7	184000	0.24	500	660	0.03	0.12	0.00
32		0.06	33	6.6	184000	0.3	5000	4710	0.015	0.26	-0.02
33		0.06	33	6.1	184000	2.26	20000	16140	0.09	0.79	-0.04
34		0.06	33	12.5	184000	0.47	500	1070	0.14	0	0.00
35		0.06	33	7.3	184000	0.47	5000	4910	0	0.46	-0.02
36		0.06	33	3.8	184000	1.48	20000	14910	-0.01	1.66	-0.07
37		0.06	33	10.8	184000	0.11	500	890	0.05	0.03	0.00
38		0.06	33	8.7	184000	0.26	5000	5300	0.02	0.19	-0.01
39		0.06	33	5.7	184000	0.54	20000	15900	-0.03	0.9	-0.05
40		0.06	33	10.7	184000	0.3	500	880	0.055	0.14	-0.01
41		0.06	33	8.4	184000	0.38	5000	5200	0	0.39	-0.03
42		0.06	33	6.4	184000	0.71	20000	16280	-0.01	0.95	-0.03
43		0.07	33	6.3	184000	0.88	500	580	0.13	0	0.00
44		0.07	33	3.1	184000	1.5	5000	3890	0.045	0.46	-0.02
45		0.07	33	1.4	184000	2.87	20000	13670	-0.055	-	-0.06

323

Case No.	Source and Description	L (m)	ϕ_b (°)	JRC	JCS (kPa)	δ_p (mm)	σ_n (kPa)	τ_p (kPa)	$(\delta_h)_p$ (mm)	$(\delta_v)_{@(\delta_h)=0}$	$\min(\delta_h)$
46		0.06	35	9.1	172000	0.79	500	800	0.11	0.17	-0.01
47		0.06	35	6.7	172000	0.6	5000	5040	0.005	0.59	-0.03
48		0.06	35	4.6	172000	2.37	20000	16380	0.13	1.16	-0.05
49		0.06	35	5.3	172000	1.46	5000	4680	0.19	0.34	-0.02
50		0.06	35	2.1	172000	4.16	20000	15040	0.27	0.95	-0.05
51	Jacobsson & Flansbjer [199, 208]; KL10-117; Avro Granite	0.06	35	10.6	172000	1.26	500	940	0.02	0.06	-0.02
52		0.06	35	3.1	172000	3.13	20000	15580	0.11	0.095	-0.04
53		0.07	35	7.8	172000	1.15	500	710	0.29	0.08	0.00
54		0.07	35	5.3	172000	0.35	5000	4680	0.08	0.23	-0.01
55		0.07	35	4.3	172000	0.63	20000	16180	0	0.61	-0.30
56		0.06	35	9.9	172000	0.45	500	870	0.06	0.19	0.00
57		0.06	35	7.8	172000	0.58	5000	5350	0.01	0.48	-0.02
58		0.06	35	4.4	172000	0.94	20000	16280	-0.03	1.29	-0.05
59		0.07	35	10.9	175000	0.13	500	970	0.04	0.02	0.00
60		0.07	35	7.3	175000	2.38	5000	5220	0.44	0.09	-0.01
61	Jacobsson & Flansbjer [200, 209]; KLX12A-117; Avro Granite and Quartz monzodiorite	0.07	35	5.6	175000	2.68	20000	16950	0.11	0.73	-0.02
62		0.06	34	11.8	268700	0.71	500	1140	0.2	0.15	0.00
63		0.06	34	6.5	268700	0.76	5000	5030	0.04	0.56	-0.04
64		0.06	34	3.9	268700	2.73	20000	15880	0.05	1.13	-0.05
65		0.06	34	13.4	268700	0.63	500	1420	0.2	0.1	0.00
66		0.06	34	6.4	268700	0.34	5000	5000	-0.01	0.37	-0.02
67		0.06	34	2.4	268700	3.13	20000	14910	-0.02	-	-0.04
68		0.06	35	8.4	250000	0.49	500	790	0.09	0.13	0.00
69		0.06	35	6.0	250000	1.69	5000	5040	0.2	0.46	-0.04
70		0.06	35	3.9	250000	3.12	20000	16370	-0.02	4.2	-0.09
71		0.05	35	9.3	250000	0.18	500	870	0.03	0.1	0.00
72	Jacobsson & Flansbjer [201, 210]; KFM09A-117; Medium-grained granite	0.05	태	6.2	250000	0.42	5000	5100	-0.03	0.56	-0.04
73		0.05	35	2.0	250000	1.09	20000	15190	-0.1	-	-0.11
74		0.05	35	6.6	250000	0.47	500	660	0.07	0.3	-0.01
75		0.05	35	3.1	250000	0.57	5000	4240	-0.01	0.62	-0.04
76		0.05	35	1.5	250000	4.13	20000	14900	-0.06	-	-0.12
77		0.05	35	9.4	250000	0.18	500	880	0.08	0	0.00
78		0.05	35	3.6	250000	1.25	5000	4370	0.11	0.33	-0.02
79		0.05	35	1.1	250000	3.62	20000	14620	0.02	2.51	-0.07
80		0.06	30	13.4	185000	0.11	500	1040	0.04	0.03	0.00
81		0.06	30	8.8	185000	0.23	5000	4790	0.01	0.13	0.00
82		0.06	30	5.4	185000	0.39	20000	14130	0	0.39	-0.09
83		0.06	30	10.2	185000	0.21	500	750	0.04	0.08	0.00
84	Jacobsson & Flansbjer [195, 203]; KFM06A-117; Medium-grained granite	0.06	30	7.8	185000	1.52	5000	4530	0.24	0.25	-0.01
85		0.06	30	7.5	185000	0.46	20000	15200	-0.02	0.64	-0.03
86		0.06	30	5.2	185000	1.14	500	470	0.12	0.27	0.00
87		0.06	30	4.8	185000	1.53	5000	3840	0.1	0.49	-0.01
88		0.06	30	5.5	185000	5.05	20000	14160	0.06	2.22	-0.04
89		0.06	30	8.6	185000	0.31	500	640	0.05	0.04	0.00
90		0.06	30	5.9	185000	0.44	5000	4090	-0.01	0.5	-0.02

Table A.1-Continued: MDST database: pre-peak behavior

Case No.	Source and Description	L (m)	ϕ_b (°)	JRC	JCS (kPa)	δ_p (mm)	σ_n (kPa)	τ_p (kPa)	$(\delta_h)_p$ (mm)	$(\delta_v)_{@(\delta_h)=0}$	$\min(\delta_h)$
91		0.06	30	5.9	185000	2.56	20000	14350	-0.13	-	-0.23
92	Jacobsson & Flansbjer [195, 203]; KFM06A-117; Medium-grained granite	0.06	30	11.4	185000	0.1	500	840	0.005	0.04	0.00
93		0.06	30	8.5	185000	0.29	5000	4720	-0.01	0.35	-0.02
94		0.06	30	9.5	185000	2.24	20000	16290	0	2.19	-0.08
95		0.07	30	13.4	185000	0.15	500	1040	0.01	0.12	0.00
96		0.07	30	12.1	185000	0.32	5000	5750	-0.02	0.39	-0.03
97		0.07	30	10.6	185000	0.98	20000	16900	-0.06	1.71	-0.08
98		0.05	28	15.5	230000	0.12	500	1330	0.02	0.06	0.00
99		0.05	28	11.2	230000	0.38	5000	5290	0	0.38	-0.02
100		0.05	28	9.5	230000	1.12	20000	15690	-0.08	2.51	-0.09
101		0.05	28	14.7	230000	0.11	500	1190	0.03	0.02	0.00
102		0.05	28	11.5	230000	0.33	5000	5380	0	0.29	-0.01
103		0.05	28	8.7	230000	0.94	20000	15170	-0.07	1.83	-0.08
104		0.06	28	7.8	230000	0.46	500	570	0.1	0	0.00
105		0.06	28	2.9	230000	0.38	5000	3220	-0.005	0.49	-0.02
106		0.06	28	0.9	230000	6.69	20000	11060	-0.05	-	-0.06
107	Jacobsson & Flansbjer [193, 194, 204]; KFM05A-117; Medium-grained granite	0.06	28	12.2	230000	0.15	500	880	0.04	0.06	0.00
108		0.06	28	10.6	230000	0.24	5000	5100	0	0.25	-0.02
109		0.06	28	8.1	230000	0.47	20000	14840	0	0.52	-0.02
110		0.07	30	14.2	230000	0.15	500	1230	0	0.12	0.00
111		0.07	30	12.8	230000	0.25	5000	6220	0	0.24	-0.01
112		0.07	30	11.8	230000	0.46	20000	18370	0.21	0.77	-0.04
113		0.06	30	9.5	230000	0.21	500	720	0.03	0.12	0.00
114		0.06	30	7.4	230000	0.46	5000	4540	0	0.46	-0.02
115		0.06	30	5.2	230000	3.02	20000	14290	-0.06	0	-0.08
116		0.06	30	13.8	230000	0.1	500	1160	0.03	0.05	0.00
117		0.06	30	9.0	230000	0.28	5000	4980	0.02	0.14	0.00
118		0.06	30	6.2	230000	0.84	20000	14830	0.01	0.75	-0.03
119		0.06	30	13.0	230000	0.05	500	1060	0.02	0.03	0.00
120		0.06	30	10.2	230000	0.24	5000	5340	0.01	0.15	0.00
121		0.06	30	7.7	230000	0.58	20000	15720	-0.03	0.96	-0.05
122		0.06	31	15.8	173000	0.16	500	1460	0.07	0.05	0.00
123		0.06	31	12.0	173000	0.34	5000	5860	0.02	0.28	-0.01
124		0.06	31	6.7	173000	0.72	20000	15230	-0.03	0.99	-0.04
125		0.05	31	11.0	173000	0.13	500	830	0.03	0.04	0.00
126		0.05	31	8.8	173000	0.33	5000	4910	0.02	0.27	-0.01
127	Jacobsson & Flansbjer [197, 206]; KFM08A-117; Medium-grained granite	0.05	31	8.9	173000	2.99	20000	16390	0.07	0.99	-0.04
128		0.05	31	15.4	173000	0.22	500	1380	0.06	0.12	0.00
129		0.05	31	12.8	173000	0.39	5000	6110	0.02	0.33	-0.02
130		0.05	31	10.3	173000	2.78	20000	17180	0.1	1.26	-0.07
131		0.06	31	9.1	173000	0.3	500	690	0.06	0.12	0.00
132		0.06	31	7.6	173000	0.38	5000	4610	0.03	0.31	-0.02
133		0.06	31	4.8	173000	0.58	20000	14250	-0.02	0.72	-0.04
134		0.06	31	10.8	173000	0.29	500	810	0.06	0.15	0.00
135		0.06	31	8.1	173000	0.42	5000	4740	0.03	0.32	-0.01
136		0.06	31	7.0	173000	2.48	20000	15400	0.14	0.84	-0.04

325

Table A.1-Continued: MDST database: pre-peak behavior

Case No.	Source and Description	L (m)	ϕ_b (°)	JRC	JCS (kPa)	δ_p (mm)	σ_n (kPa)	τ_p (kPa)	$(\delta_h)_p$ (mm)	$(\delta_v)_{@(\delta_h)=0}$	$\min(\delta_h)$
137		0.05	35	6.6	158000	1.18	500	630	0.23	0.04	0.00
138		0.05	34	7.1	158000	0.99	5000	4930	0.1	0.27	-0.01
139		0.05	34	7.3	158000	1.92	20000	17140	0.02	1.5	-0.05
140		0.06	34	10.0	158000	0.42	500	830	0.08	0.1	0.00
141		0.06	34	4.1	158000	1.23	5000	4220	0.03	0.69	-0.02
142		0.06	34	3.2	158000	1.79	20000	15010	-0.05	-	-0.17
143		0.06	34	6.1	158000	0.33	500	80	0.04	0.05	0.00
144		0.06	34	5.5	158000	0.43	5000	4530	0	0.41	-0.01
145		0.06	34	2.7	158000	3.33	20000	14770	0.09	1.18	-0.04
146	Jacobsson &	0.06	34	7.9	158000	0.13	500	680	0.01	0	0.00
147	Flansbjer	0.06	34	4.9	158000	1.84	5000	4390	0.19	0.33	-0.01
148	[196, 205];	0.06	34	4.2	158000	2.23	20000	15490	0.09	0.56	-0.01
149	KLX03A-117;	0.06	34	11.4	158000	0.18	500	960	0.02	0	0.00
150	Avro Granite and Quartz	0.06	34	8.4	158000	0.4	5000	5290	0.01	0.34	-0.01
151	monzodiorite	0.06	34	4.9	158000	0.99	20000	15850	-0.01	1.1	-0.03
152		0.05	34	7.2	158000	1.16	500	640	0.09	0.35	-0.01
153		0.05	34	4.0	158000	1.3	5000	4200	0.05	0.77	-0.03
154		0.05	34	1.7	158000	5.1	20000	14280	0	4.96	-0.06
155		0.06	34	6.1	158000	0.56	500	580	0.02	0.37	-0.01
156		0.06	34	3.4	158000	0.67	5000	4060	-0.02	0.83	-0.05
157		0.06	34	1.9	158000	1.32	20000	14360	-0.05	2.3	-0.10
158		0.06	31	12.7	176000	0.17	500	1000	0.03	0.11	-0.01
159		0.06	31	9.3	176000	0.32	5000	5060	0	0.32	-0.02
160		0.06	31	4.9	176000	1.07	20000	14330	-0.04	3.01	-0.05
161		0.06	35	9.4	206000	0.1	500	850	0.03	0.05	0.00
162		0.06	35	9.7	206000	0.24	5000	6090	0.01	0.2	-0.01
163		0.06	35	5.1	206000	0.5	20000	16890	-0.01	0.66	-0.03
164		0.06	35	9.4	206000	0.07	500	850	0.02	0.04	0.00
165		0.06	35	9.0	206000	0.23	5000	5850	0.01	0.19	-0.01
166	Jacobsson &	0.06	35	5.1	206000	0.75	20000	16870	-0.01	1.06	-0.03
167	Flansbjer	0.06	35	8.8	206000	0.17	500	800	0.02	0.08	0.00
168	[198, 207];	0.06	35	4.8	206000	1.11	5000	4610	0.11	0.23	-0.01
169	KFM07A-117;	0.06	35	4.6	206000	3.93	20000	16610	0.09	1.1	-0.03
170	Medium-grained granite	0.05	35	8.3	206000	0.19	500	760	0.03	0.08	0.00
171		0.05	35	5.2	206000	0.32	5000	4740	-0.005	0.36	-0.02
172		0.05	35	3.2	206000	1.88	20000	15760	0	1.46	-0.03
173		0.06	35	8.9	206000	0.23	500	810	0.07	0.03	0.00
174		0.06	35	6.8	206000	0.27	5000	5180	0.02	0.18	-0.01
175		0.06	35	5.8	206000	1.85	20000	17290	0.06	0.55	-0.02
176		0.15	34	11.0	75000	8.16	400	640	1.17	3	0.00
177	Homand *et al.*	0.15	34	11.0	75000	9.63	800	1150	2.12	1	0.00
178	[169];	0.15	34	11.0	75000	8.17	1200	1670	1.56	0.25	0.00
179	Schist replicas	0.15	34	11.0	75000	7.68	1800	2360	1.35	0.5	0.00
180		0.15	34	11.0	75000	12.65	2400	2870	1.17	5.31	-0.18

Table A.1-Continued: MDST database: pre-peak behavior

Case No.	Source and Description	L (m)	ϕ_b (°)	JRC	JCS (kPa)	δ_p (mm)	σ_n (kPa)	τ_p (kPa)	$(\delta_h)_p$ (mm)	$(\delta_v)_{@(\delta_h)=0}$	$\min(\delta_h)$
181		0.06	34	5.8	202300	0.65	500	570	0.11	0.14	0.00
182		0.06	34	2.3	202300	1.47	5000	3800	0.13	0.8	-0.02
183		0.06	34	0.9	202300	2.12	20000	13690	0.11	1.27	-0.03
184		0.06	34	10.3	202300	0.48	500	880	0.11	0.05	0.00
185		0.06	34	9.0	202300	0.52	5000	5540	0.04	0.31	-0.01
186		0.06	34	8.2	202300	0.9	20000	17840	0.02	0.68	-0.03
187		0.05	34	7.4	202300	0.22	500	660	0.02	0.05	0.00
188		0.05	34	4.1	202300	1.93	5000	4220	0.1	0.49	-0.01
189		0.05	34	3.6	202300	3.98	20000	15120	0.07	1.05	-0.02
190		0.05	34	12.2	202300	0.13	500	1090	0.02	0.11	0.00
191		0.05	34	7.7	202300	0.28	5000	5160	0	0.27	-0.01
192		0.05	34	5.3	202300	0.7	20000	16090	0	0.71	-0.03
193	Jacobsson [188, 189]; KLX02-117; Avro Granite	0.06	34	7.1	202300	1.1	500	640	0.07	0	0.00
194		0.06	34	6.4	202300	3.11	5000	4790	0.21	0.93	-0.02
195		0.06	34	7.8	202300	2.95	20000	17570	0.1	1.76	-0.05
196		0.05	34	12.7	202300	0.1	500	1150	0.03	0	0.00
197		0.05	34	7.4	202300	0.26	5000	5060	0.01	0.21	-0.02
198		0.05	34	4.8	202300	0.48	20000	15790	0	0.49	-0.01
199		0.06	34	10.5	202300	0.47	500	900	0.11	0.1	0.00
200		0.06	34	9.8	202300	0.49	5000	5790	0.02	0.41	-0.02
201		0.06	34	7.7	202300	1.09	20000	17510	0.02	0.87	-0.04
202		0.06	34	11.4	202300	0.14	500	990	0.03	0.08	0.00
203		0.06	34	8.7	202300	0.4	5000	5460	0.01	0.32	-0.02
204		0.06	34	7.3	202300	2.66	20000	17290	0.09	1.09	-0.04
205		0.06	34	4.6	202300	1.09	500	510	0.07	0.13	0.00
206		0.06	34	2.0	202300	4.54	5000	3730	0.26	1.19	-0.03
207		0.06	34	0.8	202300	5.68	20000	13660	0.12	2.94	-0.04
208	Yoshinaka and Yamabe [154]; Diamond Sawed; Welded-tuff (Ohya stone)	0.14	39	0.0	11200	1.25	490	22.9			
209		0.14	39	0.0	11200	1.45	980	11.4			
210		0.14	39	0.0	11200	1.55	1460	7.7			
211		0.14	39	0.0	11200	1.55	1950	5.7			
212		0.14	39	0.0	11200	1.80	2930	3.8			
213	Yoshinaka and Yamabe [154]; Sand Blasted; Welded-tuff (Ohya stone)	0.13	33	0.0	11200	0.25	480	23.3			
214		0.13	33	0.0	11200	1.10	910	12.3			
215		0.13	33	0.0	11200	0.75	1190	9.4			
216		0.13	33	0.0	11200	0.90	1800	6.2			
217		0.13	33	0.0	11200	1.20	2600	4.3			
218		0.13	33	0.0	11200	1.30	3050	3.7			
219	Van Sint Jan [185]; Plaster	0.15	48	20.0	14700	1.50	500	29.4			
220		0.15	48	20.0	14700	1.70	1000	14.7			
221		0.15	48	20.0	14700	1.70	2000	7.35			
222		0.15	48	20.0	14700	2.20	4000	3.675			
223		0.15	48	20.0	14700	2.40	6000	2.45			
224	Aydan et al. [186]; Plaster	0.16	36	13.0	920	1.20	30	30.67			
225		0.16	36	13.0	920	2.00	70	13.14			
226		0.16	36	11.0	920	1.80	20	46.00			
227		0.16	36	11.0	920	2.45	40	23.00			

Table A.1-Continued: MDST database: pre-peak behavior

Case No.	Source and Description	L (m)	ϕ_b (°)	JRC	JCS (kPa)	δ_p (mm)	σ_n (kPa)	τ_p (kPa)	$(\delta_h)_p$ (mm)	$(\delta_v)_{@(\delta_h)=0}$	$\min(\delta_h)$
228		0.09	32	6.5	2000	0.47	10	11.28			
229		0.09	32	7.5	2000	0.55	10	15.4			
230		0.09	32	10.6	2000	0.73	10	17.34			
231		0.09	32	16.6	2000	0.73	10	31.16			
232		0.09	32	6.5	2000	0.56	34	32.38			
233	Bandis *et al.* [79];	0.09	32	7.5	2000	0.61	34	35.77			
234	Figure 4; Tension	0.09	32	10.6	2000	0.8	34	41.4			
235	fracture	0.09	32	16.6	2000	0.85	34	52.9			
236		0.09	32	6.5	2000	1.18	90	71.5			
237		0.09	32	7.5	2000	1.07	90	81.8			
238		0.09	32	10.6	2000	0.99	90	90.5			
239		0.09	32	16.6	2000	1.33	90	123			
240		0.06	32	17.5	2000	0.57	24.5	56.56	0.15	0.2	0.00
241		0.12	32	14.2	1375.5	0.74	24.5	52.35	0.14	0.2	0.00
242	Bandis *et al.* [79];	0.18	32	12.6	1105.1	1.17	24.5	41.50	0.1	0.4	0.00
243	Figures 9-21;	0.36	32	10.2	760.03	2.7	24.5	35.96	0.16	0.8	0.00
244	Bedding plane in	0.06	32	17.5	2000	0.75	24.5	54.68			
245	limestone	0.12	32	14.2	1404.4	0.91	24.5	41.24			
246		0.18	32	12.6	1142.1	1.87	24.5	45.96			
247		0.36	32	10.2	802	2.17	24.5	41.96			
248		0.06	32	17.5	2000	1.13	24.5	44.81			
249		0.12	32	14.2	1404.4	1.74	24.5	33.07			
250	Bandis *et al.* [79];	0.18	32	12.6	1142.1	2.13	24.5	35.07			
251	Figures 9-21;	0.36	32	10.2	802	3.5	24.5	26.13			
252	Vertical tension	0.06	32	17.5	2000	1.13	24.5	54.68			
253	joints in siltstone	0.12	32	14.2	1479.4	1.22	24.5	39.25			
254		0.18	32	12.6	1240.2	1.45	24.5	34.00			
255		0.36	32	10.2	917.35	2.17	24.5	27.65			
256		0.06	32	17.5	2000	1.13	24.5	43.21			
257		0.12	32	14.2	1510.5	1.37	24.5	41.29			
258		0.18	32	12.6	1281.7	1.67	24.5	32.40			
259		0.36	32	10.2	968.01	2.91	24.5	29.60			
260	Bandis *et al.* [79];	0.06	32	17.5	2000	0.9	24.5	37.43			
261	Figures 9-21;	0.12	32	14.2	1558.3	1.05	24.5	31.65			
262	Bedding plane in	0.18	32	12.6	1346.7	1.15	24.5	27.84			
263	slightly	0.36	32	10.2	1049.3	1.4	24.5	24.18			
264	metamorphosed	0.06	32	17.5	2000	0.75	24.5	28.09			
265	fine grained	0.12	32	14.2	1693.5	1.15	24.5	25.78			
266	sandstone	0.18	32	12.6	1536.5	1.1	24.5	24.00			
267		0.36	32	10.2	1301	1.2	24.5	21.60			
268		0.06	32	17.5	2000	0.75	24.5	21.73	0.02	0.39	0.00
269		0.12	32	14.2	1798.8	1.15	24.5	20.89	0.03	0.39	0.00
270		0.18	32	12.6	1690.6	1.1	24.5	19.84	0.02	0.39	0.00
271		0.36	32	10.2	1520.5	1.25	24.5	18.75	0	0.94	0.00
272	Bandis *et al.* [79];	0.06	32	17.5	2000	0.6	24.5	61.96			
273	Figures 9-21;	0.12	32	14.2	1464.1	0.7	24.5	49.61			
274	Bedding plane in	0.18	32	12.6	1219.9	0.9	24.5	33.70			
275	limestone	0.36	32	10.2	893.02	1.8	24.5	26.67			

Case No.	Source and Description	L (m)	ϕ_b (°)	JRC	JCS (kPa)	δ_p (mm)	σ_n (kPa)	τ_p (kPa)	$(\delta_h)_p$ (mm)	$(\delta_v)_{@(\delta_h)=0}$	$\min(\delta_h)$
276		0.05	32	18.5	2000	0.7	24.5	58.59	0.02	0.34	0.00
277		0.10	32	15.0	1361.3	0.8	24.5	39.47	0.03	0.59	0.00
278	Bandis *et al.* [79];	0.20	32	12.2	926.59	1.1	24.5	30.50	0.12	0.34	0.00
279	Figures 9-21;	0.40	32	9.9	630.69	1.9	24.5	25.34	0.11	0.56	0.00
280	Bedding plane in	0.05	32	18.5	2000	0.7	24.5	58.59			
281	Course grained	0.10	32	15.0	1419.1	0.8	24.5	39.89			
282	sandstone	0.20	32	12.2	1007	1.1	24.5	30.98			
283		0.40	32	9.9	714.5	1.7	24.5	25.81			
284		0.30	30	0.0	30000	0.05	35	20.7			
285		0.30	30	0.0	30000	0.1	138	79.67			
286		0.30	30	0.0	30000	0.75	345	199.2			
287		0.30	30	2.0	30000	1.2	35	23.61			
288	Desai and Fishman	0.30	30	3.0	30000	1.1	35	25.43			
289	[106];	0.30	30	2.0	30000	1.25	69	46.54			
290	Figures 11-18; Concrete replica	0.30	30	3.0	30000	1.2	69	50.13			
291		0.30	30	2.0	30000	1.6	138	93.08			
292		0.30	30	3.0	30000	2.5	138	100.3			
293		0.30	30	2.0	30000	1.8	345	232.7			
294		0.30	30	3.0	30000	4	345	250.7			
295		0.10	35	0.0	8500	0.33	300	184			
296		0.10	35	0.0	8500	0.65	500	308			
297		0.10	35	0.0	8500	1.96	1000	777			
298		0.10	35	0.0	8500	2.71	1500	1200			
299		0.10	35	8.7	8500	0.6	100	103.2	0.05	0	0.00
300		0.10	35	8.7	8500	1.16	300	412.5	0	1.05	-0.04
301	Huang *et al.* [184];	0.10	35	8.7	8500	0.99	500	523.4	0	1.57	-0.03
302	Figures 3-8;	0.10	35	8.7	8500	1.49	1000	928.5	-0.03	1.57	-0.03
303	Replica	0.10	35	8.7	8500	2.48	1500	1278	-0.07		-0.06
304		0.10	35	15.8	8500	0.84	100	191.2	0.07	0.54	0.00
305		0.10	35	15.8	8500	1.16	300	606.4	0.04	0.39	-0.04
306		0.10	35	15.8	8500	2	500	785.1	0.03	1.42	0.00
307		0.10	35	15.8	8500	1.84	1000	1067	0.01	1.42	0.00
308		0.10	35	15.8	8500	2.5	1500	1530	-0.02		-0.03
309		0.14	32	14.6	27600	1.28	276	381.3	0.128		
310	Wibowo [162] and	0.14	32	14.6	27600	1.94	1380	1479	0.1552		
311	Wibowo *et al.* [161]; G2; Replica	0.14	32	14.6	27600	2.29	2755	30401	0.2748		
312		0.14	32	14.6	27600	3.95	5516	5488	0.0395		
313		0.10	32	9.9	27600	0.34	283.3	306.1	0.0544		
314	Wibowo [162] and	0.10	32	9.9	27600	0.55	1375	1422	0.066		
315	Wibowo *et al.* [161]; F2; Replica	0.10	32	9.9	27600	1.07	2749	2417	0.0642		
316		0.10	32	9.9	27600	1.08	5509	4482	0.108		
317		0.11	32	9.8	27600	0.10	272.7	366.6	0.038		
318	Wibowo [162] and	0.11	32	9.8	27600	0.67	1380	1297	0.067		
319	Wibowo *et al.* [161]; F3; Replica	0.11	32	9.8	27600	0.78	2760	3232	0.117		
320		0.11	32	9.8	27600	2.08	5512	4233	0.208		

Table A.1-Continued: MDST database: pre-peak behavior

Case No.	Source and Description	L (m)	ϕ_b (°)	JRC	JCS ekPa)	δ_p (mm)	σ_n (kPa)	τ_p (kPa)	$(\delta_h)_p$ (mm)	$(\delta_v)_{@(\delta_h)=0}$	$\min(\delta_h)$
321		0.11	32	15.5	27600	0.42	275.6	464.4	0.0504		
322	Wibowo [162] and	0.11	32	15.5	27600	1.34	1378	1532	0.2144		
323	Wibowo *et al.*	0.11	32	15.5	27600	1.56	2756	2845	0.1872		
324	[161]; F4; Replica	0.11	32	15.5	27600	1.90	4134	4370	0.171		
325		0.11	32	15.5	27600	2.09	5512	55263	0.1881		
326		0.14	36	20.5	25000	0.5	1070	2200			
327		0.14	36	19.7	25000	0.52	1070	2100			
328	Grasselli and	0.14	36	24.1	25000	0.53	3720	5500			
329	Egger [127];	0.14	36	25.7	25000	0.31	2450	4600			
330	Limestone	0.14	36	24.4	25000	0.24	3110	5000			
331		0.14	36	20.2	25000	0.37	1020	2100			
332		0.14	36	23.9	25000	0.74	3110	4900			
333		0.14	34	18.1	173000	0.38	2300	5700			
334		0.14	34	17.9	173000	0.65	2300	5600			
335		0.14	34	16.6	173000	0.45	2190	4800			
336	Grasselli and	0.14	34	14.2	173000	0.62	1120	2400			
337	Egger [127];	0.14	34	15.9	173000	0.38	1120	2900			
338	Granite	0.14	34	15.6	173000	0.23	1120	2800			
339		0.14	34	16.2	173000	0.56	1120	3000			
340		0.14	36	3.3	184000	0.3	2650	2400			
341		0.14	36	12.9	160000	0.48	1900	3400			
342		0.14	36	7.4	184000	0.2	3520	4000			
343	Grasselli and	0.14	36	6.7	184000	0.31	3570	3900			
344	Egger [127];	0.14	36	8.6	184000	0.35	3520	4300			
345	Gneiss	0.14	36	1.8	184000	0.31	4080	3300			
346		0.14	36	9.4	184000	0.35	2600	3500			
347		0.14	37	13.0	87000	0.28	870	1707			
348		0.14	37	11.7	87000	0.27	1730	2655			
349		0.14	37	16.6	87000	0.5	870	2417			
350		0.14	37	13.5	87000	0.88	3780	5477			
351		0.14	37	9.2	87000	0.29	2600	3214			
352	Grasselli and	0.14	37	9.0	87000	0.44	2600	3179			
353	Egger [127];	0.14	37	14.8	87000	0.44	3780	5856			
354	Marble	0.14	37	15.0	87000	0.39	3830	5976			
355		0.14	37	14.3	87000	0.42	2600	4293			
356		0.14	37	13.7	87000	0.27	870	1816			
357		0.14	37	16.3	87000	0.55	1790	3752			
358	Grasselli and	0.14	37	27.2	10000	0.65	1020	2088			
359	Egger [127];	0.14	37	16.3	10000	0.67	4130	3886			
360	Sandstone	0.14	37	15.0	10000	0.67	2090	2257			
361	Grasselli and	0.14	39	17.0	74000	0.4	1940	4334			
362	Egger [127]; Serpentines	0.14	39	20.9	74000	0.5	970	4702			

Table A.2: Monotonic Direct Shear Test (MDST) database: post-peak behavior

Case No.	Source and Description	Post-peak shear displacements				Post-peak shear stress				Post-peak dilation displacement			
		1	2	3	4	1	2	3	4	1	2	3	4
1	Barton [115]; Figure 5.1; Tension Fracture	1.0	1.5	2.0	3.0					0.29	0.38	0.45	0.53
2		1.0	1.5	2.0	3.0					0.21	0.32	0.38	0.49
3		1.0	1.5	2.0	3.0					0.17	0.27	0.35	0.44
4		1.0	1.5	2.0	3.0					0.13	0.21	0.27	0.35
5		1.0	1.5	2.0	3.0					0.15	0.23	0.28	0.33
6		1.5	2.0	2.3	2.5					0.17	0.19	0.20	0.21
7	Bandis [113]	1.0	2.0	3.0	5.0	35.34	32.13	30.74	29.29				
8		1.0	2.0	3.0	6.0	30.81	28.29	27.40	26.71				
9		1.0	2.0	3.0	6.0	26.40	25.77	25.77	24.25				
10		1.0	2.0	3.0	6.0	23.62	23.25	23.31	22.55				
11	Barton [115]; Figure 6.2	2.0	3.0	4.0	5.0	47.12	43.52	38.70	36.61	0.41	0.60	0.78	0.97
12		2.0	3.0	4.0	5.0	37.62	34.96	32.37	31.22	0.27	0.44	0.66	0.86
13		2.0	3.0	5.0	6.0	34.03	33.52	32.01	31.51	0.27	0.44	0.72	0.83
14		3.0	4.0	5.0	6.0	30.86	39.86	39.35	39.06	0.25	0.42	0.57	0.65
15	Barton *et al.* [81]; Figure 20	3.0	6.0	12.0	21.0	3980	3790	3630	3500	0.15	0.31	0.56	0.85
16		3.0	6.0	12.0	21.0	13130	12970	12730	12560	0.05	0.11	0.22	0.33
17		3.0	6.0	12.0	21.0	3670	3600	3520	3380	0.08	0.21	0.43	0.68
18		3.0	6.0	12.0	21.0	12540	12520	12430	12260	0.02	0.06	0.06	0.19
19	Barton *et al.* [81]; Figure 22	4.0	8.0	14.0	22.0	910	760	880	860	0.38	0.76	1.23	1.71
20		4.0	8.0	14.0	22.0	2310	2220	2240	2240	0.28	0.56	0.91	1.27
21		4.0	8.0	14.0	22.0	7100	6940	6860	6770	0.17	0.34	0.56	0.79
22		4.0	8.0	14.0	22.0	19310	19000	18860	18810	0.07	0.15	0.26	0.35
23	Barton *et al.* [81]; Figure 23	8.0	14.0	18.0	24.0	7660	7490	7390	7340	0.45	0.66	0.81	0.97
24		8.0	14.0	18.0	24.0	7490	7310	7200	7160	0.34	0.55	0.67	0.81
25		8.0	14.0	18.0	24.0	7210	7130	7080	7000	0.22	0.39	0.49	0.62
26		8.0	14.0	18.0	24.0	7000	6930	6860	6860	0.12	0.25	0.33	0.43
27	Olson and Barton [176]; Figure 16	1.0	2.5	4.0	5.5	2230	1890	1770	1740	0.02	0.4	0.7	0.95
28	Jacobsson & Flansbjer [192, 202]; KLX06A; Avro Granite	0.6	1.0	1.7	2.0	800	690	610	570	0.23	0.36	0.52	0.58
29		1.0	2.0	3.2	3.5	4870	4450	3970	3900	0.14	0.3	0.43	0.46
30		2.6	3.2	4.6	5.0	16040	15180	14190	14410	0.09	0.11	0.14	0.14
31		0.5	1.0	1.6	2.0	550	450	450	450	0.11	0.21	0.31	0.35
32		1.0	2.0	2.7	3.0	4320	4170	4150	4130	0.12	0.23	0.29	0.31
33		3.0	4.0	4.5	5.0	1520	15060	14580	14230	0.12	0.15	0.16	0.16
34		1.0	1.4	1.7	2.0	770	730	670	620	0.32	0.41	0.5	0.65
35		1.0	2.0	2.8	3.0	4730	4270	4000	4000	0.1	0.26	0.34	0.37
36		2.0	3.0	4.5	5.0	15060	14460	13840	13580	0.02	0.06	0.06	0.05
37		0.6	1.0	1.7	2.0	660	570	520	500	0.15	0.24	0.38	0.42
38		1.0	2.0	2.7	3.0	4600	4000	3900	3900	0.11	0.24	0.32	0.35
39		1.0	3.0	4.4	5.0	15350	14460	14120	13940	0.01	0.1	0.11	0.1
40		0.7	1.0	1.7	2.0	690	630	610	610	0.1	0.24	0.36	0.42
41		1.0	2.0	2.7	3.0	4460	4560	4290	4280	0.1	0.23	0.29	0.31
42		1.0	3.0	4.4	5.0	15840	15360	14150	14000	0	0.1	0.11	0.11
43		1.0	1.2	1.7	2.0	590	530	520	500	0.14	0.17	0.2	0.23
44		2.0	2.3	3.0	3.2	3730	3720	3530	3550	0.06	0.08	0.1	0.1
45		3.0	4.0	4.4	5.0	13770	13280	13220	13410	-0.06	-0.06	-0.05	-0.05

331

Table A.2-Continued: MDST database: post-peak behavior

Case No.	Source and Description	Post-peak shear displacements				Post-peak shear stress				Post-peak dilation displacement			
		1	2	3	4	1	2	3	4	1	2	3	4
46		1.0	1.3	1.7	2.0	690	690	640	640	0.21	0.25	0.3	0.34
47		1.0	2.0	2.7	3.0	4990	4670	4600	4360	0.58	0.76	0.85	0.89
48		3.0	4.0	4.5	5.0	15430	14510	14140	13390	0.69	0.73	0.74	0.74
49			2.0	2.7	3.0		4190	4050	4080		0.26	0.34	0.38
50				4.5	5.0			14860	14690			0.29	0.32
51	Jacobsson &			1.7	2.0			790	780			0.05	0.07
52	Flansbjer [199,		4.0	4.4	5.0		14890	14840	14650		0.11	0.1	0.1
53	208]; KL10-117;			1.7	2.0			650	650			0.41	0.46
54	Avro Granite	1.0	2.0	2.7	3.0	4340	4330	4110	4040	0.16	0.37	0.45	0.49
55		2.0	4.0	4.4	5.0	14840	14440	14390	13790	0.17	0.34	0.36	0.41
56			1.0	1.7	2.0		710	640	560		0.26	0.45	0.51
57		1.0	2.0	2.7	3.0	4980	4460	4170	4070	0.11	0.33	0.43	0.47
58		2.0	4.0	4.5	5.0	15010	13960	13710	13060	0.04	0.05	0.04	0.02
59			1.0	1.7	.0		800	820	790		0.32	0.49	0.55
60				2.7	3.0			4930	4750			0.5	0.55
61	Jacobsson &	3.0	4.0	4.5	5.0	16440	15610	15400	14730	0.13	0.16	0.16	0.17
62	Flansbjer [200,		1.0	1.8	2.0			1040	910	790		0.3	0.48	0.51
63	209]; KLX12A-	1.0	2.0	2.8	3.0	4920	4700	4560	4540	0.09	0.25	0.36	0.38
64	117; Avro Granite	3.0	4.0	4.5	5.0	15200	13680	13630	13370	0.07	0.05	0.04	0.03
65	and Quartz		1.0	1.7	2.0		1140	930	850		0.32	0.46	0.52
66	monzodiorite	1.0	2.0	2.7	3.0	4330	4120	4230	4280	0.11	0.19	0.22	0.24
67			4.0	4.6	5.0		14730	14590	14470		-0.04	-0.05	-0.06
68			1.0	1.7	2.0		610	650	630		0.24	0.4	0.46
69			2.0	2.7	3.0		4540	4410	4330		0.24	0.31	0.34
70			4.0	4.4	5.0		15370	15150	14970		0	0	-0.01
71			1.0	1.7	2.0		610	610	580		0.26	0.39	0.45
72	Jacobsson &	1.0	2.0	2.7	3.0	4500	3880	3660	3490	0.08	0.21	0.28	0.31
73	Flansbjer [201,	2.0	4.0	4.4	5.0	14110	13300	12970	12830	-0.05	-0.04	-0.04	-0.07
74	210]; KFM09A-		1.0	1.7	2.0		580	500	440		0.22	0.39	0.45
75	117; Medium-	1.0	2.0	2.7	3.0	3920	3950	4100	4080	0.07	0.22	0.31	0.35
76	grained granite			4.4	5.0			13300	13270			-0.07	-0.08
77			1.0	1.7	2.0		530	520	440		0.23	0.33	0.35
78			2.0	2.7	3.0		3840	3760	3710		0.18	0.23	0.25
79			4.0	4.5	5.0		13760	14000	13770		0.02	0	0
80			1	1.69	2		569	490	442		0.28	0.38	0.42
81		1	2	2.71	3	3981	3476	3360	3374	0.13	0.23	0.28	0.3
82		2	4	4.71	5	13624	12929	12720	12450	0.11	0.19	0.21	0.215
83	Jacobsson &		1	1.67	2		501	530	439		0.25	0.4	0.45
84	Flansbjer [195,		2	2.38			3911	4050			0.31	0.36	
85	203]; KFM06A-	2	4	4.44	5	14367	13828	13900	13665	0.12	0.19	0.2	0.22
86	117; Medium-			1.7	2			450	441			0.21	0.25
87	grained granite		1	2.87	3		3702	3500	3564		0.14	0.2	0.21
88				5.05				14160				0.06	
89			1	1.72	2		441	420	441		0.15	0.26	0.3
90		1	2	3.01		3916	3904	3820		0.03	0.08	0.12	

332

Table A.2-Continued: MDST database: post-peak behavior

Case No.	Source and Description	Post-peak shear displacements				Post-peak shear stress				Post-peak dilation displacement			
		1	2	3	4	1	2	3	4	1	2	3	4
91		3.0	4.0	4.5	5.0	13990	13637	13650	13494	-0.14	-0.18	-0.2	-0.23
92	Jacobsson & Flansbjer [195, 203]; KFM06A-117; Medium-grained granite		1.0	1.7	2.0		592	590	554		0.24	0.38	0.46
93		1.0	2.0	2.7	3.0	4319	4276	4380	4281	0.09	0.22	0.28	0.3
94		3.0	4.0	4.5	5.0	15488	15108	15220	14922	0.03	0.06	0.06	0.06
95			1.0	1.7	2.0		554	500	491		0.27	0.39	0.44
96		1.0	2.0	2.9	3.0	4391	4278	3800	3574	0.11	0.25	0.33	0.34
97		2.0	4.0	4.7	5.0	15276	13590	13020	12734	0.02	0.12	0.13	0.13
98	Jacobsson & Flansbjer [193, 194, 204]; KFM05A-117; Medium-grained granite		1	1.7	2		608	570	529		0.32	0.46	0.51
99		1	2	2.71	3	4127	3810	3790	3492	0.13	0.29	0.36	0.39
100		2	4	4.46	5	14287	14340	14370	13811	-0.02	0.02	0.02	0.01
101			1	1.68	2		608	510	423		0.33	0.5	0.57
102		1	2	2.7	3	4339	4021	4070	4180	0.15	0.34	0.41	0.45
103		4	5	4.45	5	14287	13811	14330	14499	0.01	0.07	0.08	0.09
104			1	1.83	2		423	400	423		0.19	0.29	0.31
105		1	2	2.69	3	2990	2778	2750	2752	0.03	0.07	0.08	0.09
106				7				11030				-0.06	
107			1	1.67	2		555	500	476		0.34	0.51	0.59
108		1	2	2.7	3	4180	3810	3470	3333	0.16	0.3	0.38	0.41
109		2	4	4.43	5	13864	12917	13160	13202	0.13	0.25	0.27	0.28
110		1	2	2.67	3	530	680	670	610	0.32	0.59	0.79	0.89
111		1	2	2.66	3	4590	5060	4510	4030	0.21	0.44	0.57	0.63
112		3	4	4.43	5	16550	16130	16600	15730	0.26	0.31	0.33	0.35
113			1	1.68	2		600	520	480		0.2	0.29	0.33
114		1	2	2.86	3	4180	3860	3520	3460	0.06	0.15	0.23	0.25
115			4	5.52	5		13220	13400	13060		-0.06	-0.07	-0.09
116			1	1.66	2		596	550	546		0.34	0.48	0.55
117		1	2	2.64	3	4159	3816	3660	3600	0.19	0.34	0.41	0.44
118		2	4	4.52	5	13435	12050	13690	12750	0.12	0.17	0.17	0.16
119			1	1.66	2		503	480	398		0.33	0.45	0.5
120		1	2	2.67	3	3941	3550	3520	3525	0.18	0.32	0.4	0.43
121		2	4	4.39	5	13183	12260	12920	11721	0.09	0.16	0.17	0.17
122	Jacobsson & Flansbjer [197, 206]; KFM08A-117; Medium-grained granite	1	2	2.36		596	470	480		0.36	0.58	0.64	
123		1	2	2.76	3	4212	3755	3470	3378	0.17	0.33	0.42	0.44
124		2	4	4.61	5	13628	13142	13000	13002	0.07	0.12	0.11	0.11
125			1	1.73	2		545	530	520		0.31	0.48	0.53
126		1	2	2.78	3	4465	4389	4110	4082	0.17	0.33	0.42	0.44
127			4	4.54	5		15175	15180	14412		0.06	0.04	0.02
128			1	1.7	2		697	680	660		0.36	0.54	0.62
129		1	2	2.72	3	5366	4503	4380	4123	0.19	0.39	0.5	0.54
130		3	4	4.52	5	16554	15679	14950	14981	0.11	0.15	0.16	0.16
131			1	1.71	2		457	420	444		0.25	0.37	0.41
132		1	2	2.81	3	3679	3514	3340	3438	0.15	0.25	0.32	0.33
133		2	4	4.56	5	13307	12316	12790	12418	0.09	0.13	0.13	0.13
134			1	1.78	2		672	710	672		0.27	0.46	0.54
135		1	2	2.77	3	4567	4541	3980	3932	0.16	0.35	0.48	0.52
136		3	4	4.72	5	14550	14068	14040	14106	0.16	0.18	0.2	0.2

333

Table A.2-Continued: MDST database: post-peak behavior

Case No.	Source and Description	Post-peak shear displacements				Post-peak shear stress				Post-peak dilation displacement			
		1	2	3	4	1	2	3	4	1	2	3	4
137	Jacobsson & Flansbjer [196, 205]; KLX03A-117; Avro Granite and Quartz monzodiorite			1.72	2			580	570			0.32	0.36
138			2	2.81	3		4612	4490	4385		0.24	0.33	0.35
139		3	4	4.85	5	16703	16557	16570	16412	0.07	0.09	0.11	0.11
140		1	2	2.22		693	567	550		0.17	0.28	0.3	
141			2	2.72	3		4121	4020	3944		0.05	0.06	0.07
142		3	5	5.36	6	14589	15769	14800	14454	-0.08	-0.14	-0.15	-0.17
143			1	1.72	2		495	490	444		0.15	0.23	0.26
144		1	2	2.69	3	4151	3834	3810	3796	0.15	0.16	0.21	0.23
145			4	4.49	5		14576	14200	13698		0.11	0.12	0.12
146			1	1.68	2		571	570	546		0.2	0.32	0.37
147		2	3	3.71	4	4189	3580	3460	3529	0.21	0.32	0.37	0.39
148		3	4	5	5.51	14700	14903	14910	14993	0.11	0.12	0.12	0.12
149			1	1.68	2		635	550	444		0.28	0.42	0.48
150		1	2	2.7	3	4697	4367	3980	3948	0.12	0.25	0.32	0.34
151		2	3	4.45	5	15686	15094	14620	14459	0.05	0.14	0.15	0.17
152				1.84	2			550	533			0.21	0.24
153			2	2.7	3		4012	3890	3897		0.12	0.19	0.21
154													
155			1	1.68	2		495	490	444		0.11	0.23	0.27
156		1	2	2.71	3	3948	3872	3640	3517	0.03	0.13	0.18	0.2
157		2	4	4.6	5	13685	13558	13630	13489	-0.01	0.06	0.06	0.07
158			1	1.87	2		635	560	521		0.22	0.36	0.39
159		1	2	2.73	3	4532	4075	4010	3859	0.09	0.2	0.26	0.29
160		2	4	4.58	5	14128	12664	12720	12501	-0.03	-0.01	-0.02	-0.03
161	Jacobsson & Flansbjer [198, 207]; KFM07A-117; Medium-grained granite		1	1.7	2		647	560	546		0.29	0.42	0.47
162		1	2	2.7	3	4494	4443	4370	4329	0.16	0.29	0.37	0.4
163		2	4	4.45	5	15729	15259	15010	14929	0.09	0.17	0.17	0.18
164			1	1.67	2		647	560	546		0.25	0.36	0.41
165		1	2	2.67	3	4722	4595	4250	4164	0.14	0.25	0.31	0.33
166		2	4	4.45	5	16541	15530	15630	15475	0.02	0.1	0.1	0.1
167			1	1.68	2		571	570	533		0.18	0.28	0.33
168			2	2.69	3		4329	4260	4291		0.19	0.24	0.26
169			4	4.66	5		16524	16500	16524		0.09	0.1	0.1
170			1	1.66	2		609	540	482		0.2	0.27	0.3
171		1	2	2.68	3	4265	3986	4000	3935	0.08	0.16	0.19	0.21
172		3	4	4.52	5	15443	15029	14790	14294	0.01	0.01	0.01	0.01
173			1	1.7	2		597	580	571		0.25	0.37	0.42
174		1	2	2.72	3	4519	4443	4470	4380	0.13	0.24	0.32	0.3
175		3	4	4.45	5	16851	16490	16240	16071	0.09	0.11	0.12	0.12
176	Homand *et al.* [169]; Schist replicas	10	15	20		562	454	432		1.7	2.57	3.14	
177		10	15	20		1119	880	780		2.27	3.4	4.13	
178		10	15	20		1492	1416	1265		1.94	2.96	3.78	
179		10	15	20		2189	2005	1789		2.04	2.96	3.46	
180		15	0			2470	2486			1.49	2.03		

Case No.	Source and Description	Post-peak shear displacements				Post-peak shear stress				Post-peak dilation displacement			
		1	2	3	4	1	2	3	4	1	2	3	4
181			1	1.73	2		520	470	444		0.17	0.34	0.4
182			2	2.9	3		3654	3590	3604		0.23	0.39	0.43
183		3	4	4.63	5	13462	12945	12700	12751	0.23	0.37	0.44	0.49
184			1	1.7	2		647	660	609		0.28	0.48	0.54
185		1	3	3.69	4	5278	4694	4470	4466	0.16	0.52	0.61	0.65
186		2	4	4.7	5	16177	14883	14360	14337	0.16	0.34	0.38	0.41
187			1	1.98			295	620			0.12	0.21	
188			3	3.2			4009	4020			0.15	0.17	
189				4.46	5			14990	14705			0.08	0.08
190			1	1.7	2		660	530	444		0.26	0.41	0.46
191	Jacobsson [188, 189]; KLX02-117; Avro Granite	1	2	2.71	3	4225	3844	3610	3578	0.14	0.29	0.35	0.37
192		2	4	4.52	5	13944	11102	10900	10900	0.11	0.19	0.19	0.19
193				1.88	2.22			590	596			0.14	0.17
194				3.7	4			4480	4377			0.28	0.33
195			4	4.95	5.55		15783	15480	15720		0.19	0.24	0.28
196			1	1.92	2		634	580	533		0.29	0.44	0.46
197		1	2	3.18		4352	3743	3050		0.13	0.24	0.33	0.34
198		2	4	4.64	5	12967	12600	12180	11936	0.12	0.2	0.2	0.2
199			1	1.68	2		749	630	596		0.28	0.46	0.53
200		1	2	2.75	3	5189	4223	3860	3730	0.13	0.33	0.47	0.51
201		2	4	4.44	5	16634	13969	14240	14908	0.12	0.3	0.32	0.34
202		1	2	2.48	2.81	787	647	580	609	0.29	0.49	0.57	0.63
203		1	3	3.65	4	5188	4365	4180	4060	0.1	0.38	0.46	0.49
204		3	4	4.96	5.53	17102	16662	16150	16050	0.1	0.12	0.12	0.12
205				1.74	2			460	444			0.14	0.16
206													
207					6				13512				0.13
228		2	3	4	6	12.07	11.57	11.82	11.19				
229		2	3	4	6	14.84	14.71	13.96	12.32				
230		2	3	4	6	16.73	15.85	14.84	13.83				
231		2	3	4	6	24.02	22.26	18.74	16.85				
232		2	3	5	7	33.07	31.19	29.55	27.67				
233	Bandis *et al.* [79]; Figure 4; Tension fracture	2	3	5	7	34.83	33.83	30.56	27.67				
234		2	3	5	7	40	38.48	35.21	33.07				
235		2	3	5	7	45.02	43.13	39.86	36.85				
236		2	4	6	7	71.09	69.42	68.24	67.4				
237		2	4	6	7	78.97	75.45	72.1	71.43				
238		2	4	6	7	88.19	82.5	77.63	77.3				
239		2	4	6	7	118.9	110.2	105.1	102.1				
240	Bandis *et al.* [79]; Figures 9-21; Bedding plane in limestone	2	3	4		48.31	44.7	41.86		0.39	0.55	0.66	
241		2	3	4		46.23	42.41	40.44		0.41	0.63	0.79	
242		2	3	4	6	39.4	38.86	35.9	34.26	0.28	0.48	0.63	0.96
243			3	4	6		35.9	35.9	34.7		0.24	0.45	0.8

Table A.2-Continued: MDST database: post-peak behavior

Case No.	Source and Description	Post-peak shear displacements				Post-peak shear stress				Post-peak dilation displacement			
		1	2	3	4	1	2	3	4	1	2	3	4
268	Bandis *et al.* [79]; Figures 9-21; Bedding plane in slightly metamorphosed fine grained sandstone	2	3	4	5	21.88	21.14	21.29	21.09	0.06	0.09	0.11	0.13
269		2	3	4	5	20.34	20.29	19.94	19.94	0.06	0.08	0.11	0.12
270		2	3	4	5	19.5	19.15	19.2	18.85	0.04	0.07	0.1	0.11
271		2	3	4	5	18.65	18.65	18.4	18.5	0.03	0.05	0.08	0.09
276	Bandis *et al.* [79]; Figures 9-21; Bedding plane in Course grained sandstone	2	3	4		49.57	44.52	41.54		0.26	0.5	0.64	
277		2	3	4	6	40.72	38.08	36.63	35.19	0.3	0.47	0.61	
278		2	3	4	6	30.91	30.14	30.24	29.85	0.27	0.43	0.54	0.66
279		2	3	4	6	25.58	25.96	26.25	25.67	0.17	0.3	0.44	0.56
299	Huang *et al.* [184]; Figures 3-8; Replica	2	3	4		111.8	117.5	121.3		0.44	0.72	1.04	
300		2	3	4		434.0	430.2	422.7		0.1	0.25	0.45	
301		2	3	4		500.4	477.6	462.5		0.02	0.08	0.14	
302		2	3	4		898.4	860.5	851		0	0	-0.01	
303			3	4			1257	1192			-0.06	-0.06	
304		2	3			210	210			0.75	1.3		
305		2	3	4		570	520	500		0.2	0.32	0.44	
306			3	4			760	730			0.13	0.27	
307		2	3	4		1040	920	820		0.01	0.01	0	
308			3	4			1480	1390			-0.03	-0.03	
309	Wibowo [162] and Wibowo *et al.* [161]; G2; Replica	13				236.4							
310		13				1139							
311		13				2493							
312		13				4171							
313	Wibowo [162] and Wibowo *et al.* [161]; F2; Replica	13				104.1							
314		13				767.6							
315		13				1547							
316		13				3316							
317	Wibowo [162] and Wibowo *et al.* [161]; F3; Replica	15				135.7							
318		15				842.7							
319		15				2230							
320		15				3386							
321	Wibowo [162] and Wibowo *et al.* [161]; F4; Replica	15				222.9							
322		15				812.1							
323		15				1821							
324		15				3015							
325		15				3813							
327	Grasselli and Egger [127]	1	2	3	5	1998	1680	1557					
337		1	2	3	5	2057	1787	1720					
339		1	1.5	2	3	2200	1978	1800					
344		1	2	3	5	2855	2643	2643					
359		1	2	3		3682	3652	3623					

TableA.3: Cyclic Direct Shear Test (CDST) database

Case No.	Source and Description	Shear strength			Dilation displacement		
		δ_h (mm)	Cycle no.	τ (KPa)	δ_h (mm)	Cycle no.	δ_v (mm)
1	Celestino and Goodman [174]; Figure 4; Cyclic direct shear test (1 cycle) on a 0.35 m long specimen of Plaster with *UCS*=40 MPa, under normal stress of 1030 KPa	0.62		1279	0.2		-0.22
		2.38		718	0.58		0
		2.29		0	1.57		0.81
		2.03		-785	2.3		0.68
		0.3		-647	1.9		0.31
		-0.51		-1116	0.67		0
		-2.57	1	-700	-0.1	1	-0.54
		-2.33		0	-1.35		-0.08
		-2.22		816	-2.02		-0.08
		-0.42		681	-2.46		-0.28
		0.3		966	-2.22		-0.45
		1.73		773	-1.51		-0.45
					-0.33		-0.9
					1.74		-0.9
2	Homand *et al.* [169]; Figure 10-a; Cyclic direct shear test (10 cycles) on a 0.145 m long specimen of schist replicas with *UCS*=75 MPa, under normal stress of 500 KPa; the base friction angle of the replica is 34º	0.63		416	2		0.56
		10		202	6		1.28
		10		0	10		1.85
		9.45		-101	6		1.28
		0.5	1	-15	2	1	0.56
		-1.5		-313	0		0
		-10		-210	-2		0.39
		-10		0	-6		1.24
		-9.46		43	-10		1.73
		-0.43		11	-6		1.24
		0.92		364	-2		0.39
		10		208	0		0
		10		0	dN10		0.66
		9.45		-154	6		1.37
		0.5	2	-18	10	10	1.91
		-1.5		-327	6		1.37
		-10		-227	2		0.66
		-10		0	0		0
		-9.46		45	-2		0.5
		-0.54		26	-6		1.37
		0.92		334	-10		1.77
		10		327	-6		1.37
		10		0	-2		0.5
		9.45		-166	0		0
		0.5	2	-54			
		-1.5		-425			
		-10		-294			
		-10		0			
		-9.46		101			
		-0.88		75			

Case No.	Source and Description	Shear strength			Dilation displacement		
		δ_h (mm)	Cycle no.	τ (KPa)	δ_h (mm)	Cycle no.	δ_v (mm)
3	Homand *et al.* [169]; Figure 10-b; Cyclic direct shear test (10 cycles) on a 0.145 m long specimen of schist replicas with *UCS*=75 MPa, under normal stress of 4000 KPa; the base friction angle of the replica is 34º	0.61	1	3911	2	1	0.51
		10		2214	6		1.32
		10		0	10		1.92
		10		-1119	6		1.32
		1.03		-696	2		0.51
		-1.59		-4163	0		0
		-10		-2963	-2		0.41
		-9.75		0	-6		1.32
		-9.35		1652	-10		1.86
		-1.19		1355	-6		1.32
		0.89	2	3733	-2		0.41
		10		2622	0		0
		10		0	2	2	0.41
		9.85		-1481	6		1.26
		1.26		-896	10		1.85
		-1.59		-4160	6		1.26
		-10		-3111	2		0.41
		-9.75		0	0		0
		-9.38		1696	-2		0.35
		-1.33		1408	-6		1.24
		4.41	10	4303	-10		1.8
		10		4006	-6		1.24
		10		0	-2		0.35
		9.61		-2044	0		0
		2.35		-1844	2	10	0.17
		-1.46		-4415	6		0.92
		-10		-4126	10		1.6
		-9.75		0	6		0.92
		-9.54		2118	2		0.17
		-1.73		2052	0		0
					-2		0.21
					-6		0.98
					-10		1.62
					-6		0.98
					-2		0.21
					0		0

Table A.3-Continued: Cyclic Direct Shear Test (CDST) database

Case No.	Source and Description	Shear strength			Dilation displacement		
		δ_h (mm)	Cycle no.	τ (KPa)	δ_h (mm)	Cycle no.	δ_v (mm)
4	Huang *et al.* [103]; Figure 6; Cyclic direct shear test (1 cycle) on a 0.15 m long specimen of artificial joint (Hydrostone & water) with *UCS*=38 MPa, under normal stress of 1000 KPa; the base friction angle of the replica is 34º	0.65	1	1092	1	1	0.07
		6.26		1132	3		0.41
		5.82		-471	5		0.76
		0.68		-506	6.3		0.98
		-0.41		-1022	5		0.8
		-5.93		-1070	3		0.47
		-5.5		524	1		0.12
		-0.17		590	0		0
					-1		0.13
					-3		0.46
					-5		0.81
					-5.9		0.96
					-5		0.86
					-3		0.51
					-1		0.17
					0		0
5	Huang *et al.* [103]; Figure 7; Cyclic direct shear test (5 cycles) on a 0.15 m long specimen of artificial joint (Hydrostone & water) with *UCS*=38 MPa, under normal stress of 500 KPa; the base friction angle of the replica is 34º	0.29	1	531	3	1	0.58
		6.01		478	6		1.09
		5.77		-221	3		0.58
		0.29		-214	0		0
		-0.46		-490	-3		0.51
		-6.08		-506	-6		1.02
		-5.86		235	-3		0.51
		-0.22		223	0		0
		0.29	2	500	3	5	0.51
		6.01		529	6		1.05
		5.77		-221	3		0.51
		0.32		-241	0		0
		-0.46		-492	-3		0.48
		-6.08		-540	-6		1.01
		-5.86		235	-3		0.48
		-0.24		246	0		0
		0.29	5	512			
		6.01		563			
		5.77		-221			
		0.38		-248			
		-0.46		-520			
		-6.08		-540			
		-5.86		235			
		-0.25		265			

Case No.	Source and Description	Shear strength			Dilation displacement		
		δ_h (mm)	Cycle no.	τ (KPa)	δ_h (mm)	Cycle no.	δ_v (mm)
6	Huang *et al.* [103]; Figure 8; Cyclic direct shear test (5 cycles) on a 0.15 m long specimen of artificial joint (Hydrostone & water) with *UCS*=38 MPa, under normal stress of 1750 KPa; the base friction angle of the replica is 34º	1.29		1906	0		0
		5.82		1876	0.5		-0.07
		5.39		-760	3		0.3
		1.27	1	-774	5		0.65
		-1.27		-1597	3		0.3
		-5.73		-1635	0.5	1	-0.08
		-5.35		876	0		-0.15
		-0.83		986	-0.5		-0.1
		1.29		1679	-3		0.24
		5.9		1789	-5		0.58
		5.39		-760	-3		0.26
		1.5	2	-913	-0.5		-0.1
		-1.14		-1336	0		-0.15
		-5.75		-1482	0.5		-0.15
		-5.35		876	3		0.14
		-0.99		1088	5		0.47
		1.29		1416	3		0.14
		6		1402	0.5		-0.15
		5.39		-760	0	2	-0.2
		1.86		-1117	-0.5		-0.13
		-1.14	5	-1336	-3		0.15
		-5.9		-1351	-5		0.44
		-5.35		876	-3		0.16
		-1.13		1190	-0.5		-0.13
					0		-0.2
					0.5		-0.2
					3		-0.07
					5		0.1
					3		-0.15
					0.5	5	-0.2
					0		-0.2
					-0.5		-0.27
					-3		-0.03
					-5		0.22
					-3		-0.05
					-0.5		-0.27

Case No.	Source and Description	Shear strength			Dilation displacement		
		δ_h (mm)	Cycle no.	τ (KPa)	δ_h (mm)	Cycle no.	δ_v (mm)
7	Huang *et al.* [103]; Figure 9; Cyclic direct shear test (20 cycles) on a 0.15 m long specimen of artificial joint (Hydrostone & water) with *UCS*=38 MPa, under normal stress of 2000 KPa; the base friction angle of the replica is 34º	0.55	A1	1470	1	0	0
		6.88	B1	1382	1	1	-0.1
		6.65	C1	-412	1	4	0.36
		0.57	D1	-485	1	6.75	0.85
		-0.25	E1	-1360	1	4	0.42
		-6.94	F1	-1205	1	1	-0.1
		-6.83	G1	544	1	0	-0.23
		-0.17	H1	632	1	-1	-0.1
		0.55	A5	1500	1	-4	0.4
		6.88	B5	1426	1	-6.75	0.92
		6.65	C5	-470	1	-4	0.4
		1.07	D5	-492	1	-1	-0.1
		-0.4	E5	-1264	1	0	-0.3
		-6.94	F5	-1264	5	0	-0.4
		-6.78	G5	625	5	1	-0.37
		-0.38	H5	845	5	4	0.13
		0.55	A10	1530	5	6.75	0.63
		6.88	B10	1426	5	4	0.2
		6.65	C10	-536	5	1	-0.3
		2.55	D10	-617	5	0	-0.41
		-0.4	E10	-1264	5	-1	-0.28
		-6.94	F10	-1302	5	-4	0.23
		-6.6	G10	625	5	-6.75	0.74
		-0.74	H10	1087	5	-4	0.23
		0.55	A15	1550	5	-1	-0.28
		6.88	B15	1521	5	0	-0.41
		6.65	C15	-860	20	0	-0.63
		6.22	D15	-904	20	1	-0.57
		-0.4	E15	-1264	20	4	-0.47
		-6.94	F15	-1382	20	6.75	-0.32
		-6.65	G15	1007	20	4	-0.47
		-1.19	H15	1411	20	1	-0.57
		0.55	A20	1550	20	0	-0.63
		6.88	B20	1521	20	-1	-0.66
		6.65	C20	-860	20	-4	-0.52
		6.22	D20	-904	20	-6.75	-0.21
		-0.4	E20	-1264	20	-4	-0.43
		-6.94	F20	-1382	20	-1	-0.57
		-6.65	G20	1007	20	0	-0.63
		-1.19	H20	1411	20	0	-0.63
					20	1	-0.57

Table A.3-Continued: Cyclic Direct Shear Test (CDST) database

Case No.	Source and Description	Shear strength			Dilation displacement		
		δ_h (mm)	Cycle no.	τ (KPa)	δ_h (mm)	Cycle no.	δ_v (mm)
8	Huang *et al.* [103]; Figure 11; Cyclic direct shear test (20 cycles) on a 0.15 m long specimen of artificial joint (Hydrostone & water) with *UCS*=38 MPa, under normal stress of 3000 KPa; the base friction angle of the replica is 34º	0.15	1	2273	0	1	0
		7		1966	4		0.58
		6.54		-1057	7		1.1
		0.02		-977	4		0.58
		-0.87		-2364	0		-0.11
		-7.11		-2273	-4		0.33
		-6.69		852	-7		0.85
		-1.24		875	-4		0.33
		0.2	2	2148	0	2	-0.33
		7		1966	0		-0.33
		6.54		-1057	4		0.33
		0.47		-1114	7		0.8
		-0.87		-2284	4		0.4
		-7.11		-2273	0		-0.27
		-6.69		852	-4		0.2
		-1.05		1046	-7		0.65
		0.25	4	1966	-4	4	0.2
		7		1966	0		-0.39
		6.39		-1591	0		-0.39
		2.19		-1739	4		0
		-0.87		-2159	7		0.36
		-7.08		-2159	4		0.08
		-6.56		1273	0		-0.39
		-2.33		1739	-4		-0.12
		0.25	7	1966	-7	7	0
		7		1966	-4		-0.24
		6.34		-1863	0		-0.39
		3.08		-2103	0		-0.53
		-0.87		-2159	4		-0.52
		-7.08		-2159	7		-0.35
		-6.53		1534	4		-0.4
		-2.63		1933	0		-0.53
		0.25	20	1966	-4		-0.54
		7		1966	-7		-0.39
		6.34		-1863	-4		-0.45
		3.08		-2103	0		-0.53
		-0.87		-2159	0	20	-0.64
		-7.08		-2159	4		-0.65
		-6.53		1534	7		-0.5
		-2.63		1933	4		-0.56
					0		-0.64
					-4		-0.62
					-7		-0.5
					-4		-0.55
					0		-0.64

342

Table A.3-Continued: Cyclic Direct Shear Test (CDST) database

Case No.	Source and Description	Shear strength			Dilation displacement		
		δ_h (mm)	Cycle no.	τ (KPa)	δ_h (mm)	Cycle no.	δ_v (mm)
9	Lee *et al.* [167]; Figure 8; Cyclic direct shear test (2 cycles) on a 0.12 m long specimen of Granite with *UCS*=151 MPa, under normal stress of 1000 KPa; the base friction angle of the replica is 35°	1.23		1937	0		0
		15		773	0.6		-0.06
		12.97		492	1.23		0
		0.68	1	-367	5		1.03
		-1.86		-1125	15		2.17
		-14.83		-828	5		1.03
		-13.7		453	0	1	0.08
		-1.19		352	-0.72		0
		1.79		922	-5		0.84
		14.97		851	-15		2.13
		13.87		-469	-5		0.76
		0.98	2	-437	-0.72		0
		-2.97		-960	0		-0.05
		-14.76		-891	0.68		0
		-13.57		477	15		1.91
		-1.87		398	13.95		1.91
					-0.72	2	0
					-15		1.84
					-13.78		1.8
					-1.02		0
					0		-0.05
10	Lee *et al.* [167]; Figure 9-a; Cyclic direct shear test (15 cycles) on a 0.12 m long specimen of Granite with *UCS*=151 MPa, under normal stress of 500 KPa; the base friction angle of the replica is 35°	0.4		851	0		0
		15.14		351	0.4		-0.11
		14.44		-277	0.62		0
		0.75	1	-186	10.19	1	1.93
		-1.5		-787	15		2.42
		-14.74		-497	8.55		1.95
		-12.98		213	0		-0.13
		-1.58		111	-15		3.16
		0.92		480	0		-0.14
		15.14		351	15		2.16
		14.44		-277	0	2	-0.145
		0.92	2	-200	-15		2.76
		-2.46		-601	0		-0.15
		-14.74		-561	0		-0.22
		-12.98		213	15		1.6
		-1.76		145	0	15	-0.225
		0.97		412	-15		1.94
		15.14		456	0		-0.23
		14.44		-277			
		1.45	15	-250			
		-3.26		-466			
		-14.74		-622			
		-12.98		213			
		-2.33		223			

Table A.3-Continued: Cyclic Direct Shear Test (CDST) database

Case No.	Source and Description	Shear strength			Dilation displacement		
		δ_h (mm)	Cycle no.	τ (KPa)	δ_h (mm)	Cycle no.	δ_v (mm)
11	><p *et al.* [167]; Figure 9-b; Cyclic direct shear test (10 cycles) on a 0.12 m long specimen of Marble with *UCS*=72 MPa, under normal stress of 500 KPa; the base friction angle of the replica is 38º	0.29	1	1123	0	1	0
		14.91		413	0.21		-0.53
		14.62		-298	6.5		1.66
		1.76		-204	15		2.64
		-1.27		-668	7.49		1.52
		-14.99		-574	0		-0.33
		-14.3		277	-15		2.06
		-1.68	2	225	0	2	-0.33
		1.47		634	15		2.29
		14.95		451	0		-0.33
		14.62		-298	-15		1.81
		2.58		-247	0	10	-0.33
		-2.01		-557	15		1.84
		-15.03		-621	0		-0.33
		-14.3		277	-15		1.19
		-1.92		277	0		-0.33
		1.68	10	460			
		14.95		489			
		14.62		-298			
		4.05		-311			
		-2.66		-468			
		-15.03		-655			
		-14.3		277			
		-2.38		374			
12	Lee *et al.* [167]; Figure 10-a; Cyclic direct shear test (8 cycles) on a 0.12 m long specimen of Granite with *UCS*=151 MPa, under normal stress of 3000 KPa; the base friction angle of the replica is 35º	2.58	1	4785	0	1	0
		15.01		2298	15		2.04
		11.83		-1314	0		0
		1.12		-1251	-15		1.46
		-1.08		-2690	0		0
		-14.75		-2017	0	8	0
		-11.53		1798	15		1.27
		-1.12		1251	0		0
		2.62	8	2408	-15		0.78
		15.01		2877	0		0
		12.43		-1423			
		2.62		-1830			
		-1.94		-2174			
		-14.7		-2455			
		-11.1		1611			
		-2.06		1970			

Table A.3-Continued: Cyclic Direct Shear Test (CDST) database

Case No.	Source and Description	Shear strength			Dilation displacement		
		δ_h (mm)	Cycle no.	τ (KPa)	δ_h (mm)	Cycle no.	δ_v (mm)
13	Lee *et al.* [167]; Figure 10-b; Cyclic direct shear test (4 cycles) on a 0.12 m long specimen of Marble with *UCS*=72 MPa, under normal stress of 3000 KPa; the base friction angle of the replica is 38º	0.56	1	4466	0	1	0
		15.06		1870	3.73		0.89
		13.6		-1274	15.06		1.96
		3.19		-1451	11.87		1.3
		-2.59		-2902	-0.82		0.22
		-15.02		-2225	-9.38		1.15
		-13.2		1628	-15		1.35
		-1.38		1984	-0.86	2	0.15
		1.51		2693	15		1.5
		15.06		2322	-2.24		0.25
		13.6		-1645	-15		0.74
		3.54	2	-1757	-1.29	3	0.14
		-3.63		-2483	15		1.67
		-15.02		-2402	-3.4		0.22
		-13.08		1919	-15		0.26
		-1.81		2354	-5.12	4	0.03
		1.63		2483	15		1.41
		15.06		2402	0		0.1
		13.6		-1854	-15		-0.04
		3.63	4	-1935	-8		-0.1
		-4.32		-2306	0		0.11
		-15.02		-2610			
		-12.99		2161			
		-2.07		2483			
14	Lee *et al.* [167]; Figure 11; Cyclic direct shear test (16 cycles) on a 0.12 m long specimen of Granite with *UCS*=151 MPa, under normal stress of 1000 KPa; the base friction angle of the replica is 35º	0.58	1	1325	0	1	0
		15		732	15	1	2.73
		14.18		-438	-1.08	1	-0.07
		0.8	1	-402	-15	1	2.17
		-1.89		-1237	-1.08	2	-0.09
		-14.76		-778	15	2	2.43
		-14.07		387	-1.08	2	-0.1
		-2.91		355	-15	2	1.73
		0.98		1000	-1.08	16	-0.15
		15		856	15	16	1.55
		14.7		-459	-1.08	16	-0.16
		0.95	2	-428	-15	16	1.06
		-3.16		-954			
		-14.84		-886			
		-13.89		438			
		-2.95		376			
		1.27		798			
		15		995			
		14.7		-459			
		1.75	16	-629			
		-3.6		-835			
		-14.8		-984			
		-13.34		541			
		-3.89		624			

Table A.3-Continued: Cyclic Direct Shear Test (CDST) database

Case No.	Source and Description	Shear strength			Dilation displacement		
		δ_h (mm)	Cycle no.	τ (KPa)	δ_h (mm)	Cycle no.	δ_v (mm)
15	Jing *et al.*[99]; Figure 3; Cyclic direct shear test (2 cycles) on specimens of concrete replica with *UCS*=52 MPa, under normal stress of 2000 KPa; the base friction angle of the replica is 33°	2.24		2352	0		0
		10.32		2017	1.37		-0.2
		7.44		-1282	8.5		0.72
		1.44	1	-1282	10.25	1	0.81
		-1.61		-2246	8.5		0.72
		-9.58		-2189	0		-0.15
		-7.87		1249	-7.74		0.7
		0		1437	-10.62		0.92
		5.09		2090	-7.74		0.7
		8.94		2049	0		-0.14
		6.1		-1380	2.08		-0.17
		1.44	2	-1510	3.95		0
		-2.8		-2131	8.94	2	0.46
		-10.78		-2025	7.17		0.44
		-8.74		1315	3		0
		-0.9		1494	0		-0.15
					-9.51		0.62
					-7.74		0.54
					0		-0.15
16	Amadei *et al*. [213]; Figure 4; Cyclic direct shear test (5 cycles) on a 0.11 m long specimens of replica with *UCS*=27.6 MPa, under normal stress of 1378 KPa; the base friction angle of the replica is 32°	1.34		1456	0		0
		15.00		767	10		1.45
		14.45		-735	15		2.04
		1.62	1	-863	10	1	1.27
		-1.50		-1892	0		0
		-13.50		-1176	-10		1.09
		-13.20		304	-13.2		1.36
		-2.25		314	-10		0.99
		0.81		879	0		0
		15.00		663	10		1.18
		14.45		-627	15		1.84
		1.62	2	-863	10	2	1.13
		-1.50		-1411	0		0
		-13.50		-1176	-10		0.94
		-13.20		206	-13.2		1.28
		-2.25		314	-10		0.94
		0.35		706	0		0
		15.00		637	10		0.98
		14.45		-627	15		1.65
		1.62	5	-863	10	5	0.98
		-1.50		-1245	0		0
		-13.50		-1176	-10		0.83
		-13.20		206	-13.2		1.19
		-2.25		314	-10		0.83
					0		0

Case No.	Source and Description	Shear strength		
		δ_h (mm)	Cycle no.	τ (KPa)
17	Grasselli and Egger [127]; Figure 7; Cyclic direct shear test (6 cycles) on a 0.14 m long specimens of Serpentinite with *UCS*=74 MPa, under normal stress of 2000 KPa; the base friction angle of the replica is 39º	0.4	1	4400
		1		2820
		2.74		2740
		0.37	2	3400
		1		2300
		2.74		1740
		0.46	3	2000
		1		1980
		2.74		1740
		0.49	4	1800
		1		1840
		2.74		1740
		0.5	5	1600
		1		1720
		2.74		1740
		0.53	6	1600
		1		1700
		2.74		1740
18	Grasselli and Egger [127]; Figure 7; Cyclic direct shear test (6 cycles) on a 0.14 m long specimens of Granite with *UCS*=173 MPa, under normal stress of 1120 KPa; the base friction angle of the replica is 34º	0.56	1	3024
		1		2228.8
		3		1780.8
		0.1	2	1680
		1		1310.4
		3		1232
		0.34	3	1120
		1		1176
		3		1120
		0.49	4	1008
		1		1108.8
		3		1120
		0.68	5	1008
		1		1108.8
		3		1120
		0.55	A6	1008
		1		1030.4
		3	B6	1075.2

APPENDIX B: EXAMPLES OF BS3D INPUT FILES

B.1 "*INPUT.DAT*"

The example is the same as the one introduced in Section 5.5; just the loading condition is different here. The block is depicted in Figure 5.12-(a) and the mechanical properties of intact rock, rock mass, and fractures are summarized in Table 5.7. The input file, "*input.dat*", required to define the problem for BS3D is given in Figure B.1. It is assumed that there are no *in situ* stresses and additional forces. At the second stage (simulating the excavation), the lowermost face of the block ($A_1A_2A_3A_4$) is left unconstrained. Modified Barton's model is adopted as the constitutive model of fractures. BEM approach is to be used to determine the normal stiffness of the fractures. There is no need to consider the effect of excavation on *in situ* stresses and high-velocity jet impact. The analysis of the first stage is to be done with step stage of 0.5 up to maximum λ of 1. In addition, the analysis of the second stage is to be done with step stage of 0.1 up to maximum λ of 5. Maximum increment and maximum iteration numbers are chosen to be 100 and 50, respectively.

A.2 "*TUNNEL_STRESS.DAT*"

In order to consider the effect of excavation on *in situ* stresses in the surrounding rock mass another input file, "*tunnel_stress.dat*", should be read by BS3D. Figure B.2 and Figure B.3 give examples of "*tunnel_stress.dat*" in which the tunnel reference system is the same and is not the same as principal stress directions, respectively. In both cases, the tunnel diameter is 3.6 m, the tunnel axis is along the *x*-axis, and the excavation face is located 5 m far from the origin. Figure B.2 introduces hydrostatic *in situ* stress of 2.6 MPa, while Figure B.3 defines the following stress tensor:

$$\sigma = \begin{bmatrix} 0.5 & 0.1 & 0.4 \\ 0.1 & 1 & -0.3 \\ 0.4 & -0.3 & 3 \end{bmatrix}$$

```
Number-of-vertices(block&mould)          8

vertex(1)           0          0          0
vertex(2)           1          0          0
vertex(3)           1          1          0
vertex(4)           0          1          0
vertex(5)           0          0          1
vertex(6)           1          0          1
vertex(7)           1          1          1
vertex(8)           0          1          1


***************************************************
Block-Geometry
***************************************************
Number_of_faces                                    6
Number_of_faces_with_more_than_one_boundary        0

Number_of_Vertices_in_boundary(1)_of_Face(1)       4
Number_of_Vertices_in_boundary(1)_of_Face(2)       4
Number_of_Vertices_in_boundary(1)_of_Face(3)       4
Number_of_Vertices_in_boundary(1)_of_Face(4)       4
Number_of_Vertices_in_boundary(1)_of_Face(5)       4
Number_of_Vertices_in_boundary(1)_of_Face(6)       4

Face(1)_boundary(1)_Vertex(1)                      1
Face(1)_boundary(1)_Vertex(2)                      5
Face(1)_boundary(1)_Vertex(3)                      8
Face(1)_boundary(1)_Vertex(4)                      4
Face(2)_boundary(1)_Vertex(1)                      4
Face(2)_boundary(1)_Vertex(2)                      8
Face(2)_boundary(1)_Vertex(3)                      7
Face(2)_boundary(1)_Vertex(4)                      3
Face(3)_boundary(1)_Vertex(1)                      2
Face(3)_boundary(1)_Vertex(2)                      3
Face(3)_boundary(1)_Vertex(3)                      7
Face(3)_boundary(1)_Vertex(4)                      6
Face(4)_boundary(1)_Vertex(1)                      1
Face(4)_boundary(1)_Vertex(2)                      2
Face(4)_boundary(1)_Vertex(3)                      6
Face(4)_boundary(1)_Vertex(4)                      5
Face(5)_boundary(1)_Vertex(1)                      6
Face(5)_boundary(1)_Vertex(2)                      7
Face(5)_boundary(1)_Vertex(3)                      8
Face(5)_boundary(1)_Vertex(4)                      5
Face(6)_boundary(1)_Vertex(1)                      1
Face(6)_boundary(1)_Vertex(2)                      4
Face(6)_boundary(1)_Vertex(3)                      3
Face(6)_boundary(1)_Vertex(4)                      2


Number_of_sensor_points_per_edge                   6
***************************************************
Mould-Geometry
***************************************************
Number_of_faces                                    6
Number-of-same-faces-in-mould-and-block            6

Face(1)-index-same-in-mould-and-block              1
Face(2)-index-same-in-mould-and-block              2
Face(3)-index-same-in-mould-and-block              3
Face(4)-index-same-in-mould-and-block              5
Face(5)-index-same-in-mould-and-block              4
Face(6)-index-same-in-mould-and-block              6
```

Figure B.1: Example of "*input.dat*"

```
**************************************************
Mechanical-Properties
**************************************************
Unit_weigth_of_the_block                        0.03
Gravity                                          9.806
Young's_Modulus_of_the_Block                     30000
Poisson's_Ratio_of_the_Block                     0.3
Young's_Modulus_of_the_Rock_Mass                 7000
Poisson's_Ratio_of_the_Rock_Mass                 0.2
Isotropic_dilatancy(1)_Anisotropic(2)            1
Init_stiff&max_closure&Joint_Len&Lab_Face(1)     10000    0.0001    1
Init_stiff&max_closure&Joint_Len&Lab_Face(1)     10000    0.0001    1
Init_stiff&max_closure&Joint_Len&Lab_Face(1)     10000    0.0001    1
Init_stiff&max_closure&Joint_Len&Lab_Face(1)     10000    0.0001    1
Init_stiff&max_closure&Joint_Len&Lab_Face(1)     10000    0.0001    1
Init_stiff&max_closure&Joint_Len&Lab_Face(1)     10000    0.0001    1
JRC0(1&2)_JCS0(MPa)_Base_Friction_Face(1)        10       70        30
JRC0(1&2)_JCS0(MPa)_Base_Friction_Face(1)        10       70        30
JRC0(1&2)_JCS0(MPa)_Base_Friction_Face(1)        10       70        30
JRC0(1&2)_JCS0(MPa)_Base_Friction_Face(1)        10       70        30
JRC0(1&2)_JCS0(MPa)_Base_Friction_Face(1)        10       70        30
JRC0(1&2)_JCS0(MPa)_Base_Friction_Face(1)        10       70        30


**************************************************
Stage-Analysis-Characteristics
**************************************************
Number_of_Permanent_Faces                        5
Number_of_Stages                                 2
fa_Additional_Stage_1                            0        0        0        0        0        0
fa_Additional_Stage_2                            0        0        0        0        0        0
Step_stage_1                                     0.5
Step_stage_2                                     0.1
Max_increment_Number                             100
Max_iteration_Number                             50
Max_Lambda_Stage_1                               1
Max_Lambda_Stage_2                               5
Residual_Tollerance                              0.0001
Limit_Eigenvalues                                0.00002
Limit_Stiffness_Ratio                            0.3

Mohr_Coloumb(0)_Barton(1)_Modified_Barton(2)     2
Block_Normal_Stiffness_Analytical(0)_BEM(1)      1
In_Situ_Stress_Circular_Tunnel:No(0)_Yes(1)      0
Water_pressure_due_to_jet_impact:No(0)_Yes(1)    0
```

Figure B.1-Continued: Example of "*input.dat*"

```
NOTE: The origin of the global reference system should be on the tunnel axis
Tunnel_Diameter            3.6
Tunnel_axis(x_y_z)         1          0          0
Ditance_of_excavation_face_from_the_origin          5
(The excavation face is to be located in the negative direction of tunnel exis from the origin)

Tunnel_ref_system_is_the_same_as_principal_stress_dir:yes(1)_no(0)          1
Depth_of_Tunnel            100
Unit_Weight_of_Rock_Mass   0.026
Lateral_Pressure_Coefficient   1
```

Figure B.2: Example of "*tunnel_stress.dat*"; the tunnel reference system is the same
as principal stress directions

350

```
NOTE: The origin of the global reference system should be on the tunnel axis
Tunnel_Diameter                    3.6
Tunnel_axis(x_y_z)                   1        0        0
Ditance_of_excavation_face_from_the_origin          5
(The excavation face is to be located in the negative direction of tunnel exis from the origin)

Tunnel_ref_system_is_the_same_as_principal_stress_dir:yes(1)_no(0)        0
In Situ Stress in global ref System
(Sxx_Syy_Syz_Txy_Txz_Tyz)           0.5      1        3        0.1      0.4      -0.3
```

Figure B.3: Example of "*tunnel_stress.dat*"; the tunnel reference system is not the same as principal stress directions

B.3 "*WATER_PRESSURE.DAT*"

In order to consider dynamic water pressure caused by high-velocity jet impact on the block located in the bottom of a plunge pool, another input file, "*water_pressure.dat*", should be read by BS3D. Figure B.4 gives an example of input file for a plunge pool with following characteristics:

- $Y = 140$ m; $r = 20$ m; $D_j = 20$ m; $V_j = 24.5$ m/s
- Free over fall; Circular jet; Moderate turbulence
- Maximum duration of extreme hydrodynamic pressure: 5 ms

```
Depth_of_Water_in_the_pool                                          140
Considering_all_combinations(1)_Or_the_most_critical_one(0)         0

Distance_to_the_jet_center_line              20
Jet_diameter_at_the_pool_surface             20
Jet_diameter_is_the_same_as_jet_width_for_rectangular_jet

Circular(0)_Or_rectangular(1)_jet            0
Rough(0)_Moderate(1)_Smooth(2)_turbulent     1
Jet_length                                   1
Jet_Velocity_at_the_pool_surface             24.5

Type_of_outlet_structure:
Free_overfall(0)_Ski_jump_outlet(1)_Valve(2) 0
Hydrodynamic_pressure_max_Duration           0.005
```

Figure B.4: Example of "*water_pressure.dat*"

APPENDIX C: COMPUTATION OF POLYHEDRAL MASS PROPERTIES

The location of a body's center of mass, and its moments and products of inertia about various axes are important physical quantities for any type of dynamic simulation or physical based modeling. Mirtch [236] presented an algorithm for computing these quantities for a general class of rigid bodies: uniform density polyhedrons. The mass integrals may be converted into volume integrals under his assumption. The algorithm is based on a three-step reduction of the volume integrals to successively simpler integrals. The algorithm is designed to minimize the numerical errors that can result from poorly conditioned alignment of a polyhedral faces. It is also designed for efficiency. All required volume integrals of the polyhedron; exploiting common subexpressions reduces floating point operations [236].

In this dissertation, Mirtch's [236] algorithm has been implemented as a subroutine called "*massProperties*". Whenever BS3D needs to compute the mass properties of a block (a polyhedron), it calls "*massProperties*" subroutine. Figure C.1 shows the pseudo code implemented in "*massProperties*" subroutine which is the same as what proposed by Mirtch [236].

```
SUB MassProperties (Block)
    $T_1, T_x, T_y, T_z, T_{x^2}, T_{y^2}, T_{z^2}, T_{xy}, T_{yz}, T_{zx} \leftarrow 0$
    For each face, $F$, on the boundary of the block, $B$:
        Choose α-β-γ as a right-handed permutation of $x$-$y$-$z$ that maximized $|\hat{n}_\gamma|$ (see Section 5.2.3 for details)
        $\pi_1, \pi_\alpha, \pi_\beta, \pi_{\alpha^2}, \pi_{\alpha\beta}, \pi_{\beta^2}, \pi_{\alpha^3}, \pi_{\alpha^2\beta}, \pi_{\alpha\beta^2}, \pi_{\beta^3} \leftarrow 0$
        For each edge, ε, in counterclockwise order around $F$:
            $\alpha_0 \leftarrow \alpha -$ coordinate of start point of $\varepsilon$ ;   $\beta_0 \leftarrow \beta -$ coordinate of start point of $\varepsilon$
            $\alpha_1 \leftarrow \alpha -$ coordinate of end point of $\varepsilon$ ;   $\beta_0 \leftarrow \beta -$ coordinate of end point of $\varepsilon$
            $\Delta\alpha \leftarrow \alpha_1 - \alpha_0;$  $\Delta\beta \leftarrow \beta_1 - \beta_0$
            $C_1 \leftarrow \alpha_1 + \alpha_0;$  $C_\alpha \leftarrow \alpha_1 \cdot C_1 + \alpha_0{}^2;$  $C_{\alpha^2} \leftarrow \alpha_1 \cdot C_\alpha + \alpha_0{}^3;$  $C_{\alpha^3} \leftarrow \alpha_1 \cdot C_{\alpha^2} + \alpha_0{}^4$
            $C_\beta \leftarrow \beta_1{}^2 + \beta_1 \cdot \beta_0 + \beta_0{}^2;$  $C_{\beta^2} \leftarrow \beta_1 \cdot C_\beta + \beta_0{}^3;$  $C_{\beta^3} \leftarrow \beta_1 \cdot C_{\beta^2} + \beta_0{}^4$
            $C_{\alpha\beta} \leftarrow 3\alpha_1{}^2 + 2\alpha_1 \cdot \alpha_0 + \alpha_0{}^2;$  $K_{\alpha\beta} \leftarrow \alpha_1{}^2 + 2\alpha_1 \cdot \alpha_0 + 3\alpha_0{}^2$
            $C_{\alpha^2\beta} \leftarrow \alpha_0 \cdot C_{\alpha\beta} + 4\alpha_1{}^3;$  $K_{\alpha^2\beta} \leftarrow \alpha_1 \cdot K_{\alpha\beta} + 4\alpha_0{}^3$
            $C_{\alpha\beta^2} \leftarrow 4\beta_1{}^3 + 3\beta_1{}^2 \cdot \beta_0 + 2\beta_1 \cdot \beta_0{}^2 + \beta_0{}^3;$  $K_{\alpha\beta^2} \leftarrow \beta_1{}^3 + 2\beta_1{}^2 \cdot \beta_0 + 3\beta_1 \cdot \beta_0{}^2 + 4\beta_0{}^3$
            $\pi_1 \leftarrow \pi_1 + \Delta\beta \cdot C_1$
            $\pi_\alpha \leftarrow \pi_\alpha + \Delta\beta \cdot C_\alpha;$  $\pi_{\alpha^2} \leftarrow \pi_{\alpha^2} + \Delta\beta \cdot C_{\alpha^2};$  $\pi_{\alpha^3} \leftarrow \pi_{\alpha^3} + \Delta\beta \cdot C_{\alpha^3}$
            $\pi_\beta \leftarrow \pi_\beta + \Delta\alpha \cdot C_\beta;$  $\pi_{\beta^2} \leftarrow \pi_{\beta^2} + \Delta\alpha \cdot C_{\beta^2};$  $\pi_{\beta^3} \leftarrow \pi_{\beta^3} + \Delta\alpha \cdot C_{\beta^3}$
            $\pi_{\alpha\beta} \leftarrow \pi_{\alpha\beta} + \Delta\beta \cdot (\beta_1 \cdot C_{\alpha\beta} + \beta_0 \cdot K_{\alpha\beta});$  $\pi_{\alpha^2\beta} \leftarrow \pi_{\alpha^2\beta} + \Delta\beta \cdot (\beta_1 \cdot C_{\alpha^2\beta} + \beta_0 \cdot K_{\alpha^2\beta})$
            $\pi_{\alpha\beta^2} \leftarrow \pi_{\alpha\beta^2} + \Delta\alpha \cdot (\alpha_1 \cdot C_{\alpha\beta^2} + \alpha_0 \cdot K_{\alpha\beta^2})$
        End For
        $\pi_1 \leftarrow \pi_1/2;$  $\pi_\alpha \leftarrow \pi_\alpha/6;$  $\pi_{\alpha^2} \leftarrow \pi_{\alpha^2}/12;$  $\pi_{\alpha^3} \leftarrow \pi_{\alpha^3}/20$
        $\pi_\beta \leftarrow -\pi_\beta/6;$  $\pi_{\beta^2} \leftarrow -\pi_{\beta^2}/12;$  $\pi_{\beta^3} \leftarrow -\pi_{\beta^3}/20$
        $\pi_{\alpha\beta} \leftarrow \pi_{\alpha\beta}/24;$  $\pi_{\alpha^2\beta} \leftarrow \pi_{\alpha^2\beta}/60;$  $\pi_{\alpha\beta^2} \leftarrow -\pi_{\alpha\beta^2}/60$
        $\omega \leftarrow -\hat{n} \cdot p$ for some point, $p$, on $F$
        $k_1 \leftarrow \hat{n}_\gamma{}^{-1};$  $k_2 \leftarrow k_1{}^2$ ;  $k_3 \leftarrow k_1{}^3;$  $k_4 \leftarrow k_1{}^4$
        $F_\alpha \leftarrow k_1 \cdot \pi_\alpha;$  $F_\beta \leftarrow k_1 \cdot \pi_\beta;$  $F_\gamma \leftarrow -k_2 \cdot (\hat{n}_\alpha \cdot \pi_\alpha + \hat{n}_\beta \cdot \pi_\beta + \omega \cdot \pi_1)$
        $F_{\alpha^2} \leftarrow k_1 \cdot \pi_{\alpha^2};$  $F_{\beta^2} \leftarrow k_1 \cdot \pi_{\beta^2}$
        $F_{\gamma^2} \leftarrow k_3 \cdot (\hat{n}_\alpha{}^2 \cdot \pi_{\alpha^2} + 2\hat{n}_\alpha \cdot \hat{n}_\beta \cdot \pi_{\alpha\beta} + \hat{n}_\beta{}^2 \cdot \pi_{\beta^2} + 2\hat{n}_\alpha \cdot \omega \cdot \pi_\alpha + 2\hat{n}_\beta \cdot \omega \cdot \pi_\beta + \omega^2 \cdot \pi_1)$
        $F_{\alpha^3} \leftarrow k_1 \cdot \pi_{\alpha^3};$  $F_{\beta^3} \leftarrow k_1 \cdot \pi_{\beta^3}$
        $F_{\gamma^3} \leftarrow -k_4 \cdot (\hat{n}_\alpha{}^3 \cdot \pi_{\alpha^3} + 3\hat{n}_\alpha{}^2 \cdot \hat{n}_\beta \cdot \pi_{\alpha^2\beta} + \hat{n}_\beta{}^2 \cdot \pi_{\beta^2} + 3\hat{n}_\alpha \cdot \hat{n}_\beta{}^2 \cdot \pi_{\alpha\beta^2} + \hat{n}_\beta{}^3 \cdot \pi_{\beta^3} +$
                $3\hat{n}_\alpha{}^2 \cdot \omega \cdot \pi_{\alpha^2} + 6\hat{n}_\alpha \cdot \hat{n}_\beta \cdot \omega \cdot \pi_{\alpha\beta} + 3\hat{n}_\beta{}^2 \cdot \omega \cdot \pi_{\beta^2} + 3\hat{n}_\alpha \cdot \omega^2 \cdot \pi_\alpha + 3\hat{n}_\beta \cdot \omega^2 \cdot \pi_\beta + \omega^3 \cdot \pi_1)$
        $F_{\alpha^2\beta} \leftarrow k_1 \cdot \pi_{\alpha^2\beta};$  $F_{\beta^2\gamma} \leftarrow -k_2 \cdot (\hat{n}_\alpha \cdot \pi_{\alpha\beta^2} + \hat{n}_\beta \cdot \pi_{\beta^3} + \omega \cdot \pi_{\beta^2})$
        $F_{\gamma^2\alpha} \leftarrow k_3 \cdot (\hat{n}_\alpha{}^2 \cdot \pi_{\alpha^3} + 2\hat{n}_\alpha \cdot \hat{n}_\beta \cdot \pi_{\alpha^2\beta} + \hat{n}_\beta{}^2 \cdot \pi_{\alpha\beta^2} + 2\hat{n}_\alpha \cdot \omega \cdot \pi_{\alpha^2} + 2\hat{n}_\beta \cdot \omega \cdot \pi_{\alpha\beta} + \omega^2 \cdot \pi_\alpha)$
        If (α = x) Then
            $T_1 \leftarrow T_1 + \hat{n}_\alpha \cdot F_\alpha$
        Else If (β = x) Then
            $T_1 \leftarrow T_1 + \hat{n}_\beta \cdot F_\beta$
        Else
            $T_1 \leftarrow T_1 + \hat{n}_\gamma \cdot F_\gamma$
        End IF
        $T_\alpha \leftarrow T_\alpha + \hat{n}_\alpha \cdot F_{\alpha^2};$  $T_\beta \leftarrow T_\beta + \hat{n}_\beta \cdot F_{\beta^2};$  $T_\gamma \leftarrow T_\gamma + \hat{n}_\gamma \cdot F_{\gamma^2}$
        $T_{\alpha^2} \leftarrow T_{\alpha^2} + \hat{n}_\alpha \cdot F_{\alpha^3};$  $T_{\beta^2} \leftarrow T_{\beta^2} + \hat{n}_\beta \cdot F_{\beta^3};$  $T_{\gamma^2} \leftarrow T_{\gamma^2} + \hat{n}_\gamma \cdot F_{\gamma^3}$
        $T_{\alpha\beta} \leftarrow T_{\alpha\beta} + \hat{n}_\alpha \cdot F_{\alpha^2\beta};$  $T_{\beta\gamma} \leftarrow T_{\beta\gamma} + \hat{n}_\beta \cdot F_{\beta^2\gamma};$  $T_{\gamma\alpha} \leftarrow T_\gamma + \hat{n}_\gamma \cdot F_{\gamma^2\alpha}$
    End For
    $(T_x, T_y, T_z) \leftarrow (T_x, T_y, T_z)/2;$  $(T_{x^2}, T_{y^2}, T_{z^2}) \leftarrow (T_{x^2}, T_{y^2}, T_{z^2})/3;$  $(T_{xy}, T_{yz}, T_{zx}) \leftarrow (T_{xy}, T_{yz}, T_{zx})/2$
    volume $\leftarrow T_1;$  centroid $\leftarrow (T_x, T_y, T_z);$  inertia Tensor $\leftarrow \begin{bmatrix} T_{x^2} & T_{xy} & T_{zx} \\ T_{xy} & T_{y^2} & T_{yz} \\ T_{zx} & T_{yz} & T_{z^2} \end{bmatrix}$
End MassProperties
```

Figure C.1: Pseudo code of the algorithm that computes polyhedral mass properties
(after Mirtch [236])

APPENDIX D: IMPLEMENTATION AND VERIFICATION OF BOUNDARY ELEMENT METHOD IN ELASTOSTATIC PROBLEM

D.1 IMPLEMENTATION

BS3D triangulates each face of the block into a set of triangles and subdivides each triangle into a set of subtriangles. Subsequently, a point (node) is assigned to the centroid of each subtriangle. Figure 5.3 schematically depicts the discretization process. In BS3D, all elements of H and G matrices in Equation (5.1) are calculated by using Gaussian integration over triangles [260-263]. G_{ii} components are calculated by following Li's and Han's method [264] for evaluating singular integrals in stress analysis of solids by the direct BEM. Body force vector, B, are obtained using Galerkin Vector approach, which transforms the domain integrals into boundary integrals [237].

Figure D.1 presents subroutines that calculates BEM matrices, H, G, and B, based on the algorithm given in [237, 260-264]. It should be mentioned that, in Figure D.1, all vectors are shown in bold; *Po* is a matrix containing coordinates of all (boundary) elements; *ne* presents the coordinate of sensor points (nodes).

D.1 VERIFICATION

In order to verify the implementation of elastostatic BEM matrices, two examples have been checked. In both examples, a cubic block with sides of 1 m (Figure D.2) is considered. The block seats on a table on its lowermost face, $A_1A_2A_3A_4$. The block has Young's modulus of 30 GPa and Poisson's ratio of 0.3. Two loading conditions are considered:

1) The block is weightless and subjected to uniformly distributed load of 50 kPa on the uppermost face, $A_5A_6A_7A_8$. Stress on face $A_1A_2A_3A_4$ which is in contact with the table should be 50 kPa as well. This stress is calculates using BEM assuming the following loading and boundary conditions:

```
SUB BEMMatrices (numSen, ne, Po, area, v, E, n, HMatrix, GMatrix, BMatrix)
    w_g ←{0.07215780, 0.04754582, 0.04754582, 0.04754582, 0.01622925, 0.01622925, 0.01622925, 0.05160869,
          0.05160869, 0.05160869, 0.01361516, 0.01361516, 0.01361516, 0.01361516, 0.01361516, 0.01361516}
    x_g ←{0.3333333, 0.08141482, 0.4592926,0. 4592926, 0.8989055, 0.05054723, 0.05054723, 0.6588614,
          0.1705693, 0.1705693, 0.008394777, 0.008394777, 0.7284924, 0.7284924, 0.2631128, 0.2631128}
    y_g ←{0.3333333, 0.4592926, 0.08141482, 0.4592926, 0.05054723, 0.8989055, 0.05054723, 0.1705693,
          0.6588614, 0.1705693, 0.7284924, 0.2631128, 0.008394777, 0.2631128, 0.008394777, 0.7284924}
```
$GE \leftarrow \frac{E}{2(1+v)}$

$GMatrix, HMatrix, BMi, BMatrix \leftarrow 0$

```
For i = 1 to numSen
    For j = 1 to numSen
        If (i = j) Then
            CALL GMatrix (ne_i, Po_j, n_j, v, GMatrix_{i,j})
```
$GMatrix_{i,j} \leftarrow \frac{area_j}{3} \cdot \frac{GMatrix_{i,j}}{16\pi\cdot(1-v)\cdot GE}$; $HMatrix_{i,j} \leftarrow \begin{bmatrix} 0.5 & 0 & 0 \\ 0 & 0.5 & 0 \\ 0 & 0 & 0.5 \end{bmatrix}$

```
        ELSE
            If (i < j) Then
                CALL HGMatrice (ne_i, Po_j, n_j, , v, GE, HMatrix_{i,j}, GMatrix_{i,j})
                GMatrix_{i,j} ← 2area_j · GMatrix_{i,j};   HMatrix_{i,j} ← 2area_j · HMatrix_{i,j}
            Else
                CALL HMatrice (ne_i, Po_j, n_j, v, HMatrix_{i,j})
                GMatrix_{i,j} ← GMatrix_{j,i};   HMatrix_{i,j} ← 2area_j · HMatrix_{i,j}
            End If
        End If
        CALL bodyForce (ne_i, Po_j, n_j, v, BMi_j)
        BMatrix_i ← BMatrix_i + 2area_j · BMi_j
    End For
End For
END BEMMatrices
```

```
SUB HGMatrice (ne, Po, n, v, GE, h, g)
    h, g ← 0
    For i =1 to 16
        r ← (1 − xg_i − yg_i) · Po_1 + xg_i · Po_2 + yg_i · Po_3 − ne
        For j = 1 to 3
            For k = 1 to 3
                If (j = k) Then
```
$h_{jj} \leftarrow (\frac{-1}{r\cdot r} \cdot \frac{r\cdot n}{|r|} \cdot (1 - 2v + \frac{3r_j{}^2}{r\cdot r})) \cdot wg_i + h_{jj}$

$g_{jj} \leftarrow \frac{1}{|r|} \cdot \left(3 - 4v + \frac{r_j{}^2}{r\cdot r}\right) \cdot wg_i + g_{jj}$

```
                Else
```
$h_{jk} \leftarrow (\frac{-1}{r\cdot r} \cdot (\frac{r\cdot n}{|r|} \cdot \frac{3r_j\cdot r_k}{r\cdot r} - (1 - 2v) \cdot \frac{n_k\cdot r_j - n_j\cdot r_k}{|r|})) \cdot wg_i + h_{jk}$

$g_{jk} \leftarrow \frac{1}{|r|} \cdot \left(\frac{r_j\cdot r_k}{r\cdot r}\right) \cdot wg_i + g_{jj}$

```
                End If
            End For
        End For
    End For
```
$g \leftarrow \frac{g}{16\pi\cdot GE\cdot(1-v)};$ $h \leftarrow \frac{h}{8\pi\cdot(1-v)}$
```
END HGMatrice
```

Figure D.1: Pseudo code of subroutines that determine BEM matrices

```
SUB GMatrix (ne, Po, n,v, g)
    For i =1 to 3
        T_{i1} ← ne
    End For
    T_{12} ← Po_1;   T_{13} ← Po_2;   T_{22} ← Po_2;   T_{23} ← Po_3;   T_{32} ← Po_3;   T_{33} ← Po_1
    a1, a2, a3, g ← 0
    For i =1 to 3
        x21_i ← T_{i2} − T_{i1};   x32_i ← T_{i3} − T_{i2}
    End For
    For i =1 to 3
        For j =1 to 3
            a1_i ← a1_i + 2x21_{i,j};   a2_i ← a2_i + 2x21_{i,j} · x32_{i,j};   a3_i ← a3_i + 2x32_{i,j}
        End For
    End For
    For i =1 to 3
        sa_i ← a1_i + a2_i + a3_i;   ea_i ← 4a1_i · a3_i − a2_i^2
    End For
    For i =1 to 3
```

$$I0_i \leftarrow \frac{1}{\sqrt{a3_i}} \cdot \log_{10}\left(\frac{2\sqrt{sa_i \cdot a3_i} + a2_i + 2a3_i}{2\sqrt{a1_i \cdot a3_i} + a2_i}\right); \quad I1_i \leftarrow \frac{\sqrt{sa_i}}{a3_i} - \sqrt{\frac{a1_i}{a3_i}} - \frac{a2_i \cdot I0_i}{2a3_i}$$

$$I2_i \leftarrow \frac{2(a2_i + 2a3_i)}{ea_i \cdot \sqrt{sa_i}} - \frac{2a2_i}{ea_i \cdot \sqrt{a1_i}} \quad ; \quad I3_i \leftarrow \frac{-2(2a1_i + a2_i)}{ea_i \cdot \sqrt{sa_i}} + \frac{4a1_i}{ea_i \cdot \sqrt{a1_i}}$$

$$I4_i \leftarrow \frac{(2a2_i^2 - 4a1_i \cdot a3_i + 2a1_i \cdot a2_i)}{a3_i \cdot ea_i \cdot \sqrt{sa_i}} - \frac{2a1_i \cdot a2_i}{a3_i \cdot ea_i \cdot \sqrt{a1_i}} + \frac{I0_i}{a3_i}; \quad I5_i \leftarrow \frac{2I3_i}{a3_i} - \frac{a2_i \cdot I4_i}{2a3_i} - \frac{1}{a3_i \cdot \sqrt{sa_i}}$$

```
    End For
    For i =1 to 3
        For j =1 to 3
            If (i = j) Then
                For k =1 to 3
                    gS_{ijk} ← 2(3 − 4v) · I0_k + 2x21_{k,i} · x21_{k,j} · I2_k +
                               2(x32_{k,j} · x21_{k,i} + x32_{k,i} · x21_{k,j}) · I3_k + 2x32_{k,i} · x32_{k,j} · I4_k
                End For
            Else
                For k =1 to 3
                    gS_{ijk} ← 2x21_{k,i} · x21_{k,j} · I2_k + 2(x32_{k,j} · x21_{k,i} + x32_{k,i} · x21_{k,j}) · I3_k
                               +2x32_{k,i} · x32_{k,j} · I4_k
                End For
            End If
        End For
    End For
    For i =1 to 3
        For j =1 to 3
            For k =1 to 3
                g_{i,j} ← g_{i,j} + gS_{i,j,k}
            End For
        End For
    End For
END GMatrix
```

Figure D.1-Continued: Pseudo code of subroutines that determine BEM matrices

```
SUB HMatrix (ne, Po, n, v, h)
    h ← 0
    For i =1 to 16
        r ← (1 − xg_i − yg_i) · Po₁ + xg_i · Po₂ + yg_i · Po₃ − ne
        For j = 1 to 3
            For k = 1 to 3
                If (j = k) Then
```

$$h_{jj} \leftarrow (\frac{-1}{r \cdot r} \cdot \frac{r \cdot n}{|r|} \cdot (1 - 2v + \frac{3r_j^2}{r \cdot r})) \cdot wg_i + h_{jj}$$

```
                Else
```

$$h_{jk} \leftarrow (\frac{-1}{r \cdot r} \cdot (\frac{r \cdot n}{|r|} \cdot \frac{3r_j \cdot r_k}{r \cdot r} - (1 - 2v) \cdot \frac{n_k \cdot r_j - n_j \cdot r_k}{|r|})) \cdot wg_i + h_{jk}$$

```
                End If
            End For
        End For
    End For
```

$$h \leftarrow \frac{h}{8\pi \cdot (1 - v)}$$

```
END HMatrix
SUB bodyForce (ne, Po, n, v, b)
    b = 0
    For i = 1 to 16
        r ← (1 − xg_i − yg_i) · Po₁ + xg_i · Po₂ + yg_i · Po₃ − ne
        For j =1 to 3
```

$$b_j \leftarrow \frac{1}{2(1-v)} \cdot \frac{r_3}{|r|} \cdot n_j \cdot wg_i + b_j$$

$$\text{If } (j = 3): \; b_j \leftarrow -\frac{r.n}{|r|} \cdot wg_i + b_j$$

```
        End For
    End For
```

$$b \leftarrow \frac{b}{8\pi \cdot v}$$

```
End bodyForce
```

Figure D.1-Continued: Pseudo code of subroutines that determine BEM matrices
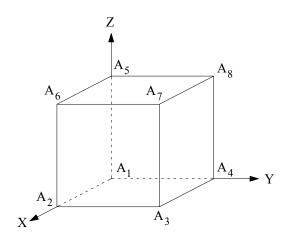
Figure D.2: Geometry of the cubic block considered in the verification example

a. Body forces: $B = 0$.

b. Face $A_5A_6A_7A_8$: $U = 0$ and $P =$ Unknown.

c. Face $A_1A_2A_3A_4$: $U =$ Unknown and $P = \{0, 0, -0.05\}$.

d. All other faces: $U=$ Unknown and $P = 0$.

Figure D.3 shows the percent error of average stresses calculated using BEM for the nodes located on face $A_5A_6A_7A_8$. It can be seen that BEM implementation works very well with nominal errors which verifies implementation of H and G matrices.
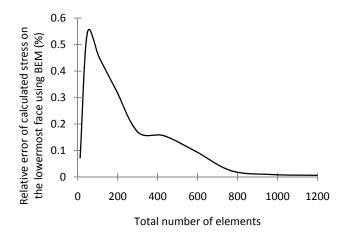
Figure D.3: Percent error of average stresses calculated using BEM (Example of weightless block on table)

2) The unit weight of the block is 30 kN/m³. Stress on face $A_1A_2A_3A_4$ which is in contact with the table should be 30 kPa. This stress is calculated using BEM assuming the following loading and boundary conditions:

e. Body forces: due weight of the block and will be calculated by the code.

f. Face $A_5A_6A_7A_8$: $U = 0$ and $P =$ Unknown.

g. All other faces: $U=$ Unknown and $P = 0$.

Figure D.4 shows the percent error of average stresses calculated using BEM for the nodes located on face $A_5A_6A_7A_8$. It can be seen that BEM implementation works very well with nominal errors which verifies implementation of B martrix.
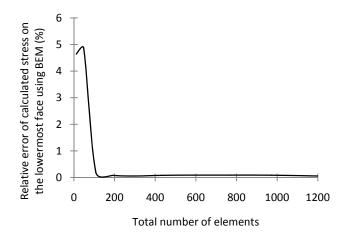
Figure D.4: Percent error of average stresses calculated using BEM (Example of a block on a table subjected to its own weight)

APPENDIX E: MATRIX M IS POSITIVE DEFINITE

Matrix **M** is defined in Section 2.3 as follows:

$$\mathbf{M} = \begin{bmatrix} m \cdot \mathbf{I}_{3\times3} & 0 \\ 0 & \mathbf{E_G} \end{bmatrix} \tag{E.1}$$

where m is the block mass, $\mathbf{E}_G$ is inertia operator relative to point G (centroid of the block) [16, 38-41], and $\mathbf{I}_{3\times3}$ is the 3×3 identity matrix. By defining, $\mathbf{E}_G$ as:

$$\mathbf{E_G} = \begin{bmatrix} I_{xx} & I_{xy} & I_{xz} \\ I_{xy} & I_{yy} & I_{yz} \\ I_{xz} & I_{yz} & I_{zz} \end{bmatrix}, \tag{E.2}$$

M can be expressed as follows:

$$\mathbf{M} = \begin{bmatrix} m & 0 & 0 & 0 & 0 & 0 \\ 0 & m & 0 & 0 & 0 & 0 \\ 0 & 0 & m & 0 & 0 & 0 \\ 0 & 0 & 0 & I_{xx} & I_{xy} & I_{xz} \\ 0 & 0 & 0 & I_{xy} & I_{yy} & I_{yz} \\ 0 & 0 & 0 & I_{xz} & I_{yz} & I_{zz} \end{bmatrix}, \tag{E.3}$$

which is clearly real and symmetric.

An 6×6 real symmetric matrix **M** is positive definite if $v^T \cdot \mathbf{M} \cdot v > 0$ for all non-zero real entries ($v \in \mathrm{R}^6$) [54, 361]. Let:

$$v = \begin{bmatrix} v_1 & v_2 & v_3 & v_4 & v_5 & v_6 \end{bmatrix}^T \tag{E.4}$$

By substituting Equations (E.3) and (E.4) in the condition of positive definite matrices ($C = C_1 + C_2 = v^T \cdot \mathbf{M} \cdot v$), the following expressions are obtained:

$$C_1 = m \cdot \left(v_1^{\,2} + v_2^{\,2} + v_3^{\,2} \right) \tag{E.5}$$

$$C_2 = I_{xx} \cdot v_4^{\,2} + I_{yy} \cdot v_5^{\,2} + I_{zz} \cdot v_6^{\,2} + 2I_{xy} \cdot v_4 \cdot v_5 + 2I_{yz} \cdot v_5 \cdot v_6 + 2I_{xz} \cdot v_4 \cdot v_6 \tag{E.6}$$

Since the mass of the block, m, and sum of squares of three real entries $\left(v_1^{\,2} + v_4^{\,2} + v_3^{\,2} \right)$ are positive, C_1 is a positive value. Therefore, to prove that **M** is a positive definite matrix, it is enough to demonstrate that C_2 is always positive.

Consider a rigid body comprising N parts, B_1, ..., B_N, each being a uniform density polyhedron. The inertia tensor relative to point G (centroid of the block which is assumed to be the same as the origin of reference system), $\mathbf{E}_G$, can be determined as follows [236, 362-364]:

$$\mathbf{E_G} = \begin{bmatrix} I_{xx} & I_{xy} & I_{xz} \\ I_{xy} & I_{yy} & I_{yz} \\ I_{xz} & I_{yz} & I_{zz} \end{bmatrix} = \begin{bmatrix} \sum_{i=1}^{N} m_i \cdot (y_i^2 + z_i^2) & -\sum_{i=1}^{N} m_i \cdot x_i \cdot y_i & \sum_{i=1}^{N} m_i \cdot x_i \cdot z_i \\ -\sum_{i=1}^{N} m_i \cdot x_i \cdot y_i & \sum_{i=1}^{N} m_i \cdot (x_i^2 + z_i^2) & -\sum_{i=1}^{N} m_i \cdot y_i \cdot z_i \\ \sum_{i=1}^{N} m_i \cdot x_i \cdot z_i & -\sum_{i=1}^{N} m_i \cdot y_i \cdot z_i & \sum_{i=1}^{N} m_i (x_i^2 + y_i^2) \end{bmatrix}, \qquad \text{(E.7)}$$

in which x_i, y_i, and z_i are coordinates of mass center of polyhedron B_i.

By substituting Equations (E.7) in Equation (E.6), C_2 can be expressed as follows:

$$C_2 = v_4^2 \cdot \sum_{i=1}^{N} m_i \cdot (y_i^2 + z_i^2) + v_5^2 \cdot \sum_{i=1}^{N} m_i \cdot (x_i^2 + z_i^2) + v_6^2 \cdot \sum_{i=1}^{N} m_i (x_i^2 + y_i^2)$$

$$- 2 \cdot v_4 \cdot v_5 \cdot \sum_{i=1}^{N} m_i \cdot x_i \cdot y_i - 2 \cdot v_5 \cdot v_6 \cdot \sum_{i=1}^{N} m_i \cdot y_i \cdot z_i - 2 \cdot v_4 \cdot v_6 \cdot \sum_{i=1}^{N} m_i \cdot x_i \cdot z_i, \qquad \text{(E.8)}$$

which can be simplified as:

$$C_2 = \sum_{i=1}^{N} m_i \cdot \left\{ \begin{array}{l} v_4^2 \cdot (y_i^2 + z_i^2) + v_5^2 \cdot (x_i^2 + z_i^2) + v_6^2 \cdot (x_i^2 + y_i^2) \\ - 2 \cdot (v_4 \cdot v_5 \cdot x_i \cdot y_i + v_5 \cdot v_6 \cdot y_i \cdot z_i + v_4 \cdot v_6 \cdot x_i \cdot z_i) \end{array} \right\} \qquad \text{(E.9)}$$

By rearranging Equation (E.16), C_2 can be expressed as follows:

$$C_2 = \sum_{i=1}^{N} m_i \cdot \left\{ (v_4 \cdot y_i - v_5 \cdot x_i)^2 + (v_4 \cdot z_i - v_6 \cdot x_i)^2 + (v_5 \cdot z_i - v_6 \cdot y_i)^2 \right\}, \qquad \text{(E.10)}$$

which is the summation of multiplication of two positive terms:

- m_i: mass of the i-th polyhedron.

- $(v_4 \cdot y_i - v_5 \cdot x_i)^2 + (v_4 \cdot z_i - v_6 \cdot x_i)^2 + (v_5 \cdot z_i - v_6 \cdot y_i)^2$: sum of the squares of three real quantities.

Therefore, C_2 is positive. Since both C_1 and C_2 are positive values, their summation, C, is also positive. Thus, $v^T \cdot \mathbf{M} \cdot v > 0$ and matrix $\mathbf{M}$ is a positive definite matrix.

APPENDIX F: STRESS TENSORS (PARAMETRIC STUDY OF SECTION 7.4.2)

A sensivity analyses has been performed in Section 7.4.2 to investigate the effect of principal stress directions on the stability of the prism (see Figure 7.25). The results of the parametric study are depicted in Figure 7.33. The stress tensors in the global reference system of

Figure 7.26 are given in Table F.1.

Table F.1: Tensors of *in situ* stresses in the global reference system (parametric study of Section 7.4.2)

β	α	σ_{xx}	σ_{yy}	σ_{zz}	τ_{xy}	τ_{xz}	τ_{yz}
0	0	5.175	1.725	3.450	0.000	0.000	0.000
	10	5.071	1.829	3.450	0.590	0.000	0.000
	20	4.771	2.129	3.450	1.109	0.000	0.000
	30	4.313	2.588	3.450	1.494	0.000	0.000
	40	3.750	3.150	3.450	1.699	0.000	0.000
	50	3.150	3.750	3.450	1.699	0.000	0.000
	60	2.588	4.313	3.450	1.494	0.000	0.000
	70	2.129	4.771	3.450	1.109	0.000	0.000
	80	1.829	5.071	3.450	0.590	0.000	0.000
	90	1.725	5.175	3.450	0.000	0.000	0.000
10	0	5.175	1.777	3.398	0.000	0.000	-0.295
	10	5.071	1.878	3.401	0.581	0.102	-0.277
	20	4.771	2.168	3.410	1.092	0.193	-0.226
	30	4.313	2.614	3.424	1.471	0.259	-0.147
	40	3.750	3.159	3.441	1.673	0.295	-0.051
	50	3.150	3.741	3.459	1.673	0.295	0.051
	60	2.588	4.286	3.476	1.471	0.259	0.147
	70	2.129	4.732	3.490	1.092	0.193	0.226
	80	1.829	5.022	3.499	0.581	0.102	0.277
	90	1.725	5.123	3.502	0.000	0.000	0.295
20	0	5.175	1.927	3.248	0.000	0.000	-0.554
	10	5.071	2.019	3.260	0.554	0.202	-0.521
	20	4.771	2.283	3.295	1.042	0.379	-0.425
	30	4.313	2.688	3.349	1.404	0.511	-0.277
	40	3.750	3.186	3.415	1.596	0.581	-0.096
	50	3.150	3.715	3.485	1.596	0.581	0.096
	60	2.588	4.212	3.551	1.404	0.511	0.277
	70	2.129	4.617	3.605	1.042	0.379	0.425
	80	1.829	4.881	3.640	0.554	0.202	0.521
	90	1.725	4.973	3.652	0.000	0.000	0.554

Table F.1-Continued: Tensors of *in situ* stresses in the global reference system

β	α	σ_{xx}	σ_{yy}	σ_{zz}	τ_{xy}	τ_{xz}	τ_{yz}
30	0	5.175	2.156	3.019	0.000	0.000	-0.747
	10	5.071	2.234	3.045	0.511	0.295	-0.702
	20	4.771	2.459	3.120	0.960	0.554	-0.572
	30	4.313	2.803	3.234	1.294	0.747	-0.373
	40	3.750	3.225	3.375	1.471	0.849	-0.130
	50	3.150	3.675	3.525	1.471	0.849	0.130
	60	2.588	4.097	3.666	1.294	0.747	0.373
	70	2.129	4.441	3.780	0.960	0.554	0.572
	80	1.829	4.666	3.855	0.511	0.295	0.702
	90	1.725	4.744	3.881	0.000	0.000	0.747
40	0	5.175	2.438	2.737	0.000	0.000	-0.849
	10	5.071	2.499	2.780	0.452	0.379	-0.798
	20	4.771	2.675	2.904	0.849	0.713	-0.651
	30	4.313	2.944	3.094	1.144	0.960	-0.425
	40	3.750	3.274	3.326	1.301	1.092	-0.147
	50	3.150	3.626	3.574	1.301	1.092	0.147
	60	2.588	3.956	3.806	1.144	0.960	0.425
	70	2.129	4.225	3.996	0.849	0.713	0.651
	80	1.829	4.401	4.120	0.452	0.379	0.798
	90	1.725	4.462	4.163	0.000	0.000	0.849
50	0	5.175	2.737	2.438	0.000	0.000	-0.849
	10	5.071	2.780	2.499	0.379	0.452	-0.798
	20	4.771	2.904	2.675	0.713	0.849	-0.651
	30	4.313	3.094	2.944	0.960	1.144	-0.425
	40	3.750	3.326	3.274	1.092	1.301	-0.147
	50	3.150	3.574	3.626	1.092	1.301	0.147
	60	2.588	3.806	3.956	0.960	1.144	0.425
	70	2.129	3.996	4.225	0.713	0.849	0.651
	80	1.829	4.120	4.401	0.379	0.452	0.798
	90	1.725	4.163	4.462	0.000	0.000	0.849
60	0	5.175	3.019	2.156	0.000	0.000	-0.747
	10	5.071	3.045	2.234	0.295	0.511	-0.702
	20	4.771	3.120	2.459	0.554	0.960	-0.572
	30	4.313	3.234	2.803	0.747	1.294	-0.373
	40	3.750	3.375	3.225	0.849	1.471	-0.130
	50	3.150	3.525	3.675	0.849	1.471	0.130
	60	2.588	3.666	4.097	0.747	1.294	0.373
	70	2.129	3.780	4.441	0.554	0.960	0.572
	80	1.829	3.855	4.666	0.295	0.511	0.702
	90	1.725	3.881	4.744	0.000	0.000	0.747
70	0	5.175	3.248	1.927	0.000	0.000	-0.554
	10	5.071	3.260	2.019	0.202	0.554	-0.521
	20	4.771	3.295	2.283	0.379	1.042	-0.425
	30	4.313	3.349	2.688	0.511	1.404	-0.277
	40	3.750	3.415	3.186	0.581	1.596	-0.096
	50	3.150	3.485	3.715	0.581	1.596	0.096
	60	2.588	3.551	4.212	0.511	1.404	0.277
	70	2.129	3.605	4.617	0.379	1.042	0.425
	80	1.829	3.640	4.881	0.202	0.554	0.521
	90	1.725	3.652	4.973	0.000	0.000	0.554

Table F.1-Continued: Tensors of *in situ* stresses in the global reference system

β	α	σ_{xx}	σ_{yy}	σ_{zz}	τ_{xy}	τ_{xz}	τ_{yz}
80	0	5.175	3.398	1.777	0.000	0.000	-0.295
	10	5.071	3.401	1.878	0.102	0.581	-0.277
	20	4.771	3.410	2.168	0.193	1.092	-0.226
	30	4.313	3.424	2.614	0.259	1.471	-0.147
	40	3.750	3.441	3.159	0.295	1.673	-0.051
	50	3.150	3.459	3.741	0.295	1.673	0.051
	60	2.588	3.476	4.286	0.259	1.471	0.147
	70	2.129	3.490	4.732	0.193	1.092	0.226
	80	1.829	3.499	5.022	0.102	0.581	0.277
	90	1.725	3.502	5.123	0.000	0.000	0.295
90	0	5.175	3.450	1.725	0.000	0.000	0.000
	10	5.071	3.450	1.829	0.000	0.590	0.000
	20	4.771	3.450	2.129	0.000	1.109	0.000
	30	4.313	3.450	2.588	0.000	1.494	0.000
	40	3.750	3.450	3.150	0.000	1.699	0.000
	50	3.150	3.450	3.750	0.000	1.699	0.000
	60	2.588	3.450	4.313	0.000	1.494	0.000
	70	2.129	3.450	4.771	0.000	1.109	0.000
	80	1.829	3.450	5.071	0.000	0.590	0.000
	90	1.725	3.450	5.175	0.000	0.000	0.000

NOMENCLATURE

a	Area of equivalent footing of each face of the block (Chapter 2); Tunnel radius (Chapter 5); Acceleration of the block caused by the unbalance force (Chapter 8)
$\mathbf{a}$	Line of action of the normal component of the surface force
a_j	Aperture thickness
a_s	Proportion of total fracture area sheared through the asperities
A_0	Maximum possible contact area
$\mathbf{b}_i$	Unit vector parallel to the i-th bisector
B	Rock block
B	Body force vectors in BEM formulation
$\mathbf{B}_i$	Bisector of an apical angle of ith face
c	Cohesion (Chapter 3); Pressure wave celerity and for a mixed fluid (Chapter 8)
c_{air}	Pressure wave celerity in air
c_{liq}	Pressure wave celerity in the liquid
C	Constraint space or face of constraint space
C	Vector that defines the virtual work for non-ideal constraints
C_p^{+}	Positive extreme fluctuation dynamic pressure coefficient (pool floor)
C_p^{-}	Negative extreme fluctuation dynamic pressure coefficient (pool floor)
C^{up}_p	Net upward pressure coefficient
C_{pa}	Mean dynamic pressure coefficient (pool floor)
C_{pd}	Mean dynamic pressure coefficient (fractures)
C_{pd}^{+}	Positive extreme fluctuation dynamic pressure coefficient (fractures)
C_{pr}	Mean pressure coefficient at distance r to the jet centerline

C_{pr}^{+}	Maximum extreme pressure coefficient at distance r to the jet centerline
C_{pr}^{+}	Minimum extreme pressure coefficient at distance r to the jet centerline
d	Distance between sensor point and constraint boundary in the direction of incremental displacement (Chapter 2); Diameter of equivalent foundation (Chapter 2); Distance from excavation face (Chapter 5)
d_h	Horizontal (or shear) displacement
d_p	Peak tangent dilation angle
$d_{s,peak}$	Peak secant dilation angle (also called initial dilation angle)
d_t	Mobilized dilation angle
$d_{t,peak}$	Peak tangent dilation angle
$\bar{d}$	Distance travelled by a sensor point either in or outside C during an increment
D	Fractal dimension in the considered direction
D_e	Equivalent core diameter in Point Load Test (PLT)
$\mathbf{e}$	Base unit vector for the global frame
E	Young's modulus
$\mathbf{E}_G$	Inertia operator relative to point G (centroid of the block)
EI	Annandale's Erodibility Index
$\mathbf{f}$	Resultant force applied to the centroid; Resultant moment calculated with respect to the centroid
f^s	Sinusoidal function in OH's model
F	Face of rock block (Chapter 2); Unbalance force due to the maximum dynamic pressure fluctuation (Chapter 8)
$\mathbf{F}$	Generalized force

F_z	Net vertical force associated with surface forces
$F_{\Delta t}$	Net impulse on the block
FS	Factor of safety
G	Centroid of the block
$\mathbf{G}$	Coefficient matrix in BEM formulation
h	Height of the block
h_{up}	Maximum upward displacement of the block
$\mathbf{H}$	Coefficient matrix in BEM formulation
H_0	The horizontal force applied to the wedge by the surrounding rock mass
i	Effective roughness (dilation angle)
i_0	Dilation angle at zero normal stress
$\mathbf{I}_{3\times3}$	3×3 Identity matrix
I_{eff}	Effective nonstationary trend angle for considered direction
$\mathbf{l}_{i,j}$	Line of intersection of faces i and j
$I_{(s)}$	Point load index
J_a	A coefficient in Annandale's EI method
J_n	A coefficient in Annandale's EI method (representing number of joints)
J_r	A coefficient in Annandale's EI method
J_s	Fracture orientation (Annandale's EI method)
JRC	Joint Roughness Coefficient; JRC_0 and JRC_n are JRC of samples with length of L_0 and L_n, respectively; JRC_1 and JRC_2 are magnitudes of JRC along the major and minor semi-axes of JRC angular distribution, respectively; $JRC_{mobilized}$ is mobilized magnitude of JRC; JRC_{peak} is peak value of JRC; JRC_{θ} is magnitude of JRC along the given direction of θ.
JCS	Joint Compressive Strength; JCS_0 and JCS_n are JCS of samples with length L_0 and L_n, respectively.

K_0	Lateral pressure coefficient
K_b	A coefficient in Annandale's EI method (representing block size)
K_d	A coefficient in Annandale's EI method (representing fracture shear strength)
K_j	A "stiffness number" varying from 3.49 to 30.19 MPa/mm
K_n	Normal Stiffness
K_{ni}	Initial normal stiffness
K_s	Shear Stiffness
kn1	Discontinuity normal stiffness
kn2	Block normal stiffness
kn3	Rock mass normal stiffness
l_i	Length of the block along the x_i axis
L	Length (Chapter 2); L_0 is sample length in direct shear test; and L_n is block length; Jet length (Chapter 8); Fissure length (Chapter 8)
L_b	Jet breakup length
m	Block mass
M	Mass matrix
M	Damage coefficient (ranges between 1 and 2) (Chapter 3); A function of the mechanical properties of the fractures and wedge apical angle
M_s	A coefficient in Annandale's EI method
N	Number (Chapter 2); Normal force (Chapter 7)
n	Unit normal (block side if normal to ∂B, into unconstrained space if normal to ∂C)
n_j	Stiffness exponent
no	Unbalanced force
P	Sensor point, contact point, or generic point of the rock block
P	Traction vector in BEM formulation

P_0	Pullout resistance of the wedge, which is the resultant of all forces applied to the wedge except for its weight and the supporting forces
P_{max}	Maximum dynamic pressure
P_{min}	Minimum dynamic pressure
Q	Total discharge of the jet
q	First quaternion component (scalar) (Chapter 2); Discharge per unit length of the jet (Chapter 8)
$\mathbf{q}$	Vector quaternion component
Q	Intersection between a plane and a segment
$\mathbf{r}$	Residual or unit vector about which the block rotates
r	Schmidt rebound on wet fracture surface (Chapter 3 and 4); Distance from tunnel axis (Chapter 5); Distance from jet centerline (Chapter 8)
R	Schmidt rebound on dry unweathered sawn surface (Chapter 3 and 4); Tunnel radius (Chapter 7)
R_f	Failure ratio (τ/τ_{ult}) ranging from 0.652 to 0.887
RQD	Rock Quality Designation
s	Initial discontinuity stiffness
S	Ordered list of face vertices listed in consecutive order (Chapter 2); Resultant of support forces (Chapter 7); Shear force (Chapter 7)
$\mathbf{S}$	Spin operator
s_r	Shear strength of the asperity intact rock
sr	Spin operator
t_n	Normal component of traction at any point on the fracture surface
T	Set of normalized vectors in the null space of the stiffness matrix at a bifurcation point
T_c	Natural period of an open-ended joint
T_u	Issuance turbulence intensity
$\mathbf{u}$	Displacement or vector of degrees of freedom

369

$\mathbf{\bar{u}}$	Small displacement or vector of degrees of freedom for small rotations
U	Displacement vector (BEM formulation)
U	Displacement (of any point of the medium) along the x axis
U_∞	Displacement far from excavation face
$u1$	Displacement caused by the deformability of the discontinuity
$u2$	Displacement caused by the deformability of the rock block
$u3$	Displacement caused by the deformability of the constraint space
UCS	Uniaxial Compressive Strength
v	Maximum discontinuity closure
$v_{\Delta t}$	Initial velocity
$\mathbf{V}$	Velocity
V	Displacement (of any point of the medium) along the y axis (Chapter 7); Mean axial flow velocity of the jet (Chapter 8)
V'	**R**oot mean square value of the fluctuating velocity
V_i	Jet velocity at issuance
V_j	Jet velocity at the pool surface
V_m	Maximum closure of fractures
W	Force applied to a parallelepiped
W	Displacement (of any point of the medium) along the z axis (Chapter 5); Weight of the block (Chapter 7)
W_p	Plastic work
x_b	Length of the block
Y	Plunge pool depth
z	Vertical co-ordinate, positive upwards
$\mathbf{z}$	Eigenvector in the null space of the stiffness matrix
z_b	Height of the block
Z	Plunging jet length depicted

Greek Letters

α	Semi-apical angle of the wedge
α_0	Initial asperity angle
α_1	Major semi-axis of the ellipse (asperity angle in Jing *et al.* model)
α_2	Minor semi-axis of the ellipse (asperity angle in Jing *et al.* model)
α_n	Shear-through component obtained by laboratory test
β	Free air content
γ_r	Unit weight of the rock
γ_w	Unit weight of water
δ	Accumulated shear displacement
δ_h	Shear displacement
$(\delta_h)_p$	Peak dilation displacement (Appendix A)
$\min(\delta_h)$	Maximum negative value of dilation (Appendix A)
δ_p	Peak shear displacement (Appendix A)
δ_{peak}	Peak shear displacement of fractures
δ_v	Normal displacement (dilation displacement)
$(\delta_v)_{@(\delta_h)=0}$	Shear displacement at which dilation displacement is zero (Appendix A)
$(\delta_v)_{peak}$	Dilation displacement at peak shear displacement
δ_s^p	Plastic shear displacement
Δ	Increment
Δt	Maximum duration of extreme pressure fluctuation
θ_{max}^*	Maximum apparent dip angle in the shear direction
λ	Step stage (in BS3D analysis); wavelength of asperity (in OH's model)
υ	Poisson's ratio
ξ	Virtual displacement

ρ_{air}	Density of the air
ρ_{liq}	Density of the liquid
ρ_{mix}	Density of mixed liquid and air
σ	Stress
σ_1	Axial stress at failure
σ_3	Effective confining pressure
σ_c	Unconfined compression strength
σ_j	Joint compressive strength
σ_n	Normal stress
σ_r	Radial component of stress
σ_t	Tensile strength of intact rock
σ_z	Vertical component of stress
σ_θ	Tangential component of stress
τ	Shear stress
τ_p	Shear strength
τ_{peak}	Peak shear strength
$\tau_{r\theta}, \tau_{rz}, \tau_{\theta z}$	Shear stress components
ϕ	Friction angle
ϕ_b	Base friction angle
$\phi_{mobilized}$	Mobilized base friction angle
ϕ_r	Residual friction angle
ϕ_u	Angle of friction for sliding along the asperities
ψ	Angle to the major semi-axis (asperity angle in Jing *et al.* model)

Subscripts (Chapter 2)

B	Block
c, h	h^{th} face making up the boundary of the constraint space
c, i, j, k	Normal to ∂C at the point where $P_{i,j,k}$ entered C
d	Caused by dilatancy
f	Faces making up the rock block
m	Rock mass
n	Normal
(n)	n^{th} increment
v, i	Vertices of ith face of the rock block
t	Tangential
t,i	Triangles of ith face of the rock block
tt	Subdivisions of a face triangle
u	Unconstrained motion

Superscripts (Chapter 2)

(l)	l^{th} iteration

Symbols (Chapter 2)

∂	Boundary
#	Cardinality: number of elements in a set or list

REFERENCES

1. Tonon, F., *Analysis of single rock blocks for general failure modes under conservative and non-conservative forces.* International Journal for Numerical and Analytical Methods in Geomechanics, 2007. **31**(14): p. 1567-1608.

2. Goodman, R.E. and G.H. Shi, *Block theory and its application to rock engineering.* 1985, Englewood, NJ: Wiley.

3. Yarahmadi Bafghi, A. and T. Verdel, *The probabilistic key-group method.* International Journal for Numerical and Analytical Methods in Geomechanics, 2003. **27**: p. 495-511.

4. Brady, B.H.G., *Stress analysis for rock masses*, in *Engineering in Rock Masses*, F.G. Bell, Editor. 1992, Butterworth-Heinemann Ltd: Oxford, UK.

5. Palassi, M. and P. Asadollahi. *Design or rockbolts and shotcrete for tunnel in jointed rock.* in *the 57th Canadian Geotechnical Conf. (QeoQuebec 2004).* 2004. Quebec, Canada: On CD, Sec. 5G, pp. 33-40.

6. John, K., *Graphical stability analysis of slopes in jointed rock.* J Soil Mech Found Div ASCE, 1968. **94**: p. 497-526.

7. Londe P, V.G., Vormeringer R., *Stability of rock slopes, a three-dimensional study.* J Soil Mech Found Div (ASCE), 1969. **95**(1): p. 235–62.

8. Hendron AJ, C.E., Aiyer AK., *Analytical and graphical methods for the analysis of slopes in rock masses.* 1980, Technical Report GL-80-2, US Army Engineers Nuclear Cratering Group, Livermore, CA.

9. Hoek ET, B.J., *Rock Slope Engineering*, ed. 3rd. 1981, London, England: Institute of Min and Metallurgy.

10. Warburton, P.M., *Vector stability analysis of an arbitrary polyhedral rock block with any number of free faces.* Int. J. of Rock Mech. and Mining Sci. & Geomech. Abstracts, 1981. **18**: p. 415–427.

11. Priest, S.D., *Hemispherical Projection Methods in Rock Mechanics.* 1985, London: George Allan & Unwin.

12. Wittke, W., *Methods to analyze the stability of rock slopes with and without additional loading*, in *Rock Mechanics and Engineering Geology Supplement 2.* 1965, Springer-Verlag KG: Vienna, Austria.

13. Wittke, W., *Felsmechanik. Springer-Verlag KG, Berlin, Germany, 1984. Also, Rock Mechanics. Springer-Verlag KG, Berlin, Germany, 1990.*

14. Chan, H. and H.H. Einestein, *Approach to complete limit equilibrium analysis for rock wedges-the method of "artificial supports".* Rock Mech Rock Eng, 1981. **14**: p. 59-86.

374

15. Mauldon, M., and Goodman, RE., *Vector analysis of keyblock rotation.* J Geotech Geoenviron Eng (ASCE), 1996. **122**: p. 976–987.

16. Tonon, F., *Generalization of Mauldon's and Goodman's vector analysis of keyblock rotations.* J Geotech Geoenviron Eng ASCE, 1998. **124**(10): p. 913-22.

17. Jiang, Q.H. and M.R. Yeung, *A model of point to face contact for three-dimensional discontinuous deformation analysis.* Rock Mech Rock Eng, 2004. **37**: p. 95-116.

18. Yeung, M.R., Q.H. Jiang, and N. Sun, *Validation of block theory and three-dimensional discontinuous deformation analysis as wedge stability analysis methods.* Int J Rock Mech Min Sci, 2003. **40**: p. 265-75.

19. Sun, N., et al., *Design method coupling block theory and three-dimensional discontinuous deformation analysis*, in *40th US rock mech symp.* 2005: Anchorage, Alaska.

20. Sofianos, A.I., P. Nomikos, and C.E. Tsoutrelis, *Stability of symmetric wedge formed in the roof of a circular tunnel: nonhydrostatic natural stress field.* Int J Rock Mech Min Sci, 1999. **36**: p. 687-691.

21. Barton, N., *Review of a new shear strength criterion for rock joints.* Engineering Geology, 1973. **7**: p. 287-332.

22. Barton, N. and V. Choubey, *The Shear Strength of Rock Joints in Theory and Practice.* Rock Mechanics, 1977. **10**: p. 1-54.

23. Tonon, F., *A Probabilistic Evaluation of Scour Threshold and Extent in Fractured Rock Plunge Pools*, in *Unsolicited proposal to the Bureau of Reclamation, Department of the Interior. Unfunded.* 2006.

24. Manso, P.A., *The influence of pool geometry and induced flow currents in rock scour by high-velocity plunging jets*, A. Schleiss, Editor. 2006, Communiction No. 25 of the Laboratory of Hydraulic Constructions, EPFL: Lausanne, Switzerland (ISSN 1661-1179).

25. Coulomb, C.A., *Essai sur une application des regles des maximis et mnimis a quelquels problemesde statique relatifs.* a la architecture. Mem. Acad. Ray. Div. Sav., 1776. **7**: p. 343-387.

26. Kumsar H., A.O., and Ulusay R., *Dynamic and static stability assessment of rock slopes against wedge failure.* Rock Mechanics and Rock Engineering, 2000. **33**(1): p. 31-51.

27. Federspiel, M.P.E.A., E.F.R. Bollaert, and A.J. Schleiss, *Respose of an intelligent block to symmetrical core jet impact*, in *IAHR.* 2009: Vancouver.

28. Schleiss, A.J. and M.P.E.A. Federspiel, *Response of an intelligent block to symmetrical core jet impact*, P. Asadollahi, Editor. 2009.

29. Martins, R., *Contribuution to the knowledge on the scour action of free jets on rocky river-beds*, in *Commision Interhnationale Des Grands Barrages, Onzieme Congres des Grands Barrages*. 1973: Madrid.

30. Bollaert, E., *Transient water pressures in joints and formation of rock scour due to high-velocity jet impact*, A. Schleiss, Editor. 2002, Communication No. 13 of the Laboratory of Hydraulic Constructions, EPFL: Lausanne, Switzerland. (ISSN 1661-1179).

31. Bollaert, E.F.R. and A.J. Schleiss, *Physically based model for evaluation of rock scour due to high-velocity jet impact.* Journal of Hydraulic Engineeirng, ASCE, 2005. **March**: p. 153-165.

32. Sun, N., Yeung, M.R., Lee, C.F., Jiang, Q.H. *Design Method Coupling Block Theory and Three-Dimensional Discontinuous Deformation Analysis.* in *Alaska Rocks 2005, 40th U. S. Rock Mechanics Symposium Rock Mechanics for Energy, Mineral and Infrastructure Development in the Northern Regions (Eds.: G. Chen, S. Huang, W. Zhou, J. Tinucci)*. June 25-29, 2004. Anchorage, Alaska.

33. Goodman, R.E., *Block theory and its applications.* Geotechnique, 1995. **45**: p. 383-432.

34. Argyris, J., *An excursion into large rotations.* Computer Methods in Applied Mechanics and Engineering, 1982. **32**: p. 85-155.

35. Hibbitt Karlsson & Sorensen, I., *ABAQUS Theory Manual Version 6.3*. 2002, Hibbitt, Karlsson & Sorensen, Inc.

36. Spring, K.W., *Euler parameters and the use of quaternion algebra in the manipulation of finite rotations: a review.* Mechanisms and Machine Theory, 1986. **21**: p. 365-373.

37. Hamilton, W.R., *Elements of Quaternions*. 3 ed. 1969, New York: Chelsea Pub. Co.

38. Truesdell, C.A., *A First Course in Rational Continuum Mechanics* 2ed. 1991, New York: Academic Press.

39. Sheck, F., *Mechanics from Newton's Laws to Deterministic Chaos*. 2004, Berlin: Springer.

40. Tonon, F., *Explicit exact formulas for the 3-D tetrahedron inertia in terms of its vertex coordinates.* Journal of Mathematics and Statistics, 2004. **1**: p. 8-11.

41. Tonon, F., *Analytical formulas for the geometric and inertia quantities of the largest removable blocks around tunnels.* International Journal for Numerical and Analytical Methods in Geomechanics 2007. **31**(11): p. 1301-1327.

42. Udwadia, F.E. and R.E. Kalaba, *Analytical Dynamics-A New Approach*. 1996, New York: Cambridge University Press.

43. Kalaba, R.E. and F.E. Udwadia, *Analytical dynamics with constraint forces that do work.* Applied Mathematics and Computation, 2001. **121**: p. 211-217.

44. Kalaba, R.E., H. Natsuyama, and F.E. Udwadia, *An extension of Guass's principle of least constraint.* International Journal of General Systems, 2004. **33**(1): p. 63-69.

45. Udwadia, F.E. and R.E. Kalaba, *Non-ideal constraints and Lagrangian dynamics.* Journal of Aerospace Engineering, 2000. **13**: p. 17-22.

46. Udwadia, F.E. and R.E. Kalaba, *What is the general form of the explicit equations of motion for constrained mechanical system?* Journal of Applied Mechanics, 2002. **69**: p. 335-339.

47. Udwadia, F.E. and R.E. Kalaba, *On the foundations of analytical dynamics.* International Journal of Nonlinear Mechanics, 2002. **37**: p. 1079-1090.

48. Udwadia, F.E. and R.E. Kalaba, *Explicit equations of motion for systems with non-ideal constraints.* Journal of Applied Mechanics, 2001. **68**: p. 462-467.

49. Udwadia, F.E., R.E. Kalaba, and P. Phohomsiri, *Mechanical systems with nonideal constraints: explicit equations without the use of generalized inverses.* Journal of Applied Mechanics, 2004. **71**(5): p. 618-621.

50. Udwadia, F.E., *New general principle of mechanics and its application to general nonideal nonholonomic systems.* Journal of Applied Mechanics, 2005. **131**(4): p. 444-450.

51. Udwadia, F.E., *On constrained motion.* Applied Mathematics and Computation, 2005. **164**: p. 313-320.

52. Guass, C.F., *Uber Ein Neues Allgemeines Grundgesetz der Mechanik.* journal fur Reine und Angewandte Mathematik, 1829. **4**: p. 232-235.

53. Whittaker, E.T., *A Treatise on the Analytical Dynamics of Particles and Rigid Bodies*, Cambridge, UK: Cambridge University Press.

54. Horn, R. and C. Johnson, *Matrix Analysis*. 1985, Cambridge, UK: Cambridge University Press.

55. Hart, R.D., P.A. Cundall, and J. Lemos, *Formulation of a three-dimensional distinct element model - Part II. Mechanical calculations for motion and interaction of a system composed of many polyhedral blocks.* International Journal of Rock Mechanics and Mining Sciences and Geomechanical Abstracts, 1988. **25**(3): p. 117-125.

56. Itasca, *3DEC User's Manual*. 1999, Minneapolis, MN: Itasca.

57. Wang, B. and V.K. Garga, *A numerical method for modelling large displacements of jointed rocks. I. Fundamentals.* Canadian Geotechnical Journal, 1993. **30**: p. 96-108.

58.   Wang, B. and V.K. Garga, *A numerical method for modelling large displacements of jointed rocks. II. Modelling of rock bolts and groundwater and applications.* Canadian Geotechnical Journal, 1993. **30**: p. 109-123.

59.   Li, G.G. and J. Vance. *A 3-D block-spring model for simulating the behavior of jointed rocks*. in *Proceeding of the 37th US Rock Mechanics Symposium*. 1999. Vail, USA: Balkema: Rotterdam.

60.   Jang, H.I. and C.I. Lee. *Development of a three-dimensional discontinuous deformation analysis technique and its application to toppling failure*. in *Proceeding of the Fifth International Conference on Analysis of Discontinuous Deformation*. 2002. Wuhan, China: Balkema: Rotterdam.

61.   Shi, G.H. *Three dimensional discontinuous deformation analysis*. in *Proceedings of the 38th US Rock Mechanics Symposium*. 2001. Washington, DC: Balkema: Rotterdam.

62.   Shi, G.H. *Application of discontinuous deformation analysis (DDA) to rock engineering*. in *International Symposium on Computational Mechanics, July 30 - August 1, 2007*. 2007. Beijing, China.

63.   Shi, G.H. *Manifold method. Discontinuous deformation analysis (DDA) and simulations of discontinuous media*. in *Proceedings of the First International Forum on Discontinuous Deformation Analysis (DDA) and Simulations of Discontinuous media*. 1996. Berkeley, CA: TSI Press: Albuquerque, NM.

64.   Riks, E., *The application of Newton's method to the problem of elastic stability.* Transactions of the ASME Journal of Applied Mechanics, 1972. **39**: p. 1060-1065.

65.   Wempner, G.A., *Discrete approximations related to nonlinear theories of solids.* International Journal of Solids and Structures, 1971. **7**: p. 1581-1599.

66.   Felippa, C., *Nonlinear Finite Element Methods*. (accessed 12/29/05), Department of Aerospace Engineering, University of Colorado at Boulder. www.colorado.edu/engineering/CAS/courses.d/NFEM.d/.

67.   Quarteromi, A., R. Sacco, and F. Saleri, *Numerical Methematics*. 2000, New York: Springer.

68.   Pars, L.A., *A Treatise on Analytical Dynamics*, London: Heinemann.

69.   Seidel, R., *A simple and fast incremental randomized algorithm for computing trapezoidal decompositions and for triangulating polygons.* Computational Geometry: Theory and Applications, 1991. **1**(1): p. 51-64.

70.   Narkhede, A. and D. Manocha, *Fast polygon triangulation based on Seidel's algorithm*, in *Graphics Gems*, V. Alan Paeth, Editor. 1995, Academic Press: New York. p. 394-397. http://www.cs.unc.edu/~dm/CODE/GEM/chapter.html.

71. O'Rourke, J., *Computational Geometry in C.* 2 ed. 1998, NY: Cambridge University Press.

72. van den Bergen, G., *Efficient collision detection of complex deformable models using AABB trees.* Journal of Graphics Tools, 1998. **2**: p. 1-13.

73. Henle, M., *A Combinatorial Introduction to Topology.* 1979, San Francisco: W.H. Freeman.

74. Haines, E., *Point in polygon strategies*, in *Graphics Gems IV*, P. Heckbert, Editor. 1994, Academic Press: New York. p. 24-46. http://www.acm.org/pubs/tog/editors/erich/ptinpoly/.

75. Franklin, R.W., *http://www.ecse.rpi.edu/Homepages/wrf/Research/Short-Notes/pnpoly.html*.

76. Gottschalk, S., M.C. Lin, and D. Manocha. *OBB-Tree: a hierarchical structure for rapid interfence detection*. in *Proceedings of ACM Conference SIGGRAPH 96* 1996. Chicago.

77. Terdiman, P., *http://www.codercorner.com/Opcode.htm*.

78. Goodman, R.E., *The deformability of joints.* ASTM Special Technical Publication, 1970. **477**: p. 174-196.

79. Bandis, S.C., A.C. Lumsden, and N. Barton, *Experimental studies of scale effects on the shear behaviour of rock joints.* 1981. **18**: p. 1-21.

80. Bandis, S.C., A.C. Lumsden, and N.R. Barton, *Fundamentals of Rock Joint Deformation.* Int. J. Rock Mech. Min. Sci. & Geomech. Abstr., 1983. **20**(6): p. 249-268.

81. Barton, N., S.C. Bandis, and K. Bakhtar, *Strength, Deformation and Conductivity Coupling of Rock Joints.* Int. J. Rock Mech. Min. Sci. & Geomech. Abstr., 1985. **22**(3): p. 121-140.

82. Chrisfield, M.A., *Non-linear Finite Element Analysis of Solids and Structure-Volume 1.* 1991, Wiley: Chichester.

83. Sagaseta, C., *Modes of instability of a rigid block on an inclined plane.* Rock Mechanics and Rock Engineering, 1986. **19**: p. 261-266.

84. Brown, E.T., *Rock characterization, testing and monitoring, ISRM Suggested Methods.* 1981, Oxford: Pergamon Press.

85. Muralha, J., *Evaluation of mechanical characteristic of rock joints under shear loads*, in *International Symposium on Rock Joints*. 1990, A.A. Balkema: Leon, Norway.

86. Swan, G. *Tribbology and the characterization of rock joints*. in *22nd US Symp. on Rock Mechanics* 1981. Boston.

87.   Plesha, M.E., *Constitutive models for rock discontinuities with dilatancy and surface degradation.* Int. J. Numerical and Analytical Methods in Geomechanics, 1987. **11**: p. 345-362.

88.   Kane, F.W. and E.C. Drumm. *A modified 'cap' model for rock joints*. in *28th US Symp. on Rock Mechanics*. 1987. Tuscon.

89.   Desai, C.S. and K.L. Fishman. *Constitutive models for rocks and discontinuities (joints)*. in *28th US Symp. on Rock Mechanics*. 1987. Tuscon.

90.   Hsu-Sun, K. *Non-linear analysis of the mechanical properties of joints and weak intercalations in rock*. in *3rd Int. Conf. on Numerical Methods in Geomechanics*. 1979. Aachen.

91.   Ladanyi, B. and G. Archambault, *Simulation of the shear behaviour of a jointed rock mass*, in *The 11th Symposium on Rock Mechanics*. 1969: Berkeley, p. 105-125.

92.   Barton, N., *Estimation of in situ shear strength from back analysis of failed rock slopes*, in *Int. Symp. Rock Mech. Rock Fracture*. 1971, Paper II-27: Nancy.

93.   Goodman, R.E. *The mechanical properties of joints*. in *Proc. 3rd Congr. ISRM, Vol. 1A, p. 127-140*. 1974. Denver.

94.   Pande, G.N. *A constitutive model of rock joints*. in *Int. Symp. on Fundamentals of Rock Joints*. 1985. Bjorkliden, Sweden.

95.   Heuze, F.E. and T.G. Barbour. *Models for jointed rock structures*. in *1st Int. Conf. on Computing in Civil Engng*. 1981. NY, ASCE.

96.   Bandis, S.C., *Mechanical properties of rock joints*, in *International Symposium on Rock Joints*. 1990, A.A. Balkema: Leon, Norway.

97.   Goodman, R.E., *Methods of Geological Engineering in Discontinuous Rock*. 1976: West, New York.

98.   Amadei, B. and S. Saeb, *Constitutive models of rock joints*, in *Internation Symposium on Rock Joints*. 1990, A.A. Balkema: Leon, Norway.

99.   Jing, L., O. Stephansson, and E. Nordlund, *Study of rock joints under cyclic loading conditions.* Rock Mech. Rock Engng., 1993. **26**(3): p. 215-232.

100.   Jing, L., *Numerical modeling of jointed rock masses by distinct element method for two and three-dimensional problems* 1990, Lulea University of Technology: Lulea, Sweden.

101.   Qiu, X., et al., *An investigation of the mechanics of rock joints-Part II: Analytical investigation* int. J. Rock. Mech. Min. Sci. & Geomech. Abstr., 1993. **30**(3): p. 271-287.

102.   Patton, F.D., *Multiple modes of shear failure in rock*, in *The 1st Congress of the International Society of Rock Mechanics*. 1966: Lisbon, p. 509-513.

103. Huang, X., et al., *An investigation of the mechanics of rock joints-Part I: Laboratory investigation.* Int. J. Rock Mech. Min. Sci. & Geomech. Abstr., 1993. **30**(3): p. 257-269.

104. Saeb, S., *A variance on Ladanyi and Archambault's shear strength criterion*, in *Rock Joints*, S. Barton, Editor. 1990, Balkema: Rotterdam. p. 701-705.

105. Gens, A., I. Carol, and E.E. Alonso, *A constitutive model for rock joints, formulation and numerical implementation.* Computers and Geotechnics, 1990. **9**: p. 3-20.

106. Desai, C.S. and K.L. Fishman, *Plasticity-based constitutive model with associated testing for joints.* Int. J. Rock Mech. Min. Sci. & Geomech. Abstr., 1991. **28**(1): p. 15-26.

107. Wang, J.G., Y. Ichikawa, and C.F. Leung, *A constitutive model for rock interfaces and joints.* Int. J. Rock Mech. Min. Sci., 2003. **40**: p. 41-53.

108. Leichnitz, W., *Mechanical properties of rock joints.* Int. J. Rock Mech. Min. Sci. & Geomech. Abstr., 1985. **22**(5): p. 313-321.

109. Kana, D.D., D.J. Fox, and S.M. Hsiung, *Interlock/friction model for dynamic shear response in natural jointed rock.* Int. J. Rock. Mech. Min. Sci. & Geomech. Abstr., 1996. **33**(4): p. 371-386.

110. Fox, D.J., D.D. Kana, and S.M. Hsiung, *Influence of interface roughness on dynamic shear behavior in jointed rock.* Int. J. Rock. Mech. Min. Sci., 1998. **35**(7): p. 923-940.

111. Samadhiya, N.K., M.N. Viladkar, and M.A. Al-Obaydi, *Three-dimensional joint/interface element for rough undulating major discontinuities in rock masses.* Int. J. Geomechanics, 2008. **8**(6): p. 327-335.

112. Pratt, H.R., A.D. Black, and B. W.F., *Friction and deformation of jointed quartz diorite*, in *Proc. 3rd Congr. ISRM, Vol IIA, p. 306-310*. 1974: Denver.

113. Bandis, S.C., *Experimental studies of scale effects on shear strength and deformation of rock joints, PhD thesis.* 1980, University of Leeds, 385 p.

114. Barton, N. and S.C. Bandis, *Effects of block size on t he shear behavior of jointed rock*, in *23rd US Symposium on Rock Mechanics*. 1982: Berkely, California.

115. Barton, N., *Modelling Rock Joint Behavior from In Situ Block Tests: Implications for Nuclear Waste Repository Design*. 1982, Office of Nuclear Waste Isolation, Columbus, OH, 96p., ONWI-308, September 1982.

116. Barton, N., *Scale effects or sampling bias?*, in *1st Int. Workshop on Scale Effects in Rock Masses*. 1990: Leon, Norway.

117. Hencher, S.R., J.P. Toy, and A.C. Lumsen, *Scale dependent shear strength of rock joints*. Scale effect in Rock Masses. 1993, Rotterdam: Balkema.

118. Hencher, S.R. and L.R. Richards, *The basic frictional resistance of sheeting joints in Hong Kong grantie.* Hong Kong Engineer, 1982. **11**(2): p. 21-25.

119. Hencher, S.R. and L.R. Richards, *Laboratory dircet shear testing of rock discontinuities.* Ground Engineering, 1989. **March 1989**: p. 24-31.

120. Cording, E.J., *Shear strength of bedding and foliation surface*, in *A speciality conference, ASCE.* 1976.

121. Cording, E.J. and J.W. Mahar, *The effect of natural goelogic discontinuities on behavior of rock in tunnels*, in *1974 Rapid Excavation and Tunneling Conference* 1974: San Francisco, CA.

122. McMahon, B.K., *Some practical considerations for the estimation of shear strength of joints and other discontinuities*, in *Int. Symp. on Fundamentals of Rock joints.* 1985: Bjorkliden, Sweden.

123. Lee, S.W., *Stability around underground openings in rock with dilative, non-persistent and multi-scale wavy joints using a discrete element method*, in *Civil Engineering* 2003, Univeristy of Illinois: Urbana-Champaign.

124. OH, J.M., *Three dimensional numerical modeling of excavation in rock with dilatant joints*, in *Civil Engineering.* 2005, University of Illinois: Urbana-Champaign. p. 232.

125. Huang, T.H. and Y.S. Doong, *Anisotropic shear strength of rock joints*, in *International Symposium on Rock Joints.* 1990, A.A. Balkema: Leon, Norway.

126. Jing, L., E. Nordlund, and O. Stephansson, *An experimental study on the anisotropy and stress-dependency of the strength and deformability of rock joints.* Int. J. Rock Mech. Min. Sci. & Geomech. Abstr., 1992. **29**(6): p. 535-542.

127. Grasselli, G. and P. Egger, *Constitutive law for the shear strength of rock joints based on three-dimensional parameters.* Int. J. Rock Mech. Min. Sci., 2003. **40**: p. 25-40.

128. Grasselli, G., J. Wirth, and P. Egger, *Quantitative three-dimensional description of a rough surface and parameter evolution with shearing.* Int. J. Rock Mech. Min. Sci., 2002. **2002**: p. 789-800.

129. Kulatilake, P.H.S.W., B.B. Panda, and N. Nghiem, *Development of new peak shear-strength criterion for anisotropic rock joints.* Journal of Engineering Mechanics, 1999. **125**(9): p. 1010-1017.

130. Kulatilake, P.H.S.W., et al., *New peak shear strength criteria for anisotropic rock joints.* Int. J. Rock. Mech. Min. Sci. & Geomech. Abstr., 1995. **32**(7): p. 673-697.

131. Byerlee, J.D., *The fracture strength and frictional strength of Weber sandstone.* Int. J. Rock Mech. Min. Sci. & Geomech. Abstr., 1975. **12**: p. 1-4.

132. Barton, N., *Rock Mechanics Review: The Shear Strength of Rock and Rock Joints.* Int. J. Rock Mech. Min. Sci. & Geomech. Abstr., 1976. **13**: p. 255-279.

133.   Jaeger, J.C., *The frictional properties of joints in rock* Geofis. Pura Appl., Milano, 1959. **43**: p. 148-158.

134.   Krsmanovic, D. and Z. Langof, *Large scale laboratory tests of the shear strength of rocky material.* Rock Mech Eng. Geol., Suppl., 1964. **1**: p. 20-30.

135.   Lane, K.S. and W.J. Heck. *Triaxial testing for strength of rock joints.* in *6th Symp. Rock Mech.* 1964. Rolla, MI, p. 98-108.

136.   Patton, F.D., *Multiple modes of shear failure in rock and related materials, Thesis.* 1966, University of Illinois.

137.   Goldstein, M., et al., *Investigation of mechanical properties of cracked rock*, in *1st Congr. Int. Soc. Rock Mech.* 1966, Vol. 1, p. 521-524: Lisbon.

138.   Newland, P.L. and B.H. Alley, *Volume changes in drained triaxial tests on granular materials.* Geotechnique, 1957. **7**: p. 17-34.

139.   Rowe, P.W., L. Barden, and I.K. Lee, *Energy components during the triaxial cell and direct shear tests.* Geotechnique, 1964. **14**: p. 247-261.

140.   Patton, F.D. and D.U. Deere. *Significant geologic factors in rock slope stability.* in *Symp. Theor. Background Plann. Open Pit Mines with spec. Ref. to Slope Stab.* 1970. Johannesburg: p. 143-151, Balkema, Cape Town.

141.   Coulson, J.H. *Shear strength of flat surfaces in rock.* in *13th Symp. on Rock Mech.* 1972. Urbana, IL: p.77-105.

142.   Hutchinson, J.N. *Field and laboratory studies of a fall in Upper Chalk cliffs at Joss Bay, Isle of Thanet. Stress-strain behaviour of soils.* in *Roscoe Mem. Symp.* 1972. Cambridge University: p. 692-706. G.T.Foulis, Henley-on-Thames.

143.   Krsmanovic, D., *Initial and residual shear strength of hard rocks.* Geotechnique, 1967. **17**: p. 145-160.

144.   Ripley, C.F. and K.L. Lee, *Sliding friction tests on sedimentary rock specimens*, in *7th Congr. Large Dams.* 1962, Vol. 4, p. 657-671: Rome.

145.   Wallace, G.B., E.J. Slebir, and F.A. Anderson. *Foundation testing for Auburn Dam.* in *11th Symp. Rock Mech.* 1970. Berkely, CA: p. 461-498.

146.   Miller, R.P., *Engineering classification and index properties for intact rock.* 1965, PhD Thesis, University of Illinois. p. 282.

147.   Jaeger, J.C., *Friction of rocks and stability of rock slopes.* Geotechnique, 1971. **21**: p. 97-134.

148.   Bieniawski, Z.T., *Estimating the strength of rock materials.* J. S. Afr. Inst. Min. Metal., 1972. **74**: p. 312-320.

149.   Hoek, E. and J.W. Bray, *Rock Slope Engineering.* 1977, London: Institution of Minning and Metallurgy.

150. Jing, L., E. Nordlund, and O. Stephansson, *A 3-D constitutive model for rock joints with anisotropic friction and stress dependency in shear stiffness.* Int. J. Rock Mech. Min. Sci. & Geomech. Abstr., 1994. **31**(2): p. 173-178.

151. Goodman, R.E., R.L. Taylor, and T.A. Brekke, *A model for the mechanics of jointed rock.* J. Soil Mech. Fdns Div., Proc. Am. Soc. Civ. Engrs., 1968. **94(SM3)**: p. 637-659.

152. Iwai, K., *Fundamental studies of fluid flow through a single fracture, PhD thesis.* 1976, University of California, Berkeley, 208 p.

153. Shehata, W.M., *PhD thesis (1971), queted in Sharp J.C. and Miani Y.N.T., in fundamental considerations on the hydrualic characteristics of joints in rock*, in *Proc. Symp. on Percolation Through Fissured Rock, Paper No. T1-F*. 1972: Stuttgart.

154. Yoshinaka, R. and T. Yamabe, *Joint stiffness and the deformation behaviour of discontinuous rock.* Int. J. Rock Mech. Min. Sci. & Geomech. Abstr., 1986. **23**(1): p. 19-28.

155. Yoshinaka, R. and H. Nishimaki, *Experimenal and numerical studies on bearing capacity of soft rock foundation.* Proc. Japan Soc. Civ. Engrs, 1980. **304**: p. 113-128.

156. Alvarez, T.A., E. Cording, and R.A. Mikhail, *Hydromechanical behavior of rock joints: A re-interpretation of published experiments*, in *35th US Symp on Rock Mechanics*. 1995, Balkema: Lake Tahoe, NV.

157. Barton, N., *A model study of rock joint deformation.* Int. J. Rock Mech. Min. Sci., 1972. **9**: p. 570-602.

158. Asadollahi, P., *Modeling Rockbolts and Shotcrete in Tunnels Excavated Through Jointed Rock and Comparison with an Empirical Method, MSc Thesis*, in *Civil Engineering*. 2004, University of Tehran: Tehran.

159. Barton, N. and K. Bakhtar, *Rock joint description and modelling for the hydrothermomechanical design of nuclear waste repositories*. 1983, Terra Tek Engineering. p. 270.

160. Kulhaway, F.H., *Stress-deformation properties of rock and rock discontinuities.* Engineering Geology, 1975. **8**: p. 327-350.

161. Wibowo, J., et al., *Effect of boundary conditions on the strength and deformability of replicas of natural fractures in welded tuff: data report*. 1993, Sandia National Laboratories: Albuquerque, New Mexico.

162. Wibowo, J., *Effect of boundary conditions and surface damage on the shear behavior of rock joints: tests and analytical predictions*, in *Civil Engineering*. 1994, University of Colorado at Boulder: Boulder, CO. p. 200.

163. Kondner, R.L., *Hyperbolic stress-strain response: cohesive soils.* J. Soil Mech. Fdns Div., Proc. Am. Soc. Civ. Engnrs, 1963. **89(SMI)**: p. 115-143.

164. Duncan, J.M. and C.Y. Chang, *Non-linear analysis of stress and strain in soils.* J. Soil Mech. Fdns. Div. Am, Soc. Civ. Engrs., 1970. **96**: p. 1629-1655.

165. Chen, E.P., *A constitutive model for jointed rock mass with orthogonal sets of joints.* Journal of Applied Mechanics, 1989. **56**: p. 25-32.

166. Zubelewicz, A., et al. *A constitutive mpdel for cyclic behavior of dilatant rock joints*. in *The second International Conference on Constitutive laws for Engineering Materials* 1987.

167. Lee, H.S., et al., *Influence of asperity degradation on the mechanical behavior of rough rock joints under cyclic shear loading.* Int. J. Rock Mech. Min. Sci., 2001. **38**: p. 967-980.

168. Homand-Etienne, F., et al., *Rock joints behaviour under cyclic direct shear tests*, in *Rock Mechanics for Industry*, K. Amadei, Scott Smealie, Editor. 1999, Balkema: Rotterdam. p. 399-406.

169. Hommand, F., T. Belem, and M. Souley, *Friction and degradation of rock joint surfaces under shear loads.* Int. J. Numerical and Analytical Methods in Geomechanics, 2001. **25**: p. 973-999.

170. Hutson, R.W. and C.H. Dowding, *Joint asperity degradation during cyclic shear.* Int. J. Rock. Mech. Min. Sci. & Geomech. Abstr., 1990. **27**(2): p. 109-119.

171. Hutson, R.W., *Preparation of duplicate rock joints and their changing dilatancy under cyclic shear*. 1987, Northwestern University: Evanston, Illinois.

172. Weissbach, G. and H.K. Kutter. *The influence of stress and strain history on the shear strength of rock joints*. in *The 3rd International Congress of Engineering Geologists*. 1978. Madrid, Spain.

173. Martin, G.R. and P.J. Millar. *Joint strength characteristics of a weathered rock*. in *The 3rd International Congress on Rock Mechanics*. 1974. Denver, Colorado.

174. Celestino, T.B. and R.E. Goodman. *Path dependency of rough joints in bi-directional shearing*. in *4th International Congress on Rock Mechanics*. 1979. Montreux, Switzerland.

175. Schneider, H.J., *The friction and deformation behavior of rock joints*, in *Rock Mech. 8*. 1976, Springer-Verlag. p. pp. 169-185.

176. Olsson, R. and N. Barton, *An Improved Model for Hydromechanical Coupling During Shearing of Rock Joints.* Int. J. Rock Mech. Min. Sci. , 2001. **38**: p. 317-329.

177. Tse, R. and D.M. Cruden, *Estimating joint roughness coefficient.* Int J Rock Mech Min Sci, 1977. **16**: p. 303-307.

178. ISRM, *Suggested methods for the quantitative description of discontinuities in rock masses.* Int. J. Rock. Mech. Min. Sci. & Geomech. Abstr., 1978. **15**: p. 319-68.

179. Saeb, S., *Effect of boundary conditions on the behavior of a dilatant rock joint.* 1989, University of Colorado at Boulder, PhD.

180. Saeb, S. and B. Amadei. *Effect of boundary conditions on the shear behavior of a dilatant rock joint.* in *30th US Symp. Rock Mech.* 1989. Morgantown, WV.

181. Saeb, S. and B. Amadei, *Modelling joint response under constant or variable normal stiffness boundary conditions.* Int. J. Rock. Mech. Min. Sci. & Geomech. Abstr., 1990. **27**: p. 213-217.

182. Saeb, S. and B. Amadei, *Modelling rock joints under shear and normal loading.* Int. J. Rock Mech. Min. Sci. & Geomech. Abstr., 1992. **29**(3): p. 267-278.

183. Kutter, H.K., *Results of Laboratory Direct Shear Tests on Four Rock Types*, in *Rock Mechanics Research Report, No. 28*. 1974, Imperical Colledge, London.

184. Huang, T.H., C.S. Chang, and C.Y. Chao, *Experimental and mathematical modeling for fracture of rock joint with regular asperities.* Engineering Fracture Mechanics, 2002. **69**: p. 1977-1996.

185. Van Sint Jan, M.L., *Shear tests of model rock joints under stiff normal loading*, in *International Symposium on Rock Joints*. 1990, A.A. Balkema: Leon, Norway.

186. Aydan, O., et al., *Studies on interfaces and discontinuities and an incremental elasto-plastic constitutive law*, in *International Symposium on Rock Joints*. 1990, A.A. Balkema: Leon, Norway.

187. Wibowo, J., et al., *Effect of boundary conditions on the strength and deformability of replicas of natural fractures in welded tuff: data analysis*. 1994, Sandia National Laboratories: Albuquerque, New Mexico.

188. Jacobsson, L., *Oskarshamn Site Investigation - Borehole KLX02 - Uniaxial compression test of intact rock*. 2004, Svensk Kärnbränslehantering AB.

189. Jacobsson, L., *Oskarshamn Site Investigation - Borehole KLX02 - Normal Loading and Shear Tests on Joints*. 2004, Svensk Kärnbränslehantering AB (SKB).

190. Jacobsson, L., *Oskarshamn Site Investigation - Borehole KLX04A - Normal Loading and Shear Tests on Joints*. 2004, Svensk Kärnbränslehantering AB (SKB).

191. Jacobsson, L., *Oskarshamn Site Investigation - Borehole KLX04A - Triaxial compression test of intact rock*. 2004, Svensk Kärnbränslehantering AB (SKB).

192. Jacobsson, L., *Oskarshamn Site Investigation - Borehole KLX06A - Triaxial compression test of intact rock*. 2005, Svensk Kärnbränslehantering AB (SKB).

193. Jacobsson, L., *Fotsmark Site Investigation - Borehole KFM05A - Triaxial compression test of intact rock*. 2005, Svensk Kärnbränslehantering AB (SKB).

194. Jacobsson, L., *Forsmark Site Investigation - Borehole KFM05A - Normal Loading and Shear Tests on Joints*. 2005, Svensk Kärnbränslehantering AB (SKB).

195. Jacobsson, L., *Fotsmark Site Investigation - Borehole KFM06A - Uniaxial compression test of intact rock*. 2005, Svensk Kärnbränslehantering AB (SKB).

196. Jacobsson, L., *Oskarshamn Site Investigation - Borehole KLX03A - Triaxial compression test of intact rock*. 2005, Svensk Kärnbränslehantering AB.

197. Jacobsson, L., *Fotsmark Site Investigation - Borehole KFM08A - Triaxial compression test of intact rock*. 2005, Svensk Kärnbränslehantering AB (SKB).

198. Jacobsson, L., *Fotsmark Site Investigation - Borehole KFM07A - Uniaxial compression test of intact rock*. 2005, Svensk Kärnbränslehantering AB (SKB).

199. Jacobsson, L., *Oskarshamn Site Investigation - Borehole KLX10 - Triaxial compression test of intact rock*. 2006, Svensk Kärnbränslehantering AB.

200. Jacobsson, L., *Oskarshamn Site Investigation - Borehole KLX12A - Triaxial compression test of intact rock*. 2006, Svensk Kärnbränslehantering AB (SKB).

201. Jacobsson, L., *Forsmark Site Investigation - Borehole KFM09A - Triaxial compression test of intact rock*. 2006, Svensk Kärnbränslehantering AB (SKB).

202. Jacobsson, L. and M. Flansbjer, *Oskarshamn Site Investigation - Borehole KLX06A - Normal Loading and Shear Tests on Joints*. 2005, Svensk Kärnbränslehantering AB (SKB).

203. Jacobsson, L. and M. Flansbjer, *Forsmark Site Investigation - Borehole KFM06A - Normal Loading and Shear Tests on Joints*. 2005, Svensk Kärnbränslehantering AB (SKB).

204. Jacobsson, L. and M. Flansbjer, *Fotsmark Site Investigation - Borehole KFM05A - Normal test with direct and indirect deformation measurement together with shear test on joints*. 2005, Svensk Kärnbränslehantering AB (SKB).

205. Jacobsson, L. and M. Flansbjer, *Oskarshamn Site Investigation - Borehole KLX03A - Normal Loading and Shear Tests on Joints*. 2005, Svensk Kärnbränslehantering AB.

206. Jacobsson, L. and M. Flansbjer, *Fotsmark Site Investigation - Borehole KFM08A - Normal load and shear test on joints*. 2005, Svensk Kärnbränslehantering AB (SKB).

207. Jacobsson, L. and M. Flansbjer, *Forsmark Site Investigation - Borehole KFM07A - Normal Loading and Shear Tests on Joints*. 2005, Svensk Kärnbränslehantering AB (SKB).

208. Jacobsson, L. and M. Flansbjer, *Oskarshamn Site Investigation - Borehole KLX10 - Normal Loading and Shear Tests on Joints*. 2006, Svensk Kärnbränslehantering AB.

209. Jacobsson, L. and M. Flansbjer, *Oskarshamn Site Investigation - Borehole KLX12A - Normal Loading and Shear Tests on Joints*. 2006, Svensk Kärnbränslehantering AB (SKB).

210. Jacobsson, L. and M. Flansbjer, *Forsmark Site Investigation - Borehole KFM09A - Normal Loading and Shear Tests on Joints*. 2006, Svensk Kärnbränslehantering AB (SKB).

211. Heok, E. and E.T. Brown, *Underground Excavation in Rock*. 1980: London Instn. Min. Metall.

212. Heok, E. and E.T. Brown, *Empirical srength criterion for rock masses.* J. Geotech. Engng Div. ASCE, 1980. **106**: p. 1013-1035.

213. Amadei, B., et al., *Applicability of existing models to predict the behavior of replicas of natural fractures of welded tuff under different boundary conditions.* Geotechnical and Geological Engineering, 1998. **16**: p. 79-128.

214. John, K.W., *Civil engineering approach to evaluate strength and deformability of regularly jointed rock*, in *Proc. 11th Symp. on Rock Mechanics, p. 68-82*. 1970.

215. Szirtes, T., *Applied dimensional analysis and modeling*. 1997: McGraw-Hill.

216. Asadollahi, P. and F. Tonon. *Anisotropy of the strength, deformability, and dilatancy of rock fractures*. in *43rd US Rock Mechanics Symposium and 4th US-Canada Rock Mechanics Symposium*. 2009. Ashville, NC.

217. Aufmuth, R.E., *A systematic determination of rock hardness by rebound hammer method.* ASTM Standard, 1973. **0409 (D 5873-00)**.

218. Cargill, J.S. and A. Shakoor, *Evaluation of empirical methods for measuring the uniaxial compressive strength.* Int J Rock Mech Min Sci, 1990. **27**: p. 495-503.

219. Dearman, W.R. and T.Y. Irfan. *Assesment of the degree of weathering in granite using petrographic and physical index tests*. in *Proc. Int. Symp. on Deterioration and Protection of Stone Monuments*. 1978. Unesco, Paris, pp. 1-35, Paper 2.3.

220. Deere, D.U. and R.P. Miller, *Engineering classification and index properties for intact rocks*, in *Tech Report, Air Force Weapons Lab*. 1966: New Mexico, No. AFNL-TR, pp. 65-116. Kirtland.

221. Ghose, A.K. and S. Chakraborti, *Empirical strength indices of Indian coals-an investigation*, in *27th US Symp. on Rock Mech.* 1986, Balkema, Rotterdam, pp. 59-61.

222. Haramy, K.Y. and M.J. DeMarco, *Use of Schmidt hammer for rock and coal testing*, in *26th US Symp. on Rock Mech.* 1985, Balkema, Rotterdam, pp. 549-555: Rapid City.

223. Kahraman, S., *Evaluation of simple methods for assessing the uniaxial compressive strength of rock.* Int J Rock Mech Min Sci, 2001. **38**: p. 981-994.

224. Katz, O., Z. Reches, and J.C. Roegiers, *Evaluation of mechanical rock properties using a Schmidt Hammer.* Int J Rock Mech Min Sci, 2000. **37**: p. 723-728.

225. Kidybinski, A., *Method of investigation, estimation and classification of roofs in the USA for the selection of suitable mechanized support for long walls*, in *Project No. 14-01-0001-1450*. 1980, Centeral Mining Institute: Katowice, Poland.

226. Sachpazis, C.I., *Correlating Schmidt hardness with compressive strength and Young's modulus of carbonate rocks.* Bull. Int. Assoc. Eng. Geol., 1990. **42**: p. 75-83.

227. Shorey, P.R., et al., *Schmidt hammer rebound data for estimation of large scale in situ coal strength.* Int J Rock Mech Min Sci Geomech Abstr, 1984. **21**: p. 39-42.

228. Singh, R.N., F.P. Hassani, and P.A.S. Elkington, *The application of strength and deformation index testing to the stability assessment of coal measures excavations*, in *24th US Symp. on Rock Mech.* 1983, Balkema, Rotterdam: Texas A and M Univ. AEG.

229. Tugrul, A. and I.H. Zarif, *Correlation of mineralogical and textural characteristics with engineering properties of selected granitic rocks from Turkey* Engineering Geology, 1999. **51**: p. 303-317.

230. Xu, S., P. Grasso, and A. Mahtab, *Use of Schmidt hammer for estimating mechanical properties of weak rock*, in *Proc. 6th International IAEG Congress, vol. 1*. 1990, Balkema, Rotterdam.

231. Yasar, E. and Y. Erdogan, *Estimation of rock physiomechanical properties using hardness methods.* Engineering Geology, 2004. **71**: p. 281-288.

232. Aydin, A. and A. Basu, *The Shmidth hammer in rock material characterization.* Engineering Geology, 2005. **81**: p. 1-14.

233. Aydin, A., *ISRM Suggested method for determination of the Schmidt hammer rebound hardness: Revised version.* Int J Rock Mech Min Sci, 2009. **46**: p. 627-634.

234. ISRM, *Suggested Methods for Determining Point Load Strength.* International Journal of Rock Mechanics & Mining Sciences, 1985. **22**(2): p. 51-60.

235. Brady, B.H.G. and E.T. Brown, *Rock Mechanics for underground mining*, ed. T. edition. 2004, Dordrecht, The Netherlands: Kluwer Academic Publishers.

236. Mirtich, B., *Fast and accurate computation of polyhedral mass properties.* Journal of graphics tools, 1995. **1**(2): p. 31-50.

237. Aliabadi, M.H., *The Boundary Element Method (Volume 2: Applications in Solids and Structures)*. Vol. 2. 2002, West Sussex, England: John Wiley & Sons, Ltd.

238. Balas, J., J. Sladek, and V. Sladek, *Stress Analysis by Boundary Element Method.* 1989, Amesterdam: Elsevier.

239. Brebbia, C.A., J.C.F. Telles, and L.C. Wrobel, *Boundary Element Techniques, Theory and Applications in Engineering* 1984, Berlin: Springer.

240. Paris, F. and J. Canas, *Boundary Element Method, Fundamentals and Applications.* 1997, Oxford: Oxford University Press.

241. Vodicka, R., V. Mantic, and F. Paris, *Note on the removal of rigid body motions in the solution of elastostatic traction boundary value problems by SGBEM.* Engineering Analysis with Boundary Elements, 2006. **30**: p. 790-798.

242. Bonnet, M., G. Maier, and C. Polizzotto, *Symmetric Galerkin boundary element method.* Appl. Mech. Rev., 1998. **15**: p. 669-704.

243. Szabo, B. and J. Babuska, *The finite element method.* 1991, New York: Wiley.

244. Zienkiewicz, O.C. and R.L. Taylor, *The finite element method, vol. 1: the basis.* 2000, Oxford: Butterworth-Heinemann.

245. Blazquez, A., et al., *On the removal of rigid body motions in the solution of elastostatic problems by direct BEM.* International Journal for Numerical Methods in Engineering, 1996. **39**: p. 4021-4038.

246. Chen, G. and J. Zhou, *Boundary Element Methods.* 1992, London: Academic Press.

247. Prossdorf, S. and V.G. Mazya, *Linear and boundary integral equations.* 1991, Berlin: Springer.

248. Costabel, M., *Principles of boundary element methods.* Comput. Phys. Reports, 1987. **6**: p. 243-274.

249. Hsiao, G. and W.L. Wendland. *On a boundary integral method for some exterior problems in elasticity* in *Tbiliski University* 1985: Tbiliski University Press.

250. Karrila, S.J. and S. Kim, *Integral equations of the second kind for Stokes flow: direct solution for physical variables and removal of inherent accuracy limitations.* Chem Eng Comm, 1989. **82**: p. 123-61.

251. Greenbaum, A., L. Greengard, and G.B. McFadden, *Laplace's equation and the Dirichlet-Neumann map in multiply connected domains.* J. Comput. Phys. , 1993. **105**: p. 267-278.

252. Heise, U., *Removal of zero eigenvalues of integral operators in elastostatic boundary value problems.* Acta Mech., 1981. **41**: p. 41-61.

253. Lutz, E., W. Ye, and S. Mukherjee, *Elimination of rigid body modes from discritized boundary integral equations.* Int. J. Solids Struct., 1998. **35**: p. 4427-36.

254. Phan-Thien, N. and D. Tullock, *Compeleted double layer boundary element method in elasticity.* J Mech Phys Solids, 1993. **41**: p. 1067-86.

255. Power, H. and G. Miranda, *Second kind integral equation formulation of Stokes' flows past a particle of arbitrary shape.* SIAM J Appl Math, 1987. **47**: p. 689-98.

256. Ugodchikov, A.G. and N.M. Khutorianskii, *Boundary Element Method in the Mechanics of the Deformable Solid Body (in Russian).* 1986, Kazan: Kazan Univeristy Publishers.

257. Vable, M., *Importance and use of rigid body mode in boundary element method.* International Journal for Numerical Methods in Engineering, 1990. **29**: p. 453-72.

258. Chen, G. and S. Sun, *Augmenting a Fredholm operator of zero index to achieve invertibility for elliptic boundary value problems.* J. Math. Anal. Appl., 1993. **176**: p. 24-48.

259. Telles, J.C.F. and F.A. De Paula, *Boundary elements with equilibrium satisfaction-a consistent formulation for potential and elastostatic problems.* International Journal for Numerical Methods in Engineering, 1991. **32**: p. 609-21.

260. Cowper, G.R., *Gaussian Quadrature Formulas for Triangles.* International Journal of Numerical Methods in Engineering 1973. **7**: p. 405-408.

261. Lyness, J.N. and D. Jespersen, *Moderate Degree Symmetric Gaussian Quadrature Rules for the Triangle.* International Journal for Numerical Methods in Engineering, 1985. **21**: p. 1129-1148.

262. Dunavant, D.A., *High Degree Efficient Symmetrical Gaussian Quadrature Rules for the Triangle.* International Journal for Numerical Methods in Engineering, 1985. **21**: p. 1129-1148.

263. Hammer, P.C. and A.H. Stroud, *Numerical Integration over Simplexes and Cones.* Mathematical Tables and other Aides to Computation, 1956. **X**(54): p. 130-139.

264. Li, H. and G. Han, *A new method for evaluating singular integrals in stress analysis of solids by the direct Boundary Element Method.* International Journal for Numerical Methods in Engineering, 1985. **21**: p. 2071-2098.

265. Rump, S., *Inversion of extremely ill-conditioned matrices in floating-point.* JJIAM, 2008. **Submitted for publication**.

266. Sadd, M.H., *Elasticity : Theory, Applications, and Numerics* 2004, Amsterdam ; Boston: Elsevier Butterworth Heinemann.

267. Vandebril, R., G. Golub, and M. Van Barel, *On solving the definite tridiagonal symmetric generalized eigenvalue problem*, in *Celestijnenlaan 200A - B-3001 Heverlee*. 2007, Katholieke Universiteit Leuven, Department of Computer Science: Belgium.

268. Golub, G.H. and C.F. Van Loan, *Matrix Computations*, ed. 3. 1996: The Johns Hopkins University Press.

269. Moreau, J.P. *Module feigen0.f90 (http://pagesperso-orange.fr/jean-pierre.moreau/Fortran/feigen0_f90.txt)*. (accessed 02/2009) [cited.

270. Engeln-Mueller, G. and F. Uhlig, *Numerical Algorithms with C*. 1996: Springer-Verlag.

271. Peters and Wilkinson, *Eigenvectors of real and complex matrices by LR and QR triangularisations*. Num. Math., 1970. **16**: p. 184-204.

272. Martin and Wilkinson, *Similarity reductions of a general matrix to Hessenberg form*. Num. Math., 1968. **12**: p. 339-358.

273. Parlett and Reinsch, *Balancing a matrix for calculations of eigenvalues and eigenvectors*. Num. Math., 1969. **13**: p. 293-304.

274. Rego, J. *Subroutine to find the inverse of a square matrix (http://www.dreamincode.net/code/snippet1296.htm)*. [cited 02/2009].

275. McFarland. *Help center for mathematical students (http://math.uww.edu/~mcfarlat/inverse.htm)*. [cited 02/2009].

276. Sniedovich, M. *Matrix Inverse (http://www.tutor.ms.unimelb.edu.au/matrix/matrix_inverse.html)*. [cited 02/2009].

277. Itasca, *UDEC (Universal Distinct Element Code) Special Features*. 2000, Minneapolis, MN: Itasca.

278. Guangqi, C., *Numerical modelling of rock fall using extended DDA*. Chinese Journal of Rock Mechanics and Engineering, 2003. **22**(16): p. 926-931.

279. Shi, G.H., *Discontinuous deformation analysis-a new model for the statics and dynamics of block systems*, in *Civil Engineering*. 1988, University of California: Berkeley.

280. Ke, T.C., *Simulated testing of two-dimensional heterogeneous and discontinuous rock masses using discontinuous deformation analysis*, in *Civil Engineering*. 1993, University of California: Berkeley.

281. Ke, T.C. *Modification of DDA with respect to rigid body rotation*. in *the First International Conference on Analysis of Discontinuous Deformation*. 1995. Chungli, Taiwan, ROC, 260-273.

282. Ke, T.C. *The issue of rigid body rotation in DDA*. in *he First International Forum on Discontinuous Deformation Analysis (DDA) and Simulations of Discontinuous Media*. 1996. Berkeley, CA: TSI Press: Albuquerque, NM; 318–325.

283. MacLaughlin, M.M. and N. Sitar. *Rigid body rotations in DDA*. in *the First International Forum on Discontinuous Deformation Analysis (DDA) and*

Simulations of Discontinuous Media. 1996. Berkeley, CA: TSI Press: Albuquerque, NM, 1996; 620–636.

284. Cheng, Y.M. and Y.H. Zhang, *Rigid body rotation and block internal discretization in DDA analysis.* International Journal for Numerical and Analytical Methods in Geomechanics, 2000. **24**: p. 567-578.

285. MacLaughlin, M.M. and D.M. Doolin, *Review of validation of the discontinuous deformation analysis (DDA) method.* Int. J. Numer. Anal. Meth. Geomech., 2006. **30**: p. 271-305.

286. Amadei, B., *Rock anisotropy and theory of stress measurements*. 1983, Germany: Springer-Verlag Berlin Heidelberg.

287. Amadei, B. and R.E. Goodman. *Formulation of complete plane strain for regularly jointed rocks*. in *Proc. 222d Symp. on Rock. Mech. (M.I.T.)*. 1981.

288. Lekhnitskii, S.G., *Theory of elasticity of an anisotropic elastic body*. 1963, San Francisco: Holden Day, Inc.

289. Milne-Thomson, L.M., *Antiplane elastic systems*. 1962, Berlin: Springer Verlag.

290. Brady, B.H.G. and J.W. Bray, *The boundary element method for determining stresses and displacements around long openings in a triaxial stress field.* Int J Rock Mech Min Sci, 1978. **15**(1): p. 21-28.

291. Panet, M. and A. Guenot, *Analysis of convergence behind the face of a tunnel*, in *Int Symposium Tunneling 1982*. 1982: Brington, 249–268.

292. Babuska, J. and T. Oden, *Verification and validation in computational engineering and science: basic concepts.* Comp Meth Appl Mech Eng, 2004. **193**: p. 4057-66.

293. Easterling, R.C., *Statistical foundations for model validation: two papers*, in *Sandia Nat Lab rep SAND2003-0287*. 2003: Albuquerque, NM.

294. Hills, R.G. and I.H. Leslie, *Statistical validation of engineering and scientific models: validation experiments to application*, in *Sandia Nat Lab rep SAND2003-0706*. 2003: Albuquerque, NM.

295. Oberkampf, W.L. and T.G. Trucano, *Verification and validation in computational fluid dynamics*, in *Sandia Nat Lab rep SAND2002-0529*. 2002: Albuquerque, NM.

296. Oberkampf, W.L., T.G. Trucano, and C. Hirsch, *Verification, validation, and predictive capability in computational engineering and physics*, in *Sandia Nat Lab Rep SAND2003-3769*. 2003: Albuquerque, NM.

297. Trucano, T.G., M. Pilch, and W.L. Oberkampf, *General concepts for experimental validation of AISC code applications*, in *Sandia Nat Lab rep SAND2002-0341*. 2002: Albequerque, NM.

298. Tonon, F. and P. Asadollahi, *Validation of general single rock block stability analysis (BS3D) for wedge failure.* International Journal of Rock Mechanics and Mining Sciences, 2008. **45**: p. 627-637.

299. Bandis, S.C., N. Barton, and M. Christianson. *Application of a New Numerical Model of Joint Behaviour to Rock Mechanics Problems*. in *International Symposium on Fundamentals of Rock Joints*. 1985. Bjorkliden.

300. Rosso, R.S., *A comparison of joint stiffness measurements in direct shear triaxial compression and In situ.* Int. J. Rock Mech. Min. Sci. & Geomech. Abstr., 1976. **13**: p. 167-172.

301. Asadollahi, P. and F. Tonon. *Validation of single rock block stability analysis*. in *42nd US Rock Mechanics Symposium*. 2008. San Fransisco, CA.

302. Liu, J., X. Kong, and G. Lin, *Formulations of the three dimesional discontinuous diformation analysis method.* Acta Mechanica Sinica, 2001. **20**: p. 270-282.

303. Wang, J., L. G., and J. Liu, *Static and dynamic stability analysis using 3D DDA with incision body scheme.* Earthquake Engineering and Engineering Vibration, 2006. **5**: p. 273-283.

304. Hatzor, Y.H. and A. Feintuch, *The validity of dynamic block displacement prediction using DDA.* Int J Rock Mech Min Sci. , 2001. **38**: p. 599-606.

305. Hatzor, Y.H., A.A. Arzi, and Y. Zaslavsky, *Dynamic stability analysis of jointed rock slopes using the DDA method: King Herod's Palace, Masada, Israel.* . Int J Rock Mech Min Sci., 2004. **41**: p. 813-832.

306. Bray, J.W., *Unpublished note*. 1977, Imperial College: London.

307. Sofianos, A.I., *Stability of wedges in tunnel roofs.* int J Rock Mech Min Sci Geomech Abstr, 1986. **23**(2): p. 119-130.

308. Elsworth, D., *Wedge stability in the roof of a circular tunnel: plane strain condition* Int J Rock Mech Min Sci Geomech Abstr, 1986. **23**(2): p. 177-181.

309. Nomikos, P., A.I. Sofianos, and C.E. Tsoutrelis, *Symmetric wedge in the roof of a tunnel excavated in an inclined stress field.* Int J Rock Mech Min Sci, 2002. **39**: p. 59-67.

310. Hudson, J.A. and J.P. Harrison, *Engineering Rock Mechanics: An Introduction to the Principles*, ed. t. Edition. 2005, Amesterdam, The Nederlands: Elsevire Ltd.

311. Rocscience, *Unwedge Theory Manual – Factor of Safety Calculations (http://www.rocscience.com/downloads/unwedge/unwedge_theory.pdf)*. Accessed online in Feb. 2009.

312. Yow, J.L. and R.E. Goodman, *A ground reaction curve based upon block theory.* Rock Mechanics and Rock Engineering, 1987. **20**: p. 167-190.

313. Muskhelishvili, N.I., *Some basic problems of the mathematical theory of elasticity*, ed. 4. 1963: J.R.M. Radok. Noodhof: Gronigen.

314. Timoshenko, S.P. and J.N. Goodier, *Theory of elasticity*, ed. 3. 1970, Wiley: New York.

315. Poulos, H.G. and E.H. Davis, *Elastic solutions for soil and rock mechanics*. 1974: Wiley: New York.

316. Yow, J.L., *Field investigation of keyblock stability*. 1985, Lawrence Livermore National Laboratory Report UCRL 53632.

317. Rocscience, *Field stress tutorial (http://www.rocsience.com/downloads/unwedge/webhelp/unwedge.htm)*. Accessed online in Feb. 2009.

318. Holmes, P. and J.E. Marsden, *Bifurcation to divergence and flutter in flow-induced oscillations: an infinite dimensional analysis. Automatica*. J. IFAC, 1978. **14**: p. 367-384.

319. Iudovich, V.I., *The onset of auto-oscillations in a fluid*. J. Applied Math.Mech, 1971. **35**: p. 587-603.

320. Kounadis, A.N., *The existence of regions of divergence instability for nonconservative systems under follower forces*. Int. J. of Solids and Structures, 1983. **19**: p. 725-733.

321. Kounadis, A.N., *On the failure of static stability analyses of nonconservative systems in regions of divergence instability*. Int. J. of Solids and Structures, 1994. **31**: p. 2099-2120.

322. Fiorotto, V. and A. Rinaldo, *Turbulent pressure fluctuations under hyraulic jumps*. J. Hydraulic Research. **30**: p. 499-519.

323. Hoek, E. and E.T. Brown, *Underground Excavation in Rock*. 1980: London Instn. Min. Metall.

324. Annandale, G.W., *Erodibility*. Journal of Hydraulic Research, 1995. **33**(4): p. 471-494.

325. Annandale, G.W., *Scour Technology - Mechanics and Engineering Practice*. 2006, New York, NY: McGraw Hill.

326. Goodman, R.E. and C. Powell, *Investigations of blocks in foundations and abutments of concrete dams*. J. Geotech. and Geoenvir. Engrg,, 2003. **129**: p. 105-116.

327. USBR, *Engineering Geology Field Manual*, in *Engineering Geology, Technical Service Center, Bureau of Reclamation, U.S. Department of Interior, Denver, CO., http://www.usbr.gov/pmts/geology/*. 2006.

328. BS5930, *Code of Practice for Site Investigations*. British Standards Institution (BSI). 1981, London.

329. Ervine, D.A., H.T. Falvey, and W. Withers, *Pressure fluctuations in plunge pool floors*. J. Hydraulic Research, 1997. **35**: p. 257-279.

330. Franzetti, V. and M.G. Tanda, *Getti deviati a simmetria assiale*, in *Report of Istituto di Idraulica e Costruzioni Idrauliche, Politecnico di Milano*. 1984.

331. Franzetti, V. and M.G. Tanda. *Analysis of turbulent pressure fluctuation caused by a circular impinging jet*. in *International Symposium on New Technology in Model Testing in Hydraulic Research*. 1987. India, pp. 85-91.

332. Xu-Duo-Ming. *Pressao no fundo de um canal devido ao choque de um jacto plano*. in *e suas caracteristicas de fluctuacao,Translation from chinese by J.A. Pinto de Campos*. 1983. Lisboa.

333. Tao, C.G., L. JiYong, and L. Xiangrong. *Efeito do impacto, no leito do rio, da lamina descarregada sobre uma barragem-abobada*. in *Laboratorio Nacianal de Engenharia Civil, Translation from Chinese by de Campose, J.A.P.* 1985. Lisboa.

334. Lopardo, R.A. *Stilling basin pressure fluctuations*. in *Conference Proceedings, Model-prototype Correlation of Hydraulic Structures*. 1988. P.Burgi, pp. 56-73.

335. Armengou, J., *Disipacion de energia hidraulica e pie de presa en presas boveda*. 1991, Universitat Politechnica de Catalunya: Barcelona.

336. May, R.W.P. and I.R. Willoughby, *Impact pressures in plunge pool basins due to vertical falling jets*, R.S. 242, Editor. 1991: HR Wallingford, UK.

337. Puertas, J. and J. Dolz, *Criterios hidraulicos para el diseno de cuencos de disipacion de energia en presas boveda con vertido libre por coronacion*. 1994, University of Catalunya: Barcelona.

338. Hartung, F. and E. Hausler. *Scours, stilling basins and downstream protection under free overfall jets at dams*. in *Proceedings of the 11th Congress on Large Dams*. 1973. Madrid, pp. 39-56.

339. Beltaos, S. and N. Rajaratnam, *Plane turbulent impinging jets*. Journal of Hydraulic Research, IAHR, 1973. **11**(1): p. 29-59.

340. Cola, R. *Energy dissipation of a high-velocity vertical jet entering a basin*. in *Proceedings of the 11th Congress of the I.A.H.R.* 1965. Leningrad.

341. Bollaert, E. and A. Schleiss, *Scour of rock due to the impact of plunging high velocity jets. Part I: A state-of-the-art review*. Journal of Hydraulic research, 2003. **41**(5): p. 451-464.

342. Bollaert, E. and A. Schleiss, *Scour of rock due to the impact of plunging high velocity jets. Part II: Experimental results of dynamic pressures at pool bottoms and in one- and two-dimensional closed-end rock joints*. Journal of Hydraulic Research, 2003. **41**(5): p. 465-480.

343. Horeni, P., *Desintegration of a Free Jet of Water in Air*. 1956, Sesit 93, Praha, Pokbaba.

344. Ervine, D.A. and H.T. Falvey, *Behavior of Turbulent Jets in the Atmosphere and in Plunge Pools*. Proceedings of the Institution of Civil Engineers, 1987. **83**(2): p. 295-314.

345. Ervine, D.A., *The entrainment of air in water*. Water Power & Dam Construction, 1976. **December**: p. 27-30.

346. Ervine, D.A. and E.M. Elsawy. *Model scale effect in air-regulated siphon spillways*. in *BHRA Symposium on Siphons and Siphon Spillways*. 1975. London, May, Paper B2.

347. Melo, J.F. *Reduction of plunge pool floor dynamic pressure due to jet air entrainment*. in *Rock Scour due to falling High-velocity Jets*. 2002. Lausanne, Switzerland.

348. Ervine, D.A., *Air Entrainment in Hydraulic Structures: A Review* Proceedings of the Institution of Civil Engineers, Wat., Marit. & Energy, 1998. **130**: p. 142-153.

349. Mason, P.J. and K. Arumugam, *Free Jet Scour below Dams and Flip Buckets*. Journal of Hydraulic Engineeirng, 1985. **111**(2): p. 220-235.

350. Castillo, L.G., *Personal Communication*. 2004.

351. Liu, P.Q., J.R. Dong, and C. Yu, *Experimental investigation o fluctuating uplift on rock blocks at the bottom of the scour pool downstream of Three-Gorges spillway*. J. Hydraulic Research, 1998. **36**: p. 55-68.

352. Fiorotto, V. and P. Salandin, *Design of anchored slabs in spillway stilling basins*. Journal of Hydraulic Engineeirng, 2000. **126**: p. 502-512.

353. Bellin, A. and V. Fiorotto, *Direct dynamic force measurement on slabs in spillway stilling basins*. ASCE J. Hydrualic Eng., 1995. **121**: p. 686-693.

354. Melo, J.F., A.N. Pinheiro, and C.M. Ramos, *Forces on plunge pool slabs: influence of joints location and width*. ASCE J. Hydrualic Eng., 2006. **131**: p. 49-60.

355. Hausler, E., *Dynamische Wasserdrucke auf Tosbeckenplatten infolge freier Uberfallstrhlen bei Talsperren*. Wasserwirtschaft, 1966. **2**: p. 42-49.

356. Yuditski, G.A., *Actual pressure on the channel bottom below ski-jump spillways*. Izvestiya Vsesoyuznogo Nauchno-Issledovatel-Skogo Instuta Gidrotekhiki, 1967. **67**: p. 231-240.

357. Yuditski, G.A., *Experimental Prediction of Rock Bed Scour Below a Ski-jump Spillway Dam*, ed. I.P.f.S.T.I. Translated from Russian. 1971.

358. Ramos, C.M. *Energy dissipation on free jet spillways. Bases for its study in hydraulic models.* in *Proc. Transactions of the Int. Symp. on the Layout of Dams in Narrow Gorges, Vol. 1, ICOLD.* 1982. Rio de Janeiro, Brazil, 263-268.

359. Cunha, L.V. and A.C. Lencastre. *La dissipation de l'energie dans un evacuateur en saut de ski.* in *Observation de l'erosion, Lisboa, LNEX, 1966 (Technical Paper no. 288).* 1966.

360. Kamenev, I.A., *Excavacao de um leito por um jacto em queda livre (2)*, in *LNEC, Transl. no. 474 from Trudy gidravlicheskoi laboratorii, no. 11.* 1965.

361. Bhatia, R., *Positive definite matrices*. Princeton Series in Applied Mathematics. 2007.

362. Greenwood, D.T., *Principles of Dynamics*. 1988, Englewood Cliffs, NJ: Prentice-Hall.

363. Meriam, J.L. and L.G. Kraige, *Engineering Mechanics Volume 2: Dynamics*. 1986, New York: John Wiley Sons.

364. Tenenbaum, R.A., *Fundamental of Applied Dynamics*. 2004: Springer.

VITA

Pooyan Asadollahi was born on April 22, 1980 in Tehran, Iran, to Maryam Tavoosian and Mohammad Asadollahi. Pooyan attended Alborz High School, Tehran, Iran, and graduated in June 1997. In the same year, he entered the University of Tehran for his undergraduate studies. He graduated with a Bachelor of Science degree in Civil Engineering in June 2002. Pooyan remained at the University of Tehran to pursue a graduate degree in Civil Engineering with a focus on Soil Mechanics and Foundation Engineering. He received a Master of Science degree in December 2004. His master thesis was entitles "*Modeling Rockbolts and Shotcrete in Tunnels Excavated Through Jointed Rock and Comparison with an Empirical Method*". Pooyan was employed as a Geotechnical Engineer at Mahab Ghodss Consulting Engineering Company from October 2003 to June 2006. In Fall 2006, he entered the PhD program of the Department of Civil Engineering (the Geotechnical Engineering Group) of the University of Texas at Austin. Pooyan has published 8 papers in international conferences and 4 technical articles in international journals

Permanent Address: 107 Dastour St., Soheil St., Shariati Av., Tehran, 193144855, Iran

This manuscript was typed by the author.